(NASA-SP-416)   AIRCRAFT SAFETY AND OPERATING
PROBLEMS (NASA)   644 p HC A99/MF A01
                                          CSCL 01C

N77-18081
THRU
N77-18116
Unclas
H1/03   17162

PREFACE

The Proceedings of the NASA Aircraft Safety and Operating
Problems Conference held at Langley Research Center, Hampton,
Virginia, on October 18-20, 1976, are reported in this NASA
Special Publication.

The purpose of this conference was to discuss the results
of research of the National Aeronautics and Space Administration
in the field of aircraft safety and operating problems. The
program components include the following:

    (1) Terminal Area Operations
    (2) Flight Dynamics and Control
    (3) Ground Operations
    (4) Atmospheric Environment
    (5) Structures and Materials
    (6) Powerplant
    (7) Noise
    (8) Human Factors

Contributions to this compilation were made by representatives
from NASA Headquarters; NASA Ames, Langley, and Lewis Research
Centers; NASA Dryden Flight Research Center; NASA Johnson Space
Center; NASA Marshall Space Flight Center; NASA Wallops Flight
Center; the Federal Aviation Administration; The George Washington
University, Joint Institute for Advancement of Flight Sciences;
University of Virginia; University of Kansas; General Electric
Company; and Beech Aircraft Corporation.

CONTENTS

INTRODUCTORY REMARKS

Kenneth E. Hodge
NASA Headquarters

I'm pleased to be here with you this morning to welcome you all to the Conference on behalf of NASA Headquarters. Your participation in this Conference is indicative, I believe, of both your interest and the interest of your organizations in NASA research programs which address aircraft safety and operating problems.

During the next several days you will hear reports on results of a number of recently completed programs and status reports on still other programs now underway. The papers cover a wide range of topics - from safety in flight to safety on the runway, from problems related to the cockpit environment to problems related to the atmospheric environment, and from problems induced by one aircraft on another to problems induced by the aircraft on airport neighbors. Obviously the presentations will not provide solutions to all these problems. We are hopeful that the ideas and knowledge reflected by the presentations do help with some of your problems and provide the basis to improve the usefulness of air vehicles to some degree. Many times, it seems, our problems are not completely eliminated or solved. Today's so-called solutions are merely acceptable for this period in history. New vehicles, flight regimes, modes of operation, and levels of public concern place continuing demands both for more refined solutions to old or lingering problems and for fresh solutions to brand new problems: problems often spawned by the use of new vehicles in our air transporation system. And of course we must recognize problems which could occur as a consequence of extending aircraft operating life-times well beyond initial design objectives as appears to be the tendency under the present economic environment.

As aviation's role in public transportation has become firmly established, more and more attention has been devoted to ensuring the reliability, and therefore the safety, of flight. Safety is difficult to define, but can be thought of as the absence or control of factors which can cause injury, loss of life, or loss of property. Survival and expansion of air travel demand the lowest operational risk commensurate with economic well-being of the air transportation system. Consequently, the field of aviation safety and operating problems provides a continuing challenge to raise the levels of our knowledge and understanding of the aircraft operating environment.

A difficult and formidable task confronts the research planner or headquarters manager who is called upon to not only respond to identified problems but to anticipate where the next serious problem area will be. Funding for the problems of tomorrow is difficult to justify, and impatience for quick, low-cost solutions to difficult problems is a natural reaction. Despite the difficulty of the task, working in the safety research and technology area is exciting and provides the satisfaction of contributing towards a most worthwhile goal: reduction of suffering, misery, and loss.

Some research efforts have just recently been initiated; too new for even a status report at this time. For example, an NASA Twin Otter has recently been modified with a research type cross-wind landing gear to enable as to investigate trigear cross-wind landing problems and methods of extending cross-wind limits for landing of STOL aircraft.

Wake vortex minimization is an area of high-priority research in NASA; a survey paper is included in this Conference. We have very recently been asked by FAA to examine a number of questions which must be answered before operational application of certain promising minimization concepts would be proposed. In addition to quantifying benefits and costs, we are presently working with FAA on details of additional ground tests and flight research with the most promising concept to assess possible impacts on noise, approach and landing performance, fuel consumption, structural loads, and other. This program is a coordinated effort involving the Ames and Langley Research Centers and Dryden Flight Research Center. I believe this Conference to be a multifaceted program that is representative of NASA's research efforts in the aviation safety and aircraft operating problems areas. We hope you will enjoy the Conference and benefit from the technical papers presented. We would welcome comments on how the Conference met your expectations and needs.

This Conference is historically under the aegis of the NASA Research and Technology Advisory Council, Panel on Aviation Safety and Operating Systems. As many of you know, our Panel Chairman since 1969, Frank Kolk of American Airlines, passed away last summer. Frank would have liked to have been here and would want us to carry on in the tradition of our prior Conferences, and so we will!

REVIEW OF OPERATIONAL ASPECTS OF INITIAL EXPERIMENTS UTILIZING

THE U.S. MLS

Thomas M. Walsh, Samuel A. Morello, and John P. Reeder
NASA Langley Research Center

SUMMARY

An exercise to support the Federal Aviation Administration in demonstrating the U.S. candidate for an international microwave landing system (MLS) was satisfactorily accomplished at the National Aviation Facilities Experimental Center in May 1976. It was demonstrated that in automatic three-dimensional (3-D) flight, the volumetric signal coverage of the MLS can be exploited to enable a commercial carrier class airplane to perform complex curved, descending paths with precision turns into short final approaches terminating in landing and roll-out, even when subjected to strong and gusty tail- and cross-wind components and severe wind shear. The avionics technique used in the demonstration for processing and utilization of the MLS signals is illustrative of application to future system design.

Of equal importance were the advanced displays that allowed the flight crew and observers to follow the flight situation and aircraft tracking performance very accurately from the aft flight deck of the Terminal Configured Vehicle Program Boeing 737 research airplane without outside reference. Elements of these displays enabled the pilots to proceed after take-off toward the initial way point of the flight profiles, where automatic 3-D flight was initiated. During the initial phase of automatic 3-D navigation, elements of the displays were driven by conventional navigation signals. Upon entering the MLS coverage region, MLS signals were used to drive the display elements for monitoring of the automatic control system performance during transition from conventional RNAV to MLS RNAV; curved, descending flight; flare; touch-down; and roll-out. Of greater importance, particularly with respect to implications for future systems, the displays enabled the pilots, when traffic situations or their interruptions occurred, to control manually for diversionary maneuvers. The situation presented by the displays was clear enough to allow the pilots to perform the appropriate maneuvers readily in the RNAV environment to reenter the desired profiles with precision. Such capability is lacking today in commercial operations and will be required for acceptance of complex, close-in maneuvers in the future. In addition, the pilots flew several manually controlled approaches using the same display formats that had been used for monitoring purposes during the automatic flights. Data for these manual approaches indicate that the performance compares favorably with the performance achieved under automatic flight control.

3

The growing congestion associated with the rapid expansion of air travel and the noise impact of the jet fleet on airport neighbors have led to technology developments in ground and airborne electronic systems and in noise suppression. In this area, the Department of Transportation (DOT) and the Federal Aviation Administration (FAA) have undertaken an effort to upgrade the air traffic control system. This revised system, known as the Upgraded Third-Generation Air Traffic Control System (UG3RD ATCS), has the following features (ref. 1):

(1) Intermittent positive control
(2) Discrete address beacon system
(3) Area navigation
(4) Microwave landing system
(5) Upgraded air traffic control automation
(6) Airport surface traffic control
(7) Wake-vortex avoidance system
(8) Aeronautical satellites for transoceanic flight
(9) Automation of flight service stations

It is recognized that additional development and evaluation activities should make maximum use of the potential of these system developments. In formulating the joint DOT-NASA Civil Aviation Research and Development Policy Study Report (ref. 2, p. 6-28) the question of U.S. Government conduct or support of demonstration programs in civil aviation is introduced with:

"Demonstration programs are needed to prove out new systems and technologies, to assess market potentials, or to remove major institutional constraints temporarily. Demonstration programs are experiments designed to embrace new concepts, procedures, regulations, or the blending of new technologies into existing systems. These programs should collect information and required data in a real-world environment involving the ultimate users of the system. . . ."

In recognition of this need, the NASA Langley Research Center has implemented the Terminal Configured Vehicle (TCV) Program (ref. 3). Its goal is to identify, evaluate, and demonstrate aircraft and flight management technology that will improve the efficiency and acceptability of conventional aircraft in terminal-area operations. The reason for emphasis on terminal-area operations (fig. 1) is that this region is recognized as the system bottleneck as well as the major area of possible unfavorable impact with the community environment.

The TCV Program is conducting analytical, simulation, and flight test research which will support improvements in (1) terminal-area capacity and efficiency, (2) approach and landing capability in adverse weather, and (3) operating procedures to reduce noise impact. In this research, major emphasis is being placed on the development of advanced concepts for applications to avionics and displays for aircraft operations in the UG3RD and post UG3RD ATCS's. Particular emphasis is being placed on operations in an MLS environment. One example of this effort is the participation of NASA through its TCV Program with the FAA in the demonstration of the U.S. national microwave landing system to the

4

All Weather Operations Panel of the International Civil Aviation Organization (ICAO). This demonstration took place at the FAA's National Aviation Facilities Experimental Center (NAFEC) in May 1976 (ref. 4). During this demonstration the MLS was utilized to provide the TCV Boeing 737 research airplane with guidance for automatic control during transition from conventional RNAV to MLS RNAV in curved, descending flight; flare; touchdown; and roll-out. The purpose of this paper is to describe some of the operational aspects of the demonstration. Flight profiles, system configuration, displays, and operating procedures used in the demonstration are described, and preliminary results of flight data analysis are discussed. Recent experiences with manually controlled flight in the NAFEC MLS environment are also discussed.

ABBREVIATIONS AND SYMBOLS

AFD   aft flight deck

ATC   air traffic control

AWOP   All Weather Operations Panel

Az   azimuth angle from MLS azimuth beam

C-band   5000-MHz frequency signal

CWS   control wheel steering

DME   distance measuring equipment

DME/DME   dual DME navigation mode

DOT   Department of Transportation

EADI   electronic attitude director indicator

EHSI   electronic horizontal situation indicator

El   elevation angle

EL1   elevation angle from MLS glide slope beam

EL2   elevation angle from MLS flare beam

FAA   Federal Aviation Administration

GCA   Ground Controlled Approach

ICAO   International Civil Aviation Organization

IDD   inertially smoothed DME/DME navigation mode

ILS   instrument landing system

INS   inertial platform

K_u 15,000-MHz frequency signal

LAT   latitude

LAT_{ORIGIN} latitude of origin of MLS runway-referenced coordinates

LONG   longitude

$LONG_{ORIGIN}$ longitude of origin of MLS runway-referenced coordinates

MLS   microwave landing system

MLS RNAV   navigation in the MLS environment

NAFEC   National Aviation Facilities Experimental Center

NASA   National Aeronautics and Space Administration

NCDU   navigation control/display unit

R   range measurement

RNAV   area navigation

RSFS   Research Support Flight System

TCV   Terminal Configured Vehicle

UG3RD ATCS   Upgraded Third-Generation Air Traffic Control System

VFR   visual flight rules

V_E east velocity

V_N north velocity

$\dot{h}$ altitude rate or sink rate

h_{msl} altitude above mean sea level

h_{td} altitude above desired touchdown point

x,y,z   aircraft position in runway-referenced coordinates

$\dot{y}$ cross runway velocity

$\ddot{y}$ cross runway acceleration

6

ΔLAT	latitude deviation of aircraft from origin of runway-referenced coordinate system
ΔLONG	longitude deviation of aircraft from origin of runway-referenced coordinate system
β	angle of glide-path deviation
η	angle of lateral-path deviation
θ	aircraft pitch angle
ϕ	aircraft roll angle
ψ	aircraft yaw angle
3-D	three-dimensional navigation mode (3 positions)
4-D	four-dimensional navigation mode (3 positions and velocity or time schedule)

TCV PROGRAM OVERVIEW

It has been recognized that new ATC equipment and procedures cannot solve the problems that they are intended to solve unless the airborne systems and flight procedures are developed to take full advantage of the capabilities of the ground-based facilities. The airborne system is considered to be the basic airframe and equipment, the flight-control systems (automatic and piloted modes), the displays for monitoring or pilot control, and the crew as manager and operator of the system. Because of the urgent need to develop the required airborne system capability, the NASA Langley Research Center has implemented a long-term research effort known as the Terminal Configured Vehicle Program. The program is conducting analytical, simulation, and flight-test work to develop advanced flight-control capability for

4-D RNAV and transition to MLS

Precision, curved, steep, decelerating, and time-sequenced approaches utilizing MLS

Zero-visibility landings through turnoff

This capability will be developed by means of

Advanced automatic controls

Advanced pilot displays for monitoring and control

Reduced crew workload

Improved interfaces of avionics, aircraft, and crew

Advanced airframe configurations

The primary facility used in the flight research is the Research Support Flight System (RSFS). The system consists of a Boeing 737 airplane (fig. 2) equipped with onboard reprogrammable all-digital integrated navigation, guidance, control, and display systems.

RSFS Description

A cutaway view of the airplane shown in figure 3 illustrates the palletized installation of the RSFS avionics and depicts a second cockpit for research (aft flight deck, AFD). The value of the RSFS for research purposes is enhanced by several notable design features:

(a) The system functions are controllable and variable through software.

(b) The hardware is easily removed, modified, repaired, and installed.

(c) Flight station changes are readily accomplished in the research cockpit, which has a fly-by-wire implementation for control of the airplane.

The arrangement of the AFD is shown in the photograph of figure 4. The center area of the cockpit is seen to resemble a conventional 737 cockpit, whereas the area immediately in front of the pilot and copilot has been opened up by removing the wheel and wheel column and replacing them with "brolly handle" controllers. This open area has been utilized as the location for advanced electronic displays. The displays illustrated in figure 4 consist of an electronic attitude director indicator (EADI) at the top, the electronic horizontal situation indicator (EHSI) in the middle, and the navigation control display unit (NCDU) at the bottom. A control mode select panel is shown located at the top of the instrument panel and centered between the two pilots. The display system is all digital and can be readily reprogramed with regard to formats and symbology for research purposes. The NCDU is used to call up preplanned routes and flight profile information or for entering new or revised information to be displayed. Inserted information and flight progress information can be called up on the NCDU for review. The EADI instrument provides basic attitude information to control the airplane; the EHSI shows the horizontal plan of the flight, either with a heading-up or north-up mode, and the flight progress. The display formats and their functions will be described in more detail in a later section of this paper.

TCV Program Goals

The basic goals of the TCV Program are illustrated in figure 5. As seen in this figure, operations in the MLS environment can, perhaps with proper controls and displays, allow operators to take advantage of steep, decelerating curved approaches with close-in capture which result in shorter common paths. These paths can be planned for reduced noise over heavily populated areas and for increased airport capacity. Onboard precision navigation and guidance systems including displays are required for 3-D and 4-D navigation and for sequencing and closer lateral runway spacing. Displays are under development

8

with the intent of achieving lower visibility operations in this future environ ment with sufficient confidence that they become routine. Finally, programmed turnoffs at relatively high speed should clear the runway to allow operations to proceed with perhaps 40 to 45 seconds between aircraft, should the vortex wake problems be solved.

U.S. MICROWAVE LANDING SYSTEM

In 1977, the ICAO is scheduled to select a new international standard approach and landing guidance system that will replace both the instrument landing system (ILS) at civil airports and the ground controlled approach (GCA) at military airports (ref. 5). The ICAO All Weather Operations Panel is presently evaluating candidate microwave landing systems submitted by Australia, Britain, France, West Germany, and the United States. All candidate systems operate in the microwave region, which is expected to serve the full range of aircraft operating in all-weather conditions.

The U.S. MLS basically transmits three time-reference scanning fan-shaped radio beams from the runway, as illustrated in figure 6. One beam scans $\pm 60^\circ$ from side to side of the runway center at a rate of $13\frac{1}{2}$ times per second to provide azimuth (Az) referencing. The second beam scans up 20° and down to a reference plane parallel to the runway surface at a rate of 40 times per second to provide basic glide slope guidance (EL1). The third beam, which scans up $7\frac{1}{2}$ and down to the same plane parallel to the runway at a rate of 40 times per second, is used for flare guidance (EL2). A fourth nonscanning fan-shaped beam transmitted from a distance measuring equipment (DME) site provides ranging information. This DME beam is transmitted at a rate of 40 times per second and has an angular coverage of 120° in azimuth and 20° in elevation. Time reference means that receiving equipment onboard the aircraft will measure the time difference between successive "to" and "fro" sweeps of the scanning beams to determine aircraft position relative to the runway center line and to a preselected glide path. This time-difference measurement technique gives rise to the designation of the U.S. MLS as a Time Reference Scanning Beam MLS.

JOINT FAA/NASA ICAO DEMONSTRATION AGREEMENT

Early in the TCV Program, a joint NASA/FAA agreement recognized the long-term objectives of the NASA Program, and NASA agreed to provide use of the TCV airplane for support of specific FAA system evaluations, including that of the MLS. In July 1975, at the request of the FAA, NASA agreed to participate in a flight demonstration of the U.S. MLS capabilities to the All Weather Operations Panel (AWOP) of ICAO at NAFEC. The ground rules adopted for the demonstration were

(1) Fly 3-D automatic, curved, descending approaches with RSFS navigation control laws used for the curved-path portions and with MLS guidance substituted for inertial platform (INS) guidance.

(2) Make transition from curved-path portions to short, straight final approaches and land with the RSFS autoland control laws modified to use MLS guidance substituted for INS and ILS guidance.

(3) Perform flares using EL2 and/or radio altimeter signals.

(4) Perform roll-out using MLS guidance.

(5) Modify the RSFS displays to accept MLS derived information. These displays include (a) horizontal situation, (b) curved trend vector, and (c) center-line and glide-path deviations.

All the capabilities implied by the ground rules were to be demonstrated in an automatic mode without use of the inertial smoothing technique which is a basic part of the conventional RSFS. The FAA asked that no acceleration signals be used to augment the MLS data if possible. However, the FAA stated that the use of body-mounted accelerometers or direct measurement of INS acceleration signals were permissible if parameters of this type were needed for the basic control systems. The FAA also stated that the use of attitude data from the INS was permissible in lieu of attitude from high-quality vertical and directional attitude reference systems for display purposes. The philosophical approach taken by Langley Research Center was to make minimum modifications in the existing navigation guidance and control systems and to derive all necessary parameters from the MLS data for interface with these systems.

DEMONSTRATION FLIGHT PROFILES

The flight profiles selected for the demonstration are shown in figure 7 superimposed on a photograph of the NAFEC area. The two profiles shown in this figure are designated as a 130° azimuth capture and an S-turn azimuth capture. Each flight profile contains a 3 n. mi. straight final approach representative of many VFR approaches being flown at the present time at congested airports near heavily populated areas. These profiles, which can be used to provide alleviation of noise over populated areas, are also illustrative of the types of curved paths that have potential for increasing airport capacity in an advanced ATC environment.

A more detailed description of flight events along the demonstration profiles is given in figures 8 and 9. As seen in figure 8, take-off was from runway 22 with the airplane controlled manually from the front cockpit during take-off. Shortly after take-off, control was shifted to the aft cockpit, where a control wheel steering (CWS) mode had been selected by the AFD pilot. Prior to encountering the first way point, the AFD pilot selected a 3-D automatic RNAV mode for airplane control. This control mode used inertially smoothed DME/DME (IDD) as the source of guidance information. Altitude was maintained at 1220 m (4000 ft) until the way point indicated by "Begin 3° descent" was passed. From this point the airplane continued descending at 3° until flare was initiated. After crossing the Az boundary and approximately 15 seconds after crossing the EL1 boundary, the pilot received an indication of valid MLS data, at which time he selected the MLS RNAV mode which used MLS data as the source of guidance

10

information. This latter event is noted as "MLS enable" in figure 8. Just prior to entering the final turn, the pilot switched to Land Arm. The airplane continued to fly under the MLS RNAV mode until both selected glide slope and lateral path were acquired; then the control of the airplane was switched to autoland, which then controlled the aircraft along the 3 n. mi. final approach. At an altitude consistent with the sink rate and altitude criteria of the flare laws in the flight control system, flare was initiated. Flare was executed using EL2 and DME data as the source of vertical guidance information on most of the touchdowns. On a few flights during the demonstration, a radio altimeter was used as the source of vertical guidance information for comparison purposes.

The events along the S-turn profile are very similar to the events of the 130° azimuth capture profile, as shown in figure 9. It may be noted that the S-turn profile resulted in a greater time period of MLS RNAV than did the 130° profile. On touch-and-go approaches, control was switched from aft flight deck automatic control to front flight deck manual control for the take-off portion of repeat flights. On landings that continued to a full stop, roll-out was conducted in an automatic mode that used the Az beam for runway center-line guidance information.

RSFS CONFIGURATION FOR THE ICAO DEMONSTRATION

The basic configuration of the RSFS that was used during the ICAO Demonstra-tion is illustrated in figure 10. It should be noted that the original RSFS was not configured to use MLS data for navigation, guidance, or control. The principal task to which NASA addressed its efforts was the integration of the MLS signals into the navigation, guidance, and control laws and display formats of the original RSFS that had been designed to use INS, DME, ILS, and radio altimeter data. The major development effort involved with the configuration of figure 10 was directed at aircraft antenna design and location, interface of the MLS receiver with the RSFS, and design of the MLS guidance signal processor. Wherever possible, the functions of this signal processor were designed to per-mit integration of MLS derived navigation, guidance, and control parameters with existing laws of the navigation and guidance computer and the autoland computer with minimal modifications to these computers. Minor changes were made to the existing display formats, with features added to indicate validity of MLS sig-nals and to improve the perspective runway format.

MLS Processor

Details of the MLS processor are illustrated in figure 11. As shown in this figure, the inputs to the MLS processor from the MLS receiver are Az, R, EL1, and EL2. These signals were prefiltered to remove extraneous noise and then transformed to a runway-referenced coordinate frame which produced position data (x,y,z) relative to the selected glide-path intercept point.

The function of the closed-loop estimator of figure 11 was to produce esti-mates of position and velocity parameters required for interface with the navi-gation and guidance computer, the autoland computer, and the displays. The Air

11

Data input to the closed-loop estimator consisted of calibrated airspeed and sink rate as derived from a barometric altimeter. These two pieces of data were used to initialize the closed-loop estimator. The Accelerations input to the closed-loop estimator was used to produce the quality of velocity data required in the flight control system. These acceleration data were extracted from the INS during the ICAO Demonstration. However, on subsequent flights this Accelerations input was derived from body-mounted accelerometers, with no notable degradation of flight performance. A description of the closed-loop estimator outputs is given in the following paragraphs.

MLS Processed Signals for Navigation and Guidance

The MLS processor outputs to the navigation and guidance computer are indicated in figure 12. The parameters derived from MLS data for navigation are ΔLAT and ΔLONG, which are latitude and longitude deviations from the origin of the MLS runway-referenced coordinate frame. The terms LAT_{ORIGIN} and $LONG_{ORIGIN}$ in figure 12 are the latitude and longitude values for the origin of the runway-referenced coordinate frame. These latitude and longitude origin values are known a priori and stored in the navigation computer. It is then a simple task to determine the aircraft latitude and longitude, as indicated by the equations in figure 12. The MLS processor outputs used for guidance are latitude LAT, longitude LONG, altitude to mean sea level h_{msl}, north velocity V_N, east velocity V_E, and sink rate $\dot{h}$. These MLS processor outputs and way points defining the desired flight path which are prestored in the navigation and guidance computer are then operated upon by the RSFS guidance laws to produce path correction commands to the autopilot while operating in an automatic RNAV mode.

MLS Processed Signals for Autoland

The MLS processor outputs to the autoland computer as shown in figure 13 are glide-path-angle deviation β, lateral-path-angle deviation η, altitude to touchdown h_{td}, vertical velocity, or sink rate $\dot{h}$, and cross runway velocity $\dot{y}$. These inputs to the autoland guidance laws are processed in the autoland computer along with a prestored runway heading during the final approach to produce pitch and roll commands to the autopilot. It should be noted here that airspeed is controlled by the autothrottle according to a preset airspeed selected by the pilot.

MLS Processed Signals Used for Displays

Before discussing the MLS processor outputs used for driving the displays, it is appropriate to describe the EHSI and EADI display formats used during the MLS demonstration. The photograph of figure 14 shows the arrangement of the electronic displays in the research cockpit. The display system consists of the electronic attitude director indicator (EADI) at the top, an electronic horizontal situation indicator (EHSI) in the middle, and the navigation control display unit (NCDU) at the bottom. The EADI provides basic attitude information

12

used to control the airplane. The EADI format of figure 14 shows an en route format, with the star and circle symbology providing information on the position of the airplane relative to a programed flight profile. Details of the EADI symbology used for approach to landing will be discussed later.

The EHSI format of figure 14 shows a horizontal view of the preprogramed flight path and obstacles, such as the towers shown in the display. The present position of the airplane is indicated by the apex of the triangle symbol. The dashed trend vector in front of the airplane symbol is predictive information and represents where the airplane will be in 30, 60, and 90 seconds if it maintains the current turn rate. The map also shows way points along with the path and ground navigation aids. The current track angle is displayed at the top of the screen. The moving time box shown in the photograph can be displayed if the pilot wishes to fly a 4-D path manually or automatically.

The NCDU is used by the pilot to call up or revise preplanned routes and flight profiles. Flight progress information can also be called up on the NCDU for review.

The EADI format used for the automatic approach and landing mode is shown in the photograph of figure 15. This format provides basic attitude information in both pitch and roll. Lines of pitch angle in 5° increments are indicated above and below the horizon, and the roll pointer at the top of the display shows bank angles of 10°, 20°, 30°, and 45°. The reference airplane symbol is biased 5° up to reduce clutter in the middle of the screen. Flight-path angle is displayed in the form of two wedge-shaped symbols that move vertically as a function of flight-path angle and laterally as a function of drift angle. Flight-path acceleration is displayed by the rectangular-shaped symbol that is just to the left of the flight-path symbols. Deviation from the vertical and lateral paths is displayed by the movement of the autoland box symbol in relation to the boresight dot of the reference airplane symbol. When desired, a computer-generated perspective runway with extended center line (ref. 6) can be displayed for approach situation information. The triangle symbol on the horizon gives present track-angle information. The box-shaped symbols on the horizon represent 10° track increments from the runway heading and are plotted relative to the junction of the rearward extended runway center line and the horizon. The pilot uses the track angle and relative track symbology to establish his path intercept for runway alinement. The computer-generated runway symbology shows good registration with the real runway, shown by the forward-looking television image. Time of day is displayed in the top left-hand corner so that video tapes of the displays can be correlated with the onboard data system. Radio altitude is displayed in the top right-hand side of the screen.

The MLS processor outputs used to drive these display symbols are indicated in figure 16 as north velocity V_N, east velocity V_E, sink rate $\dot{h}$, lateral-path deviation η, glide-path deviation ϵ, latitude LAT, and longitude LONG. The display symbols which are driven from these parameters are flight-path angle wedges, which indicate the projected touchdown point; trend vector, which indicates the predicted flight path of the aircraft; aircraft position; ground speed; lateral-path and glide-path deviations; and a computer-generated perspective runway with an extended center line. Additional inputs to the display

13

compucations as shown in figure 16 are cross runway acceleration $\ddot{y}$, which is used to stabilize the trend vector; and pitch θ, roll ϕ, and yaw ψ, which are used to correct the perspective runway symbol for aircraft attitude changes. The acceleration and attitude inputs were derived from the inertial platform during the ICAO Demonstration. During later flights the acceleration inputs were measured from body-mounted accelerometers and transformed to an inertial reference frame.

RSFS Reconfiguration Summary

Changes to the RSFS configuration for the ICAO Demonstration may be seen by comparing figure 17 with figure 3. As shown in figure 17, three antenna locations were selected for the demonstration. The C-band antennas on the tail and lower aft fuselage were used for diagnostic purposes during the development flights. The C- and K_u-band antennas located above the front cabin were the primary antennas used for guidance. The cabin-mounted C-band antenna was used to receive Az, EL1, and R signals, and the K_u-band antenna was the receiving antenna for EL2 signals. The MLS receivers, processor, and special MLS signal recorders are shown located just in front of the aft flight deck. Special in-flight diagnostic oscillographs and a backup MLS receiver are shown located at the right rear of the airplane.

OVERVIEW OF FLIGHT RESULTS

During the development, demonstration, and post-demonstration data-collection flights in the NAFEC MLS environment, 208 automatic approaches and 205 automatic flares were flown. These flares were terminated in touch-and-go maneuvers and full-stop landings that included automatic roll-out operations. During the demonstration flights, final approaches of 3 n. mi. were achieved. Following the demonstration, shorter final automatically controlled approaches of 2 n. mi. were flown. Manually controlled flights conducted after the demonstration included 41 approaches with final segments of 3, $1\frac{1}{2}$, and 1 n. mi. Reduction of flight data gathered on these flights is underway. Analysis of these data is expected to result in an assessment of path tracking accuracy; speed control system performance; display format utility for monitoring aircraft path tracking performance and for interpretation of flight situation and usefulness in changes in flight plans; wind shear and turbulence conditions during all flight phases; quality of the MLS signals in terms of precision and multipath characteristics; and total performance of the navigation, guidance, and flight control systems. However, a limited amount of quantitative data has been reduced and the results will be summarized here. In addition, qualitative comments of pilots and observers regarding overall airplane performance will be discussed.

Automatic Flight Control Performance

An example of path tracking accuracy during the demonstration flights of May 20, 1976, is shown in figures 18 and 19. The data of these two figures

14

were obtained through a comparison of unprocessed MLS Az, EL1, EL2, and R signals with phototheodolite tracking data. The ordinates of figure 18 are in degrees and each abscissa is in nautical miles, as measured from the MLS Az and DME transmitter site. In figure 18, it can be seen that the azimuth error is quite small throughout the approach and is usually less than 0.05°. The error in elevation (EL1 reference) is somewhat larger but appears to be of the order of 0.05° along most of the final approach. The abscissa scales of figure 19 are the same as for figure 18. The upper plot of this figure has range signal error along the ordinate; the lower plot has degrees of elevation (flare signal) error along its ordinate. The range-error plot of figure 19 shows a bias of approximately 8 m (25 ft), with maximum errors appearing to be of the order of 15 m (50 ft). The elevation error shown in this figure agrees well with the elevation error in figure 18. In fact, these two elevation-error plots agree so well that it is highly probable that the major portion of this error may be attributable to phototheodolite error rather than errors in either EL1 or EL2 signals. The source of this error is under study. The growth of EL1 and EL2 error in the vicinity of the runway threshold can be attributed chiefly to the geometry of the phototheodolite sites.

Flight-path deviations for the same flight as in figures 18 and 19 are shown in the plots of figure 20. The upper plot of this figure shows the lateral-path deviation that occurred from final turn into the final approach fix through touchdown and roll-out. These lateral deviations are typically less than 15 m (50 ft). The lower plot of figure 20 is representative of the glide-path deviations experienced during the demonstration flights. These deviations were usually less than 6 m (20 ft). The growth of glide-path deviation starting at 1.3 n. mi. is due to the flare maneuver.

An example of the effects of wind shear along the flight track on tracking performance during final approach is shown in figure 21. The plot on the left of figure 21 shows an ideal 3° glide slope (dashed line) and the glide-slope performance (solid line) achieved when the airplane was subjected to the influence of the evident wind shear shown in the calibrated-airspeed plot on the right of this figure. The airspeed plot shows variations in the tail wind component of approximately 20 knots. An examination of this plot indicates that the airplane experienced a wind shear gradient along the flight path of approximately 15 knots over an altitude range of 8 m (25 ft). Examination of the glide-slope performance plot shows that the flight deviations were quite small and of the order of 3 m (10 ft) or less. This performance is considered to be excellent for such severe wind conditions. Other wind conditions experienced during the demonstration flights include strong gusts, tail wind components of 20 to 25 knots, and 20-knot cross-wind components.

No conclusions may be made at this time regarding correlations among airspeed at flare initiation, mean tail winds during flare, sink rates at touchdown, and touchdown dispersion. Analysis is underway to develop correlation criteria for the results of these flights and the data gathered during the development and demonstration flights. However, it can be noted that touchdown dispersion data obtained for EL2 flares and radio altimeter flares appear to have similar characteristics. These dispersion data are considered to compare favorably with performance of commercial airlines. Following the ICAO

Demonstration, several automatic approaches were successfully flown with acceleration data sensed from body-mounted accelerometers instead of from the INS. During these latter flights the final approach was shortened to 2 n. mi.

Display Utilization

In exploiting the MLS capabilities in an RNAV and MLS environment and in utilizing profiles such as those demonstrated before the ICAO, it is essential that the flight crew be continually oriented with respect to its flight and navigation situation. Today's aircraft flight instrumentation is not considered operationally adequate, either for monitoring automatic flight or for contingency reversion to manual control in the environment anticipated, that is, close-in, curved, descending, precision approach profiles with very low visibility and in proximity to other traffic. Consequently, the advanced electronic display system has been provided in the aft flight deck of the TCV airplane with which to explore and develop this all-important interface of the pilot with his environment.

During the ICAO Demonstration, the ability to observe the position of the airplane at all times and its tracking performance by means of the displays was as impressive as the automatic operation itself. After take-off, the displays permitted the pilots to position the airplane manually for a smooth, maneuverless transition to 3-D automatic flight into the first way point of the automatic profile. Also, during the development flights prior to the demonstration, numerous interruptions in flying the profiles were encountered. Several diversions due to intrusion of traffic were encountered, and there were many programing errors and malfunctions of various kinds that led the pilot to take over. The displays, in combination with control wheel steering, resulted in effortless navigation during reprograming or redirected flight and facilitated expeditious maneuvering by the pilots to reenter the desired patterns without lost time or excessive airspace for orientation and without the need for vectoring from the ground. The EADI symbology provided an effective means of monitoring flight progress on the final approach. In particular, the excellent registration of the computer-generated perspective runway with the television-generated image of the real-world runway established confidence in the potential utility of computer-generated runway symbology for monitoring landing operations.

The implications for the future are clear with respect to automatic flight. Advanced displays will have to be provided to

Maintain crew orientation

Permit manual maneuvering within constraints in airspace, fuel, and time in order to cope with diversions due to traffic, weather, or loss of automatic capability

Permit continued controlled navigation when new clearances and/or flight profiles must be defined

16

Manually Controlled Approaches

Upon completion of the automatic flights related to the ICAO Demonstration, additional flights were conducted to evaluate display effectiveness for manually controlled flight along the same profiles, since this is considered to be the best way to evaluate display information for monitoring purposes and takeover if necessary. The runway symbology and track information relative to the runway presented in the EADI appear to be effective means of integrating horizontal information into the vertical situation display for the landing approaches. The runway and relative-track symbology aid the pilot in maintaining a current mental picture of his situation relative to the runway.

The velocity vector control mode was used during the approaches. In this mode, the pilot commands pitch rate by pulling or pushing the panel-mounted controllers. When the pilot perceives that the desired flight-path angle has been reached, he releases the controllers and the system maintains that flight-path angle. The pilot also commands roll rate by rotating the panel-mounted controllers. When he attains the desired track angle relative to the runway, he releases the controllers with wings level and that track angle is maintained until further inputs are made.

During the manual approaches the pilot's task was to capture and hold the localizer center line while maintaining the 3° glide-slope center line. Several approaches with 3 n. mi. finals were flown using the runway and relative-track symbology as primary information for capturing and holding the localizer center line. The resulting lateral errors were less than 5 m (15 ft) at the 30-m (100-ft) altitude window. This small error indicates that the pilot was able to make the localizer offset correction quickly and come through this window with satisfactorily stable attitudes and conditions. The vertical errors at the 30-m window were less than 2 m (6 ft).

Flight-path deviations for a typical manually controlled approach are shown in the plots of figure 22. The upper plot of this figure shows the lateral-path deviations that occurred from the final approach fix to an altitude of 30 m (100 ft). The lateral deviation at the final approach fix is approximately 30 m. This offset was easily handled by the pilot, and as indicated by the plot, the lateral deviations were reduced to 3 m (10 ft) or less prior to flare initiation. The lower plot of figure 22 is illustrative of the glide-path deviations during these approaches. The maximum vertical deviation is seen to be 6 m (20 ft).

The manual approach performance achieved with the runway and relative-track symbology is very encouraging considering that these were the first close-in approaches flown by these pilots. The performance data for these manual approaches compare very favorably with the flight director criteria for glide slope and localizer performance stated in reference 7 for Category I and Category II approach conditions. Additional manual approaches with final segments of $1\frac{1}{2}$ and 1 n. mi. were successfully flown. Quantitative data relating to these latter approaches are not available at this time.

CONCLUDING REMARKS

The system development effort undertaken by NASA in support of the ICAO Demonstration presented NASA with the opportunity to gain experience with the U.S. MLS characteristics and an opportunity to develop operational techniques for utilization of this system in a real-world environment. The demonstration also provided an opportunity for a wide and varied audience to observe proof of concept of the MLS in flight and to witness presentations of the techniques used to integrate the MLS capability into an existing avionics system on a commercial carrier class airplane.

The flights demonstrated the utility of the wide area coverage of the MLS for curved, descending paths commencing with a standard RNAV approach into a terminal area and continuation of this approach throughout the MLS coverage area and onto the runway. The ability to fly precision curved navigation paths with use of MLS signals highlights the potential of this system for design of noise alleviation and high-capacity flight paths in a terminal area. During these flights, transition from a curved path to the final approach was executed smoothly, with lateral excursions of the order of 15 m (50 ft). These small excursions, or overshoots, indicate that an 800-m (2500-ft) separation of final approach paths, and therefore runway separation, is a reasonable goal.

These flights also demonstrated the feasibility of shorter final approaches for terminal-area operations during very low visibility conditions. Shorter final approaches coupled with improved ATC techniques give promise of shorter common paths for merging aircraft and therefore a potential for increased airport capacity. Flare performance using the MLS flare beam (EL2) was seen to compare favorably with that accomplished when conventional radio altimeter techniques were used; and use of the MLS for roll-out demonstrated the potential for improved guidance on the runway.

Advanced display concepts developed under the TCV Program were shown to be compatible with the MLS, and the accuracy of the MLS signals permitted these displays to be used to their fullest advantage by the pilots both in monitoring and controlling with precision the close-in flight profiles. Also, the EHSI proved to be of significant value for execution of flight plan changes or manual performance of diversionary maneuvers.

It should be noted that the demonstration flights were conducted under severe wind conditions which would ordinarily have required runway assignment changes for final approaches or rerouting to other airports in the cases of commercial airline traffic. Atmospheric conditions included high winds with strong gusts resulting in tail wind components of 20 to 25 knots, cross-wind components of 20 knots, steady tail quartering winds of 20 to 25 knots, and shears in excess of 50 knots per 30 m (100 ft).

Problems currently existing in terminal-area operations of the civil air transportation system can be expected to intensify in the future. New flight procedures and advancements in flight control, navigation, and guidance systems designed to take maximum advantage of MLS, and other advanced ATC equipment, offer potential solutions to these problems as well as economic advantage. The

development and demonstration of these advantages is an urgent requirement. The NASA Terminal Configured Vehicle program has demonstrated through flight research during the ICAO evaluation period that the TCV research airplane and its advanced equipment can effectively utilize these new capabilities for improved terminal-area operations.

REFERENCES

1. An Overview of the FAA Engineering and Development Programs, 1973-1974. FAA-EM-73-2, Mar. 1973.

2. Joint DOT-NASA Civil Aviation Research and Development Study — Supporting Papers. DOT-OST-P-10-, NASA   , Part.

3. Reeder, John P.; Taylor, Robert T.; and Walsh, Thomas M.: New Design and Operating Techniques and Requirements for Improved Aircraft Terminal Area Operations. NASA TM X-72006, 1974.

4. Stein, Kenneth J.: Microwave Landing System Demonstrated. Aviat. Week & Space Technol., vol. 104, no. 24, June 14, 1976, pp. 96-99.

5. McLucas, John L.: MLS: Breakthrough in Landing Systems. Air Force Mag., July 1976, pp. 66-72.

6. Steinmetz, George G.; Morello, Samuel A.; Knox, Charles E.; and Person, Lee H., Jr.: A Piloted-Simulation Evaluation of Two Electronic Display Formats for Approach and Landing. NASA TN D-5183, 1976.

7. Criteria for Approving Category I and Category II Landing Minima for FAR 121 Operators. AC No. 120-29, FAA, Sept. 25, 1970.
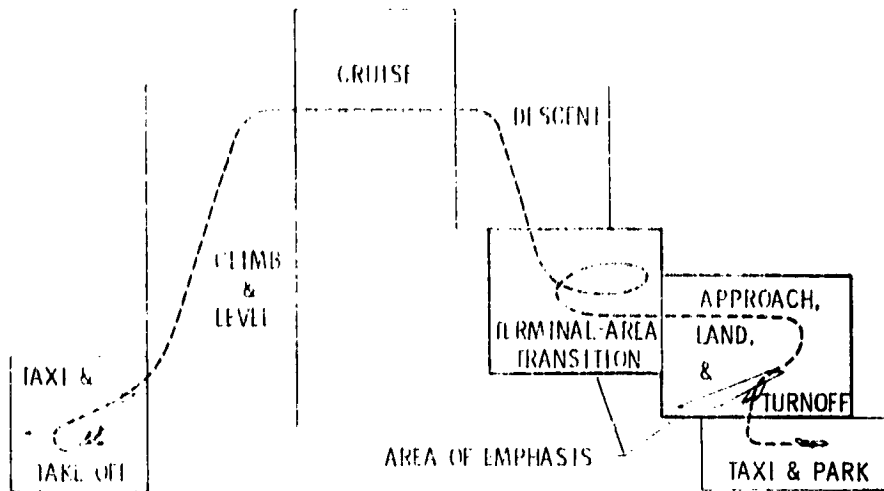
Figure 1.- Flight modes and areas of emphasis in
Terminal Configured Vehicle Program.

Figure 2.- Terminal Configured Vehicle
Program research airplane.

20
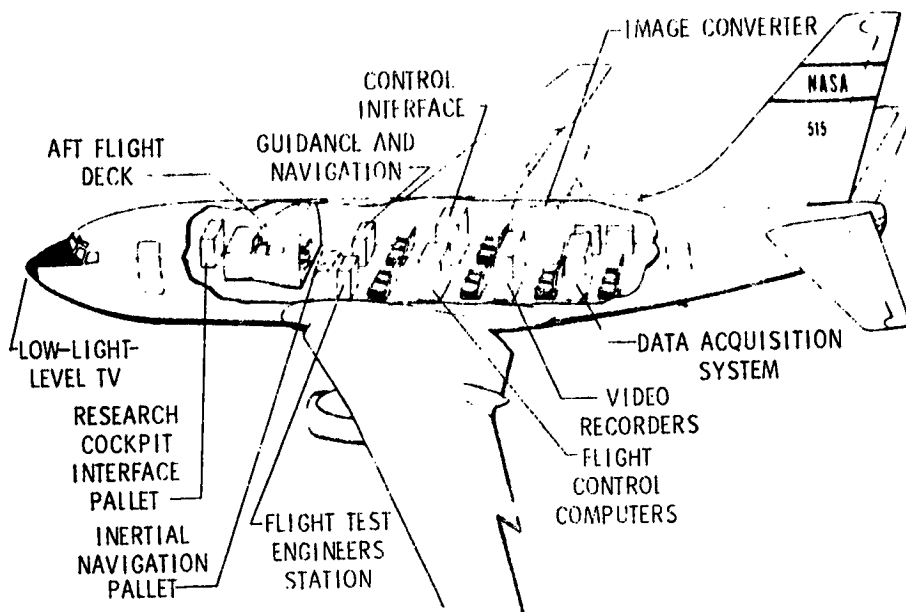
Figure 3.- Research Support Flight System internal arrangement.
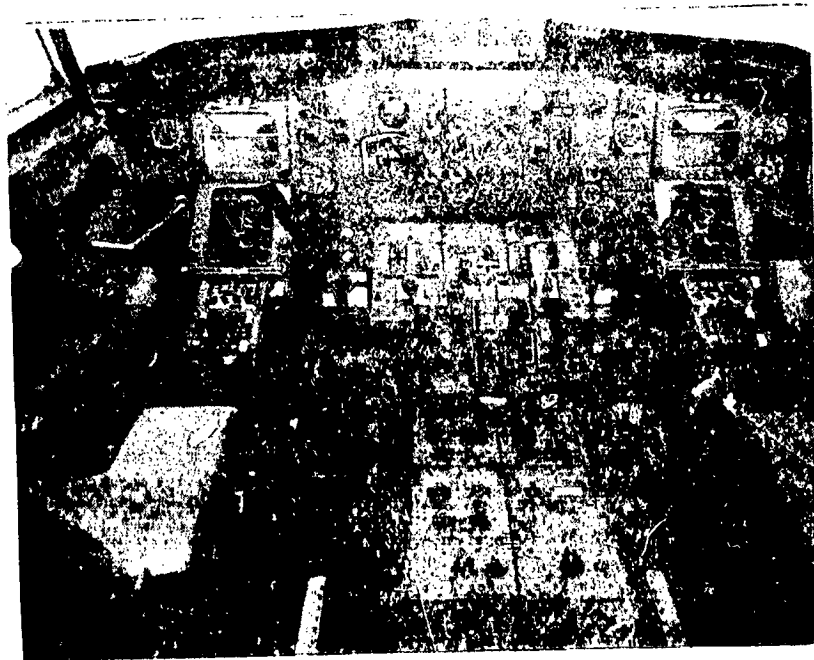
Figure 4.- Aft flight deck display arrangement.
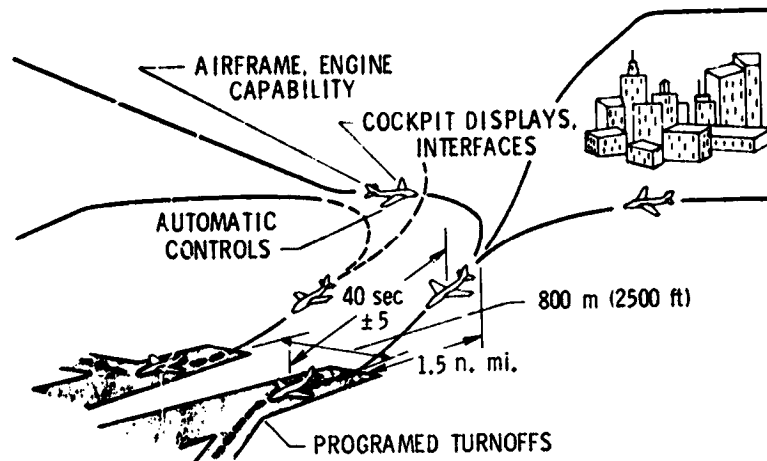
Figure 5.- Terminal Configured Vehicle operational goals.
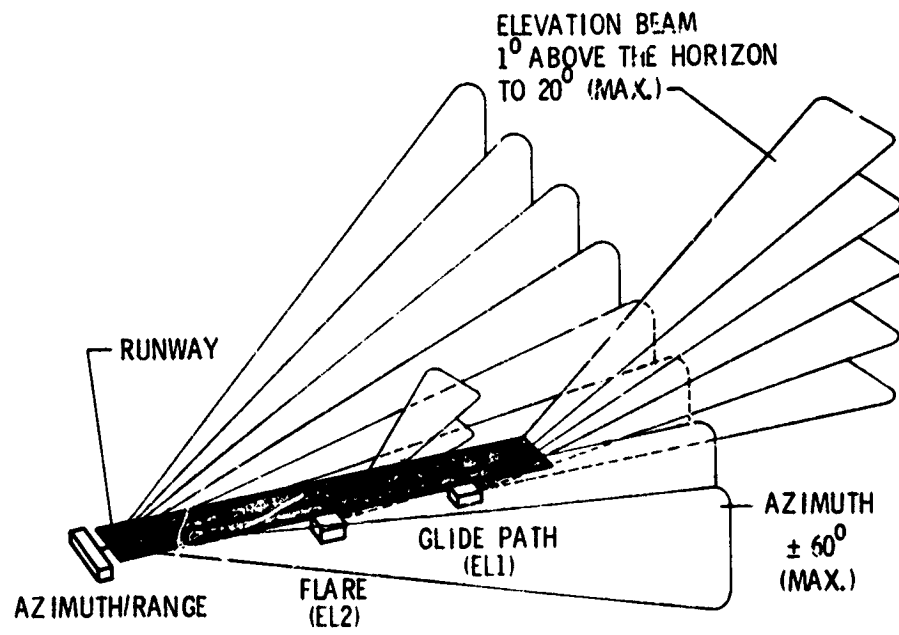
Figure 6.- Microwave landing system.

Figure 7.- ICAO Demonstration profiles at NAFEC.
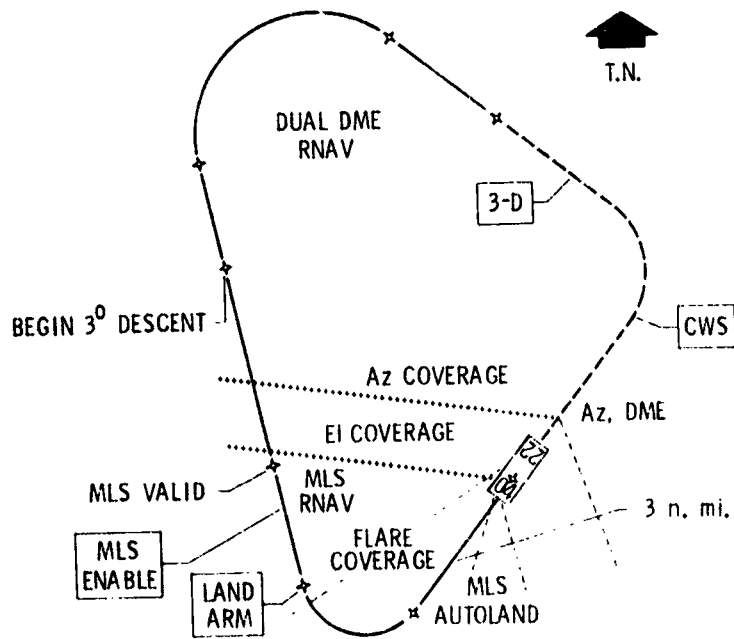
Figure 8.- 130° azimuth capture.

23
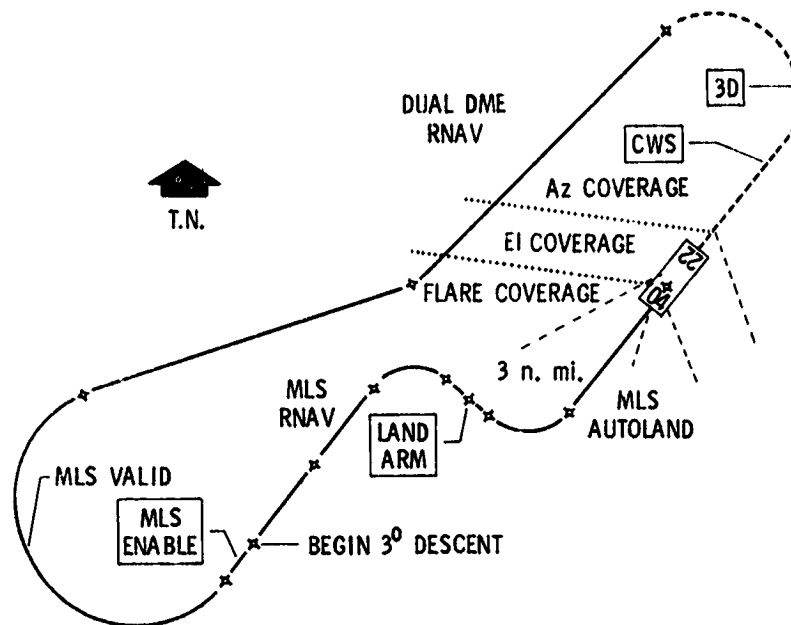
Figure 9.- S-turn azimuth capture.
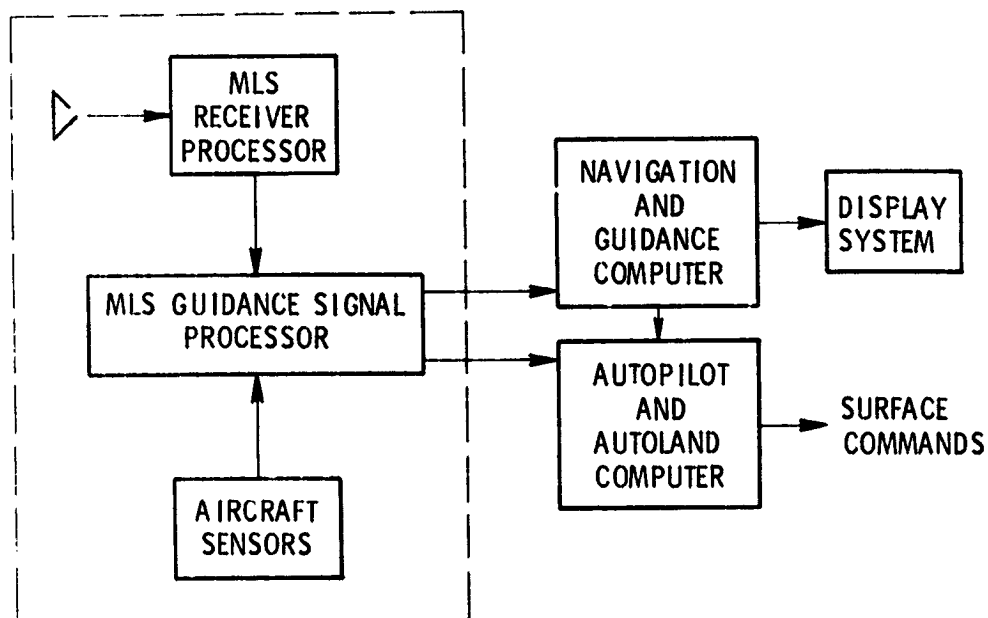
Figure 10.- MLS integration with TCV airplane.
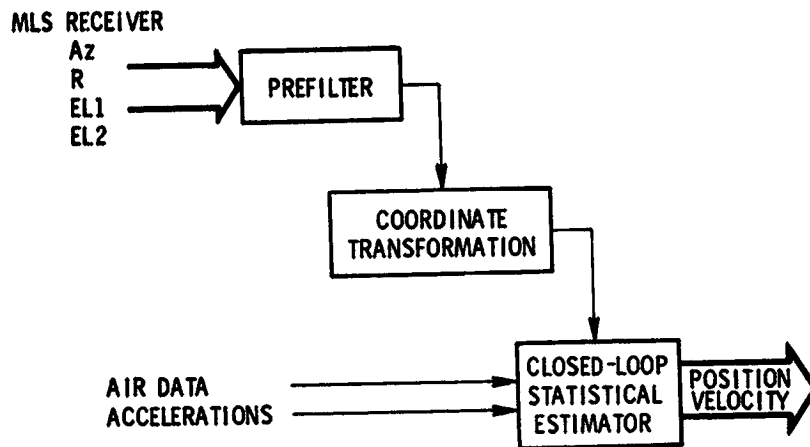
Figure 11.- Major functions of MLS processor.

NAVIGATION

$$LAT = LAT_{ORIGIN} + \Delta LAT$$
$$LONG = LONG_{ORIGIN} + \Delta LONG$$

GUIDANCE
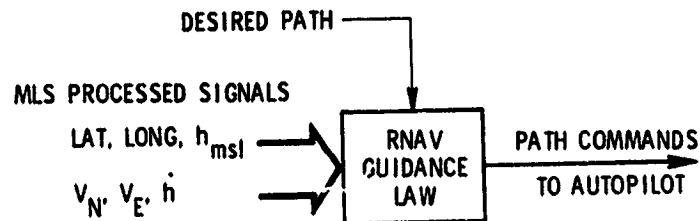
Figure 12.- MLS processed signal use for navigation and guidance.

PATH DEVIATIONS, β & η
ALTITUDE, h_{td}
VERTICAL VELOCITY, $\dot{h}$
CROSS RUNWAY VELOCITY, $\dot{y}$

AUTOLAND

PITCH & ROLL
COMMANDS

TO AUTOPILOT
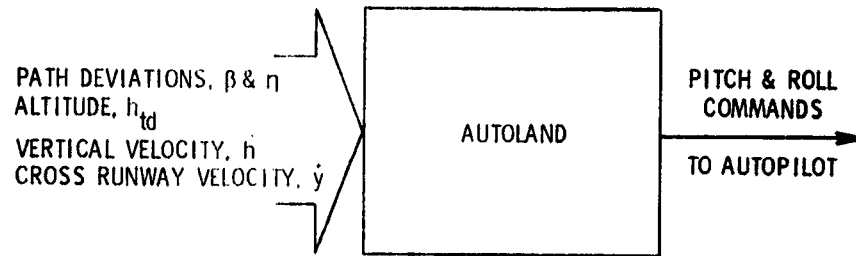
Figure 13.- MLS processed signal use for autoland computer.
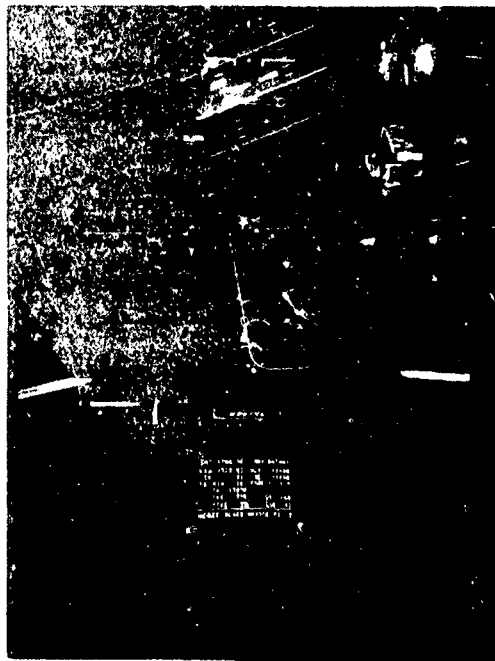
Figure 14.- EADI and EHSI displays.

26
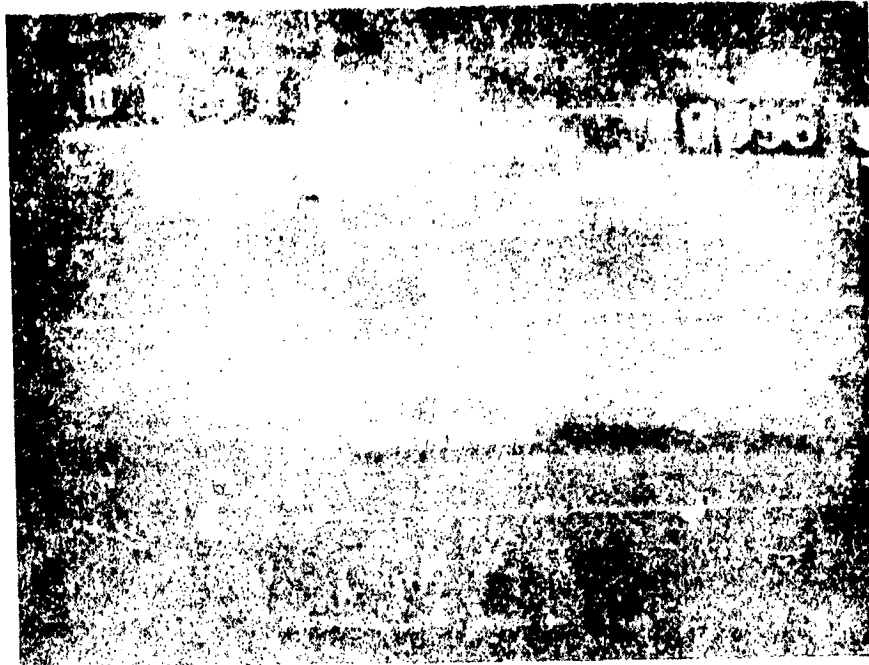
Figure 15.- EADI symbology.
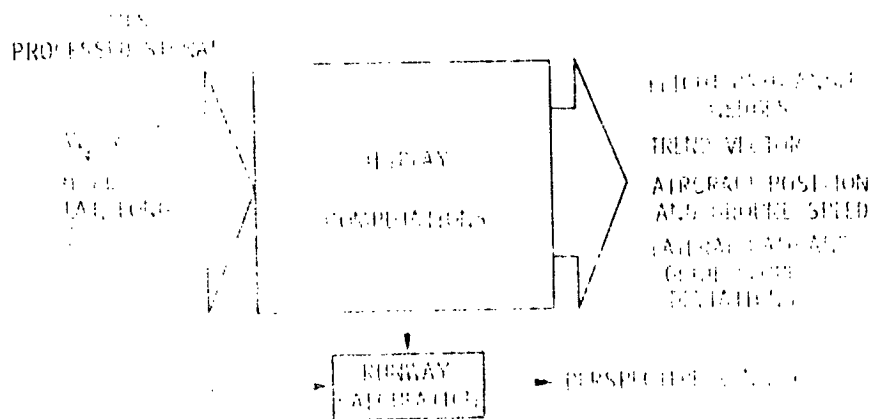
Figure 16.- ILS processed signal use for displays.
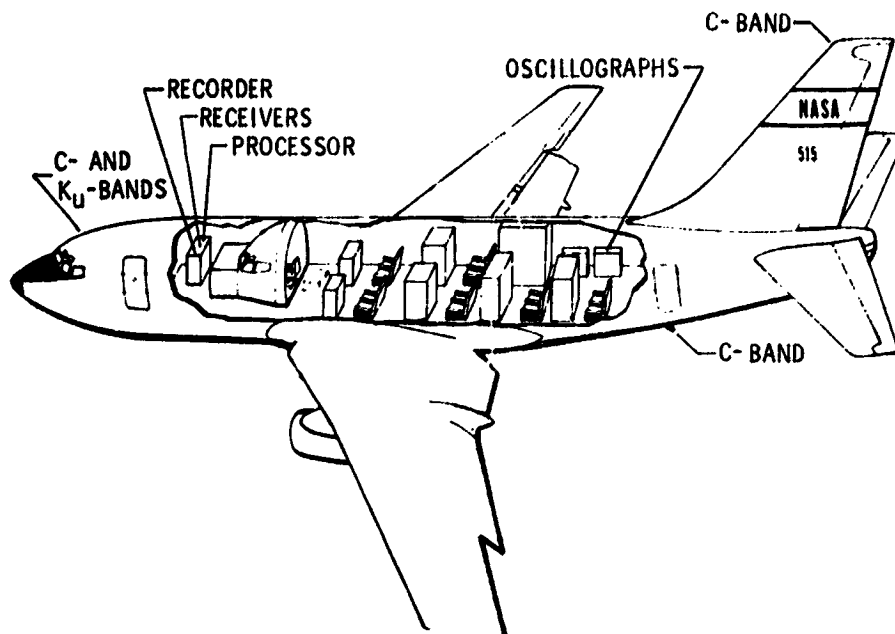
Figure 17.- Research Support Flight System internal arrangements with MLS.
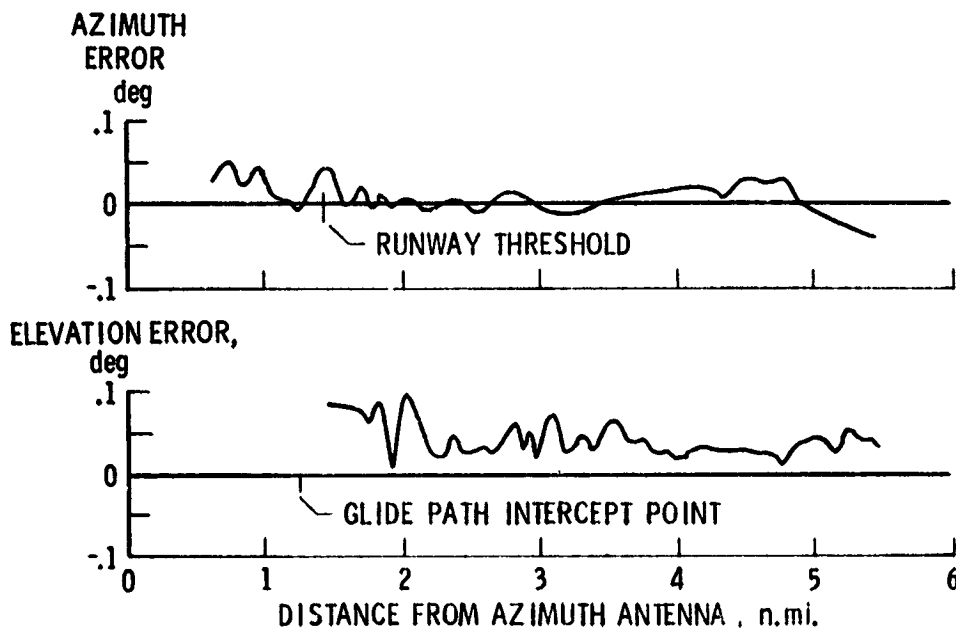
Figure 18.- Typical azimuth and elevation signal errors.

DME ERROR
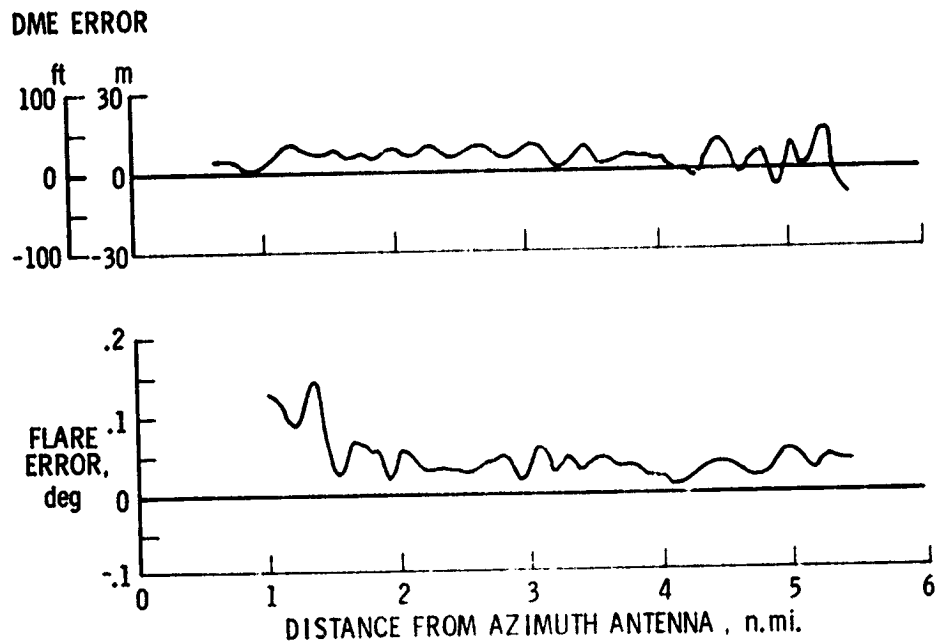
Figure 19.- Typical DME and flare signal errors.
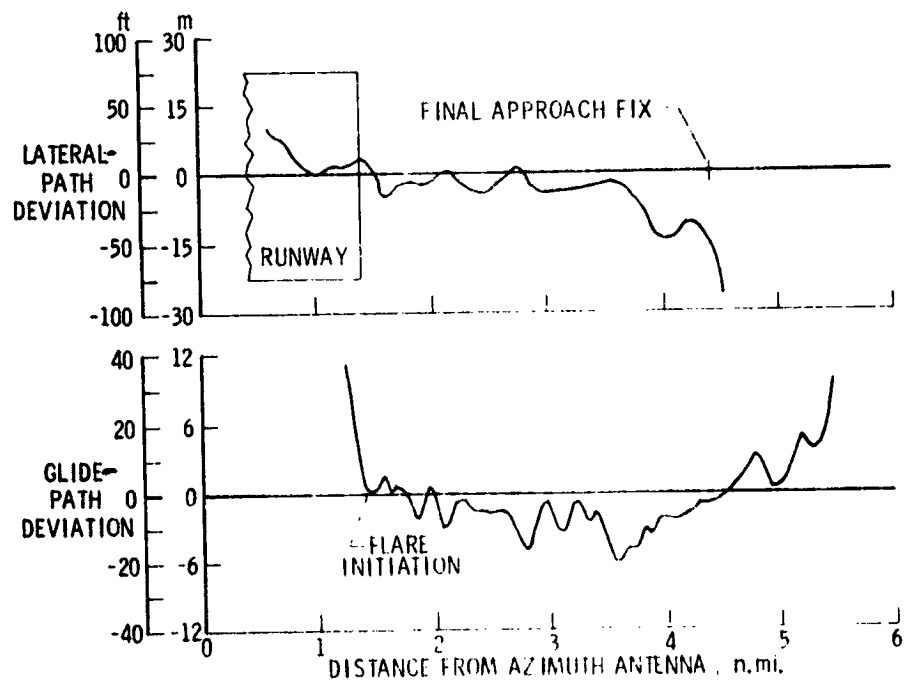
Figure 20.- Typical autoland flight-path deviations.

29
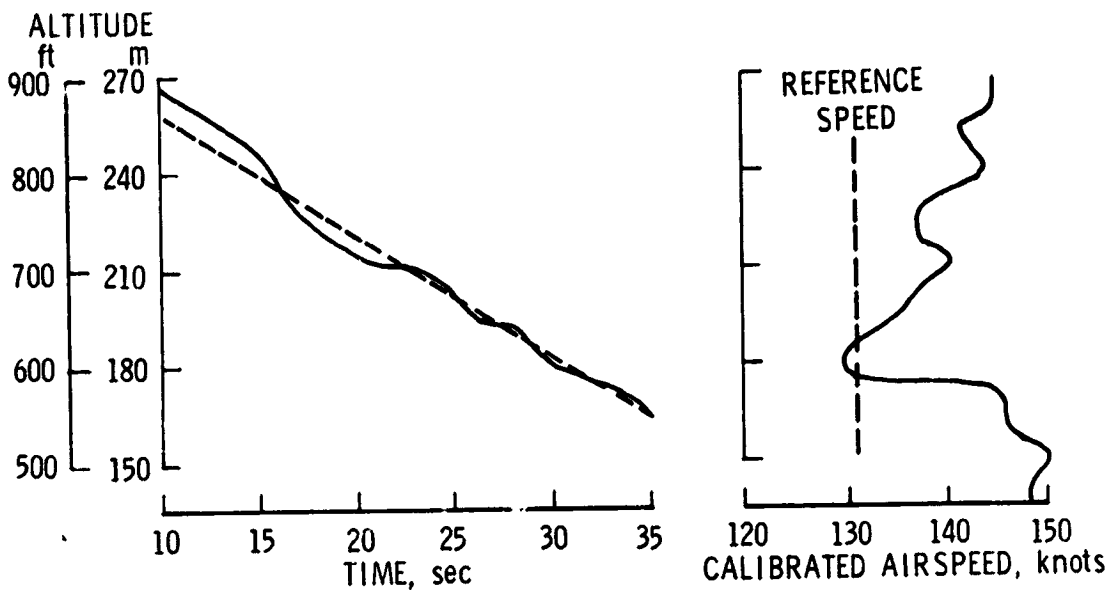
Figure 21.- Typical autoland shear performance.
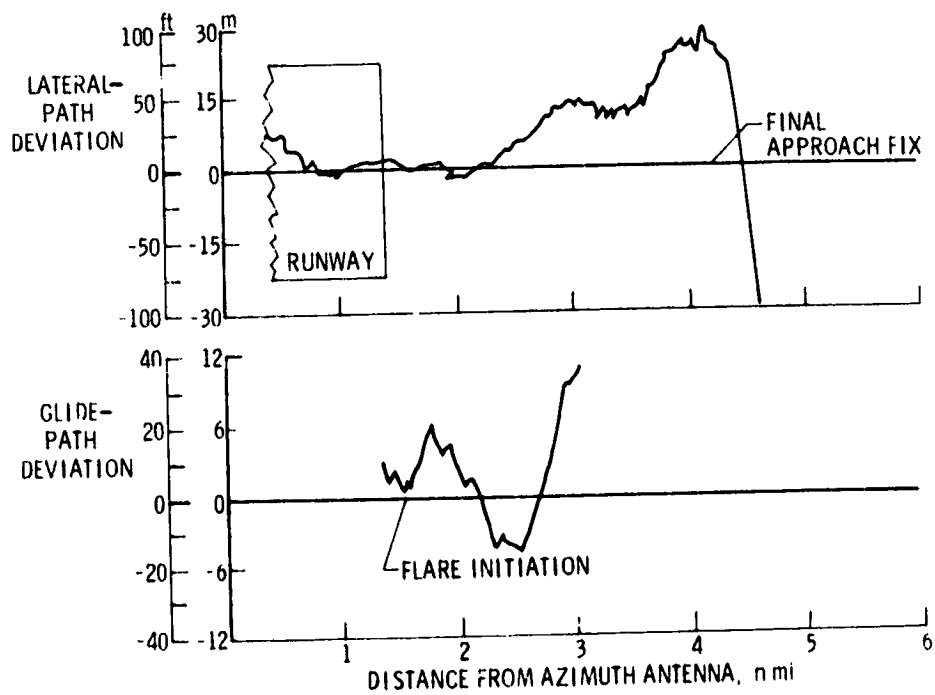
Figure 22.- Typical manual control flight-path deviations.

ł Ꞩ ꞟ 𝚊 ~ ʈ 𝖺 𝟢 𝟪 ?

OPERATIONAL EXPERIENCE WITH

POWERED-LIFT STOL

Robert C. Innis and Hervey C. Quigley
NASA Ames Research Center

SUMMARY

The experience gained in over four years of experience with the Augmentor Wing Research Aircraft and the background operation of other STOL powered-lift aircraft have identified several characteristics that will be basic to most STOL aircraft designs. The factors are that the use and percent of lift achieved by powered lift have a significant effect on the operational characteristics of STOL aircraft and on the performance that can be achieved. A brief description of the aircraft including the means by which it achieves its powered lift is presented. Specific problem areas relating to the control of the aircraft flight path are discussed as well as the consequences these factors have on the design and operation of this class of aircraft.

INTRODUCTION

This paper reviews the experience gained during the first four years of operation of a powered-lift jet STOL airplane, the Augmentor Wing Research Aircraft. It reflects some 330 flight hours and over 3,100 STOL approaches and landings. While the concept for achieving powered lift with this airplane is perhaps unique, the design is such that it allows considerable flexibility to the pilot in the means by which he controls the aircraft. With the incorporation of an advanced digital flight control system, designed and built by Sperry Flight Systems, it is possible to examine a wide range of handling qualities and flight control concepts. It is for this reason we feel that the conclusions presented here apply in general to those aircraft which derive a substantial portion of their lift from the primary propulsion system. The contents of this paper address primarily the approach and landing phase of flight where the consequences of the powered lift are most pronounced, and the resultant characteristics most different from those of conventional aircraft.

DESCRIPTION OF AIRCRAFT

The augmentor wing was designed as a low-cost, low-speed research vehicle that could be used to investigate the operational characteristics of a powered-lift jet STOL aircraft in the environment of the terminal area including takeoff, transition, approach, and landing. The aircraft, shown in figures 1, 2, and 3, was modified from a deHavilland C-8A Buffalo which was donated by the USAF. The G. E., T-64 turboprop engines were replaced by R. R. Spey turbofans. The wing area was reduced by removing about 2 m from each wing tip, and fixed, full-span slats were installed on the leading edge. The landing gear was fixed in the down position and modified to accommodate a higher gross weight. The spring tab controlled elevator system was changed to a hydraulic powered unit, and the conventional double slotted flaps were replaced with an entirely new augmented jet flap system. This flap, illustrated in figure 4, consists of two nearly parallel surfaces with a continuous double slot nozzle located between them which acts as an ejector pump with air drawn in from both the upper and lower surface of the wing.

Air for the flap nozzles is provided by the fan section of the Spey compressors. The lower nozzle is supplied by air from the engine on the same side of the airplane, while air for the upper nozzle is cross ducted from the opposite engine. This arrangement reduces the asymmetry which would occur should an engine fail during takeoff, approach, or landing. The purpose of all this is to augment the thrust from the ejector nozzle and also to induce airflow over the surface of the wing which increases its lift. The aft portion of the lower surface of the flap is hinged so that it can be closed thereby choking the augmentor and spoiling the lift. The outboard chokes are used for lateral control while the inboard chokes are modulated for direct lift control. Additional lateral control is obtained from drooped ailerons provided with BLC and from spoilers located in front of the ailerons.

The hot gases from the Spey engines are exhausted through Pegasus-type swiveling nozzles which are located on both sides of each engine nacelle. They can be positioned from nearly straight aft to slightly forward of the vertical and are controlled by levers located adjacent to the overhead throttles in the cockpit. During the approach where the nozzles are deflected nearly normal to the flight path, they contribute about 1800 newtons (8000 lb) of direct lift to the airplane. However, this is only a small part of the powered lift that is achieved by the augmentor wing as shown in figure 5. This bar graph compares the airspeed that corresponds to a given angle of attack with varying amounts of thrust. The center bar represents our nominal approach conditions, 65 knots at 4° angle of attack, utilizing about 2/3 of the available thrust. If there were no thrust, the airspeed corresponding to this angle of attack would increase to 100 knots. The thrust from the swiveling nozzles would account for only about 7 knots of this difference. Applying maximum thrust, which might occur during a wave off, would decrease the airspeed by about 10 knots.

32

Following the initial documentation and proof-of-concept flight testing,
the aircraft was equipped with STOLAND. This is an experimental digital
avionics system which, through its computer, sensors and servos, can drive
any or all of the primary and secondary controls. This allows us to indepen-
dently vary the lift, drag and stability characteristics of the augmentor wing
so as to represent the response characteristics of a wide range of aircraft
of this class. Subsequent flight testing has emphasized the examination of
STOL handling qualities over as broad a range of these characteristics as is
practical.

Most of these flight tests were conducted at a Naval Auxiliary Landing
Facility called Crows Landing, located in the San Joaquin Valley of California.
The approaches were conducted on a 7-1/2° glide slope with guidance provided
by an experimental microwave landing system called MODILS. Some of these
approaches were hooded to simulate instrument meteorological conditions. The
landings were made to a 518 m × 30 m (1700 × 100 ft) STOL strip marked out on
one of the main runways.

DISCUSSION OF RESULTS

The environment in which the airplane has operated, in terms of wind and
turbulence, is indicated in figure 6. The points represent the maximum wind
velocities and direction relative to the landing runway. The lines extending
from the points indicate the gust factor. The grid resolves them into their
headwind and crosswind components. These are tower reported winds which do not
accurately depict the conditions at the touchdown zone but are at least
representative. Approaches with headwinds of 30 to 40 knots and 10- to
15-knot gusts were negotiated without great difficulty although they did take
a considerable length of time and were sometimes subject to large flight path
excursions. Landings with crosswind components in excess of 20 knots were
relatively easy even though the decrab maneuver of some 20° required full
rudder. The most critical condition in terms of both safety and performance
was approach and landing with a tailwind component. The higher descent rates
tax the capabilities of both the aircraft and the pilot, and landing distance
increases dramatically. This is illustrated in figure 7 which depicts the
results of some landing performance tests. These landings were performed
on two back-to-back flights, the first of which was made with a light tail
wind which steadily increased to about 10 knots as the flight progressed.
The second set of landings was made into the wind. It is apparent that as the
wind velocity approaches 10 knots, landing with the wind rather than into it
effectively doubles the stopping distance.

It was recognized early in the design of the augmentor wing that stabil-
ity augmentation would be required to achieve satisfactory handling qualities.
This is typical of those aircraft which operate at high lift coefficients and
low dynamic pressure. The initial flight tests were made with a lateral-
directional SAS which provided positive spiral stability, increased roll and
yaw damping, and improved turn coordination. Later in the program, more
advanced augmentation schemes were examined. Attitude command and rate-

33

command attitude hold were evaluated in both the pitch and roll axis. With attitude command, the ability to return the aircraft to wings level and trimmed pitch attitude was appreciated by the pilots; however, the sustained control forces and deflections required when maneuvering in either pitch or roll were objectionable. With those configurations which required pitching the aircraft for flight path control, the trim button which was used to change the reference pitch attitude became a primary but somewhat awkward controller. Because of this the pilots settled on rate command attitude hold as the basic SCAS configuration. It should be pointed out that acceptable STOL approaches and landings were performed without any SAS or SCAS in light to moderate turbulence, but only under visual flight conditions.

Having arrived at an acceptable stability and control augmentation scheme, we proceeded to examine those characteristics which are peculiar to powered lift. These, of course, occur primarily in the longitudinal axis as shown in figure 8. With conventional aircraft, the thrust exerts a force along this axis which in steady flight balances the drag force. Changes in thrust produce a longitudinal acceleration.

The concept of powered lift implies that the lift produced by the wing is dependent upon the amount of thrust applied. In order to achieve a low approach speed and maintain a steep descent angle, the thrust must be also deflected or turned so as to properly balance the longitudinal and normal forces. In this example, the thrust vector includes the contribution of both the cold air from the flap nozzle and the hot gases from the swiveling nozzles. Changes in thrust now increase the lift which produces more change in normal force than longitudinal acceleration and in some cases may even cause the aircraft to decelerate when thrust is increased. This provides the pilot with a powerful means by which he can change flight path angle but leaves him somewhat at a loss as to how to manage airspeed control. In the case of the augmentor wing, the swiveling nozzles which divert the hot gases from the Spey engines provide an effective means of changing airspeed. As the pilots gained experience and familiarity with the airplane, they learned to use the nozzles in conjunction with the throttles to adequately control the flight path (and airspeed). However, in the presence of turbulence and wind shears, the pilot workload became quite high and there was sometimes confusion as to which set of levers to move first. In an IFR environment, glide slope tracking was poor, therefore the pilots concluded that the use of three different controllers for the management of the longitudinal task was too much to cope with for everyday operation.

Leaving the nozzles fixed at some predetermined value requires the pilot to control airspeed by changing pitch attitude. If the effective thrust turning exceeds about 80°, adverse coupling can occur between thrust and longitudinal acceleration which will compound the control problem. As thrust is increased at constant attitude, airspeed decays, which puts the aircraft further on the backside of the thrust required curve. As this occurs, the flight path response diminishes and the pilot is forced to add still more power. The problem is illustrated in figure 9 which is a time history of an approach with a configuration which has substantial adverse thrust-airspeed coupling.

34

Glide slope intercept is from above and is initiated by a change in pitch. Tracking is accomplished with thrust while attitude is held relatively constant. At about 80 sec the aircraft starts to descend below the glide slope which prompts the pilot to add thrust. Airspeed decays though, and the aircraft descends still lower until the thrust is at the maximum allowable and the airspeed is well below the desired value.

The obvious solution to this problem, to everyone but the pilot, is to lower the nose to gain airspeed. However, to be effective, this requires a fairly large change in attitude — at least $5°$, and the initial response of the airplane is to descend even steeper. Furthermore, the recovery time to regain airspeed is such that the approach had best be abandoned.

One question which the pilot must address with a powered-lift aircraft is how much power can be used in the approach. Assuming he has the option of changing the inclination of the effective thrust vector by either flap or nozzle deflection or by some other means, he can increase the amount of thrust used and thereby reduce the approach speed while maintaining the low effective lift to drag required for the steep flight path angle. In other words, the approach speed depends upon the amount of thrust used; but the margins in terms of flight path capability depend on the excess thrust available.

Our pilots felt that they would like to have the capability of achieving level flight without requiring a change in configuration. Assuming that this performance is available under standard conditions, the pilot must also concern himself with what adjustments must be made to accommodate temperatures above standard and higher altitudes. Figure 10 presents a chart which was used for this purpose with the augmentor wing. It allows the pilot to determine what rpm is required to achieve the thrust that would be realized on a standard day. For example, our approach speed was predicated on a nominal 93 percent rpm for standard day conditions. For a day on which the temperature was 10 degrees above standard, 94.5 percent rpm would be required, and if in addition, the field elevation was 1000 m (3280 ft), about 97 percent would be needed. Under these conditions, there would be insufficient thrust remaining to allow adequate flight path corrections. In this case our pilots would select a lesser nozzle deflection and accept a higher approach speed with its reduced thrust requirement.

SUMMARY OF OPERATING PROBLEMS AND CONSEQUENCES

Perhaps the greatest asset of a STOL airplane in terms of safety is its low closure rate to the intended touchdown point. It allows the pilot time in which he can observe, react, and make corrections. Powered lift is an attractive means of achieving this performance while still maintaining the high speed cruise and efficiency of a jet airplane. There are, however, certain operating problems which are inherent to the concept. Some of these

are listed in table I along with the implications they might have on either
the design or operation of the aircraft. They are divided into two categories,
the first of which includes those problems which are brought about by
operating at low dynamic pressures and high lift coefficients. Our experience
has shown that the low aerodynamic stability and damping associated with this
condition will require some form of augmentation in order to provide satisfac-
tory handling qualities. The effect of wind naturally becomes more pronounced
as its velocity becomes greater relative to the approach speed. More direc-
tional control is required to accommodate the higher sideslip or crab angles
associated with a given crosswind component. In addition, turbulence or
gustiness will probably dictate a requirement for increased flight path
control. Runways whose length is determined by no-wind stopping distance are
comfortable to land on in a head wind but suddenly become too short with a
light tailwind component.

The second category includes operating problems which are the direct
result of powered lift. The first three of these are the subject of discussion
in reference 1. I would like to comment on them from the viewpoint of a pilot.
The first two items should actually go together, since the adverse effects of
speed variations are due in part to the poor ability to control airspeed.
Because of the operation on the backside of the thrust required curve, these
aircraft will probably experience greater flight path excursions when encoun-
tering wind shears. Airspeed management through the use of an additional
controller to be operated by the pilot seems impractical, so some form of
automatic speed stabilization may be required. Adverse coupling can, of
course, be minimized by design, but if the full performance benefits of the
powered lift system are to be realized, some form of control augmentation
may be required. The final item is a fact of life which must be accounted for
in the day-to-day operation of this type of aircraft. The use of flat-rated
engines will alleviate the situation because takeoff thrust will be available
under all conditions up to the rating limits. However, charts will still have
to be used to determine proper thrust settings, and operation outside these
limits will sometimes require a configuration change if adequate safety
margins are to be preserved.

REFERENCE

1. Franklin, James A.; Smith, Donald W.; Watson, De Lamar M.; Warner,
     David N., Jr.; Innis, Robert C.; and Hardy, Gordon H.: Flight
     Evaluation of Advanced Flight Control Systems and Cockpit Displays for
     Powered-Lift STOL Aircraft. Aircraft Safety and Operating Problems,
     NASA SP-416, 1976. (Paper no. 4 of this compilation.)

TABLE I.- SUMMARY

Operating problems	Consequences
Due to low speed Reduced stability and damping Effects of wind and turbulence	SAS or SCAS required Increased control required Field length more sensitive to wind
Due to powered lift Poor ability to control airspeed Adverse effects of speed variation Possible adverse coupling between thrust and airspeed Increased effect of temperature and altitude on landing performance	More sensitive to wind shear May require speed stabilization Can be minimized by powered-lift system design May require SCAS Landing performance must be computed like takeoff performance
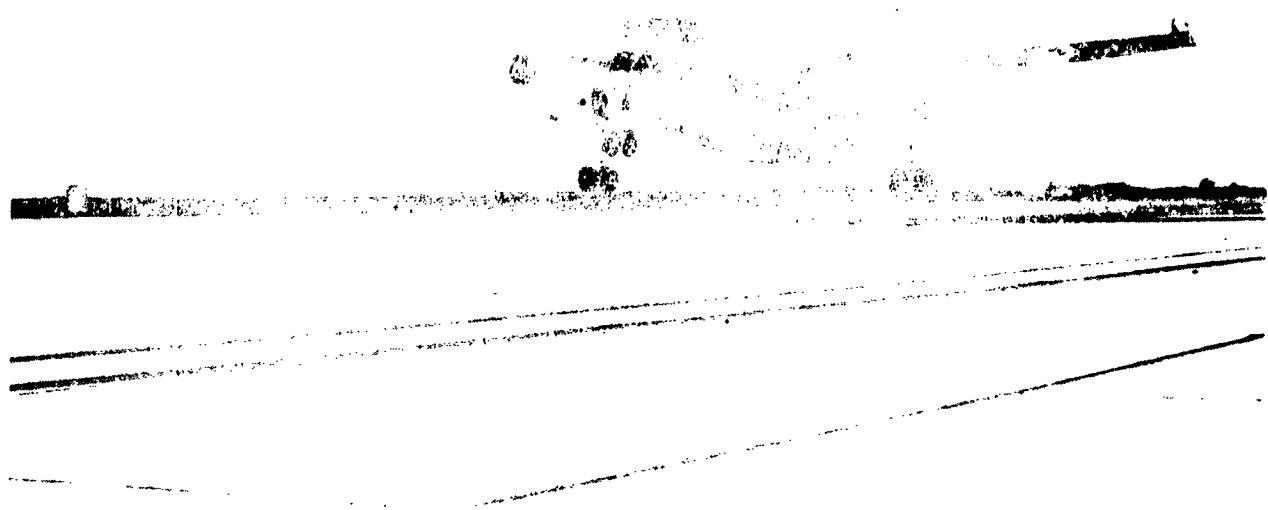
Figure 1.- Operational experience of [...] aircraft.
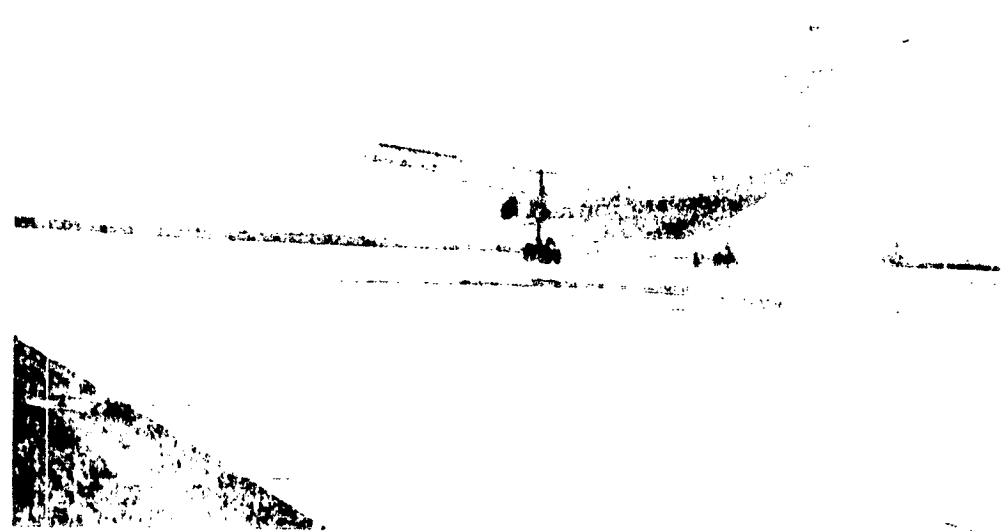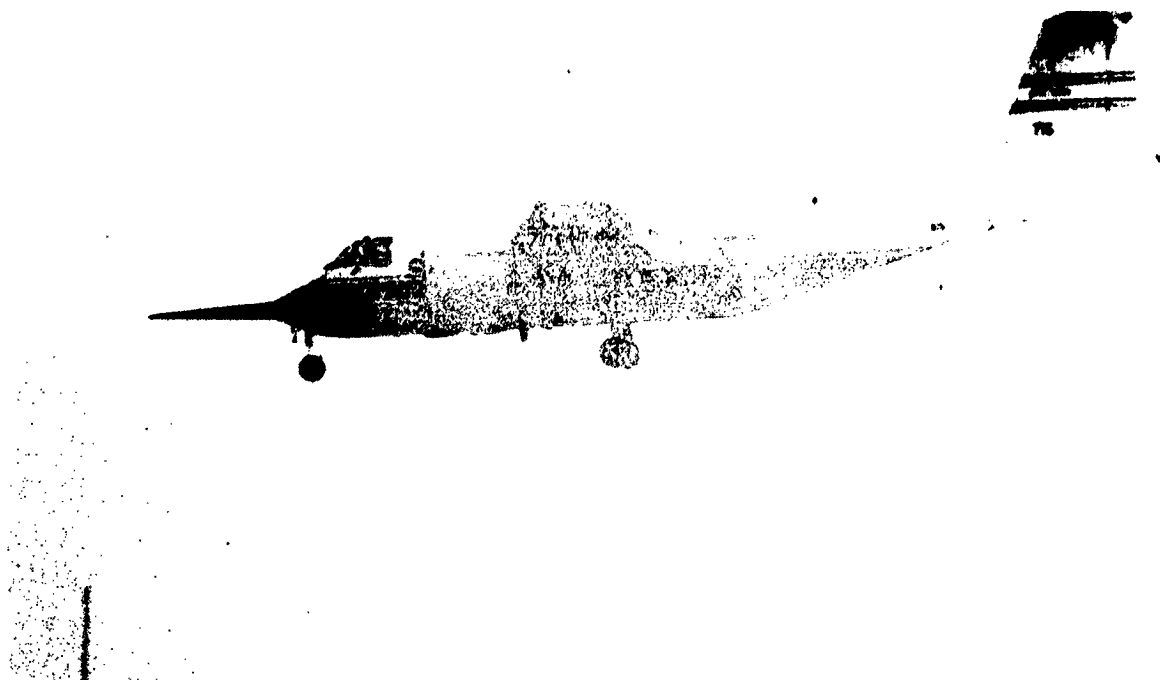
Figure 3.- Augmentor wing research aircraft approach.

INNER DUCT

OUTER DUCT

FLAP PIVOT

FLAP

SHROUD

CHOKE
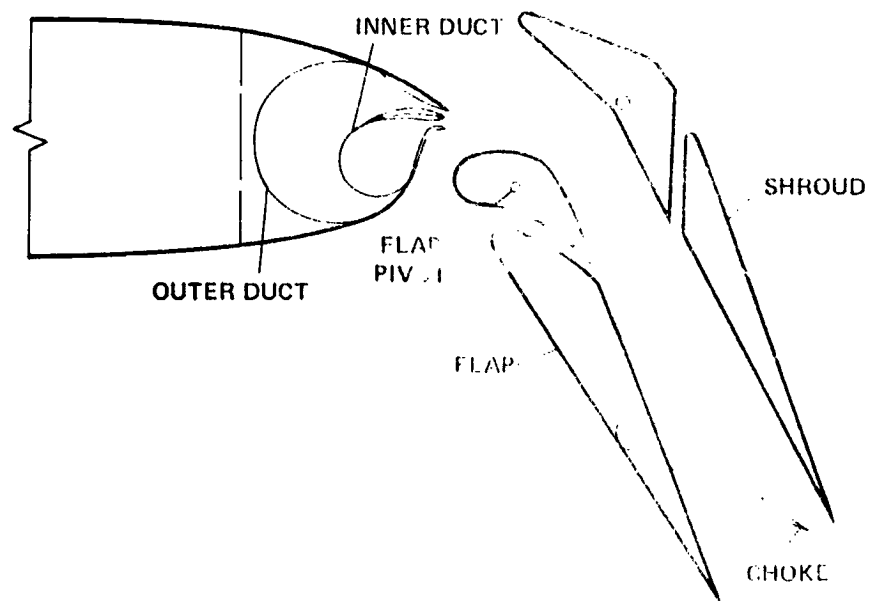
Figure 4.- Augmented jet flap.

**SEA LEVEL
STANDARD DAY
GROSS WEIGHT, 18,700 kg**
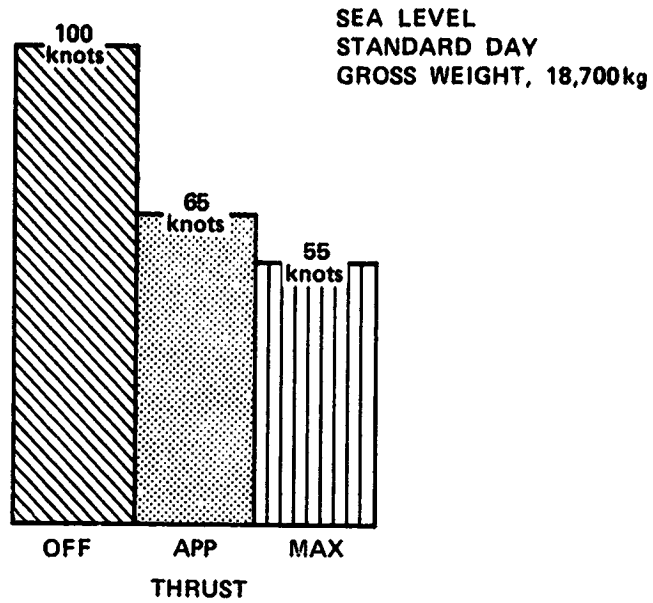
Figure 5.- Effect of thrust on approach airspeed constant angle of attack (4°).
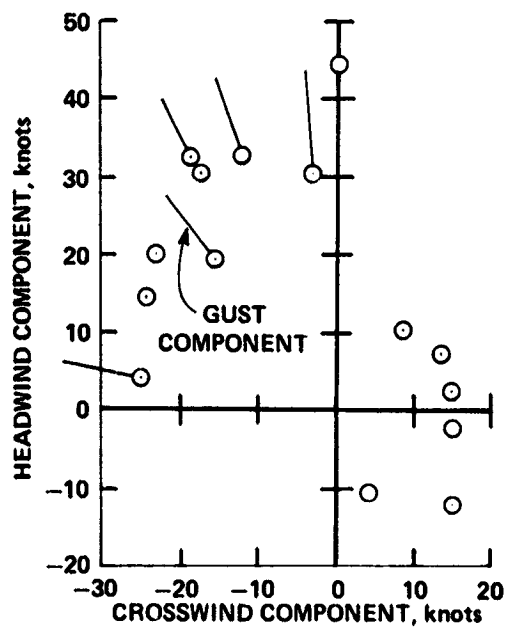
Figure 6.- Maximum wind conditions encountered in flight tests.

40
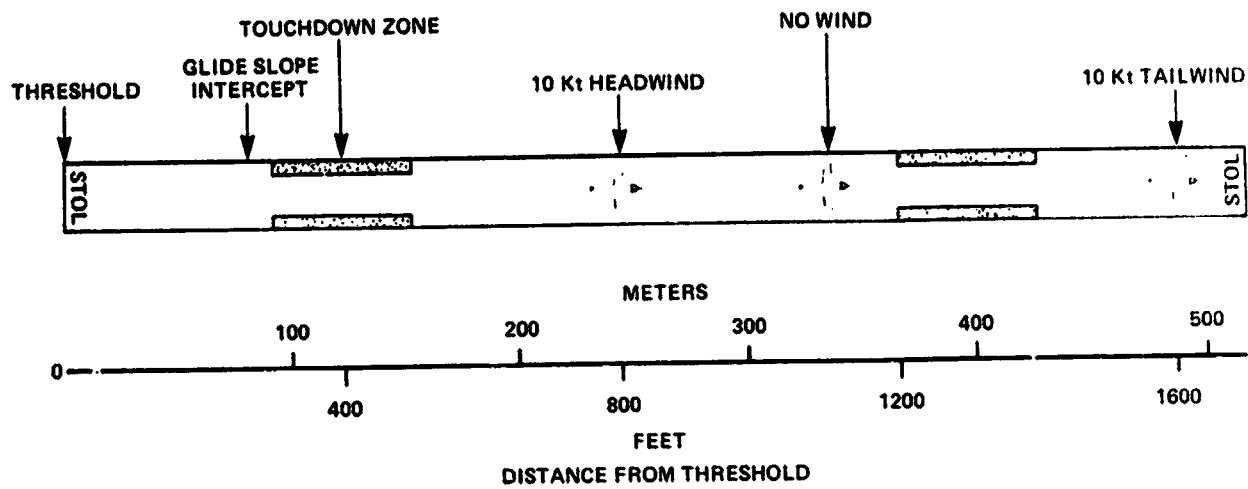
Figure 7.- Effect of wind on landing distance.
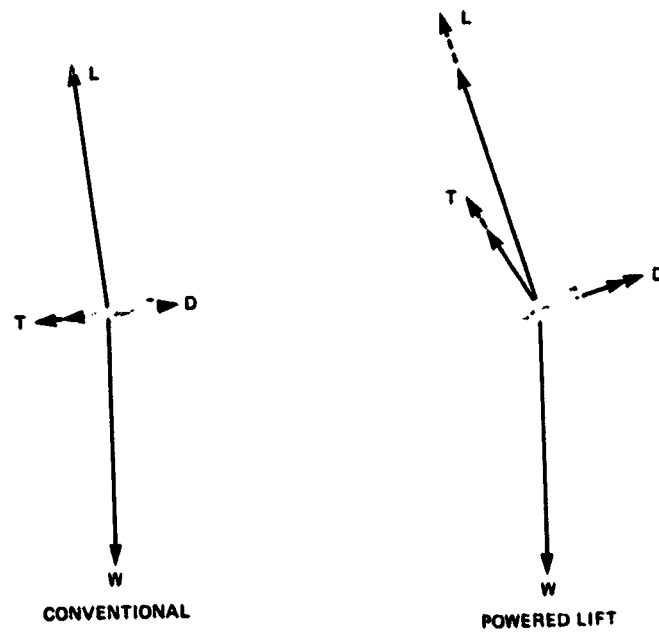
Figure 8.- Effect of thrust variation.

41
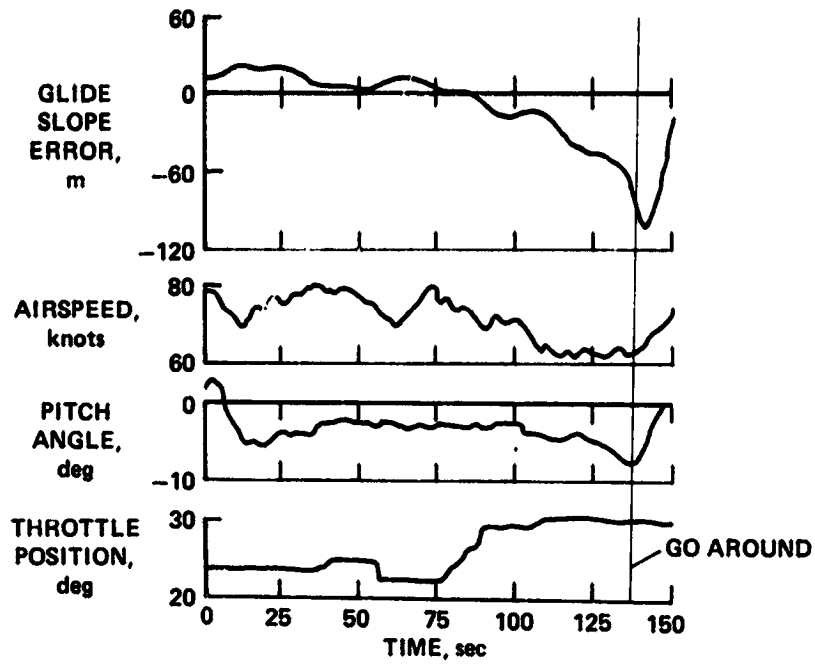
Figure 9.- Effect of thrust-airspeed coupling.
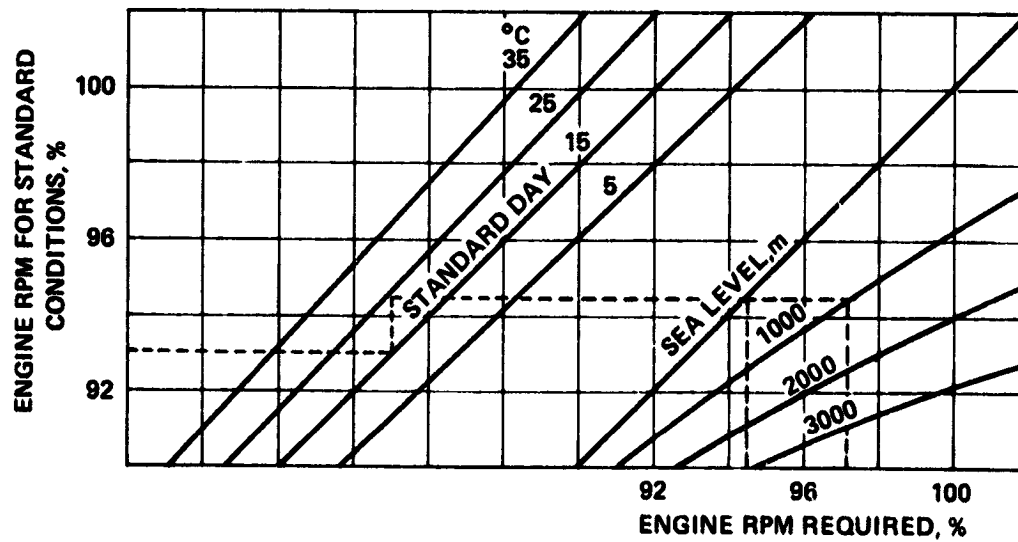
Figure 10.- Effect of temperature and altitude on approach thrust.

FLIGHT EVALUATION OF ADVANCED FLIGHT CONTROL SYSTEMS AND COCKPIT

DISPLAYS FOR POWERED-LIFT STOL AIRCRAFT

James A. Franklin, Donald W. Smith, De Lamar M. Watson,
David N. Warner, Jr., Robert C. Innis, and Gordon H. Hardy

NASA Ames Research Center

SUMMARY **N77-18084**

4

A flight research program was conducted to assess the improvements, in longitudinal path control during a STOL approach and landing, that can be achieved with manual and automatic control system concepts and cockpit displays with various degrees of complexity. NASA-Ames powered-lift Augmentor Wing Research Aircraft was used in the research program. Satisfactory flying qualities were demonstrated for selected stabilization and command augmentation systems and flight director combinations. The ability of the pilot to perform precise landings at low touchdown sink rates with a gentle flare maneuver was also achieved. Flight research is in progress to demonstrate fully automatic approach and landing to Category IIIa minimums.

INTRODUCTION

Demands which are anticipated to be placed on the operation of STOL transport aircraft due to requirements for precise glide-slope tracking, short field landing performance, acceptable landing sink rates, and adequate safety margins, are expected to dictate a precision of control during the transition, approach, and landing exceeding that which is realized by current-generation jet transport aircraft. The ability of STOL aircraft, particularly those utilizing substantial amounts of powered-lift, to meet these demands may be impeded by tendencies toward sluggish and highly coupled response associated with the low-speed operation, high wing-loading, and substantial thrust turning representative of these designs. For example, pitch attitude control is compromised by poor static stability, by substantial trim changes due to thrust and flaps, by turbulence disturbances, and by an easily excited phugoid mode. Left unattended, the phugoid substantially upsets flight-path and airspeed and degrades glide-slope tracking during the approach. Even if precise attitude control is achieved, the aircraft's response to pitch attitude is adversely influenced by operation at low speed and on the backside of the drag curve (at speeds where induced drag exceeds profile drag). Sluggish initial flight-path response to pitch attitude and the inability to sustain long-term path corrections with a change in attitude make path control with attitude unsuitable. While thrust is a very powerful path control, coupling of flight-path and airspeed (as a consequence of large effective thrust turning angles) and thrust response lags make thrust control of flight path unsatisfactory or even unacceptable. Consequently, it may be necessary to develop flight control and

display concepts that improve the inherent control characteristics of this type of aircraft if the operational requirements are to be met.

The Ames Research Center's Augmentor Wing Research Aircraft is a propulsive-lift jet STOL transport that, because of its configuration and operational flight conditions, exhibits some of the control characteristics noted in t^ foregoing discussion. The aircraft was developed for the purpose of demonstrating the augmented jet flap concept for powered-lift STOL operation and to provide a powered-lift STOL transport aircraft for flight dynamics, navigation, guidance and control, and STOL operations flight research. It was initially procured with flying qualities sufficient to permit the exploration of its flight envelope and to demonstrate the performance, stability and control characteristics associated with the augmented jet flap. Following the proof-of-concept flight tests, a versatile digital avionics system and an array of cockpit displays were installed in the aircraft to extend its capability to support the research program noted above. Two major efforts have been under way to

- define and evaluate stabilization and command augmentation systems (SCAS) and displays for improving flying qualities associated with a manually flown IFR approach and landing

- define and determine the approach and landing performance and pilot acceptance of fully automatic flight control systems and associated displays for visibility conditions down to Category IIIa.

Among the more challenging tasks for either the pilot or an automatic system to perform with these aircraft is glide-slope tracking and flare to a precise touchdown. The following sections describe the results to date of flight research conducted to assess the improvement, in longitudinal path control during the approach and landing, which can be achieved for a given degree of control system and display complexity. Although these control systems and displays have been demonstrated on a specific powered-lift concept, the nature of the path-control improvement is considered to be applicable to other powered-lift aircraft configurations.

SYMBOLS

IFR	instrument flight rules
MLS	microwave landing system
VFR	visual flight rules
Z_{δ_T}	vertical acceleration derivative with respect to the throttle control
$\Delta u_{ss}/\Delta\gamma_{ss}$	ratio of change of steady-state airspeed to flight path due to a change in thrust at constant pitch attitude

44

$d\gamma/du$ — gradient of flight with airspeed at the stabilized approach condition — constant thrust

$\Delta\gamma_{MAX}/\Delta\gamma_{ss}$ — ratio of the peak to steady-state change in flight path due to a change in thrust at constant pitch attitude

$\Delta\gamma_{MAX}/\Delta\theta_{ss}$ — ratio of the peak change in flight path to the steady-state change in pitch attitude

$\Delta\gamma_{ss}/\Delta\theta_{ss}$ — ratio of the steady-state changes in flight path to pitch attitude

DESCRIPTION OF THE BASIC AIRCRAFT

The Augmentor Wing Research Aircraft (fig. 1) a de Havilland C-8A Buffalo, modified by The Boeing Company, de Havilland of Canada, and Rolls Royce of Canada to incorporate a propulsive-lift system. It has a maximum gross weight of 21,792 kg (48,000 lb) and a range of operational wing loadings of 215-272 kg/m^2 (44-55 lb/ft^2). The propulsive-lift system utilizes an augmentor jet flap designed for deflections up to 75°. Rolls Royce Spey MK 801-SF engines power the aircraft with fan air, used to blow the augmentor flap, and with hot thrust which can be deflected over a range of 98° through two conical nozzles on each engine. Primary flight controls consist of a single-segment elevator for pitch maneuvering and trim; ailerons, spoilers, and outboard augmentor flap chokes used in combination for roll control; a two-segment rudder for yaw control; vectored hot thrust for path and speed control; and inboard augmentor flap chokes for lift control. A more detailed physical description of the aircraft and its characteristics is given in reference 1.

Before describing the SCAS, display, and autopilot concepts investigated in this research program, it is useful to review the flight-path control characteristics of the basic aircraft and to identify the objectives for improving flying qualities. Longitudinal path control can be accomplished during the approach and landing by either modulating thrust or deflecting the hot thrust component; however, neither the throttle nor nozzle controls are satisfactory for approach or flare control. Since the approach is conducted on the backside of the drag curve, pitch attitude is primarily used for speed control. Sufficient, short-term path control in response to attitude exists to provide at least marginally acceptable flare and landing precision.

Figure 2 illustrates the aircraft's stabilized path control capability using either throttle or nozzle controls. Throttle control characteristics are shown at the left for the approach flap setting, a nominal approach thrust vector angle of 80°, and for thrust levels corresponding to engine speeds from 90 percent rpm to a maximum setting of 100 percent. A typical approach would be conducted on a 7.5° glide slope at a speed of 65 knots. At the approach speed, the aircraft is only capable of achieving flight-path angles from -4° to -11° for this range of thrust settings. If pitch attitude is maintained constant by the pilot or by an attitude stabilization system, this path control capability is reduced to a range from -4.8° to -9.9° as a consequence of flight-path/airspeed coupling ($\Delta u_{ss}/\Delta\gamma_{ss}$ = -2.2 knots/deg) and the operation on the backside

45

of the drag curve. The steady flight-path/speed relationship at constant thrust for the backside condition is $d\gamma/du = 0.15°$/knot and it degrades climb and descent performance when speed is allowed to vary about the approach reference.

Flight-path control capability that can be achieved by deflecting the nozzles at a nominal approach thrust setting of 94 percent rpm is illustrated at the right. The flight-path envelope is expanded over that available using thrust control, with capability of achieving path angles of $2.7°$ to $-13.3°$ for the maximum range of nozzle angles from $6°$ to $104°$. The relationship of path and speed response to the nozzle control at constant attitude is conventional in that positive path increments are accompanied by increased airspeed and vice versa.

The transient response of flight-path and airspeed to thrust for constant attitude is shown in the time histories of figure 3. Flight-path initially responds quickly to the change in thrust and with an acceptable throttle sensitivity ($Z_{\delta_T} = -0.04$ g/cm or -0.1 g/in.). The equivalent first-order thrust time constant is approximately 0.75 sec. However, the initial path response washes out to a lower value ($\Delta\gamma_{MAX}/\Delta\gamma_{ss} = 2.1$). Airspeed response is decidedly unconventional in that speed decays following an increase in thrust and is in turn reflected in the constant attitude path-speed coupling noted previously.

Time histories of path and speed response to the nozzle control at constant attitude are also presented in figure 3 for comparison with thrust control characteristics. The initial path response to nozzle deflection is sluggish compared to the response to a thrust increment and the response may not be sufficient for tight glide-slope tracking in turbulence. If quicker path response is desired, the pilot must initiate the correction with pitch attitude and follow-up with the nozzle control to sustain the long-term correction. Coupling between flight path and airspeed at constant attitude is conventional as was previously noted. Some pitch control may be coordinated with the nozzle control if the pilot desires to maintain airspeed.

These characteristics of flight-path and airspeed response to the throttle and nozzle controls dictate that the throttles be used for precise glide-slope tracking and that the nozzles be used to augment thrust control for gross path corrections. Due to the amount of flight-path overshoot and path-speed coupling associated with thrust control, it is difficult for the pilot to anticipate the amount of thrust required to initiate and stabilize a path correction. As a consequence, he must devote considerable attention to path and speed control. Attitude control may be used to reduce path-speed coupling by coordinating attitude changes with the thrust control to minimize the speed excursions. However, this requirement for continuous control in the pitch axis increases the pilot's control workload for glide-slope tracking. Furthermore, the control technique is unfamiliar in that nose-down attitude changes are required to maintain speed when the pilot increases thrust to reduce the descent rate, and vice versa.

Raw data IFR glide-slope control down to a decision height of 60 m (200 ft) with the throttles alone was given pilot ratings of 5 to 6. These ratings were based on the Cooper-Harper scale of reference 2 and were due to large path-speed coupling and unpredictable flight-path response. Path-control authority was also considered insufficient for glide-slope tracking in turbulence. As a

consequence, glide-slope control required coordinated use of the throttles and nozzle controls and still was given pilot ratings of 5 to 6 due to the sluggish path response to changes in the nozzle deflection and the workload associated with manipulation of the various controls.

The landing flare was routinely performed by pitching the aircraft to a touchdown attitude with some adjustment in thrust to offset high angles of attack or high sink rates at flare entry or to compensate for any floating tendency. Response of the aircraft to the pitch rotation develops adequate normal acceleration to check the sink rate to an acceptable level ($\Delta\gamma_{MAX}/\Delta\theta_{ss} = 0.55$). However, a pitch rotation on the order of 10° at a rate of 2 to 3°/sec is required to check the sink rate to 1.8 m/sec (6 ft/sec) and this is considered unsatisfactory for commercial operation. Flare and landing accomplished primarily using pitch with an assist as required from thrust was given ratings from 3-1/2 to 5.

In summary, the requirement to coordinate the use of three controls for precise tracking and to establish the proper flare conditions presented the pilot with an unsatisfactory workload. As a consequence, it is desirable to improve approach path control by eliminating the path-speed coupling, by reducing the number of controls required for path control, by quickening path response for glide-slope tracking and flare, by desensitizing response to winds and turbulence, and by providing better tracking commands to the pilot.

DESCRIPTION OF THE FLIGHT RESEARCH PROGRAM

To achieve desired improvements in control and reductions in pilot workload, combinations of experimental SCAS, display, and autopilot configurations were chosen for evaluation in the flight research program. The SCAS configurations that were evaluated are described in table I. The program proceeded with a buildup in complexity of the control system for improving manual path control, including a throttle-nozzle interconnect to reduce the number of path controllers and to provide path-speed decoupling; speed stabilization to eliminate the backside of the drag curve operation and to reduce the requirement for thrust modulation; and flight-path SCAS to allow the pilot to control the flight-path vector with pitch attitude so as to reduce the path-tracking requirement to a single control. A fully automatic system was also mechanized for glide-slope capture, tracking, and flare. Evaluations of various displays were obtained for selected SCAS options and for the autopilot mode. Raw data glide-slope tracking was assessed for all the SCAS configurations. A flight director was evaluated for straight-in approaches with the throttle-nozzle interconnect and with the flight-path SCAS, and as an approach monitor for the automatic flight mode. Detailed descriptions of the flight control and display modes are subsequently provided with the discussion of results obtained during the flight experiments. Pitch, roll, and yaw SCAS was provided with all configurations.

Landing approaches were flown on a 7.5° glide slope at airspeeds from 65 to 70 knots to landings on a 30 m by 518 m (100 ft by 1700 ft) STOL runway at NASA Ames' experimental flight facility at the Crows Landing Naval Airfield. Landing approach guidance was provided by a prototype microwave landing system

47

(MODILS). Research pilots from NASA Ames, the Canadian Department of Transport and National Aeronautical Establishment conducted the flight evaluations in this program. Both VFR and IFR approaches were flown in calm to light wind conditions. Additional evaluations were obtained when possible with surface conditions ranging from strong headwinds to light tailwinds and in light to moderate turbulence. Pilot commentary and opinion ratings based on the Cooper-Harper scale were obtained for all configurations. The pilots' assessments of the acceptability of the manually controlled flare and touchdown were based on the consistency of landing performance (touchdown point and sink rate) which could be achieved for a particular configuration rather than on the ability to land at a specific point within a prespecified sink rate. Flared landings were performed to reduce the approach sink rate (4.3 m/sec or 14 ft/sec) to levels well within the aircraft's landing gear limits (3.8 m/sec or 12.6 ft/sec).

DESCRIPTION OF THE EXPERIMENTAL FLIGHT CONTROL SYSTEM AND DISPLAYS

The aircraft's primary flight controls described previously can be driven through servos commanded by an experimental digital avionics system (STOLAND). This system was developed for NASA Ames by Sperry Flight Systems and is described in reference 3. The major components of the system are a Sperry 1819A general-purpose digital computer and a data adapter to interface the aircraft's sensors, controls, displays, and navigation aids. The controls used for longitudinal path tracking are the elevator for pitch attitude stabilization and the inboard augmentor chokes, throttles, and nozzles for vertical path and airspeed control. The pitch stabilization system is driven by an electro-hydraulic series servo actuator limited to 38.5 percent of total elevator authority. The inboard augmentor flap chokes are full authority controls which are also driven by electro-hydraulic servos. The Spey engines' throttles and hot thrust nozzles are driven by electro-mechanical parallel servos with full control authority. Commands to these controls appropriate for the various SCAS or automatic modes of interest are generated through suitable combinations of sensor information processed when necessary by complementary filters to retain high frequency content while removing undesirable noise or gust disturbances.

The primary instrument displays and system mode controls available to the pilot are an electronic attitude director indicator (EADI), which presents pitch and roll attitude; aerodynamic flight path; raw glide-slope and localizer deviation; and calibrated airspeed, vertical speed, and radar altitude in digital readout. Flight director command bars can be called up on the display if desired. A multifunction display provides a moving map presentation of the aircraft's position with respect to the desired flight path, as well as heading and altitude status information. A mechanical horizontal situation indicator (HSI) presents aircraft heading and bearing to the navigational aid as well as glide-slope and localizer deviation. A mode select panel provides switches for engaging SCAS modes, the flight director, and various autopilot modes. A keyboard and status display on the center console permits manual entry and readout of instructions to the digital computer.

DISCUSSION OF RESULTS

Results of manual control for raw data IFR approaches with the various SCAS modes will be reviewed first. Contribution of these modes to control of the flare and landing will be noted where appropriate. Next, the influence of improved displays on manually flown approaches will be discussed. Finally, experience to date with fully automatic glide-slope tracking modes will be reviewed. A summary of pilot ratings for the manual SCAS modes for raw data IFR and flight director displays is provided in table II. The results shown encompass the range of pilot ratings obtained in the flight evaluations for each experimental configuration.

Contribution of Manual SCAS Modes

Throttle-nozzle interconnect — A simple means for reducing the flight path-airspeed coupling and improving closed-loop flight-path control for the basic aircraft can be provided by interconnecting the aircraft's throttle and nozzle controls. This interconnect is mechanized by a constant-gain linear crossfeed from the throttle to the nozzle control servo. The sense of this interconnect is to reduce the hot thrust deflection for an increase in thrust, and vice versa. An illustration of the influence of this interconnect on the aircraft's performance envelope is presented in figure 4 for a value of the interconnect gain which essentially eliminates path-speed coupling at constant attitude for the approach condition. The contours on the diagram are for constant throttle position and nozzle angles. In comparison to the performance envelope of the basic aircraft, which is reproduced on the figure, this control configuration provides a substantial increase in path-control capability. A positive climb angle of 1.7° can now be generated at 100 percent rpm, while a quite steep descent of -14.5° can be obtained at 90 percent rpm. Improvements in dynamic path response can also be recognized in the time histories for a step thrust application shown in the figure. Flight-path responds quickly with no overshoot, and very little change in airspeed is noted. This behavior would permit the pilot to track the glide slope with the throttle alone and not require significant pitch control to improve path response or maintain speed.

Pilot ratings from 4-1/2 to 5 for raw data IFR operation to a 60 m (200 ft) decision height represented some improvement over the basic aircraft and were a consequence of the improved path response and reduced workload for speed control. The requirement to modulate both the throttles and nozzle controls for glide-slope tracking is relieved and with the disturbances to speed reduced substantially, the approach can be flown with a single control, the throttle. Increased path-control authority provides better capability for coping with disturbances due to turbulence and wind shears. The primary remaining deficiency in path tracking and one that accounts for the unsatisfactory pilot rating is the instrument scan workload for lateral path tracking associated with the raw data display. No modification of flare control characteristics or technique is associated with this configuration.

49

<u>Airspeed stabilization</u> — Another means of eliminating the flight-path/ airspeed coupling induced by thrust control is to stabilize airspeed at the selected approach condition. By prohibiting significant variation in airspeed response to thrust, the dynamics of flight-path response to thrust can be improved to the same extent as that provided by the throttle/nozzle interconnect. Speed stabilization also inhibits the backside of the drag curve characteristics associated with the aircraft's response to pitch attitude variations thus permitting attitude to be used for flight-path control. This system also reduces variations of speed and flight-path in response to longitudinal gust components.

The system operates by driving the nozzles in proportion to speed error. In the approach condition with the hot thrust deflected 80°, incremental changes in nozzle deflection provide essentially longitudinal force control and can produce up to ±0.1 g of longitudinal acceleration within the nozzle control limits. With this authority, it is possible to counteract longitudinal force perturbations of a magnitude associated with 6° changes in pitch attitude or 1.9 knot/sec horizontal wind gradients.

Figure 5 illustrates the aircraft's dynamic response to pitch attitude at constant thrust with the speed stabilization system operating. It is apparent in the figure that, within the authority of the nozzles the aircraft is very markedly operating on the frontside of the drag curve. Substantial changes in flight path can be obtained with little change in airspeed. Capability exists to achieve level flight with no throttle adjustments although large attitude changes may be required. The dynamic response of flight path to the change in attitude occurs with no overshoot. Consequently, the pilot may use a control technique for the landing approach that relies primarily on pitch attitude corrections for glide-slope tracking and requires only infrequent adjustments in thrust for sustaining gross changes in rate of descent. When nozzle limits are reached, the aircraft's response will, of course, revert to the backside characteristics associated with the basic aircraft, and thrust modulation will be required for glide-slope corrections.

The speed stabilization system also has capability to suppress flight-path disturbances due to horizontal wind shear. When the system is engaged, it drives the nozzles to counteract the accelerations associated with the shear gradient, thereby reducing the magnitude of the change of airspeed, and consequently suppressing the source of the flight-path disturbance. As indicated previously, tne nozzle authority is equivalent to a 1.9 knot/sec horizontal gradient, which, for the nominal approach sink rate (4.3 m/sec or 14 ft/sec at 65 knots on a 7.5° glide slope) at which this aircraft is operated, corresponds to a spatial gradient of 13.3 knots/30 m (13.3 knots/100 ft). When the nozzles reach an authority limit, the pilot still has substantial capability to counteract subsequent path disturbances with an application of thrust.

Stabilization of airspeed at this selected approach reference permitted the pilot to track the glide slope with the pitch control with only occasional adjustments of thrust for large path angle changes. The flare could also be performed with pitch as it could for the basic aircraft, although some thrust reduction was required to inhibit a tendency to float. These characteristics were the basis for pilot ratings in the 3-1/2 to 4-1/2 category for raw data

50

approaches. The pilots expressed a desire for a more authoritative path control, and quicker heave responses for flight path changes on short final and for the flare maneuver. Hence, they were unwilling to give the system clearly satisfactory ratings. Speed excursions during maneuvers and in the presence of turbulence were substantially reduced by the system and hence path disturbances which would ordinarily be induced were largely suppressed.

Flight-path command and stabilization- Improvements in flight-path response for glide-slope tracking and flare can be achieved by quickening the initial path response to pitch attitude control, by providing increased steady-state path control authority with pitch attitude, and by reducing path disturbances due to winds and turbulence. To obtain these improvements, capability must be incorporated in the flight control system for quickly generating increments in lift on the order of ±0.1 to 0.2 g. This capability in the Augmentor Wing Aircraft is provided by the inboard augmentor flap chokes. In the approach configuration, the chokes have an authority of ±0.12 g. Flight-path stabilization is achieved by driving the chokes in proportion to flight-path angle error based on a reference established at the time of system engagement. Changes in flight-path can be commanded by the pilot through changes in pitch attitude which drive the chokes through the feedforward path. Additional path command quickening could be obtained through a feedforward of column force (the attitude command input); however, simulation studies indicated this additional command quickening did not produce significant improvement in path tracking.

The speed stabilization system described previously was used in conjunction with the flight-path SCAS to permit a frontside control technique to be adopted for glide-slope tracking. An indication of the quickened response and increased path control authority is shown in comparison with the basic aircraft and the speed stabilization system in figure 5. The incremental changes in path angle in response to attitude are essentially equal $(\Delta \gamma_{ss}/\Delta \theta_{ss} = 1.0)$; hence, it is possible to effectively point the flight path vector in the desired direction with the aircraft's pitch attitude. With this path quickening and path-control authority, glide-slope tracking can be accomplished through attitude control alone, thus considerably simplifying the pilot's longitudinal control workload.

This system also provides a flare capability that permits a less dramatic flare maneuver than that required for the basic aircraft to arrest the sink rate prior to touchdown. It can be seen in figure 6 that the landing sink rate for the basic aircraft is approximately 2 m/sec (6 ft/sec) as compared to 1 m/sec (3 ft/sec) with the flight path SCAS. Furthermore, where a pitch rotation in excess of 10° is required for the basic aircraft, this maneuver is reduced to approximately 5° with this SCAS configuration.

The combination of flight-path SCAS with the speed stabilization system allowed the pilot to fly the approach and to perform the landing using attitude control alone. No throttle manipulation was required other than a conventional reduction of thrust during the latter stages of the flare to counteract any tendency to float (as noted in the previous discussion). As indicated in table II, pilot ratings from 2 to 4 were given to this configuration for approach path-tracking and ratings of 2-1/2 to 3 for the flare. Favorable comments were expressed with regard to the reduced workload, the improved heave response, and more docile flare requirements. Although path disturbances due to winds and

turbulence were noticeably suppressed, this configuration offered very little better performance than the speed stabilized configuration in this regard. The pilot rating of 4 for glide-slope tracking was based on the workload associated with the instrument scan for a raw data IFR approach. Improvements in this evaluation that can be obtained with a flight director will be discussed subsequently.

Influence of Displays

Raw data — The raw data information was provided by a conventional cross pointer display located on the HSI. In comparison to a conventional ILS, the glide slope and localizer cross-pointer needles were desensitized in proportion to the approach path angle and the range from the runway landing zone to the localizer transmitter. Sensitivity was set at approximately 1°/dot for both indicators. A cross bar representing aerodynamic flight-path angle in the vertical plane was available on the EADI, superimposed on the pitch attitude scale. This display was useful in providing lead information for glide-slope acquisition and tracking, and for alerting the pilot to incipient glide-slope deviations caused by variation in horizontal and vertical winds and turbulence. An MLS box, superimposed on the EADI, offered a more integrated display for MLS tracking and a potentially reduced scanning workload for the pilot. The EADI and HSI displays are illustrated in figure 7.

Pilot evaluations for the SCAS modes noted in the previous section were performed with the raw data information. Objections were registered concerning the instrument scan workload between the EADI and HSI and one pilot could not justify a rating better than 4 for glide-slope tracking with the best SCAS configuration; this was because of the overall task workload contributed by the instrument scan. Favorable comments were given to use of the flight-path angle bar for glide-slope tracking. In some instances, the pilots felt this information improved their ability to control glide slope enough to warrant a one-half to one unit improvement in pilot rating. Although the presentation of raw MLS deviation on the EADI provided a more integrated display, the pilots felt this offered little improvement for the task because it was still necessary to refer to the HSI to get heading information for localizer tracking.

Flight director — The three-axis flight director consisted of commands for the pilot's throttle, column, and wheel controls for glide-slope and localizer tracking, maintaining the desired airspeed, and safe angle-of-attack margins. This flight director was designed for the Augmentor Wing Aircraft under contract by Systems Technology, Inc. and is described in detail in reference 4. Complementary filtered vertical velocity, vertical beam deviations and deviation rate are generated for use in holding altitude, and capturing and tracking the glide slope. When in level flight, the inputs to the pitch bar present commands to the pilot to maintain the altitude at the time the flight director was engaged. Glide-slope capture is initiated when the aircraft is within 30 m (100 ft) of the glide-slope beam. Subsequent glide-slope tracking may either be done with throttles or pitch control, depending on the flight control system configuration. Schedule changes in thrust and pitch attitude are commanded as a function of flap angle and initiation of glide-slope capture. Angle-of-attack margins are protected through commands for increased thrust introduced to the throttles when the angle of attack exceeds 10°. A limit on the thrust command

52

corresponding to maximum authorized thrust (rpm = 98.5 percent) is included in the throttle logic. Commands to maintain the reference airspeed are introduced to the pitch bar in the event a speed stabilization system is not utilized during the approach. Complementary filtered lateral beam deviation and deviation rate are generated for lateral path capture and tracking.

The flight director provided a significant reduction in scanning workload and a reduction in vertical and lateral excursions during the approach. The aircraft generally arrived at a 30 m (100 ft) decision height better established for a precise flare and landing when the flight director was used, and in these cases improvements in pilot ratings from one to two units were obtained. As indicated in table II, evaluation of the throttle/nozzle interconnect configuration was improved from pilot ratings of 4-1/2 to 5 with raw data to 2 to 3 with the director for operation to 30 m (100 ft) minimums. In this case, the director logic was structured to command vertical path control through the throttles. The flight-path SCAS configuration was given ratings of 1-1/2 to 2-1/2 with the director. For this configuration, path tracking commands were oriented to the attitude control. The throttle and choke controls were integrated by the SCAS for flight path command and stabilization.

Although very good results have been obtained with the flight director, it should not be inferred that this is the only acceptable means of improving the pilot's IFR landing guidance information. A well-integrated situation display has potential for producing similar results. However, display system limitations and the time available for further experiments did not permit these concepts to be explored in flight.

Moving map display — A simulation evaluation of the coordinated use of a moving map presentation on the electronic multifunction display (MFD) in conjunction with the HSI and EADI was carried out to define the best use of the MFD during manual approach and landing operation (ref. 5). The operation included acquisition of reference terminal area flight paths leading to the final landing approach, the approach itself, and go-arounds to and including holding patterns. These operations were flown on raw data with either the map or HSI or using the flight director for guidance with the MFD and HSI available to provide status information. An indication of the display content is provided in figure 7. While there appeared to be no consistent differences in tracking errors using the map or HSI, the pilots had more confidence in their ability to maintain geographical orientation during curved path tracking and establishing holding patterns when using the map. Course predictor and history dots permitted the pilots to better anticipate control requirements to capture the reference path, acquire and maintain the curved track, and to enter a holding pattern. The HSI provided better capability for localizer tracking during the final approach segment. Pilot evaluations of task controlability and precision, utility of status information, display clutter, and attentional workload indicated a preference for the map although it was felt that improvements could be made on this display as well as on the HSI cr EADI displays. One suggested improvement was to include a heading scale on the EADI; in combination with the MLS deviation data on this instrument the heading scale could eliminate the need to refer to the HSI during the final approach.

Automatic Glide-Slope Tracking Modes

To date, approximately 105 automatic approaches and 25 automatic landings have been made using the STOLAND flight control system. The early results have been characterized by glide-slope deviations of ±8 m (±25 ft) accompanied by significant fluctuations in rate of climb and engine rpm with resulting inconsistent flare entries. Steps have been taken to improve the glide-slope tracking performance and to make the flare entries consistent. The results to be presented demonstrate some of the problems related to providing good glide-slope tracking for STOL aircraft and one solution to these problems.

In normal cruise flight the STOLAND automatic control system uses pitch attitude to maintain path tracking and the throttles to control airspeed. When the aircraft is in the STOL approach mode the control functions are reversed such that throttles are used for vertical path tracking and pitch attitude is used to maintain airspeed.

Figure 8 indicates that with the original automatic system design, the aircraft oscillates about the nominal -7.5° glide slope with a 10- to 12-sec period and engine rpm varies from 92 to 98 percent. Gain optimization studies carried out in flight and on the simulator showed that little improvement could be achieved using the existing autothrottle system. Due to hysteresis in the throttle-fuel control, the automatic system apparently has inadequate bandwidth for good glide-slope tracking. Consequently, the augmentor chokes were introduced to quicken and improve the precision of path control. Figure 8 shows the significant improvement in the glide-slope tracking resulting from the use of direct lift control through chokes. The glide-slope error has been reduced to less than ±3 m (±10 ft), path excursions are less than 1° and overall rpm variations reduced to 3 percent. On other STOL airplanes the thrust control may provide the required bandwidth for good tracking but if it does not, direct lift control devices are likely to be required.

The poor path tracking evident in figure 8 did not greatly concern the pilots monitoring the approach. They were much more aware of the elevator activity, pitch oscillations, and normal acceleration levels. The source of the elevator activity was a noisy airspeed signal that substantially reduced the elevator activity when smoothed.

Two solutions to the pitch activity problem were evaluated. First, the velocity control gains were reduced; this proved unsatisfactory because velocity transients that occurred during glide-slope capture persisted for an objectionable duration. Second, the cutoff frequency on the airspeed component in the complementary filter was lowered; this reduced pitch activity without compromising velocity tracking performance. The reduced control column and normal acceleration activity did not greatly affect the path tracking but did make the system more acceptable to the pilots.

54

CONCLUSIONS

A flight research program was conducted to assess the improvements, in longitudinal path control during a STOL approach and landing, that can be achieved with manual and automatic control system concepts and with cockpit displays with various degrees of complexity.

Substantial improvements in manually flown IFR approaches can be obtained with stabilization and command augmentation systems ranging in complexity from simple thrust-thrust deflection interconnects to sophisticated path-speed stabilization and command configurations. With the augmented aircraft given pilot ratings in the 5-6 range for raw data IFR approaches to a 60 m (200 ft) decision height, ultimate improvement to the 2-1/2 to 4 range can be achieved with the most complex SCAS. The addition of a flight director to overcome deficiencies of the raw data instrument scan permit the rating to be improved to the 1-1/2 to 2-1/2 category for operation to a 30 m (100 ft) decision height. Thus it is apparent that fully satisfactory capability to manually perform IFR approaches to current instrument flight minimums can be obtained for an aircraft of this class. The ability to accomplish a gentle flare maneuver to a low touchdown sink rate can also be achieved with systems which augment the basic aircraft's heave response. Improvements in pilot ratings for the flare from the 4-5 to the 2-3 category can be obtained.

Flight research is in progress to demonstrate fully automatic approach and landing operation to Category IIIa minimum conditions. A substantial number of fully automatic approaches and landings have been performed and recent improvements in the glide-slope tracking logic have produced a satisfactory system concept. Fully automatic flares to touchdown have been performed and refinement of the automatic flare control is in progress. Once acceptable automatic glide slope and flare controls are established, operational evaluations will be conducted to explore operational procedures and approach path geometry.

55

REFERENCES

1. Quigley, H. C.; Innis, R. C.; and Grossmith, S.: A Flight Investigation of the STOL Characteristics of an Augmented Jet Flap STOL Research Aircraft. NASA TM X-62,334, 1974.

2. Cooper, G. E.; and Harper, R. P.: The Use of Pilot Rating in the Evaluation of Aircraft Handling Qualities. NASA TN D-5153, 1969.

3. Neuman, F.; Watson, D. M.; and Bradbury, P.: Operational Description of an Experimental Digital Avionics System for STOL Airplanes. NASA TM X-62,448, 1975.

4. Hoh, R. H.; Klein, R. H.; and Johnson, W. A.: Design of a Flight Director/ Configuration Management System for Piloted STOL Approaches. NASA CR-114688, 1973.

5. Clement, W. F.: Investigation of the Use of an Electronic Multifunction Display and an Electromechanical Horizontal Situation Indicator for Guidance and Control of Powered-Lift Short-Haul Aircraft. NASA CR-137922, 1976.

56

TABLE 1.— COMPARISON OF SCAS CONCEPTS

SCAS concept	Mechanization	Effect on aircraft response	Pilot's control technique
Throttle-nozzle interconnect	Linear, constant gain command from throttles to nozzle servos	Decouples flight path and airspeed response for throttle control. Expands flight envelope.	Backside (flight-path with throttle, airspeed with pitch). Reduces pitch control activity.
Airspeed stabilization	Error between pilot selected reference and actual airspeed commands nozzle servos. Airspeed derived from complementary filter.	Eliminates path-speed coupling for throttle control. Eliminates path response decay for pitch control. Reduces path and speed excursions to horizontal gusts.	Frontside (flight-path with pitch). Throttle activity significantly reduced. Some thrust may be required to quicken path tracking and flare.
Flight-path airspeed command and stabilization	Airspeed error command nozzle servos. Combination of flight-path and pitch attitude error drives throttle and choke servos (washout for chokes).	Same as for speed stabilization. Quickens path response to attitude. Authoritative path control $\Delta\gamma_{ss}/\Delta\theta_{ss} \doteq 1.0$.	Frontside. Only pitch control required for approach and flare.

57

TABLE II

IFR GLIDESLOPE TRACKING AND FLARE
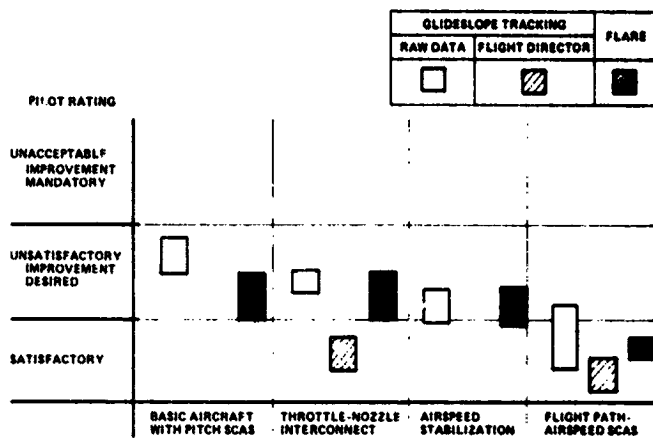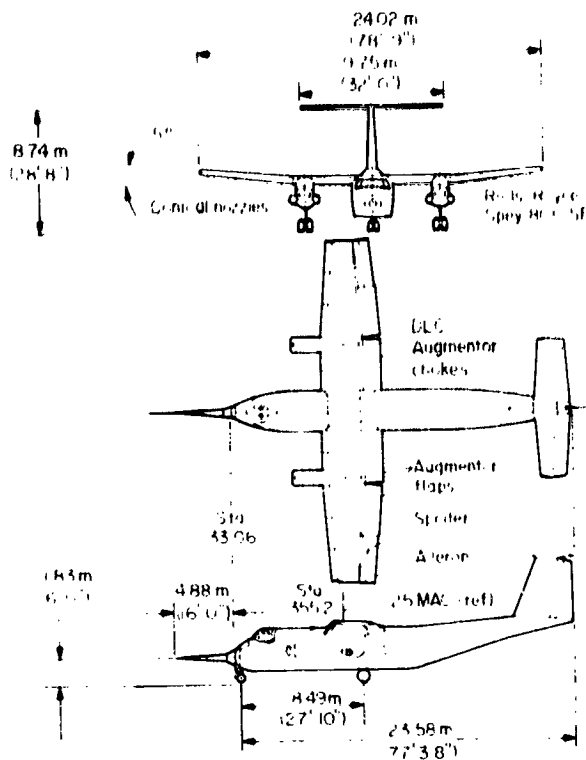
Figure 1.- The Augmentor Wing Research Aircraft.

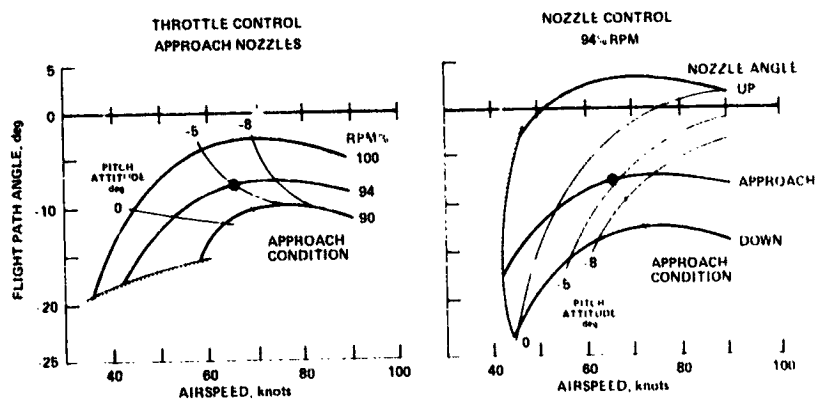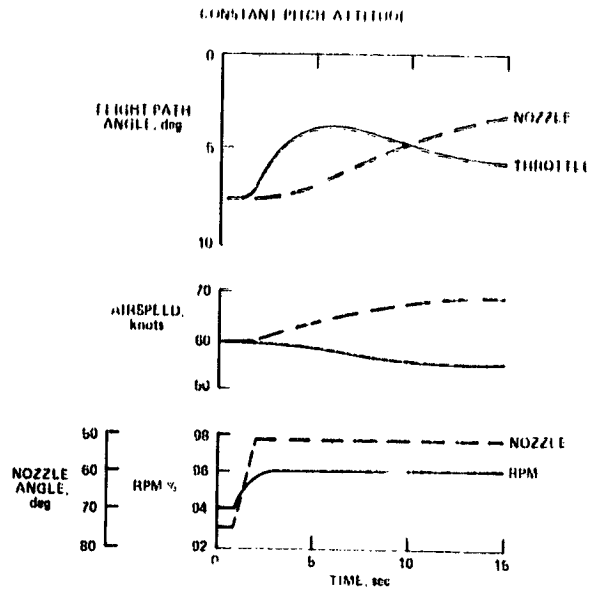Figure 2.- Performance characteristics: approach configuration.

Figure 3.- Dynamic response characteristics:
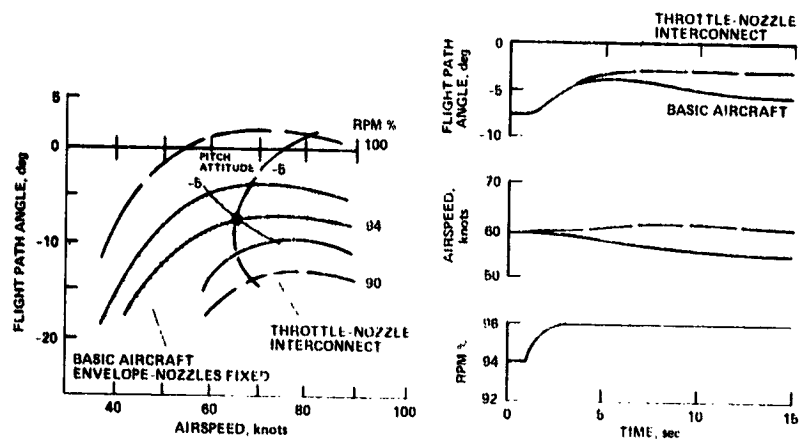approach configuration.

Figure 4.- Throttle-nozzle interconnect.

60
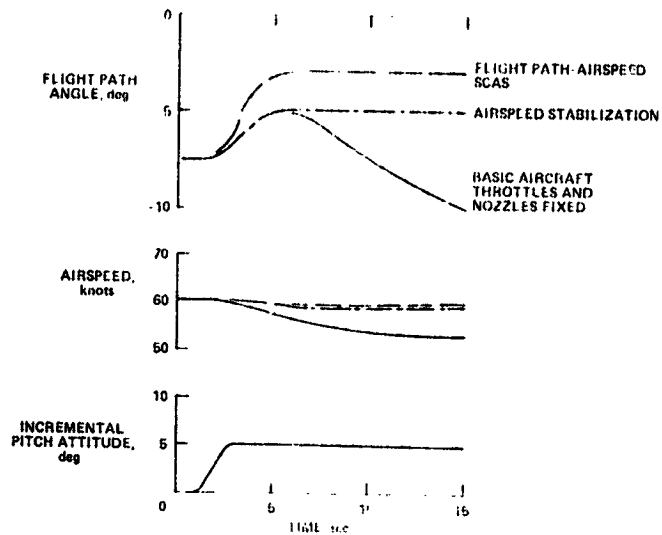
Figure 5.- Speed stabilization and flight path-airspeed SCAS:
glide-slope tracking.
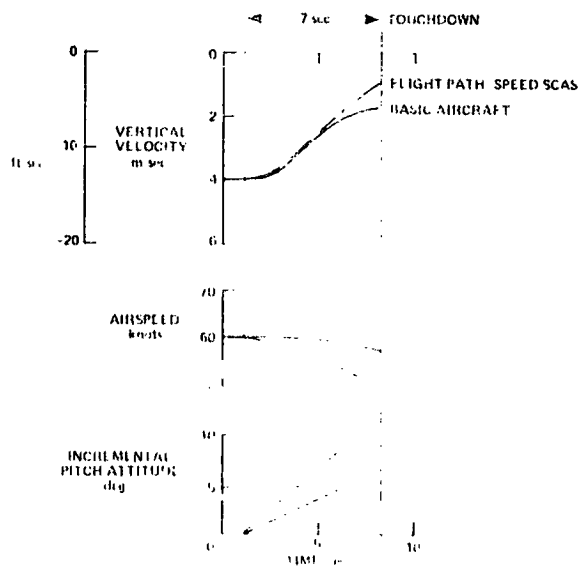
Figure 6.- Flight path-airspeed SCAS: flare control.

61
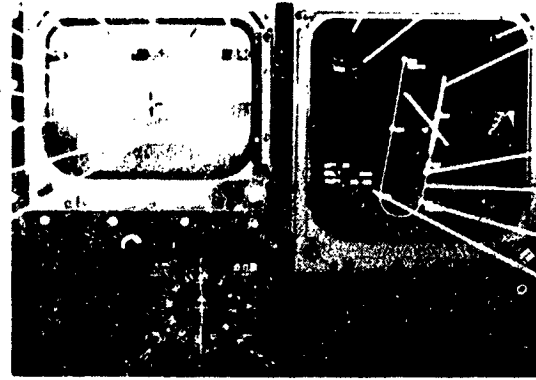
Figure 7.- Avionics system displays.
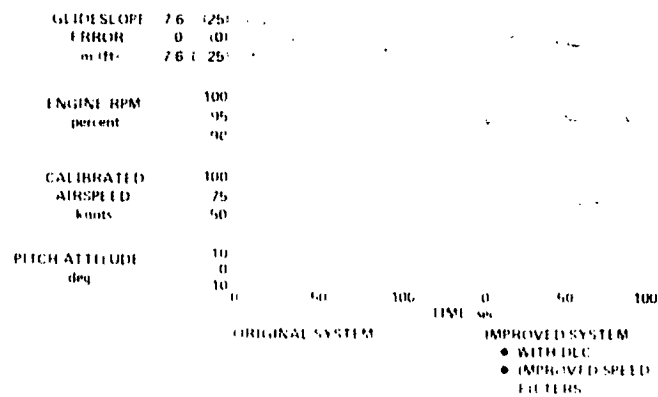
Figure 8.- Automatic glide-slope tracking.

FACTORS INFLUENCING TOLERANCE TO WIND SHEARS IN LANDING APPROACH

Richard S. Bray
NASA Ames Research Center

SUMMARY **N77-18085**

Flight simulator studies were conducted to examine the piloting problems resulting from encounters with unusual atmospheric disturbances late in landing approach. Simulated encounters with disturbances, including examples derived from accident data, provided the opportunity to study aircraft and pilot performance. It was observed that substantial delays in pilot response to shear-induced departures from glide slope often seriously amplified the consequences of the encounter. In preliminary assessments, an integrated flight instrument display featuring flight path as the primary controlled element appeared to provide the means to minimize such delays.

INTRODUCTION

This paper reports findings from piloted simulator tests conducted to obtain a better understanding of the piloting problems induced by encounters, in landing approach, with localized atmospheric disturbances such as wind shears or downdrafts. This work was motivated by the increased concern that followed recent major accidents in which such disturbances were convincingly identified as the cause. The formulation and conduct of these tests were influenced by the background gained during NASA consultation with the National Transportation Safety Board (NTSB) during their investigations of these accidents.

To illustrate the real hazards of wind shear, this paper begins with a review of two accidents from which descriptions of the atmospheric disturbances were derived. The simulator tests, which include encounters with similar wind environments, are described. Data and observations from these tests are discussed. A flight instrument display principle that appears to have potential for improving tolerance to disturbances in landing approach is then described.

Examples of Wind-Shear Accidents

In December 1973, a DC-10 descended below glidepath on an approach to Logan Airport (Boston), striking the approach light standards short of the runway. The aircraft was destroyed, but fortunately there were no fatalities. The aircraft had performed a normal coupled ILS approach, with autothrottle, to an altitude of 60 m. At this point, while the pilot was completing his transfer from instrument to visual reference, he disengaged the autopilot, but left the autothrottle engaged. Data from the flight recorder indicate a

subsequent 10-knot loss in airspeed, accompanied by an increasing sink rate. Corrective action was first too little, then too late. This aircraft was equipped with a very comprehensive digital flight data recorder (DFDR) that provided the data defining the winds shown in figure 1. The shear from a strong tailwind component at 150-m altitude to a light headwind at 50 m caused the aircraft to overshoot the desired approach speed, even though the auto-throttle had reduced thrust to near flight idle. When the shear terminated, the aircraft decelerated toward its target speed, and an undetected sink rate developed. This wind-shear-induced accident is notable for its unusual circumstances, not for the severity of the disturbance. At no time was the performance capability of the airplane challenged — in fact, it struck the obstructions at a speed slightly above its reference approach speed.

In June 1975, at John F. Kennedy Airport (New York), during local thunder-storm activity, several aircraft encountered severe shears late on final approach. The last of these, a 727, hit approach light standards well short of the runway, with catastrophic results. This aircraft was equipped with the more common four-parameter foil recorder, providing insufficient data to define winds with confidence. Six minutes before the accident, an L-1011 aircraft, encountering a severe disturbance, had successfully executed a go-around. This aircraft was equipped with a DFDR. The maneuvers of these two aircraft are described in figure 2. Examining the flight paths and speed variations, the observer is led to conclude that the disturbances experienced by the two aircraft must have been very similar. Flight-path departure rates and speed losses are nearly identical; however, the L-1011 had the good fortune to suffer its encounter at a higher altitude than did the 727. Note that, in each case, downward departure from the ILS path preceded the sharp speed decay by about 6 sec. The pitch and thrust data, as well as angle-of-attack data, from the L-1011 enabled the derivation of the winds that aircraft encountered (fig. 3). These data are plotted to the same time reference as the previous figure. The initial disturbance, a substantial downdraft of nearly 10 knots (1000 ft/min), was followed by a 30-knot change in the along-track wind component. This disturbance has been hypothesized to result from a localized cold air downflow from a thunderstorm cell which, impinging on the surface, produced a high-velocity horizontal flow radially outward. The meteorological situation at New York at the time of the accident is analyzed in detail in reference 1. The wind profile (fig. 3) played a prominent role in the simulator program discussed here.

Atmospheric disturbances of the type documented at New York have since been identified in accidents at Denver (727 take-off) and Philadelphia (DC-9 go-around). Unfortunately, these airplanes were not DFDR equipped, and thus winds cannot be determined with certainty. Further details of the Boston, New York, and Denver accidents can be found in references 2 through 4.

SIMULATOR TESTS

Objectives

The examples of shear encounters just discussed contrast the case of subtly induced sinking in the Boston accident with the awesome disturbances experienced by the airplanes at New York. Fortunately, the severe cases are rare, and warning is offered by the thunderstorms that breed them. It appears that many other approach accidents and "near misses" have been induced by the more modest type of disturbance. Thus it was intended that the simulator tests explore encounters with a wide variety of shears. Answers to the following questions were sought:

    1. In the present operational environment, what type and magnitude of disturbance represent an obvious hazard in landing approach?

    2. What are the pilot factors that might escalate the effects of a modest disturbance to produce an accident?

    3. What "onboard" means or techniques to reduce shear hazards appear worthy of development?

Simulation

Facility — The tests were conducted in the Ames Flight Simulator for Advanced Aircraft (fig. 4). This facility includes a transport-aircraft-type cockpit, large-amplitude cockpit motion, and a Redifon TV-model board visual simulation system. During these tests, the pilot station incorporated a pneumatic "G-seat," on loan from the Air Force, which was intended to produce the cues of sustained or lower frequency vertical accelerations.

Simulated aircraft — Airplane characteristics used in the simulator tests were typical of a short-range, twin-jet transport of the 737, DC-9 category. The engines were assumed to be aft-fuselage-mounted, with thrust contributing essentially no pitching moment to the aircraft. A landing weight of 43,100 kg (95,000 lb) was used for all tests. Take-off static thrust per engine was 62,274 N (14,000 lb) with 10-percent overboost available. The approach reference speed, V_{ref}, or "bug" speed, was established as 125 knots, approximately 1.25 times the speed for maximum lift in 1-g flight.

Cockpit controls and displays were conventional for transport category aircraft. The attitude indicator/horizontal situation display (ADI-HSI) were of the Sperry HZ-6 configuration. The ADI included an "expanded" pitch scale, a "fast-slow" indicator needle that was activated only for special tests, and a glide-slope deviation needle. The flight director needles were driven by signals computed in the basic simulation computer. The pitch command signal did not employ the HZ-6 system logic; it was computed using the logic of another commonly used flight director system. Pitch attitude commands were derived from a summation of pitch attitude and beam error. This system

65

incorporated a major attenuation of the beam-error input at middle-marker passage.

An ILS-coupled autopilot mode was available in the simulation. Glide-slope guidance computation for the autopilot included beam-error rates derived from vertical acceleration and was representative in its capabilities of the newer "autoland" autopilot systems.

A "head-up" display system was used late in the tests to evaluate modified flight data display concepts. The symbology (discussed later) was optically combined (with a mirror beamsplitter) with the scene presented by the Redifon visual simulation system. The combined images were viewed through collimating lenses.

Visibility simulation. - Reduced visibility due to cloud or fog was simulated electronically. Visibility conditions as low as 30-m ceiling and 300-m visual range (RVR) were simulated to the satisfaction of the pilots who participated in the tests. In this program, no cases of interrupted visibility were simulated; the RVR never decreased as altitude decreased.

Wind and turbulence simulation. - A large number of wind profiles (velocity varying with altitude below 250 m) were established for the program. Three "logarithmic" profiles characteristic of widely disparate atmospheric lapse rates, constituted the basic program. On these shear profiles were superimposed perturbations that defined discrete shears varying in altitude of initiation, total amplitude, and gradient (knots per unit altitude). Examples of the along-track shear profiles used in the tests are shown in figure 5. Crosstrack wind profiles were defined as percentages of the along-track amplitudes. A "40-percent" crosswind component from either the left or right was commonly used. In addition to these generalized altitude-dependent wind profiles, a facsimile of the atmospheric variations recorded in the L-1011 (discussed earlier) was programmed as a function of distance along the approach path, initiating at a point corresponding to that of the 727 encounter. Discrete geographically defined vertical drafts were also programmed. Simulated random turbulence, appropriate to the wind conditions, was superimposed on the shear profiles.

TESTS

Six pilots who currently fly transport category aircraft participated in the tests. After appropriate familiarization with the simulated aircraft, they each flew approaches in 20 to 30 different combinations of atmospheric disturbance and visibility. All but a few approaches were manually controlled, with flight director guidance available. Exposure to the New York thunderstorm profile was included well along in each pilots experience in the simulation while he was evaluating disturbances of lesser magnitude. A strong effort was made to create the logic of warning, readiness, and surprise that characterized the real encounters.

66

All approaches were initiated at an altitude of about 300 m. Normal control tower information regarding winds and visibility were transmitted to the pilot. In most cases of large disturbance, tower reports of previous encounters were included. Use of conventional cockpit procedures, including standard call outs, was encouraged. All pertinent pilot inputs and aircraft responses were recorded, and the pilots' observations were recorded on voice tape after each approach. At the end of the simulator exercise, and during a brief opportunity several months later, panel display modifications and several electronic head-up display formats were evaluated subjectively in the presence of disturbances.

RESULTS AND DISCUSSION

Aircraft Performance Potential

Since the response to a shear encounter involves both pilot and aircraft performance, it is appropriate to preface a discussion of the results with a review of aircraft performance capabilities assumed in these tests.

Figure 6 represents an attempt to put in perspective the level of disturbances experienced in the simulator relative to airplane performance capabilities for both the generalized shear cases and for the New York profile. Any point on this graph represents the duration of a "head-wind to tail-wind" or "negative" shear of given rate of change (in knots/sec). A useful approximation is the equivalence, in terms of energy loss, of a 6-knot downdraft to 1-knot/sec shear. The top line defines the theoretical shear (or equivalent combination of shear and downdraft) that can be tolerated without leaving the glidepath or falling below stall-warning speed — *if* take-off thrust is instantaneously available at the onset of the disturbance and appropriate pitch corrections are made. The lower curve represents the case of continued approach thrust. The crosshatched area is an envelope of all the generalized disturbances experienced in the simulator tests. Also indicated is the disturbance level of the New York profile. It can be seen that the generalized shear cases do not challenge the aircraft's performance potential. On the other hand, the New York profile leaves a comparatively small margin of performance.

Observations from Simulated Encounters

The simulator exercises provided a wealth of observations — and generated some new questions — regarding the significance in shear encounter of factors such as training, individual piloting techniques, flight director logic, and concurrent transfer from instrument to visual references. However, most of these points deserve more analysis and perhaps more experimentation before they are reported. This paper is limited to a discussion of pilot response delays in wind-shear encounters and means to reduce those delays.

New York shear profile — As indicated earlier, each of the six pilots in the simulator program suffered one well-conditioned encounter with a model of

the New York downdraft-wind-shear phenomenon. In two of the six simulated encounters, the aircraft descended to altitudes where they would have encountered obstructions, in almost exact duplication of the 727 accident. A third resulted in a near miss, and the remaining three recovered with sizeable terrain clearance. Figure 7 compares the smallest and the largest altitude divergences seen in these encounters. While one of the simulated aircraft in effect "crashes," the other executes a successful go-around with a minimum altitude of 40 m, only 20 m below ILS glide-slope altitude. The single most important difference in pilot response is seen in the record of thrust. The successful pilot perceived the sink rate induced by the downdraft and had added substantial thrust by the time the shear was encountered. The pilot also pitched the aircraft to regain near normal sink rate. When the speed was seen to decay even farther, even with the initial addition of power, take-off thrust was immediately applied. Speed did not fall below 124 knots. The other pilot made no significant response to the downdraft. In response to the rapid decrease in airspeed due to the shear, power was tentatively added. By the time this response was recognized as inadequate, the aircraft was below 30 m, in a high sink-rate condition, and 10 knots below approach reference speed — recovery was highly improbable.

Further evidence of the value of quick response is seen in figure 8, which illustrates the performance of an autopilot-autothrottle system in an encounter with the same profile. Flight path was held tightly, but with significant speed loss. The automatic systems perceived and acted with a very modest delay. As indicated in figure 7, the pilot cannot be counted on to act as effectively.

Generalized shear program — The performances recorded in the other disturbances can be reviewed for further evidence of the perception problem. As might be expected, since these disturbances did not seriously challenge airplane performance and the pilots were considered well warned, no simulated accidents occurred. There was a small number of aborted approaches and several hard landings. Subjective observations by the pilots were highly variable for the lesser disturbances — sometimes the disturbance was hardly noticed; at other times, the same disturbance caused a very significant workload. The shears that the pilots considered hazardous were of the highest amplitudes and gradients, for example, 15-20 knots in 30 m of altitude, and initiating below 100-m altitude. Figure 9 shows characteristic values of speed and altitude losses for several levels of shear intensity. The shaded points represent the larger disturbances. Generally, these levels of speed and flight-path deviation do not seem large or dangerous; however, if they are considered to occur very low in the approach, at times in low visibility, the hazard is more apparent. The observation can be made that the energy losses represented in these excursions represent roughly 75 percent of the energy loss in the disturbance input. This would indicate delay in effective countering of this loss by the pilot.

Figure 10 illustrates example response times for thrust and pitch inputs. From the data represented by the circled points, a wide variation of responses is seen. This might be expected due to differences in rates of onset of the disturbance, as well as variations in flight condition at the point of onset.

68

Initial thrust responses are seen within 3 to 4 sec, indicating tight monitoring of airspeed. However, pitch attitude increases required to arrest the increased sink rate occur 6 to 10 sec after shear initiation, indicating that flight-path angle or rate-of-descent divergences are slow to be recognized.

The response lags shown for the simulated New York shear encounters are ev   re pronounced. The quickest responses were exhibited by the pilot that s   _aneously added thrust and pitched up within 5 sec of the disturbance onset. The delays in thrust addition are presumed due to the fact that the initial disturbance was a downdraft that did not create an immediate speed decay. The delays in pitch response are more surprising in view of the immediate increase in sink rate induced by the downdraft.

Means for Improving Flight-Path Control

These observations of performance in shears led to the conclusion that conventional displays do not provide the pilot with the means for uninterrupted awareness of his flight path, and that visual cues outside the aircraft can also be tenuous. As indicated earlier, the tests were concluded with evaluations of display concepts aimed at improving the pilot's capability to control speed and flight path in strong disturbances. By far the most encouraging results were obtained using the electronic head-up display equipment available to the simulator to create integrated displays of various configurations. The format described in figure 11, which has been the subject of very brief experience in the simulator, appears to essentially eliminate the path and speed perception delays demonstrated with conventional displays. In addition to the fixed airplane symbol and moving horizon, the display includes the following elements: a runway symbol, in approximate perspective, with a touchdown reference point; a glide slope angular error indication, referenced to a negative three-degree pitch scale index; a flight-path symbol, referenced to the horizon; and a speed error indication referenced to the airplane symbol.

The effectiveness of the display in reducing time delays in the perception of flight-path changes results from the fact that the flight-path indicator can be substituted for the airplane symbol as the primary controlled element. To correct the flight situation illustrated, the glide-slope line is simply tracked with the flight-path symbol, resulting in a convergence as indicated in figure 12. In the experiments, the flight-path information was assumed to be inertially derived, and a small component of lagged pitch rate was added to compensate for the normal time lag between attitude and flight-path response. The speed error symbology was well received and could usually be sensed in peripheral vision while concentrating on the flight-path symbol.

Several points regarding this display concept must be discussed. The concept of flight path as the primary element is not original here; it is utilized in a well publicized commercial HUD system. The format shown is not a developed display. While it demonstrates effectiveness in tracking the glide slope, it is inadequate for lateral guidance without additional information. There is no reason that the concept cannot be used in a panel-mounted display.

69

CONCLUSIONS

Analysis of simulator data and accident records indicates that the consequences of wind-shear encounters are seriously aggravated by delays in perception of speed and flight-path divergences when conventional cockpit displays or visual references are used. The significance of these delays is apparent when piloted performance is compared with the performance of a modern autothrottle system in the same disturbance. Cockpit display concepts, integrating flight-path and speed information, hold promise of eliminating delays in pilot perception and are worthy of concerted development efforts.

REFERENCES

1. Fujita, T. Theodore: Spearhead Echo and Downburst Near the Approach End of a John F. Kennedy Airport Runway, New York City. SMRP Research Paper, The Univ. of Chicago, March 1976.

2. Aircraft Accident Report — Iberian Airlines DC-10 at Logan Airport, Boston, Mass., Dec. 17, 1973. NTSB-AAR-74-14, Nov. 8, 1974.

3. Aircraft Accident Report — Eastern Airlines Boeing-727 at John F. Kennedy Airport, Jamaica, New York, June 24, 1975. NTSB-AAR-76-8, Mar. 12, 1976.

4. Aircraft Accident Report — Continental Airlines Boeing-727 at Stapleton Airport, Denver, Col., Aug. 7, 1975. NTSB-AAR-76-14, May 5, 1976.
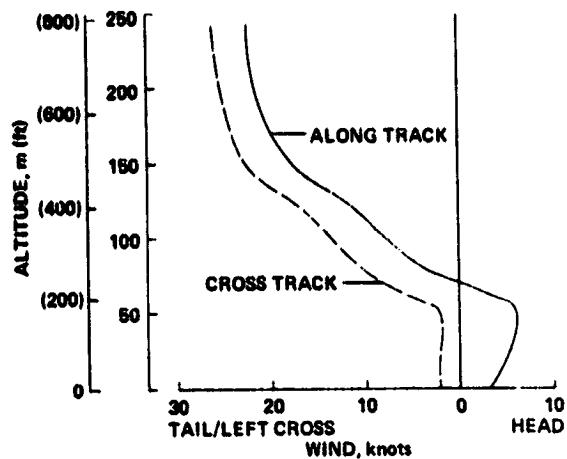
Figure 1.- Winds derived from digital flight data
recorder, DC-10, Boston.
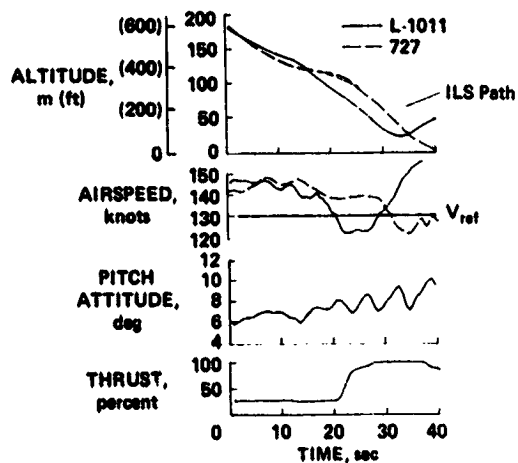
Figure 2.- Encounters with thunderstorm-related
wind shears, New York.
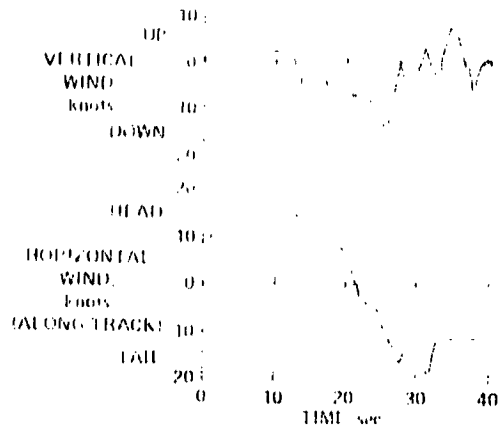
Figure 3.- Downdraft and wind shear encountered
by L-1011 aircraft, New York.
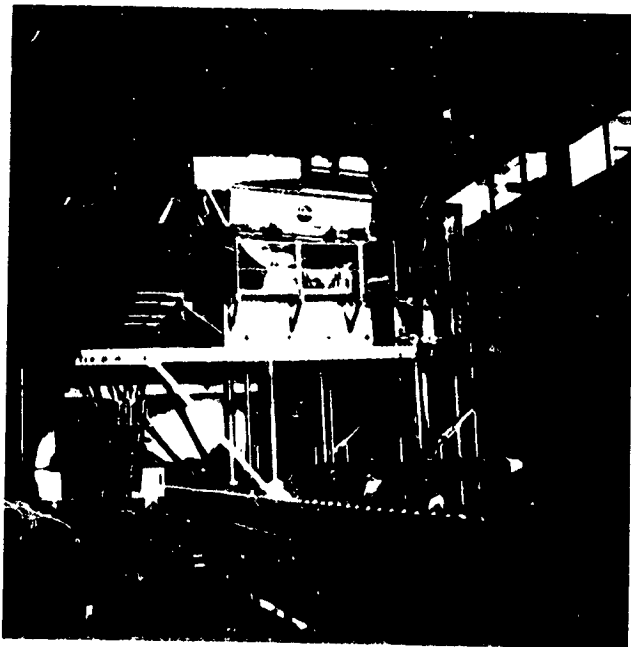
Figure 4.- Flight simulator for advanced aircraft.

72
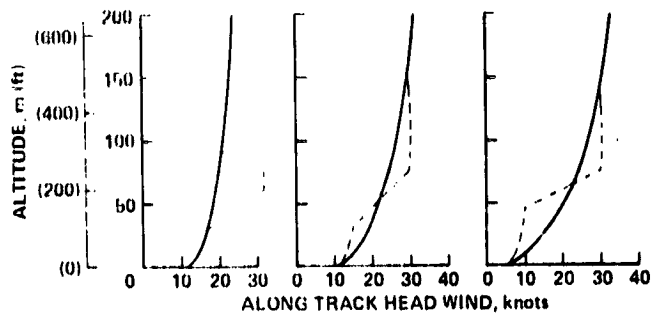
Figure 5.- Examples of simulated shears.
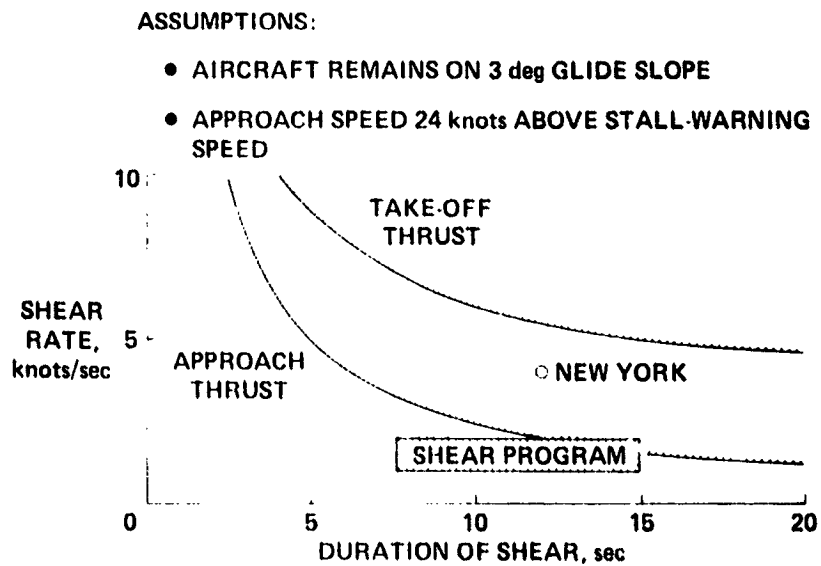
Figure 6.- Performance available to counter wind
shear on approach.

73
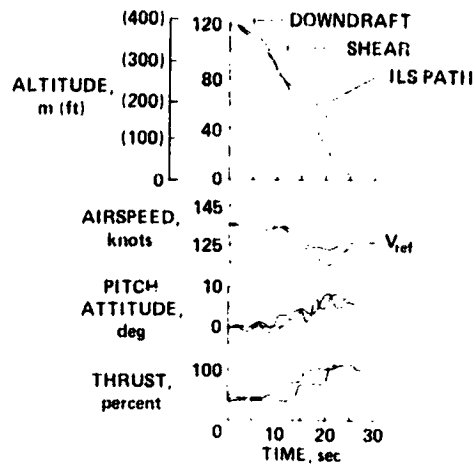
Figure 7.- Effects of response delays,
New York profile.
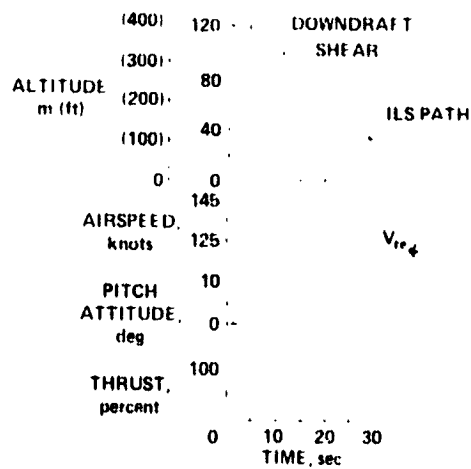
Figure 8.- Automatic systems performance
in New York profile.

74
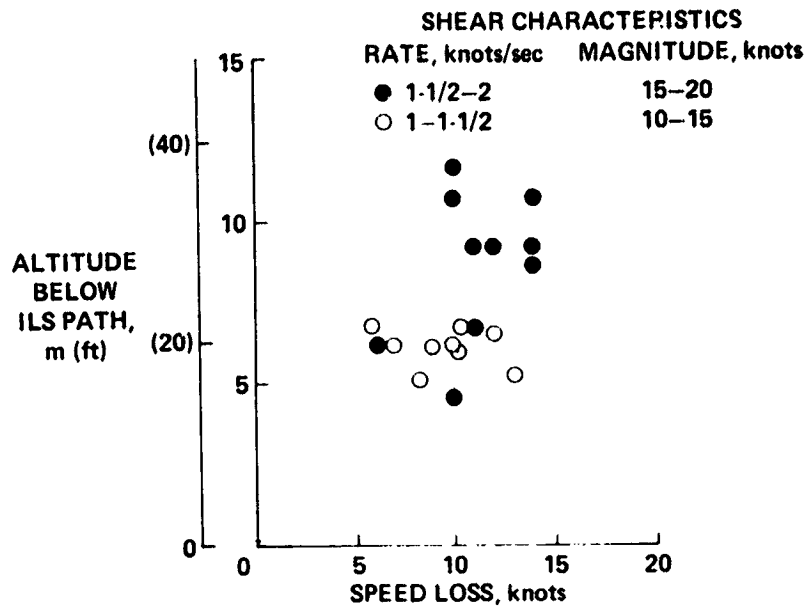
Figure 9.- Altitude and speed perturbations in
simulated shear encounters.
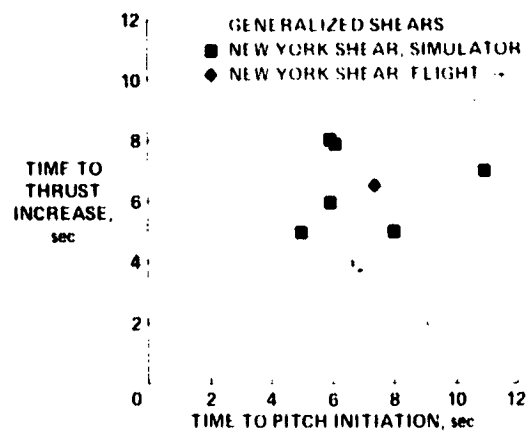
Figure 10.- Reaction times in shear encounters.

FLIGHT CONDITIONS:

- FLIGHT PATH, —4.2 deg
- "ONE DOT" BELOW GLIDE PATH
- 5 knots SLOW

SPEED-ERROR INDICATOR   AIRCRAFT SYMBOL

GLIDE-SLOPE INDICATOR   HORIZON

ILS RUNWAY INTERCEPT

—3°, REFERENCE FOR GLIDE-SLOPE INDICATOR

FLIGHT-PATH INDICATOR
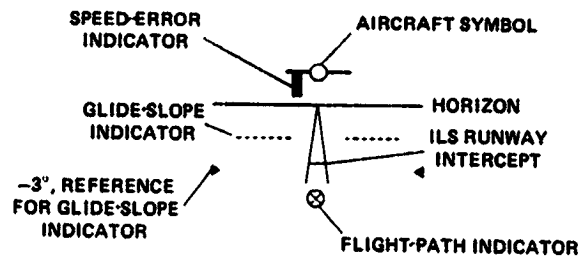
Figure 11.- Integrated flight-path display.

CORRECTING FLIGHT PATH AND SPEED

ON GLIDE SLOPE, ON SPEED
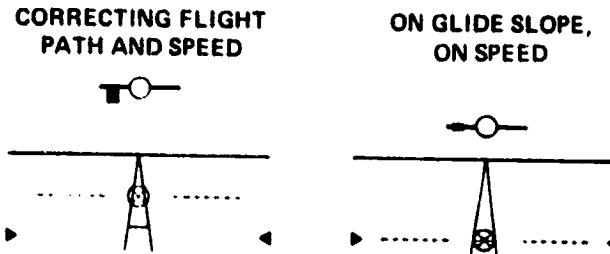
Figure 12.- Integrated flight-path display.
Correction to glide slope.

76

DELAYED FLAP APPROACH PROCEDURES FOR NOISE ABATEMENT

AND FUEL CONSERVATION

Fred G. Edwards, John S. Bull, John D. Foster,
Daniel M. Hegarty, and Fred J. Drinkwater, III
NASA Ames Research Center

SUMMARY

N78-18086

The objective of this program is to investigate the Delayed Flap Approach, which is an operational procedure designed to reduce fuel and noise in the landing approach of a jet transport. This report will describe the delayed flap operational procedures, discuss pilot acceptability of those procedures and displays, and show fuel/noise benefits resulting from flight tests and simulation.

INTRODUCTION

The conventional jet transport stabilized landing approach procedure requires moderately high thrust settings for an extended time, with the accompanying community noise impact and relatively high fuel consumption. Significant reductions in both noise generation and fuel consumption can be gained through careful tailoring of the approach flight path, the operational procedures, and the airspeed profile. For example, the noise problem has been attacked in recent years with development of the two-segment approach, which brings the aircraft in at a steeper angle initially and achieves noise reduction through lower thrust settings and high altitudes during most of the approach (refs. 1, 2).

Also, the Air Transport Association (ATA) member airlines have developed and instituted the "reduced flap" noise abatement landing procedures throughout most of the domestic airline systems (ref. 3). For this approach, the aircraft flies the standard straight-in path, but maintains a flap setting "one notch less" than minimum landing flap setting until final landing flap deployment at about 305 m (1000 ft) altitude. The final landing flap selected would be the minimum certified landing flap setting which is permissible for the particular landing. The intent is to assure that final approach stabilization is achieved at not less than 152 m (500 ft) above field elevation.

More recently, Lufthansa German airlines pioneered a low-drag/low-power approach technique (known as the TIPTOE approach) and has made it their standard ILS approach procedure (ref. 4). This technique is being considered for adoption by the International Air Transport Association (IATA) for use by all member airlines at landing fields where ground facilities permit. The target stabilization altitude for the IATA approach is 305 m (1000 ft) above field

elevation. Both the ATA and IATA techniques comprise a decelerating process, employing delays and/or reductions in the extension of the landing gear and the use of flaps, with a consequent reduction in the amount of power required to conduct the approach. Both are "thumb-rule" techniques, where pilot action is keyed on aircraft velocity and altitude above the ground and DME information when available.

The NASA/Ames Research Center is currently investigating the so-called "delayed flap" approach (refs. 5-7) where pilot actions are determined and prescribed by an onboard digital computer. The onboard digital computer determines the proper timing for the deployment of the landing gear and flaps based on the existing winds and airplane gross weight. Advisory commands are displayed to the pilot. The approach is flown along the conventional ILS glide slope but is initiated at a higher airspeed and in a clean aircraft configuration that allows for low thrust and results in reduced noise and fuel consumption.

The procedure is an application of energy management concepts, where the proper timing of the deployment of the landing gear and flaps is used to dissipate the energy in a controlled manner while the engines are at low throttle setting.

This procedure has several advantages over the ATA and the Lufthansa types of approaches. The computation capability provides for consistency of operations and allows additional noise relief and fuel savings. The system has the potential for increasing operational safety by lessening pilot workload and providing an energy management engine-out landing capability and a wind shear detection and warning function. The primary disadvantage is, of course, the requirement for additional avionics. Definition of this equipment and associated costs are the subject of an ongoing study.

The elements of the Ames delayed flap program consist of operation with the NASA Convair 990 airplane (shown in fig. 1) and application of the concept to other aircraft.

The program has proceeded through an analysis and a piloted simulation phase and more than 100 hr of flight test evaluation onboard the CV-990.

The results of the flight test evaluation which show the fuel and noise benefits will be presented and discussed. The results of a limited guest pilot evaluation of the procedures will also be presented.

Ames has contracted with the Boeing Commercial Airplane Company to investigate the benefits and problems associated with the application of the delayed flap concepts to an aircraft in the current fleet. The results of the Boeing analysis of the fuel and noise benefits for the Boeing 727 airplane are complete and will be presented.

78

OPERATIONAL PROCEDURES AND DISPLAY CONCEPT

Figure 2 shows a typical delayed flap approach for the CV-990. In contrast to a conventional stabilized approach, which is flown at a constant airspeed of about 150 knots and moderately high thrust settings throughout the approach, the delayed flap approach begins at a higher initial airspeed, 240 knots and decelerates at idle thrust through most of the approach. The pilot intercepts the ILS glidepath at about 10 n. mi. from touchdown and at approximately 900 m altitude. He then retards the throttles to the idle detent and begins a slow deceleration. At about 6 n. mi. and 230 knots, the pilot is given a command from the digital computer to lower the landing gear. At about 5 n. mi. and 220 knots a command is given to lower approach flaps, and flaps are commanded to the landing position at about 4 n. mi. and 200 knots. The aircraft decelerates to final approach airspeed at about 150 m altitude, at which point the pilot advances the throttles to approach power and the last portion of the approach is flown at a stabilized airspeed similar to a conventional approach. In headwinds, extension of landing gear and flaps is delayed and in a tailwind condition, they are commanded farther out in the approach. Thus, regardless of wind conditions, the aircraft is always stabilized for landing at 150 m altitude, which is consistent with current airline procedures.

Figure 3 shows the CV-990 cockpit and displays that the pilot uses to perform a delayed flap approach. In addition to the normal instruments are a fast/slow indicator which is part of the ADI, an alphanumeric message display, and a data entry keyboard.

The fast/slow display, which is commonly found in many current jet transports, allows the pilot to monitor the energy state of the aircraft. While on the glide path, this instrument tells the pilot how the a rcraft is decelerating relative to the desired airspeed schedule. This is similar to the way fast/slow displays are normally used, except that the usual reference airspeed is constant and not changed as in this case for a delayed flap approach.

The message display signals the pilot when to extend landing gear, approach and landing flaps, and when to apply approach power. The proper timing of signals is accomplished by a digital computer onboard the CV-990 aircraft. In essence, the computer predicts the manner in which the aircraft will decelerate during the approach to landing, taking into account the wind and changing aircraft weight. Based upon this computed deceleration, the computer signals the pilot when the flaps or gear is to be lowered by flashing a command on the message display. When the pilot has taken the required action, the display goes blank again until the next event is to occur. All this is accomplished so that the aircraft arrives at the final approach airspeed at precisely the right altitude and desired distance from touchdown.

The data entry keyboard provides a means for communicating with the digital computer. For a delayed flap approach, it would be used to input landing site data, such as the field elevation or ILS glide slope angle.

The equipment shown in figure 3 is not meant to represent an actual airline installation. The digital computer system and the CV-990 airplane were used in this program because of their availability and their ability to perform the required tasks. The avionics that could be installed in a conventional jet transport in order to have a delayed flap approach capability would be tailored to meet the requirements of the airlines.

RESULTS AND DISCUSSIONS

CV-990 Operations

Noise Measurement Results

A series of noise measurements was made during the flight test evaluation of the delayed flap approach in the NASA CV-990 aircraft at the Edwards Air Force Base (EAFB) test range. The purpose was to measure and compare the noise level on the ground under the flight path while using different types of operational procedures which included the conventional, the ATA reduced flap and the delayed flap approaches.

A total of 10 noise measurement sites was utilized. Six of the sites were located on the extended runway centerline from one to 6 n. mi. from the runway threshold. The remaining four sites were located at various sideline distances along the test range. These measurements were made with the assistance of Dryden Flight Research Center personnel during a flight test series in September 1975. The noise recording equipment and the ground radar tracking data were time correlated to provide the position of the aircraft relative to the sound measurement equipment during the tests.

The approaches were conducted during several days of flight testing under conditions where the low altitude winds varied from 1 to 16 knots and the aircraft weight varied from 59,000 kg (135,000 lb) to 64,000 kg (141,000 lb) on the different approaches. In addition, the elevation of the test site at EAFB was 696 m above mean sea level, and the ILS glide-slope angle was 2.5° which is lower than the typical 3° glide-slope found at most airports. These factors complicate the analysis and interpretation of the data since they affect the geometry of the flight path, the sequence of operational procedures and the jet engine settings during the approaches and thus, the noise and fuel measurements. In order to present a consistent set of data for direct comparisons between the different types of approaches, it was decided to use the inflight results primarily to validate existing aircraft aerodynamics, engine noise, and fuel use models. By adjusting the parameters of the computer models to correlate closely with the flight data, the resulting models could be used with confidence to generate data for direct comparison under identical test conditions. The details of the

The CV-990 aircraft is a four engine jet transport of the same B-707 vintage. This aircraft is equipped with General Electric CJ-805-23B turbofan jet engines, trailing edge Fowler flaps and leading edge Krueger flaps.

computer analysis are given in reference 7. The subsequent figures present the results of this computer analysis.

Figure 4 shows the centerline noise level generated by the CV-990 aircraft on each of three types of approaches: the conventional, the ATA reduced flap and the delayed flap. These data are for the more typical $3°$ approach path. The approaches are all for a no-wind condition at an aircraft weight of 81,650 kg (180,000 lb). Plotted is the effective perceived noise level in dB (EPNLdB) versus the range to touchdown in nautical miles. Beyond glide-slope capture the aircraft in each case is flying at a constant 900 m altitude. Glide-slope capture occurs at about 9-1/2 n. mi. from touchdown.

The 150 m stabilization altitude for the delayed flap approach is indicated at about 2 n. mi. Inside of 2 n. mi. the aircraft configuration and thrust level are about the same for each approach and the noise levels are about equal. Between 8 n. mi. and 2 n. mi. there is a significant reduction in noise generated by the aircraft on a delayed flap approach. A 10- to 12-dB reduction is indicated over both the conventional and reduced flap approach.

The sideline noise data was also generated for each of the three approach types. These data were generated by the computer noise model, which used the flight test sideline noise measurements to refine the model parameters. The areas of the resulting contours were then calculated so that a direct comparison of the noise impacted areas could be made. The 90-EPNLdB contour areas for each of the three types of approaches are included in figure 5.

Figure 5 shows the CV-990 benefits comparison for the three different approach techniques: the conventional, reduced flap and delayed flap approach, in terms of the 90-EPNLdB noise contour area under each flight path (in km^2); the time expended on the approach (in minutes) from the common initial point at 15 n. mi. out, to touchdown; and the fuel consumed by the aircraft during each approach (in kg).

The current airline procedure (the reduced flap approach) has a contour area only 80 percent that of the conventional approach. Thus, the airlines have been able to achieve some noise reduction using operational procedures which do not require the additional studies.

The delayed flap procedure offers considerable additional noise relief. This contour area is only 1/3 as large as that for the conventional approach and less than 1/3 the size of that of the current airline procedure.

and it had additional benefits

Presented in the upper right in bar chart form is the fuel used during each of the three types of approaches.

A fuel measurement system was developed and installed in the CV-990 aircraft to sample and provide a continuous measurement of the fuel flow to each of the four engines. Fuel flow to each engine is summed in the digital computer to update the weight of the aircraft in real-time. A continuous record of the fuel use is therefore available throughout the flight mission. As mechanized, the system has a resolution of 3.6 kg (8 lb). It has been estimated that during the approximate 5-min duration of an approach the fuel used can be determined to within +7 kg (+15 lb).

During the flight test onboard the CV-990, the fuel consumed was measured for a series of each of the different types of approaches (the conventional, ATA reduced flap, and the delayed flap). The same initial condition was established prior to beginning each approach. This initial condition was: range from touchdown 15 n. mi.; altitude approximately 900 m (3000 ft); indicated airspeed 240 knots; and flaps and landing gear up. The resulting flight data was again used to validate a computer model from which a directly comparable set of data could be generated for identical test condition. This data is shown in the bar charts of figure 5.

The current airline procedure (Reduced Flap Approach) saves 50 kg of fuel over the conventional approach, while the delayed flap approach saves an additional 130 kg over the reduced flap approach.

The delayed flap approach does require additional avionics, but the cost of this avionics could possibly be recovered in a reasonable period of time from the cost of fuel saved.

Time savings are also important to airline operations, and it is shown in figure 5 that the delayed flap approach saves a minute of operating time over both the reduced and conventional approaches.

Application to Current Airlines Aircraft

NASA has contracted with the Boeing Commercial Airplane Company to evaluate the delayed flap concept on an aircraft which is representative of those in current airline use. The objective is to examine some of the problems associated with the application of the delayed flap concept to a current aircraft and to evaluate the fuel and noise benefits. The operational flight procedures, computer algorithm and benefits will be different for each type of aircraft. Presented in this section will be a portion of the study results for the Boeing 727 airplane. Complete study results are presented in reference 8.

Boeing 727 Operational Procedure

Presented in figure 6 is an example of the delayed flap procedure as adapted to the Boeing 727 aircraft. The figure shows the altitude and airspeed profiles as a function of range to touchdown. The various events which occur during the approach are indicated on the airspeed profile. The

aircraft provides five flap detents to control the energy during the approach. If the approach is initiated from 900 m and 220 knots, as shown here, idle thrust is commanded just prior to glide-slope capture. The commands are illuminated on an annunciator on the Pilots Panel of the B-727. As the approach progresses the command will be generated in the sequence shown in the figure (i.e., flap = 2°, 5°, 15°, etc.).

For non-icing conditions the deceleration is arrested by reapplying thrust in two steps, first to an engine pressure ratio (EPR) of 1.1 (at about 2.5 n. mi.) and then to normal approach power setting (about EPR 1.3) at the target altitude of 150 m. The first step to EPR 1.1 initiates engine acceleration to a power setting near the surge bleed valve operating point from which further acceleration can be obtained more rapidly when required. This is a characteristic of the particular engine in the B-727-200 airplane (i.e., JT8D-9). From 150 m through to landing, the aircraft is operated as on a conventional or stabilized approach. For an icing condition, the throttle setting would be maintained above idle at about 55 percent rpm for inlet anti-icing. An EPR of 1.2 is the minimum which would insure this thrust level. The flap and gear extensions will always occur in the same sequence but will not always occur at the same speeds. This will depend on the wind condition, the weight of the aircraft, and the initial conditions. For head-wind conditions the sequence of procedures becomes more compressed, while in tailwinds the events will be strung out.

Weight variations have little effect on the deceleration distance or general shape of the airspeed-range curve. Increased weights generally shift the airspeed curve upward by an amount equal to the increase in V_{ref}. Thus, configuration changes occur at a higher airspeed.

The flap speed schedule shown on the figure is selected to minimize the pitch attitude changes during flap extension on the final approach. This is desirable for good glide-slope tracking by both the pilot and autopilot. It was shown in reference 8 that the current 727 autopilot controls those disturbances quite well. Fortunately, the minimum pitch disturbance schedule also provides adequate speed margins from safety limits, as represented by the stall speed region and flap placard boundaries, and is a good compromise with respect to fuel and noise benefits, which will be discussed next.

Noise, Fuel, and Time Benefits

The results of a benefits analysis for the B-727 aircraft are shown in figure 7. Computed fuel usage, elapsed time on the approach and noise footprint areas are compared for three different operational procedures in still air conditions. All approaches are initiated in a clean aircraft configuration at the same flight conditions. The data show that consistent benefits are realized for the B-727 when conducting a delayed flap approach as compared to either the conventional and reduced flap. For example, compared to the current airline procedure (reduced flap), a fuel saving of 1.9 kg is achieved, almost 1-1/2 min in time is saved, and a reduction in the noise area to 1/3 the size of that generated by the B-727 on a reduced flap approach is realized.

Although the data presented is for a no-wind condition, the relative benefit comparison for fuel, time and noise is not significantly different for headwind and tailwind conditions. The effects of a 30-knot headwind and a 10-knot tailwind are included in reference 8, in addition to the noise effects with acoustically treated nacelles.

Pilot Evaluation

In November 1975 nine guest pilots participated in an inflight evaluation of the delayed flap procedure and display concepts onboard the CV-990 airplane. These guests represented United and American Airlines, the Boeing, Douglas, and Lockheed companies, and the FAA, ALPA, and ATA organizations. The flight operations were conducted at the Sacramento Metropolitan Airport, Sacramento, California, under VFR conditions.

During this series of flight tests, each guest pilot conducted from three to six of the different types of approaches either as command pilot in the left-hand seat or as safety pilot/observer in the right-hand seat. The pilots acted upon the sequence of messages as they were displayed on the message display and manually deployed the landing gear and flaps, and operated the throttles. The approaches were primarily conducted in a coupled autopilot mode. Generally, the approach was stabilized in airspeed and aircraft configuration at 150 m altitude and continued through to touchdown. Comments and opinions were solicited from each guest pilot after the flights. A preliminary assessment of the operational procedures is summarized as follows.

Under the conditions of these tests most pilots indicated no significant increase in pilot workload for the delayed flap approach over the conventional approach, and felt that reversion to a conventional approach could be made safely and easily in the event of delayed-flap equipment malfunction. Consistent performance by the pilots and system was demonstrated in controlling the deceleration to achieve the reference velocity at 150 m altitude on the approach regardless of aircraft gross weight and existing wind conditions. The higher airspeeds existing during the approaches were not indicated as a problem by any of the guest pilots.

There were several comments made by the guests pointing out the potential difficulty of integrating the high-speed delayed flap procedure into the existing Air Traffic Control environment. It was indicated that this might be especially difficult at high density airports such as Chicago's O'Hare or Los Angeles International.

Generally, the guests were in agreement that the operational procedure and displays were acceptable and that the technique provided benefits for noise relief and fuel saving, but it was also the consensus that additional research would be required before the delayed flap technique could be considered an acceptable alternative for the current airline approach procedures.

84

CONCLUSIONS

Analytical, simulation, and inflight studies have been conducted to investigate the delayed flap approach technique. Inflight measurements of fuel usage and ground measurements of perceived noise were made during flight test with the NASA CV-990 airplane to assess potential benefits of the approach technique. Results show that significant benefits may be obtained using the delayed flap approach technique. Onboard the CV-990, guest pilots conducted a limited investigation of the acceptability of the operational procedures. A generally favorable response was obtained from these guests. Studies are underway to apply the delayed flap concepts to an example of a current airline aircraft. Application of the approach technique to the operation of a B-727-200 airplane shows that when compared to the reduced flap approach, significant savings in fuel, flight time and reduction in the noise impact area are achieved by using the delayed flap approach.

Several critical areas of research need study before the delayed flap approach could be considered an alternative to the present airline approach techniques. These areas include avionics retrofit costs, operational safety, and compatibility with the existing air traffic control environment.

REFERENCES

1. Denery, D. G.; White, K. C.; and Drinkwater, F. J., III: A Resume of the Status and Benefits of the Two-Segment Approach and Its Applicability to the Jet Transport Fleet. AIAA Paper 74-978, Aug. 1974.

2. Schwind, G. K.; Morrison, W. E.; and Anderson, E. B.: Operational Flight Evaluation of the Two-Segment Approach for Use in Airline Service. NASA CR 2515, 1975.

3. ATA Operations Policy Manual, Noise Abatement Approach and Landing Procedures. OPS-8, Jan. 15, 1974.

4. Elsner, Hermut: The One Segment Tiptoe Approach. J. ATC, Jan.-March 1975.

5. Bull, John S.; and Foster, John D.: Jet Transport Energy Management for Minimum Fuel Consumption and Noise Impact in the Terminal Area. AIAA Paper 74-811, Aug. 1974.

6. Bull, J. S.: Jet Transport Fuel Conservation and Noise Abatement in the Landing Approach Through Operational Procedures. 1977 NASA Authoriza- tion Hearings, Congressional Record, vol. 2, part 2, Feb. 10, 1976, pp. 134-155.

7. Foster, J. D.; and Lasagna, P. L.: Flight Measurements of the Noise Reduction of a Jet Transport Delayed Flap Approach Procedure. NASA TM X-73,172, 1976.

8. Allison, Robert L.: Application of the Delayed Flap Approach Procedures to Boeing 727 Airplane. NASA CR 137907, 1976.
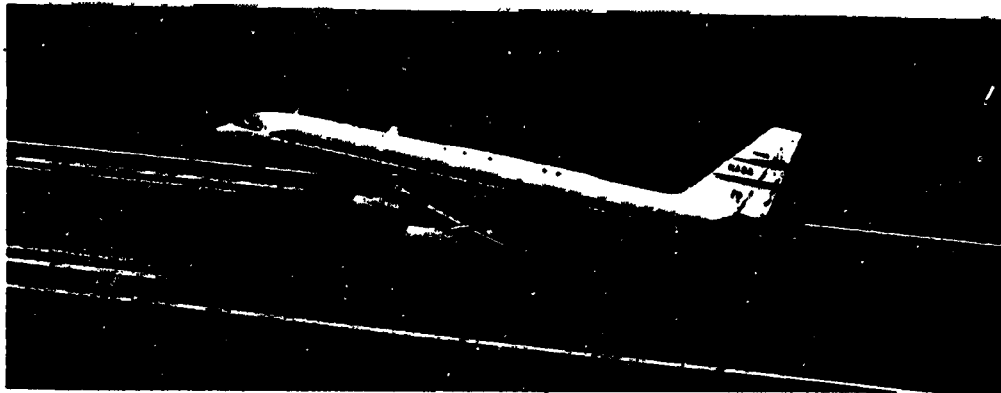
Figure 1.- CV-990 aircraft.
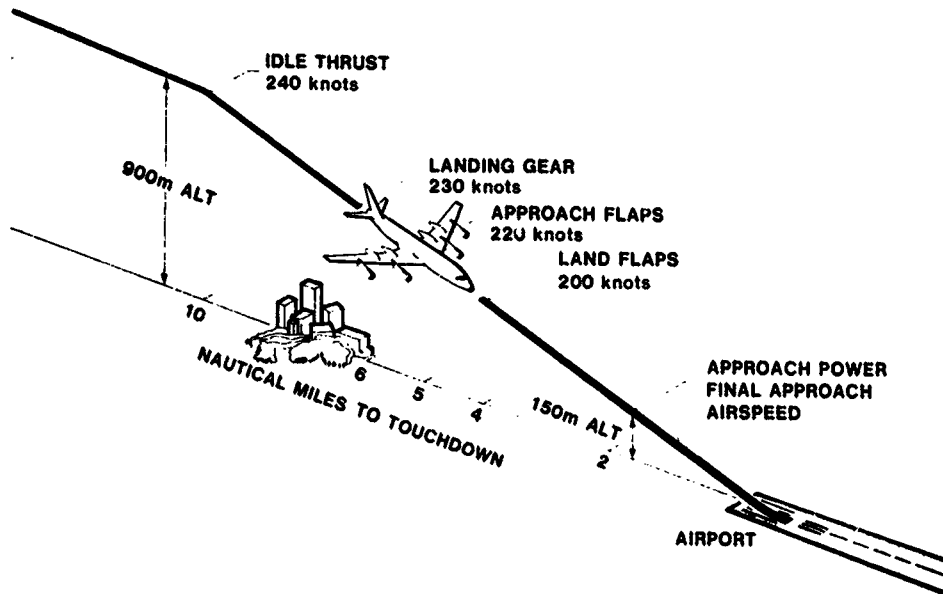
Figure 2.- CV-990 delayed flap approach profile.
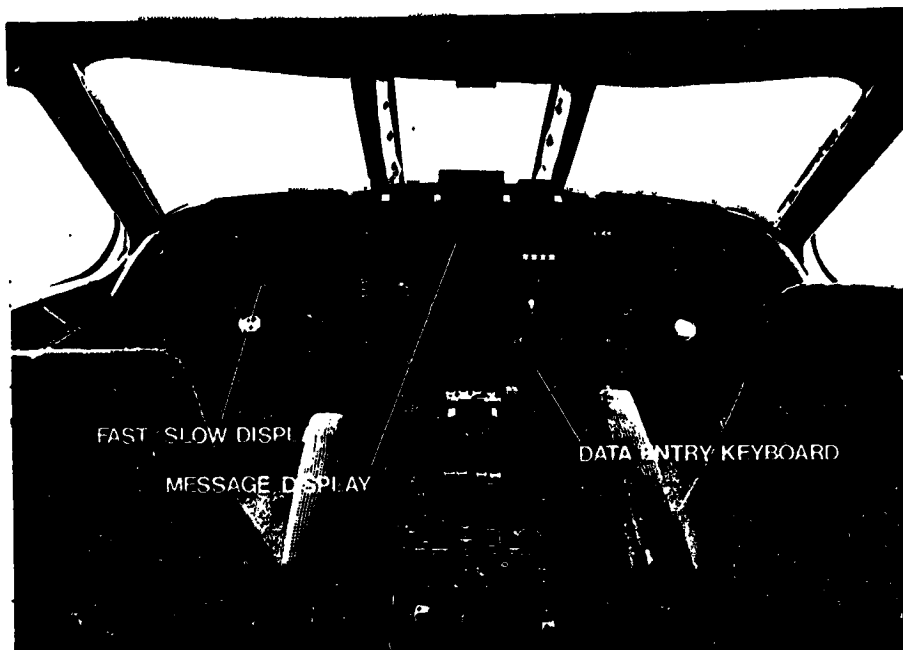
Figure 3.- CV-990 cockpit and displays used in delayed
flap approach.
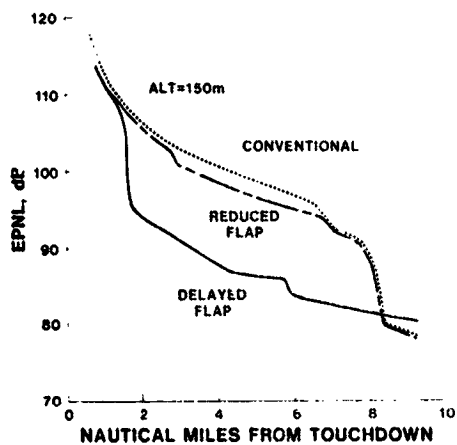
Figure 4.- CV-990 centerline noise
comparison for 3° glidepath.

88
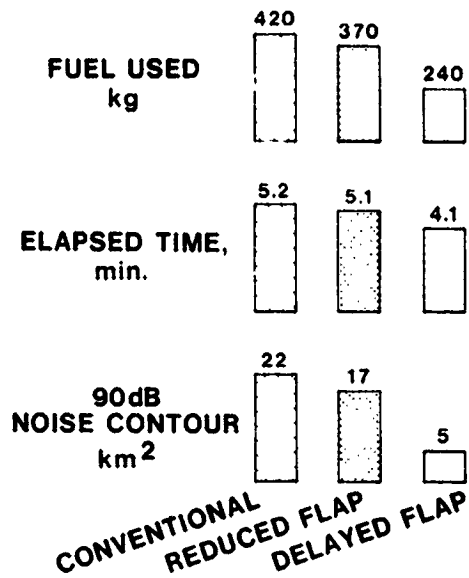
Figure 5.- CV-990 benefits comparison.
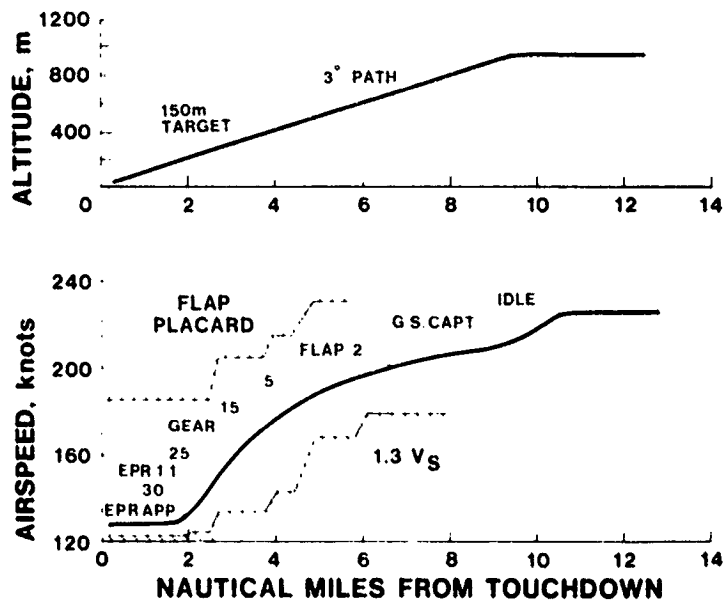
Figure 6.- Boeing 727 delayed flap approach profile.
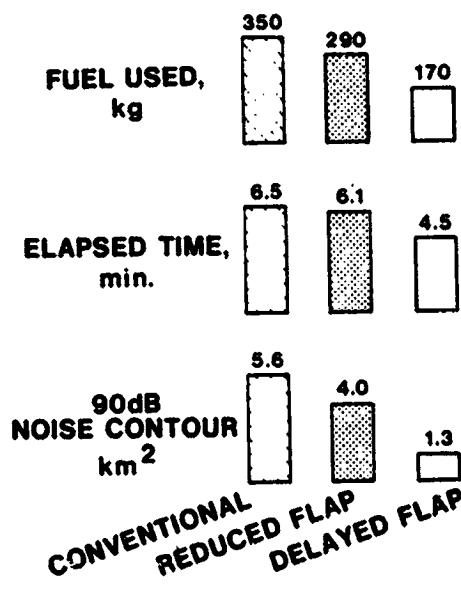
Figure 7.- B-727 benefits comparison.

 N 77-18087

GENERAL AVIATION APPROACH AND LANDING PRACTICES

Loyd C. Parker
NASA Wallops Flight Center

Maxwell W. Goode
NASA Langley Research Center

SUMMARY

The characteristics of air traffic patterns at uncontrolled airports and techniques used by a group of general aviation pilots in landing light airplanes have been documented. The report contains the results of some 1600 radar tracks taken at four uncontrolled airports and some 600 landings made by 22 pilots in two, four-place, single-engine light airplanes. The results show that the uncontrolled traffic pattern is highly variable. The altitudes, distances, and piloting procedures utilized may affect the ability for pilots to see-and-avoid in this environment. Most landing approaches were conducted at an airspeed above recommended, resulting in significant floating during flare and touchdowns that were relatively flat and often nose-low.

INTRODUCTION

The National Aeronautics and Space Administration has undertaken research programs to document the practices used by general aviation pilots in the traffic pattern and during final approach and landing. These efforts were prompted by the general aviation safety records reflected in accident summary reports, reference 1, and mid-air collision reports, references 2, 3, and 4. These reports indicate that the most frequent accidents, under visual flight rules (VFR), occur at the airport during the approach and landing of single-engine light planes flown for pleasure. Additionally, most mid-air collisions occur in the traffic pattern at uncontrolled airports on final approach and involve lack of adherence to proper pattern procedures and failure of pilots to see-and-avoid. The vast majority of all accidents are attributed to the pilot, as the cause or a factor contributing to the accident.

For the air traffic pattern studies a tracking radar system was used to measure and record the position-time histories of general aviation airplanes on pattern entry and in the pattern legs. Data were collected at four uncontrolled airports each having a different environment and pattern procedures. Airplane separation data in the pattern was measured at the last airport visited using two radar systems. For each radar

track, the runway, type airplane, surface winds, barometric pressure, visibility, and cloud ceilings were also recorded. Approximately 1400 individual radar tracks were taken to define air traffic pattern characteristics and 200 radar tracks taken to define normal general aviation separation practices. Preliminary results of the air traffic pattern studies were reported in reference 5.

Two modern, four-place, single-engine light airplanes (a low-wing and a high-wing) were leased from a fixed-based operator (FBO) and instrumented to obtain final approach and landing performance data. A cadre of 22 general aviation pilots with various backgrounds and experience was provided by the FBO to perform a series of landings on a long runway (1524 m - 5000 ft) and a short runway (762 m - 2500 ft). Approach and landing data were collected using the instrumented aircraft and a ground tracking system for approximately 150 landings of each airplane at each runway. All pilots were briefed on the purpose of the study and operation of the equipment prior to participating in the program. Pilots were asked to turn on the airborne data system just prior to final approach and to make normal landings based on their training and experience. Each pilot was scheduled to make a maximum of six landings in one day on one runway. To alleviate traffic conjestion on the long runway, touch-and-go landings with a significant ground roll were permitted. All landings on the short runway were completed to a full stop. Preliminary results of the low-wing aircraft phase of the approach and landing study were presented in reference 6.

TEST EQUIPMENT

Air traffic pattern measurements in the uncontrolled airport environment were made utilizing the MPS-19 tracking radar system, figure 1. Position-time histories of arriving airplanes were recorded on magnetic tape at one sample-per-second. Operators maintained a log of each track which included active runway, type airplane, surface wind, ceiling and visibility data. Radar data were rotated to the magnetic bearing of the landing runway and parallaxed to the landing runway threshold to create a normalized runway referenced coordinate system which permits direct comparison of pattern legs at each airport. During data reduction, operator log data were combined with each track and stored on computer disc files for retrieval and analysis. Position accuracy of the radar system is $\pm$ 9.5 m (10 yds) RMS in range and $\pm$ 1 mil RMS in angles.

Final approach and landing data were obtained using two instrumented airplanes, figure 2, and a ground tracking system, figure 3. Both airplanes, widely used in general aviation private flying, were leased from an FBO and instrumented to measure and record 21 different flight parameters, including airspeed, pitch attitude, flap position, and altitude. Modifications to the airplanes included a test boom on the left wing tip to measure airspeed, angle of attack and angle of sideslip; control switches

92

on the instrument panel; and an instrumentation package located aft of the pilot's seat. The airborne data system increased the basic weight of the test airplanes approximately 86.2 kilograms (190 pounds). Both airplanes were flight tested by NASA research pilots before and after modification with the determination that the instrumentation had a negligible effect on the airplane handling characteristics.

The ground tracking system was used to obtain the flight path and touchdown data with respect to the runway. This system was comprised of a 16-mm motion picture camera and a 3.05 m (10 ft) high by 67.0 m (220 ft) long photographic grid. The grid consisted of a series of vertical and horizontal plastic strips which formed squares of 0.6 m (2 ft) on a side within the grid frame. Normal photogrammetric techniques were used to obtain the trajectory data from the motion picture film. The airplanes were assumed to be aligned with the runway center line for photographic analysis. A field survey of a typical grid installation indicated a tracking accuracy of $\pm$ 0.3 m ($\pm$ 1 ft) or less.

AIRPORTS AND RUNWAYS

The location of the airports where data was taken during these studies are shown in figure 4. Air traffic pattern data were collected at Salisbury-Wicomico (SBY), Gaithersburg (GAI), Hyde (HYD), and Manassas (MAN) airports. Approach and landing data were collected at Hummel and Patrick Henry airports.

The Salisbury-Wicomico airport is located near Salisbury, Maryland, in a rural, low density traffic environment and has an airport elevation of 15.5 m (51 ft) above mean-sea-level (MSL), traffic pattern altitude (TPA) of 244 m (800 ft), three 1524 m (5000 ft) runways, an FAA Flight Service Station (FSS), VOR facility, commuter service, active flight school, airplane maintenance and service facilities, and approximately 25,000 operations per year of which one-third are estimated to be twin-engine aircraft. The Gaithersburg, Maryland, airport is located in a high density traffic environment north of the Washington, D.C., Terminal Control Area (TCA) and has an airport elevation of 165 m (540 ft) MSL, TPA of 183 m (600 ft), one 960 m (3150 ft) runway, right-hand pattern for runway 31, active flight school, significant airplane maintenance facilities, large number of resident private and corporate airplanes, and operations estimated at 50,000 per year of which 89% are single-engine airplanes. The Hyde airport is located near Clinton, Maryland, beneath the 457 m (1500 ft) floor of the Washington, D.C., TCA whose surface boundaries north, east, and west require all VFR traffic to enter from a south to southwest direction. The airport has an elevation of 76 m (249 ft) MSL, TPA of 244 m (800 ft), two runways - one of 976 m (3200 ft) and one of 640 m (2100 ft), another uncontrolled airport located approximately 1.5 n. mi. to the west, local pattern procedures which specify upwind pattern

leg entry for runways 5 and 31, active flight school and flying club, large number of resident airplanes, service and maintenance facilities, and operations estimated at 25,000 per year of which 94% are single-engine airplanes. The Manassas, Virginia, (MAN) airport is located west of the Washington, D.C., TCA in a relatively low density traffic environment and has an elevation of 57 m (186 ft), TPA of 244 m (800 ft), one 1128 m (3700 ft) runway, commuter service, flight school, service and maintenance facilities, large number of resident airplanes and operations estimated at 25-35,000 per year.

Approach and landing data for a long runway of 1524 m (5000 ft) were collected on runway 2 and 20 at the Patrick Henry airport in Newport News, Virginia. The elevation of the airport is 12.5 m (41 ft) MSL and controlled traffic at the airport was very heavy at times necessitating extended downwind and long straight-in final approach legs. The short runway airport, Hummel, located near Saluda, Virginia, is a small uncontrolled airport with an elevation of 9.1 m (30 ft) serving a rural area. All landings were made on runway 18 which is 762 m (2500 ft) long. Final approach to the runway is over water with a tree line approximately one-quarter of a mile from threshold. The airport had very light traffic; consequently, the test subjects could fly the pattern without interference.

RESULTS AND DISCUSSIONS

The results of the uncontrolled air traffic pattern measurements study are based on a total of 1409 individual radar tracks at three airports and 208 radar tracks of airplane separation distance at one airport. Of the individual tracks obtained approximately 83% were single-engine airplanes and 17% were twin-engine airplanes. The results of the approach and landing performance study covers a total of 616 landings made by both airplanes at both runways. A total of 299 landings (144 long runway, 155 short runway) were made in the low-wing airplane and 307 (163 long runway, 154 short runway) were made in the high-wing airplane.

Uncontrolled Air Traffic Pattern

The generally recognized standard uncontrolled air traffic pattern is characterized by entry to the downwind leg at a 45-degree angle at a 244 m (800 ft) altitude above ground level (AGL) and "left-hand" turns from downwind to base and base to final legs, reference 7. A different pattern may be adopted at an individual airport to avoid a local problem. Two of the airports had local variations from the standard pattern. HYD has a local procedure of an upwind pattern leg entry for runways 31 and 5. GAI has a local pattern altitude of 183 m (600 ft) and a right-hand pattern for runway 31. At the time traffic measurements were conducted the FAA had issued NPRM 71-20, "Operations at Airports Without Control

94

Towers," which proposed a new uncontrolled traffic pattern concept,
figure 5. FSS personnel at SBY encouraged local pilots to try out this
proposal during the period air traffic measurements were conducted.

Pattern Entry

The lack of adherence to pattern entry procedures is a possible
cause of mid-air collisions. The pattern leg entry locations were examined
to determine the variations from local procedure. The results of this
analysis for arriving airplanes, figure 6, illustrates the variations
from local pattern entry procedure. In the higher traffic density environ-
ment of GAI, adherence to the pattern procedure was significantly better
than either HYD or SBY. Approximately 51% at SBY, 12% for downwind and
66% for upwind runways at HYD, and 11% at GAI of the arriving traffic did
not adhere to the local pattern entry procedure. Normal left- and right-
hand traffic entering downwind at GAI are shown as a right-hand entry on
figure 6 to illustrate deviations from the standard. At GAI 2% of the
traffic failed to recognize the right-hand pattern established for runway
31 and used a left-hand approach opposite to local pattern. At SBY 4% of
the traffic used a right-hand base entry opposite to the left-hand
pattern.

Pattern Leg Distributions

In addition to the variation in pattern entry location, the distance
and altitude variations within the pattern legs may increase the pilot's
see-and-avoid problem. The ground track distributions observed in the
pattern legs at SBY and HYD, figure 7, illustrate this variation between
a low density (SBY) and high density (HYD) environment. Another factor
affecting this difference is that SBY's traffic was 33% twin-engine as
compared to only 6% twin-engine traffic of HYD. In either case, the
pattern legs are wide and extend from a few tenths of a nautical mile out
to greater than 1.5 n. mi. from the runway. General aviation pilots
should expect conflicting traffic at distances up to several nautical
miles when entering an uncontrolled traffic pattern. The cumulative
distributions of distance for the downwind, base and final pattern legs
are shown in figure 8. This figure further illustrates the difference
between HYD's constrained environment and SBY. Conversely, the downwind
cumulative distribution, figure 8a, for SBY and GAI, which has twice the
traffic of SBY, are essentially the same out to the median pattern distance.
The divergence beyond the median for the SBY and GAI suggest that this
portion of the distribution may be a result of the twin-engine traffic
percentage of 33% at SBY and 11% at GAI. On base and final legs little
difference in the cumulative distribution is shown up to the 97% level,
figure 8b and 8c.

Traffic Pattern Altitude Variation

A factor which may seriously influence a pilot's ability to detect another airplane is adherence to the established TPA. The cumulative distributions of the average altitude for all traffic at each airport on downwind, base and final legs are compared in figure 9. The variation from the downwind TPA of 183 m (600 ft) at GAI and 244 m (800 ft) at HYD and SBY is shown in figure 9a. Less than 1% of the traffic observed on downwind is below an altitude of approximately 122 m (400 ft). This figure also illustrates that 99% of the traffic on downwind for GAI and HYD was below 305 m (1000 ft) and at SBY was below 430 m (1410 ft). Variations of at least 183 m (600 ft) or greater in the TPA flown are shown at all airports. At HYD and SBY where the TPA was 244 m (800 ft), greater than 65% (SBY) and 90% (HYD) of the traffic was below this altitude on downwind leg. In comparison the GAI median altitude is essentially equal to the specified TPA, indicating that 183 m (600 ft) may be the more natural pattern altitude. In reference 8, pilots overwhelmingly indicated they preferred a TPA of 244 m (800 ft) or 305 m (1000 ft). Most pilots (95%) indicated they did not deviate from the TPA more than 45.6 m (150 ft),substantially less than was actually observed. The significant altitude variations on downwind leg are continued through base and final legs as shown on figures 9b and 9c. Most data shown for the final leg were taken at a distance greater than 762 m (2500 ft) from the runway threshold.

Croswind Leg

Departure airplanes may pass through portions of the crosswind leg creating potential mid-air collision (MAC) situation. This is illustrated by figure 10 which shows a cross section of a bivariate log-normal distribution of the crosswind leg at SBY and typical departure paths of a single-engine and twin-engine airplane. The conflict between departing and arriving airplanes has been recognized. The latest FAA Advisory Circular AC 90-60 "Recommended Standard Traffic Patterns for Airline Operations at Uncontrolled Airports", reference 9, recommends that a downwind entry mid-point of the runway be used and established specific departure procedures to minimize conflict with traffic using the crosswind leg. At airports where a crosswind pattern leg is utilized, specific procedures are needed for arrival and touch-and-go traffic.

Type of Aircraft

A comparison of the mean distance and altitude for single-engine high-wing (SEHW), single-engine low-wing (SELW), and twin-engine (TWIN) airplanes at SBY is shown in figure 11. The mean pattern distance, figure 11a, of the SEHW airplanes is approximately 0.2 n. mi. less than

96

SELW airplanes, and up to 0.5 n. mi. less than SEHW on base leg. TWINS were also found to fly above SEHW and SELW airplanes on all pattern legs, figure 11b, except base and final where TWINS transitioned to the lowest mean altitude. In the higher density environment of GAI and HYD, the difference in the mean pattern leg distance and altitude was found to have essentially the same characteristics.

In general SEHW airplanes fly closer to the runway and higher than SELW airplanes. TWIN airplanes fly higher and further from the runway than SEHW and SELW, except on base and final where they have transitioned to a lower mean altitude.

Closure Rate

Since all traffic generally occupies the same airspace in the uncontrolled air traffic pattern environment, closure rates between airplanes whose pilots fail to see the other becomes an important consideration in the development of any systems solution to the mid-air collision (MAC) problem. The average cumulative horizontal and vertical closure rates in the traffic pattern were determined for GAI and HYD, figure 12. The median closure rate between airplanes expected in a typical general aviation uncontrolled traffic pattern is 18 knots horizontally and 1.3 m/sec (258 ft/min) vertically. Peak closure rates in a typical general aviation environment within the pattern legs should not exceed 85 knots and 5.4 m/sec (1,068 ft/min) more than 2% of the time. If turbo-prop powered twin-engine airplanes use the environment, such as the case at SBY, the average closure rate in the pattern legs will be increased. For SBY, the median horizontal closure rate was found to be approximately 45 knots and exceeded 144 knots 2% of the time - a significant increase over the peak rates for HYD and GAI. Vertical closure rates also increased to a median of 1.9 m/sec (375 ft/min) and exceeded 7.3 m/sec (1437 ft/min) 2% of the time. The possible closure rates during and prior to pattern entry are even higher and exceed 360 knots in the SBY environment. Closure rates determine how far in advance of a MAC that a warning must be issued. To provide a 20-second warning time at a 360 knot closure rate would require issuing the warning when the airplanes were separated by greater than 2 n. mi. It is not considered unusual to have several airplanes with separations of less than 2 n. mi. at relatively high closure rates in a high density uncontrolled airport traffic area.

Separation Distance

Another factor which may affect MAC systems performance and required accuracy is the normal separation distances used by general aviation pilots in the uncontrolled traffic pattern. In reference 8, pilots indicated they used an average of approximately 1 n. mi. separation in the traffic pattern. The actual separation distances measured at a typical

uncontrolled airport were generally less than 1 n. mi. This is illustrated by figure 13 in which a typical separation track shows much less separation than 1 n. mi. In fact, the minimum separation distance for a number of tracks was less than 0.1 n. mi. during a portion of the track. The cumulative distributions of the average separation distance and the minimum distance observed for each track are shown in figure 14. The median average separation distance for each pair of aircraft tracks was found to be 0.73 n. mi.; however, a significant percentage (16%) used an average separation of less than 0.5 n. mi. The median minimum separation distance observed for each pair of tracks was found to be 0.49 n. mi. and 10% of the aircraft closed to less than 0.2 n. mi. The separation distances observed illustrate that general aviation pilots often use separations in the uncontrolled traffic pattern that are extremely close.

Final Approach Trajectories

Final approach trajectories, generally considerable variation from stabilized, steady flight paths. Profiles of the final approach trajectories for the high-wing airplane at the long runway are presented in figure 15. Included in the figure are the median and the 5- to 95-percentile spread of the data for the height of the airplane at the threshold and the touchdown distance from the threshold. For reference, 3° and 6° slopes passing through the median height at the threshold are included.

For both airplanes at both runways the average flight path angle ranged from 4.7^{O} at the long runway to 6.1^{O} at the short runway with individual flight paths ranging from 1^{O} to 14° during portions of the approaches. The average flight path angle was approximately 1^{O} steeper at the short runway than at the long runway.

The median height at the threshold was lower for the low-wing airplane than for the high-wing airplane at both runways. However, both airplanes were brought in lower over the threshold at the short runway than at the long runway, even though the average flight path angle was approximately 1^{O} steeper.

The median touchdown distance was in direct relation to the median height of the respective airplanes at the threshold. That is, the lower the median height at the threshold the closer the median touchdown was to the threshold. The median touchdown distance for both airplanes at both runways was within the first third of the runway, but well beyond the runway designation numbers just past the threshold. The median touchdown for both airplanes at both runways ranged from 10 percent to 16 percent of the runway length.

Final Approach Airspeed

The average final approach airspeed and the average flap deflection measured at 5-second intervals for the 60-second period prior to touchdown are presented in figure 16 for the high-wing airplane at both runways. Also included in the figure are reference approach speeds and the measured stall speeds of the airplane at the nominal test weight. The reference approach speeds are interpolated values of the manufacturer's recommended approach speeds using the average flap deflection at each time period.

In general, the pilots flew the final approach with an average speed considerably faster than the reference speed. In fact, the average approach speeds were more than 5 knots in excess of the reference speeds until within 15 seconds or less of the touchdown, as indicated by the solid symbols in figure 16. The exception to this result was the low-wing airplane at the short runway in which case the average speed was only slightly in excess of the reference speed for the final 40 seconds prior to touchdown.

Another point of interest shown by the data is that the final approach speeds at the short runway were slower than those at the long runway for both airplanes. This correlates directly with the larger average flap deflection used at the short runway. However, the reduction in average approach speed (6 to 12 knots) was much greater than the difference in the reference approach speeds (1 to 2 knots). This difference would indicate that the pilots were concerned about the runway length and were paying closer attention to airspeed during the approaches to the short runway to assure landings with a comfortable margin between the stopping point and the end of the runway. Based on the manufacturer's published landing distances for the airplanes, the designated short runway was not, in fact, a "short runway" requiring maximum performance from either airplane or pilot to achieve a normal landing in the available distance.

Touchdown Airspeed

Cumulative distribution of airspeed at touchdown for the high-wing airplane at both runways is presented in figure 17. Included in the figure are the measured stall speeds of the airplane at the nominal test weight and the reference approach speeds based on the flap settings for the last 10 seconds of the approaches.

The data generally show that the pilots landed the airplane with speeds considerably in excess of the stall airspeed; this is most probably a direct result of the excessive airspeed used during the final approach. The median touchdown speed ranged from 13 percent to 48 percent above the measured flaps-up stall speed, and less than 6 percent of the landings were within the stall speed range. Except for the low-wing airplane at the short runway, a rather high percentage of the landings were made in

excess of the reference approach speeds. The touchdown speeds at the short runway were significantly less than those at the long runway by approximately the same amount as the difference in the final approach speeds between runways.

Touchdown Pitch Attitude

Associated with the high touchdown speeds were pitch attitudes that were relatively flat for both airplanes at both runways. The cumulative distributions of pitch attitude at touchdown for the high-wing airplane are presented in figure 18. Included in the figure is a line indicating the in-flight three-point touchdown attitude which separates the regions of nose-wheel and main-wheel landing attitudes. In general, the touchdown pitch attitudes show little to no difference with respect to runways.

The data show that the pitch attitudes at touchdown were relatively flat for both airplanes at both runways. The median touchdown attitude ranged from only 1.4° to 2.6° above the three-point attitude (pitch-up). A significant percentage of the landings was made in which the nose wheel contacted the runway before the main wheels. Approximately 12 percent of the landings were nose wheel first, except for the low-wing airplane at the short runway where the percentage was 22 percent. Nose-wheel landings are almost invariably a direct result of allowing an airplane to touch down with an excessively high airspeed and certainly present the potential for a landing accident due to nose wheel collapse, porpoising of airplane, or unstable airplane motions referred to as wheel-barrowing.

Mid-Air Collision Simulation

Using the approach data presented in this paper a math model capable of simulating uncontrolled air traffic patterns has been developed. MAC simulations which duplicate the existing environment can provide a baseline for evaluating the effect of changing the uncontrolled pattern concept or the effect or improvements in general aviation piloting procedure. The technique utilized is illustrated in figure 19 which shows the position time histories of two airplanes in a typical approach procedure that are time normalized to have a MAC on final approach. The view angle from both airplanes to the other was computed based on their heading, bank angle, and relative positions. A time history of this data is plotted on the view envelope of each airplane, figure 20, and the percent of time each airplane is visible to the other pilot determined, reference 10. The result, figure 21, illustrates the cumulative percent of time each pilot had to detect the other from a separation distance of approximately 3 n. mi. The case shown is representative of normal general aviation approaches, yet, neither pilot could have seen the other airplane approximately 65 percent of his approach time. Using this technique the cumulative probability of a MAC can be estimated by including the probability of

each pilot looking and the probability of seeing when he looks as a function of the separation distance. By simulating thousands of such MAC's in this manner and defining the baseline for the existing uncontrolled traffic pattern environment, the relative improvements that may be achieved through changes in piloting procedure or by new pattern concepts can be determined. Typical pattern concepts under consideration are shown in figure 22. General aviation pilots have indicated, reference 8, that approximately 44 percent preferred the standard left-hand pattern and 30 percent preferred the proposed pattern shown.

Systems Studies

The uncontrolled air traffic studies indicate that new piloting and/or pattern concepts may not adequately reduce the MAC hazard at high density uncontrolled airports. Based on the traffic characteristics observed a systems definition study is in progress to determine the feasibility of a low-cost Automated Pilot Advisory System (PAS), reference 11, for high density, uncontrolled airports. The system concept, figure 23, under evaluation would utilize a small skin tracking radar, microprocessors, weather sensors, and a VHF transmitter. The system functions identified for evaluation are:

1. Broadcast an airport advisory voice message once every two minutes which specifies the active runway, surface winds, barometric pressure, and temperature.

2. Broadcast an air traffic advisory voice message every two minutes which specifies the location of all traffic within 3 n. mi. of the airport.

3. Broadcast a mid-air collision advisory voice message whenever two airplanes exceed a 15-second Modified Tau Criteria, reference 12.

4. Provide the FBO with runway select and override functions and the capability to record limited cautionary messages to be included in airport advisory message.

5. Provide for remote access of system information, via telephone.

Pulse, pulse-doppler, and doppler radar systems are under evaluation for this application. Low-cost X-band radars which appear suitable for this application are readily available as marine and airborne weather radars.

The computer would provide the essential system logic and control functions. These include radar data processing, clutter rejection, track-while-scan, weather data processing, logic and generation of pre-stored advisory word message formats, power failure auto-restart function,

FBO control functions and system self checks.

Whenever the various computer logic conditions are met, a voice
message in a standard word sequence would be generated. Computer software
will interlace proper key words into the standard format to complete the
advisory message. Pre-recorded digital message sequences and vocoder
voice sythesis techniques are under evaluation for this system. Typical
message sequences with underlined key words follow:

AIRPORT ADVISORY - HYDE - ACTIVE RUNWAY - THREE-ONE - RIGHT HAND PATTERN -
WIND - TWO-ONE-FIVE AT SIX KNOTS - ALTIMETER THREE ZERO POINT ZERO FOUR -
TEMPERATURE IS TEN DEGREES.

<center>or</center>

- TRAFFIC ADVISORY - HYDE - AIRCRAFT AWAITING DEPARTURE - AIRCRAFT ON
FINAL - TWO AIRCRAFT DOWNWIND - ARRIVING AIRCRAFT THREE MILES - NORTHEAST ---
DEPARTING AIRCRAFT ONE MILE SOUTHEAST.

An experimental PAS will be configured to evaluate the various
system performance options, message formats, and pilot reaction to system
utility.

<center>CONCLUING REMARKS</center>

The characteristics of general aviation piloting procedures during
approach and landing have been documented. Data presented illustrate the
variability with which the uncontrolled air traffic patterns, and the
approach and landing maneuvers are performed. Results confirm that
pattern entry location and procedure are often inconsistent with the
local or accepted standard pattern. The uncontrolled traffic pattern
legs are up to 1 n. mi. wide for typical general aviation airports and
may exceed 2 n. mi. in width in environments including high performance
twin-engine airplanes. Significant variation from the established pattern
altitude, $\pm$ 75 m (246 ft), is not unusual. At airports where a crosswind
pattern leg is utilized, specific procedures are needed for arrival and
touch-and-go traffic. Departure traffic should abide by the recommendations
of FAA Advisory Circular AC No. 90-66. Systems to prevent MAC at high
density uncontrolled airports must cope with very low and high closure
rates and normal VFR traffic separation distances of 0.1 n. mi. or less.

The average final approach airspeeds were generally higher than
recommended which produced significant floating during the landing flare,
average touchdown speeds well above airplane stall speed and landing
pitch attitudes that were generally flat or nose-low. On the average,
pilots used higher flap deployment angles, steeper approaches, less speed
and achieved landings closer to threshold on the short runway when

compared to the long runway approaches.

The time available for pilots to see-and-avoid a MAC with other airplanes in the uncontrolled pattern environment may be relatively short. Manuevers and vision view field restrictions create this situation; however, the ability to detect other airplanes at greater than 1 n. mi., the percentage of time pilots spend looking for other airplanes, and rapid closure rates often involved are factors which increase the MAC hazard. The Pilot Advisory System concept may provide pilots with greater ability to locate and avoid conflicting traffic, if low-cost system feasibility is demonstrated.

REFERENCES

1. Anon.: Aircraft Accident Reports, Brief Format. National Transportation Safety Board. NTSB-BA-71-3, 1970.

2. Mid-Air Collisions in U. S. Civil Aviation 1969 - 1970. Special Study, National Transportation Safety Board, Report No. NTSB-AAS-72-6, Washington, D. C. June 7, 1972.

3. Near Mid-Air Collision Report of 1968. Department of Transportation, Federal Aviation Administration, Air Traffic and Flight Standards Technical Report, prepared by NMAC Study Group, July 15, 1969.

4. Mid-Air Collisions in U. S. Civil Aviation - 1968 - A Special Accident Prevention Study. National Transportation Safety Board, Washington, D. C., July 1969.

5. Parker, L. C.: General Aviation Air Traffic Pattern Safety Analysis. NASA TM-X-6955, The System Safety Society Symposium, July 17, 1973.

6. O'Bryan, Thomas C.; Goode, Maxwell W.; and Harris, Randall L.: A Study of Light Airplane Pilot Landing Performance. Society of Automotive Engineers, Inc. 740350, 1974.

7. Anon.: Jeppesen Private Pilot Course. Times Mirror 1971.

8. Parker, Loyd C.: Pilot Preference and Procedures at Uncontrolled Airports. NASA TN D-7928, 1975.

9. Anon.: Recommended Standard Traffic Patterns for Airline Operations at Uncontrolled Airports. Department of Transportation, Federal Aviation Agency, AC 90-66, 1975.

10. Bashir, J. and Singh, R. P.: Aircraft Cockpit Vision Math Model. NASA CR-141406, July 1975.

11. Parker, Loyd C.: NASA Study of An Automated Pilot Advisory System. 760460, Society of Automotive Engineers, April 1976.

12. Britt, C. L.: A Look at Alarm Rates in Collision Warning Systems. Trans. of the 16th Annual Air Safety Forum, Airlines Pilots Association, July 1969.

14
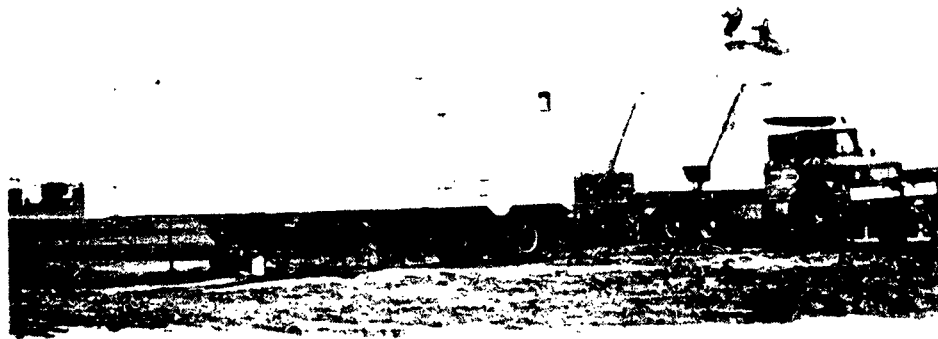
Figure 1.- MPS-19 radar system.

LANGLEY RESEARCH CENTER

Figure 2.- test airplanes.
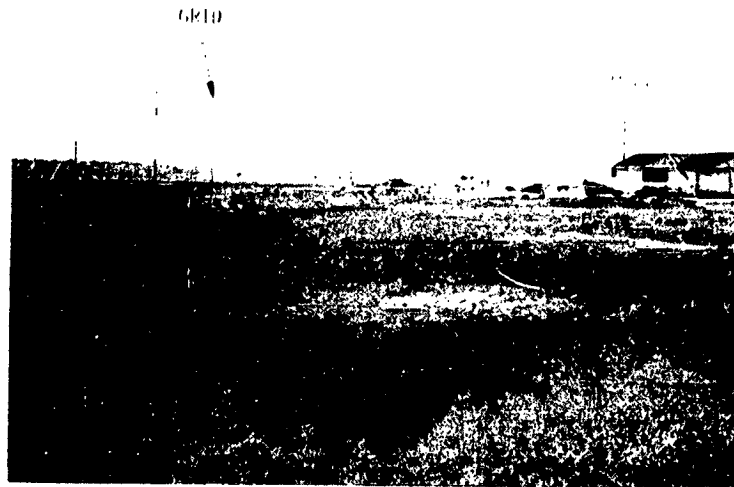
Figure 3.- Ground tracking system.
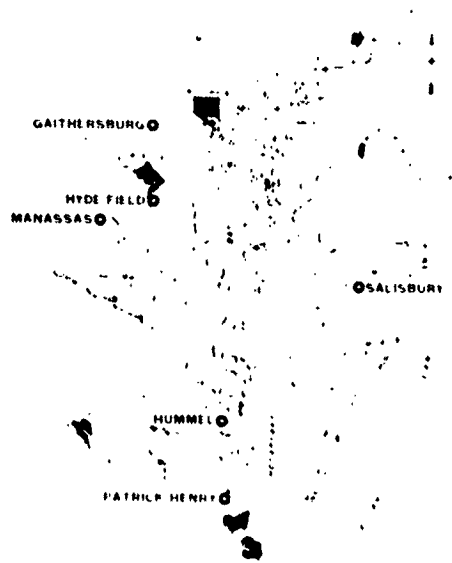
Figure 4.- Airport locations.

TPA-1000 FT.
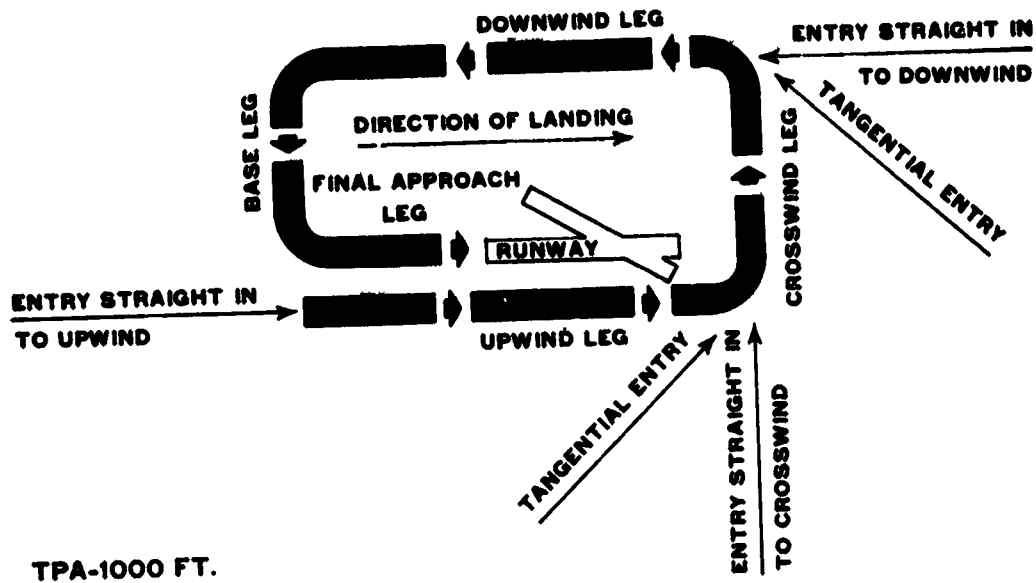
Figure 5.- Proposed uncontrolled air traffic pattern.
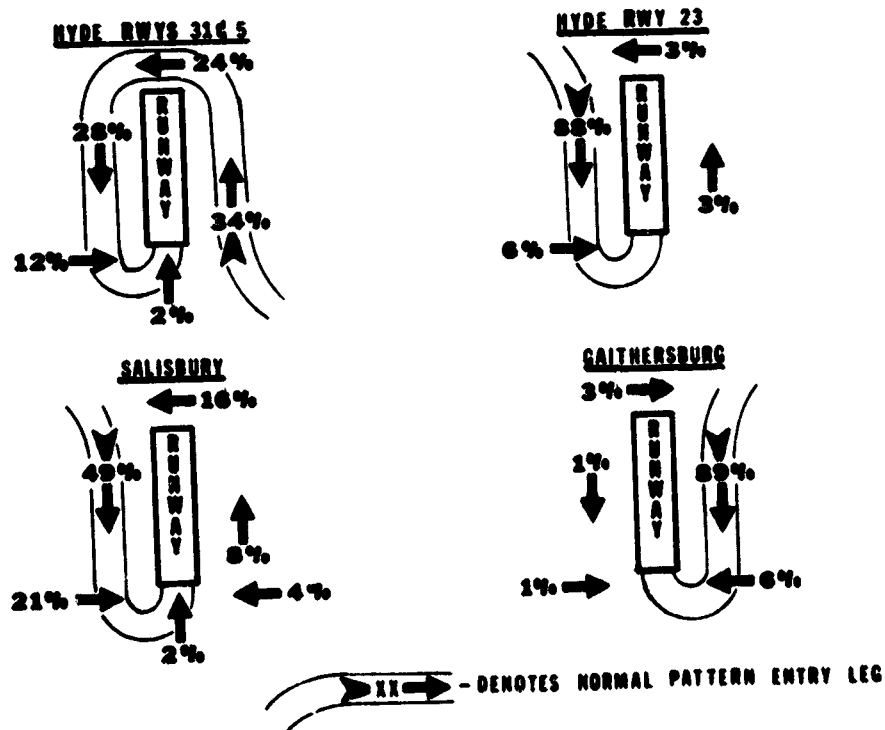
Figure 6.- Traffic pattern entry location.
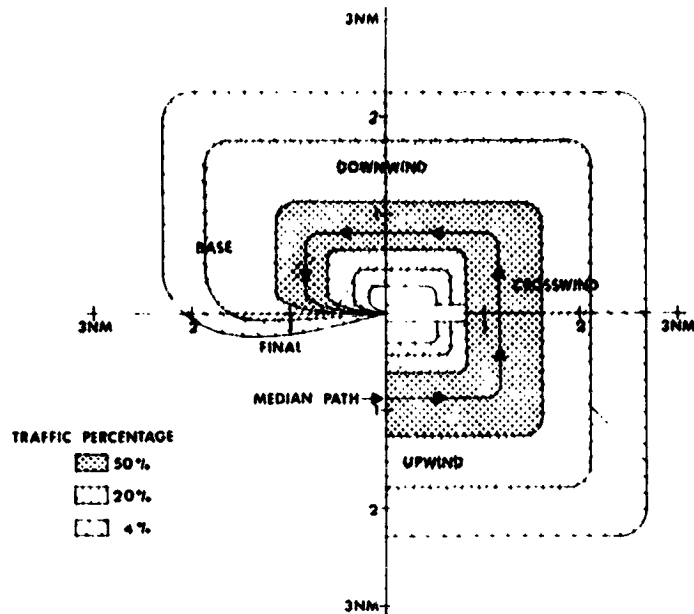
(a) Salisbury.
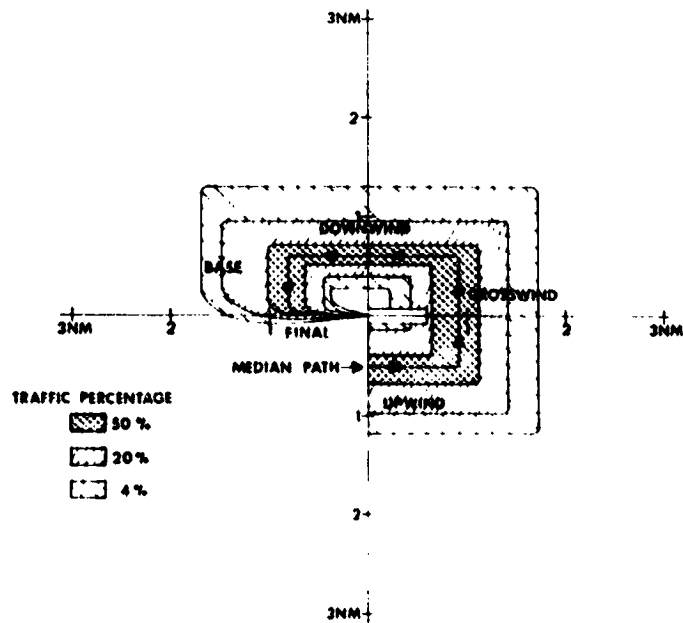
(b) Hyde.

Figure 7.- Traffic pattern leg distance distribution.

108
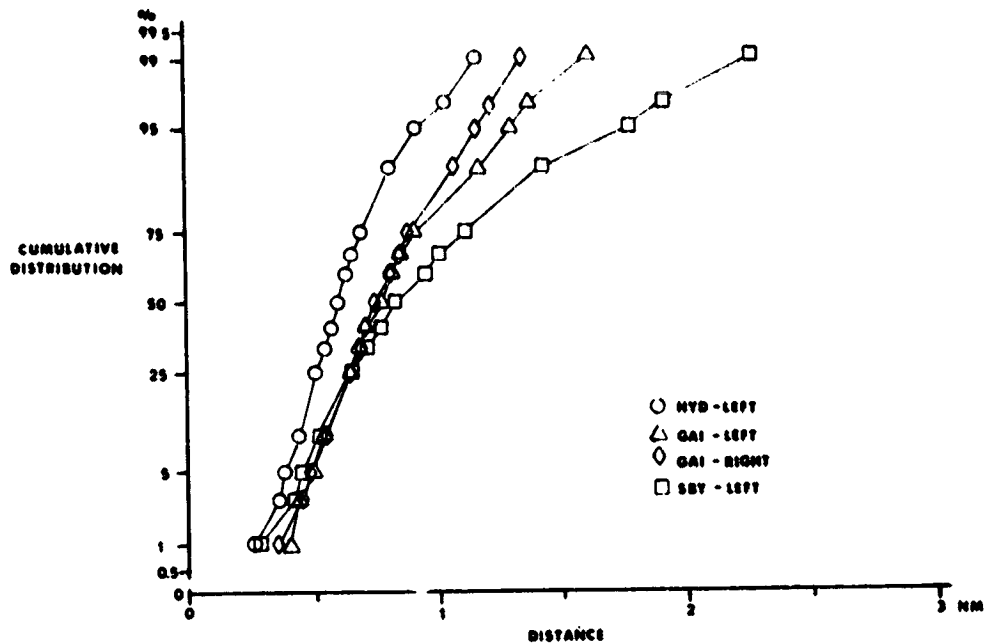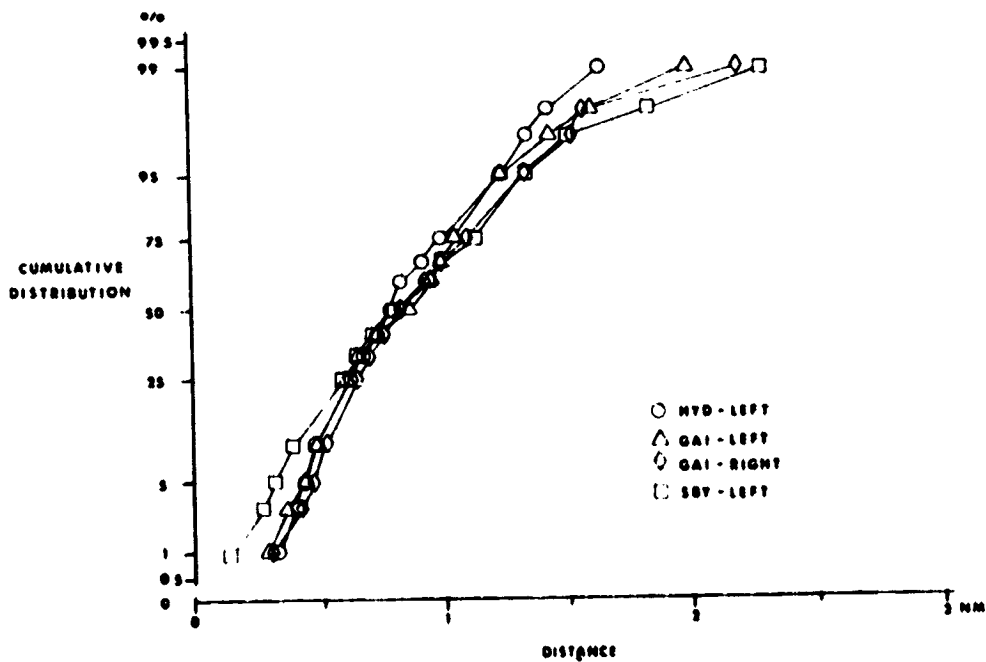
(a) Downwind leg.

(b) Base leg.

Figure 8.- Cumulative distribution of pattern leg distance.

109
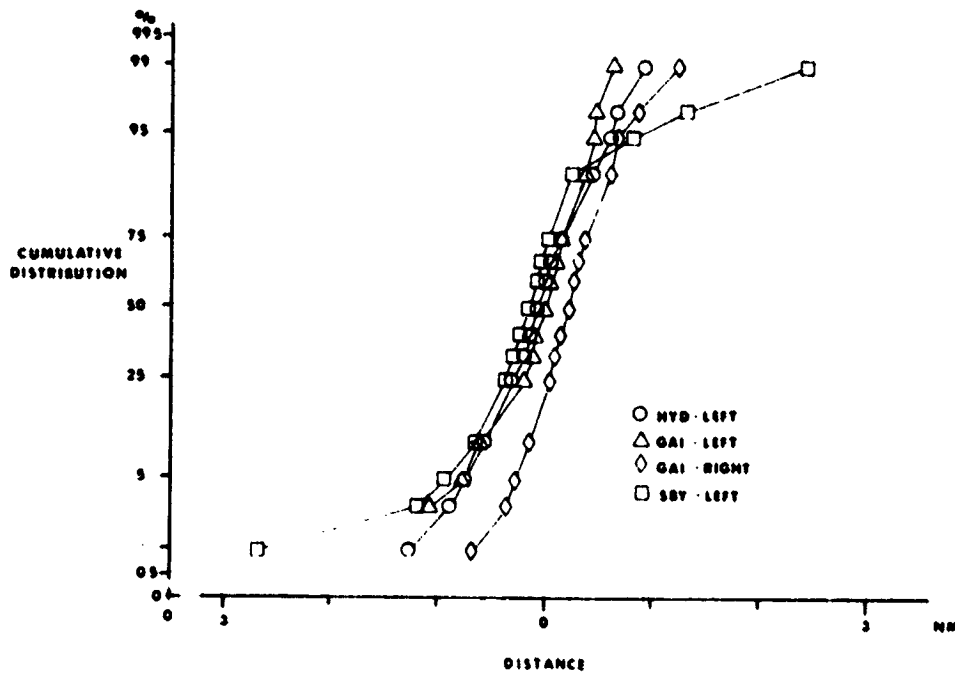
(c) Final leg.

Figure 8.- Concluded.

110
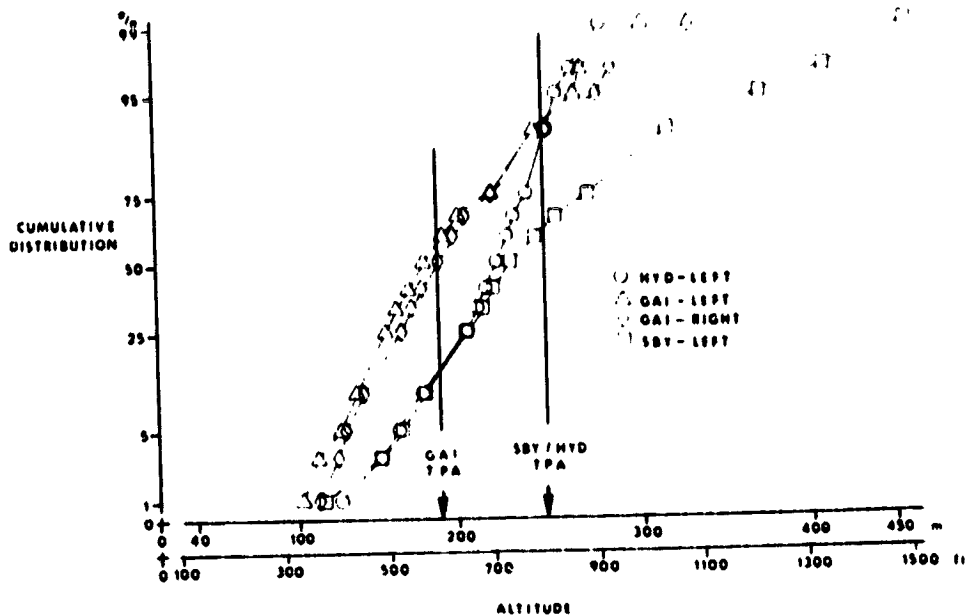
(a) Downwind leg.
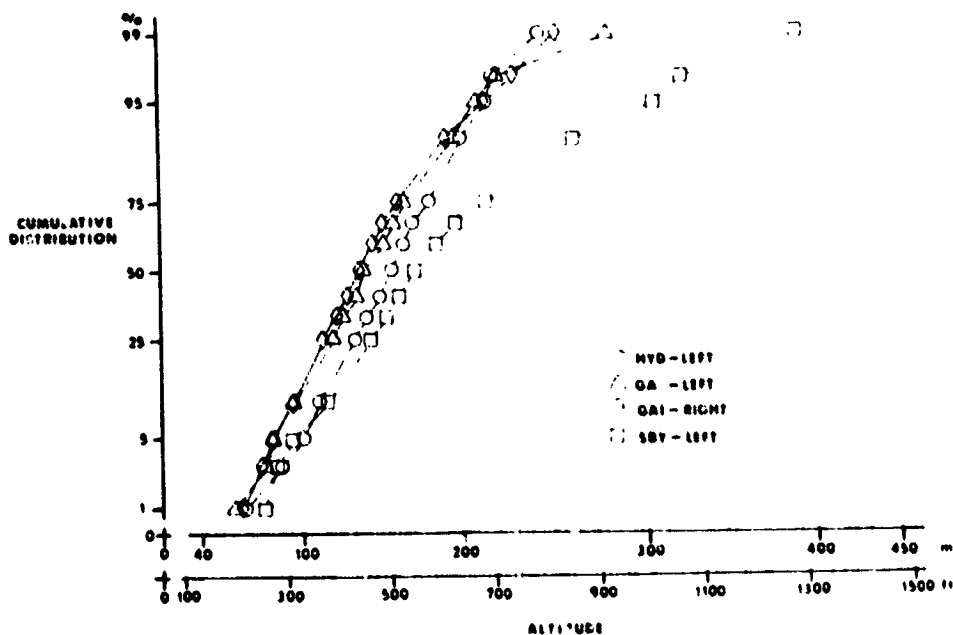
(b) Base leg.

Figure 9.- Cumulative distribution of pattern leg altitude.
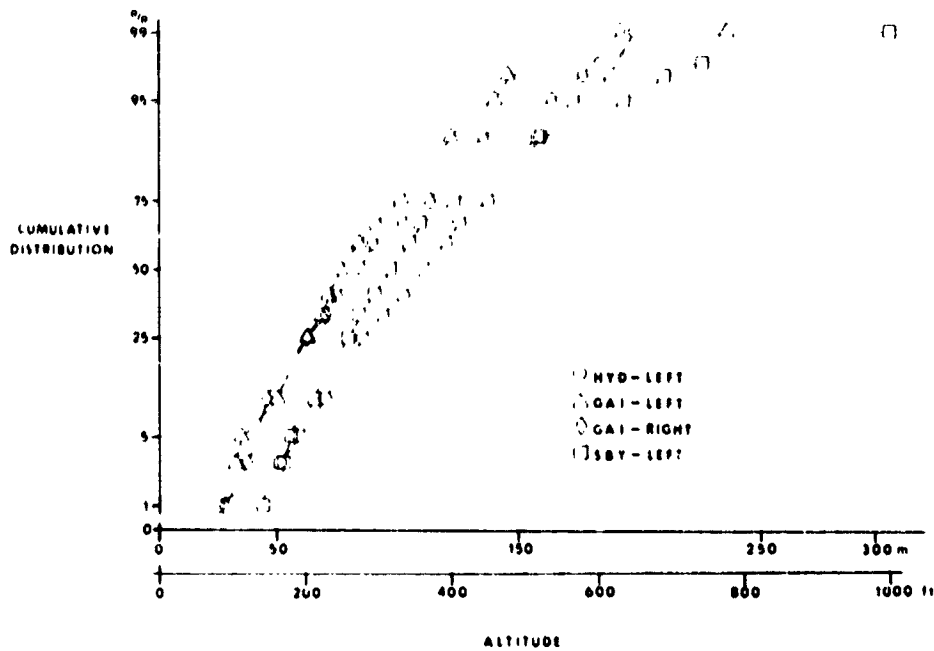
(c) Final leg.

Figure 9.- Concluded.
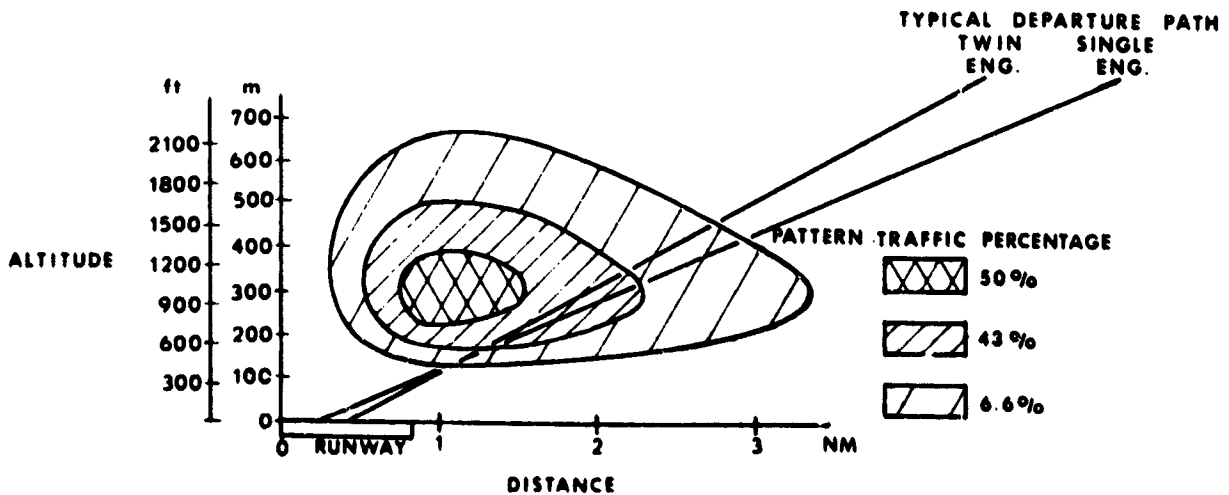
Figure 10.- Crosswind leg traffic percentage and typical departure paths.
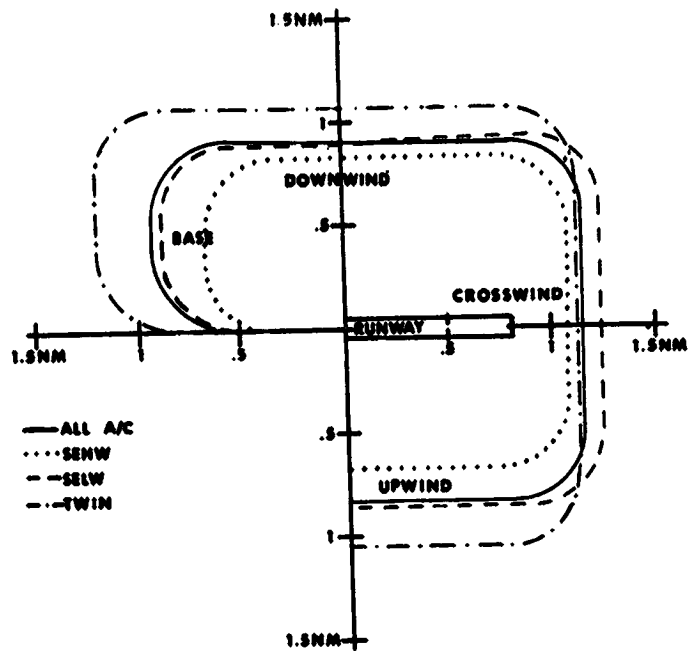
(a) Mean distance.
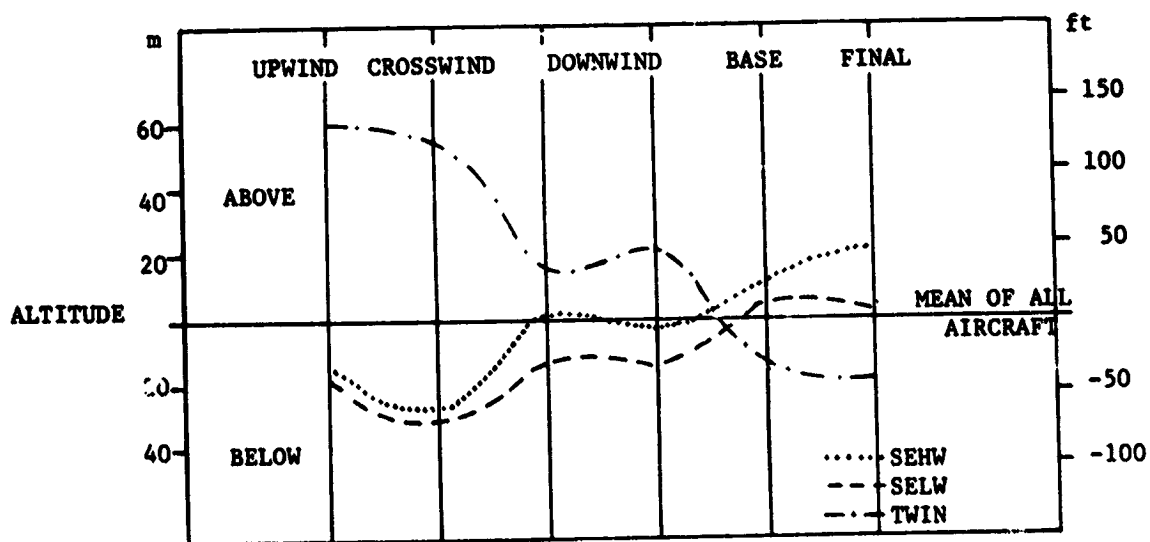
(b) Mean altitude.

Figure 11.-- Comparison of mean distance and altitude by type of aircraft at SBY.

113
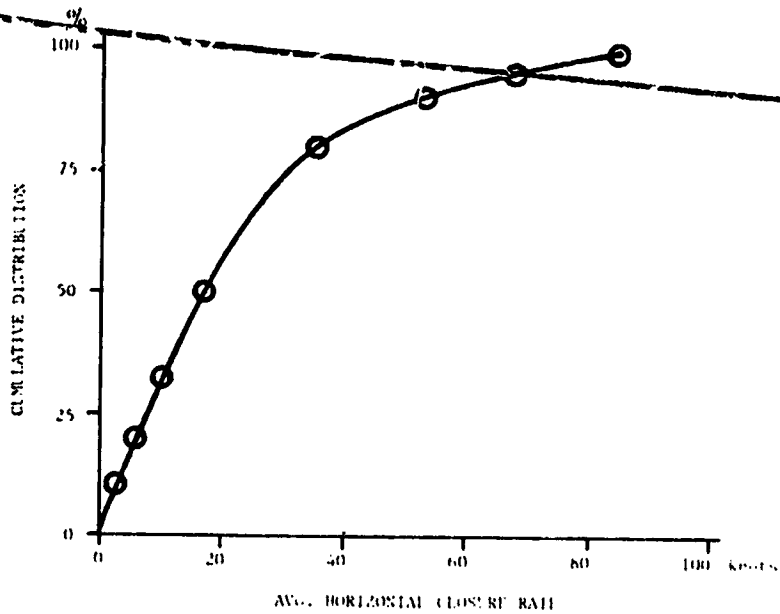
(a) Horizontal closure rate.
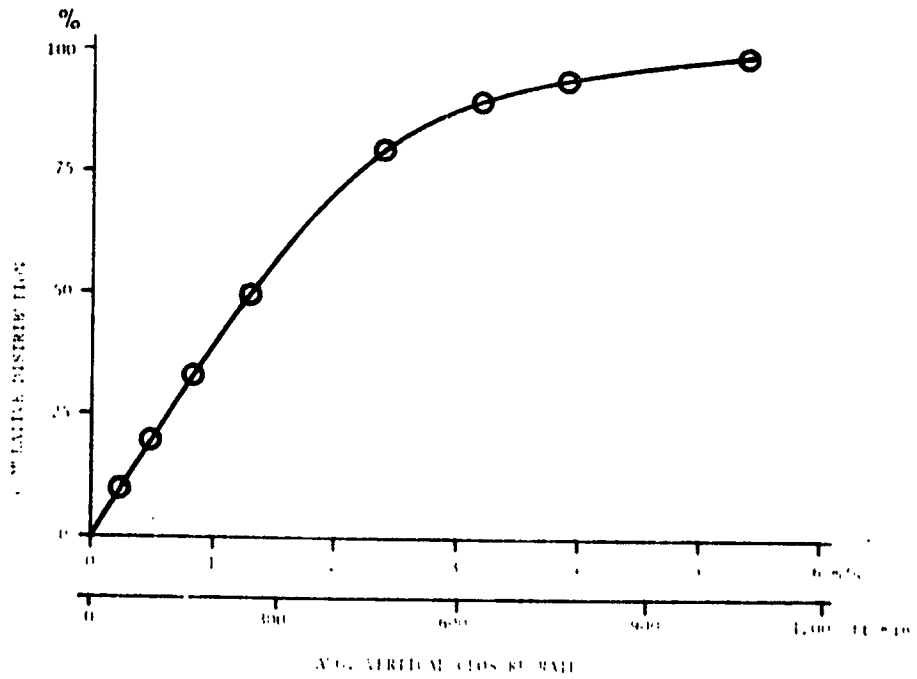
(b) Vertical closure rate.

Figure 12.- Expected horizontal and vertical closure rates.

114
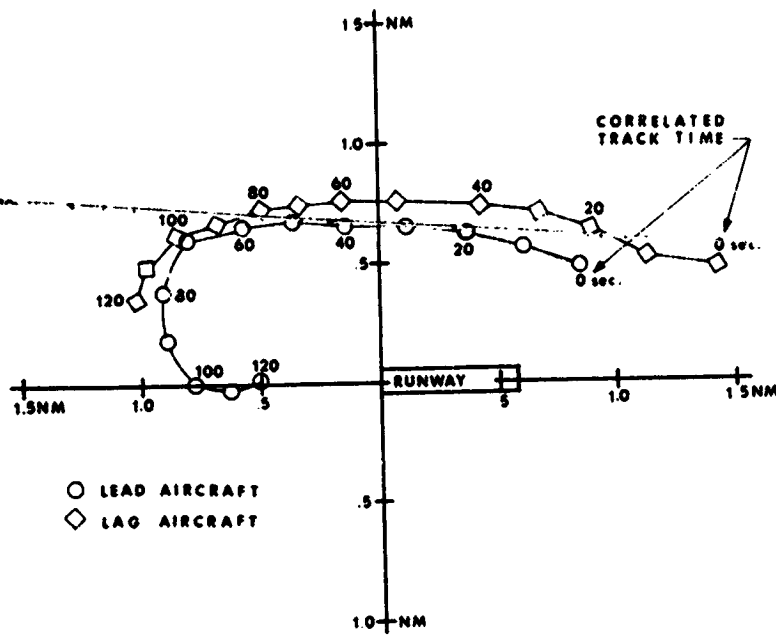
Figure 13.- Aircraft position — time separation tracks.
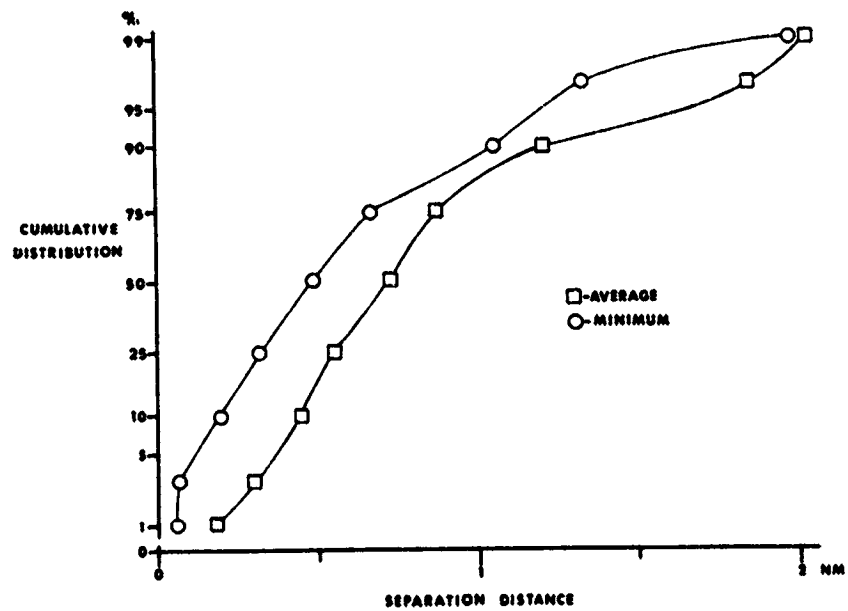
Figure 14.- Cumulative distribution of average and
minimum separation distance.
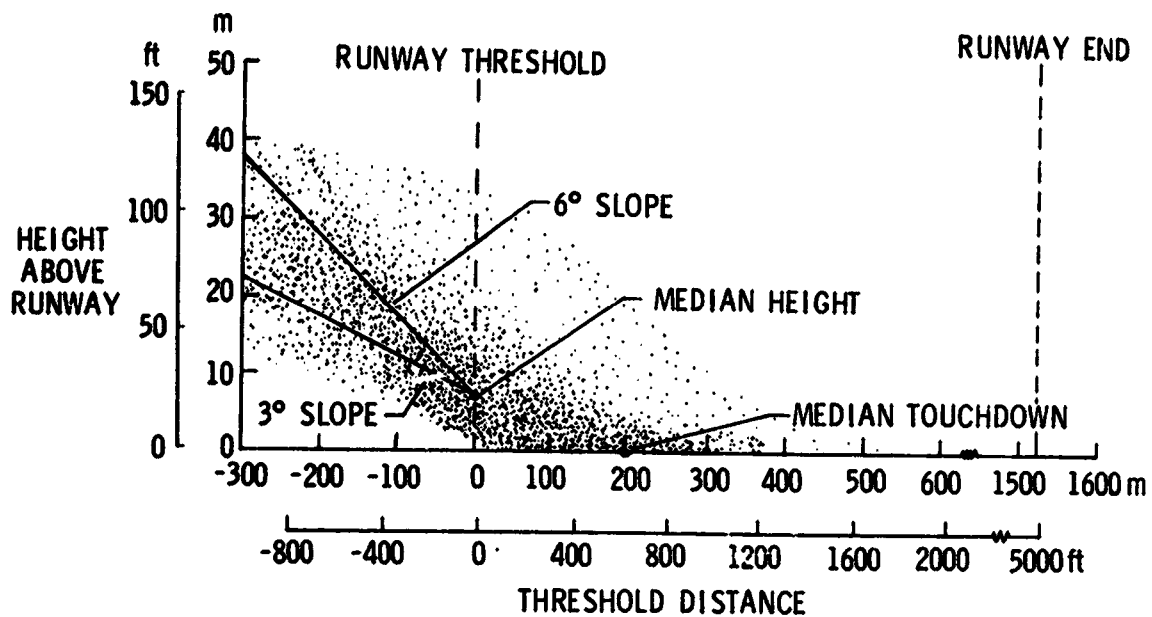
Figure 15.- Final approach trajectories for high-wing
airplane on long runway.
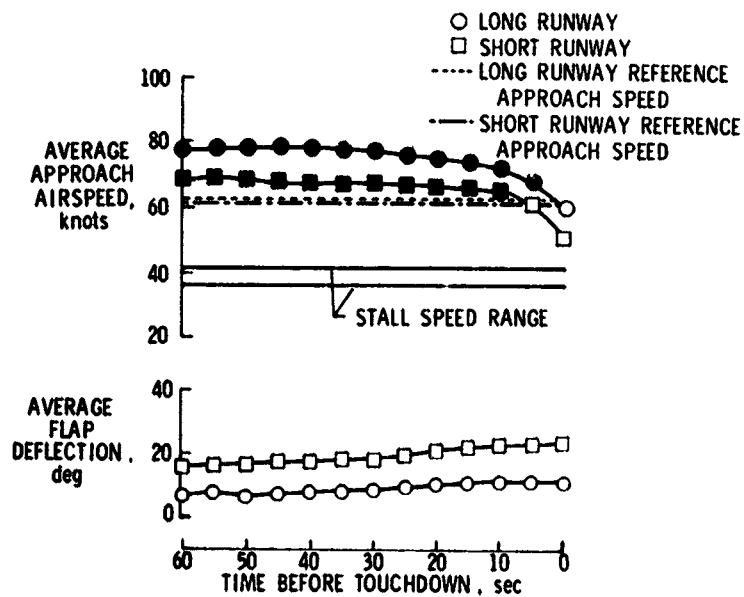
Figure 16.- Final approach airspeed and flap deflection for
high-wing airplane.

116
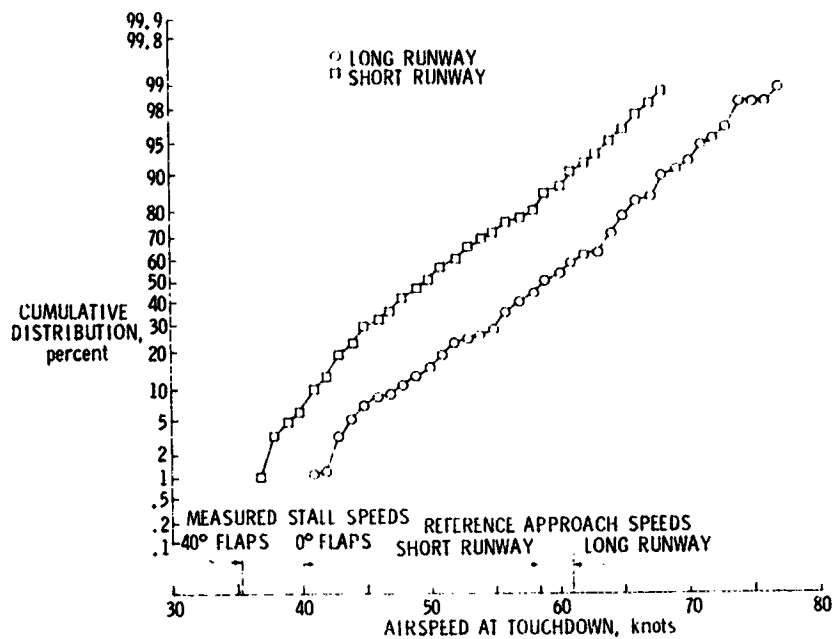
Figure 17.- Cumulative distribution of airspeed at touchdown for high-wing airplane.
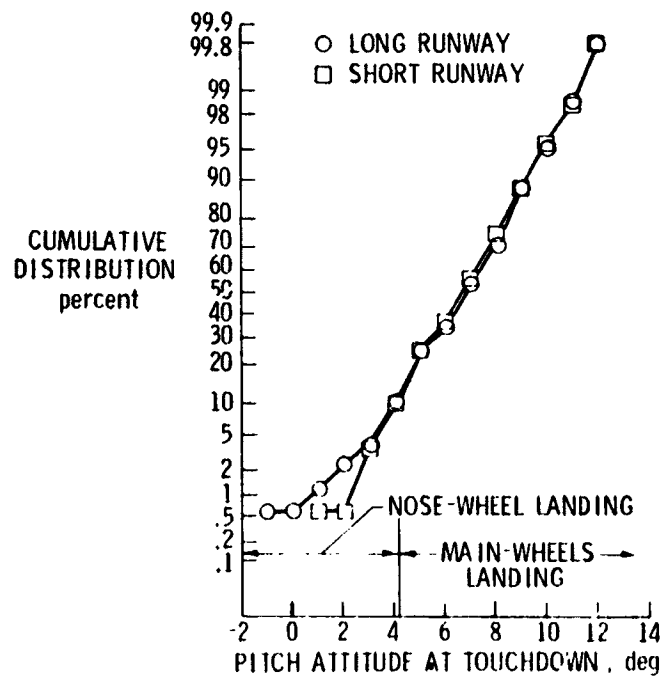
Figure 18.- Cumulative distribution of pitch attitude at touchdown for high-wing airplane.

117
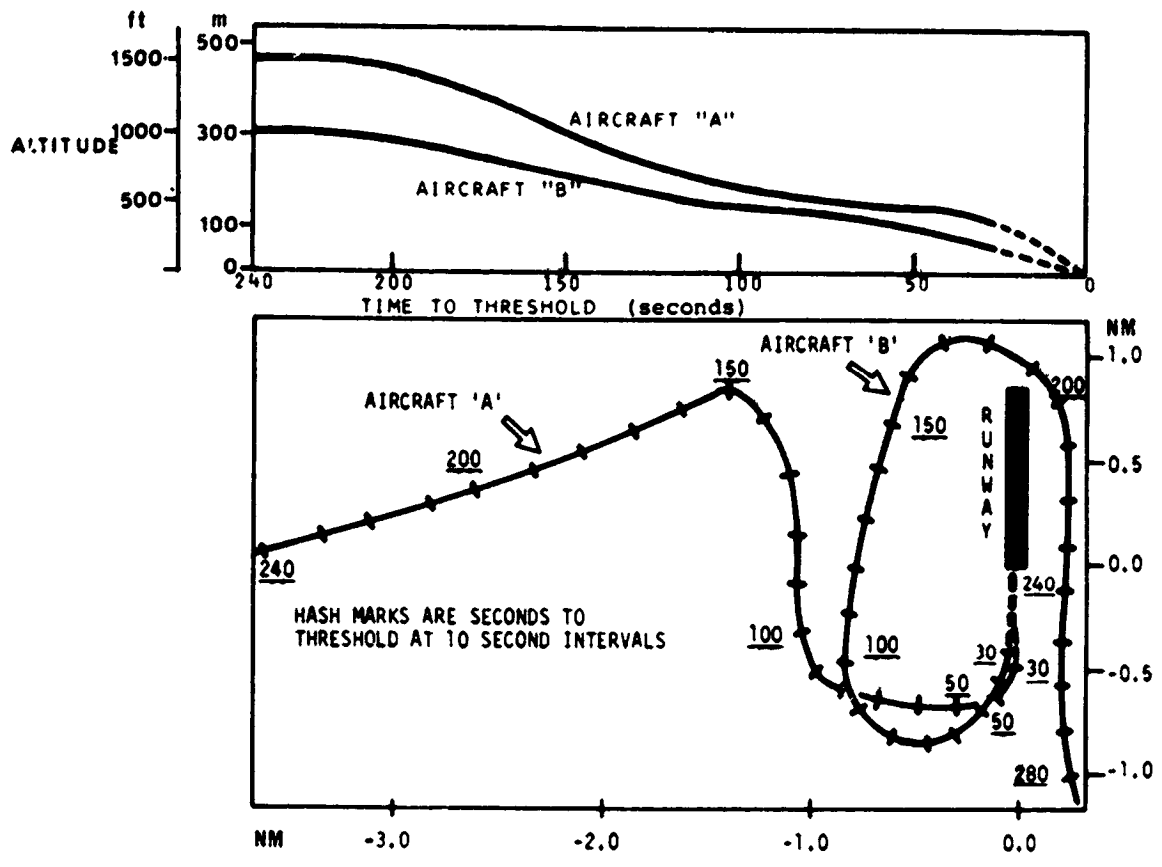
Figure 19.- Mid-air collision position and altitude time history.
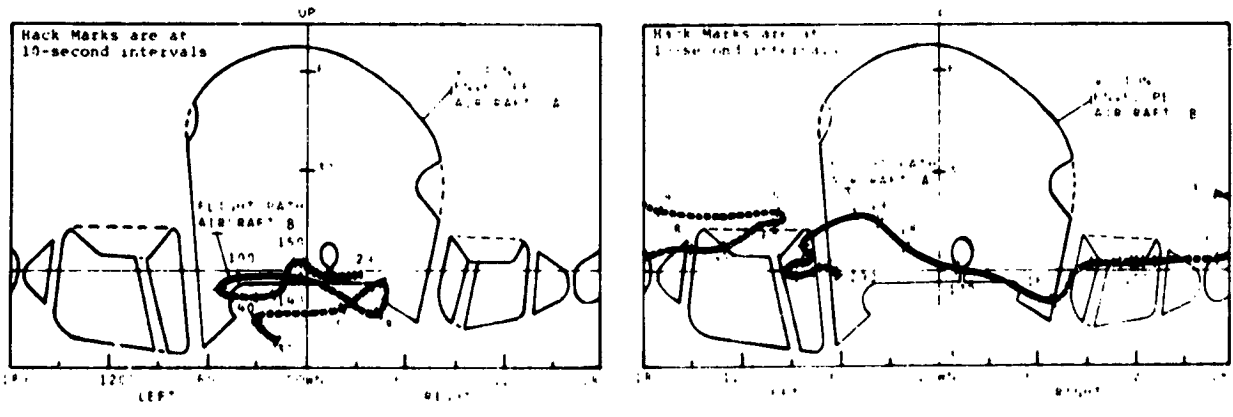
Figure 20.- Aircraft view envelopes.
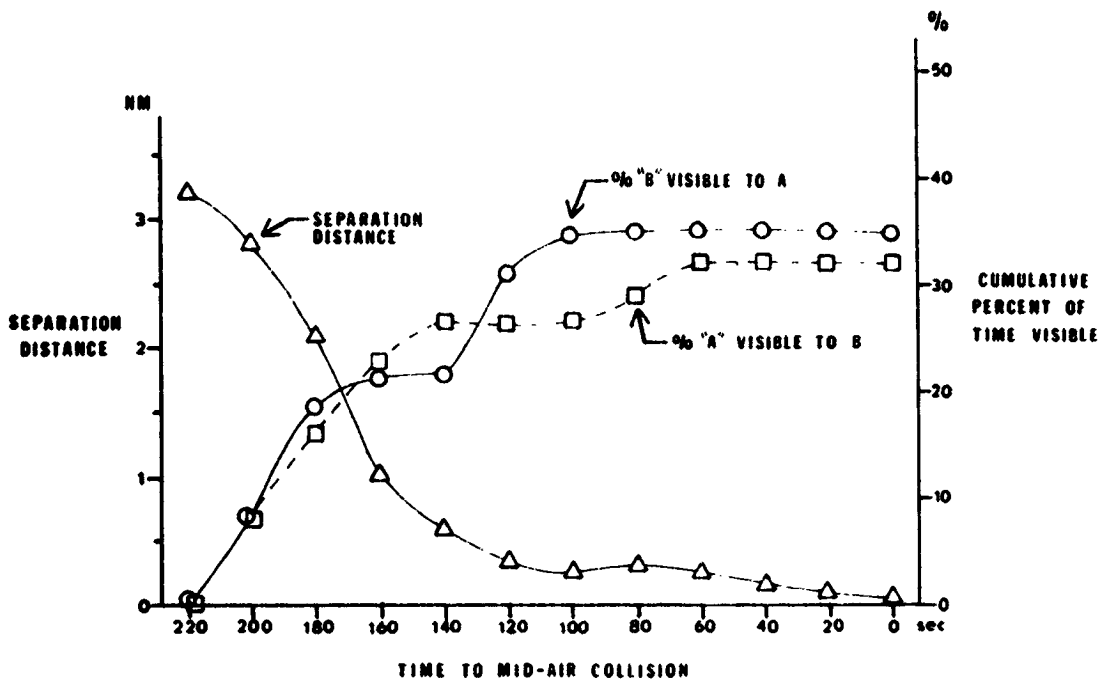
Figure 21.- Separation distance and cumulative percent of time visible as a function of time to MAC.
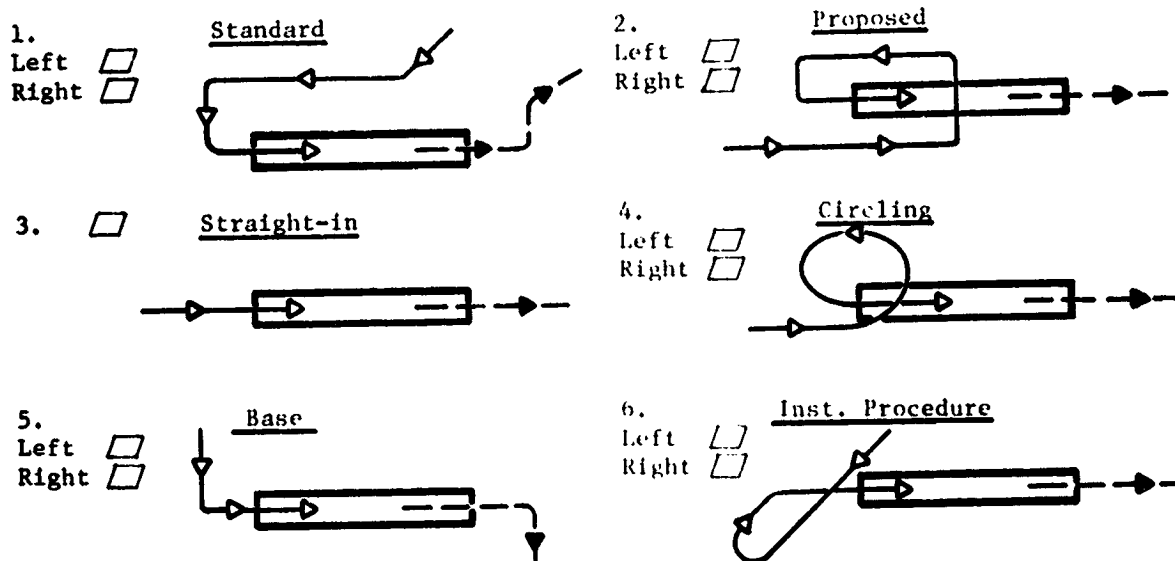
Figure 22.- Uncontrolled air traffic pattern concepts.
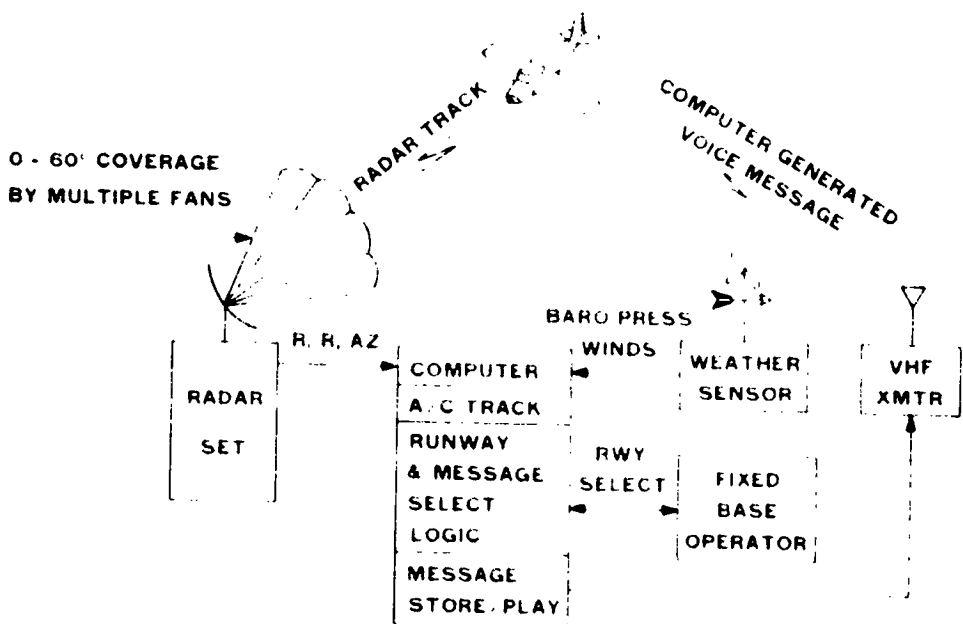
Figure 23.- Conceptual pilot advisory system.

FLIGHT TEST EVALUATION OF A SEPARATE SURFACE ATTITUDE

COMMAND CONTROL SYSTEM ON A BEECH 99 AIRPLANE

Shu W. Gee
NASA Dryden Flight Research Center

Gerald E. Jenks and Jan Roskam
Flight Research Laboratory, University of Kansas

and

Robert L. Stone
Beech Aircraft Corporation

SUMMARY

A joint NASA/university/industry program was conducted to flight evaluate a potentially low cost separate surface implementation of attitude command in a Beech 99 airplane. Saturation of the separate surfaces was the primary cause of many problems during development. Six experienced professional pilots made simulated instrument flight evaluations in light-to-moderate turbulence. They were favorably impressed with the system, particularly with the elimination of the control force transients that accompanied configuration changes. For ride quality, quantitative data showed that the attitude command control system resulted in all cases of airplane motion being removed from the uncomfortable ride region.

INTRODUCTION

One of the problems associated with general aviation is the large number of accidents due to pilot error. Improvements in airplane handling qualities in the presence of turbulence and a reduction in pilot workload would tend to reduce pilot error and improve flight safety.

Past studies at the Dryden Flight Research Center have shown that an attitude command control system could provide these improvements in general aviation aircraft (refs. 1 to 3). Attitude command is a control concept in which the pilot's control wheel position controls the attitude of the aircraft. This differs from the conventional control system, in which the pilot's control wheel deflection causes a rate of change of attitude; the pilot must neutralize his controls to stop the attitude from changing. When the control wheel position is neutral, the aircraft could be in an infinite number of different attitudes. With attitude command, however, neutral control wheel position results in only one attitude, straight and level; and any control wheel deflection results in a new airplane attitude.

In the meantime, the University of Kansas has been studying the application of separate surfaces for general aviation (refs. 4 to 6). The use of separate surfaces to achieve attitude command appears to be logical in that its cost is low, it meets flight safety requirements, and it is easy to install in existing airplanes. Consequently, a grant was awarded to the University of Kansas to study the feasibility of and designs for attitude command using separate surfaces (ref. 7). Improvements in handling and ride qualities in commuter airline operations would provide an economic advantage, and a Beechcraft Model 99 airplane was chosen because it was representative of commuter airline transports. The University was eventually awarded a contract to design, fabricate, install, and flight test a separate surface system on this airplane. Much of this work is reported in references 8 to 11. The Beech Aircraft Corporation and The Boeing Company, Wichita Division, also participated in the program.

SYMBOLS AND ABBREVIATIONS

F_w	pilot-applied control wheel force, newtons (pounds)
IFR	instrument flight rules
ILS	instrument landing system
K	gain constant
KIAS	knots indicated airspeed
p	roll rate, degrees per second
q	pitch rate, degrees per second
r	yaw rate, degrees per second
rms	root mean square
s	Laplace operator function
TIMS	turbulence-intensity measurement system
t	time, seconds
β	sideslip, degrees
δ	control surface deflection, degrees
θ	pitch attitude, degrees
$\dot{\theta}$	pitch rate, degrees per second

122

τ	time constant, seconds
φ	roll attitude, degrees
$\dot{\varphi}$	roll rate, degrees per second
ψ	heading attitude, degrees
$\Delta\psi$	increment of heading change, degrees

Subscripts:

ap	primary aileron (right)
as	separate surface aileron (right)
ep	primary elevator
es	separate surface elevator
f	wing flap
H	horizontal stabilizer
rp	primary rudder
rs	separate surface rudder

PROGRAM OBJECTIVES

The program objectives were to perform a flight evaluation of the operational characteristics and performance of a potentially low cost separate surface implementation of attitude command on a Beech 99 airplane and to provide the general aviation industry with a first hand evaluation of the control concept by allowing their participation.

SYSTEM DESCRIPTION

Aircraft

Figure 1 is a three-view drawing of the Beech 99 aircraft with separate control surfaces. The aircraft is a twin-engine, turboprop, 17-place commuter airliner. It has a wingspan of 14 meters (46 feet), a length of 13.7 meters (45 feet), and a maximum gross weight of 4716 kilograms (10,400 pounds). It has a maximum cruise of 244 knots at 4877 meters (16,000 feet) and a service ceiling of approximately 8534 meters (28,000 feet). Its approach speed is 96 knots, and it is capable of operating off a 914-meter (3000-foot) runway.

Hardware Implementation

The flight control system modifications consist of electrically interconnected components and include a gyro package, a management and control panel, an operator's console, and electromechanical actuators, which drive small separate control surfaces.

The gyro package consists of a vertical gyro, directional gyro, and three rate gyros; and it is mounted in the proximity of the center of gravity of the airplane.

The management and control panel (fig. 2) contains switches, lights, surface position indicators, and potentiometers; it is installed in the copilot's instrument panel.

The operator's console contains all the electronics for control law computations, gain adjustment, servo amplifiers, ground tests, and power supplies. The unit is installed in the main cabin.

The control actuators are of the electromechanical screw jack type. They require 28 volts dc and produce approximately 181 kilograms (400 pounds) of linear force at a maximum current of approximately 10 amperes. The frequency response of the actuators is approximately 1.5 hertz. They are located in the wings and tail with the separate control surfaces.

Separate Control Surfaces

The separate control surfaces for attitude command are obtained by the dichotomy of the primary control surfaces. In sizing the separate surfaces, consideration was given to static control and the avoidance of saturation. The sizes calculated met the military and civil aircraft performance standards (MIL-F-8785C and FAR Part 23, respectively) for failed hardover conditions. In the roll axis, 39 percent of the total roll control power is provided by the separate surface ailerons; in the pitch axis, 25 percent of the total pitch control power is provided by the separate surface elevators; and in the yaw axis, 27 percent of the total yaw control power is provided by the separate surface rudder.

System Operational Modes

Three modes of system operation are provided: off, slave, and command. A control panel in the copilot's instrument panel allows the pilot to select one of these control modes and the control loops in the command mode.

In the off mode, the separate surfaces are deenergized, and the aircraft flies with approximately two-thirds of its original control power.

In the slave mode, the separate surfaces are electronically slaved to and operate in unison with the primary control surfaces; thus, the basic Beech 99 configuration is restored.

124

In the command mode, all three axes can be operated individually or in combination; however, all tests were combined-axis tests. The separate surfaces hold the aircraft in the attitude commanded by the position of the pilot's control wheel in the pitch, roll, and yaw axes. Heading is maintained by a combination of roll and yaw heading hold control loops. Yaw-damper-only operation is available in the yaw axis.

The system is designed to operate at the approach and cruise flight conditions.

Pitch axis.—A block diagram of the pitch axis is shown in figure 3(a). The pilot controls the primary surface through the mechanical control system and has an electric trim system to position the horizontal stabilizer.

In the slave mode, the primary surface position, through the appropriate slave gain, is used to position the separate surface; thus, the separate surface operates in unison with the primary surface.

In the command mode, when the pilot commands a pitch attitude through the control column, the primary surface position is fed back through the appropriate gain and compared with the actual pitch attitude. The difference between commanded and actual attitudes is filtered and drives the separate surface to reduce the difference to zero by changing the actual attitude of the aircraft. Thus, the attitude of the aircraft becomes proportional to control column displacement.

The separate surface has a streamline position detector which moves the horizontal stabilizer through the autotrim system to keep the separate surface at a near zero position.

Roll axis.—A block diagram of the roll axis is shown in figure 3(b). It functions like the pitch axis except that it is coupled with the yaw axis. In the command and heading hold modes, and when zero bank is commanded, the yaw axis heading is locked. When the pilot applies an aileron wheel force to roll, the yaw axis unlocks to permit aircraft maneuvering.

Yaw axis.—A block diagram of the yaw axis is shown in figure 3(c). In the command, yaw damper, and heading hold modes, heading and heading rate are fed back to the separate surface to keep the aircraft on the heading sensed by the directional gyro. As explained above, the yaw axis automatically unlocks when the pilot maneuvers the aircraft for heading changes and locks when a new heading is established. The pilot can select yaw-damper-only operation, which manually unlocks the yaw axis by opening the heading feedback loop.

INSTRUMENTATION

A pulse code modulation digital data tape instrumentation system was installed in the aircraft to allow the debugging of the system, the optimization of system performance, and the acquisition of quantitative data from the flight test program. Seventy-seven channels at 200 samples per second are available for recording aircraft and system parameters.

A turbulence-intensity measuring system (TIMS) (ref. 12) was installed in the airplane to record the atmospheric gust velocity encountered during flight.

Figure 4 shows the mechanization of the turbulence-intensity measurement system. A pitot-static probe and a differential pressure transducer measure the longitudinal pressure fluctuations in front of the airplane. A bandpass filter attenuates deviations above 20 hertz and below 6 hertz to exclude unwanted high-frequency noise and low-frequency airplane response to turbulence and control inputs. The signal is then integrated in the computer and recorded in the data system. The computer also compensates for variations in the signal due to airplane velocity.

The recorded signal is directly proportional to the shaded area in the turbulence power spectrum in figure 4. The power spectrum shown represents the standard format for quantitative turbulence measurements. This format is the result of extensive turbulence research which showed empirically that the log-log plot of the gust-velocity power spectrum is linear and has a constant and repeatable slope throughout the wavelength range from 3 meters (10 feet) to 3048 meters (10,000 feet). Therefore, changes in turbulence intensity change the magnitude of the spectrum but not its slope. The invariance of the slope is illustrated in the figure by the levels of light-to-moderate and moderate-plus turbulence spectra. Therefore, the shaded area varies directly with the level of turbulence intensity. This area is also directly proportional to the root-mean-squared value of the gust velocity, which is equal to the magnitude of the area under the entire power spectral curve.

DEVELOPMENTAL PROBLEMS

As with most flight programs, problems were encountered with the system during the initial phases of flight. Some of these developmental problems, which may be unique to this system, are discussed below.

Pitch Trim Overshoot

When the pilot commanded a new pitch attitude with a trim input, the aircraft overshot the commanded attitude and then gradually returned to it. The problem was duplicated on the University of Kansas simulator, and, as shown in figure 5, the separate surface was saturated, allowing the pitch attitude to overshoot. The problem is the result of differences in aircraft responses from separate surface inputs and trim inputs. The pitch trim overshoot was eliminated by adjusting the command gain to the separate control surfaces, as shown in figure 6.

Bank Angle Overshoot

Figure 7 is a time history showing a step input of 5.6° primary aileron for a 12° bank angle, and a resulting 5° bank angle overshoot. Immediately before the bank angle overshoot, the separate surface aileron saturates (it has a 14° limit), and an overshoot ratio of 42 percent results. The forward loop gain is 15.

126

The overshoot ratio is a function of forward loop gain (fig. 8). Increasing the gain to 60 results in an acceptable overshoot. Increasing the gain requires less primary control surface deflection, and therefore less separate surface authority, for a commanded bank angle; however, the gain is limited by too abrupt control response and excessive control sensitivity.

Heading Hold Operation

The system was originally mechanized to unlock the heading loop when the pilot's control wheel was deflected more than 3°. While this technique was satisfactory for a Piper airplane (ref. 3), it was unsatisfactory for the Beech 99 airplane because of high control system friction and forces. The problem was resolved by replacing the aileron position sensor with a torque-sensitive switch on the control wheel that was activated by a very small wheel force.

Pitch Changes With Configuration Changes

One benefit of the attitude command system is the elimination of pitch changes during aircraft configuration changes. However, the elevator's separate control surfaces saturated during a go-around maneuver, which resulted in the airplane's pitching down. Analysis of the problem indicated that the nose-down pitching moment was generated by flap retraction and that the autotrim rate could not keep up with the changes. It seemed logical to limit the rate of configuration changes to avoid saturation. It was not practical to reduce the flap retraction rate; however, a successful fix resulted from interrupting the flap retraction whenever the autotrim system was operating.

TEST PLAN AND PROCEDURES

Six pilots participated in the qualitative flight evaluation. All were experienced professional pilots. Three were general aviation pilots who were twin-engine, instrument rated, but had no experience in the Beech 99 airplane. The other three were NASA research pilots. All pilots were given a 1-hour familiarization flight in the basic Beech 99 airplane.

The flight test pattern for the qualitative pilot evaluation is shown in figure 9. The vertical-S maneuver is a series of climbing and descending turns. The 90° localizer interception was initiated from the cruise configuration to increase the difficulty of the piloting task. The flights were conducted under simulated instrument flight conditions. Each pilot flew the entire pattern in the slave mode and then immediately repeated the pattern in the command mode. Only two pilots repeated the flights.

The piloting task was evaluated with the Cooper-Harper rating scale (ref. 13). The ratings ranged from 1 to 10, where 1 indicates excellent controllability and 10 indicates that control will be lost during some portion of required operation.

FLIGHT TEST RESULTS

Aircraft Response Characteristics

Roll axis.—The response to an aileron step input in the command mode is shown in figure 10. The separate surface aileron starts in the direction of the primary aileron and opposes it when the desired bank is reached; thus, the bank angle becomes proportional to the pilot's control deflection.

Pitch axis.—The response to an elevator step input in the command mode is shown in figure 11. Again, the separate surface elevator produces a change in attitude proportional to the pilot's control deflection.

The control force transients in the slave mode during configuration changes are shown in table I. The elevator wheel forces required to trim are high, and can rise as high as 311 newtons (70 pounds) during a go-around maneuver. Depending on the duration of the transient forces, pilots generally oppose the forces rather than trim. These transient forces, and the accompanying pitch changes, are eliminated in the command mode. The flap interrupt modification about doubles the normal flap retraction time, and figure 12 shows a hands-off vehicle response during a configuration change.

Yaw axis.—The most significant change that occurred in the yaw axis with the command mode is the yaw damping effect. Figure 13 shows the response of the aircraft to a rudder doublet in the slave mode. Dutch roll damping is low. Figure 14 is the aircraft response in command mode to a rudder doublet. Dutch roll damping is improved.

Pilot Evaluations

This flight test program is oriented towards the generation of pilot opinions concerning the handling and ride qualities of the modified Beech 99 airplane. The flight profile reflects this philosophy. The maneuvers are designed to task the pilot to enable him to evaluate the changes in aircraft dynamics, although the profile does not depart from being a realistic IFR mission. Therefore, the pilots' comments and the Cooper-Harper pilot ratings constitute the most important results of the flight tests.

After the pilots performed the mission in the slave and command modes, they were debriefed. The following discussion gives the pilots' consensus of opinion concerning the handling qualities of the test airplane.

The pilots were favorably impressed with the elimination of the control force transients that accompanied configuration changes. They seemed to like the pitch stabilization provided by the attitude command system; however, some pilots tended to resist adapting to the system. Comments characterizing this discussion are presented in table II.

Holding aileron force during turns was annoying. Most pilots stated that they did not like using the aircraft's manual trim. Some pilots thought that a wheel-mounted electric trim might be acceptable. One pilot said he felt that it was unsafe to trim to some bank angles.

The workload was greatly reduced by the command mode, especially for precision maneuvers like localizer and glidepath tracking. The improvement was even more pronounced in turbulence.

Most pilots agreed that with the attitude command system on, the ride qualities and turbulence response of the aircraft were substantially improved. Comments regarding ride qualities are presen'~d in table III.

Pilot Ratings

The nonresearch pilots had not used the Cooper-Harper rating scale before. Perhaps as a consequence of this, their ratings did not indicate much improvement when the attitude command system was on; however, their unrecorded comments and enthusiasm after flying with the system indicated that the airplane flew better than they had expected, and that they were pleased with the operation of the system.

The pilot ratings generated from the flight profile as a function of turbulence are presented in figure 15. The TIMS output in rms volts is correlated with the pilot assessment of the turbulence level in the slave mode. In the command mode, the pilot rating shows an improvement of at least 0.5 over the airplane in the slave mode. The mean improvement in pilot rating is between 1.25 and 1.50.

The instrument approach is the most demanding of all the piloting tasks. A measure of pilot workload for this task is shown in terms of aileron activity in figure 16. There is substantially less aileron activity in the command mode. Figure 17 shows the standard deviation in heading versus turbulence. Although the figure shows no significant improvement in performance, the pilots felt that their performance was improved.

Ride Qualities

The precision heading task is typical of enroute flight of commuter airliners. Atmospheric turbulence during these evaluations was light to moderate. The vertical and transverse accelerations of the aircraft are shown in figure 18. The solid symbols represent the averages of six flights. In terms of percentages, the data show an 18.5-percent reduction in vertical acceleration and a 32.2-percent reduction in transverse acceleration when the system is in the command mode.

The effects of attitude command on passenger comfort are also apparent in figure 18. Boundaries of passenger comfort were extracted from studies of passenger ride quality determined from commercial airline flights in which a Beech 99 airplane was one of several aircraft used (ref. 14). Passenger comfort responses in light-to-moderate turbulence are generally borderline to uncomfortable when the

airplane is in the slave mode. In all cases, putting the airplane in the command mode removes it from the uncomfortable region.

CONCLUDING REMARKS

Flight testing the Beech 99 airplane demonstrated that the use of separate surface controls is practical for general aviation and that the use of small separate surfaces is effective in controlling the response of the airplane. Because the separate surfaces were small, they were easily saturated; but the saturation problems could always be resolved. Improvements in the handling qualities and the ride qualities of the Beech 99 aircraft were demonstrated in flight tests.

REFERENCES

1. Loschke, Paul C.; Barber, Marvin R.; Jarvis, Calvin R.; and Enevoldson, Einar K.: Handling Qualities of Light Aircraft With Advanced Control Systems and Displays. NASA Aircraft Safety and Operating Problems, Volume 1, NASA SP-270, 1971, pp. 189-206.

2. Loschke, Paul C.; Barber, Marvin R.; Jarvis, Calvin R.; and Enevoldson, Einar K.: Flight Evaluations of the Effect of Advanced Control Systems and Displays on the Handling Qualities of a General Aviation Airplane. SAE Paper 720316, Mar. 1972.

3. Loschke, Paul C.; Barber, Marvin R.; Enevoldson, Einar K.; and McMurtry, Thomas C.: Flight Evaluation of Advanced Control Systems and Displays on a General Aviation Airplane. NASA TN D-7703, June 1974.

4. Roskam, J.; Collins, D.; van Deventer, F.; Berrier, F.; and Gary, S.: Windtunnel Data Report on a Hinge Moment and Force Test on a Cessna 210 Half Wing Model. FRL 72-002, Flight Res. Lab., Univ. of Kansas, Mar. 1972.

5. Roskam, J.; van Deventer, F.; and Kaul, S.: Analysis Report on Windtunnel Tests of Separate Surface Ailerons and Rudders on Cessna 210 Models. FRL 72-005, Flight Res. Lab., Univ. of Kansas, May 1972.

6. Roskam, J.; Collins, D.; van Deventer, F.; Kaul, S.; and Berrier, F.: Wind Tunnel Data Report on a Force and Moment Test of Separate Surface Ailerons and Rudders on a Cessna 210 Model. FRL 72-003, Flight Res. Lab., Univ. of Kansas, Apr. 1972.

7. Roskam, J.; Henry, S.; Collins, D.; and van Deventer, F.: An Investigation of Separate Surface Stability Augmentation Systems for General Aviation Aircraft. Third Progress Report on NASA Grant NGR 17-002-095, Flight Res. Lab., Univ. of Kansas, June 1972.

8. Buss, Marvin W.: Flight Test Program - Attitude Command Control System With Separate Control Surfaces on Beech Model 99 Airliner. Project Report, Flight Res. Lab., Univ. of Kansas, 1973.

9. Collins, Donald J.; and Bolton, Willard R., Jr.: A Separate Surface Stability Augmentation System for a General Aviation Airplane. Thesis for Doctorate of Engineering, Univ. of Kansas, Apr. 1974.

10. Schunsclaar, Henri L. J.: Flight Test Program for a Separate Surface Stability Augmented Beech Model 99 Airliner and an Investigation of Its Turbulence Intensity Measuring System. Thesis for Master of Science, Univ. of Kansas, June 1975.

11. Jenks, Gerald E.; and Ashburn, Madison H.: Implementation of an Attitude Command System Using Separate Surface Stability Augmentation on a Beech

Model 99 Airplane. Thesis for Master of Engineering, Univ. of Kansas, Aug. 1975.

12. Mac Cready, Paul B., Jr.; Williamson, Robin E.; Berman, Stephen; and Webster, Alexander: Operational Application of a Universal Turbulence Measuring System. NASA CR-62025, 1965.

13. Cooper, George E.; and Harper, Robert P., Jr.: The Use of Pilot Rating in the Evaluation of Aircraft and Handling Qualities. NASA TN D-5153, Apr. 1969.

14. Richards, L. G.; Kuhlthau, A. R.; and Jacobson, I. D.: Passenger Ride Quality Determined From Commercial Airline Flights. 1975 Ride Quality Symposium, NASA TM X-3295/DOT-TSC-OST-75-40, Nov. 1975, pp. 409-436.

132

TABLE I.—CONTROL FORCE TRANSIENTS

[120 KIAS, clean configuration, 1524 meter (5000-foot) altitude, slave mode]

Configuration change	Elevator wheel force required to maintain attitude, N (lb) (push)
Gear down	33 (7.5)
Flaps down	222 (50.0)
Half to full power	80 (18.0)

TABLE II.—HANDLING QUALITIES COMMENTS

Pitch attitude command:

I liked the decoupling effect of being able to control the glide slope and the rate of descent with the pilot trim and the speed with power.

Glide slope was more positive with the system on.

Pitch attitude command is probably the biggest improvement that I see in that the attitude tends to be locked in.

Not much change in the pitch axis except for the gear and flap transients.

Missed approach much easier, aircraft well controlled.

When the go-around was executed, I was forced to establish a climb attitude. The basic aircraft would naturally pitch up with acceleration.

Roll attitude command:

The workload is much lower, especially in the roll axis; I felt much more confident of my ability to perform the mission.

The localizer was easier to maintain.

Heading hold:

The basic aircraft wallows around. It is difficult to hold heading. The aileron forces are high. When you turn your system on, it relieves the pilot workload, particularly when maintaining heading in turbulence. If turbulence knocks you off [the heading], the system brings you back to it.

Initially I was fighting the heading hold system; I wasn't turning loose and letting it settle down. I found out later if I flew almost hands off, heading hold was pretty good.

133

TABLE III.—RIDE QUALITY COMMENTS WITH
ATTITUDE COMMAND SYSTEM ON

> In all the axes, as soon as you turn the attitude command on it seems as if the turbulence decreases by half.
>
> The ride is much smoother.
>
> The airplane seems as if it is on a rail or track.
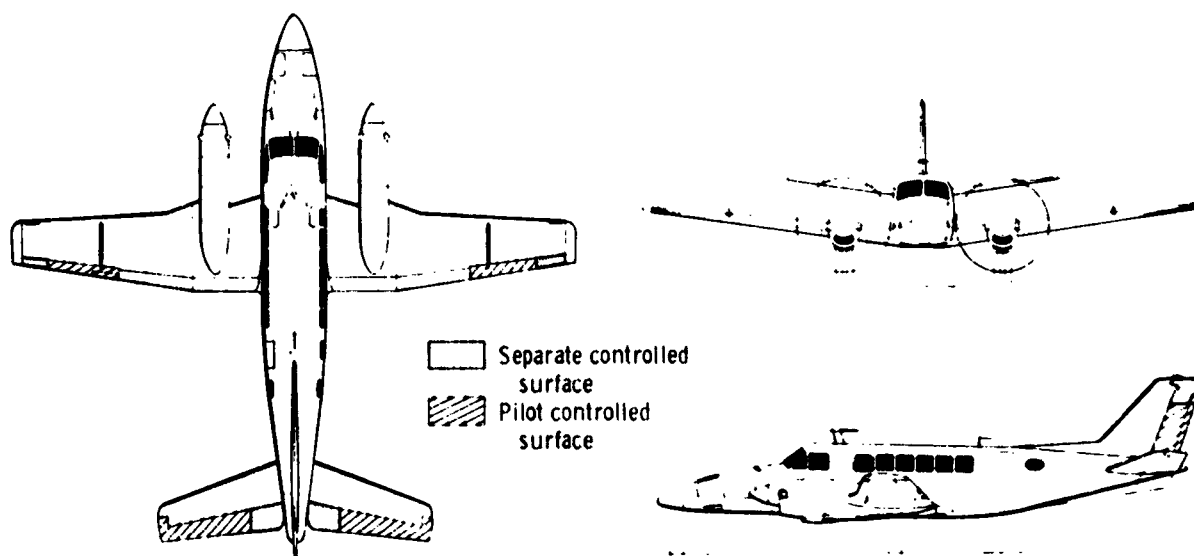
Figure 1.— Beech 99 airplane with separate surface controls.

134
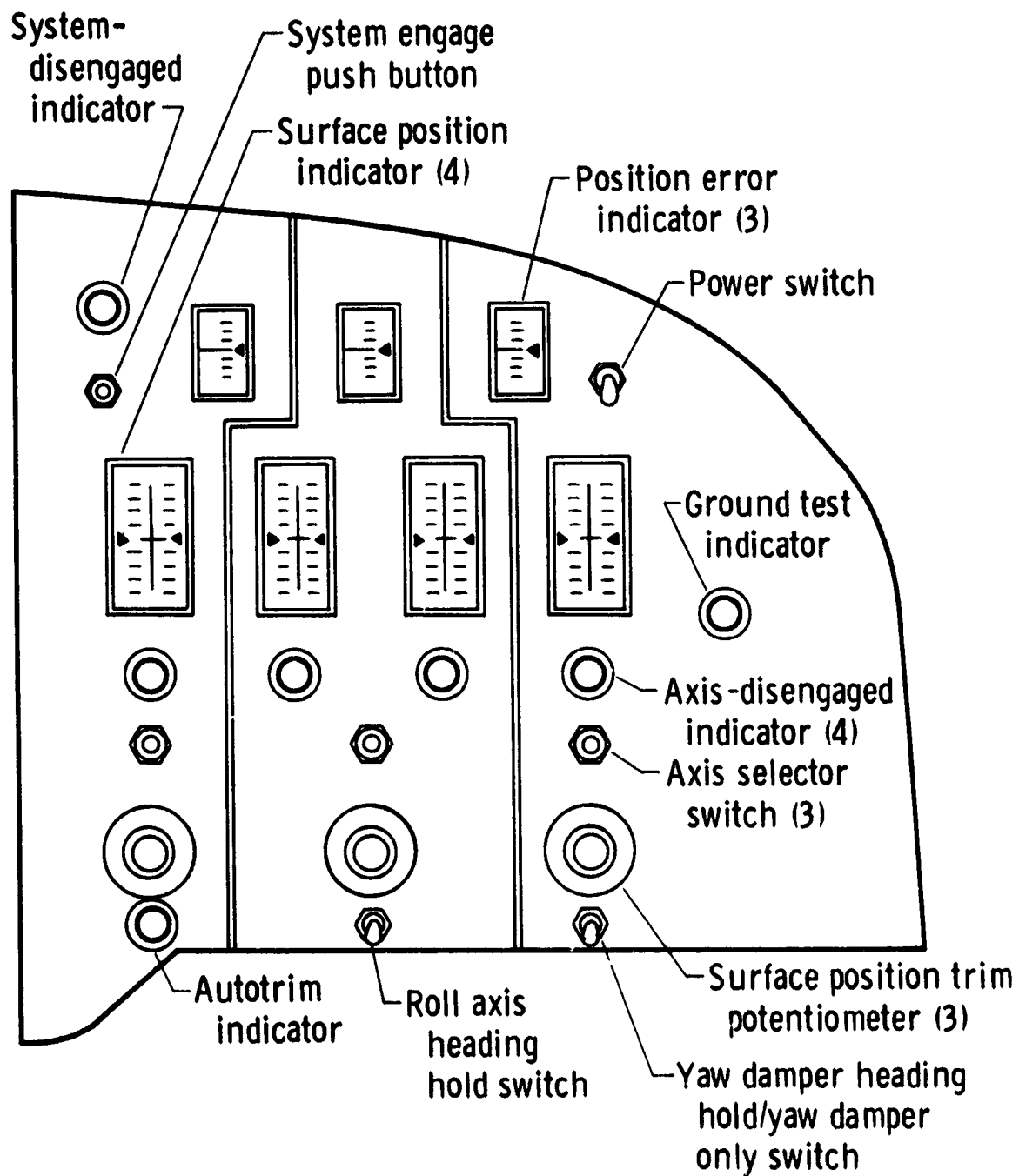
Figure 2.- Management and control panel.
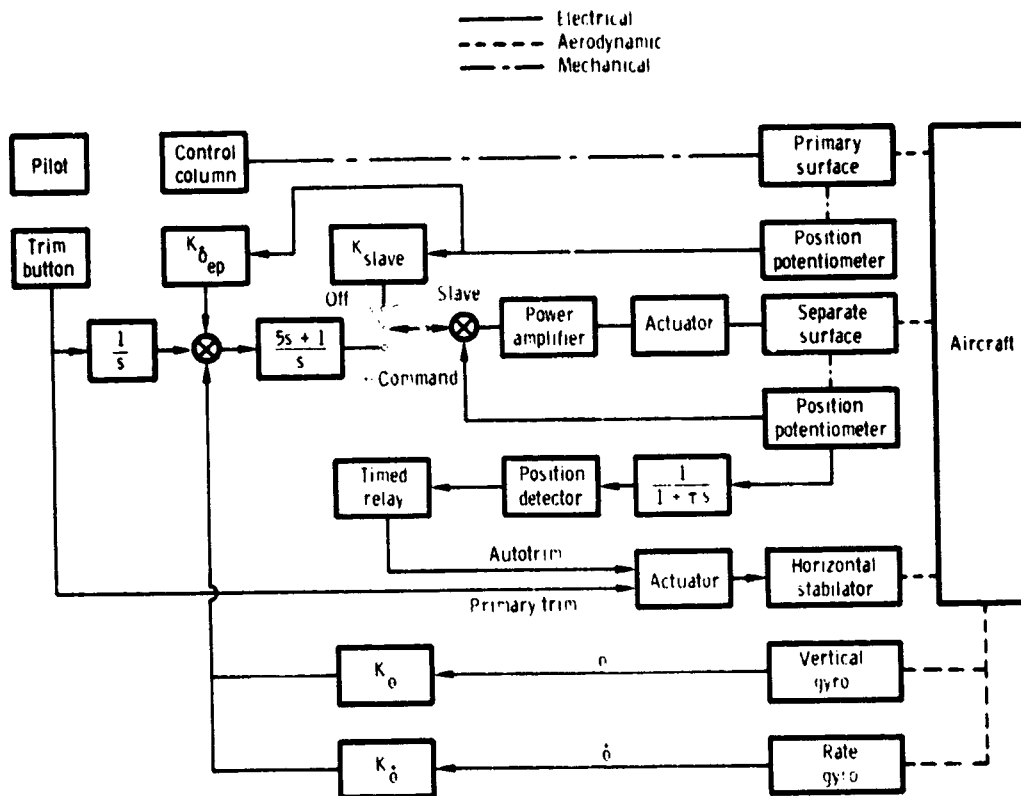
(a) Pitch axis.

Figure 3.- Mechanization of attitude command control system.

136

(b) Roll axis.

Figure 3.- Continued.
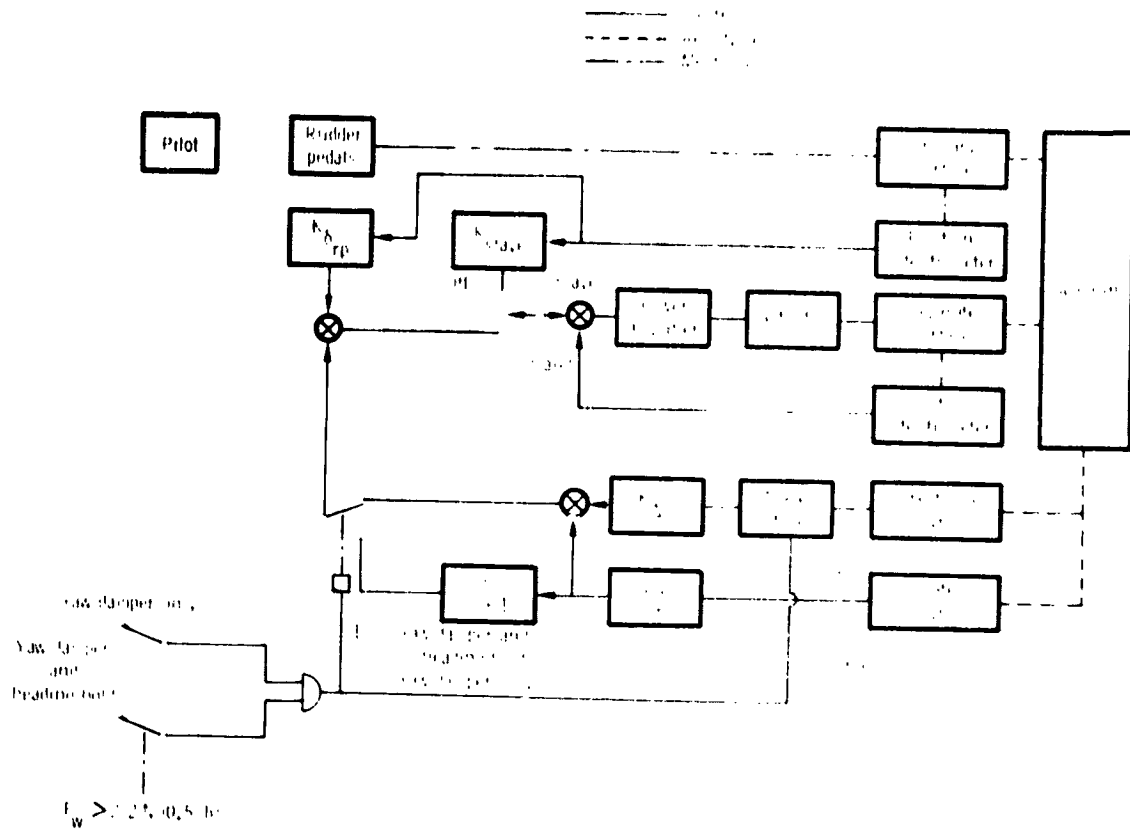
(c) Yaw axis.

Figure 3.- Concluded.

138
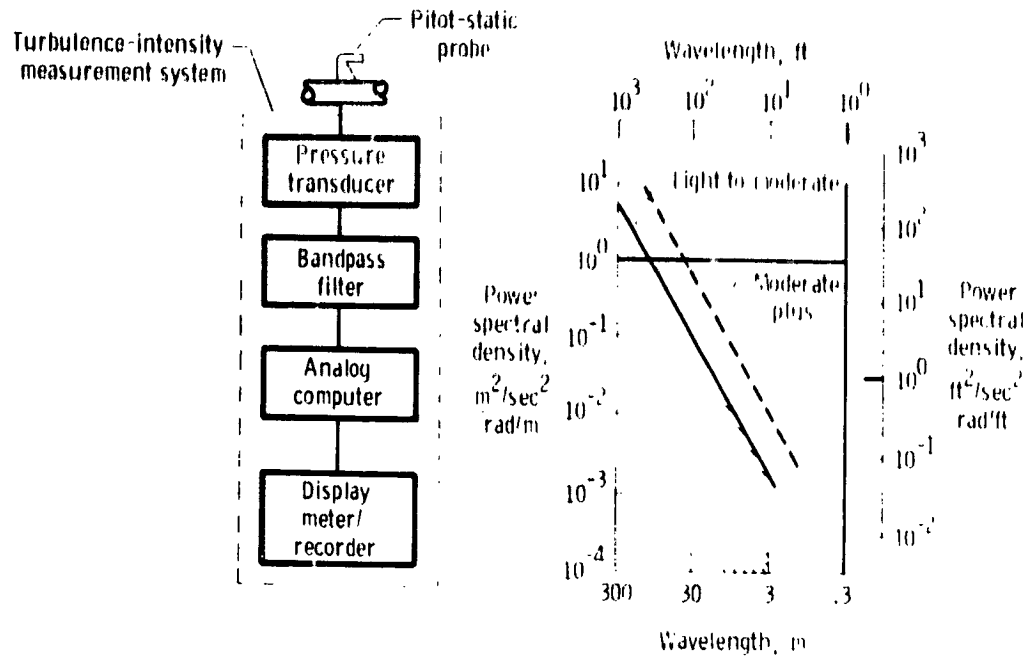
Figure 4.- Turbulence-intensity measurement system.
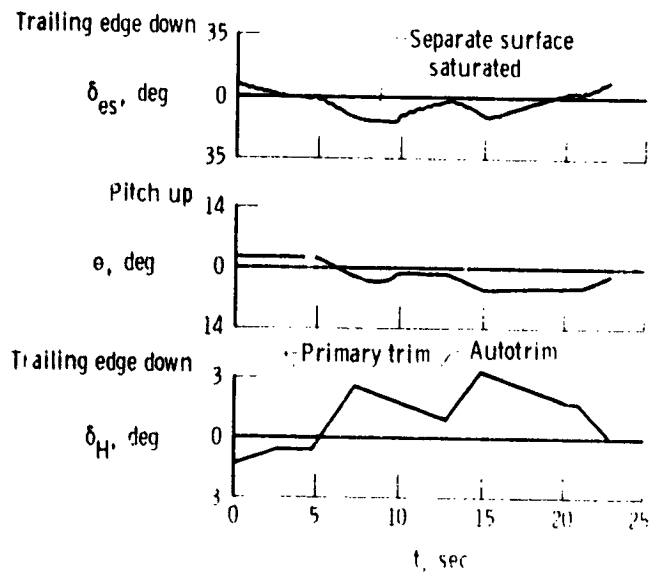
Figure 5.- Simulator pitch axis response due to
pilot trim input with K_{ep} = 10. (Pitch
angle overshoot induced by δ_{es} saturation.)
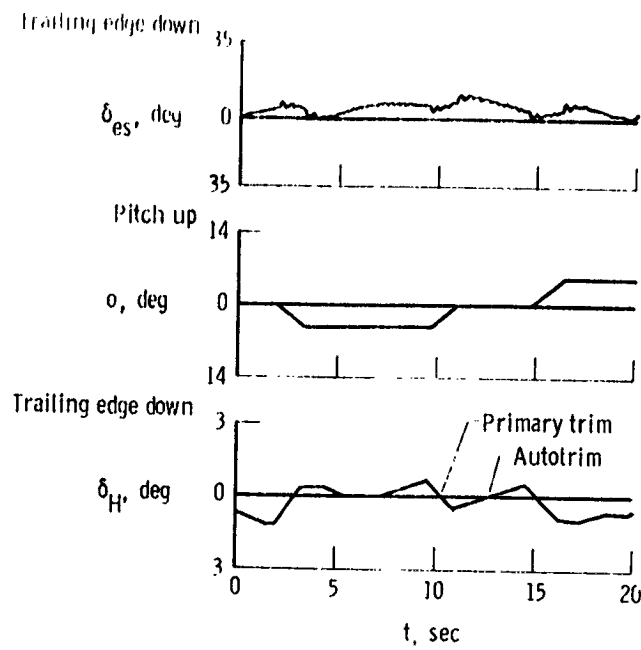
Figure 6.- Simulator pitch axis response due to pilot trim input with $K_{\delta_{ep}} = 20$.
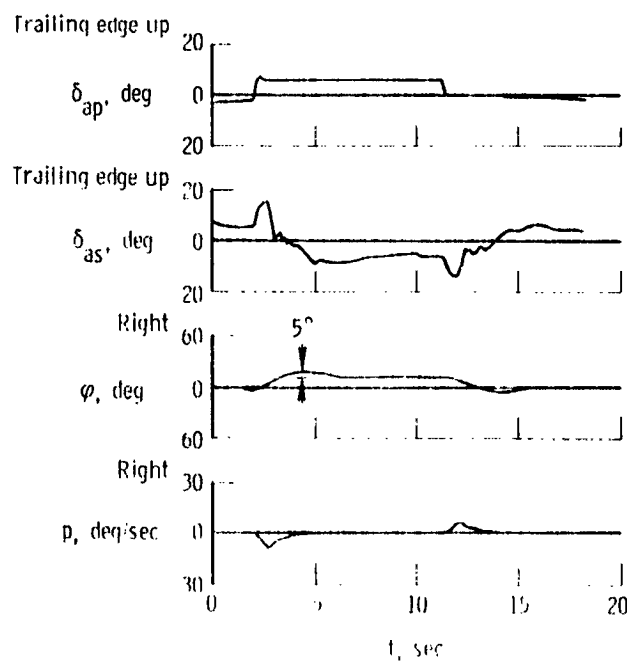
Figure 7.- Time history of bank angle overshoot. Gear and flaps down; airspeed = 110 knots; $K_{\delta_{ap}} = 15$.
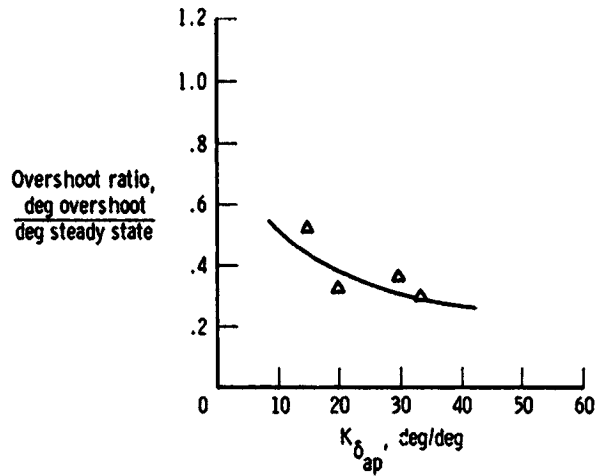
Figure 8.- Effect of $K_{\delta_{ap}}$ on overshoot
ratio. Flight data.
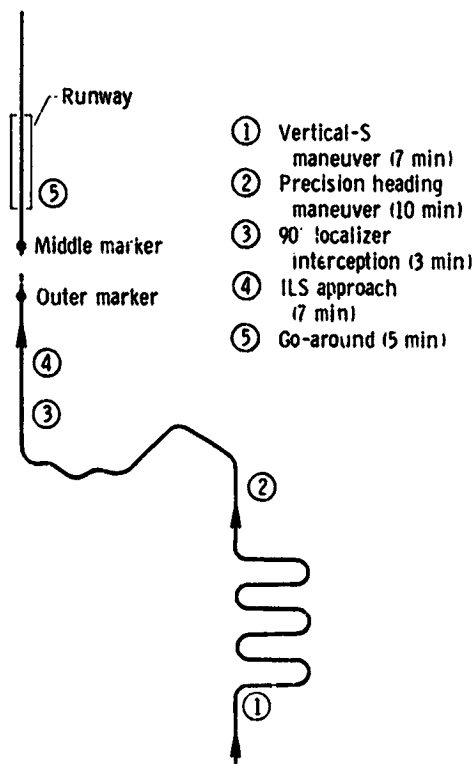
Figure 9.- Qualitative flight profile.
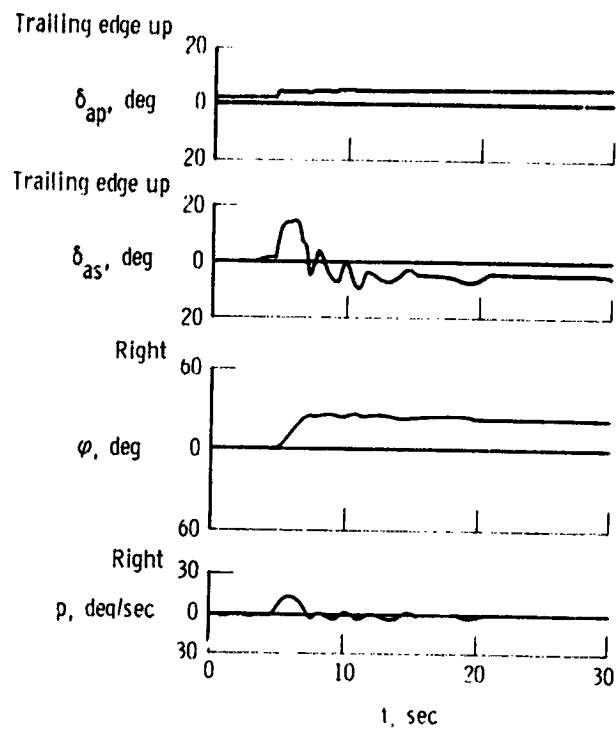
Figure 10.- Aileron step response.
Command mode.
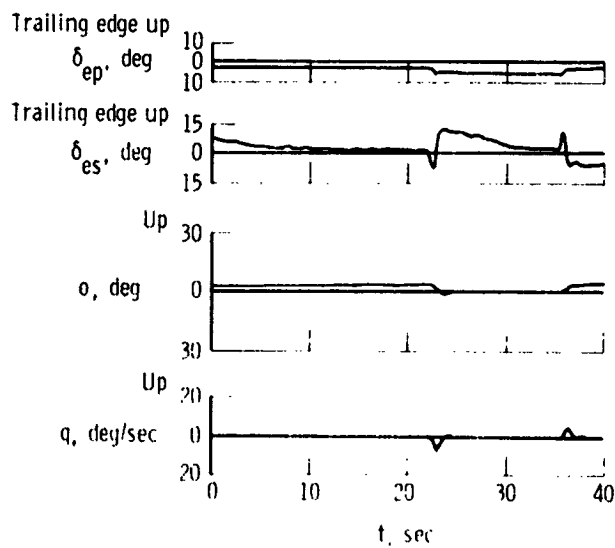
Figure 11.- Elevator step response.
Command mode.

142
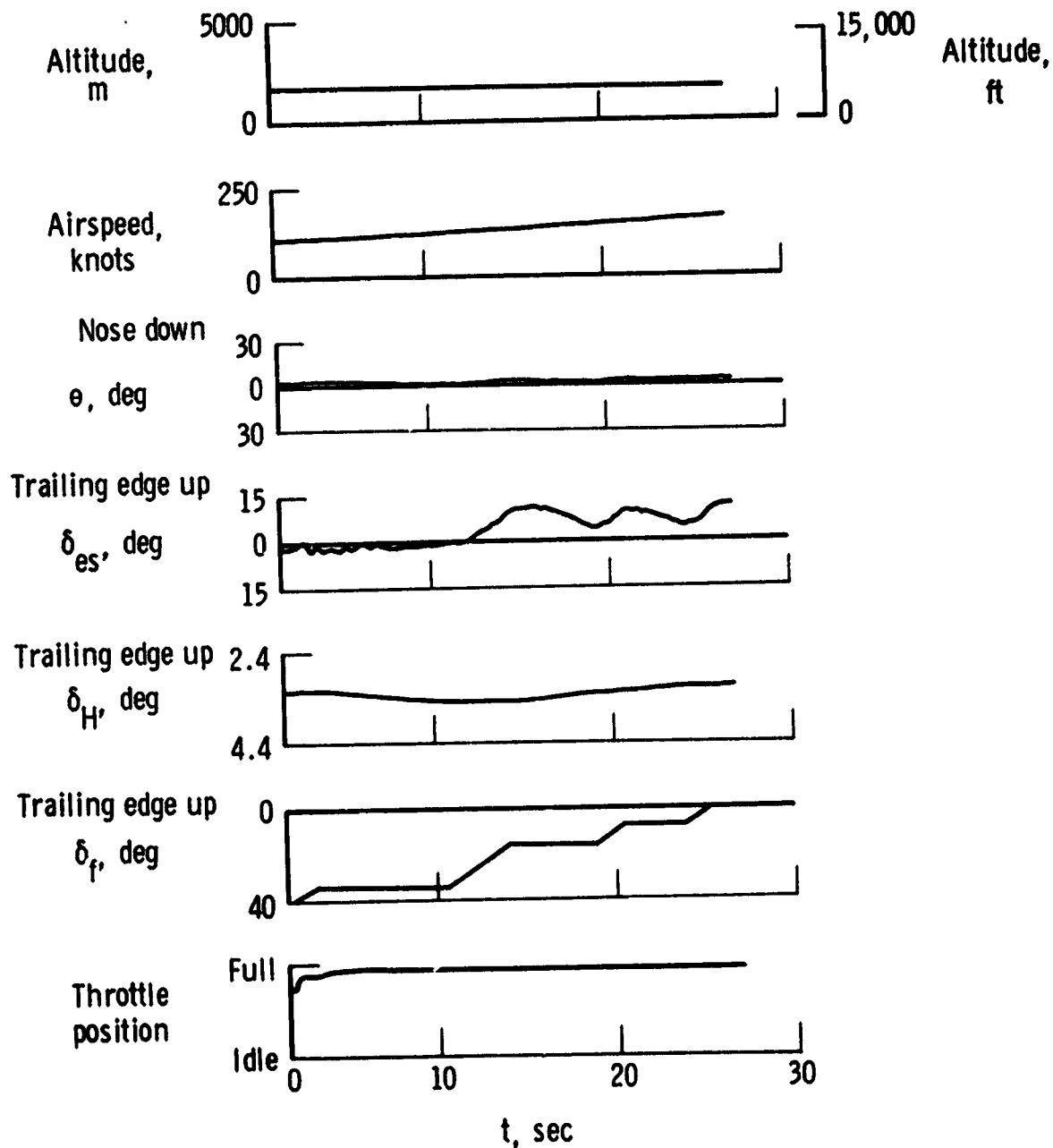
Figure 12.- Aircraft response to configuration changes. Hands off, $K_\theta = 20$, $K_{\dot\theta} = 4$, $K_{\delta_{ep}} = 24$.

143
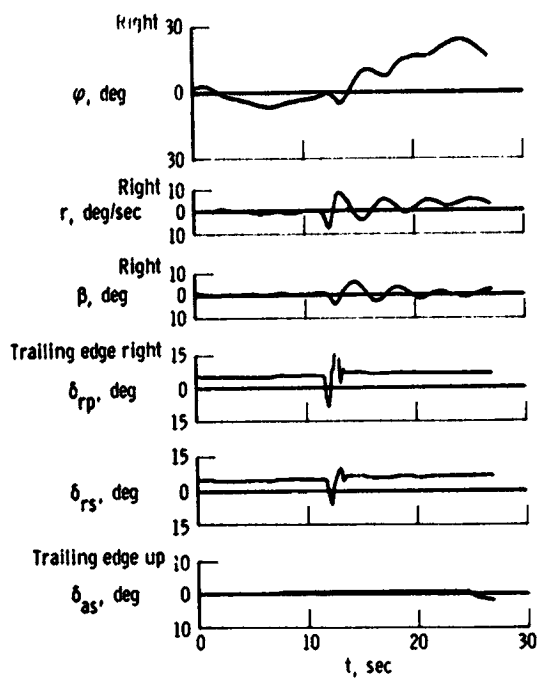
Figure 13.- Aircraft response to rudder
doublet in slave mode.
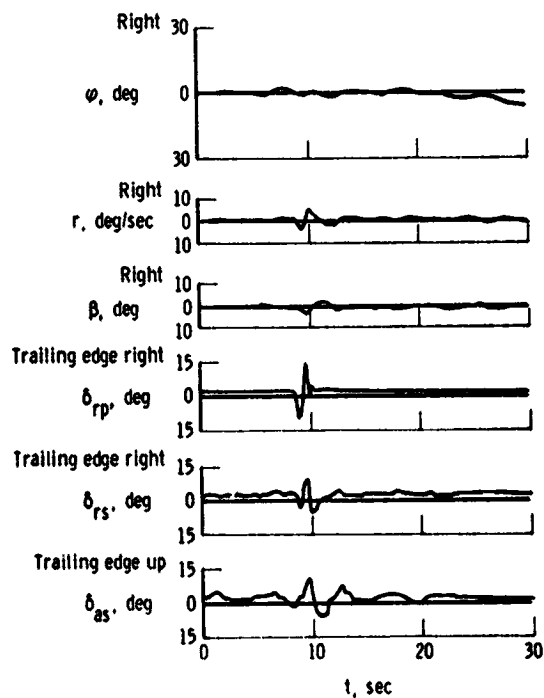
Figure 14.- Aircraft response to rudder
doublet in command mode.

144
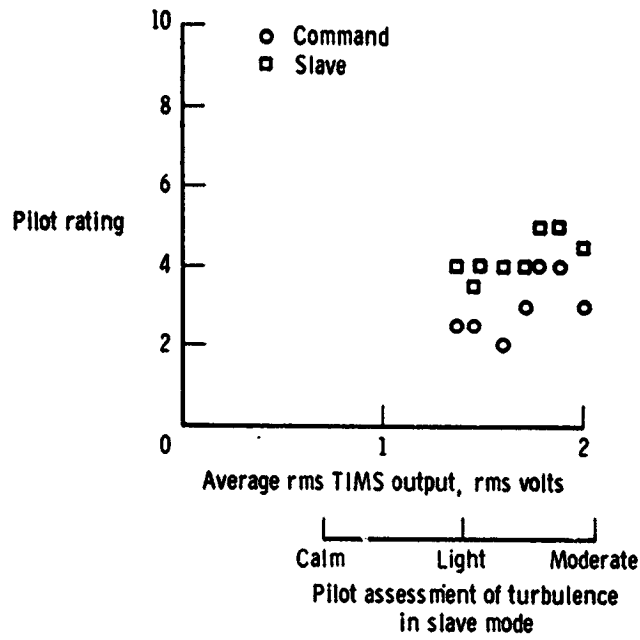
Figure 15.- Pilot ratings versus turbulence
for tasks 3, 4, 5.
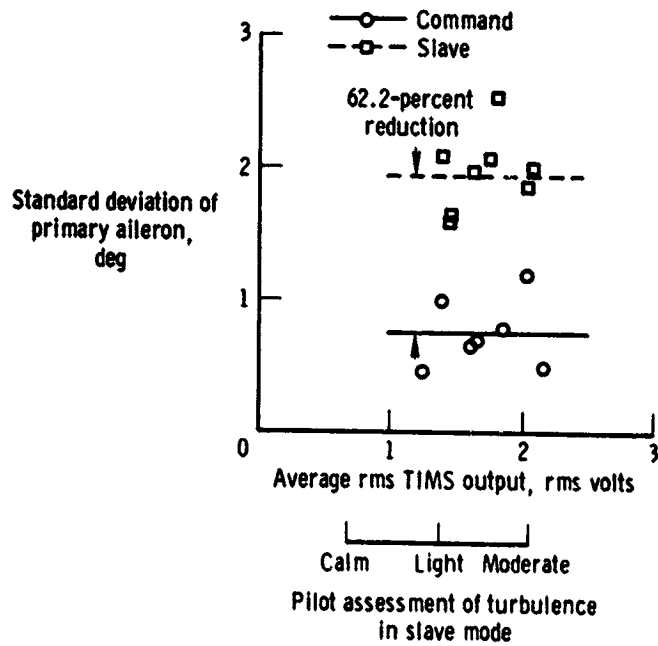
Figure 16.- Standard deviation of primary
aileron versus turbulence. Task 4.

145
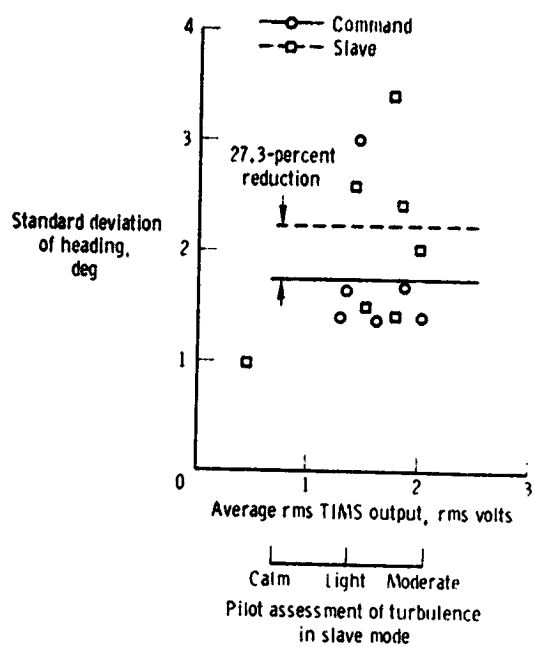
Figure 17.- Standard deviation of heading
versus turbulence. Task 2.
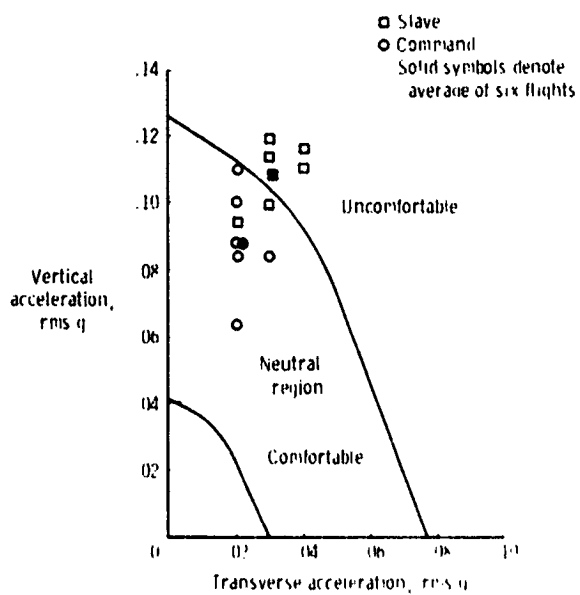
Figure 18.- Passenger comfort response
contours.

146

A REVIEW OF SUPERSONIC CRUISE FLIGHT PATH CONTROL

EXPERIENCE WITH THE YF-12 AIRCRAFT

Donald T. Berry and Glenn B. Gilyard
NASA Dryden Flight Research Center

SUMMARY

Flight research with the YF-12 aircraft indicates that solutions to many handling qualities problems of supersonic cruise are at hand. Airframe/propulsion system interactions in the Dutch roll mode can be alleviated by the use of passive filters or additional feedback loops in the propulsion and flight control systems. Mach and altitude excursions due to atmospheric temperature fluctuations can be minimized by the use of a cruise autothrottle. Autopilot instabilities in the altitude hold mode have been traced to angle of attack-sensitive static ports on the compensated nose boom. For the YF-12, the feedback of high-passed pitch rate to the autopilot resolves this problem. Manual flight path control is significantly improved by the use of an inertial rate of climb display in the cockpit.

INTRODUCTION

At the 1971 operating problems conference (ref. 1), some handling qualities problems of high altitude, supersonic cruise aircraft were discussed. An area of primary concern was longitudinal and lateral-directional flight path control. Longitudinal flight path control problems manifest themselves as altitude or Mach excursions, or both, that occur in an apparently random and unpredictable manner. These incidents have a history beginning with the XB-70 aircraft and extending to the YF-12 aircraft (ref. 1) and, more recently, the Concorde aircraft (ref. 2). Lateral-directional control problems of the YF-12 aircraft (ref. 3) manifest themselves as large forces and moments induced by inlet spike and bypass door movements and reductions in Dutch roll damping due to automatic inlet operation.

Since the last operating problems conference, research pertinent to supersonic cruise aircraft has been relatively low key. Nevertheless, significant progress has been made and solutions to several problems are at hand. Several papers and reports (refs. 3 to 7) have explored the primary areas of concern, such as airframe/propulsion system interactions, atmospheric disturbances, autopilot performance, and pilot displays.

This paper will review the high speed, high altitude flight path control problems discussed five years ago and the developments in these areas with the YF-12 aircraft since then. This study is neither final nor complete: more operating experience is required to confirm the adequacy of the solutions and to investigate additional problems.

9

147

SYMBOLS

Physical quantities are given in the International System of Units (SI) and parenthetically in U.S. Customary Units. All measurements except temperature were taken in Customary Units.

a_n normal acceleration, g

C_x longitudinal force coefficient

Δh incremental altitude, m (ft)

L normalized rolling moment, $1/\text{sec}^2$

M Mach number

N normalized yawing moment, $1/\text{sec}^2$

Δp_s static pressure error, N/m^2 (lb/ft^2)

α angle of attack with respect to wing reference plane, deg

β angle of sideslip, deg

β_i indicated angle of sideslip, deg

δ_a differential elevon deflection, deg

δ_e average elevon deflection, deg

δ_r rudder deflection, deg

ζ_{DR} Dutch roll damping ratio

$\zeta\omega_{n_{SP}}$ short period damping factor, rad/sec

η differential bypass door opening, right bypass door position minus left bypass door position, percent

τ_β sideslip sensor lag, sec

$\omega_{n_{SP}}$ short period frequency, rad/sec

Subscripts:

$M, \beta, \delta_a, \delta_r, \eta$ partial derivative with respect to subscripted variable

AIRFRAME/PROPULSION SYSTEM INTERACTIONS

Because airframe/propulsion system interactions are probably the most important factor in supersonic aircraft flight path control, this topic will be discussed first.

The demands of efficient cruise above Mach 2.0 has led to the use of variable geometry and mixed-compression inlets. A simplified schematic of a variable geometry inlet and control system is shown in figure 1. This inlet is representative of that used in the YF-12 aircraft. The inlet has a translating spike and forward bypass doors to control the position of the normal shock in the inlet. If the normal shock is positioned too far to the rear of the inlet, losses in efficiency and, thus, range will occur. If the normal shock is too far forward, it can become unstable and be expelled from the inlet (unstart), which causes large thrust losses and airflow disturbances. The desired operating position of the normal shock is a function of Mach number, angle of attack, and angle of sideslip. The inlet can be automatically controlled by a computer that varies the spike and bypass door positions as functions of these critical variables.

Dutch Roll Interactions

The propulsion system can exert a strong influence on the aircraft's stability and control characteristics. An example of a lateral-directional airframe/propulsion system interaction (ref. 3) is shown in figure 2. The airplane's response to a rudder pulse is illustrated with the inlets fixed and with the inlets operating automatically. The stability augmentation system is off. When the inlets are operating automatically, the Dutch roll motion is divergent. Because the Dutch roll motion has a relatively short period, the Mach number is constant and the only significant inlet control variable is the angle of sideslip. To compensate for local flow effects, the bypass doors on the windward side open farther with the sensed angle of sideslip than the doors on the leeward side. This causes asymmetric motion of the bypass doors with the net result that the differential bypass door deflection is in phase with the angle of sideslip. The spikes move in a similar manner. The analysis of these time histories (ref. 3) shows that the observed motions are due to the magnitude of the forces and moments produced by automatic inlet operation, the effect of those forces and moments on the aircraft's stability and control, and a 0.5-second lag (at this flight condition) in the sideslip sensor used by the inlet computer. These factors will be discussed in the following paragraphs.

Table 1 compares the effectiveness of the bypass doors in producing rolling and yawing moments to that of the aerodynamic control surfaces. Airplane control effectiveness is expressed in terms of percent of full deflection, rather than degrees of rudder or aileron. This provides a common base for comparison with the bypass

door effectiveness, which is expressed in terms of percent of full bypass door opening. In the normal operating range, the bypass doors have the same order of magnitude of effectiveness as the rudder and ailerons: in other words, 10 percent aileron deflection has approximately the same effect as 10 percent bypass door deflection. Fortunately, other YF-12 data indicate that due to choking, the effectiveness of the bypass doors as moment producers decreases considerably as the doors open beyond the normal operating position. If this effectiveness did not decrease, full bypass door openings could overpower the aerodynamic controls. (To simplify the analysis, the bypass door and spike effects have been combined, which is valid at this flight condition because the spikes move in phase with the bypass doors. In addition, investigations indicate that at this flight condition the bypass doors are more effective than the spikes.)

Table 2 shows the effect of the inlet on the static lateral-directional stability of the airplane. The bypass doors are programed by the inlet computer such that a bypass door opening of approximately 3 percent is commanded for each degree of sideslip. Thus, the moments generated by automatic inlet operation are coupled to sideslip. The table gives the static directional stability parameter (N_β) and the dihedral effect parameter (L_β) for the basic aircraft (inlets fixed) and for automatic inlet operation. The yawing moments produced by static stability are in the same sense as those produced by the bypass doors (N_η). Thus, these effects are additive and directional stability is improved 40 percent by automatic inlet operation. However, the rolling moments produced by the bypass doors oppose the rolling moments due to dihedral effect and the net result is a change in sign of the effective L_β.

The influence of automatic inlet operation on the Dutch roll damping is primarily determined by the lag in the sideslip sensor for the inlet computer, which acts in conjunction with the yawing moments induced by the bypass doors. Figure 3 illustrates the influence of the sideslip sensor lag on the Dutch roll damping ratio for a nominal value of yawing moment due to bypass door deflection for the YF-12 aircraft. The figure shows that lags cause the damping of the Dutch roll mode to become unstable. However, it is relatively easy to eliminate the lag or, possibly, provide a lead. When a lead is provided, the airframe/propulsion system interaction could be used to enhance aircraft damping. Feasibility studies indicate that Dutch roll damping can be improved by the use of passive filters or feedback loops such as the feedback of a yaw rate signal to the bypass doors.

Phugoid Interactions

Damping changes due to automatic inlet operation have also been documented for the phugoid mode. Figure 4 illustrates a typical phugoid motion of the YF-12 aircraft for fixed and automatic inlet operation. In both cases the aircraft was initially disturbed by the pilot's opening and closing the bypass doors, which momentarily increases drag and decreases thrust.

150

An unpublished analysis of YF-12 phugoid data indicates that the primary influence is on C_{x_M}, the change in longitudinal force coefficient (thrust minus drag) with respect to Mach number (table 3). For a typical subsonic jet aircraft at a constant throttle setting, drag tends to increase faster with speed than thrust, which increases phugoid damping. For high performance supersonic propulsion systems, however, efficiency increases with Mach number and, at a constant altitude, thrust can actually increase faster than drag. Conversely, when the aircraft decelerates, thrust can decrease faster than drag. Because automatic inlet operation is more efficient than fixed inlet operation, this effect is accentuated, as illustrated by the change in C_{x_M} in table 3.

It is not certain whether these changes in phugoid damping contribute to piloting difficulties. In any case, the basic phenomena are understood and can be suppressed with an autopilot or a stability augmentation system if necessary.

LONGITUDINAL FLIGHT PATH CONTROL

Many factors are involved in the long history of incidents of altitude and Mach number excursions with supersonic cruise aircraft. Some primary factors are autopilot behavior in the presence of atmospheric temperature fluctuations, system characteristics such as lags and angle of attack sensitivity, and inadequate pilot displays.

Mach Hold Autopilot Behavior

Manual control of Mach number and altitude can involve a sizable pilot workload when conditions are not ideal. In addition, the pilot must monitor a variety of aircraft systems (particularly the propulsion system) and contend with a rapid succession of air traffic control checkpoints because of the high cruise speed. Consequently, autopilot operation is essential for pilot relief.

However, some conventional autopilot modes respond unfavorably to 'mospheric temperature changes. For example, a conventional Mach hold auto, ilot uses elevons to maintain Mach number. Basically, it attempts to trade altitude for speed. At high speeds, however, large changes in altitude are required to obtain relatively small changes in speed. When atmospheric temperature changes are encountered, the autopilot interprets these as instantaneous Mach number changes and induces large altitude changes to attempt to compensate. This is illustrated in figure 5, in which the solid line shows the simulated response of a YF-12 aircraft to a 4° C (7.2° F) step change in temperature.

Unpublished studies show that a cruise autothrottle alleviates this problem by providing an additional controller which permits control of Mach number independent of altitude. The dashed line in figure 5 shows a simulator response with the autothrottle system. A cruise autothrottle was recently installed in the YF-12

aircraft and flight tests are in progress to verify these studies in an operational environment. Similar experiences with the Concorde aircraft have also led to the conclusion that a cruise autothrottle is needed (ref. 8).

Altitude Hold Autopilot Behavior

Difficulties have also been encountered with conventional altitude hold modes, and YF-12 experience (ref. 6) indicates that these cases can be quite subtle and complex. The YF-12 problems appear to be extremely random and unpredictable: sometimes the problems are associated with obvious atmospheric temperature fluctuations and sometimes they are not. The altitude hold mode on the YF-12 aircraft was designed for use below 18,288 meters (60,000 feet), but because nothing in the design precluded its use above that altitude, it was decided to investigate the behavior of the altitude hold autopilot at high altitudes. The results appear to be inconsistent in that on some occasions the altitude hold autopilot maintained altitude within ±30.5 meters (±100 feet), whereas on other occasions large altitude excursions or bursts of short period instability occurred. Figure 6 shows an example of acceptable altitude hold performance (ref. 6) and figure 7 shows an example of unacceptable performance. In figure 7, note the bursts of divergent-convergent short period oscillations, the rough ride (as indicated by the normal acceleration time history), and the poor altitude hold performance.

Analysis and simulation studies showed that adjustment of the autopilot gains could improve the long period altitude hold performance, but the short period instabilities persisted and were traced to the angle of attack sensitivity of the static ports on the compensated nose boom of the YF-12 aircraft. The compensated nose booms are used to minimize airspeed errors in the transonic speed range; unfortunately, these nose booms tend to be sensitive to angle of attack.

The nature of the angle of attack sensitivity of the nose boom is illustrated in figure 8. As angle of attack increases, the slope $(\Delta p_s/\Delta\alpha)$ of the curve of static pressure error versus angle of attack increases. Analysis has shown that $\Delta p_s/\Delta\alpha$ has a direct effect on short period stability. This is illustrated in figure 9, which is a root locus of the airplane and autopilot for various values of $\Delta p_s/\Delta\alpha$. As $\Delta p_s/\Delta\alpha$ becomes more negative, the short period mode becomes unstable.

Therefore, relatively small changes in angle of attack can cause marked changes in system stability. On days when the atmosphere is smooth and the aircraft precisely trimmed, good autopilot behavior is possible. On the other hand, any roughness in the atmosphere that would induce more autopilot activity and larger angle of attack excursions would lead to instability. Figure 7 shows that the oscillations diverge when angle of attack increases and converge when angle of attack decreases.

Simulation studies showed that the angle of attack sensitivity could be counteracted by adding a high-passed pitch rate signal to the autopilot. The addition of high-passed pitch rate increased the damping of the aircraft-autopilot system without interacting with other modes, so that the system was insensitive to the effects of angle of attack. The angle of attack sensitivity could also be counteracted by the

152

computation of a correction in the air data computer or the relocation of the static ports to a location that is insensitive to angle of attack. The use of the high-passed pitch rate feedback, however, is advantageous in that it does not require as precise a prior knowledge of the angle of attack induced errors or nose boom characteristics.

To verify these results in the flight environment, the YF-12 altitude hold autopilot mode was modified with gains optimized for higher altitudes and a high-passed pitch rate feedback signal to compensate for the angle of attack-sensitive nose boom. The performance of the modified altitude hold autopilot is illustrated in figure 10. Although the atmosphere appears to be smooth, the angle of attack range is similar to the example of figure 7, where short period instabilities occurred. In this case, however, autopilot performance is smooth with no signs of short period instability.

Manual Flight Path Control

To assist the pilot in manual flight path control tasks, an inertial rate of climb display was provided in the YF-12 cockpit (ref. 7). Vertical velocity information from the onboard inertial guidance system was used to drive a horizontal needle on the attitude/director indicator. This display circumvents the lag in the air data system and the errors due to the angle of attack sensitivity of the nose boom.

Pilots' comments on this display were highly favorable. Typical comments were: "immediately obvious this is a lot better", "a big help", "very helpful", and "nice for level accelerations." A limited semiquantitative evaluation of the display was made, and the results, which are summarized in table 4, show an average improvement in pilot rating of approximately 2 1/2 on the Cooper-Harper scale—a significant improvement.

CONCLUDING REMARKS

Solutions to several of the handling qualities problems of supersonic cruise vehicles discussed at the 1971 operating problems conference are at hand. However, more operating experience is needed to confirm the adequacy of these solutions and to investigate additional problems. The primary problems addressed in 1971 and the solutions developed with the YF-12 aircraft since then are summarized as follows:

Airframe/propulsion system interactions are caused by significant forces and moments on the airframe induced by bypass door and spike operation. For the Dutch roll mode, these forces and moments are coupled to the aircraft's responses by the inlet computer that controls the spike and bypass door positions as a function of angle of sideslip. This coupling is adversely affected by lags in the sideslip sensor. These adverse interactions can be reduced or made favorable by the use of passive filters or additional feedback loops in the propulsion or flight control system, or both.

Atmospheric temperature fluctuations can cause a conventional Mach hold auto-
pilot to induce large Mach and altitude excursions. The use of a cruise autothrottle
for Mach control alleviates this problem.

Instabilities in the altitude hold autopilot systems have been traced to the angle
of attack sensitivity of the static ports on the compensated nose boom. For the
YF-12 aircraft, the feedback of high-passed pitch rate to the autopilot resolves this
problem.

Manual flight path control is significantly improved by the use of an inertial rate
of climb display in the cockpit.

154

REFERENCES

1. Berry, Donald T.: Some Handling-Qualities Problems of High-Altitude Supersonic Cruise Aircraft. NASA Aircraft Safety and Operating Problems, NASA SP-271, Vol. II, 1971, pp. 25-38.

2. Coleman, Herbert J.: Concorde Tour Adds to Operations Data. Aviation Week & Space Technology, Aug. 7, 1972, pp. 31-32.

3. Gilyard, Glenn B.; Berry, Donald T.; and Belte, Daumants: Analysis of a Lateral-Directional Airframe/Propulsion System Interaction. NASA TM X-2829, 1973.

4. Berry, Donald T.; and Gilyard, Glenn B.: Airframe/Propulsion System Interactions — An Important Factor in Supersonic Aircraft Flight Control. AIAA Paper 73-831, Aug. 1973.

5. Berry, Donald T.; and Schweikhard, William G.: Potential Benefits of Propulsion and Flight Control Integration for Supersonic Cruise Vehicles. Advanced Control Technology and its Potential for Future Transport Aircraft. NASA TM X-3409, 1976.

6. Gilyard, G. B.; Smith, J. W.; and Falkner, V. L.: Flight Evaluation of a Mach 3 Cruise Longitudinal Autopilot. AIAA Paper 74-910, Aug. 1974.

7. McMaster, John R.; and Schenk, Frederick L.: The Development of the F-12 Series Aircraft Manual and Automatic Flight Control System. AIAA Paper 73-822, 1973.

8. World News. FLIGHT International, Oct. 9, 1975, pp. 512-514.

TABLE 1.—COMPARISON OF BYPASS DOOR AND
CONTROL EFFECTIVENESS

$$L_\eta = 0.35 \text{ deg/sec}^2\text{-percent}$$

$$L_{\delta_a} = 0.30 \text{ deg/sec}^2\text{-percent}$$

$$N_\eta = 0.11 \text{ deg/sec}^2\text{-percent}$$

$$N_{\delta_r} = -0.073 \text{ deg/sec}^2\text{-percent}$$

TABLE 2.—INFLUENCE OF AUTOMATIC INLET OPERATION ON
EFFECTIVE AIRCRAFT STATIC STABILITY

Inlet operation	Effective stability derivative	
	L_β, $1/\text{sec}^2$	N_β, $1/\text{sec}^2$
Fixed	−0.90	0.86
Automatic	0.24	1.23

TABLE 3.—EFFECT OF INLET OPERATION ON C_{x_M}

Inlet operation	C_{x_M}
Fixed	-0.028
Automatic	0.025

TABLE 4.—PILOT RATINGS OF ALTITUDE CONTROL

$M \approx 3.0$

Task	Cooper-Harper rating	
	Without inertial rate of climb display	With inertial rate of climb display
Transition from climb to level flight	6	3
Stabilization after pitch disturbance	5	3
Descent	5	3
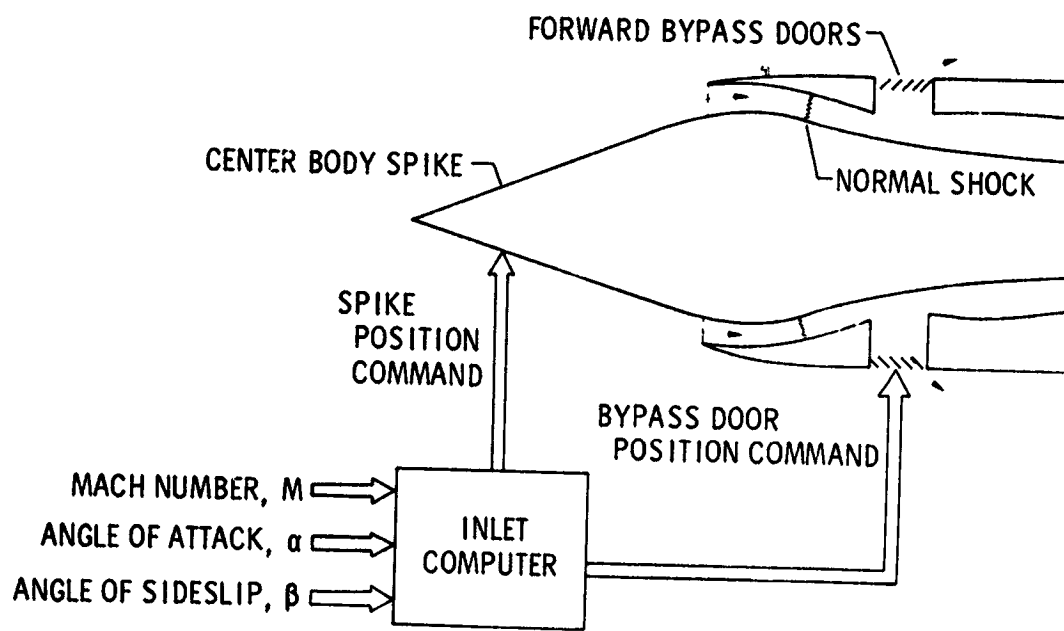
Figure 1.- Simplified schematic of variable geometry inlet and
control system.
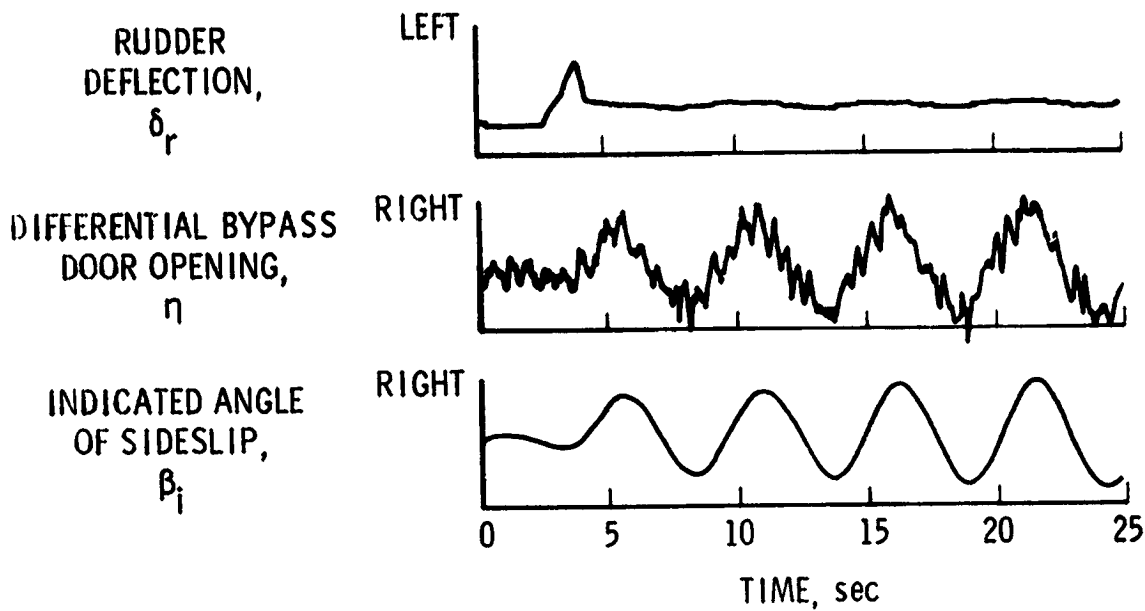
(a) Inlets automatic.
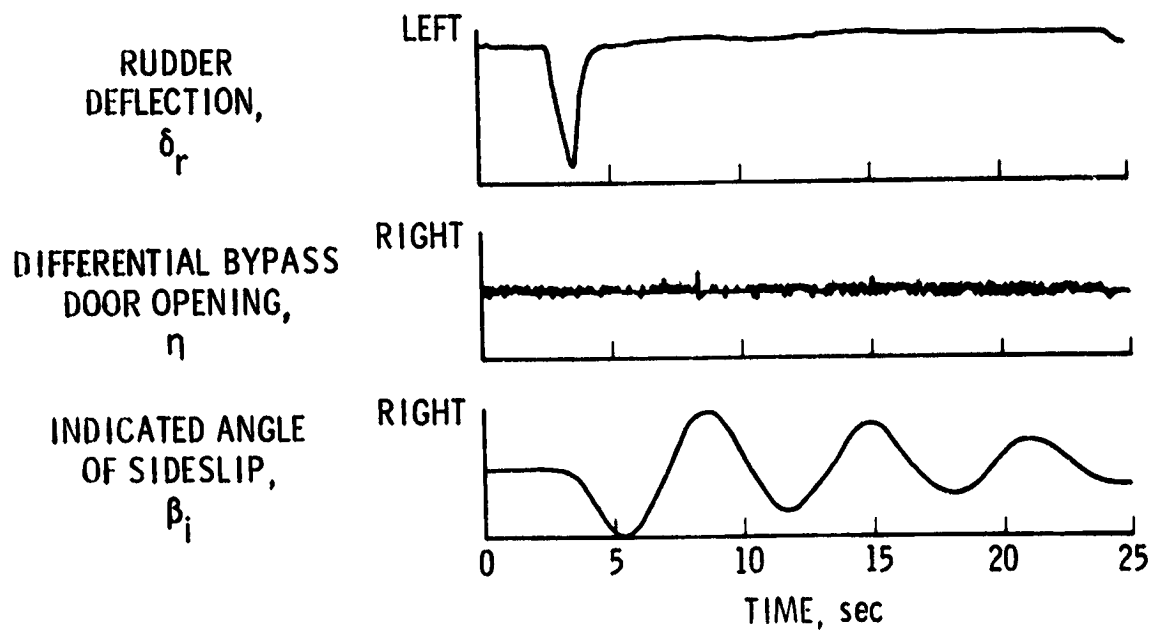
(b) Inlets fixed.

Figure 2.- Dutch roll response to rudder pulse. Yaw stability augmentation system off, $M \approx 3.0$.
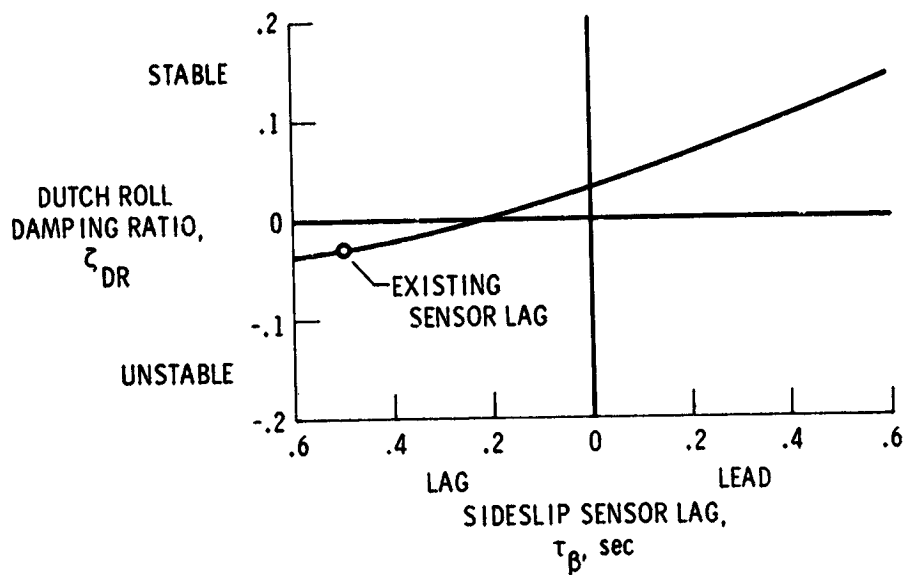
Figure 3.- Influence of sideslip sensor lag or lead
compensation on Dutch roll damping ratio.
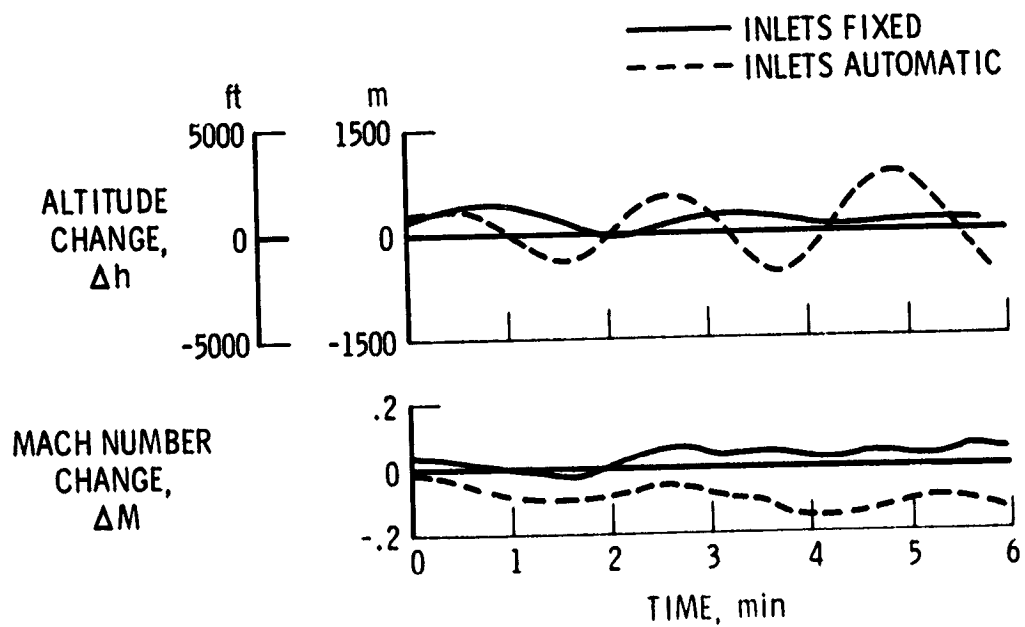
Figure 4.- Effect of inlet operation on YF-12 phugoid response.
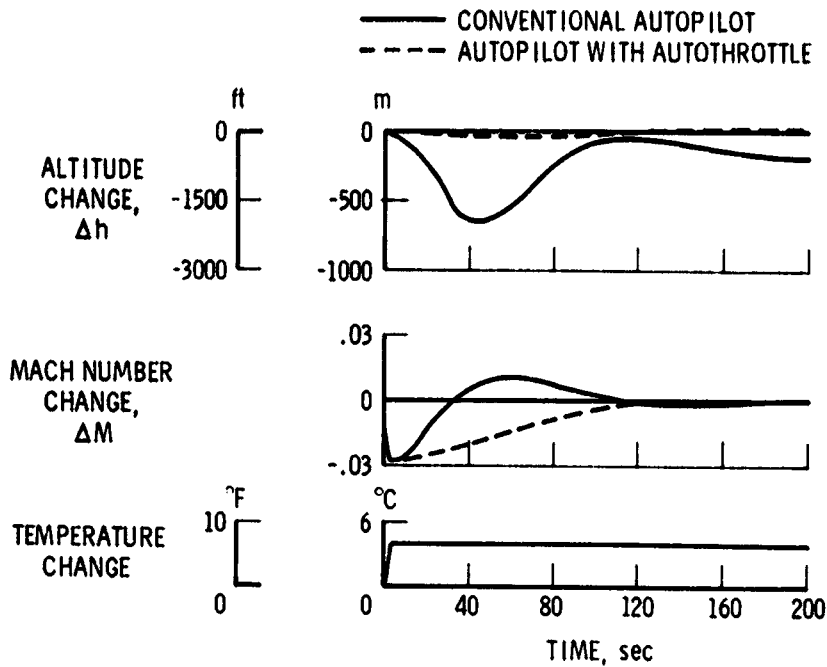
Figure 5.- Simulated response of YF-12 Mach hold autopilot.
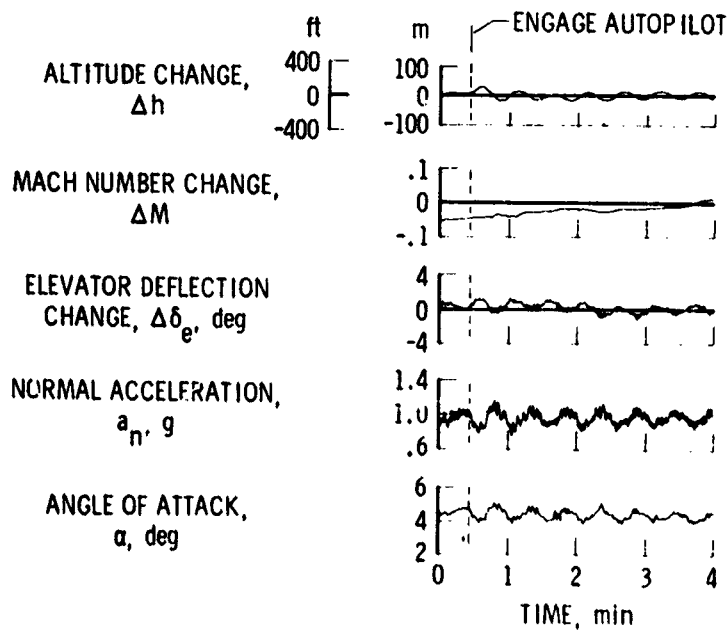
Figure 6.- Acceptable altitude hold.   Stable
   atmosphere;   M ≈ 3;   h ≈ 23,622 m (77,500 ft).

161
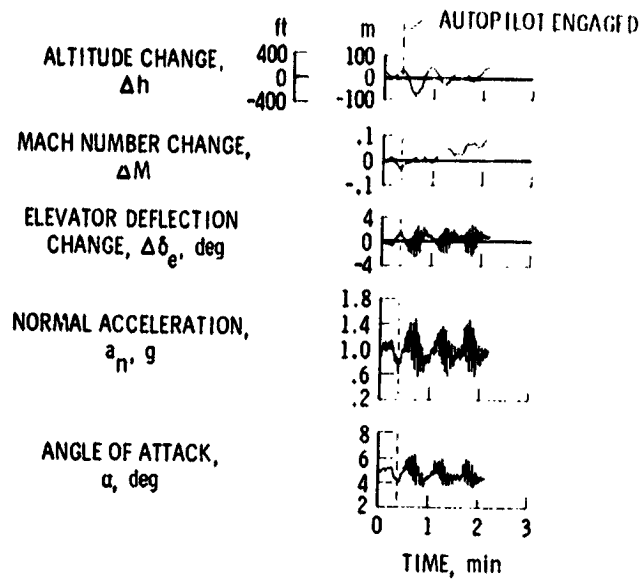
Figure 7.- Unacceptable altitude hold.
Unstable atmosphere;   M ≈ 3;
h ≈ 23,622 m (77,500 ft).
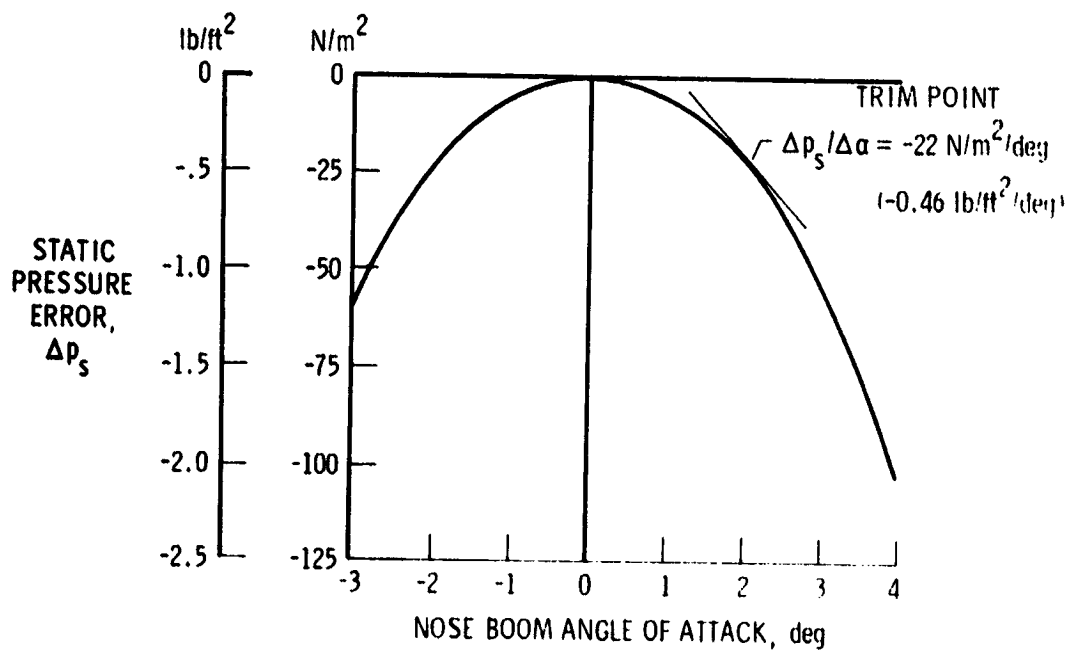
Figure 8.- Variation of static pressure error with nose boom angle of attack.
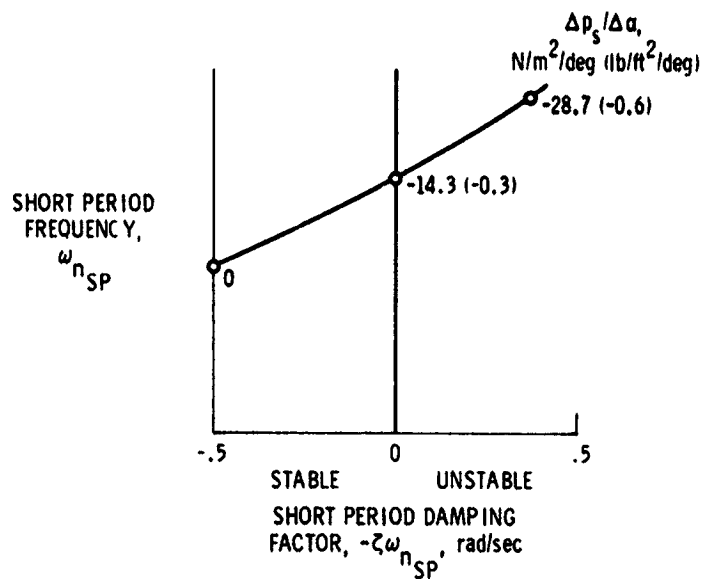
Figure 9.- Variation of short period roots with
$\Delta p_s / \Delta \alpha$ for altitude hold mode.
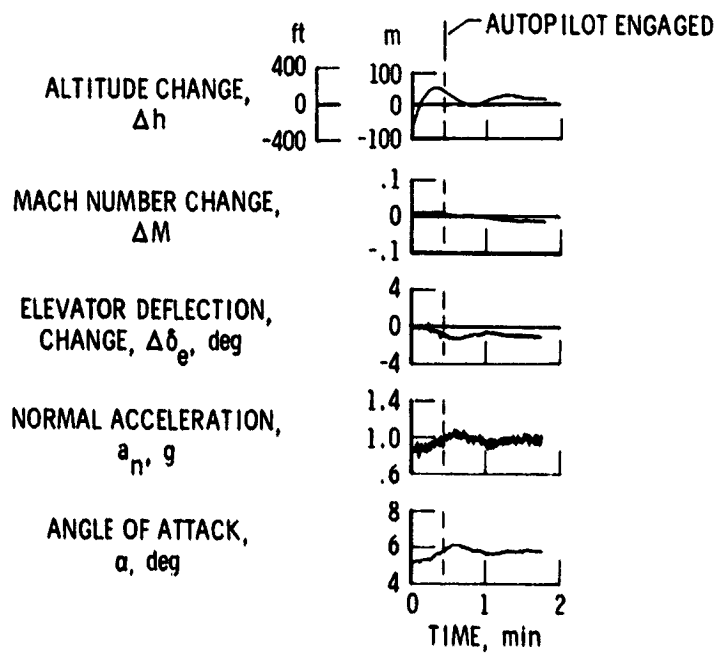
Figure 10.- Performance of modified altitude hold autopilot.

163

TENTATIVE CIVIL AIRWORTHINESS FLIGHT CRITERIA

FOR POWERED-LIFT TRANSPORTS

Charles S. Hynes
NASA Ames Research Center
and
Barry C. Scott
FAA, Ames Research Center

$N77-18034$

SUMMARY

A 3-year research program sponsored jointly by the NASA and the FAA has resulted in the formulation of tentative civil airworthiness flight criteria for powered-lift transports. Representatives of the U. S., British, French, and Canadian airworthiness authorities participated. The ultimate limits of the flight envelope are defined by boundaries in the airspeed/path-angle plane. Angle of attack and airspeed margins applied to these ultimate limits provide protection against both atmospheric disturbances and disturbances resulting from pilot actions or system variability, but do not ensure maneuvering capability directly, as the 30-percent speed margin does for conventional transports. Separate criteria provide for direct demonstration of adequate capability for approach path control, flare and landing, and for go-around. Demonstration maneuvers are proposed, and appropriate abuses and failures are suggested. Taken together, these criteria should permit selection of appropriate operating points within the flight envelopes for the approach, landing, and go-around flight phases, which are the phases likely to be most critical for powered-lift aircraft. Criteria are based (1) on simulation results obtained using the Ames Flight Simulator for Advanced Aircraft, (2) on previous ARC flight experience with a variety of experimental powered-lift aircraft, and (3) on recommendations from other sources. Additional work is needed to verify and refine the present criteria in flight, to develop criteria to define field lengths, and to treat powered-lift concepts that incorporate sophisticated guidance, displays, or advanced vehicle stability augmentation.

INTRODUCTION

This paper presents the results of a 3-year research program directed toward development of tentative civil airworthiness flight criteria for powered-lift aircraft. The objectives were to develop tentative airworthiness flight criteria (concentrating on the approach and landing flight phases), to define demonstration test techniques, and to explore design implications of the criteria.

The program was sponsored jointly by NASA and FAA, with participation by the United States, British, French, and Canadian airworthiness authorities. It is hoped that standards developed from these criteria can be adopted in substantially equivalent form by each of the participating authorities.

The development of criteria was begun by using the Ames Flight Simulator for Advanced Aircraft (fig. 1) to evaluate the operating characteristics of several representative powered-lift concepts (refs. 1-6) under realistic instrument flight conditions with atmospheric turbulence and wind shear. Together with previous Ames experience with various powered-lift research aircraft (ref. 7), this evaluation enabled identification of the principal flight hazards due to powered lift.

Preliminary criteria intended to provide protection against these hazards were drafted by the Powered-Lift Standards Development Working Group, a body organized for that purpose and constituted of representatives of the participating organizations. These preliminary criteria were then examined by additional simulator testing (refs. 8, 9), and appropriately modified. Flight testing will be necessary to verify and refine the presently proposed criteria.

These criteria are presented and discussed fully in a report (ref. 10) that has recently been distributed by the FAA for comment. Criteria have been developed in the categories of flight envelope limits, safety margins, approach path control, flare and landing, go-around, and propulsion failure, together with brief guidelines on landing field length. A section on general considerations (ref. 10) is intended to treat questions of regulatory philosophy, and to clarify certain peculiarities that tend to characterize all powered-lift vehicles supported primarily by wing lift. The forms of the criteria were considered more important than the proposed numerical quantities. Although these numerical proposals were based on the flight and simulation results available at the time, it is recognized that these numerical quantities will have to be refined as flight experience is gained.

ULTIMATE FLIGHT ENVELOPE LIMITS

Turning now to the criteria themselves, it is convenient to begin by considering those basic aerodynamic characteristics of a powered-lift aircraft that determine the ultimate limits of its flight envelope. The two graphs on the left-hand side of figure 2 illustrate the lift curves and polar characteristics of a representative powered-lift transport in the landing configuration. The augmentation of lift by the propulsion system is correlated for different concepts by the blowing momentum coefficient C_J, which represents the reaction force due to the momentum discharged by the powered-lift system. The lowest curves represent the characteristics of the wing without blowing. Increased blowing at constant angle of attack augments the lift several-fold. Powered-lift aircraft may be controllable beyond the peaks of the lift curves, so that the maximum angle of attack α_{MAX} may exceed the angle for maximum lift.

The right-hand graph of figure 2 illustrates the operating envelope that results when the aerodynamic characteristics are converted from coefficient to dimensional form. The heavy contours correspond to constant thrust settings. It can be seen that the boundaries of the central clear area constitute the ultimate limits of the flight envelope. In the shaded region at the top of the chart, the thrust required for steady flight is greater than the maximum

166

available; in the lower right-hand corner it is less than flight idle thrust. Beyond the right edge of the chart the airspeed exceeds the placard (structural) limit, and in the lower left-hand corner the aircraft is either stalled or otherwise uncontrollable. The broken minimum-speed contour V_{MIN} corresponds to $C_{L_{MAX}}$. The region of the flight envelope between the α_{MAX} and V_{MIN} contours is not useful for controlled operation, but can provide additional protection against vertical gusts. In general for powered-lift aircraft it is necessary to consider the limiting angle of attack separately from the limiting speed.

SAFETY MARGINS

Safety margins must be applied to the ultimate limits of the flight envelope to define the normal envelope. Within this normal envelope, all expected flight operations can be carried out while maintaining safe margins from the ultimate envelope limits.

Angle of Attack Margin

Considering first the angle of attack margin, it must provide protection against undesired angle of attack excursions resulting from atmospheric disturbances and unintentional pilot deviations, as well as allowing for intentional maneuvers. The proposed tentative angle of attack margin is illustrated in figure 3, and is defined by the equation

$$\Delta\alpha = \text{arc sin } \frac{20}{V_{knot}}$$

This margin enables the aircraft to encounter an abrupt 20-knot vertical gust without exceeding α_{MAX}. The criterion was proposed by the working group after reviewing the capabilities of conventional aircraft during the landing approach, and is intended to provide vertical gust protection equivalent to that of conventional jet transports. The angle of attack excursions caused by pilot actions are smaller for powered-lift aircraft which use thrust as the primary means of flight path control than for conventional aircraft, which use pitch changes for flight path control. Since α_{MAX} is generally thrust-dependent, the margin must be established at each thrust setting throughout the flight range. This process then defines the upper light solid contour in figure 3, which constitutes one boundary of the normal operating envelope.

Speed Margin

For purposes of comparison, consider the speed margin for conventional transports. The hatched boundary on the right in figure 4 illustrates the 30-percent speed margin required for conventional transports; it is based on the power-off stall speed. It will be seen that this margin would not allow

exploitation of the powered-lift envelope. The corresponding tentative speed margin proposed for powered-lift aircraft is also 30 percent (but not less than 20 knots), but it is based on the use of maximum thrust. This speed margin is intended to deal with atmospheric disturbances requiring drastic action by the pilot, such as strong wind shear. To command maximum lift, the pilot of the conventional aircraft must pitch to the stalling limit. In the powered-lift aircraft the corresponding pilot action would be to apply maximum thrust (and perhaps also to pitch moderately). It will be seen from figure 4 that the proposed criterion recognizes the effectiveness of powered lift in reducing minimum speed by allowing a corresponding reduction in approach speed. As a consequence, an aircraft with little powered lift would use an approach speed nearly the same as if it were certified under present transport-category requirements.

The right-hand chart of figure 5 illustrates a second tentative speed margin which is intended to provide protection during normal approaches not requiring drastic action by the pilot. For commercial operations it is neces- sary to fly normal approaches in light to moderate turbulence safely and routinely, with an acceptable pilot workload and without encountering nuisance warnings. After reviewing both flight and simulation experience, the working group proposed a speed margin of 15 percent (but not less than 10 knots), based on the minimum speed at the instantaneous thrust. This thrust is, of course, nominally the approach thrust. However, since the minimum speed V_{MIN} depends on thrust, it will change as thrust is set for different flight path angles. Therefore, the margin must be established at each thrust setting over the whole flight range. This process then defines the upper broken contour in the right-hand chart of figure 5. The two speed-margin criteria illustrated in figure 5 constitute two additional boundaries of the normal operating envelope.

Summary of Safety Margin Criteria

When the proposed angle of attack and speed margin criteria are applied to the ultimate flight envelope, the normal operating envelope that is thus defined is illustrated by the clear area in figure 6. The relationship of the three margin boundaries to each other determines which margin criteria govern in defining the limits of the normal envelope. This relationship will depend on design characteristics, such as the forms of lift curves and the magnitude of powered lift, and will be different for each aircraft. To reiterate, for an aircraft with little powered lift, the maximum-thrust speed margin would likely be dominant, resulting in an approach speed nearly the same as if the aircraft were certified under present requirements for conventional transport-category aircraft.

Now, where within this normal envelope should the nominal operating point be located? To answer this question, it is necessary to consider how the actual instantaneous operating point may change as the pilot makes flight path corrections during the approach. In a conventional aircraft, of course, the pilot attempts to maintain the approach airspeed nominally constant. Most of the powered-lift research aircraft have been flown to a reference angle of attack. It can be seen from figure 6 that maximum use of the powered-lift

168

envelope would result from following the maximum-thrust speed margin boundary
when flying shallow approach paths, and following the angle of attack margin
boundary when flying steeper paths. There is some question whether the pilot
can follow such contours successfully. This matter will be considered further
in the next section.

FLIGHT REFERENCE

An enlargement of the normal operating envelope (the clear area of
fig. 6) appears in figure 7. Here the concept of flight reference has been
generalized to include any contour within the flight path angle vs speed
plane, such as the arbitrary contour shown in figure 7. This generalized
flight reference could be speed, angle of attack, or perhaps some combina-
tion of these with thrust, provided only that the reference quantity be dis-
played to the pilot by a single instrument and that it be adequately reliable.
Simulation results indicate that use of such artificial references appears
quite feasible. The dotted area in figure 7 illustrates an expected range
of abuses of the flight reference resulting from atmospheric disturbances or
pilot deviations.

FLIGHT PATH CAPABILITY

What increments of flight path angle above and below the scheduled path
are necessary to enable the pilot to make adequate upward of downward correc-
tions during the approach? Based on both flight and simulation experience,
the working group proposed that the upward correction capability extend to an
angle 4° steeper than the scheduled angle. Because powered-lift aircraft tend
to operate on the back side of the thrust-required curve, slow-speed abuses
tend to reduce the upward capability, and fast-speed abuses tend to reduce
the downward capability. It is intended that appropriate abuses be included
in the flight path control demonstrations. The size of the abuse would be
related to the excursions to be expected during approaches in moderate turbu-
lence, and the demonstration would establish the flight path capability at
the abused flight reference.

Figure 7 illustrates these considerations, and shows how an appropriate
operating point can be selected. The flight reference must be chosen to
provide adequate flight path capability without violating any of the safety
margin boundaries when the flight reference itself is maintained. In
figure 7, if the chosen flight reference contour were to permit the demon-
stration of a steady gradient of only 10° with the fast-speed abuse, then
the steepest scheduled approach angle that could meet all the criteria
simultaneously would be 6°.

FLIGHT PATH CONTROL

Why is it necessary to treat the problem of flight path control separately at all? First, the characteristics of backsided operation, large thrust inclination, low lift-curve slope (heave damping), and limited pitch authority and dynamic response all tend to degrade the flight path response. Maintaining speed and angle of attack margins is not sufficient to ensure adequate maneuvering capability, as it does for conventional transports. The need for adequate flight path capability to enable the pilot to make path corrections has already been discussed.

The working group proposed several dynamic response criteria intended to ensure adequate path response without objectionable overshoot or excessive disturbance of the flight reference due to use of the primary flight path control. These proposals are presented and discussed in detail in reference 10.

Finally, the handling qualities of several powered-lift research aircraft have been objectionable during approach because of excessive complexity of controls. For example, the hot nozzles of the Augmentor Wing Research Aircraft (AWRA) are operated by a separate cockpit controller providing powerful control of thrust inclination. Flight experience with this aircraft indicates that continuous modulation of nozzles in addition to column and throttles during approach results in excessive pilot workload.

To deal with this problem, the working group proposed that there be no more than two longitudinal controls, one primarily for controlling path and the other for controlling flight reference, just as in conventional airplanes. For example, throttle might be primary for path, and column primary for flight reference. In order to limit pilot workload, any other cockpit controllers would be treated as configuration selectors not requiring continuous pilot modulation during approach.

FLARE AND LANDING

The next flight phase to be considered is the flare and landing. In this section and in those that follow, it will only be possible to indicate the general nature of the proposed criteria, concentrating on those aspects that differ significantly from conventional aircraft practice.

After considering the need for balancing various requirements on precision of control, on acceptability of dispersions in touchdown sink rate and landing distance, and on gear strength, the working group proposed that flare and landing capability be demonstrated directly in flight, with appropriate abuses. Proposed abuses of initial conditions include landing from a path 2° steeper than scheduled, as well as appropriate variations in initial flare height and in initial flight reference.' These latter abuses remain to be defined from further study of operating characteristics. The steep-path abuse corresponds to use at the flare initiation point of half the proposed

170

4° downward correction capability, and appears to correlate well with the flight path disturbances encountered during simulation of moderate turbulence.

A second category of flare and landing abuses is concerned with abuse of the secondary control. For example, for an aircraft that relies primarily on pitch rotation for landing flare, thrust would be considered the secondary control. For powered-lift aircraft in this category, a severe thrust-reduction abuse is proposed, one amounting to irrational use of thrust. The purpose of the abuse demonstration is to ensure that the flare and landing technique normally used in the conventional regime would not be catastrophic if applied to the same aircraft in the powered-lift regime. If the aircraft were flared primarily with thrust, this thrust abuse would not be needed (although the effect of an inadequate pitch rotation should then be demonstrated). Flaring with thrust alone appears acceptable if the heave response is sufficiently rapid.

GO-AROUND

The principal differences between go-around criteria for conventional aircraft and those for powered-lift aircraft are concerned with the acceptability of re-configuration. Some powered-lift aircraft may not be capable of positive climb angles without re-configuration, such as closing upper-surface spoilers, even with all engines operating. Under the proposed criteria, an acceptable re-configuration would be accomplished quickly by a single-action selection that would not require the pilot to remove his hands from the primary or secondary controls, and would not require further attention.

PROPULSION FAILURE

After considering the questions concerning propulsion failure in a powered-lift aircraft, the working group proposed the following criteria. First, failure of all critical system elements should be considered, including such elements as cross-shafting or cross-ducting as well as the engines themselves. Second, all available alternatives, such as reversion to conventional operation, should be considered. The need to take account of propulsion failure affects the specific criteria in all categories. In view of the low probability of propulsion failure following commencement of an approach, the group believed it reasonable to accept slight reductions in safety margins and flight path capability following the failure. Capability for safe landing (within structural limits) would be demonstrated following failure below a certain commit height, and capability for safe go-around would be demonstrated following failure above this commit height.

LANDING FIELD LENGTH

A great deal of work is still needed to develop methods for determining landing field length. Summarizing the general considerations the working group believed most important: the field length determination should be based on the operational (rather than maximum-effort) technique; abuses related to flare and landing should be demonstrated; and propulsion failure should be considered. It may be significant that powered-lift aircraft could be limited by landing distance rather than takeoff distance; such a limitation could complicate the determination of landing field length and lead to a complexity similar to that for determining takeoff field length for conventional transports.

CONCLUDING REMARKS

The need for flight examination of these proposed criteria is fully recognized. Ames is in the midst of a 50-hr flight program using the Augmentor Wing Research Aircraft (AWRA). This work is directed toward verification and refinement of the tentative criteria, and is planned for completion next year. It is hoped that this process of refinement can be continued by selected experiments using other powered-lift aircraft, and that the design implications of the criteria can be more thoroughly explored.

REFERENCES

1. Stapleford, R. L.; Heffley, R. K.; Rumold, R. C.; Hynes, C. S.; and Scott,
    B. C.: A STOL Airworthiness Investigation Using a Simulation of a
    Deflected Slipstream Transport. Vol. I, Summary of Results and
    Airworthiness Implications. STI TR 1014-3, FAA-RD-74-143-I, NASA
    TM X-62,392, 1974.

2. Stapleford, R. L.; Heffley, R. K.; Jewell, W. F.; Lehman, J. M.; Hynes,
    C. S.; and Scott, B. C.: A STOL Airworthiness Investigation Using a
    Simulation of a Deflected Slipstream Transport. Vol. II, Simulation
    Data and Analysis. STI TR 1014-3, FAA-RD-74-143-II, NASA TM X-62,393,
    1974.

3. Heffley, R. K.; Jewell, W. F.; Stapleford, R. L.; Craig, S. J.;
    Hynes, C. S.; and Scott, B. C.: A STOL Airworthiness Investigation
    Using a Simulation of a Deflected Slipstream Transport. Vol. III,
    Breguet 941S Simulation Model. STI TR 1014-3, FAA-RD-74-143-III,
    NASA TM X-62,394, 1974.

4. Stapleford, R. L.; Heffley, R. K.; Hynes, C. S.; and Scott, B. C.: A
    STOL Airworthiness Investigation Using a Simulation of an Augmentor
    Wing Transport. Vol. I, Summary of Results and Airworthiness Implica-
    tions. STI TR 1047-1, FAA-RD-74-179-I, NASA TM X-62,395, 1974.

5. Heffley, R. K.; Stapleford, R. L.; Rumold, R. C.; Lehman, J. M.;
    Hynes, C. S.; and Scott, B. C.: A STOL Airworthiness Investigation
    Using a Simulation of an Augmentor Wing Transport. Vol. II, Simulation
    Data and Analysis. STI TR 1047-1, FAA RD-74-179-II, NASA TM X-62,396,
    1974.

6. Rumold, R. C.; Stapleford, R. L.; Hynes, C. S.; and Scott, B. C.: A STOL
    Airworthiness Investigation Using Simulation of Representative STOL
    Aircraft. STI TR 1047-2, FAA RD-75-197, NASA TM X-62,498, 1975.

7. Innis, R. C.; Holzhauser, C. A.; and Quigley, H. C.: Airworthiness
    Considerations for STOL Aircraft. NASA TN D-5594, 1970.

8. Heffley, R. K.; Lehman, J. M.; Rumold, R. C.; Stapleford, R. L.; Scott,
    B. C.; and Hynes, C. S.: A Simulator Evaluation of Tentative STOL
    Airworthiness Criteria. Vol. I, Simulation Results and Analysis.
    STI-TR-1047-3, FAA-RD-75-222, NASA TM X-73,093, 1975.

9. Heffley, R. K.; Lehman, J. M.; Rumold, R. C.; Stapleford, R. L.; Scott,
    B. C.; and Hynes, C. S.: A Simulator Evaluation of Tentative STOL
    Airworthiness Criteria. Vol. II, Background Information, STI TR 1047-3,
    FAA RD-75-222, NASA TM X-73,094, 1975.

10. Hynes, C. S., Scott, B. C.; Martin, P. W.; and Bryder, R. B.: Progress
    Toward Development of Civil Airworthiness Criteria for Powered-Lift
    Aircraft, NASA TM X-73,124, FAA-RD-76-100, 1976.
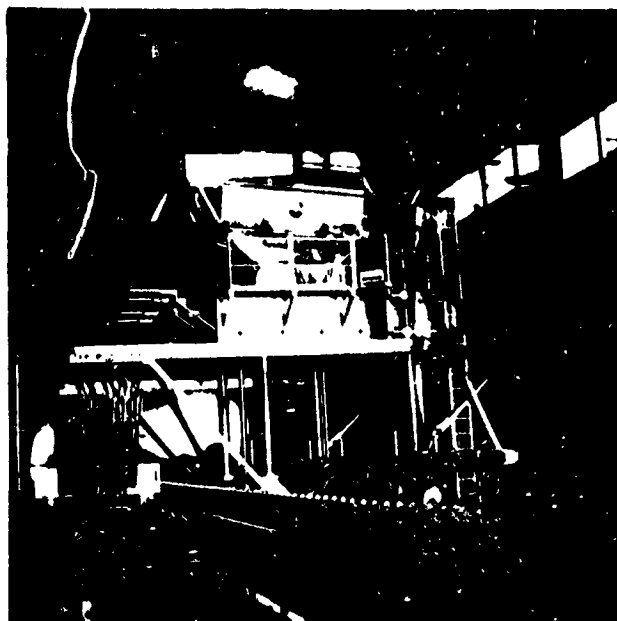
Figure 1.- Flight Simulator for
Advanced Aircraft.

AERODYNAMIC
CHARACTERISTICS

ULTIMATE FLIGHT
ENVELOPE
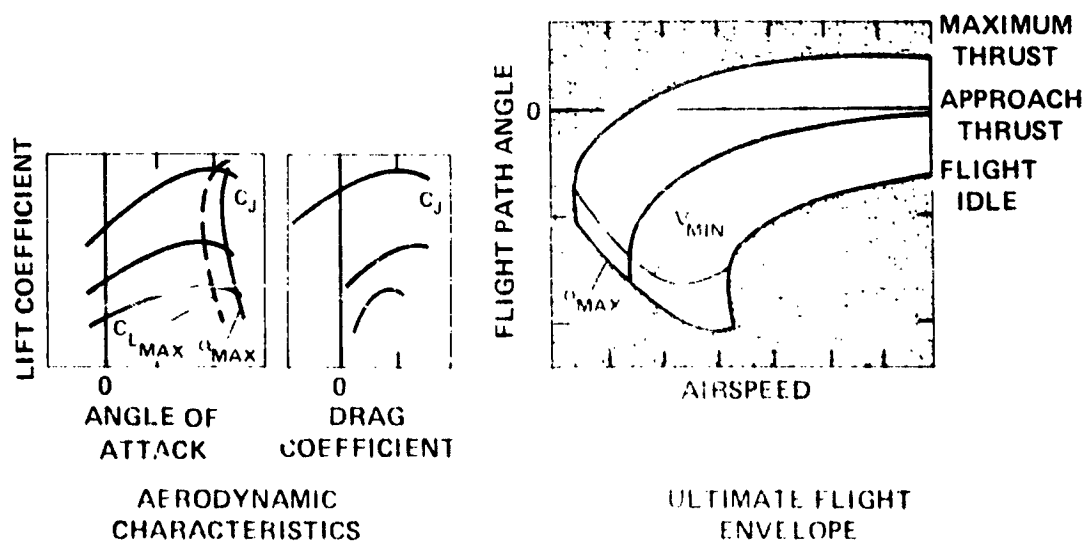
Figure 2.- Aerodynamic characteristics and flight envelope
of powered-lift transports in approach configuration.

$$\Delta \alpha = \sin^{-1} \frac{20}{V_{kt}}$$
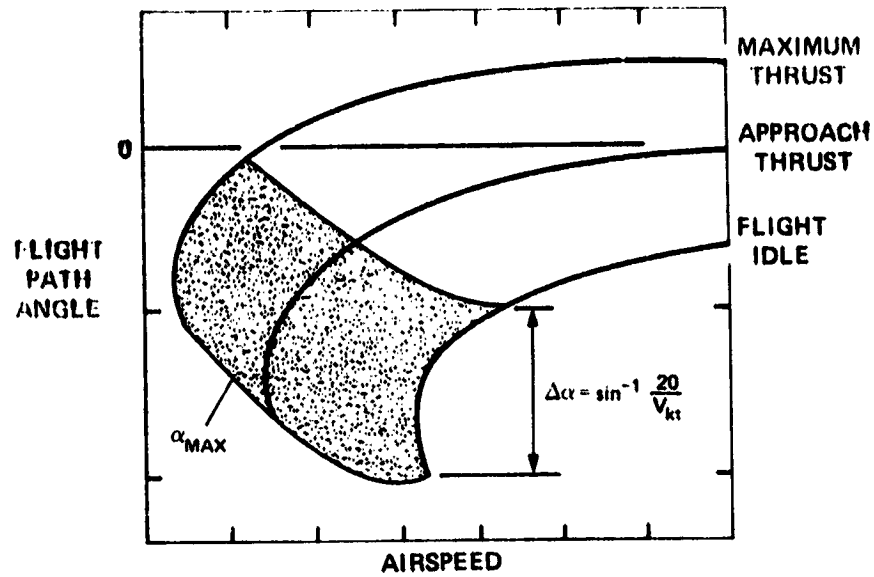
Figure 3.- Proposed angle of attack margin criterion:
all engines operating.
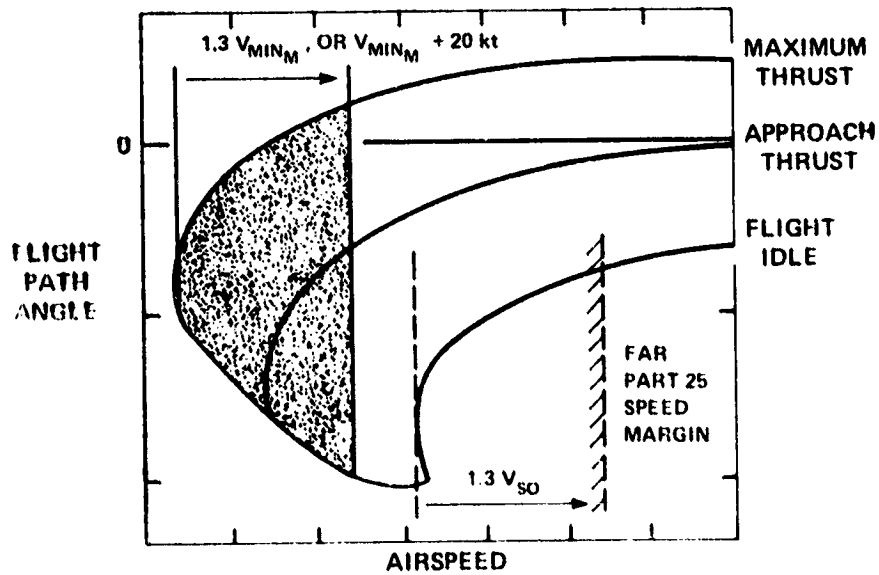
Figure 4.- Proposed speed margin criterion, maximum thrust:
all engines operating.
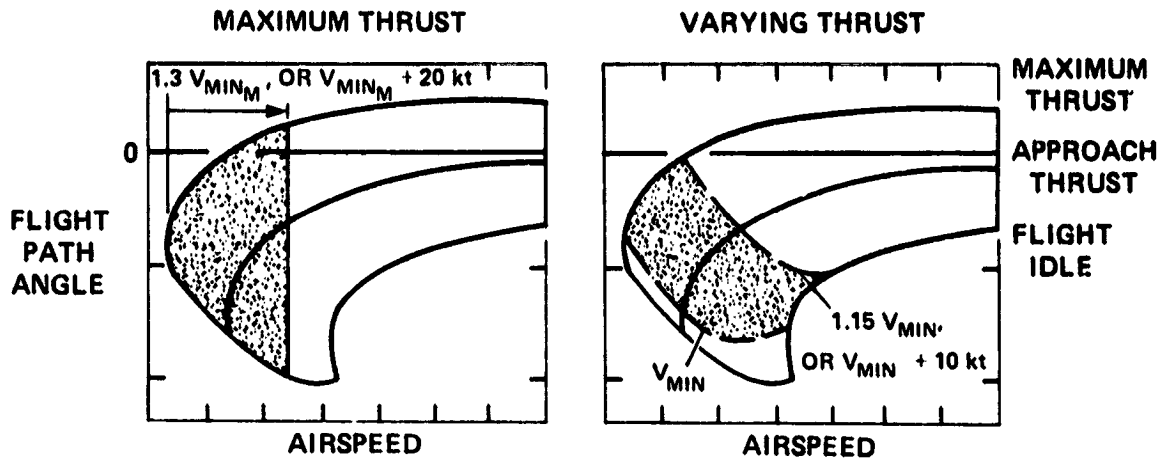
Figure 5.- Proposed speed margin criteria: all engines operating.
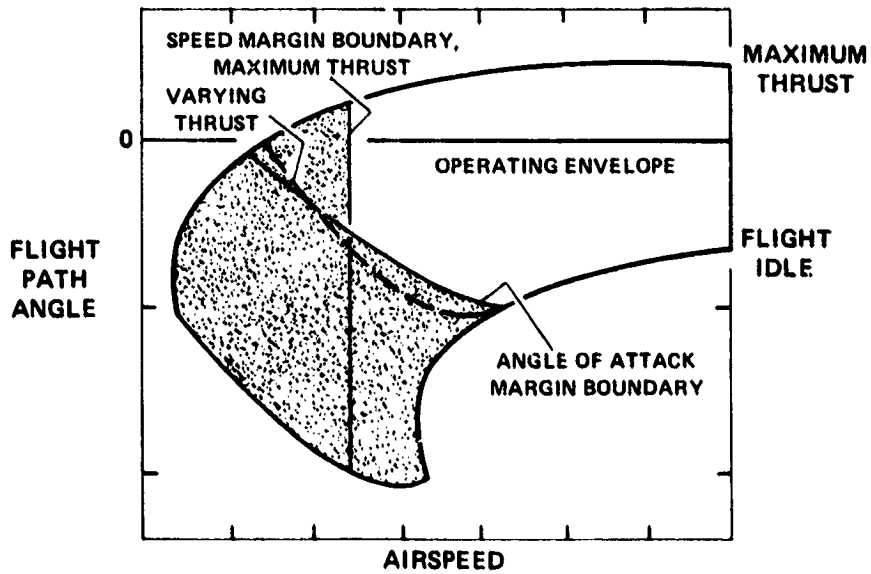
Figure 6.- Operating envelope limited by proposed margin criteria: all engines operating.

176
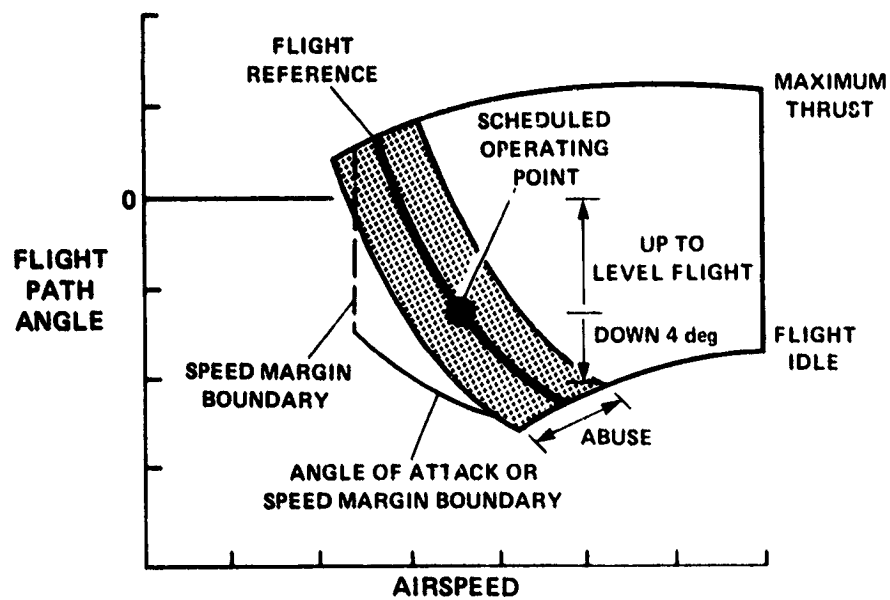
Figure 7.- Proposed criteria for flight path capability:
all engines operating.

ACCIDENT INVESTIGATION - ANALYSIS OF AIRCRAFT MOTIONS

FROM ATC RADAR RECORDINGS

N78-18091

Rodney C. Wingrove

NASA Ames Research Center

SUMMARY

Ames Research Center, in cooperation with the National Transportation Safety Board, has developed a technique for deriving time histories of an aircraft's motion from Air Traffic Control (ATC) radar records. This technique uses the radar range and azimuth data, along with the downlinked altitude data (from an onboard Mode-C transponder), to derive an expanded set of data which includes airspeed, lift, thrust-drag, attitude angles (pitch, roll, and heading), etc. This technique of analyzing aircraft motions was recently evaluated through flight experiments which used the CV-990 research aircraft and recordings from both the enroute and terminal ATC radar systems. The results indicate that the values derived from the ATC radar records are for the most part in good agreement with the corresponding values obtained from airborne measurements. In an actual accident, this analysis of ATC radar records can provide an important source of data, both to complement the flight-data recorders, now onboard airliners, and to provide a source of recorded information for other types of aircraft that are equipped with Mode-C transponders but not with onboard recorders. The number of aircraft with Mode-C transponders is expected to grow to between 70 and 80 percent of the total United States aircraft fleet (civilian, commercial, and military) in the next few years, implying increased capabilities for the use of this analysis technique.

INTRODUCTION

A valuable source of information for use in analyzing aircraft accidents has been the flight-data recorder, introduced in 1958, onboard United States air carriers. More recently, an additional source of recorded data has become available to the investigator through the introduction of radar recording capabilities at many of the ATC centers (ref. 1). These ATC recordings have proven useful, not only as an additional data source in the investigation of airline accidents (refs. 1 to 3), but also, and possibly of more importance, they can provide information for the analysis of accidents involving aircraft which do not have onboard data recorders (e.g., military, short-haul, and general aviation).

Considering the current and future potential for the use of ATC radar recordings in accident investigation, Ames Research Center (with cooperation from the National Transportation Safety Board, Bureau of Aviation Safety, and

PRECEDING PAGE BLANK NOT FILMED

Federal Aviation Agency Field Centers) has initiated a research program to investigate advanced methods for the analysis of this recorded data. The National Transportation Safety Board and the airline industry have previously developed methods to determine some of the basic aircraft quantities, such as position and velocity (ref. 1). The work at Ames Research Center has been aimed primarily at deriving an expanded set of data which includes both the short-period quantities (forces and attitude angles) as well as the long-period quantities (position and velocity).

This paper reviews the analysis techniques which have been developed and illustrates their application to CV-990 experimental flight test data. An example is also included to illustrate their application to actual accident recordings. The current limitations and future potential for the use of ATC recordings in accident investigation are discussed.

ATC RADAR RECORDINGS

ATC radar records can be analyzed in various ways to aid an accident investigation. For example, radar records can be used to derive a time-history reconstruction of the aircraft position with respect to the airways, landing fields, ground obstructions, and other aircraft. In this report, radar position data, along with the altitude data (from an onboard Mode-C transponder), are used to provide a time-history reconstruction of the aircraft dynamic motions. These derived motion data can be used to complement the flight-data recordings onboard airliners and provide a source of recorded information for other aircraft that are equipped with Mode-C transponders[1] (fig. 1) but not with flight recorders.

Current ATC radar systems use transponder beacon replies as a means of determining the position for each target aircraft under surveillance. The transponder replies are resolved into range and azimuth at each radar site. For those aircraft equipped with Mode-C transponders, pressure altitude is also transmitted to the ground. These raw data are transformed into space coordinates (x, y, h) at intervals corresponding to the radar antenna rotational rate, nominally a 5- to 12-sec interval, depending upon the type of radar system.

There are primarily two types of ATC radar systems (fig. 2) that can record these raw data. The Automated Radar Terminal System (ARTS III), located at 61 of the major terminals, provides recorded radar data at intervals of about 5 sec. The National Airspace System (NAS Stage A), located at the 20 enroute centers, provides recorded radar data at intervals of about 12 sec. The following analysis techniques, and later examples, consider data from both these systems.

---

[1]For aircraft not equipped with Mode-C, only x, y radar data are available, thus limiting the effectiveness of the three-dimensional motion analysis reported herein.

180

ANALYSIS METHOD

The technique used to determine the aircraft motions involves smoothing of the raw radar data. These smoothed results, in combination with other available information (wind profiles and aircraft performance data), are used to derive the expanded set of data (fig. 3).

Several types of smoothing techniques (e.g., least squares, Kalman filter/smoothers, etc.) are currently under evaluation at Ames. The smoothing technique used for the results in this report is based on a cubic least-square fit to the recorded raw data (ref. 4). This moving-arc procedure provides a smoothed time history of the aircraft position (x, y, h), the inertial velocities $(\dot{x}, \dot{y}, \dot{h})$ and accelerations $(\ddot{x}, \ddot{y}, \ddot{h})$. A transformation of the inertial velocities provides a direct calculation of the ground speed, the track angle, and the flight-path angle. Using the known winds (usually recorded twice a day at local weather stations), these inertial data are transformed to the aircraft stability axes to provide true airspeed, the component of force along the airspeed vector (thrust-drag), the component of force normal to the airspeed vector (lift), and the orientation of the total force vector (roll angle). The derived quantities which have been discussed so far are aircraft independent. Further derivations, based on aircraft dependent performance data, can determine the aircraft angle of attack, which is used in a transformation from the stability axes to derive the pitch and heading angles.

Thus, time histories can be derived of altitude, airspeed, attitude angles (pitch, roll, and heading), and acceleration forces (lift, thrust-drag). The accuracy of the derived information, however, will depend on several factors, such as the aircraft speed, the type of maneuvers being performed, the distance from the radar site, wind uncertainties, aircraft performance uncertainties, etc. The following examples illustrate the accuracy of the technique.

CV-990 FLIGHT-TEST EXPERIMENTS

In these experiments (fig. 4), the quantities derived from ATC radar records are compared with the actual values measured by the instrumentation system onboard the CV-990 aircraft. Figures 5 and 6 show representative comparisons of the radar-derived data (dotted lines) with the corresponding onboard measurements (solid lines). Measurements included air data (altitude and airspeed), accelerometer (lift and thrust-drag) and inertial platform (pitch, roll, and heading angles) time histories.

The experimental results presented in figure 5 were derived from ARTS III radar records obtained during CV-990 flight operations at the Los Angeles terminal. These records include a landing approach to about 60 m above the runway, followed by a go-around and a 180° turn. These radar data were recorded once each 4.7 sec.

The experimental results in figure 6 were derived from NAS Stage A (Oakland Center) radar records of the CV-990 descending into the Stockton, California

airport. These records, obtained during normal flight operations, begin from a cruise condition at an altitude of about 10 km, followed by routine trim changes and descending turns down to an altitude of about 3 km. These radar data were recorded once each 12 sec.

The accuracy of the quantities derived from both radar systems have the same general trends. There is poor accuracy in some of the quantities derived during rapid orientation changes of the aircraft; however, there is relatively good accuracy in most of the quantities derived during the steadier portions of flight.

The errors that occur during rapid orientation change are found primarily in the values of lift, pitch, and roll angle. Rapid changes in these variables can go undetected because of the large time span (4.7 to 12 sec) between the radar records.

During the steadier portion of the flight (e.g., steady turns, ascent, descent, etc.), most of the derived data are obtained with remarkably good accuracy. These radar-derived data are generally of sufficient accuracy to provide important information in the analysis of aircraft accidents. One representative application in an accident analysis is illustrated next.

APPLICATION WITH ACTUAL ACCIDENT RECORDS

This example is based on ATC radar data available from an airliner accident near Thiells, New York, on December 1, 1974. This aircraft, on a climbout from JFK, stalled at an altitude of about 8 km and entered an uncontrolled, spiralling descent into the ground. The stall was precipitated by an erroneous airspeed indication which had resulted from blockage of the pitot heads by atmospheric icing (ref. 5).

Radar data were available during the climbout, stall, and the initial portion of the uncontrolled, spiralling descent. Only limited radar data were available during the later stages of descent, below about 6 km, because of intermittent transponder returns. A derived time history of the aircraft motions is presented in figure 7 (dotted lines). Also shown for comparison are the four quantities (altitude, airspeed, normal force, and heading) available from the onboard foil-type flight recorder.

The comparison of the radar-derived airspeed with the onboard airspeed measurement clearly shows the time at which the pitot head became blocked with ice. Beyond that time, the radar-derived data indicate a decreasing airspeed that reached a minimum near the stall and then increased during the descent. The values of normal force derived from the radar data generally agree with the onboard measurement, except that the radar data cannot reproduce the short-term peak excursions which are actually experienced by the aircraft. The values of pitch angle derived from the radar data indicate a maximum angle of about 27° during stall, followed by values as steep as -25° during the initial portion of descent. The values of roll and heading angles derived from the radar data

182

indicate the point at which wing drop occurred and the aircraft started into the spiralling descent.

CURRENT LIMITATIONS AND FUTURE TRENDS

The preceding examples (figs. 5 to 7) have illustrated the capability of deriving time histories of the aircraft motions from ATC radar recordings. However, the experience gained through analyzing the CV-990 data and through applications to accident investigations indicates certain limitations in the use of ATC radar recordings for the analysis of aircraft dynamics. As noted earlier, the slow data rate from radar recordings precludes the determination of rapid orientation changes of the aircraft. Radar data also may have voids (no transponder returns) during some extreme, uncontrolled maneuvers, such as spiralling descents. Also, current ATC radar recordings do not provide coverage of all aircraft operations. For instance, radar coverage generally does not extend to the ground level (for ground roll, liftoff, touchdown, etc.) and may not be available in remote areas.

In spite of these limitations, ATC radar records can provide an important source of data, both to complement the flight-data recorders onboard airliners and to provide a source of recorded information for other types of aircraft not equipped with onboard recorders. At the present time, only about 1.5 percent of the total aircraft in the United States have onboard flight-data recorders; whereas, about 30 percent have Mode-C transponders. The number of aircraft with Mode-C transponders is expected to grow to between 70 and 80 percent of the total aircraft fleet in the next few years (ref. 6). Because of this rapidly increasing number of aircraft with Mode-C transponders (fig. 1), the number of flight operations which can be analyzed by ATC recordings is steadily growing.

A look into the future also indicates that several features of the Upgraded Third Generation ATC System (refs. 6 to 8), which is now undergoing evaluation by the Federal Aviation Agency, may ease some of the limitations noted above and could provide additional sources of data for use in accident investigations (fig. 8). For instance, the advanced transponders could provide increased accuracy and increase the number of downlinked quantities. The proposed terminal surveillance systems could extend coverage to the ground and provide increased accuracy and higher data rates. The proposed space satellite ATC systems could provide coverage over the ocean and eventually provide worldwide coverage. These future trends of increased coverage, better accuracy, higher data rates, and an increased number of downlinked quantities, along with the growing number of aircraft with transponders, imply increasing capabilities for the use of ATC records in accident investigation.

CONCLUDING REMARKS

This paper has presented some results based on a technique for deriving time histories of additional aircraft states from ATC radar records of x and y position and altitude. This technique smooths the raw radar data and, using

183

other available information (wind profiles and aircraft performance), derives an expanded set of data which includes airspeed, lift, thrust-drag, pitch, roll, and heading angles, etc.

Applications in this paper illustrate that the largest errors in the derived data occur during rapid orientation changes of the aircraft. For the steadier portions of flight (ascent, descent, turns, etc.) the derived quantities are generally of sufficient accuracy to provide important information in the analysis of aircraft accidents.

REFERENCES

1. Miller, C. O.; and Laynor, W. G.: Use of ARTS-III in Aircraft Accident Investigation. Presented at Air Traffic Control Association Annual Meeting, Miami, Florida, Oct. 16, 1973.

2. Anderson, C. M.: Civil Aircraft Accident Analysis in the United States. Presented at AGARD Symposium on Aircraft Operational Experience and Its Impact on Safety and Surveilability, Sadefjord, Norway, May 31-June 3, 1976.

3. Aircraft Accident Report - UAL at Midway Airport, Chicago, Illinois, Dec. 8, 1972. NTSB-AAR-73-16, Aug. 29, 1973.

4. Handbook of Data Reduction Methods. White Sands Technical Report, Aug. 1964.

5. Aircraft Accident Report - Northwest Airlines Near Thiells, New York, Dec. 7, 1974. NTSB-AAR-75-13, Aug. 13, 1975.

6. Hoffman, W. C.; and Hollister, W. M.: Forecast of the General Aviation Air Traffic Control Environment for the 1980's. NASA CR-137909, 1976.

7. An Overview and Assessment of Plans and Programs for the Development of the Upgraded Third Generation Air Traffic Control System. FAA-EM-75-5, March 1975.

8. Plans and Developments for Air Traffic Systems. AGARD CP-188, Feb. 1976.
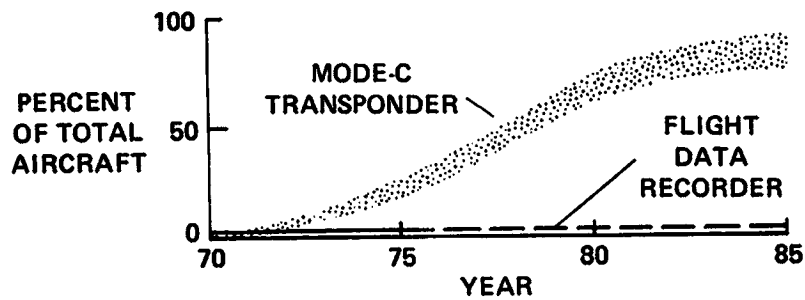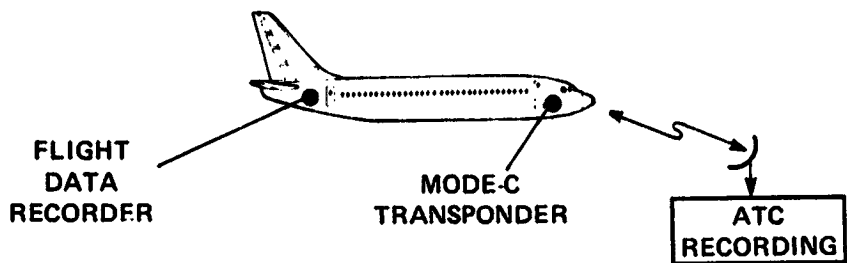
Figure 1.- Two sources of accident recordings.

	ENROUTE	TERMINAL
COVERAGE	CONTINENTAL USA	61 MAJOR AIRPORTS
RADAR SYSTEM	NAS STAGE A	ARTS III
TIME BETWEEN DATA POINTS	$\approx$ 12 sec	$\approx$ 5 sec

Figure 2.- ATC radar recording capabilities.
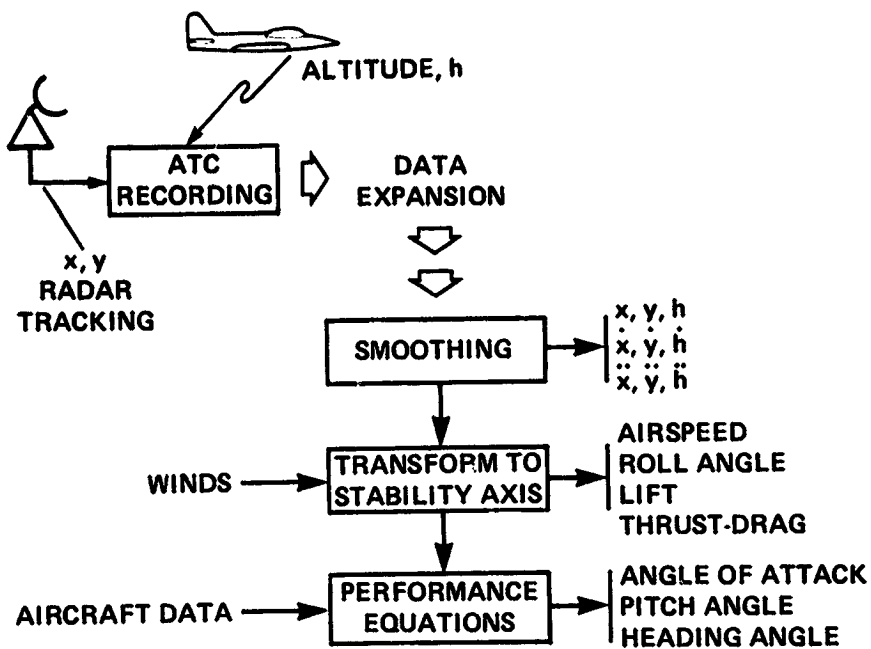
Figure 3.- Data expansion from ATC radar recordings.
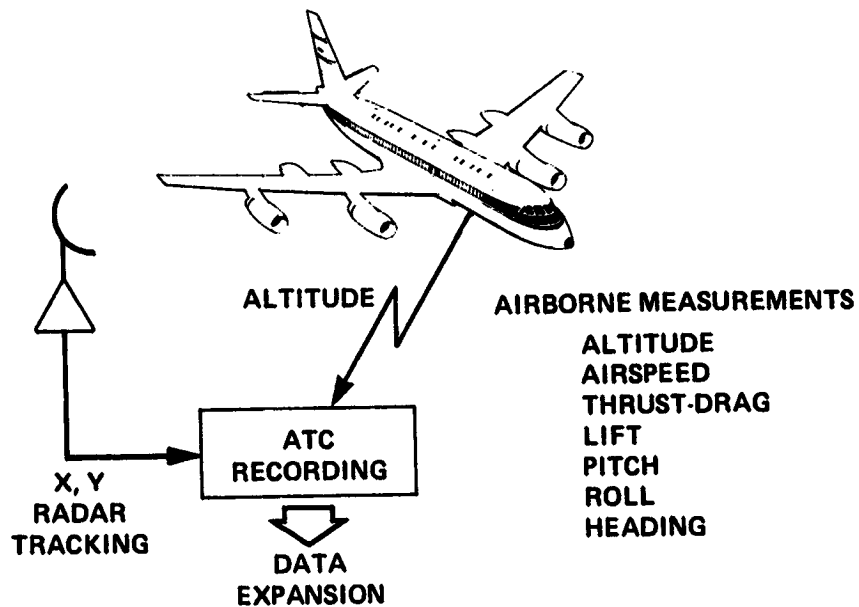
Figure 4.- Evaluation of radar derived data using CV-990 measurements
as a standard for comparison.

186
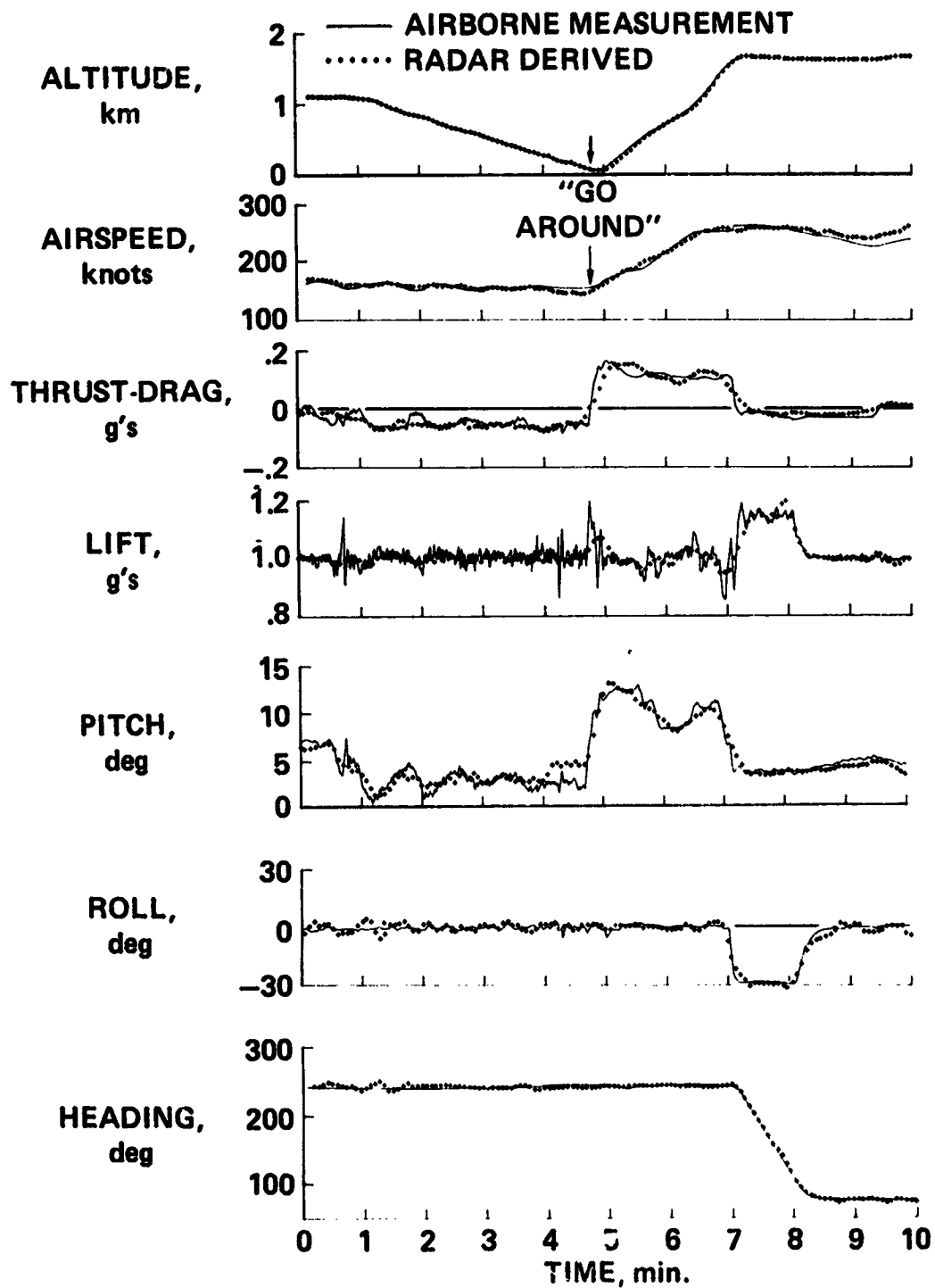
Figure 5.- ARTS III radar derived data compared with CV-990 measurements.
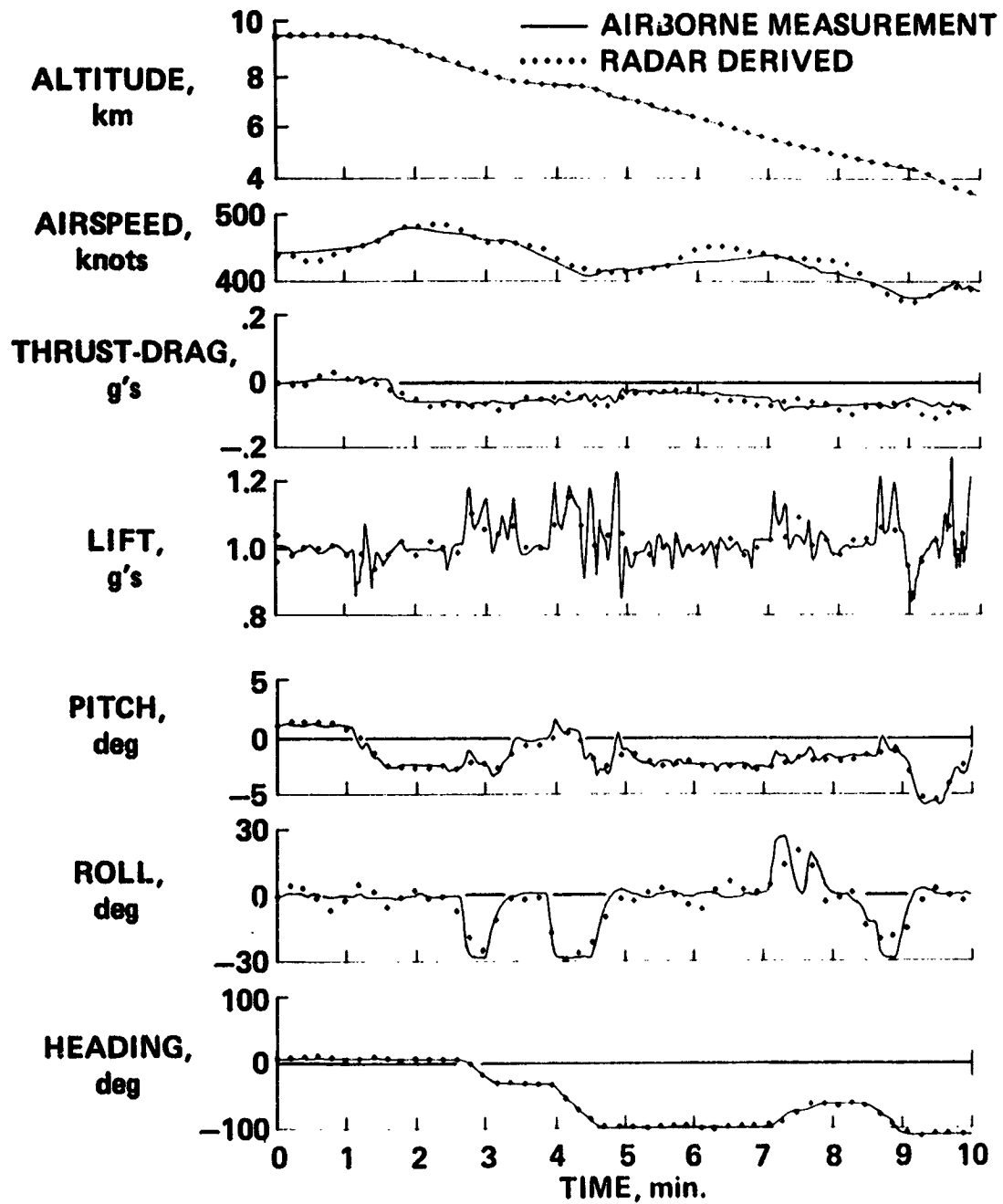
Figure 6.- NAS Stage A radar derived data compared with CV-990 measurements.
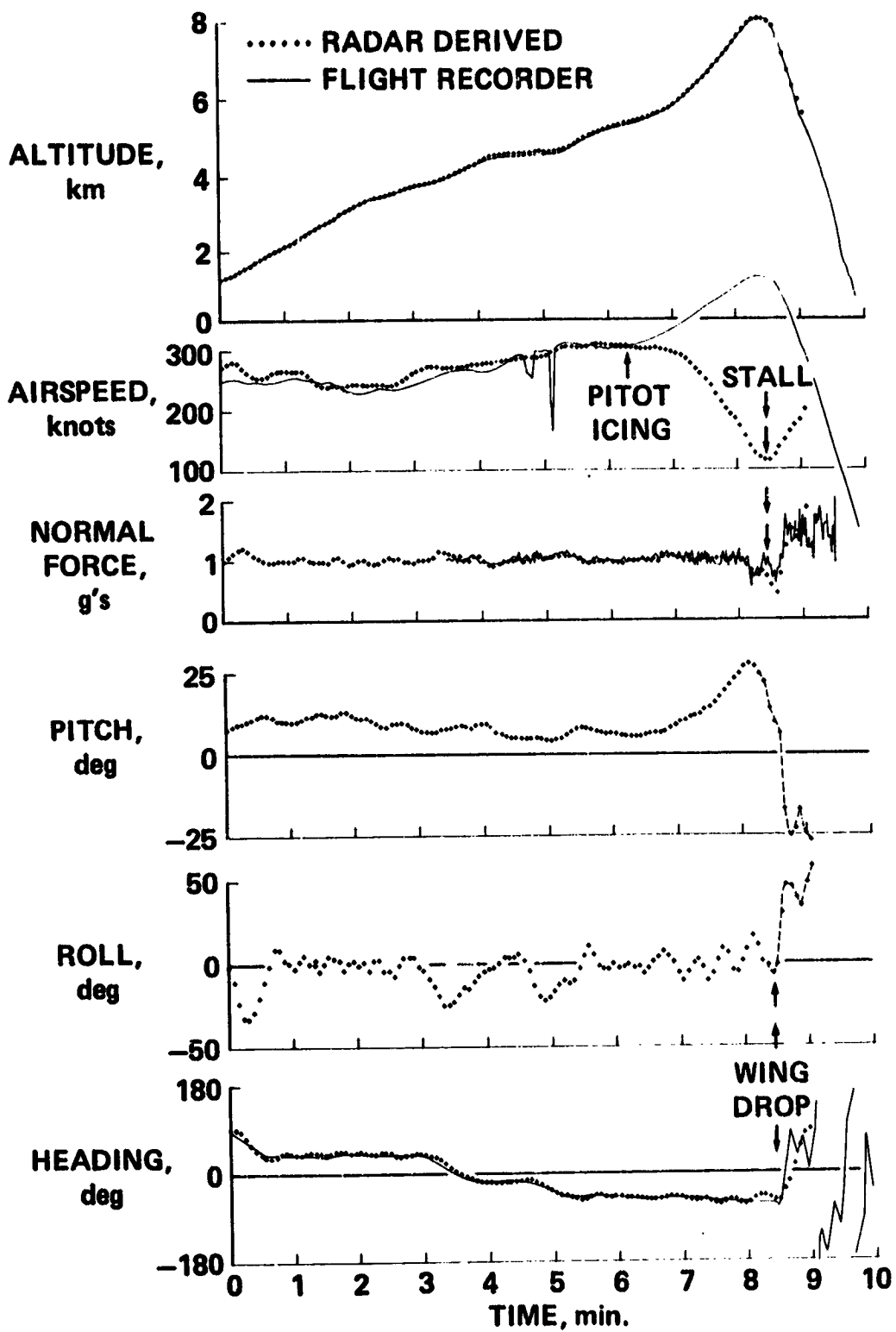
Figure 7.- Data from actual accident.

UPGRADED 3RD GENERATION ATC SYSTEM ELEMENTS	INCREASED CAPABILITIES FOR ACCIDENT INVESTIGATION			
	COVERAGE	ACCURACY	DATA RATE	DOWN LINKS
DISCRETE ADDRESS BEACON SYSTEM		X		X
UPGRADED ATC AUTOMATION	X			
AIRPORT SURFACE TRAFFIC CONTROL	X	X	X	
AERONAUTICAL SATELLITES	X			X

Figure 8.- Future trend in ATC systems.

STATUS OF RUNWAY SLIPPERINESS RESEARCH

Walter B. Horne
NASA Langley Research Center

SUMMARY

Runway slipperiness research performed in the United States and Europe since 1968 has been reviewed. This review suggests the following benefits to the aviation community: Better understanding of the hydroplaning phenomena; a method for predicting aircraft tire performance on wet runways from a ground-vehicle braking test; runway rubber deposits identified as a serious threat to aircraft operational safety; methods developed for removing rubber deposits and restoring runway traction to uncontaminated surface levels; and developed antihydroplaning runway surfaces, such as pavement grooving and porous friction course, which considerably reduce the possibility of encountering aircraft hydroplaning during landings in rainstorms.

INTRODUCTION

Extensive research has been performed in the United States and Europe since 1968 in an effort to combat problems relative to aircraft operations on slippery runways. This research has led to a more complete understanding of the sources of these operating problems and, as a result, improved methods are being introduced to control or alleviate these problems. The purpose of this paper is to review the present status of runway slipperiness research in the following areas of interest:

(1) Runway flooding during rainstorms

(2) Hydroplaning

(3) Identification of slippery runways including the results from ground vehicle friction measurements and attempts to correlate these measurements with aircraft stopping performance

(4) Progress and problems associated with the development of antihydroplaning runway surface treatments such as pavement grooving and porous friction course (PFC)

(5) Runway rubber deposits and their removal

191

RUNWAY FLOODING DURING RAINSTORMS

During 1971, the Texas Transportation Institute (TTI), Texas A&M University, published the results of a comprehensive study on the effects of rainfall intensity, pavement cross slope, surface texture, and drainage length on pavement water depths (ref. 1). From the TTI study, an equation can be derived to predict the rainfall intensity required to initiate flooding in aircraft tire paths on the runway as follows:

For SI Units:

$$I_F = 1.253 \times 10^3 \left[\frac{T^{.89}}{L^{.43}(1/S)^{.42}} \right]^{1.695} \tag{1a}$$

For U.S. Customary Units:

$$I_F = 1.543 \times 10^4 \left[\frac{T^{.89}}{L^{.43}(1/S)^{.42}} \right]^{1.695} \tag{1b}$$

where

I_F rain rate required to initiate runway flooding in tire path, mm/hr (in/hr)

T pavement surface texture depth (ATD), mm (in.)

L tire path distance from runway crown, m (ft)

S runway cross slope, m/m (ft/ft)

It should be noted that equations (1) are derived from data obtained on ungrooved pavements and from pavements that have not been treated with a porous friction course. Figure 1 illustrates how equations (1) can be used to predict whether a flooded runway condition will exist for a typical jet transport landing on the runway center line during a rainstorm. The trends shown in figure 1 suggest that a pavement must be provided with a good cross slope and a good surface texture to minimize the risk of runway flooding and dynamic hydroplaning occurring to aircraft during take-off and landing in rainstorms.

Effect of Surface Winds on Drainage

Surface winds, when present on runways, can appreciably affect runway drainage by changing the direction of water flow off the side of the runway which tends to increase the drainage path length and increase runway water depths. Observations of water drainage from a number of runways using a dye test (sodium

192

fluorescein dye injected into draining water on the runway to improve flow visualization) suggest that surface winds do not appreciably affect water drainage from runways as long as the draining water is flowing below the top of the pavement texture. Surface winds do affect water drainage from runways when flooded conditions exist and the water is flowing as a sheet above the top of the pavement texture. In the latter case, the water drainage-path angle with respect to the runway center line is determined from the vector sum of the wind and gravitational forces acting on the water. Typical examples of this behavior are shown in figure 2 (ref. 2) where the water drainage patterns (from a dye test) obtained on a conventional burlap drag and a wire-combed (plastic grooved) concrete runway surfaces during artificial wetting tests performed in a 10-knot surface wind are compared. The average texture depth (ATD) of the ungrooved burlap drag surface was 0.28 mm (0.011 in.) as measured by the NASA grease test. This texture depth was insufficient to prevent surface flooding under the artificial wetting conditions, and the water drainage path direction was rotated toward the runway center line by the action of the surface wind. Under the same surface wetting and wind condition, the grooved concrete surface with an ATD of 0.81 mm (0.032 in.) allowed most of the draining water to flow below the top of the surface texture (unaffected by wind). As a consequence, the water drainage path on this surface was nearly inline with the transverse grooves and the runway cross slope.

Flooding on Grooved Runways

NASA has constructed a concrete runway 4372 m (15 000 ft) long and 91 m (300 ft) wide at the Kennedy Space Center (KSC) for the space shuttle. (See fig. 3.) A longitudinal broom surfacing treatment was given the fresh concrete as it was paved by a slip-form paver (fig. 4). The concrete runway surface several months after paving was grooved by diamond saws to a transverse $29 \times 6 \times 6$ mm ($1\frac{1}{8} \times \frac{1}{4} \times \frac{1}{4}$ in.) pattern with the resulting surface texture shown in figures 5 and 6. The Langley Research Center (LaRC) performed drainage and traction studies on the space shuttle runway in June 1976.

On June 20, 1976, the Cape Canaveral area was subjected to a series of thunderstorms during which heavy rain fell on the shuttle runway. Figure 7 shows the rain rates and surface flooding that occurred on the shuttle runway during a 30-minute period as one of the thunderstorms passed over the runway. The space shuttle runway is oriented in a north/south direction; a wind of approximately 10 knots magnitude from the southwest was observed during the storm. For this wind condition, the data in figure 7 show that a rain rate of approximately 81 mm/hr (3.2 in/hr) is required to start runway flooding in the shuttle main gear tire paths (landing on runway center line).

The predicted rain rate (from eqs. (1)) required to flood the runway in the shuttle main tire path is 47.1 mm/hr (1.85 in/hr). This difference between observed (81 mm/hr (3.2 in/hr)) and estimated (47.1 mm/hr (1.85 in/hr)) rain rates gives added weight to features long observed on runways grooved with a diamond saw technique; that is, the polished groove channels (from the diamond saw cuts) greatly reduce water flow resistance over water draining through and over the comparatively much rougher texture of conventional surface treatments.

In addition, the draining water is forced by the groove channels to take the shortest drainage path (down the grooves) off the runway edge even on runways with longitudinal slope. As a consequence, water drainage from runways grooved with the diamond saw technique is greatly increased over ungrooved runway surfaces. (See fig. 8.) It is believed that plastic grooving techniques are not as effective as the sawed groove technique for water drainage because the grooves can be interrupted or misalined at paving lane edges and the groove channels have rougher wall surfaces.

Flooding on Porous Friction Course Runways

Water drainage from the porous friction course (PFC) runway at Farnborough, England, was personally observed during a heavy rain in 1965 and the runway did not flood while adjacent conventional surfaces did. Most PFC surfaces are 19 mm (3/4 in.) thick and have void ratios ranging between 0.1 and 0.15, which give this surface treatment a high water storage capacity before the surface floods. However, water drainage over and through this surface treatment is interstitial with many abrupt flow direction changes as well as rough flow surfaces. Consequently, the drainage-path lengths will be longer for a PFC surface than for a grooved surface, especially on runways with longitudinal slope. For these reasons, it is believed, but not yet substantiated, that PFC surfaces will not drain water from runways as effectively as grooved surfaces (diamond saws) during prolonged rainfalls having high rainfall rates.

HYDROPLANING

The three presently known types of hydroplaning were first defined in reference 2, that is, dynamic, viscous, and "reverted" rubber hydroplaning. Continuing research on hydroplaning since that time has in general supported the conclusions reached in reference 2. However, this later research has shown new aspects of hydroplaning that are significant and of importance to describe.

Wheel Spin-Up Speed

Early (1960) NASA track hydroplaning research was conducted by rolling full-size unbraked aircraft tires across dry and flooded runway sections. The aircraft tire spun up at touchdown on the dry pavement and then entered the flooded runway section at synchronous runway wheel speed and subsequently spun down or stopped completely when the carriage speed equaled or exceeded the tire hydroplaning speed. This type of test defined the well-known tire hydroplaning speed equation (ref. 3), which is given as follows:

For SI Units:

$$\left(V_P\right)_{\text{spin-down}} \approx 3.43 \sqrt{p} \tag{2a}$$

194

For U.S. Customary Units:

$$\left(V_P\right)_{\text{spin-down}} \approx 9\sqrt{p} \tag{2b}$$

where

$\left(V_P\right)_{\text{spin-down}}$ tire spin-down hydroplaning speed, knots

p tire inflation pressure, kPa (lb/in^2)

Since 1960, the aircraft industry has used this equation to define the hydroplaning speed for particular aircraft and aircraft flight manuals. Starting in 1970, investigation of aircraft hydroplaning accidents suggested that the spin-up hydroplaning speed for a nonrotating aircraft tire (as at aircraft touchdown) might be lower in magnitude than the speed predicted by equations (2) for a rolling unbraked tire. (See refs. 4 and 5.) As a consequence, references 6 and 7 defined the tire wheel spin-up hydroplaning speed on flooded runways as

For SI Units:

$$\left(V_P\right)_{\text{spin-up}} \approx 2.93\sqrt{p} \tag{3a}$$

For U.S. Customary Units:

$$\left(V_P\right)_{\text{spin-up}} \approx 7.7\sqrt{p} \tag{3b}$$

where

$\left(V_P\right)_{\text{spin-up}}$ tire spin-up hydroplaning speed, knots

p tire inflation pressure, kPa (lb/in^2)

Additional verification of this new hydroplaning equation (eqs. (3)) is given in reference 8 and shown in figure 9. It is important that aircraft flight-manual hydroplaning speeds be changed to reflect the values given by equations (3) since this hydroplaning speed represents the actual tire situation for aircraft touchdown on flooded runways.

Reverted Rubber Hydroplaning

Reverted rubber hydroplaning was first recognized and defined from friction data produced at the Langley landing-loads track (ref. 2), now called the

195

Langley aircraft landing loads and traction facility, and from investigation of NTSB (National Transportation Safety Board) aircraft skidding accident reports prior to 1965. (Data from the Langley landing-loads track or the Langley aircraft landing loads and traction facility are herein after designated "NASA track data," and the facility is designated "NASA track.") Full-scale aircraft verification of the extremely low friction values encountered during reverted rubber hydroplaning did not occur until the aircraft flight test programs that are reported in references 9 to 11. These flight test programs were conducted in 1971-73. Figure 10 shows the reverted rubber skid patch developed on a B-737 tire during a landing run on the artificially wet runway at Roswell, New Mexico, after an approximately 1829-m (6000-ft) slide-out with all four main gear tires of the B-737 in a locked-wheel condition. Figure 11 shows the comparison between the Langley friction results of 1965 and the B-727 (1971) and the B-737 (1973) full-scale braking tests. The aircraft friction data shown in this figure completely validate the 1965 NASA track data and confirm the belief that the reverted rubber skid mode is the most catastrophic for aircraft operational safety because of the low braking friction and the additional fact that tire cornering capability drops to zero when wheels are locked. (See ref. 8.)

The reverted rubber hydroplaning condition is limited to aircraft using high tire inflation pressures. This phenomenon has not been observed on ground vehicles employing low tire inflation pressures of 165 kPa (24 lb/in^2) or less when vehicle wheels are locked. Reverted rubber hydroplaning develops only when prolonged wheel lockups occur which stem from pilot/antiskid braking system inputs. Thus, the avoidance of reverted rubber hydroplaning must rest with improving pilot braking procedures and with improving locked-wheel protection circuits of aircraft antiskid braking systems. (See ref. 8.)

Combined Viscous and Dynamic Hydroplaning

Most researchers now agree that the loss of tire friction on wet or flooded pavements with speed is due to the combined effects of viscous and dynamic hydroplaning phenomena acting in the tire footprint as shown in figure 12. The tire hydroplaning model shown in this figure was first proposed by Gough in 1959 in reference 12. (See also ref. 13.) The footprint and sketch in this figure show a pneumatic rolling at medium speed across a flooded pavement. For this partial hydroplaning condition, zone 1 describes the fraction of the tire footprint that is supported by bulk water, zone 2 describes the fraction of tire footprint that is supported by a thin water film, and zone 3 describes the traction of the tire footprint that is in essentially dry contact with the peaks of the pavement surface texture. The length of zone 1 represents the time required for the rolling tire for this speed condition to expel bulk water from under the footprint; correspondingly, the length of zone 2 represents the time required for the tire to squeeze out the residual thin water film remaining under the footprint after the bulk water has been removed. Since fluids cannot develop shear forces of appreciable magnitude, it is only in zone 3 (essentially dry region) that traction forces for steering, decelerating, and accelerating a vehicle can be developed between the tire and the pavement. The ratio of the

196

dry contact area (zone 3) to the total tire footprint area (zone 1 + zone 2 + zone 3) multiplied by the friction coefficient the tire develops on a dry pavement yields the friction coefficient the tire can develop for this flooded pavement and speed condition.

As speed is increased, a point is reached where zone 3 disappears and the entire footprint is supported by either bulk water or a thin water film. This speed condition is called combined viscous and dynamic hydroplaning. As speed is further increased a point is reached where bulk water penetrates the entire tire footprint. This condition is called dynamic hydroplaning. If the runway is not flooded (no bulk water) such as on a runway covered with a heavy dew, it is possible for zone 2 to cover the entire tire footprint at speed if the pavement is very smooth. This condition is called viscous hydroplaning.

Water Pressure Propagation Under the Tire Footprint

NASA track research (ref. 2) shows that the fluid pressure developed in the bulk water (zone 1) region of the footprint follows a V^2 law and stems from fluid inertial or density properties as shown in figure 12. Correspondingly, this research shows that the fluid pressure developed in zone 2 (fig. 12) stems from fluid viscous properties; hence, the names dynamic and viscous hydroplaning are used to describe the hydroplaning phenomena.

Pavement Macro/Microtexture Effects on Hydroplaning

When flooding on a runway occurs, the pavement surface macrotexture plays the important role of providing escape channels to drain bulk water from zone 1 (fig. 12). The drainage channels are provided by the tire tread draping over the high spots (asperities) of the pavement surface texture leaving valleys between the tire tread and the low points of the surface texture through which bulk water can easily drain out from under the tire footprint. Bulk water drainage through the pavement macrotexture thus delays to much higher speeds the buildup of fluid dynamic pressure with speed found for pavements with no or poor macrotexture. This effect is illustrated in figure 12 for smooth and grooved pavements. The macrotexture of a pavement can be assessed to some degree by methods such as the NASA grease test (ref. 14), the British sand patch test (ref. 15), and the Texas Transportation Institute silicone putty test (ref. 16).

Providing the pavement with a good microtexture is the major means of combating viscous hydroplaning or preventing the development of viscous fluid pressures in zone 2 of the tire footprint. (See fig. 12.) Pavement microtexture is difficult to detect by eye but can usually be determined from touching the surface. A good pavement microtexture has a sharp-harsh-gritty feel such as obtained when touching fine sandpaper. The touch test is qualitative and not infallible and should be confirmed by ground vehicle friction tests under wet conditions. Pavement microtexture performs its function by providing the pavement surface thousands of sharp pointed projections that, when contacted by the tire tread, generate local bearing pressures of several thousand Pa (lb/in^2).

197

This intense pressure quickly breaks down the thin water film coating the pavement surface, and allows the tire to regain dry contact with the high points of the pavement surface texture.

Tire Effects on Hydroplaning

The footprint of the tire can be considered analogous to the wing on an aircraft; both are lifting surfaces, the wing to support the weight of the aircraft in flight through the atmosphere and the tire footprint to support the weight of the vehicle during hydroplaning on a wet or flooded pavement. Wings of high aspect ratio (wing length/chord length) reduce tip losses and produce the highest lift coefficient to support the aircraft in flight. Research shows the same trends for tire footprints. Smooth tread tires having high-aspect-ratio footprints (footprint width/footprint length) for similar conditions of flooded pavement, load, and inflation pressure will hydroplane at lower vehicle speeds than tires with low-aspect-ratio footprints. The aspect ratio of the tire footprint is governed by the shape of the tire cross section or the ratio of tire section height to section width (also called the tire aspect ratio).

Molding grooves (channels) in the tire tread at time of construction is the tire designers equivalent of pavement macrotexture. The tread grooves in the tire footprint are vented to atmosphere and provide escape channels for the bulk water trapped in zone 1 (fig. 12). Tread grooves thus raise the critical water depth required for a tire to suffer dynamic hydroplaning, and for water depths less than the critical depth, raise the tire hydroplaning speed. It should be noted that the benefits from grooving the tire tread decrease in proportion to tread wear (depth of groove) and vanish when the groove depth decreases to 1.6 mm (1/16 in.) or less. The tire designers equivalent of pavement microtexture is to cut or mold kerfs or sipes into the tread ribs that lie between the tread grooves. The purpose of these features is to greatly increase the number of sharp edges of tread contact with the pavement that are provided by the tread grooves. Contact of the pavement surface at these sharp cornered tread sipe and groove edges creates local bearing pressures sufficiently high to quickly breakdown and displace the thin water film (zone 2, fig. 12) that creates viscous hydroplaning.

The vertical load acting on a tire divided by the tire footprint area determines the average tire-pavement contact pressure. For smooth tread tires, this contact pressure is approximately equal or proportional to the tire inflation pressure. The difference in the pressure within and without (atmospheric pressure) the tire footprint creates forces which expel the water trapped in the tire-pavement contact zone at velocities which are proportional to the square root of the tire tread-pavement contact pressures. Thus, increasing the inflation pressure in a tire increases the rate of flow of water drainage out of the footprint and raises the tire hydroplaning speed. When grooves are cut or molded into a tire tread to form a tread pattern, the area of actual rubber contact with the pavement in the tire footprint is reduced. The result is that the contact pressures on the ribs of the tread pattern are increased which increases the rate of flow of water draining out of the footprint. This fact explains the effectiveness of tire tread patterns in improving wet traction or

198

delaying hydroplaning effects on wet or flooded pavements to higher speeds. It should be noted that while tire tread designs can reduce wet runway traction losses, the improvements obtained are relatively small in comparison to what can be obtained by providing the pavement with a good micro/macrotexture (ref. 7), and these improvements disappear when the tread becomes worn.

Tire Operating Mode Effects on Hydroplaning

The tire operating mode is controlled by the vehicle operator (pilot or driver). Depending upon the maneuver required, the vehicle tires may be undergoing free rolling, braked rolling, yawed rolling, powered rolling, a combination of braked and yawed rolling, or a combination of powered and yawed rolling. Maximum lateral or steering forces for the tire occur when the tire is neither braked nor powered (driven by the engine). Correspondingly, maximum traction for accelerating or decelerating the vehicle develops when the vehicle is moving straight ahead (unyawed) and the tires are not developing lateral forces to withstand a cross wind or to conduct a turning maneuver. If the driver applies power to the vehicle driving wheels in excess of the tire-pavement friction capability, the tire loses its grip on the pavement, and the wheel will start to spin up with respect to the pavement. The resulting relative motion between the tire and the pavement under wet conditions increases viscous-dynamic hydroplaning effects and traction for accelerating and steering the vehicle is greatly reduced. On the other hand, if the pilot or driver braking demand (brake application) exceeds the tire-pavement friction capability, the tire loses its grip with the pavement and rapidly spins down to a locked-wheel condition. This is the most hazardous tire operating mode for vehicle operational safety (refs. 7, 8, and 17) because the tire cornering capability drops to zero even on dry pavements and vehicle directional stability is greatly reduced. Research shows that on wet and flooded pavements, both viscous and dynamic fluid pressures increase in magnitude under the sliding tire footprint over those obtained for a rolling tire for the same speed condition. The result is that locked-wheel sliding or nonrotating tires have a lower hydroplaning speed than rolling tires (compare eqs. (2) and (3)). Under partial hydroplaning conditions on wet runways, the braking traction can be reduced by as much as one-third to two-thirds the maximum obtained during the braked rolling mode from this enhanced hydroplaning effect as shown in figure 11. (Compare μ_{max} with μ_{skid} for normal rubber.)

Prediction of Tire Braking and Cornering Characteristics on Wet Runways

The description of the hydroplaning process given in the preceding paragraphs was taken from the preamble of an empirically derived combined viscous-dynamic hydroplaning theory which is being developed by Horne (LaRC) and Merritt (FAA, Flight Standards). This theory is presently being refined and tested by using NASA track tire data and data obtained from aircraft-ground vehicle runway test programs. The theory was first exposed to public view at the FAA/Industry Meeting on Runway Traction and Rational Landing Rule (Washington, D.C.), February 11-13, 1975. The theory is being used to develop tire-runway friction

models for flight simulator research conducted under NASA Contract (ref. 18), and is being used by NASA to assist NTSB in the investigation of aircraft skidding accidents on wet runways.

One of the first major accomplishments of the theory is the development of a simple method for transforming experimental friction measurements made by a vehicle using one tire operating mode on a wet pavement to prediction of braking and cornering friction coefficients for other tire sizes and different tire operating modes for this same wet pavement condition. The method is described herein with the aid of figures 13 and 14 for the case of a diagonal-braked vehicle (DBV) friction measurement of the wet runway at Roswell, New Mexico, and the corresponding prediction of a B-737 main gear tire friction performance for the same runway wetness condition.

The DBV method for evaluating the slipperiness of wet runways is to lock a diagonal pair of wheels on a four-wheel ground vehicle at a speed of 52.2 knots and decelerate the vehicle to a stop under both wet and dry runway conditions. (See ref. 19.) The wet-dry stopping distance ratio (SDR) obtained is an index to the slipperiness of the runway surface; the higher the SDR, the slipperier the runway is under wet conditions. The upper left plot shown in figure 13 describes the variation of DBV ground speed with time during a typical DBV test run at Roswell during the B-737 flight test program described in references 10 and 11. This speed time history was differentiated with respect to time to obtain the curve for DBV μ_{skid} against speed shown in the upper right plot of figure 13. The values of DBV μ_{skid} were obtained from the equation

$$\text{DBV } \mu_{skid} = 2 \left[\left(\frac{dv}{dt}\right)_{braked} - \left(\frac{dv}{dt}\right)_{unbraked} \right] \tag{4}$$

The viscous-dynamic hydroplaning theory states that any experimentally obtained variation of tire friction coefficient with speed on a wet pavement can be converted to an equivalent nondimensional hydroplaning-parameter $(\bar{Y})$—speed-ratio form (lower left plot of fig. 13) by means of the relationships

$$\bar{Y} = \frac{\mu_{wet}}{\mu_{dry}} \tag{5}$$

$$\text{Speed ratio} = \frac{V_G}{V_P} \tag{6}$$

where

μ_{dry} characteristic dry friction coefficient for tire

μ_{wet} experimental or predicted friction coefficient for wet
           pavement conditions

200

V_G ground speed

V_P characteristic tire hydroplaning speed (obtained from eqs. (2))

$\bar{Y}$ tire-pavement drainage characteristic or hydroplaning parameter for pavement

$\bar{Y}_L$ $\bar{Y}$ for locked-wheel sliding (nonrotating tire)

$\bar{Y}_R$ $\bar{Y}$ for braked or yawed rolling (rotating tire)

The theory defines μ_{dry} as the maximum friction coefficient obtainable on a dry pavement under braked rolling, yawed rolling, or locked-wheel sliding conditions at low speed ($V_G < 2$ knots). For aircraft tires, μ_{dry} may be calculated from the following equation (derived from ref. 20):

For SI Units:

$$\mu_{dry} = 0.93 - 1.6 \times 10^{-4} \; p \tag{7a}$$

For U.S. Customary Units:

$$\mu_{dry} = 0.93 - 1.1 \times 10^{-3} \; p \tag{7b}$$

where

p tire inflation pressure, kPa (lb/in^2)

The value of μ_{dry} for ground-vehicle tires must be determined experimentally. Typical values of μ_{dry} found for ground-vehicle friction measuring devices are listed in table 1. If $\mu_{dry} = 1.15$ and $V_P = 44.1$ knots (from eqs. (2)) in equations (5) and (6), respectively, the curve for DBV μ_{skid} against V_G of figure 13 is converted to the curve for $\bar{Y}_L$ against V_G shown in the lower left plot of figure 13. The curve of $\bar{Y}_R$ (rolling tire) shown in this latter plot was obtained with the aid of figure 14 which is empirically derived from NASA track aircraft tire data in the viscous-dynamic hydroplaning theory.

The theory suggests that all experimental pneumatic tire friction coefficients (aircraft or ground vehicle), when converted to nondimensional form, will condense along either the $\bar{Y}_L$ curve (locked-wheel braking tests) or the $\bar{Y}_R$ curve (peak-braking or yawed-rolling tests) if the correct values for μ_{dry} and V_P for the tire conditions are used, and the pavement micro/macrotexture and wetness conditions remain constant for the pavement during the tests.

Prediction of friction coefficients for any other tire size and inflation pressure simply requires multiplying either $\bar{Y}_L$ or $\bar{Y}_R$ in figure 13 by the

appropriate μ_{dry} value for the desired tire condition and the speed ratio V_G/V_P by the appropriate value of V_P for the desired tire condition for each data point $(\bar{Y}, V_G/V_P)$. For the B-737 tire friction coefficient prediction shown in figure 13, $\mu_{dry} = 0.75$ and $V_P = 115.6$ knots were used. These values were predicted by the B-737 test tire inflation pressure of $p = 1137$ kPa (165 lb/in^2). Figure 13 shows that the prediction of the theory using DBV test data is within reasonable agreement of the NASA track friction data over the speed range studied for the B-737 tire.

IDENTIFICATION OF SLIPPERY RUNWAYS

A main goal of runway slipperiness research has been to find ways to identify slippery runways so that such runways can be remedied and made safe for aircraft adverse weather operation. It has always been realized that it would be very expensive and impractical to utilize specially instrumented aircraft for this purpose; therefore, much research attention has been devoted to developing suitable ground-vehicle friction measuring techniques and equipment for this purpose. Since 1968, extensive aircraft/ground-vehicle runway research programs have been carried out in this country and abroad to find a solution to this problem (refs. 9 to 11, 19, and 21 to 26), and to answer the fundamental questions:

(1) Do friction measuring devices correlate between themselves?

(2) Do friction measuring devices correlate with aircraft tire performance on wet runways?

(3) Do friction measuring devices correlate with aircraft stopping performance on wet runways?

The scope of this aircraft/ground-vehicle correlation problem is indicated by the data trends shown in figures 15 and 16. It can be seen that the data obtained by the various friction measuring devices and two aircraft, all of which utilize different tire operational modes in testing, literally fill the figures, and poor correlation between ground vehicle to ground vehicle, ground vehicle to aircraft, and aircraft to aircraft is indicated. The data in figures 15 and 16 were obtained from references 21, 22, and 27.

Ground-Vehicle/Ground-Vehicle Correlation

Ground-vehicle/ground-vehicle correlation is complicated by the fact that the tire sizes, operating modes, and inflation pressures, as well as test speed or test speed ranges, used by the ground-vehicle devices in measuring runway slipperiness are usually significantly different. Historically, most correlation attempts between devices have compared the measurement output of one device against that of another as shown in figures 17 and 18. These figures compare 1/SDR for the DBV against the Mu-Meter friction reading. Both measurements of runway slipperiness were obtained under identical runway wetness conditions on many different runway surfaces tested by USAF (fig. 17 (data

202

from ref. 28)) and FAA (fig. 18 (data from ref. 29)). The data shown in both figures exhibit similar trends and indicate very poor correlation between a device (DBV) which measures vehicle stopping distance over a speed range of 52.2 to 0 knots with diagonal wheels locked and a yawed-rolling trailer which measures tire cornering force at constant yaw angle ($\psi = 7.5^\circ$) and constant speed ($V_G = 34.8$ knots) for the wet runway surfaces investigated. A similar trend is noted for the Roswell smooth concrete runway surface shown in figure 19. In this instance only one runway surface was tested, but the runway wetness condition (water depth) varied. These data for the DBV and Mu-Meter were obtained from reference 11. Figures 20 and 21 show the correlation obtained between the DBV and the skiddometer and the DBV and the Miles trailer at Roswell (ref. 11), respectively. The data in these figures show that the skiddometer (fig. 20) (like the Mu-Meter) exhibits poor correlation with DBV SDR measurements, whereas the Miles trailer compares better (fig. 21). The skiddometer runway slipperiness rating was achieved by testing the pavement at a constant speed of 34.8 knots (like the Mu-Meter), whereas the Miles trailer tested the pavement over a speed range of 85 to 0 knots (similar to the DBV).

Much better correlation between ground vehicles is obtained when each vehicle is tested over a speed range and the viscous-hydroplaning theory method (described earlier) is used to compare the friction data obtained by the vehicles. This type of correlation is shown in figures 22 to 25. The data for these figures were obtained from the joint NASA-British Ministry of Technology Skid Correlation Study reported in references 21, 22, and 30. The data trends shown in figures 22 to 25 suggest that good correlation is achieved between ground vehicles when the friction measurement of a vehicle is compared over a speed range with its equivalent measurement from another ground-vehicle device. This result suggests that ground-vehicle runway slipperiness measurements can correlate if tested over a speed range and proper accounting is made for the difference in the tire operating modes between the vehicles. It should be noted that the worst correlation between devices occurs in figure 25 where the Mu-Meter is compared with several other friction measuring devices. The Mu-Meter is the only friction device that does not measure a friction boundary condition - that is, the skiddometer measures peak braking (constant 0.13 braking slip); the General Motors (GM) trailer, either μ_{max} or μ_{skid} from a pulse braking technique; the Miles trailer, μ_{skid} from a pulse braking technique; and the DBV, μ_{skid} from a continuous locked-wheel braking technique. The Mu-Meter, on the other hand, measures cornering force developed on a tire at 7.5° yaw angle. At high pavement friction values, it cannot measure the peak friction boundary condition, whereas for low friction conditions, it may measure cornering force after the peak cornering-force value has been obtained, as shown in figure 26. The data in figure 26 were obtained from reference (p. 654). These data suggest that if the yaw angle for maximum cornering (limiting coefficient of friction) is exceeded, the cornering force (and cornering friction coefficient) is reduced as yaw angle is further increased. For the case of the Mu-Meter which measures cornering force at 7.5° yaw angle, this type of tire behavior may result in an overestimation of the slipperiness of the wet pavement defined by peak boundary friction conditions.

Aircraft/Ground-Vehicle Correlation

As with ground-vehicle/ground-vehicle correlation attempts, most aircraft/ground-vehicle correlation attempts try to relate the measured output of a friction device with some measured output of the aircraft from data obtained during joint testing of the device and aircraft on artificially wet runway surfaces. Typical aircraft/ground-vehicle relationships obtained from such test programs are shown in figures 27 (Mu-Meter, ref. 24) and 28 (DBV, refs. 11 and 25). Each friction device advocate claims good correlation between the device and the aircraft. For example, reference 26 states that the Mu-Meter may predict aircraft stopping performance within 10 to 15 percent if a correlation ranking system classifying runway surfaces into different texture groups is used. On the other hand, reference 11 states that the DBV can predict aircraft stopping performance within ±15 percent by using its prediction method. The tire friction prediction method (described earlier in the paper) offers another approach to show correlation between ground-vehicle and aircraft measurements of runway slipperiness.

Equation (5) may be modified to the form

$$\mu_{eff} = \eta \; \bar{Y}_R \; \mu_{dry} \tag{8}$$

where

μ_{eff} effective braking friction coefficient realized by the aircraft through its antiskid braking system

$\bar{Y}_R$ runway tire-pavement drainage characteristic (hydroplaning parameter) determined by ground-vehicle friction test over ground speed range

μ_{dry} characteristic maximum aircraft tire friction coefficient on dry pavement

η antiskid braking system efficiency, μ_{eff}/μ_{max}

This method, using the DBV friction measuring device, is illustrated in figures 29 to 31. The correlation shown in the figures resulted from use of the arbitrarily selected antiskid braking system efficiency model depicted in figure 29 which is patterned after the one described in reference 32.

The data trends shown in figures 29 to 31 suggest that a ground-vehicle friction measuring device can be used to predict the effective friction coefficient an aircraft will develop on a wet runway providing the antiskid braking system efficiency of the aircraft is known. The data trends also suggest that each aircraft type has its own characteristic antiskid braking system efficiency which is dependent upon the landing gear, braking, and antiskid system design.

Summary of Correlation Results

The runway slipperiness research conducted since 1968 in the area of ground-vehicle/ground-vehicle and aircraft/ground-vehicle correlations has been reviewed and yields the following observations:

Ground-vehicle devices that test at constant speed do not correlate well with those devices that test over a speed range.

Ground-vehicle devices that test at constant speed can be correlated together as well as those that test over a speed range regardless of the tire operating mode during testing.

The DBV can be used to predict aircraft tire braking and cornering characteristics on wet runways. Other ground-vehicle devices have the potential to predict these tire characteristics as well if their test procedure is changed from a constant speed test to a speed range test similar to the DBV. Ground-vehicle devices that test at constant speed cannot predict aircraft tire braking and cornering friction coefficient on wet runways over the full take-off and landing speed range of aircraft.

Ground-vehicle and aircraft slipperiness measurements can be correlated. However, the precision of correlation is obtained from artificially wet runway test programs. The accuracy of prediction from the correlation may be degraded when runways are wet from natural rain (different water depths). Further, some of the older aircraft braking systems can allow locked-wheel operation during maximum braking operation on wet runways. The locked-wheel condition can result in reverted rubber hydroplaning which destroys the aircraft/ground-vehicle correlation. For these reasons, predictions of aircraft braking performance on wet runways from ground-vehicle devices should be employed only to provide guidance information to pilots.

Status of Runway Slipperiness Measurements

Standard USAF runway skid resistant tests.- Since November 1973, the Air Force Civil Engineering Center (AFCEC) has been measuring the skid resistance properties of airfields. Procedures for conducting the standard skid resistance tests are given in reference 33. This test requires that friction measurements be obtained by both the DBV and Mu-Meter when testing an airfield pavement. AFCEC feels that the friction data obtained from these friction measuring devices are complementary, and together they provide an adequate data base to evaluate the skid resistance of an airfield pavement. AFCEC intends to survey the skid resistance of all USAF runways in the United States and overseas on a periodic basis. AFCEC feels strongly that the concept of using an experienced, well-trained crew and standardized testing procedures for pavement skid resistance evaluations offers many advantages. This concept requires the Air Force to purchase and maintain a minimum quantity of equipment and ensures that the testing is properly accomplished and documented. Results from this Air Force program are reported in references 28 and 34.

FAA Advisory Circular No. 150/5320-12.- FAA Airports Service issued FAA Advisory Circular No. 150/5320-12 on June 30, 1975 (ref. 35). This advisory circular provides guidance on methods that can be used to provide and maintain airport pavement surface friction characteristics. This guidance is intended for use by airport operators, engineering consultants, and maintenance personnel. This advisory circular does not purport to provide a means to predict aircraft stopping distance. For the requirements specified in this circular, FAA Airports Service requires a friction measuring device which

(1) Can provide fast, accurate, and reliable friction values of airport pavement surfaces under varying climatic conditions

(2) Can provide a continuous graph record of the pavement surface characteristics

(3) Has minimal maintenance and recurring costs

(4) Has a simple calibration technique

(5) Indicates potential for hydroplaning conditions

This circular is worded carefully such that current friction measuring devices, the DBV for example, are not excluded from use in implementing the circular, although it is clear that the British Mu-Meter is the device favored by FAA Airports Service since it is the only device described in the circular. The advisory circular clearly indicates that its needs are met by a device which measures the relative friction of pavement surfaces and that this measurement of friction does not provide a means to predict aircraft stopping distance (determine how slippery the runway surfaces are for aircraft operation).

It is felt that issuance of this advisory circular by the FAA is a noteworthy step forward in providing guidance to install antihydroplaning runway surfaces at airports. However, the providing of relative friction measurements for engineering and maintenance purposes is secondary to the main objective of a friction evaluation which is to determine how slippery the runway surface is for aircraft operation.

PROGRESS AND PROBLEMS OF ANTIHYDROPLANING

RUNWAY SURFACE TREATMENTS

Both runway grooving and porous friction course (PFC) antihydroplaning runway surfaces were originated in England, as described in reference 36. Research on runway grooving in the United States started with NASA experiments in 1962 (reported in ref. 2). PFC pavement research in the United States was initiated by USAF (1972) and is reported in references 37 and 38.

Runway Grooving

Since 1956, approximately 160 runways have been grooved world-wide as indicated in tables 2 to 12. Figure 32 shows the development of grooved runways at U.S. civil airports since the first air carrier airport was grooved in 1967. For the past 3 years an average of 24 air carrier airport runways have been grooved each year. At this present rate, the 224 ILS runways 1524 m (5000 ft) or longer in length at U.S. air carrier airports will all be grooved by 1986. At the present time, six different methods are available for grooving runways, namely, diamond saws, abrasive (carborundum) saws, flails, plastic grooving with segmented drum, plastic grooving with wire comb, and plastic grooving with wire broom. The latter three methods can only be used for grooving portland cement concrete when it has been freshly laid and has not hardened or set up. The most popular grooving method is the diamond saw. Approximately 80 percent of the air carrier airport runways that have been grooved since 1967 have used this grooving method. The effectiveness of runway grooving as an antihydroplaning surface treatment is revealed by reviewing the DBV SDR data shown in tables 13 to 17. Tables 13 to 16 were obtained from reference 39. Table 17 shows data obtained from a recently completed FAA DBV trial application-runway friction calibration and pilot information program (ref. 40). Review of these data suggests that the greatest traction benefit is realized from closed-spaced grooves that are cut 1/4 inch deep in the pavement with diamond saws. This result follows the trend reported in reference 27 where a $25 \times 6 \times 6$ mm $(1 \times 1/4 \times 1/4$ in.) pattern was found to be superior to all other patterns studied with regard to preserving traction on wet or flooded runways. Plastic grooving treatments are considered to be an improvement over conventional ungrooved concrete surfaces but are inferior to diamond sawed grooves in both traction performance and water drainage (discussed in section "Flooding on Grooved Runways"). The uniformity of plastic grooving is poor compared with diamond sawed grooves as shown by comparing figures 5 and 6 with figure 33. The data presented in figure 34 compare the traction performance of plastic grooving using a wire comb technique (ref. 41) with other antihydroplaning pavement surface treatments. These data confirm the traction trends just discussed.

The major problem encountered with grooved runways is the chevron cutting of aircraft tires during the touchdown phase of aircraft landings on grooved runways. (See fig. 35.) This problem is discussed in detail in reference 39 and has been studied in reference 42. The civil airlines in the United States at the present time do not consider chevron cutting to be a serious operational problem to their jet transport fleet. It should be noted that the aircraft tire industry has been working in close cooperation with aircraft operators on the chevron cutting problem. During the past 5 years, the aircraft tire industry has developed new tread rubber compounds and tread designs that significantly reduce the degree of chevron cutting on aircraft tires experienced on grooved runways. In this regard, American Airlines reports that over the past 4 years, the number of landings per tire change on its jet transport fleet has increased by 50 percent. During this time period, the number of grooved runways at air carrier airports has increased from 37 to 107. The slipperiness of grooved runways is increased when heavy rubber deposits coat touchdown areas, but this problem is easily corrected by rubber removal treatments (discussed later).

Some asphaltic concrete runways have suffered collapsed grooves in trafficked areas. This type of problem is usually created by grooving the asphaltic concrete shortly after the runway has been paved and before the asphaltic concrete has cured properly.

Porous Friction Course

The first PFC surface treatment in the United States was at the Dallas Naval Air Station in 1971 as indicated in table 18. The growth of the PFC surface treatment at U.S. civil airports (through 1975) is shown in figure 36. Over the past 3 years (1973 to 1975), an average of seven air carrier airport runways per year have been given this antihydroplaning pavement surface treatment. Figure 34 shows that this surface is definitely superior in traction qualities over conventional ungrooved concrete and ranks with pavement grooving in this regard as reported in reference 19. PFC has a high storage volume to prevent runway flooding when rain first commences but does not have the free flowing drainage features common to grooved runways. Consequently (as discussed earlier in the paper), PFC surface treatments are not believed to be as effective as grooved pavements, especially those cut with diamond saws, in preventing runway flooding during sustained, high rainfall rate precipitation conditions.

A major problem that has been reported for PFC pavements is the difficulty of removing rubber from contaminated touchdown areas of the runway. AOCI (Airport Operators Council International) reports that the PFC surface at Johannesburg had to be replaced because rubber deposits could not be removed from the surface. A similar problem has been encountered at Denver Stapleton Airport where the rubber deposits could be removed only through the use of a flailing machine and high-pressure water-blast equipment. It should be stressed that the PFC surface treatments at U.S. airports have not been installed long enough at the present time to report realistically or the durability and maintainability of this type pavement surface.

Runway Rubber Deposits and Their Removal

NASA, USAF, and FAA studies (tables 13 to 17) show that the most slippery runway segments are usually those located in aircraft touchdown areas which become covered with heavy rubber deposits. The reduced macro/microtexture of the pavement surface (fig. 37) resulting from rubber deposits makes the runway much more susceptible to dynamic and viscous hydroplaning during times of rain. The dramatic runway traction loss suffered as a consequence is illustrated by figure 38. Reference 11 points out that wheel spin-up at touchdown on the Roswell smooth concrete runway (SDR = 2.17 to 2.75 for DIA, B-57, and C-1011) required as much as 2 seconds. From a comparison of figures 18 and 38, the predicted aircraft tire friction coefficient μ_{skid} available to spin the tire up on the rubber coated ungrooved runway at MIA runway 9R/27L (SDR = 4.62) is found to be much less than at Roswell. Consequently, wheel spin up times may take from 6 to 8 seconds on this wet, contaminated surface. As a consequence, pilots may apply wheel braking before the wheels are spun up with the result that the antiskid braking system fails to perform properly and poor braking, poor

208

directional control along with reverted rubber skidding may occur for the aircraft. (See refs. 8 and 11.) Obviously, runway rubber deposits pose a distinct threat to the operational safety of aircraft during landings and take-offs in adverse weather. This paper has pointed out that ground vehicles which test pavements utilizing a constant speed technique cannot predict the runway slipperiness resulting to aircraft from this effect. Therefore, the DBV, which has a demonstrated capability to perform this measurement, should be the only device permitted to assess this runway condition. Only when test procedures have been changed and the devices correlated or calibrated satisfactorily with the DBV, should other devices be allowed to measure the effects of rubber deposits on runway slipperiness for aircraft operation.

Review of the data contained in tables 13 to 17 and figures 37 and 38 indicates that grooved runways are much less affected by rubber deposits than ungrooved runways and may require less frequent cleaning. Several methods for cleaning runways of rubber deposits are available and discussed in reference 40. One of the most effective means is by high-pressure water blast as shown in figures 39 and 40.

CONCLUDING REMARKS

This paper has reviewed the runway slipperiness research performed in the United States and abroad over the time period 1968 to the present. This review suggests that this research has been extremely fruitful with the following tangible benefits resulting to the aviation community:

(1) A better understanding of the hydroplaning phenomena

(2) A method for predicting aircraft tire performance on wet runways from a ground-vehicle braking test

(3) The runway rubber deposit problem has been defined as one of the most serious threats to aircraft operational safety during landings and take-offs in adverse weather; at the same time, methods have been developed which can remove runway rubber deposits so that runway traction is effectively restored to uncontaminated levels

(4) Pavement grooving has fulfilled its promise as a runway surface treatment that minimizes runway flooding during heavy rainstorms and produces nearly dry aircraft braking and cornering performance under wet runway conditions

(5) Porous friction course surface treatments are nearly as effective as pavement grooving, but further research and time are required to assess the effects of rubber deposits (and removal), durability, and maintainability of this surface treatment

Finally, it is hoped that this report on the status of runway slipperiness research will stimulate the aviation community and the Federal Regulatory Agencies into a rapid implementation program to utilize the technological advances this research has produced and to improve airport runway safety.

REFERENCES

1. Galloway, Bob M.; Schiller, Robert E., Jr.; and Rose, Jerry G.: The Effects of Rainfall Intensity, Pavement Cross Slope, Surface Texture, and Drainage Length on Pavement Water Depths. Res. Rep. No. 138-5, Texas Transp. Inst., Texas A&M Univ., May 1971.

2. Horne, Walter B.; Yager, Thomas J.; and Taylor, Glenn R.: Review of Causes and Alleviation of Low Tire Traction on Wet Runways. NASA TN D-4406, 1968.

3. Horne, Walter B.; and Dreher, Robert C.: Phenomena of Pneumatic Tire Hydroplaning. NASA TN D-2056, 1963.

4. Aircraft Accident Report - Caribbean Atlantic Airlines, Inc.; Douglas DC-9-31, N938PR; Harry S. Truman Airport, Charlotte Amalie, St. Thomas, Virgin Islands; August 12, 1969. Rep. No. NTSB-AAR-70-23, Sept. 16, 1970.

5. Aircraft Accident Report - Piedmont Airlines; Boeing 737, N751N; Greensboro, N.C.; October 28, 1973. Rep. No. NTSB-AAR-74-7, May 22, 1974.

6. Horne, Walter B.; and Joyner, Upshur T.: Determining Causation of Aircraft Skidding Accidents or Incidents. Paper presented at the 23rd Annual International Air Safety Seminar, Flight Safety Foundation, Inc. (Washington, D.C.), Oct. 1970.

7. Horne, Walter B.: Elements Affecting Runway Traction. [Preprint] 740496, Soc. Automat. Eng., Apr.-May 1974.

8. Horne, Walter B.; McCarty, John L.; and Tanner, John A.: Some Effects of Adverse Weather Conditions on Performance of Airplane Antiskid Braking Systems. NASA TN D-8202, 1976.

9. Merritt, Leslie R.: Impact of Runway Traction on Possible Approaches to Certification and Operation of Jet Transport Aircraft. [Preprint] 740497, Soc. Automot. Eng., Apr.-May 1974.

10. Cantu, A. G.; and Chernick, B. E.: Model 737 Data - FAA Evaluation of Proposed Landing Certification Rules. Doc. No. D6-43078, Boeing Co., Dec. 1973.

11. Merritt, Leslie R.: Concorde Landing Requirement Evaluation Tests. Report No. FAA-FS-160-74-2, 1974.

12. Gough, V. E.: Discussion of Paper by D. Tabor, Frottement en Caoutchouc, Rev. Ge'n du Caoutchouc, vol. 36, 1959.

13. Frictional and Retarding Forces on Aircraft Tyres. Part I: Introduction. Eng. Sci. Data Item No. 71025 with amendment A, R. Aeronaut. Soc., Aug. 1972.

14. Leland, Trafford J. W.; Yager, Thomas J.; and Joyner, Upshur T.: Effects of Pavement Texture on Wet-Runway Braking Performance. NASA TN D-4323, 1968.

15. Lander, F. T. W.; and Williams, T.: The Skidding Resistance of Wet Runway Surfaces With Reference to Surface Texture and Tyre Conditions. RRL Rep. LR 184, Road Res. Lab., British Minist. Transp., 1968.

16. Rose, F. G.; Gallaway, R. M.; and Hankins, K. D.: Macrotexture Measurements and Related Skid Resistance at Speeds From 20 to 60 Miles Per Hour. Highway Research Record no. 341, 1970, pp. 33-45.

17. Horne, Walter B.: Skidding Accidents on Runways and Highways Can Be Reduced. Astronaut. & Aeronaut., vol. 5, no. 8, Aug. 1967, pp. 48-55.

18. Expansion of Flight Simulator Capability for Study and Solution of Aircraft Directional Control Problems on Runways. Phase I - Final Report. Rep. MDC A3304 (Contract NAS1-13378), McDonnell Aircraft Co., Mar. 15, 1975. (Available as NASA CR-145084.)

19. Yager, Thomas J.; Phillips, W. Pelham; Horne, Walter B.; and Sparks, Howard C. (appendix D by R. W. Sugg): A Comparison of Aircraft and Ground Vehicle Stopping Performance on Dry, Wet, Flooded, Slush-, Snow-, and Ice-Covered Runways. NASA TN D-6098, 1970.

20. Smiley, Robert F.; and Horne, Walter B.: Mechanical Properties of Pneumatic Tires With Special Reference to Modern Aircraft Tires. NASA TR R-64, 1960. (Supersedes NACA TN 4110.)

21. Horne, Walter B.; and Tanner, John A.: Joint NASA-British Ministry of Technology Skid Correlation Study - Results From American Vehicles. Pavement Grooving and Traction Studies, NASA SP-5073, 1969, pp. 325-359.

22. Sugg, R. W.: Joint NASA-British Ministry of Technology Skid Correlation Study - Results From British Vehicles. Pavement Grooving and Traction Studies, NASA SP-5073, 1969, pp. 361-409.

23. Anon.: Model L-1011-1 (Base Aircraft) Landing Performance Report for FAA Evaluation of Concorde SST Special Condition 25-43-EU-12. Rep. No. LR 26267, Lockheed Aircraft Corp., Jan. 14, 1974.

24. Sugg, R. W.: The Development and Testing of the Runway Friction Meter MK 1 (Mu-Meter). AF/542/043, British Minist. Def., June 1972.

25. Merritt, L. R.: Analysis of Tests Conducted by the French Ministry of Armed Forces Flight Test Center for the Service Technique Aeronautique (STAe) Utilizing a Caravelle 116 Aircraft and a Diagonal Braked Vehicle (DBV). Rep. No. FS-160-75-2, FAA, Oct. 1975.

26. Blanchard, J. W.: An Analysis of the B727 and DC9 Trials on Wet Runways With the Mu-Meter and Diagonal Braked Vehicle (DBV). Civil Aviat. Auth. (London), Dec. 1974.

27. Yager, Thomas J.: Comparative Braking Performance of Various Aircraft on Grooved and Ungrooved Pavements at the Landing Research Runway, NASA Wallops Station. Pavement Grooving and Traction Studies, NASA SP-5073, 1969, pp. 35-65.

28. Williams, John H.: Analysis of the Standard USAF Runway Skid Resistance Tests. AFCEC-TR-75-3, U.S. Air Force, May 1975.

29. Nussbaum, Peter J.; Hiering, William A.; and Grisel, Charles R.: Runway Friction Data for 10 Civil Airports as Measured With a Mu-Meter and Diagonal Braked Vehicle. Rep. No. FAA-RD-72-61, July 1972.

30. Horne, Walter B.: Results From Studies of Highway Grooving and Texturing at NASA Wallops Station. Pavement Grooving and Traction Studies, NASA SP-5073, 1969, pp. 425-464.

31. Van Eldik Thieme, H. C. A.: Cornering and Camber Experiments. Mechanics of Pneumatic Tires, Samuel K. Clark, ed., NBS Monogr. 122, U.S. Dep. Commer., Nov. 1971, pp. 631-693.

32. Preston, O. W.; Kibbee, G. W.; Muroyama, R. H.; and Storley, R. A.: Development of a Basic Methodology for Predicting Aircraft Stopping Distance on a Wet Runway. Rep. No. FAA-RD-70-62, Mar. 1971.

33. Ballentine, George D.; and Compton, Phil V.: Procedures for Conducting the Air Force Weapons Laboratory Standard Skid Resistance Test. AFWL-TR-73-165, U.S. Air Force, Sept. 1973.

34. AFCEC Pavement Surface Effects Team: Runway Skid Resistance Survey Report. Air Force Civil Eng. Center, U.S. Air Force, 1975. Production FLT/Test Instln, AF Plant 42, Palmdale, California, Mar. 1975.
    Norton AFB, California, Apr. 1975.
    March AFB, California, Apr. 1975.
    Vandenberg AFB, California, Apr. 1975.
    Williams AFB, California, Apr. 1975.
    Davis Monthan AFB, Arizona, Apr. 1975.
    Reese AFB, Texas, May 1975.
    Carswell AFB, Texas, May 1975.
    Dyess AFB, Texas, May 1975.
    Webb AFB, Texas, May 1975.
    Laughlin AFB, Texas, May 1975.
    Randolph AFB, Texas, May 1975.
    Barksdale AFB, Louisana, May 1975.
    Yokota AFB, Japan, Aug. 1975.
    Elmendorf AFB, Alaska, Aug. 1975.

35. Methods for the Design, Construction, and Maintenance of Skid Resistant Airport Pavement Surfaces. AC No. 150/5320-12, FAA, June 30, 1975.

36. Martin, F. R.: Pavement Surface Treatments at Airports in Great Britain. Pavement Grooving and Traction Studies, NASA SP-5073, 1969, pp. 235-278.

37. Tomita, Hisao; and Forrest, J. B.: Porous Friction Surfaces for Airfield Pavements. AFWL-TR-74-177, U.S. Air Force, May 1975.

38. Compton, Phil V.; and Hargett, Emil R.: Skid-Resistance Evaluation of Seven Antihydroplaning Surfaces. AFWL-TR-74-64, U.S. Air Force, May 1974.

39. Horne, Walter B.; and Griswold, Guy D.: Evaluation of High Pressure Water Blast With Rotating Spray Bar for Removing Paint and Rubber Deposits From Airport Runways, and Review of Runway Slipperiness Problems Created by Rubber Contamination. NASA TM X-72797, 1975.

40. Merritt, Leslie R.: Trial Application-Runway Friction Calibration and Pilot Information Program. Rep. No. AFS-160-76-1, FAA, Aug. 19, 1976.

41. Marlin, Eugene C.; and Horne, Walter B.: Plastic (Wire-Combed) Grooving of a Slip-Formed Concrete Runway Overlay at Patrick Henry Airport - An Initial Evaluation. Paper presented at the Southeastern Airport Managers Association (Fort Lauderdale, Fla.), Nov. 1973.

42. Byrdsong, Thomas A.; McCarty, John Locke; and Yager, Thomas J.: Investigation of Aircraft Tire Damage Resulting From Touchdown on Grooved Runway Surfaces. NASA TN D-6690, 1972.

213

KEY TO ABBREVIATIONS USED IN TABLES

Abbreviation	Meaning
AB	Air Base
AC	Asphaltic concrete
AFB	Air Force Base
AFCEC	Air Force Civil Engineering Center
ASTM	American Society for Testing and Materials
ATD	Average texture depth
C	Civil
CS	Carborundum saw
D	Depth
DBV	Diagonal-braked vehicle
DS	Diamond saw
F	Flail
FAA	Federal Aviation Administration
G	Grooved
Int.	International
L	Longitudinal
Lt	Light
M	Military
Med	Medium
Metro.	Metropolitan
Mun.	Municipal
N/A	Not available
NAS	Naval Air Station
Nat.	National
P	Pitch
PCC	Portland cement concrete
PGSD	Plastic grooving with segmented drum
PGWB	Plastic grooving with wire broom
PGWC	Plastic grooving with wire comb
RAF	Royal Air Force
SDR	Stopping distance ratio
T	Transverse
W	Width

TABLE 1.- TIRE CHARACTERISTICS OF FRICTION MEASURING DEVICES

Device	μ_{dry}	P	
		kPa	lb/in^2
DBV (ASTM E-249 smooth tread tire)	1.15	165	24
DBV (ASTM E-524 smooth tread tire)	1.20	165	24
Mu-Meter	0.84	69	10
Miles trailer	1.15	138	20
Skiddometer model BV-6 (ASTM E-249 smooth tread tire). . .	1.15	165	24

Table 2.- GROOVED RUNWAYS CONSTRUCTED DURING 1956-1966

Airport	Country	Runway	Surface	Grooving technique	Groove pattern, P × W × D (mm)	Groove pattern, P × W × D (in.)
A (1956) - M	UK	N/A	AC	T-F	25 × 3 × 3	1 × 1/8 × 1/8
B (1957) - M	UF	N/A	AC	T-F	25 × 3 × 3	1 × 1/8 × 1/8
C (1960) - M	UK	R/A	AC	T-F	25 × 3 × 3	1 × 1/8 × 1/8
D (1960) - M	UK	N/A	AC	T-F	25 × 3 × 3	1 × 1/8 × 1/8
E (1960) - M	UK	N/A	PCC	T-F	25 × 3 × 3	1 × 1/8 × 1/8
F (1961) - M	UK	N/A	AC	T-CS	25 × 3 × 3	1 × 1/8 × 1/8
Manchester (1961) - C	UK	N/A	AC	T-F	25 × 3 × 3	1 × 1/8 × 1/8
NASA LaRC (1964) - C	USA	Research track	AC	T-DS	25 × 3 × 3	1 × 1/8 × 1/8
			PCC	L-DS	25 × 6 × 6	1 × 1/4 × 1/4
Manchester (1965) - C	UK	N/A	AC	T-F	25 × 3 × 3	1 × 1/8 × 1/8
Ubon (1966) - M	USA	N/A	PCC	T-DS	51 × 6 × 6 (Skip 610)	2 × 1/4 × 1/4 (Skip 24)
Udorn (1966) - M	USA	N/A	PCC	T-DS	51 × 6 × 6 (Skip 610)	2 × 1/4 × 1/4 (Skip 24)
NASA LaRC (1966) - C	USA	Research track	PCC	I-F	25 × 3-9 × 3	1 × 1/8-3/8 × 1/8
					38 × 3-9 × 3	1 1/2 × 1/8-3/8 × 1/8
					51 × 3-9 × 3	2 × 1/8-3/8 × 1/8
				T-DS	25 × 3-9 × 6	1 × 1/8-3/8 × 1/4
					38 × 3-9 × 6	1 1/2 × 1/8-3/8 × 1/4
					51 × 3-9 × 6	2 × 1/8-3/8 × 1/4

TABLE 3.- GROOVED RUNWAYS CONSTRUCTED DURING 1967

Airport	Country	Runway	Surface	Grooving technique	Groove pattern, P × W × D (mm)	Groove pattern, P × W × D (in.)
Bien Hoa - M	USA	N/A	PCC	T-DS	51 × 6 × 6 (Skip 610)	2 × 1/4 × 1/4 (Skip 24)
Birmingham - C	UK	N/A	AC	I-F	25 × 3 × 3	1 × 1/8 × 1/8
Beale AFB - M	USA	14/32	PCC	T-DS	25 × 6 × 6	1 × 1/4 × 1/4
John F. Kennedy - C	USA	4R/22L	PCC	T-DS	38 × 10-5 × 3	1 1/2 × 3/8-3/16 × 1/8
Kansas City Mun. - C	USA	18/36	PCC/AC	T-DS	25 × 3 × 6	1 × 1/8 × 1/4
NASA Wallops - C	USA	4/22	PCC/AC	T-DS	25 × 6 × 6	1 × 1/4 × 1/4
Washington Nat. - C	USA	18/36	AC	T-DS	25 × 3 × 3	1 × 1/8 × 1/8

TABLE 4.- GROOVED RUNWAYS CONSTRUCTED DURING 1968

Airport	Country	Runway	Surface	Grooving technique	Groove pattern, P × W × D (mm)	Groove pattern, P × W × D (in.)
Atlanta Mun. - C	USA	9R/27L	PCC	T-DS	32 × 10-3 × 6	1 1/4 × 3/8-1/8 × 1/4
Chicago-Midway - C	USA	13R/31L	PCC	T-DS	32 × 6 × 6	1 1/4 × 1/4 × 1/4
Chicago-Midway - C	USA	4R/22L	PCC	T-DS	32 × 6 × 6	1 1/4 × 1/4 × 1/4
Seymour-Johnson AFB - M	USA	8/26	PCC/AC	T-DS	51 × 6 × 6 (Skip 610)	2 × 1/4 × 1/4 (Skip 24)
Tempelhof (Ger.) - M	USA	9R/27L	AC	T-DS	38 × 10 × 10	1 1/2 × 3/8 × 3/8

TABLE 5.- GROOVED RUNWAYS CONSTRUCTED IN U.S. 1969

Airport	Country	Runway	Surface	Grooving technique	Groove dimensions		
Boston Logan - C	USA	N/A	AC				
Charleston (W.Va.) - C	USA	5/23	PCC/AC				
Chicago O'Hare - C	USA	9L/27R	PCC/AC				
Dallas Love Field - C	USA	13R/31L	PCC				
Offutt AFB - M	USA	12/30	PCC				
Wellington - C	New Zealand	N/A	AC				

TABLE 6.- GROOVED RUNWAYS CONSTRUCTED U.S. IN 1970

Airport	Country	Runway	Surface	Grooving technique	Groove dimensions		
Bankok	Thailand	N/A	PCC				
Dallas Love Field - C	USA	13L/31R	AC				
Harry S. Truman - C	USA	9/27	PCC/AC				
Kadena - M	USA	N/A	PCC/AC				
Nashville Met. - C	USA	2L/20R	AC				
Nashville Met. - C	USA	13/31	PCC/AC				
Orly - C	France	N/A	PCC				
Port Hardy - C	Canada	N/A	AC				
Shemya - M	USA	10/28	AC				

TABLE 7.- GROOVED RUNWAYS CONSTRUCTED U.S. IN 1971

Airport	Country	Runway	Surface	Grooving technique	Groove dimensions		

216

TABLE 8.- GROOVED RUNWAY CONSTRUCTED DURING 1972

Airport	Country	Runway	Surface	Grooving technique	Groove pattern, P • W • D mm	Groove pattern, P • W • D in.
Baton Rouge - C	USA	4/22	PCC	T-PG	51 • 6 • 6	2 • 1/4 • 1/4
Boston Logan - C	USA	4R/22L	AC	T-DS	57 • 8 • 6	2 1/4 • 5/16 • 1/4
Cincinnati - C	USA	18/36	AC	T-DS	45 • 6 • 6	1 1/2 • 1/4 • 1/4
Cincinnati - C	USA	9R/22L	PCC	T-PG	48 • 6 • 6	1 1/2 • 1/4 • 1/4
Denver Stapleton - C	USA	17L/35R	PCC	T-PG	51 • 6 • 6	2 • 1/4 • 1/4
Detroit Metro. - C	USA	3L/21R	PCC	T-PG	51 • 6 • 6	2 • 1/4 • 1/4
Minneapolis - C	USA	4/22	PCC	T-PG	32 • 6 • 6	1 1/4 • 1/4 • 1/4
Oklahoma City - C	USA	17R/35L	PCC	T-PG	51 • 6 • 6	2 • 1/4 • 1/4
Omaha Eppley Field - C	USA	14L/32R	PCC	T-PG	25 • 13 • 13	1 • 1/2 • 1/2
Osan - M	USA	9/27	PCC	T-PG	32 • 6 • 6	1 1/4 • 1/4 • 1/4
Plattsburg - M	USA	17/35	PCC	T-PG	32 • 6 • 6	1 1/4 • 1/4 • 1/4
Shaw - M	USA	4L/22R	PCC	T-D	38 • 6 • 6	1 1/2 • 1/4 • 1/4
					51 • 6 • 6	2 • 1/4 • 1/4
Springfield (Mo.) - C	USA	1/19	PCC	T-DS	(Skip 610) 51 • 6 • 6	(Skip 24) 2 • 1/4 • 1/4
St. Paul Holman - C	USA	12/30	AC	T-DS	32 • 6 • 6	1 1/4 • 1/4 • 1/4
Waterloo Mun. - C	USA	12/30	PCC	T-DS	32 • 6 • 6	1 1/4 • 1/4 • 1/4
Washington Nat. - C	USA	15/36	AC	T-DS	32 • 6 • 6	1 1/4 • 1/4 • 1/4

TABLE 9.- GROOVED RUNWAY CONSTRUCTED DURING 1973

Airport	Country	Runway	Surface	Grooving technique	Groove pattern, P • W • D mm	Groove pattern, P • W • D in.
Allentown - C	USA	6/24	AC	T-DS	32 • 6 • 6	1 1/4 • 1/4 • 1/4
Atlanta Int. - C	USA	9R/27L	PCC	T-PG	A	N/A
Baltimore Int. - C	USA	10/28	AC	T-DS	32 • 6 • 6	1 1/4 • 1/4 • 1/4
Baltimore Int. - C	USA	15/33	AC	T-DS	32 • 6 • 6	1 1/4 • 1/4 • 1/4
Charles DeGaulle - C	France	N/A	PCC	T-DS	N/A	N/A
Clarksburg - C	USA	3/21	AC	T-DS	51 • 6 • 6	2 • 1/4 • 1/4
Cleveland Hopkins - C	USA	5R/23L	AC	T-DS	38 • 6 • 6	1 1/2 • 1/4 • 1/4
Dallas/Ft. Worth - C	USA	17L/35R	PCC	T-DS	32 • 6 • 6	1 1/4 • 1/4 • 1/4
Dallas/Ft. Worth - C	USA	17R/35L	PCC	T-DS	32 • 6 • 6	1 1/4 • 1/4 • 1/4
Dallas/Ft. Worth - C	USA	13L/31R	PCC	T-DS	38 • 6 • 6	1 1/2 • 1/4 • 1/4
Gainsville Mun. - C	USA	10/28	AC	T-DS	38 • 6 • 6	1 1/2 • 1/4 • 1/4
Griffiss - M	USA	15/33	PCC	T-DS	51 • 6 • 6	2 • 1/4 • 1/4
Huntington - C	USA	12/30	AC	T-DS	32 • 6 • 6	1 1/4 • 1/4 • 1/4
Jacksonville Int. - C	USA	7/25	AC	T-DS	51 • 6 • 6	2 • 1/4 • 1/4
Lafayette (Ind.) - C	USA	10/28	AC	T-DS	32 • 6 • 6	1 1/4 • 1/4 • 1/4
LaGuardia - C	USA	13/31	AC	T-DS	38 • 19.5 • 5	1 1/4 • 3/4-5/16 • 3/16
Miami Int. - C	USA	9L/27R	AC	T-DS	32 • 6 • 6	1 1/4 • 1/4 • 1/4
Miami Int. - C	USA	9R/27L	AC	T-DS	38 • 6 • 6	1 1/2 • 1/4 • 1/4
Patrick Henry Field - C	USA	6/24	PCC	T-P-SG	13 • 5 • 5	1/2 • 3/16 • 3/16
Peoria (Ill.) - C	USA	12/30	AC	T-DS	51-76 • 6 • 6	2-3 • 1/4 • 1/4
Savannah - C	USA	18/36	PCC	T-P-SG	N/A	N/A
South Bend - C	USA	9/27	AC	T-DS	32 • 6 • 6	1 1/4 • 1/4 • 1/4
St. Louis Lambert - C	USA	6/24	PCC	T-DS	32 • 6 • 6	1 1/4 • 1/4 • 1/4
Vance - M	USA	17R/35L	PCC	T-DS	51 • 6 • 6	2 • 1/4 • 1/4
Williamsport - C	USA	9/27	AC	T-DS	32 • 6 • 6	1 1/4 • 1/4 • 1/4

217

TABLE 10.- GROOVED RUNWAYS CONSTRUCTED DURING 1974

Airport	Country	Runway	Surface	Grooving technique	Groove pattern, P × W × D	
					mm	in.
Albany (N.Y.) - C	USA	10/28	AC	T-DS	32 × 6 × 6	1 1/4 × 1/4 × 1/4
Allentown - C	USA	13/31	AC	T-DS	38 × 6 × 6	1 1/2 × 1/4 × 1/4
Bagotville - M	Canada	11/29	PCC	T-PGWC	N/A	N/A
Bangor - C	USA	15/33	PCC	T-DS	32 × 6 × 6	1 1/4 × 1/4 × 1/4
Cedar Rapids - C	USA	8/26	AC	T-DS	32 × 6 × 6	1 1/4 × 1/4 × 1/4
Cedar Rapids - C	USA	13/31	AC	T-DS	32 × 6 × 6	1 1/4 × 1/4 × 1/4
Chattanooga - C	USA	2R/20L	AC	T-DS	38 × 6 × 6	1 1/2 × 1/4 × 1/4
Chicago O'Hare - C	USA	14L/32R	AC	T-DS	32 × 6 × 6	1 1/4 × 1/4 × 1/4
Chicago O'Hare - C	USA	14R/32L	AC	T-DS	32 × 6 × 6	1 1/4 × 1/4 × 1/4
Chicago O'Hare - C	USA	9R/27L	USA	T-DS	32 × 6 × 6	1 1/4 × 1/4 × 1/4
Cleveland Hopkins - C	USA	10L/28R	AC	T-DS	38 × 6 × 6	1 1/2 × 1/4 × 1/4
England - M	USA	14/32	PCC	T-DS	51 × 6 × 6 (Skip 610)	2 × 1/4 × 1/4 (Skip 24)
Elsworth - M	USA	12/30	AC	T-DS	38 × 6 × 6	1 1/2 × 1/4 × 1/4
Harry S. Truman - C	USA	9/27	AC	T-DS	51 × 10 × 6	2 × 3/8 × 1/4
Jacksonville Int. - C	USA	7/25	AC	T-DS	51 × 6 × 6	2 × 1/4 × 1/4
John F. Kennedy - C	USA	13L/31R	AC	T-DS	38 × 10-5 × 5	1 1/2 × 3/8-3/16 × 3/16
John / Kennedy - C	USA	4L/22R	PCC/AC	T-DS	38 × 10-5 × 5	1 1/2 × 3/8-3/16 × 3/16
Lawton - C	USA	17/35	PCC	T-PG	51 × 6 × 3	2 × 1/4 × 1/8
Los Angeles Int. - C	USA	6R/24L	PCC/AC	T-DS	38 × 6 × 6	1 1/2 × 1/4 × 1/4
Louisville - C	USA	1/19	PCC	T-PGWB	N/A	N/A
Memphis Int. - C	USA	17L/35R	PCC	T-PGWB	N/A	N/A
Minneapolis - C	USA	11R/29L	PCC/AC	T-DS	32 × 6 × 6	1 1/4 × 1/4 × 1/4
Newark - C	USA	4R/22L	AC	T-DS	38 × 10-5 × 5	1 1/2 × 3/8-3/16 × 3/16
Patrick Henry Field - C	USA	2/20	PCC	T-PGWC	13 × 3 × 3	1/2 × 1/8 × 1/8
Pittsburg - C	USA	10L/28R	PCC	T-DS	32 × 6 × 6	1 1/4 × 1/4 × 1/4
Ponca City - C	USA	17/35	PCC	T-PG	51 × 6 × 3	2 × 1/4 × 1/8
Washington Nat. - C	USA	18/36	AC	T-DS	32 × 6 × 6	1 1/4 × 1/4 × 1/4

TABLE 11.- GROOVED RUNWAYS CONSTRUCTED BEFORE 1971

Airport	Country	Runway	Surface	Grooving technique		Groove pattern, w × d
						in.
Arlanda - C	Sweden	N/A	PCC	N/A		1 × 1/8 × 1/8
Beaumont - C	USA	11/29	PCC	T-PC		2 × 1/4 × 1/4
Boston Logan - C	USA	4L/22R	AC	T-DC		2 1/4 × 1/4 × 1/4
Boston Logan - C	USA	15R/33L	AC	T-DC		2 1/4 × 1/4 × 1/4
Cannon - M	USA	3/21	PCC	T-DC		(Skip 24)
Charlotte - C	USA	5/23	PCC/AC	T-DC		1 1/4 × 1/4 × 1/4
Chicago O'Hare - C	USA	9L/27R	AC	T-DC		1 1/4 × 1/4 × 1/4
Chicago O'Hare - C	USA	4L/22R	AC	T-DC		1 1/4 × 1/4 × 1/4
Denver Stapleton - C	USA	17L/35R	PCC	T-DC		2 × 1/4 × 1/4
Des Moines Mun. - C	USA	12L/30R	AC	T-PC		1 1/4 × 1/4 × 1/4
Dunedin - C	New Zealand	N/A	N/A	N/A	N/A	N/A
Elmira - C	USA	10/28	AC	T-DC		1 1/4 × 1/4 × 1/4
Erie - C	USA	6/24	AC	T-DC		2 × 1/4 × 1/4
Fort Lauderdale - C	USA	9L/27R	AC	T-DC		1 1/2 × 1/4 × 1/4
Grand Forks - M	USA	17/35	PCC	T-DC		2 × 1/4 × 1/4
Houston Int. - C	USA	14/32	PCC	T-PC		2 × 1/4 × 1/4
Invercargill - C	New Zealand	N/A	N/A	N/A	N/A	N/A
Kansas City Int. - C	USA	9/27	PCC	T-DC		1 1/4 × 1/4 × 1/4
Kansas City Int. - C	USA	1/19	PCC/AC	T-PC		1 1/4 × 1/4 × 1/4
Kincheloe - M	USA	15/33	PCC	T-DC		2 × 1/4 × 1/4
Knoxville - C	USA	4L/22R	PCC	T-PC/R		N/A
Lubbock Int. - C	USA	8/26	PCC	T-DC		1 1/4 × 1/4 × 1/4
Monroe (La.) - C	USA	4/22	PCC	T-PC		1/2 × 1/4 × 1/8
New Haven - C	USA	2/20	AC	T-PC		1 7/8 × 1/4 × 1/4
Pittsburg - C	USA	14/32	PCC/AC	T-DC		1 1/4 × 1/4 × 1/4
Pittsburg - C	USA	10R/28L	PCC	T-DC		1 1/4 × 1/4 × 1/4
San Antonio - C	USA	12R/30L	PCC	T-PC		2 × 1/4 × 1/4
Tallahassee - C	USA	18/36	AC	T-DC		1 × 1/4 × 1/4
Tampa - C	USA	18R/36L	AC	T-DC		1 1/4 × 1/4 × 1/4
Washington Nat. - C	USA	15/33	AC	T-DC		1 1/4 × 1/4 × 1/4
Wilkes-Barre - C	USA	4/22	AC	T-PC		1 1/2 × 1/4 × 1/4
Victoria Int. - C	Canada	N/A	N/A	N/A	N/A	N/A
Zurich - C	Switzerland	N/A	N/A	N/A	N/A	N/A

TABLE 12.- GROOVED RUNWAYS CONSTRUCTED DURING 1971

Airport	Country	Runway	Surface	Grooving technique		Groove pattern,
						in.
Albany County - C	USA	N/A	AC			
Boston Logan - C	USA	N/A	AC			
Cumberland (Md.) - C	USA	N/A				
Jackson County (W.Va.) - C	USA	N/A				
Lihue (H.I.) - C	USA	N/A	AC			
NASA Kennedy - C	USA		PCC			
Raleigh Heights (W.Va.) - C	USA	N/A	PCC/AC			
Wood County (W.Va.) - C	USA	N/A	AC			

219

TABLE 13.- DBV SDR AND NASA GREASE TEST ATD OBTAINED ON RUNWAYS

EVALUATED JULY 1974 TO DECEMBER 1974 BY AFCEC
[From reference 28]

Airfield	Runway	Surface	Touchdown area, rubber deposits			Trafficked, no rubber			Untrafficked, no rubber		
			SDR (a)	ATD mm	ATD in.	SDR (a)	ATD mm	ATD in.	SDR (a)	ATD mm	ATD in.
Travis	21L	PCC	5.79	0.3759	0.0148	2.28	0.9677	0.0381	----	----	----
Fairchild	23	PCC	4.75	.1092	.0043	1.97	.4318	.0170	1.97	0.2769	0.0109
Castle	30	AC	4.60	.1448	.0057	2.00	--	----	1.59	.8306	.0327
Loring	01	AC	4.58	.1499	.0059	1.99	.4032	.0143	----	----	----
Travis	21R	AC	4.01	.3632	.0143	2.71	.4140	.0163	2.18	.5537	.0218
McGuire	24	AC	3.92	.1575	.0062	1.93	.3073	.0121	1.43	----	----
Torrejon	23	AC	3.85	.1626	.0064	1.85	1.1633	.0458	1.50	.6452	.0254
Mather	22L	PCC/AC	3.75	.2083	.0082	1.86	.4140	.0163	----	----	---
Blytheville	17	PCC	3.73	----	----	2.45	----	----	1.57	----	----
Dover	01	PCC/AC	3.62	----	----	1.73	----	----	1.47	----	----
Scott	31	AC	3.61	----	----	1.83	----	----	1.47	----	----
Robbins	32	PCC	3.59	.2896	.0114	2.01	.4928	.0194	----	----	----
Cannon	21	PCC/GPCC	3.59	----	----	1.73	----	----	1.43	----	----
Rickenbacker	23L	PCC	3.40	.2769	.0109	2.05	.4851	.0190	1.66	.5055	.0199
Homestead	05	PCC	3.37	.2235	.0088	1.92	.7061	.0278	2.17	.4140	.0163
Grissom	22	AC	3.23	.1041	.0041	1.66	.5055	.0199	1.60	.5283	.0208
Charleston	15	AC/PCC	3.21	.2159	.0085	2.55	----	----	2.21	.3302	.0130
Zaragosa	31R	AC	2.93	.2591	.0102	1.41	.5817	.0229	1.32	.5537	.0218
Mather	22R	AC	2.90	.2083	.0082	2.18	.4150	.0163	1.67	----	----
Andrews	01L	PCC	2.89	.4064	.0160	2.14	.5588	.0220	2.28	.9398	.0370
Charleston	21	AC	2.79	.3327	.0131	1.88	.5817	.0229	----	----	----
Shaw	4L	PCC/GPCC/AC	2.77	.3429	.0135	1.79	.7264	.0286	1.52	.4851	.0191
McConnel	18R	AC	2.77	----	----	2.03	----	----	----	----	----
Hector	35	PCC	2.72	----	----	1.95	.6121	.0241	1.89	----	----
Dover	31	AC	2.66	----	----	1.80	----	----	1.28	----	----
Columbus	13L	PCC/AC	2.62	.4851	.0191	1.80	.4851	.0191	1.71	.5537	.0218
Glasgow	28	PCC	2.61	.3632	.0143	2.11	.2464	.0097	2.37	.1727	.0068
Andrews	01R	PCC/AC	2.60	.3302	.0130	1.73	.635	.025	1.82	.686	.027
England	14	PCC	2.54	----	----	2.66	.5055	.0199	----	----	----
Aviano	05	AC	2.51	.889	.035	1.73	1.168	.046	1.64	.965	.038
R. Gebaur	36	PCC/AC	2.50	----	----	2.22	----	----	2.29	----	----
Vance	17R	PCC/AC/GPCC	2.50	----	----	1.50	----	----	1.53	----	----
Soesterberg	28	AC	2.42	----	----	2.20	----	----	1.52	----	----
Columbus	13R	PCC	2.40	----	----	2.28	----	----	----	----	----
England	16	PCC/AC	2.40	.6452	.0254	2.57	.6375	.0251	2.40	----	----
Moody	18R	PCC/AC	2.38	.4851	.0191	1.48	1.1633	.0458	1.52	1.1633	.0458
Zweibrucken	03	AC	2.34	.5283	.0208	1.34	.5941	.0234	1.16	.7264	.0286
Bentwaters	25	PCC/AC	2.33	.4851	.0191	1.34	1.1633	.0458	1.57	.6121	.0241
Moody	18L	PCC/AC	2.32	.3073	.0121	1.66	.5283	.0208	1.45	.6121	.0241
Craig	32L	PCC/AC	2.27	.4318	.0170	1.50	.3327	.0131	1.42	1.3462	.0530
Rickenbacker	23R	AC	2.26	----	---	1.95	--	--	----	----	----
Vance	17C	PCC/AC	2.25	.1448	.0057	1.44	.5941	.0234	1.52	----	----
Columbus	13C	PCC/AC	2.22	----	----	1.63	----	--	2.13	----	----
Woodbridge	27	AC	2.22	----	----	1.53	----	----	2.01	----	----
Niagara Falls	28	AC	2.12	.1641	.0066	1.??	.4851	.0191	1.28	.6121	.0241
Vance	17L	PCC	2.10	----	----	2.??	.481	.0191	1.34	----	----
McConnel	18L	AC	2.03	----	----	1.25	----	----	----	----	----
McGuire	36	PCC/AC	2.00	.1??	.0005	1.66	.6024	.0121	1.36	----	----
Myrtle Beach	17	PCC/AC	1.90	.4013	.0158	1.57	.5583	.0208	1.52	.6452	.0254
Cannon	30	PCC/AC	2.00	----	----	1.56	--	--	1.51	----	----
Shaw	04R	PCC/PGWC/PCC	1.99	.3150	.0124	1.14	.1534	.0063	1.35	----	----
Erding	26	PCC	1.93	.2184	.0086	2.??	.4?5?	.0154	?.??	.44??	.0176
Hurlburt	35	PCC/AC	1.89	.0355	.0109	1.02	.6833	.0269	1.34	.8306	.0327
McChord	34	AC	1.87	.??47	.130?	.???	.???	.???	.???	.???	.0306

a DBV SDR 3 minutes after wetting.

220

TABLE 14.- DBV SDR OBTAINED ON RUNWAYS EVALUATED JANUARY TO JUNE 1975 BY AFCEC
[From reference 38]

Airfield	Runway	Rubber-coated touchdown areas				Trafficked, no rubber (wheel paths)		Untrafficked, no rubber (runway edge)	
		Primary		Secondary					
		SDR (a)	Surface	SDR (a)	Surface	SDR (a)	Surface	SDR (a)	Surface
Palmdale	07/25	6.12	PCC	2.55	PCC	2.31	PCC	----	PCC/AC
March	13/31	5.19	PCC	2.46	PCC	2.21	PCC	----	AC
Barksdale	14/32	4.73	AC	3.70	AC	1.84	AC	1.40	AC
Norton	05/23	4.58	PCC	2.75	PCC	2.19	PCC	2.40	PCC
bWebb	17L/35R	2.95	PCC/AC	1.51	PCC/AC	4.51	AC	----	AC
Dyess	16/34	3.32	PCC	4.46	PCC	2.61	PCC	----	AC
Carswell	17/35	3.78	AC/PCC	4.11	PCC	2.36	AC/PCC	1.32	AC
Elmendorf	05/23	3.52	AC	1.92	AC	2.95	AC	1.52	AC
Reese	17R/35L	3.03	PCC	1.85	PCC/AC	1.80	PCC/AC	1.72	AC
Davis Monthan	12/30	2.98	AC	2.50	PCC	1.54	AC	1.39	AC
Palmdale	04/22	2.88	AC	2.43	AC	1.82	AC	2.05	AC
bWebb	17R/35L	2.82	PCC/AC	2.65	PCC/AC	2.69	AC	----	AC
Laughlin	13C/31C	2.70	PCC/AC	1.88	PCC/AC	1.69	AC	1.75	AC
Randolph	14L/32R	2.65	PCC	2.16	PCC	2.05	PCC	2.27	PCC
Yokota	18/36	2.61	PCC	1.95	PCC	1.91	PCC	1.94	PCC
Reese	17C/35C	2.37	AC	2.59	AC	2.15	AC	2.06	AC
Williams	12L/30R	2.52	PCC/AC	1.57	AC	1.68	AC	1.65	AC
cWilliams	12C/30C	2.39	PCC	----	----	----	----	----	----
Williams	12R/30L	2.36	PCC	2.16	PCC	2.22	PCC	2.03	PCC
Laughlin	13L/31L	2.15	PCC/AC	2.31	PCC/AC	1.35	AC	----	AC
Elmendorf	15/33	2.21	AC	1.86	AC	2.05	AC/PCC	----	AC
Laughlin	13R/31L	1.87	AC	2.20	AC	1.56	AC	----	AC
Randolph	14R/32L	2.13	PCC/AC	1.90	PCC	1.48	PCC/AC	1.39	PCC/AC
dVandenberg	12/30	1.59	AC	1.54	AC	1.60	AC	1.32	AC
Reese	17L/35R	----	PCC/AC	----	PCC/AC	1.39	AC	----	AC

aAverage DBV SDR 3 minutes after wetting.

bAsphalt emulsion diluted with water applied to asphaltic concrete.

cRunway under construction.

dNew runway surface.

TABLE 15.- DBV SDR OBTAINED AT 10 CIVIL AIRPORTS

EVALUATED NOVEMBER 1971 TO APRIL 1972 BY FAA.
[From reference 29]

Airport	Runway	Centerline area, rubber deposits				Trafficked, no rubber (wheel path)	
		SDR (a)	Surface	SDR (a)	Surface	SDR (a)	Surface
St. Louis Int.	12R/30L	4.79	12R:??	4.54	30L:??	2.90	AC
	6/24	_.48	24:PCC	2.13	6:PCC	1.85	PCC
	12L/30R	1.93	30L:PCC	1.35	12L:W PCC	1.81	PCC
	17/35	1.77	17:PCC	1.63	35:PCC	1.79	PCC
Miami Int.	9R/27L	4.44	9R:AC	-.88	27L:AC	1.81	AC
	9L/27R	2.88	9L:AC	1.98	27R:AC	1.72	AC
	12/30	2.01	12:AC	1.75	30:AC	1.56	AC
	17/35	1.35	17:AC	1.32	35.AC	1.33	AC
Memphis Int.	17L/35R	3.52	17:PCC	3.51	35R:PCC	2.44	PCC
	9/27	1.83	27:AC	1.58	9:AC	1.32	AC
	[b]17R/35L	----	----	----	----	1.47	PCC
	3/21	1.18	3:AC	1.16	21:AC	1.17	AC
New Orleans Int.	10/28	3.76	10:PCC	2.22	28:AC	2.26	PCC
	1/19	3.22	19:PCC	3.03	1:AC	2.17	PCC
	5/23	1.22	23:AC	----	5:AC	1.32	AC
Atlanta W. B. Hartsfield	9L/27R	2.88	9L:WCPCC	2.26	27R:WCPCC	1.38	WCPCC
	15/33	2.21	33:AC	1.72	15:AC	1.50	AC
	9R/27L	2.03	27L:GPCC	1.24	9R:GPCC	1.12	GPCC
	3/21	1.69	21:AC	1.52	3:AC	1.36	AC
Jacksonville Int.	7/25	2.77	7:PCC	2.59	25:PCC	2.12	PCC
	13/31	2.65	31:PCC	2.33	13:PCC	1.97	PCC
Greater Cincinnati	18/36	2.45	36:AC	1.93	18:AC	1.73	AC
	9R/27L	2.38	27L:AC	2.09	9R:AC	1.77	AC
	9L/27R	1.80	9L:PCC	1.15	27R:PCC	1.25	PCC
Charlotte Douglas	18/36	2.32	36:AC	1.39	18:AC	1.46	AC
	5/23	1.21	5:AC	1.38	23:AC	1.22	AC
Nashville Int.	13/31	2.12	31:AC	1.71	13:AC	1.69	AC
	2L/20R	2.08	20R:AC	1.52	2L:AC	2.04	GAC
	2R/20L	1.30	20L:AC		2:AC	1.24	AC
Charleston Kanawha	5/23	1.33	5:PCC	1.16	5:GPCC	1.09	GPCC
	14/32	1.20	32:AC	1.09	14:AC	1.16	AC

[a]Average DBV SDR.
[b]New surface; under construction.

TABLE 16.- DBV AND AIRCRAFT SDR OBTAINED ON TRANSVERSE GROOVED RUNWAY SURFACES WITH AND WITHOUT RUBBER CONTAMINATION

[From reference 34]

Airport	Date tested	Runway	Rubber deposits	SDR DBV	SDR Aircraft	Surface; date installed	Groove pattern; date installed	Source
Cannon AFB	11/73	3/21	Heavy None	[a]3.59 to 2.46 1.74	—	305 m (1000 ft) PCC, 2438 m (8000 ft) GPCC, 305 m (1000 ft) PCC; date unknown	51 × 6 × 6 mm (2 · 1/4 × 1/ in.), groove 610 mm (2 ft) skip 610 mm (2 ft); 1973	Reference 8
Shaw AFB	7/74	4L/27R	Med-lt None	2.77 to 1.97 1.79	— —	305 m (1000 ft) PCC, 1367 m (3500 ft) GPCC, 1370 m (4500 ft) GAC, 305 m (1000 ft) PCC; date unknown	51 × 6 × 6 mm (2 × 1/4 × 1/4 in.), groove 610 mm (2 ft) skip 610 mm (2 ft); 1971	Reference 8
Vance AFB	12/73	17R/35L	Lt-med None	[a]2.50 [a]1.50	—	457 m (1500 ft) PCC, 853 m (2800 ft) GPCC, 1036 m (3400 ft) AC; date unknown	51 × 6 × 6 mm (2 × 1/4 × 1/4 in.); 1973	Reference 8
Houston Int.	[b]6/70	8L/26R	Heavy-med	3.46 to 2.94	—	PCC; date unknown	Ungrooved	Unpublished
	10/71		Lt-none	2.08 to 2.52	[c]1.91 to 2.[?]		Ungrooved	
	2/25/71		None Heavy	1.13 to 1.44 2.27 to 2.43	[d]1.10 to 1.53 —		51 × 6 × 6 mm (2 × 1/4 × 1/4 in.); 2/24/71	Unpublished
Miami Int.	3/73	9R/27L 9L/27R	Heavy None Heavy-med	4.62 to 3.51 2.43 3.16 to 2.38	— — —	AC overlay; 11/72	Ungrooved	Unpublished
	5/73	9R/27L 9R/27L 9L/27R	Heavy-lt None None	2.42 to 1.51 1.51 1.22	— — —		38 × 10 × 6 mm (1 1/2 × 1/4 × 1/4 in.) [e]1973	Unpublished
John F. Kennedy	7/69 7/69 10/71	4R/22L	None Heavy Lt-none	1.75 2.20 1.47 to 1.80	[f]1.57 1.86 [c]1.50 to 1.67	PCC; 1959	38 × 10-5 ... mm (1 3/8 × 3/8-3/16 × 1/8 in.); 1967	Reference 1 Unpublished
Atlanta Int.	11/71	9R/27L	Heavy-med None	2.39 to 1.24 1.12	—	PCC; date unknown	32 × 10-3 × 6 mm (1 1/4 × 3/8-1/8 × 1/4 in.); 1969	Reference 10
Nashville Int.	4/72	2L/20R	Lt None	2.06 to 1.82 2.04	— —	AC; date unknown	32 × 6 × 6 mm (1 1/4 × 1/4 × 1/4 in.); 1970	Reference 10
Harry S. Truman	6/70	9/27	Heavy None Heavy None	2.26 1.40 1.69 1.18	— —	AC; date unknown	Ungrooved 38 × 6 × 6 mm (1 1/2 × 1/4 × 1/4 in.); 4/70	Unpublished
Stennis-Johnson AFB	7/69	8/26	None Heavy-lt	1.45 1.50	[f]1.48 1.47	PCC, 1960	51 × 6 × 6 mm (2 1/4 × 1/4 × 1/4 in.), groove 610 mm (2 ft) skip 610 mm (2 ft); 1968	Reference 1

[a] DBV test area contained both grooved and ungrooved pavements.

[b] Rubber removed after test.

[c] B-727.

[d] DC-9.

[e] 9L/27R being grooved at time of test.

[f] C-141.

TABLE 17.- DBV SDR AND NASA GREASE TEST ATD OBTAINED ON RUNWAYS EVALUATED BY THE FAA JOINT APPLICATION - RUNWAY FRICTION CALIBRATION AND PILOT INFORMATION PROGRAM DURING AUGUST AND SEPTEMBER 1975

Airport	Runway	Surface (a)		Touchdown area, rubber deposits			Trafficked, no rubber		
				DBV SDR	AFD		DBV SDR	AFD	
					mn	in.		mn	in.
Allentown	13	GAC	1.0	1.07	1.56	0.061	1.08	1.48	0.058
	31			1.29	1.49	.059	1.08	1.48	.058
	6	GAC	0.75	2.07	1.52	.060	1.66	1.48	.058
	24			1.71	1.60	.063	1.66	1.48	.058
Akron-Canton	1	AC	1.4	2.71	0.229	0.009	2.01	0.305	0.012
	19			2.19	.229	.009			
	5	AC	1.4	1.32	.254	.010	1.47	.330	.013
	23			1.26	.330	.013			
Boston Logan	4L	GAC	1.0	1.12	---	---	0.90	---	---
	22R			1.00	---	---	.90	---	---
	4R	GAC	1.0	1.62	---	---	1.96	---	---
	22L			1.75	---	---	1.96	---	---
	15R	GAC	1.0	1.39	---	---	2.00	---	---
	33L			2.50	---	---	2.00	---	---
Buffalo	5	AC	1.0	2.06	0.838	0.033	.30	0.864	0.034
	23			2.68	1.092	.043	2.30	.864	.034
	b14								
	b32								
Burlington	15	AC	1.0	2.09	0.559	0.022	1.75	0.564	0.023
	33			2.04	.508	.020			
Charleston, W.Va.	5	GPCC	0.8	1.27	0.211	0.008	1.37	0.221	0.009
	23			1.42	.165	.007			
	b14								
	b32								
Cincinnati	18	GAC	1.5	1.51	1.346	0.053	2.05	1.016	0.040
	36			1.70	1.270	.050			
	9R	GPCC	1.5	1.3	.838	.033	1.38	1.194	.047
	27L			1.78	1.270	.050			
Cleveland	5R	GAC	1.3	1.7	0.737	0.029	2.14	1.092	0.043
	23L			2.4	.279	.011			
	10L	GAC	0.8	1.30	1.118	.044	1.57	1.702	.067
	28R			1.39	.737	.029			
Detroit	3L	GPCC	1.0	1.56	1.270	0.050	1.68	1.270	0.050
	21R			1.65	1.270	.050			
	9	PCC/AC 1.0		2.10	.432	.017	1.91	.508	.020
	27			2.77	.076	.003			
Dulles	1L	PCC	1.0	5.11	0.152	0.006	2.98	0.254	0.010
	19R			3.90	.102	.004			
	1R	PCC	1.0	4.48	.229	.009	3.1	.254	.010
	19L			3.12	.279	.011			
Ft. Wayne	4	PCC/AC 0.9		2.00	0.330	0.013	1.59	.533	0.021
	22			2.05	.203	.008			
	9	PCC/AC N/A		1.77	1.016	.040	1.86	.508	.020
	27			1.81	.559	.022			
Grand Rapids	8R	PCC/AC 1.5		2.38	0.254	0.010	1.57	0.127	0.005
	26L			1.96	.254	.010			
Madison	18	PCC	1.5	1.68	0.686	0.027	1.43	1.016	0.040
	36			1.35	1.118	.044			
	13	AC	1.5	1.62	.381	.015	1.54	.127	.005
	31			1.70	.254	.010			

aNumber on right of column represents the runway transverse slope in percent.

bUnder construction.

TABLE 17.- Concluded

Airport	Runway	Surface (a)		Touchdown area, rubber deposits			Trafficked, no rubber		
				DBV SDR	ATD		DBV SDR	ATD	
					mm	in.		mm	in.
Milwaukee	b 1L								
	b 19R								
	7R	PCC	1.0	1.67	0.838	0.033	1.56	0.432	0.017
	25L			3.02	1.118	.044			
Moline	9	AC	1.0	2.34	0.508	0.020	2.65	0.508	0.020
	27			2.77	.102	.004			
	12	PCC	1.0	2.66	.216	.009	2.49	.127	.005
	30			2.91	.152	.006			
Peoria	30	GAC	1.25	1.36	0.965	0.038	1.16	1.397	0.055
	12			1.52	.991	.039			
	4	AC	1.0	1.14	.635	.025	1.43	1.270	.050
	22			1.44	.305	.012			
Philadelphia	9R	AC	1.0	4.99	0.127	0.005	2.47	0.279	0.011
	27L			3.57	.127	.005			
Pittsburg	10R	GAC	1.0	2.15	1.549	0.061	1.63	1.600	0.063
	28L			2.54	1.549	.061			
	10L	GAC	1.5	1.43	1.549	.061	1.35	1.600	.063
	28R			1.49	1.626	.064			
Portland, Maine	11	AC	1.0	1.54	0.737	0.029	1.27	0.737	0.029
	29			1.41	.762	.030			
	18	AC	1.0	1.86	.254	.010	1.77	.279	.011
	36			1.83	.279	.011			
Rochester, N.Y.	10	AC	1.0	1.74	0.559	0.022	1.79	0.356	0.014
	28			2.18	.178	.007			
	4	PCC	1.0	3.68	.102	.004	3.60	.152	.006
	22			4.50	.127	.005			

a Number on right of column represents the runway transverse slope in percent.

b Under construction.

TABLE 18.- U.S. POROUS ASPHALT RUNWAY SURFACE CONSTRUCTION

Year	Airport	Runway	Year	Airport	Runway
1970	Hahn AB - M	11/29	1973	St. Louis Lambert - C	6/24
	RAF Milden Hall - M	1/29	1974	Aberdeen (S. Dak.) - C	13/31
	Wiesbaden AB - M	8/26		Farmington (N. Mex.) - C	7/25
1971	Dallas NAS - M	17/35		Greensboro-High Point - C	14/32
	Gallup (N. Mex.) - C	6/24		Hill AFB - M	14/32
1972	Denver Stapleton - C	8L/26R		Las Vegas (Nev.) - C	7/25
	Denver Stapleton - C	8R/26L		RAF Bentwaters - M	7/25
	Great Falls Int. - C	16/34		RAF Lakerheath - M	6/24
	Hot Springs (Va.) - C	6/24		Roswell (N. Mex.) - C	17/35
	Nashville Metro. - C	2L/20R		Sioux City (Idaho) - C	17/35
	Sioux Falls (N. Dak.) - C	15/33	1975	Boise (Idaho) - C	10R/28L
	Springfield (Mo.) - C	13/31		Jackson Hole (Wyo.) - C	18/36
	Vernal (Utah) - C	16/34		Jamestown (N. Dak.) - C	12/30
	Wichita Mun. - C	N/A		Las Vegas (Nev.) - C	1R/19L
1973	Bellingham (Wash.) - C	16/34		Missoula (Mont.) - C	11/29
	Cedar City (Utah) - C	2/20		Monroe (La.) - C	4/22
	Peas AFB - M	16/34		Pierre (S. Dak.) - C	13/31
	Portland (Maine) - C	11/29			
	RAF Alconbury - M	12/30			
	Rapid City (S. Dak.) - C	14/32			
	Ramstein AB - M	9/27			
	Salt Lake City (Utah) - C	16L/34R			
	Salt Lake City (Utah) - C	16R/34L			
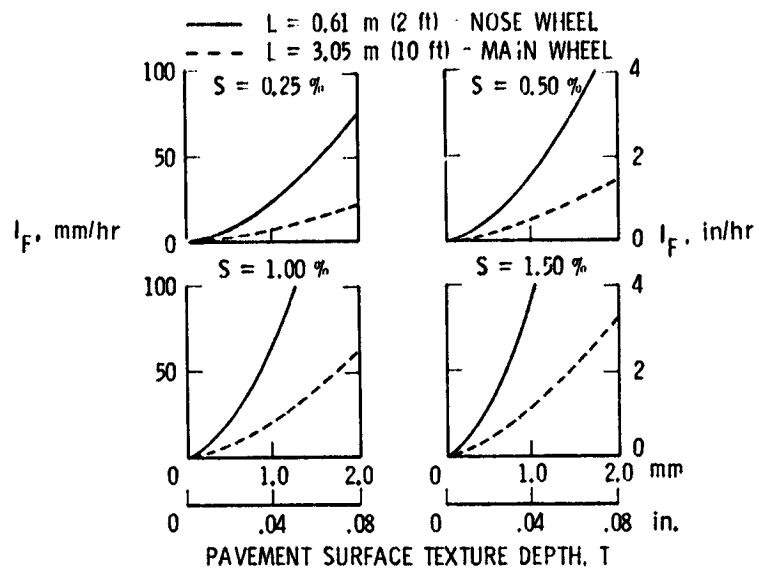
Figure 1.- Rainfall rate required to flood tire path on conventional runway surfaces. Landings on center line.
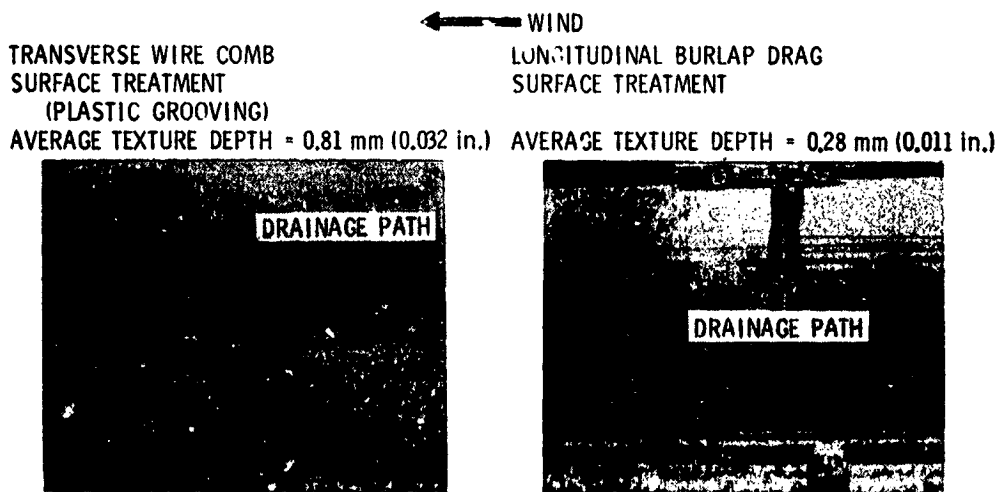
Figure 2.- Water drainage from concrete runway at PHF. Water truck wetting; runway 6/24; wind from 60° at 10 knots.
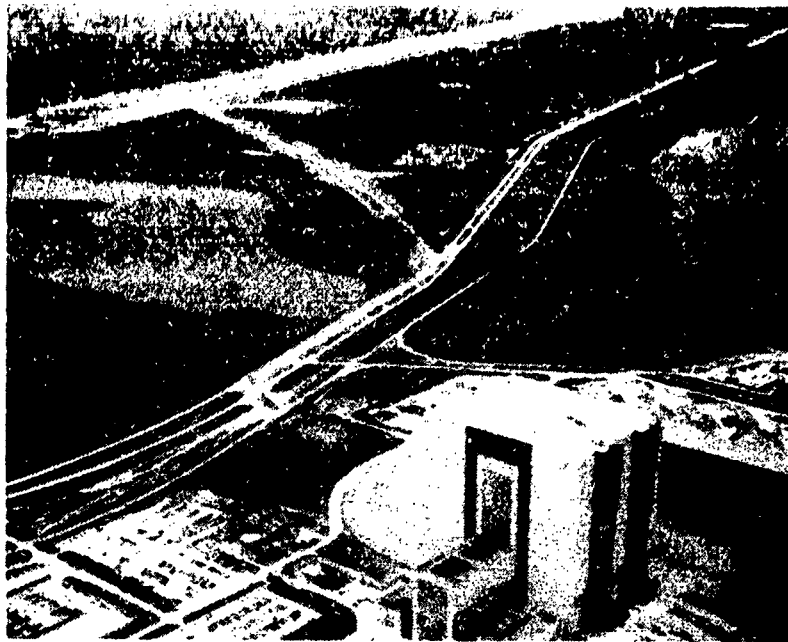
Figure 3.- Space shuttle landing facility at KSC.
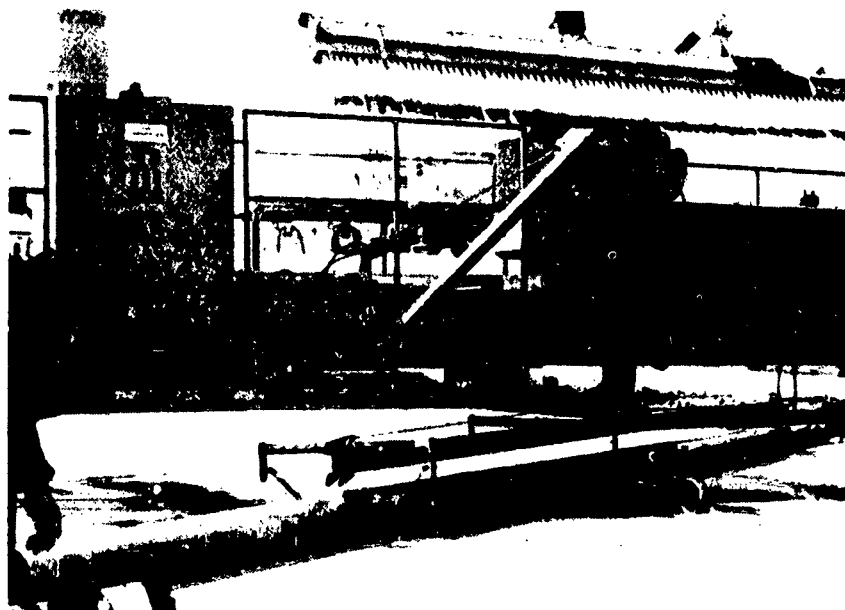
Figure 4.- Space shuttle landing facility at KSC with slip-form
paving equipment, leveling tube, and longitudinal broom.

227

Figure 5.- Space shuttle landing facility at KSC with
pavement grooving machine (diamond blades).
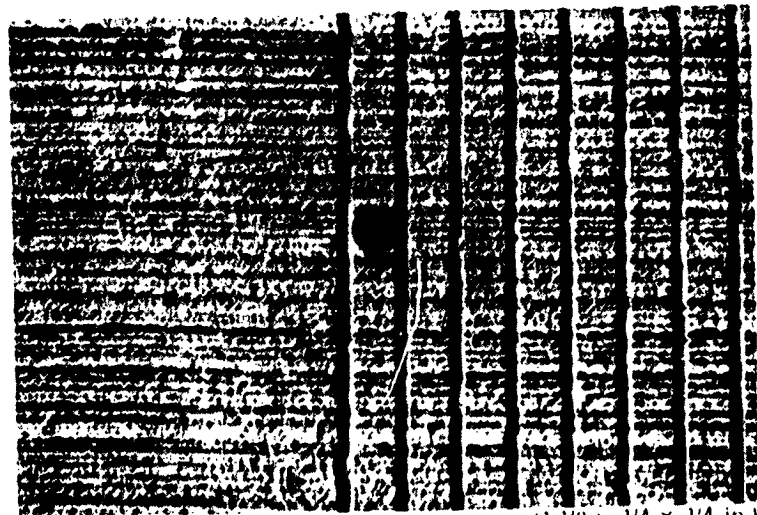
29 × 6 × 6 mm (1 1/8 × 1/4 × 1/4 in.)

LONGITUDINAL BROOM FINISH   TRANVERSE GROOVE PATTERN
ATD = 0.38 to 0.64 mm   ATD = 1.70 to 1.91 mm
(0.015 to 0.025 in.)   (0.067 to 0.075 in.)

Figure 6.- Concrete runway surface texture of
space shuttle landing facility at KSC.

228
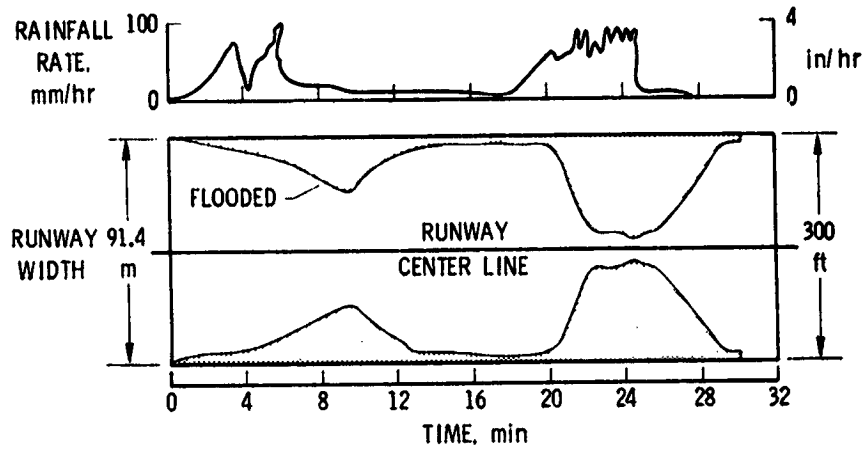
Figure 7.- Surface flooding on space shuttle grooved runway during thunderstorm 6/20/76.

Figure 8.- Water drainage from grooved and ungrooved asphalt. Grooving pattern, $38 \times 6 \times 6$ mm ($1\frac{1}{2} \times \frac{1}{4} \times \frac{1}{4}$ in.).
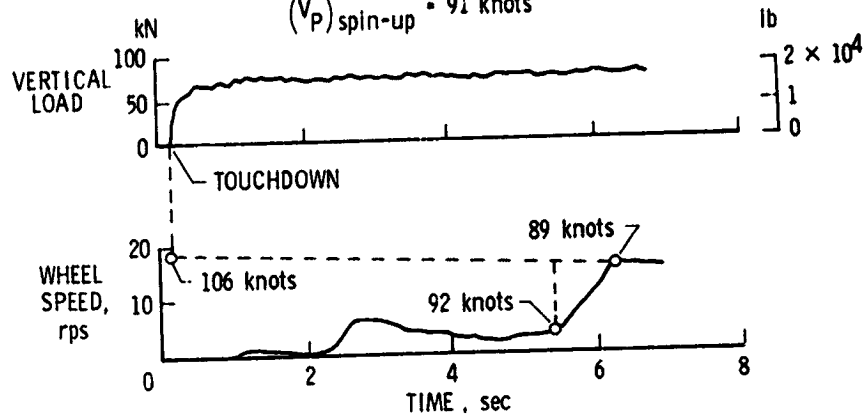
Figure 9.- Delayed wheel spin-up at touchdown
on flooded runway.

Figure 10.- B-737 tire reverted rubber skid patch after
1.8 km (6000 ft) locked-wheel skid on wet smooth
concrete.
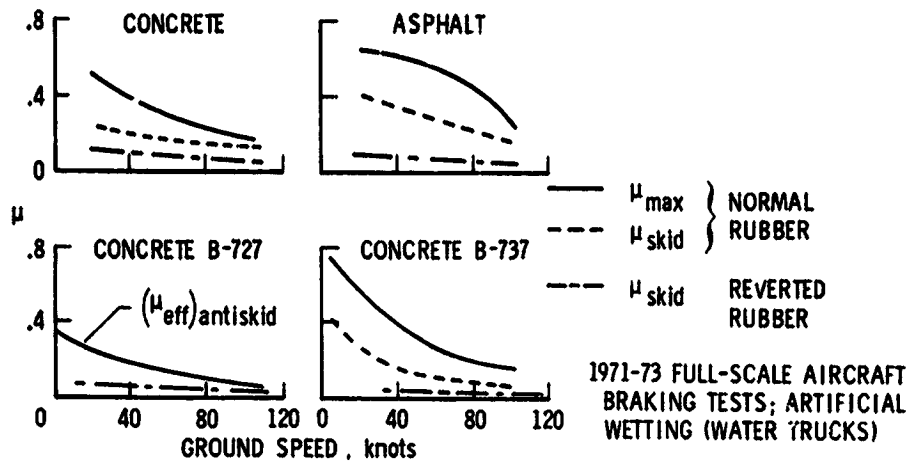
Figure 11.- Aircraft flight test confirmation of reverted
    rubber hydroplaning 1965 NASA track; 32 × 8.8 aircraft
    tire; flooded runway.
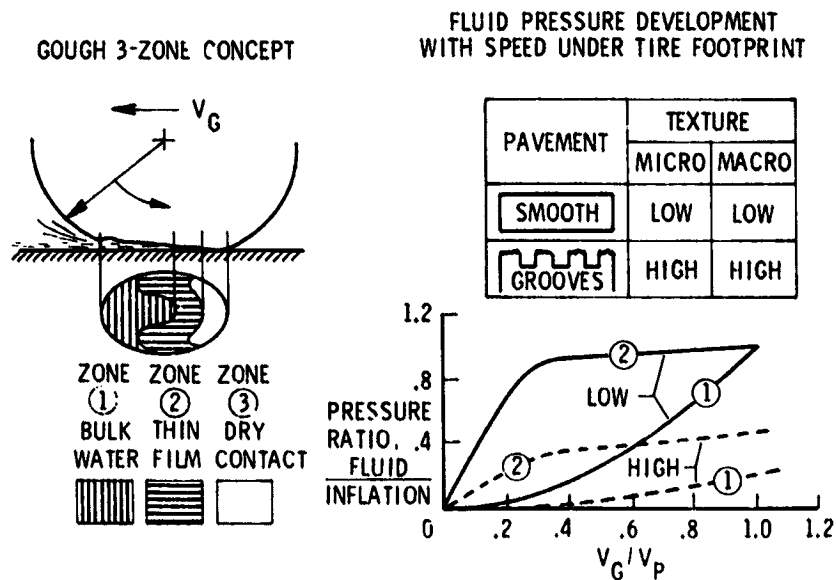
Figure 12.- NASA model for combined viscous and dynamic
                    tire hydroplaning.
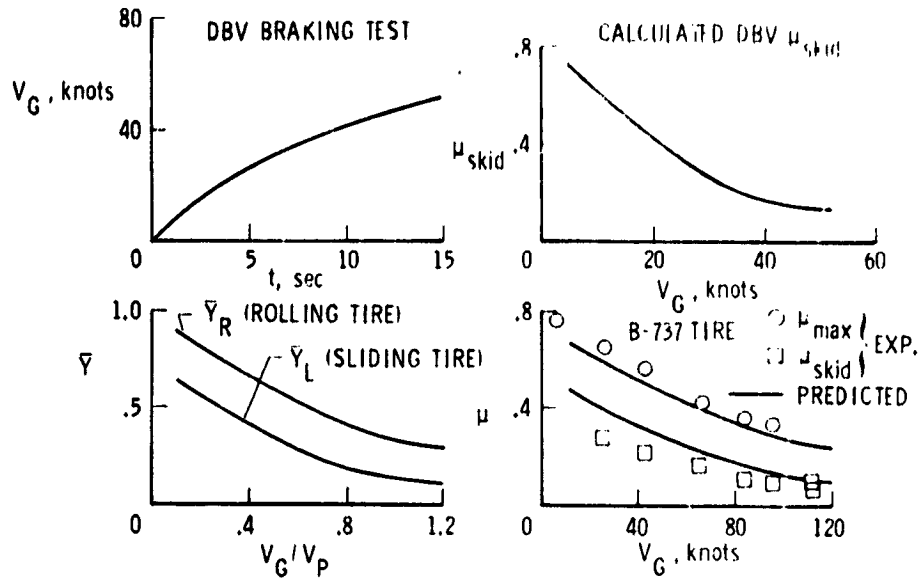
Figure 13.- Prediction of aircraft tire friction coefficient from ground-vehicle braking test on a wet runway by NASA theory.
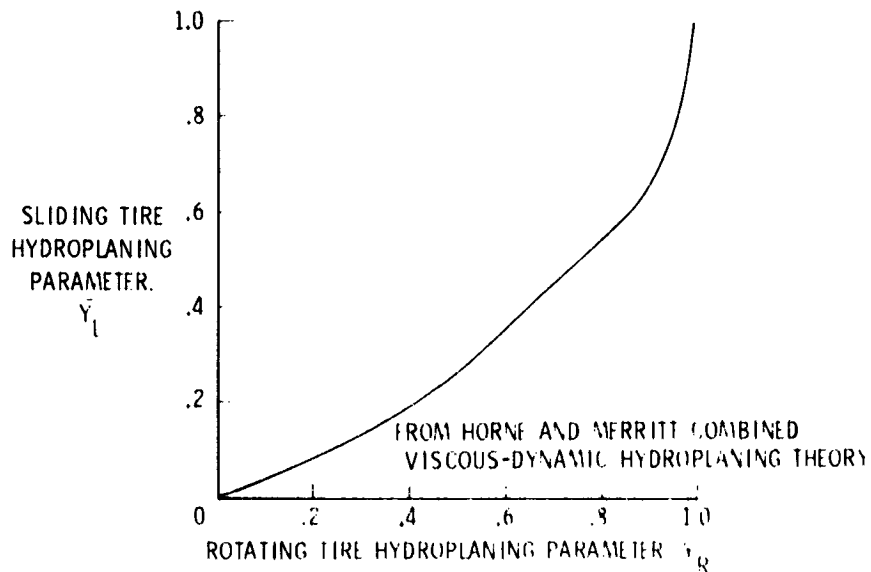
Figure 14.- Empirically derived relationship between sliding $(\bar{Y}_L)$ and rotating $(\bar{Y}_R)$ tire hydroplaning parameters.
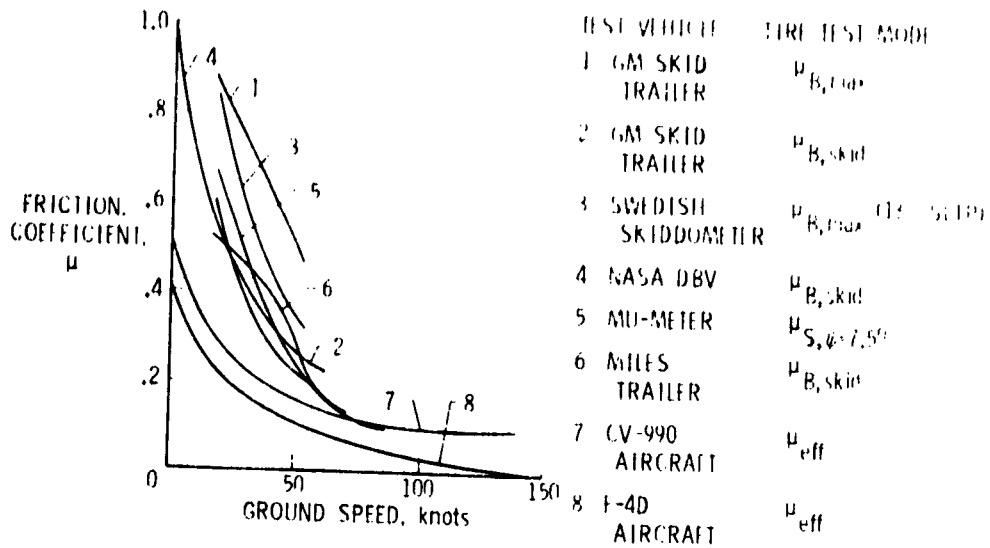
Figure 15.- Aircraft/ground-vehicle correlation problem for wet and puddled smooth concrete surface.
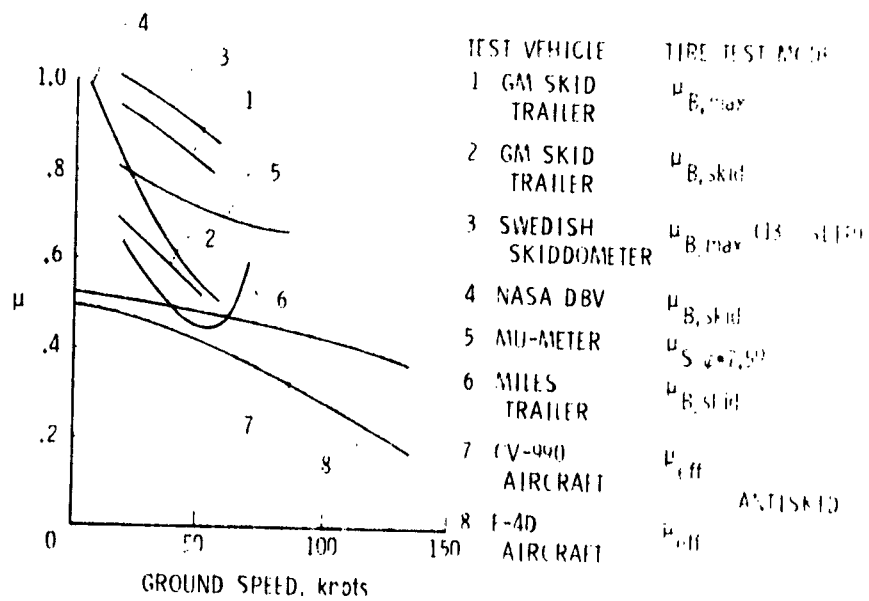
Figure 16.- Aircraft/ground-vehicle correlation problem for wet and puddled grooved asphalt.
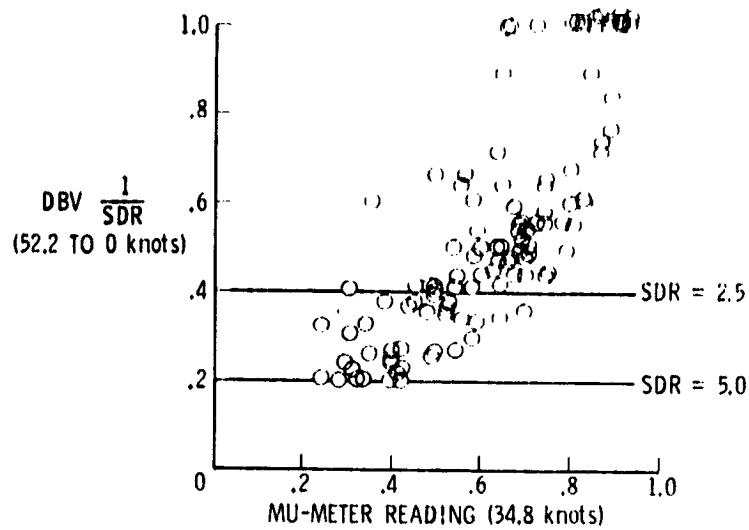
Figure 17.- DBV/Mu-Meter relationship found by
USAF tests (ref. 28).
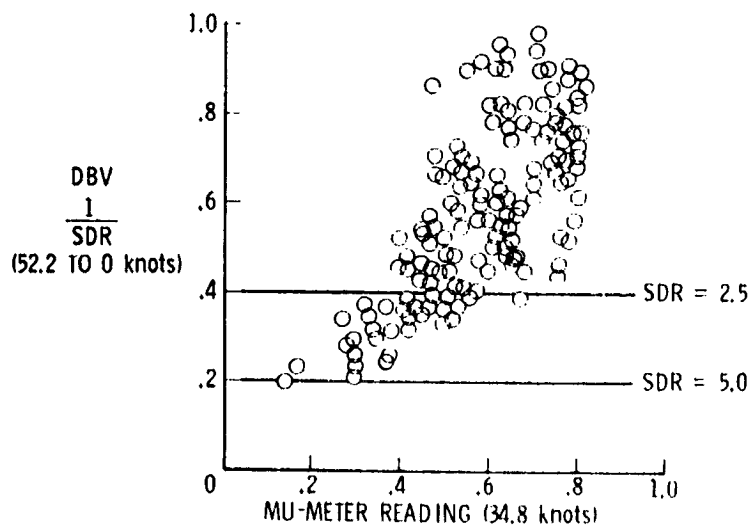
Figure 18.- DBV/Mu-Meter relationship found by
FAA tests on 31 runways.

234
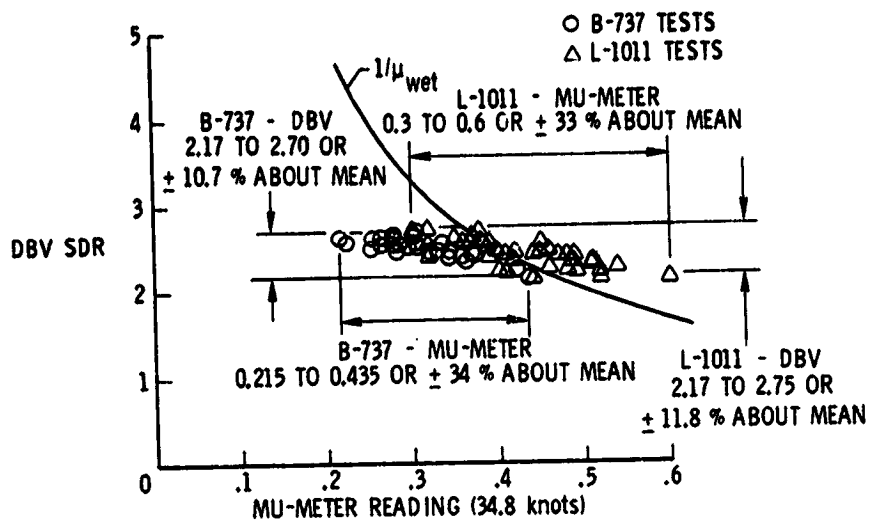
Figure 19.- Comparison of NASA DBV with Mu-Meter.
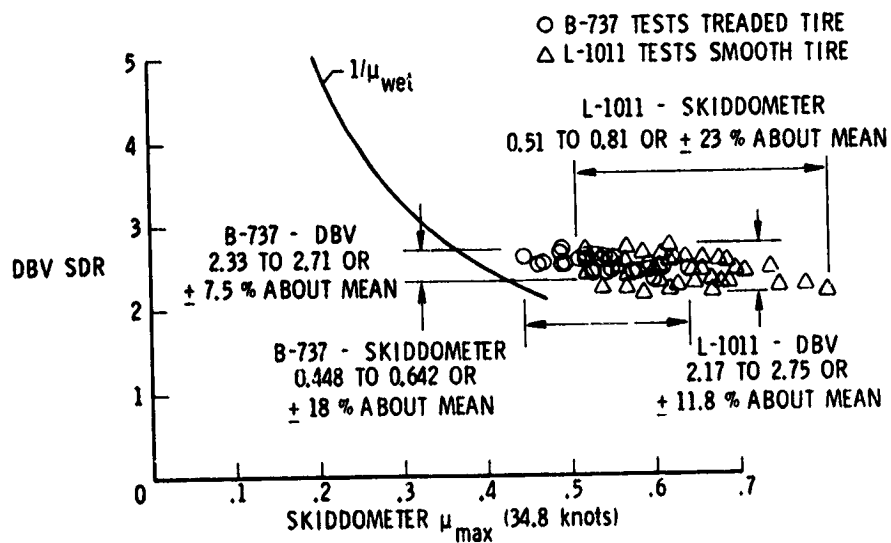
Figure 20.- Comparison of NASA DBV with skiddometer.

235
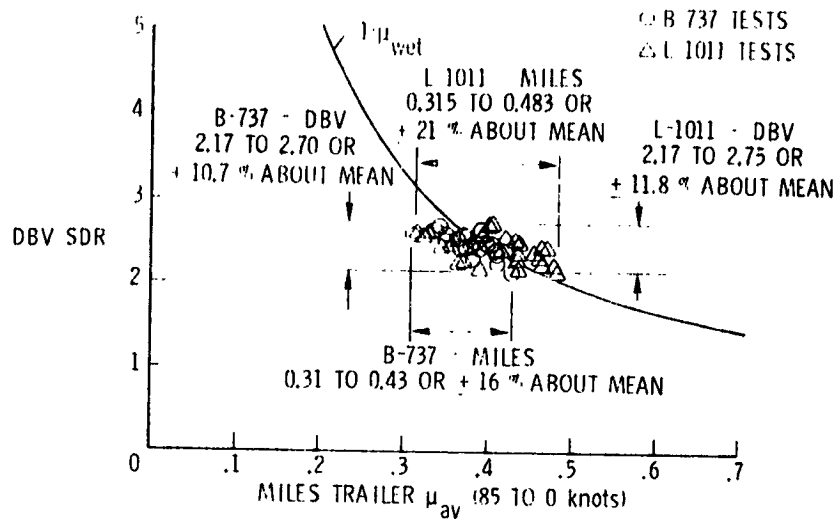
Figure 21.- Comparison of NASA DBV with Miles trailer.
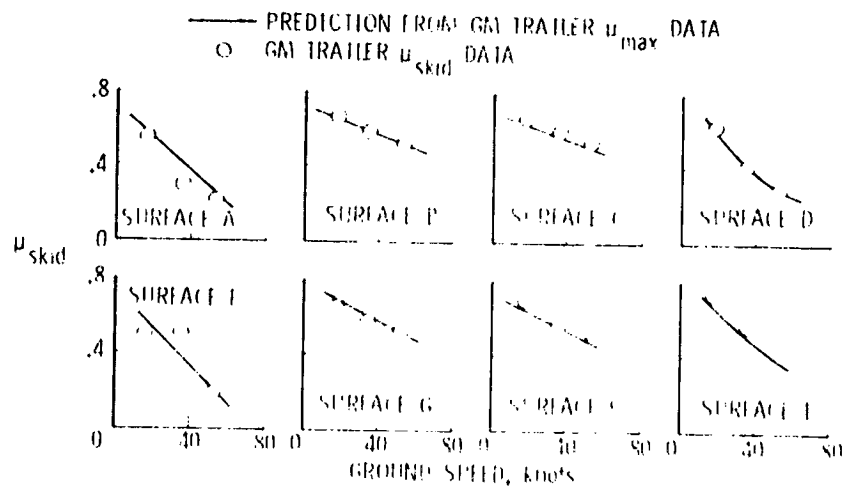
Figure 22.- Prediction of GM trailer μ_{skid} from GM trailer μ_{max} data. ASTM smooth tread tire; data from reference 22.
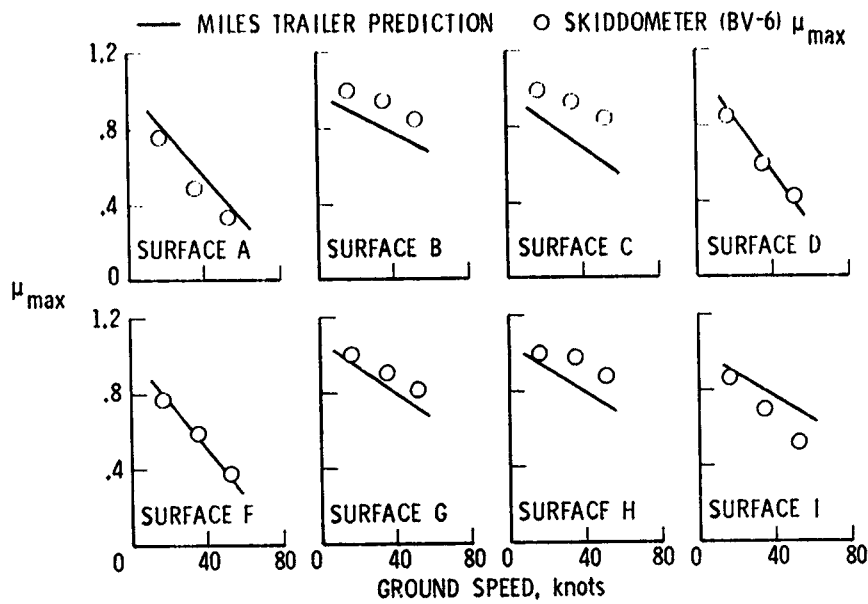
Figure 23.- Prediction of skiddometer μ_{max} from Miles trailer μ_{skid} data. Data from references 21 and 22.
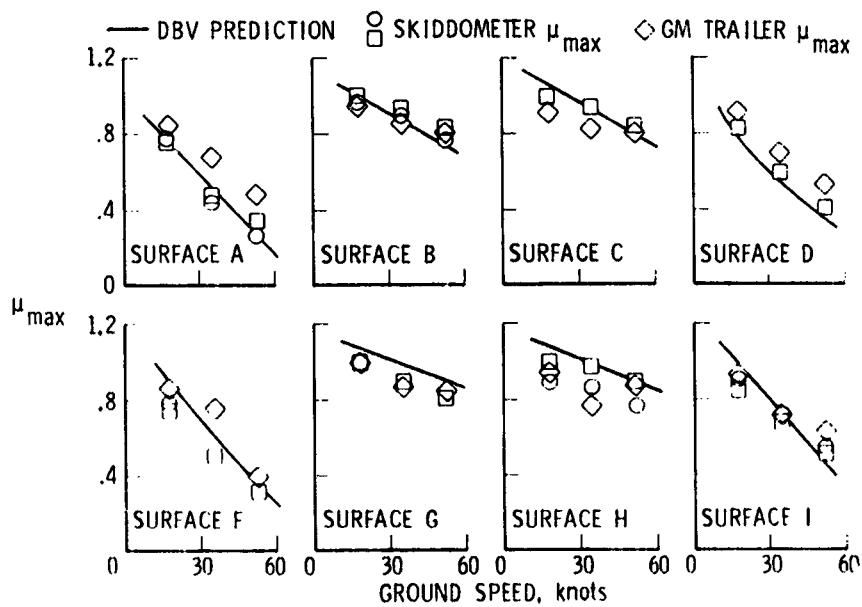
Figure 24.- Prediction of skiddometer and GM trailer μ_{max} from DBV μ_{skid} data. Data from references 21, 22, and 30.

237
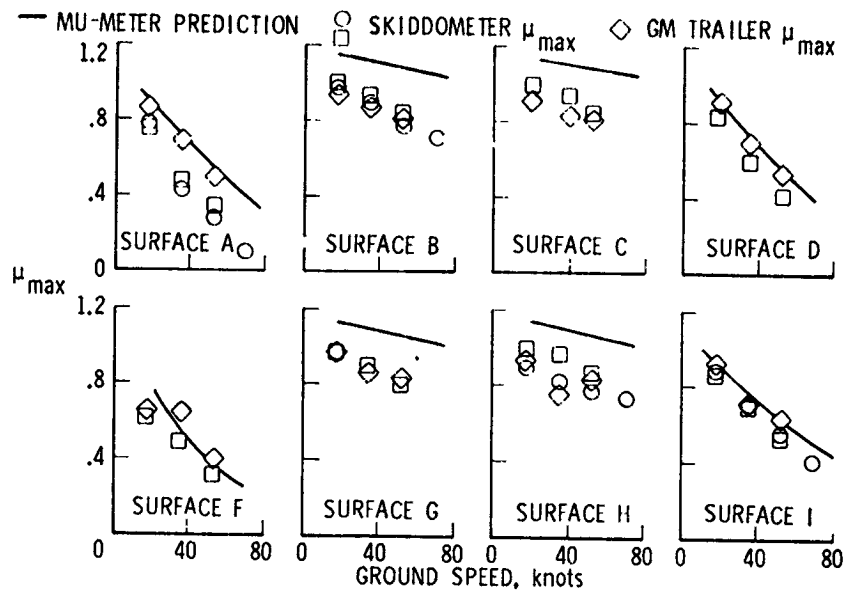
Figure 25.- Prediction of skiddometer and GM trailer μ_{max} from Mu-Meter friction reading ($\psi = 7.5^o$). Data from references 21, 22, and 30.
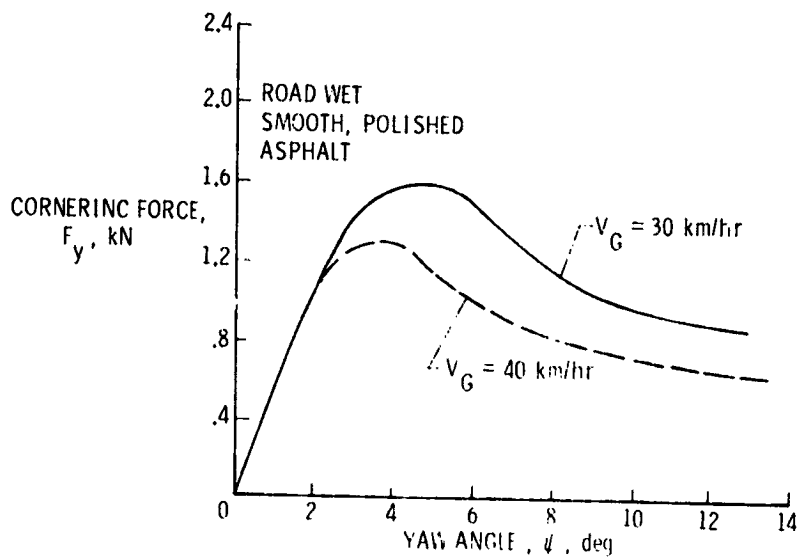
Figure 26.- Effect of ground speed on cornering-force-yaw-angle relationships for 5.60-13 automobile tire. $F_z = 2.70$ kN; $p = 167$ kPa; from reference 31.
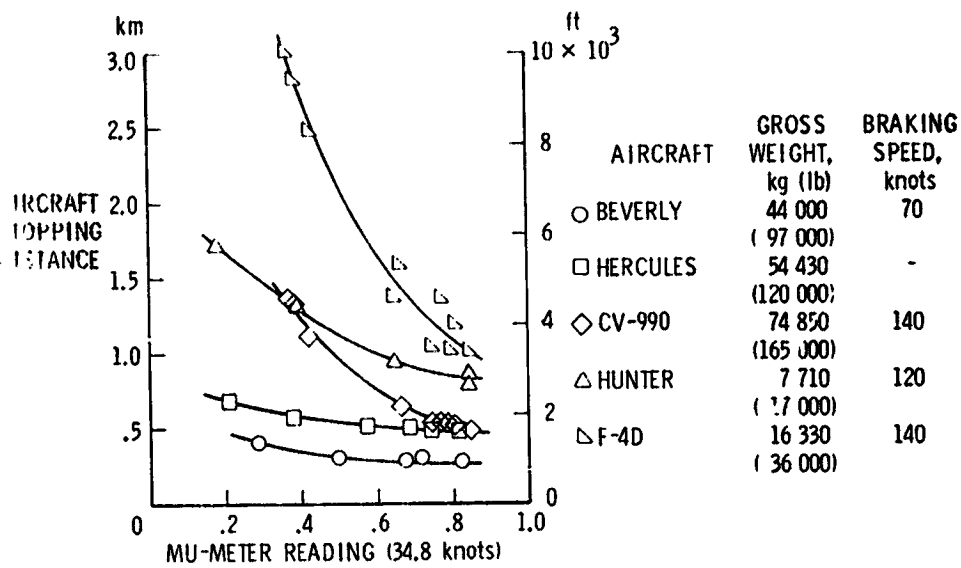
Figure 27.- Mu-Meter correlation with aircraft stopping
distances on wet surfaces.
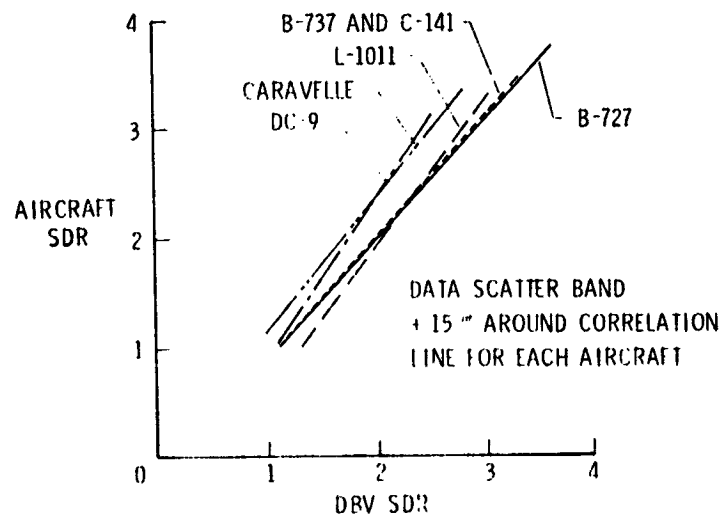
Figure 28.- Aircraft/DBV correlation on wet runways
for different jet transports.
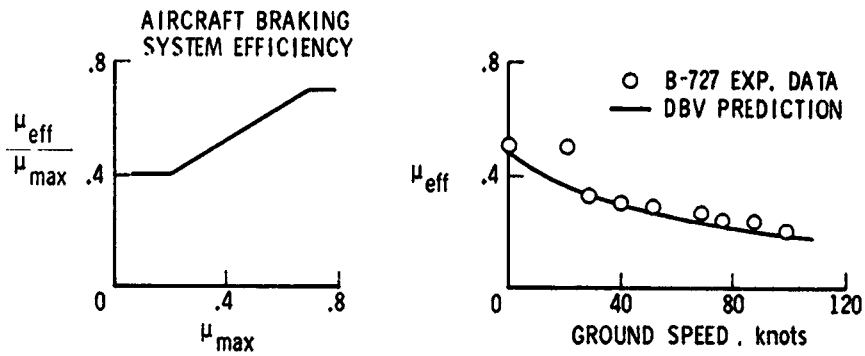
Figure 29.- Prediction of aircraft braking performance
on wet runway from DBV braking test. JFK runway 4R/22L;
grooved concrete; water truck wetting.
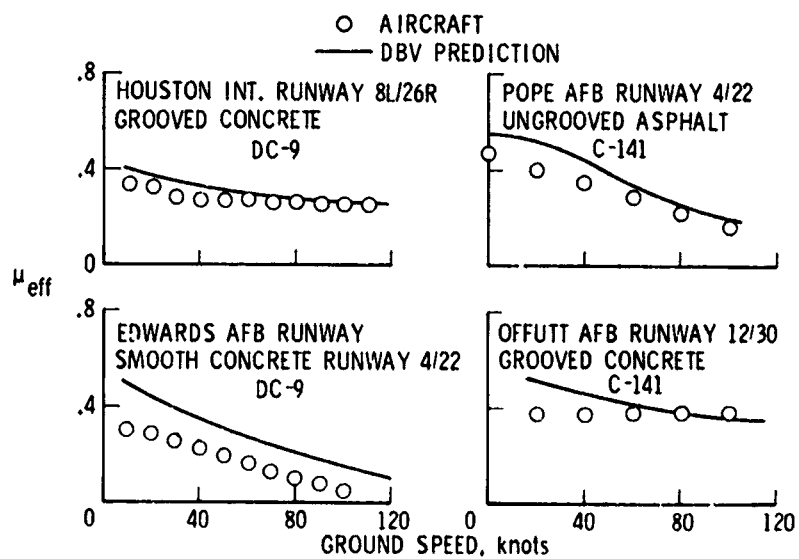
Figure 30.- Prediction of aircraft braking performance
on wet runways from DBV braking test for DC-9 and
C-141 jet transports.

240
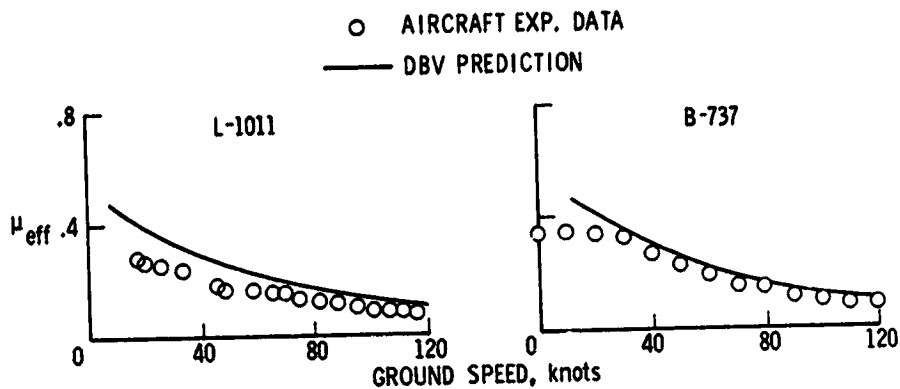
Figure 31.- Prediction of aircraft braking performance on wet
runway from DBV braking test for B-737 and L-1011 jet
transports. Roswell runway 3/21; smooth concrete.
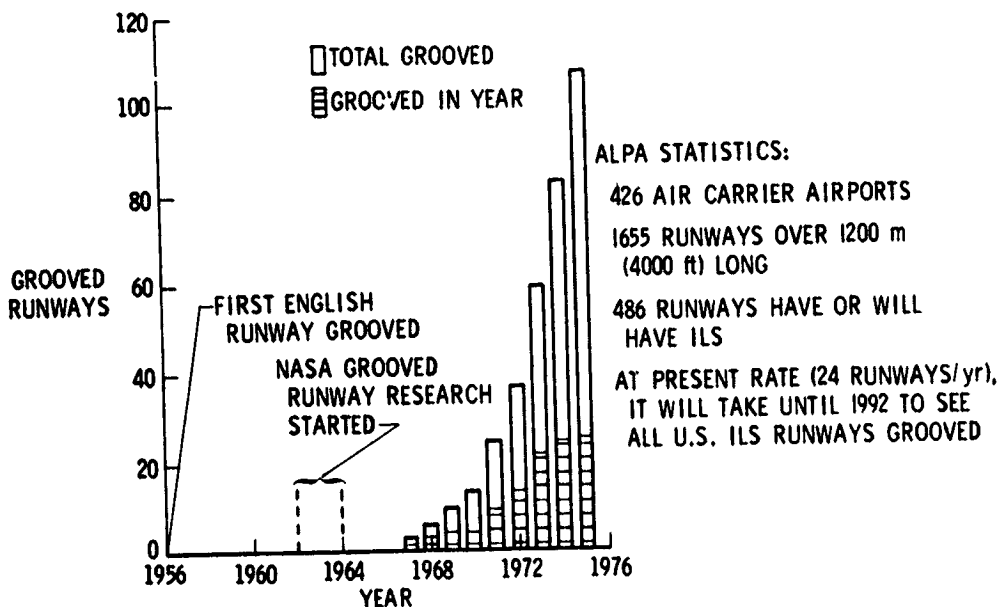
Figure 32.- Number of grooved runways at
U.S. air carrier airports.
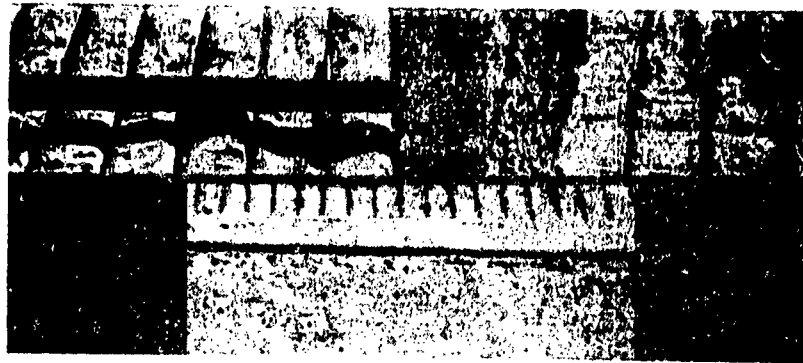
(a) Plastic grooving with segmented drum.

(b) Plastic grooving with wire comb.

Figure 33.- Examples of plastic grooving
of Portland cement concrete.
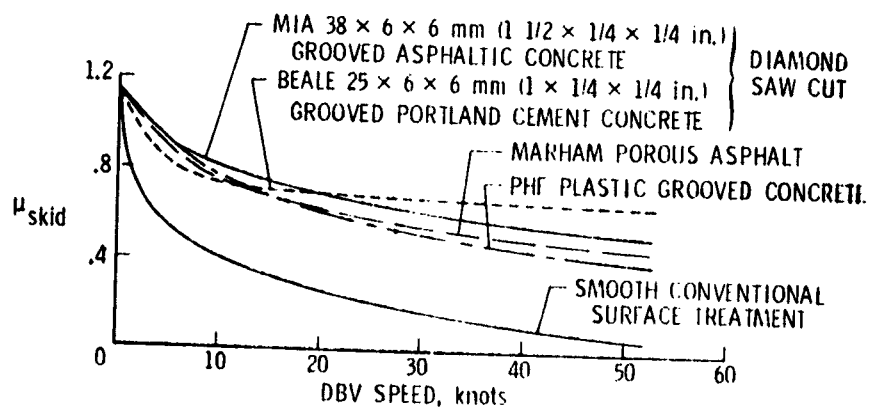
Figure 34.- Wet skid resistance of several new type
runway surface treatments. Artificial wetting.

246

Figure 35.- Tire damage from wheel spin-up at touchdown on dry grooved runway. Wallops grooved concrete; groove pattern, 25 × 6 × 6 mm (1 × 1/4 × 1/4 in.); CV-990 jet transport MLG tire, size 41 × 15.0-18; p = 1102 kPa (160 lb/in^2); V_G = 125 knots.
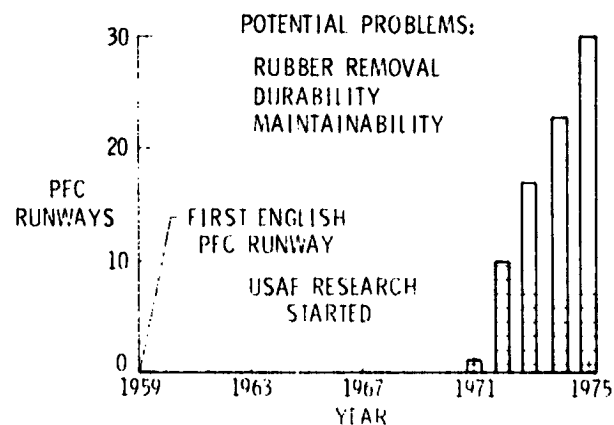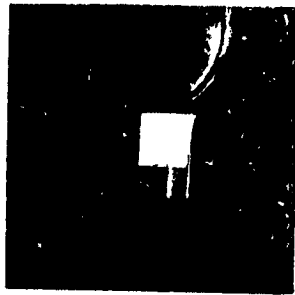

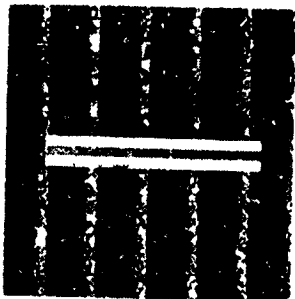Figure 36.- Number of porous friction course runways at U.S. air carrier airports.

BEFORE GROOVING:
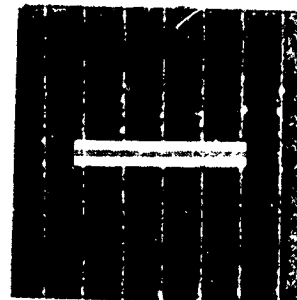MARCH 1973

CLEAN (NO RUBBER)
ATD = 0.457mm (0.018 in.)

HEAVY RUBBER DEPOSITS
ATD = 0.178mm (0.007 in.)

AFTER GROOVING:
38 x 6 x 6 mm
$(1\frac{1}{2} \times \frac{1}{4} \times \frac{1}{4}$ in.),
MAY 1973

CLEAN (NO RUBBER)
ATD = 1.439mm (0.057 in.)

HEAVY RUBBER DEPOSITS
ATD = 1.207mm (0.048 in.)

Figure 37.- Effect of rubber deposits on runway surface texture.
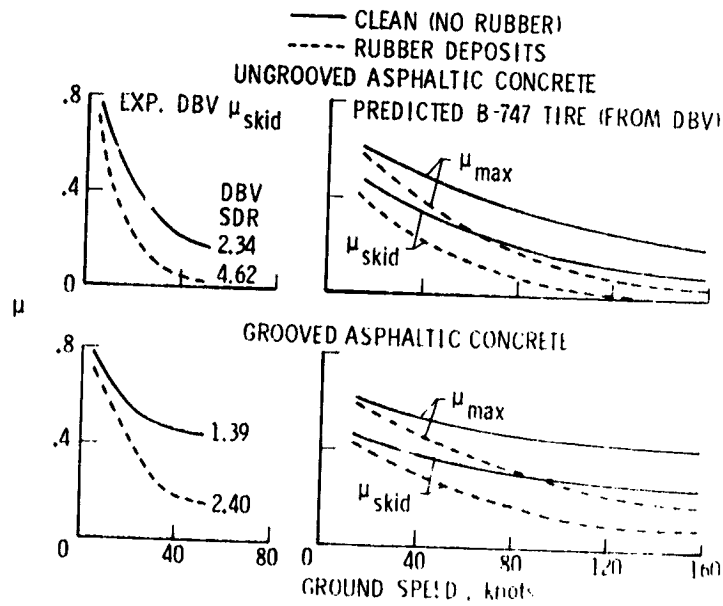

Figure 38.- Effect of rubber deposits on runway traction before and after grooving.
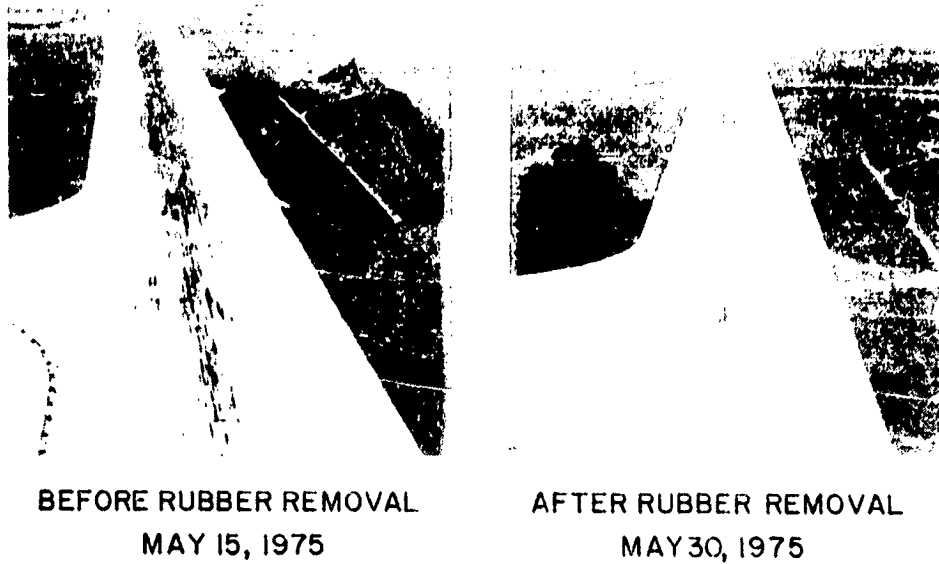
BEFORE RUBBER REMOVAL
MAY 15, 1975

AFTER RUBBER REMOVAL
MAY 30, 1975

Figure 39.- Approach end of LAFB runway 25 before and after rubber removal by high-pressure water blast.

CLEAN (NO RUBBER); DBV SDR = 1.97
CLEANED OF RUBBER; DBV SDR = 1.95
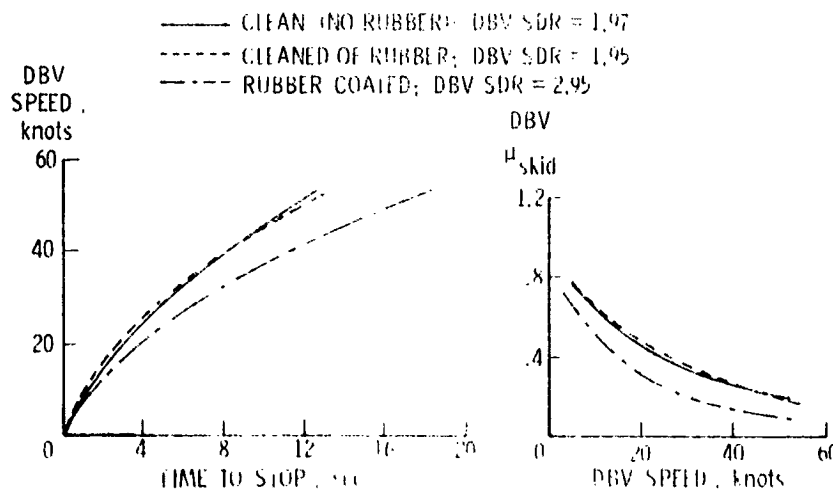RUBBER COATED; DBV SDR = 2.95

Figure 40.- Effect of rubber removal by high-pressure water blast on runway traction. LAFB runway 25; May 1975.

245

'

DEVELOPMENTS IN NEW AIRCRAFT TIRE TREAD MATERIALS

Thomas J. Yager and John L. McCarty
NASA Langley Research Center

S. R. Riccitiello and M. A. Golub
NASA Ames Research Center

13

SUMMARY

Comparative laboratory and field tests were conducted on experimental and state-of-the-art aircraft tire tread materials in a program aimed at seeking new elastomeric materials which would provide improved aircraft tire tread wear, traction, and blowout resistance in the interests of operational safety and economy. The experimental stock was formulated of natural rubber and amorphous vinyl polybutadiene to provide high thermal-oxidative resistance, a characteristic pursued on the premise that thermal oxidation is involved both in the normal abrasion or wear of tire treads and probably in the chain of events leading to blowout failures. Results from the tests demonstrated that the experimental stock provided better heat buildup (hysteresis) and fatigue properties, at least equal wet and dry traction, and greater wear resistance than the state-of-the-art stock.

INTRODUCTION

Apart from occasional traction problems on wet or icy runways, the major tire concerns of commercial and military aviation are those which lead to tire removal. The primary concern is tread wear or abrasion which results from braking and cornering maneuvers and from wheel spinup at touchdown. Cutting is another cause for tire removal and it is generally attributed to characteristics of the runway surface, such as sharp aggregate or uneven slab joints, and to the presence of foreign objects. Other causes include tearing and chunking where strips or chunks of rubber are separated from the tire during high-speed operations generally on a dry, rough runway. In the interests of operational efficiency, there is a clear need to prolong the lifetime of a tire tread to minimize replacement costs and to reduce the "downtime" of the aircraft. In the interests of aircraft safety, blowouts and related tire failures obviously need to be reduced to negligible levels.

Keeping a fleet of airplanes properly shod is a definite economic problem, particularly since the lifetime of a tire tread can extend from approximately 300 take-off and landing cycles all the way down to 10 to 15 cycles, depending upon the aircraft and the nature of its operation. Over half a million aircraft tires were manufactured in this country during 1975 to help maintain the operation of this nation's commercial and military aircraft. Fortunately, in contrast to automobile tires, the carcass of an aircraft tire

247

undergoes relatively little deterioration during the lifetime of a given tread and these tires are customarily retreaded five or six times before being scrapped. The cost of retreading is approximately one-fourth the cost of a new tire. In view of such economic and inherent safety considerations, the Chemical Research Projects Office at Ames Research Center instituted a program to seek new elastomeric materials which would provide improved tire tread wear, traction, and blowout resistance. Additional impetus for the program was provided by the NASA Research Advisory Subcommittee on Aircraft Operating Problems, which recognized in a 1968 resolution the need for high-performance aircraft tires with improved wear and safety characteristics. The purpose of this paper is to briefly describe the results from initial developments at Ames on a new elastomer formulation for aircraft tires and to present preliminary results from traction and wear experiments conducted under the guidance of Langley Research Center on tires retreaded with this new formulation.

TIRE TREAD RUBBER DEVELOPMENT

Among the many elements which make up an aircraft tire, the elastomer system constitutes the critical component since its molecular structure and chemical reactivity must offer the optimum balance of mechanochemical, thermal-oxidative stability and viscoelastic properties. State-of-the-art treads for jet transports typically comprise a 75/25 polyblend of cis-polyisoprene, either as natural rubber (NR) or "synthetic natural rubber" (SN), and cis-polybutadiene (CB). Although this is the basic blend, variations do exist between different tire manufacturers and for specific tire operational needs. (The tire tread for the Concorde, for example, is made from all natural rubber.) In addition to the elastomer system, other tread ingredients include a vulcanizing agent (sulfur or other curative), reinforcement pigments (e.g., carbon black), accelerators, stabilizers, processing aids, and cord material. Each of these ingredients, as well as assorted engineering parameters such as tread design and ply construction, must be optimized for a particular tire formulation and use.

It was decided early in the program to focus attention on the development of elastomers which would provide a higher thermal-oxidative resistance than state-of-the-art elastomers. This approach was pursued on the premise that thermal oxidation is involved in the normal abrasion or wear of tire treads and probably in the chain of events leading to blowout tire failures. It was also recognized that optimization of the tire formulation could best be accomplished by the tire industry once the enhanced thermal-oxidative stability of a new tread composition had been demonstrated.

The thermal-oxidation studies which ensued led to the view that a new elastomer, amorphous vinyl polybutadiene (VB), having its double bonds (which are required for vulcanization) outside the main polymer chain, would be more oxidatively stable at a given temperature than state-of-the-art elastomers which have their double bonds inside the main chain. An experimental tire tread stock, consisting of a 75/25 blend of NR/VB, was formulated and tested against state-of-the-art stock (75/25 NR/CB) for comparative heat buildup (hysteresis), fatigue, traction, and wear characteristics.

RESULTS AND DISCUSSION

Laboratory Tests

The initial tests on the two tread stocks were performed in the laboratory on small specimens using testing machines and procedures which have been standardized for such tests.

Heat buildup and blowout.- The results from heat buildup and blowout flexure tests are presented in figure 1. The figure shows that the temperature rise ΔT after 30 min of flexing in the two heat buildup tests is less in the experimental stock than it is in the standard or state-of-the-art stock. The difference is appreciable in the case where working of the samples commences at an elevated temperature. This comparison suggests that the experimental stock has the better thermal stability, particularly at higher temperature levels where this stability is needed. Similar temperature buildup trends are noted in the heat blowout tests in which the samples are worked at a higher energy level (sample loaded to 1110 N as opposed to 778 N in the buildup tests and a compression stroke of 6.4 mm as opposed to 5.7 mm). During the blowout test which commenced at 38° C, the standard stock failed after 36 min with a temperature rise of 81.7° C, whereas the experimental stock sample, which had not failed when the test was concluded after an hour, had a ΔT of only 62.2° C, which was measured after the sample had been subjected to a working time lasting 24 min longer. For the heat blowout test which commenced at 100° C, the temperature rise was essentially the same in both samples, even though the temperature of the experimental stock at failure was recorded after a working time approximately 50 percent longer than that of the standard stock sample. The longer blowout times associated with the experimental stock suggest that it is a stronger material than the state-of-the-art stock.

Cut growth.- Figure 2 presents the results from flexure tests on pierced samples of the experimental and standard stock to determine cut growth characteristics. The figure shows that at room temperature the experimental stock has a higher initial rate of cut growth than the standard stock; however the data suggest that the experimental stock has a lower overall cut growth after a prolonged period. More importantly, this observation of a better cut growth property of the experimental stock is reinforced by measurements taken after 1 hour at elevated temperatures where the potential for chunking is significant.

Field Tests

On the basis of the successful performance demonstrated by the experimental rubber stock during laboratory tests, a number of size 49 · 17, type VII, aircraft tires were retreaded with the new NR/VB formulation. Following qualification for aircraft use on a dynamometer at Wright-Patterson Air Force Base, Ohio, the tires were shipped to Langley Research Center for traction and wear tests under actual and simulated flight conditions. For comparison purposes, additional tires were retreaded in the same mold but with the standard state-of-the-art NR/CB rubber formulation and also shipped to Langley.

Traction.- One tire of each rubber formulation was installed on the large test carriage at the Langley aircraft landing loads and traction facility, pictured in figure 3, to ascertain whether the new tread rubber stock had any traction deficiencies. Tires equipped with both the standard and the experimental stock were exposed to braking cycles, which extended from free rolling to locked wheel skids, on similar dry, damp, and flooded concrete runway surfaces at test speeds up to approximately 100 knots. The insert in figure 3 is a photograph of the fixture which supported the tire and was instrumented to measure the forces and moments exerted on the tire during the course of a braking test. Some typical results from these tests are given in figure 4 where the maximum braking friction coefficients developed by the two tires on a dry and on a flooded surface are presented as a function of carriage ground speed. The figure shows that the level of developed friction did not deteriorate when the tire equipped with standard tread stock was replaced by one with the experimental stock. Indeed, the experimental stock provided maximum friction coefficients on both the dry and the wetted surface which were as high or higher than those measured with the standard stock.

Wear.- The extent of the tread wear associated with each tire during the traction tests was obtained by noting the gauged difference in the average tread groove depth around the tire circumference prior to and following the test program. Unfortunately, it was difficult to use this information to form the basis for comparing the wear resistance of the two tread materials because the tires were not exposed to identical test conditions of ambient temperature, speed, and the number and length of each brake cycle. However, it was interesting to note that both tires experienced essentially the same average loss in tread thickness but the tire with the experimental tread material was exposed to approximately 50 percent more brake cycles than the tire with the standard tread material. Thus, on the basis of this information the experimental stock appeared to have better wear properties than the standard stock.

To acquire meaningful tire wear data resulting from actual aircraft take-off and landing operations, NASA enlisted the services of the FAA Aeronautical Center in Oklahoma City to fly sets of tires equipped with the experimental and standard tread stocks on a Boeing 727 airplane. For these tests, tires with the experimental stock were installed on the inboard wheel of one gear and the outboard wheel of the other; at the same time, tires with standard stock were mounted on the remaining wheels for comparison purposes. The upper photograph in figure 5 was taken during the course of this program and shows the airplane immediately following main gear touchdown, the smoke from that event being quite visible. The other two photographs in this figure are closeup views of a gear with newly installed tires and with a tire worn to the removal stage. Through the highly cooperative efforts of the FAA, tread depth measurements were periodically taken across the tread and around the circumference of all four tires in a test set to define the pattern and the extent of tread wear. Four test sets involving eight tires retreaded from the NR/VB stock and a like number retreaded from the standard state-of-the-art NR/CB stock from two sources were flown in this test program. The information contained in figures 6 and 7 typify the results.

Tread profiles at selected stages of the tread lifetime are given in figure 6. The profiles shown were obtained from tread depth measurements taken on a tire equipped with standard tread stock and mounted on the left inboard wheel.

250

The wear pattern is not unique; tires retreaded with both the experimental and standard stocks at other wheel locations on the gear showed similar wear propagation. The figure identifies the original tire profile and worn profiles after a designated number of landing operations, including that after 261 landings when the tire was removed because marker cords were visible. The history of this and the other treads in the aircraft test program differed from that of treads on commercial aircraft tires because the test airplane landings were predominantly touch-and-go operations conducted during pilot training exercises. However a query of aircraft tire retreaders revealed that Boeing 727 tires worn during commercial service had similar final profiles which showed very little wear near the outer edges of the tread. In view of this wear pattern, the two tire tread compounds were compared on the basis of tread depth measurements taken only along the two inner grooves. Results of measurements from two sets of test tires, which typify all the data, are presented in figure 7 where the wear in terms of percent tread worn is plotted as a function of the number of landing operations. The percentage tread wear was derived by averaging tread depth measurements along the circumference of the two inner grooves of both experimental tread stock tires and both standard tread stock tires in each set. Note that this percentage never reached 100 percent since each tire was removed from the airplane when a wear marker was exposed, and as a result some tread remained about the circumference, as shown in figure 5. Figure 7 shows that the wear performance exhibited by the experimental stock is equivalent to or better than the standard stock. The wear performance of this experimental tread stock is most encouraging because it means that a material has been developed which possesses good hysteresis, fatigue, and friction characteristics without a sacrifice in lifetime. Indeed, the formulation of the stock tested here was an initial attempt and, as such, was not considered the optimum blend of ingredients which are added to the elastomer system to provide the best wear characteristics. It is likely that a blend could be perfected which would considerably improve tread longevity.

It is also of interest to note in figure 7 that the number of landing operations in the tread life of the tires exposed to predominantly touch-and-go operations is comparable to the number of full-stop landing operations generally available with tires in commercial service. Since touch-and-go operations involve no wheel braking and very little cornering, this agreement would suggest that perhaps the major source of tire wear occurs during wheel spinup. The fact that the wear is predominantly in the central area of the tread - the area which at touchdown first contacts the runway surface - would appear to support this possibility.

The authors are aware that the tread wear evaluation obtained from the FAA Boeing 727 aircraft operations was based on a comparatively small data sample. Arrangements are being made to retread 50 additional tires with this experimental stock for use by a commercial airline during normal operations on a variety of runway surfaces.

CONCLUDING REMARKS

Comparative laboratory and field tests were conducted on an experimental tire tread stock formulated of a 75/25 blend of natural rubber/amorphous vinyl

polybutadiene and on a state-of-the-art tire tread stock with 75/25 natural rubber/cis-polybutadiene. These tests constituted the initial effort in an overall research program aimed at seeking new elastomeric materials which would provide improved aircraft tire tread wear, traction, and blowout resistance in the interests of operational safety and economy. The experimental stock was selected to provide high thermal-oxidative resistance, a characteristic pursued on the premise that thermal oxidation is involved both in the normal abrasion or wear of tire treads and in the chain of events leading to blowout tire failures. Results from the tests demonstrated that the experimental stock provided better heat buildup (hysteresis) and fatigue properties, at least equal wet and dry traction, and greater wear resistance than the state-of-the-art stock. No attempts were made in this initial phase of the overall tread development program to optimize the experimental formulation since the intent here was only to demonstrate the concept of an improved tread stock based on amorphous vinyl polybutadiene. Such an optimization, which could result in much longer tread lifetimes, would best be accomplished by the tire industry. Meanwhile, efforts continue at Ames and Langley Research Centers to develop and evaluate new tire tread compounds aimed at improving the economy and safety of aircraft ground operations.
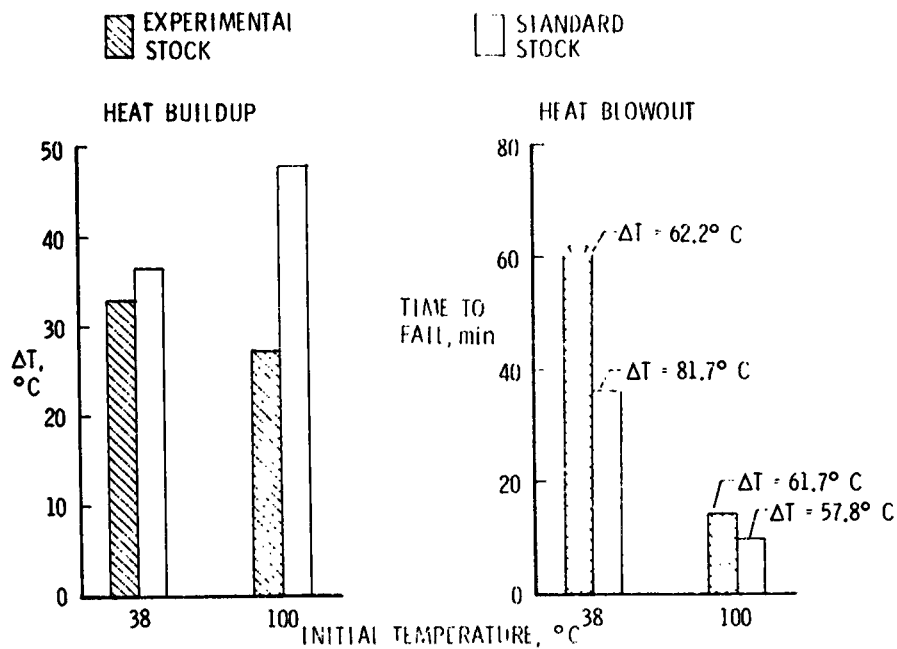
252

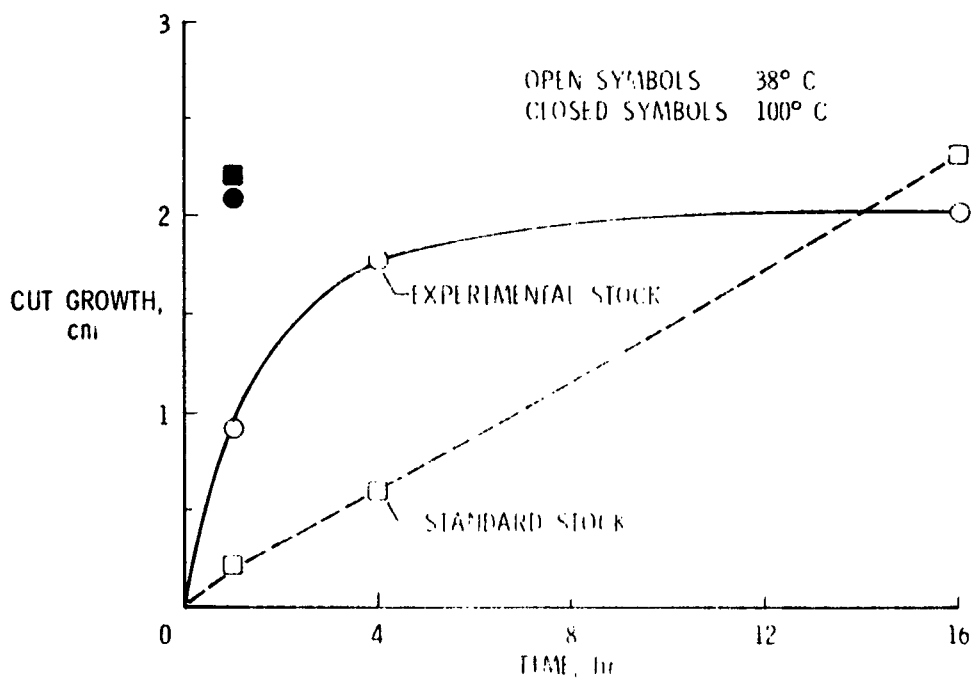**Figure 1.-** Heat buildup and blowout test results.
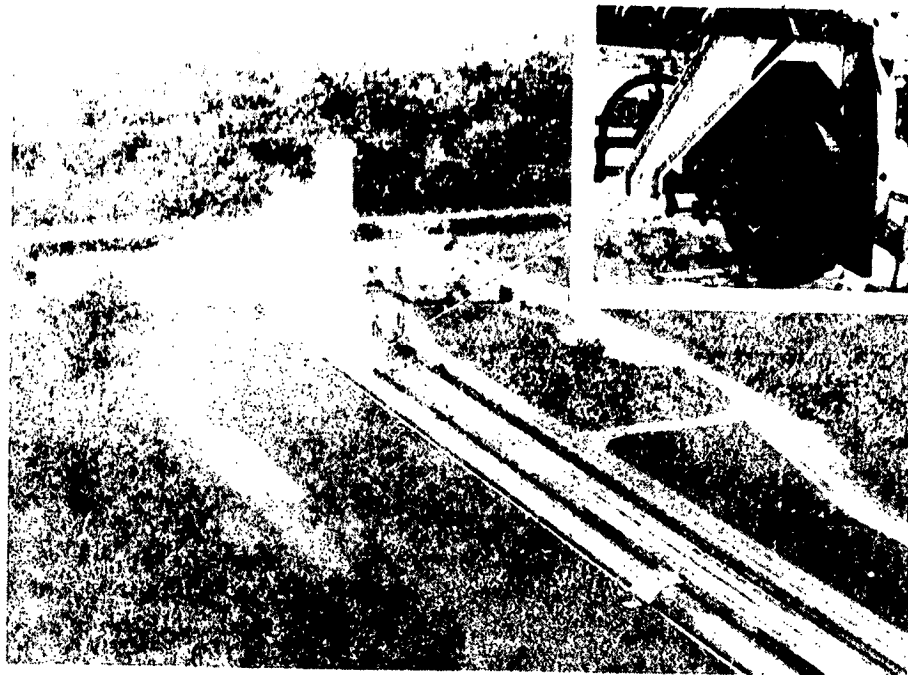

Figure 2.- Cut growth test results.

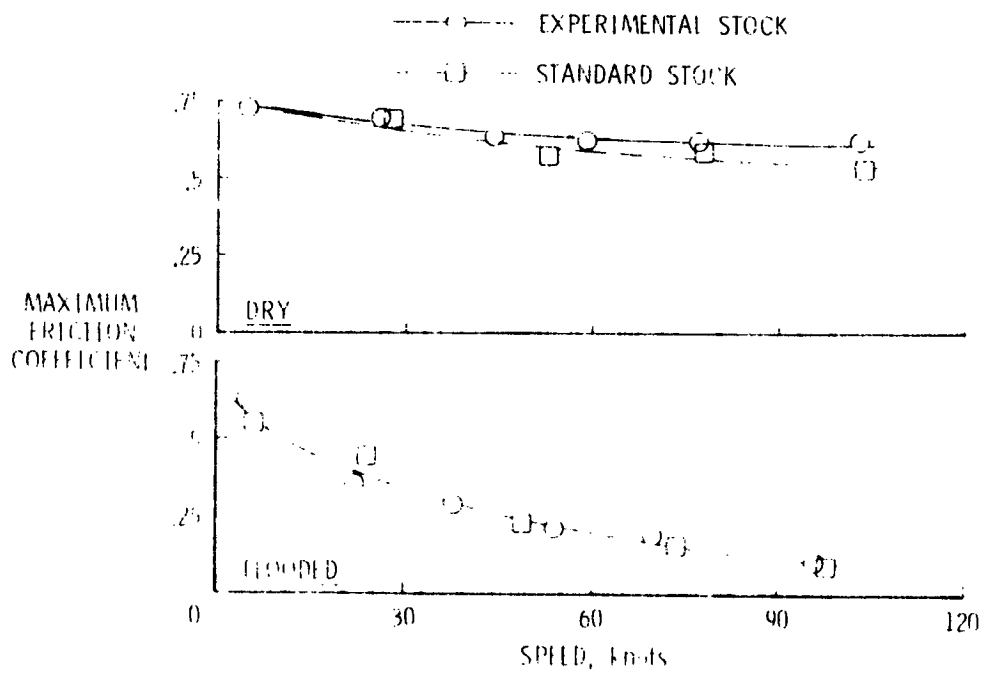Figure 3.- Langley aircraft landing loads and
traction facility.

Figure 4.- Tire traction test results.

Figure 5.- Aircraft tire tread wear evaluation.

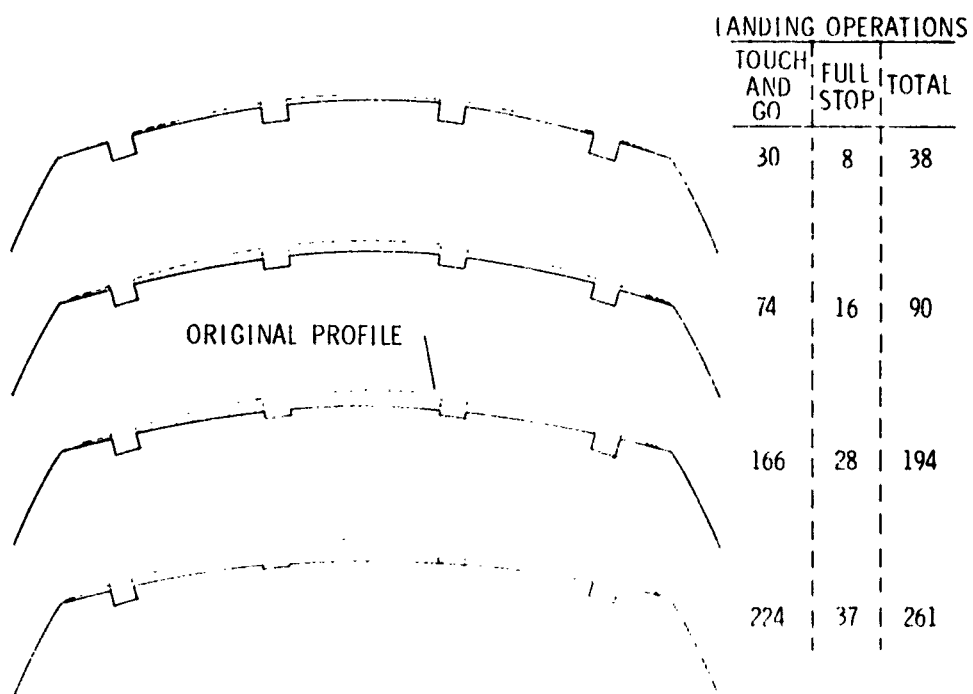|	LANDING OPERATIONS		
	TOUCH AND GO	FULL STOP	TOTAL
	30	8	38
	74	16	90
	166	28	194
	224	37	261

ORIGINAL PROFILE

Figure 6.- Typical propagation of tire tread wear of the
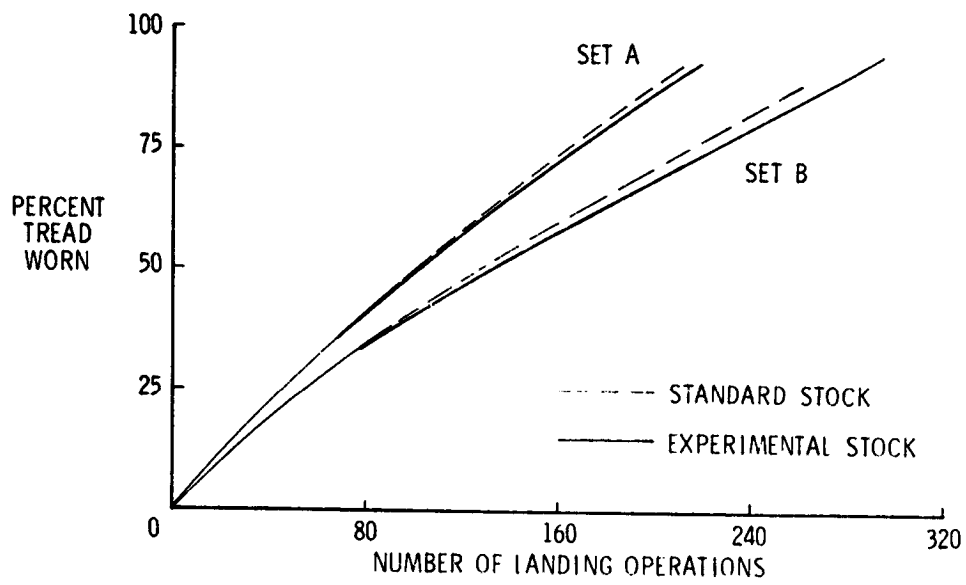main gear tire on FAA Boeing 727 airplane.

Figure 7.- Tire tread wear results from FAA Boeing 727 tests. Average wear at two inner grooves.

STATUS OF RECENT AIRCRAFT BRAKING AND CORNERING RESEARCH

Sandy M. Stubbs and John A. Tanner
NASA Langley Research Center

SUMMARY

In an effort to enhance the safety of aircraft antiskid braking and steering systems under adverse weather conditions, NASA Langley Research Center is currently conducting two parallel research programs. One program is an experimental study of antiskid braking systems and the second program is the development of an aircraft ground handling simulator.

Two antiskid systems have been investigated to date: the first was an older velocity-rate-controlled system and the second was a more recent system designed to operate at a constant slip ratio. Initial results indicate that for both systems there was a rapid deterioration in tire cornering capability with increased braking effort, and the braking performance was degraded on wet runway surfaces. As expected, however, the braking performance of the newer antiskid system was shown to be somewhat better than that of the older system on both dry and wet surfaces.

The adequacy of a simulator hardware/software program to represent aircraft ground handling characteristics has been evaluated for a wide variety of operational conditions during demonstration flights made by several experienced test pilots. Based on their recommendations, some changes are currently being made to improve the simulation capability before it is implemented at Langley Research Center.

INTRODUCTION

Operating statistics of modern aircraft indicate that the antiskid braking and steering systems used on these airplanes are both effective and dependable. The several million landings that are made each year in routine fashion with no serious operating problems attest to this fact. As aircraft avionics improve, however, the number of adverse weather landings also increases and thereby imposes greater demands on aircraft braking and steering systems. If compromises in the safety of aircraft ground operations are to be avoided, the performance of these braking and steering systems under slippery runway conditions must continue to improve.

In an effort to meet this need, NASA is currently conducting two parallel research programs. One program is an experimental study of the performance of several different aircraft antiskid braking systems under the controlled conditions afforded by the Langley aircraft landing loads and traction facility. The second is the development of a motion base aircraft landing and take-off simulator program which, when completed, will be implemented at Langley for use,

among other applications, as a research tool to study aircraft braking and steering operations under adverse weather conditions without risk to aircraft and flight crew.

The purpose of this paper is to present findings to date on the antiskid research program and to describe briefly the ongoing development and status of the aircraft landing and take-off simulator program.

ANTISKID BRAKING RESEARCH PROGRAM

Objectives

The objective of the antiskid braking research is to find the sources of degraded performance which sometimes occur under adverse runway conditions and to obtain data necessary to the development of more advanced systems in an effort to insure safe ground handling operations under all-weather conditions. Secondary objectives are to acquire tire-to-ground friction characteristics under braking conditions which closely resemble those of airplanes under heavy braking and to relate braking data from single-wheel landing loads track tests with those available from full-scale flight tests.

Apparatus

Test facility.- The antiskid tests are being performed at the Langley aircraft landing loads and traction facility utilizing the test carriage shown in figure 1. Figure 2 is a photograph of the DC-9 tire wheel and brake assembly used in the test program mounted on the instrumented dynamometer which measures the various axle loadings. DC-9 equipment is being used because of the availability of flight test data from an earlier DC-9 program. The tire is a 40 × 14, type VII bias ply aircraft tire of 22 ply rating and both new and worn tread conditions are being investigated. The 365-m runway has a smooth flat concrete surface and tests are being conducted with the surface under dry, damp, and flooded conditions. With the exception of transient runway friction tests, the entire runway is maintained at one uniform surface wetness condition and antiskid cycling generally occurs for approximately 300 m.

Skid control systems.- To date, a velocity-rate-controlled, pressure-bias-modulated, skid control system, hereafter referred to as system A, and a slip command system, hereafter referred to as system B, have been investigated. System A is of interest in that it is a relatively early skid control technique (about 10 to 15 years old) but one that is still in widespread use on many commercial and military aircraft. System B is a more recent design based on maintaining the braked wheel at a constant slip ratio while using the nose wheel speed for a reference speed input to compute that ratio. Both antiskid control systems used the same hydraulic components and line lengths for a single wheel of the dual-strut four main-wheel, McDonnell-Douglas DC-9 series 10 airplane. Schematic diagrams of both systems are shown in figure 3. Pressure from a fully open pilot metering valve (to exert maximum braking) is regulated by the antiskid control valve and is fed to the brake. For system A (fig. 3(a)), braked

wheel speed is fed to the antiskid electronic control box which senses the change in angular velocity (acceleration) of the braked wheel and generates a voltage to the control valve that is a function of the number and depth of previous skids. The antiskid control box of system B (fig. 3(b)), on the other hand, compares the speed of the braked wheel with that of the unbraked nose wheel and generates a current to the control valve to maintain pressure sufficient to control the braked wheel at 15 percent slip with respect to the unbraked nose wheel.

Test Results

Antiskid response.- Typical time histories of parameters which illustrate the nature of the response characteristics of the two antiskid systems are presented in figure 4. These parameters include the wheel speed, skid signal, brake pressure, and drag-force friction coefficient, and serve to show the adaptive characteristics of the antiskid systems as they experience an abrupt change in runway friction. At the start of the test, for system A (fig. 4(a)), the tire is operating on a dry runway and when a pressure of 20 MPa is applied to the brake, the drag friction coefficient developed between the tire and the runway increases to approximately 0.65. Approximately 3.5 seconds into the test, the runway condition changes abruptly from dry to flooded and the wheel, still under heavy braking, immediately enters into a deep skid which produces a full skid signal to the antiskid control valve. The valve, in turn, reduces the brake pressure to allow spinup of the braked wheel. When the wheel spins up to free rolling speed, the skid signal drops but not completely and allows brake pressure to be reapplied at a reduced rate which is a result of the pressure bias modulation circuit of system A. Five subsequent cycles ensue on the flooded surface as the system allows the pressure to build up to produce a skid and then decrease to permit wheel spinup. The inability of system A to prevent these deep skids on a flooded runway is attributed, at least in part, to the fact that the brake torque capacity greatly exceeds the resisting drag force, to the low spinup torque available on wet surfaces, and to the 40 ms response time required for the antiskid system to react to abrupt changes in wheel speed. The response time delay appears to be the result of electronic lags in the antiskid control box which occur when the wheel speed ac signal is converted to a dc voltage that is supplied to the antiskid control valve.

The test with system B, presented in figure 4(b), also shows a buildup in friction coefficient on the dry surface with brake application. In this test the dry surface was sufficiently long for antiskid cycling to occur. Note that the high-frequency oscillations in wheel speed correspond to skid signals and brake pressure releases and result in a fairly uniform drag-force friction coefficient. At approximately 6.2 seconds, the runway condition changes abruptly from dry to flooded and, as a result, the wheel enters a deep skid. This deep skid produces a full skid signal which reduces the brake pressure to near zero. After the initial transition, system B controls the brake pressure very well, prevents further deep skids, and, most importantly, maintains a fairly constant drag coefficient.

Typical tire frictional response to antiskid braking on dry and flooded runway surfaces is presented in figure 5 where the drag and side-force friction

coefficients for the tire yawed to 6° and operating at a nominal speed of 75 knots are plotted as a function of wheel slip ratio. A slip ratio of 0 corresponds to a freely rolling wheel and a slip ratio of 1 corresponds to a locked wheel skid. The data presented in the figure were generated by system A and illustrate the cyclic nature of the friction developed during antiskid braking control. The classical μ slip curve (ref. 1) is a smooth curve that reaches a peak somewhere between 10 percent and 20 percent slip (μ denotes friction coefficient). These data show that under realistic conditions, however, the curve is not smooth because of runway roughness, flexibility in the wheel support which would be reflected in the measured drag and side forces, variations in the runway friction characteristics, and the spring coupling between the wheel and the pavement provided by the tire. The data in the figure illustrate the traction losses associated with flooded runway operations. For example, on the dry surface the maximum drag-force friction coefficient reaches approximately 0.6 but on the flooded surface it never exceeds 0.2. A similar loss is noted in the developed side-force friction coefficient when the surface is flooded. The figure also demonstrates the rapid deterioration in the tire cornering capability with increased braking effort. For example, at a slip ratio of only 0.3, the side-force friction coefficient had decreased approximately 60 percent on the dry runway and to negligible values on the flooded runway.

Antiskid performance.- A measure of the antiskid performance can be obtained from the ratio of the average drag-force friction coefficient developed by the system to the average maximum available drag-force friction coefficient developed at the tire/pavement interface. This ratio, called the braking performance ratio for the purposes of this paper, is presented in bar graph form for systems A and B in figures 6(a) and 6(b), respectively.

The values in this figure are the numerical averages of all the data for a given test condition; for example, the 3° bar graph for the dry surface in figure 6(a) is the average of all dry runs at 3°, regardless of speed, vertical force, tire configuration or system pressure. For system A, the average performance ratio on a dry surface is shown to increase with increasing yaw angle and tire vertical force and to decrease when a new tire was replaced by one with essentially no tread. On the wet runway surfaces, the average performance ratio also decreases with a worn tire and increases with tire vertical force. There was no conclusive trend in braking performance at yaw angles of 3° and 6° but, in general, braking performance was not appreciably degraded by yaw angle; thus, the braking characteristics can be expected to be good during crosswind operations. For system A the best braking performance was obtained with a new heavily loaded tire running on a dry surface. In general, similar trends were noted with system B (fig. 6(b)). As expected, this newer system exhibits higher performance ratios for every test condition, but both systems consistently have reduced performance ratios on slippery surfaces. Thus, the stopping capability potential of an airplane on a wet runway surface is hampered not only by the reduced friction level but also by the inability of the antiskid system to effectively take advantage of the friction available.

260

AIRCRAFT LANDING AND TAKE-OFF SIMULATOR DEVELOPMENT

One of the applications of the data from the antiskid braking research program is to provide inputs necessary to the development of landing and take-off simulation technology. The following paragraphs discuss the background, current status, as well as the plans for and applications of this development.

Background

It is common knowledge that the ground operation safety margins of aircraft are reduced by combinations of such factors as slippery runways, the presence of crosswinds, poor pilot visibility, excessive touchdown velocity, and equipment malfunction, among others. Full-scale tests can be used to explore the braking capability of an airplane by simply noting the distance required to bring the vehicle to rest from some preselected ground speed. The directional control capability cannot be evaluated through full-scale testing because such tests would compromise the safety of the airplane and crew and because of the unpredictability of the key ingredient, the surface winds. In an effort to acquire the capability to safely explore aircraft directional control and braking performance under any runway environment, a major research program was recently undertaken to explore the feasibility of expanding current flight simulation technology to include the complex interactions between the runway and the landing-gear system. Such an expansion would require a definition of the runway environment (including surface crown and roughness), the magnitude and direction of crosswinds, tire/surface friction levels (including the relationship between braking and cornering), airplane characteristics (landing-gear dynamics, brake system behavior, and the contributions from reverse thrust and auxiliary braking devices), and a good runway visual scene.

Current Status

The initial simulation involved the F-4 airplane which was chosen because of the considerable amount of available tire traction data on the airplane from landing loads track tests and full-scale braking tests. A photograph of the motion base simulator used in the program development is given in figure 7. A typical time history of a simulated F-4 landing as performed by one of the test pilots on an icy runway is presented in figure 8. For this test run, the pilot touched down at approximately 125 knots in an 8 m/sec crosswind after negotiating a somewhat higher crosswind during approach. The figure shows the rollout behavior of the airplane which included some rather substantial lateral excursions.

The results of the feasibility study with the F-4 airplane were sufficiently encouraging that the development was extended to include the DC-9 jet transport. Table I is a summary of the pilot assessment of the F-4 and the DC-9 simulations during approach and touchdown, landing rollout, and aborted take-off demonstrations. Thus far, 348 simulator demonstration runs with six different pilots have been conducted with the F-4 and 186 runs with two pilots with the DC-9. Table I presents comments from two pilots in each airplane during the most recent demonstrations. These runs demonstrated the need for airplane deceleration

cues (the current motion-based simulator has five degrees of freedom and fore-
and-aft motion is not among them), a cockpit environment closely allied to the
airplane being examined (both the F-4 and the DC-9 simulations were performed
on an F-4 simulator), and good visual scene simulation (some difficulty was
experienced in getting the terrain map translator to the proper simulated eye
level for both airplanes).

Plans and Applications

Current plans in the aircraft landing and take-off simulation program
include furthering, under contract, the development of the DC-9 transport simu-
lation. This extension calls for the use of a transport cockpit on a motion
base simulator with six degrees of freedom, and the incorporation of antiskid
brake system simulation with hardware as needed. It is also planned to imple-
ment this simulator capability at Langley Research Center by starting with the
DC-9, since the simulator technology for that airplane exists, and then expand-
ing to a generalized model to accommodate the simulation of a variety of air-
craft. Such a simulation would provide a research tool for evaluating, in
perfect safety, factors which influence the ground handling performance of an
aircraft up to and beyond its normal operating limits, or for making trade-off
studies to evaluate aircraft design concepts (that is, landing gear, tire,
brake, and antiskid modifications). In addition, an aircraft ground handling
simulator could be used to establish safe operational limits for various air-
plane and runway combinations and to optimize piloting techniques under adverse
runway conditions.

CONCLUDING REMARKS

This paper has presented the status of recent braking and cornering
research at Langley Research Center. Two antiskid systems have been tested to
date and the degraded performance noted on slippery runways was attributed to
electronic lags, low wheel spinup forces, and to high brake torque capacity
relative to the resisting drag force. Antiskid performance was highest under
a heavy loading condition with a new tire on a dry runway. An aircraft landing
and take-off simulator program has been written to safely study aircraft direc-
tional control problems on slippery runways in the presence of crosswinds.
Initial runs in an aircraft landing and take-off simulation program appeared
to be quite promising and the development is being expanded to include a trans-
port cockpit utilizing a six degrees of freedom motion base simulator with the
addition of antiskid brake action and an improved visual scene. A simulator,
generalized to accommodate a variety of aircraft, is scheduled to be installed
at Langley Research Center.

REFERENCE

1. Dreher, Robert C.; and Yager, Thomas J.: Friction Characteristics of
   20 x 4.4, Type VII, Aircraft Tires Constructed With Different Tread
   Rubber Compounds. NASA TN D-8252, 1976.

TABLE I

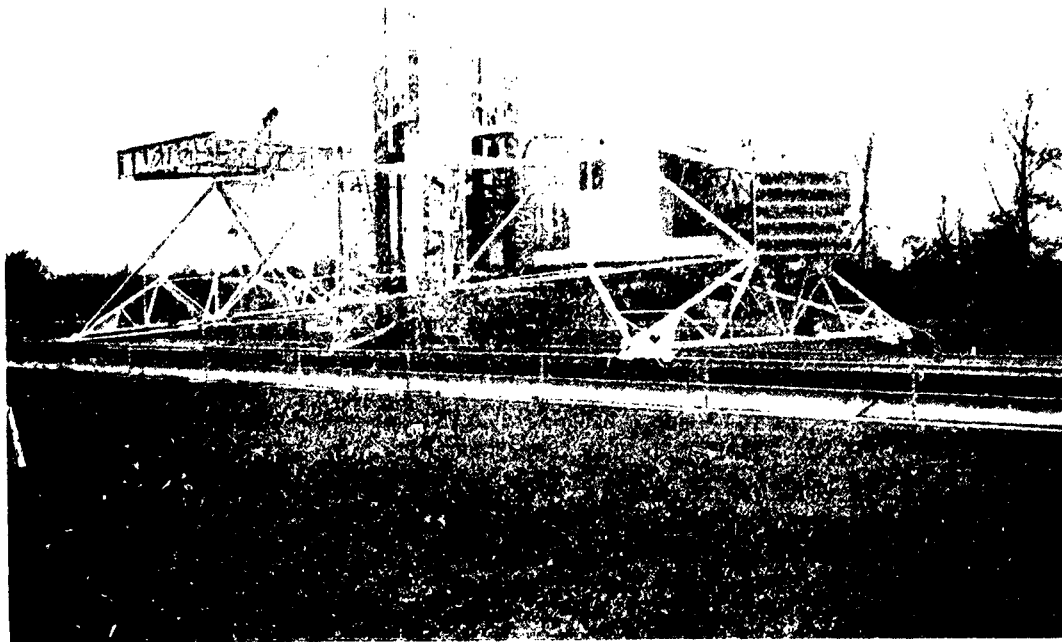| PILOT EVALUATION OF SIMULATOR DEMONSTRATION RUNS				
SIMULATION	F-4 AIRPLANE		DC-9 AIRPLANE	
	PILOT A	PILOT B	PILOT C	PILOT D
APPROACH AND TOUCHDOWN	GOOD	GOOD	GOOD	FAIR

LANDING ROLL-OUT
   DIRECTIONAL CONTROL
   BRAKING RESPONSE
	GOOD
	FAIR
		GOOD
		FAIR
			FAIR
			POOR
				GOOD
				GOOD

ABORTED TAKE-OFF
   DIRECTIONAL CONTROL
   BRAKING RESPONSE
	GOOD
	FAIR
		GOOD
		FAIR
			FAIR
			POOR
				FAIR
				FAIR

263

Figure 1.- Test carriage.
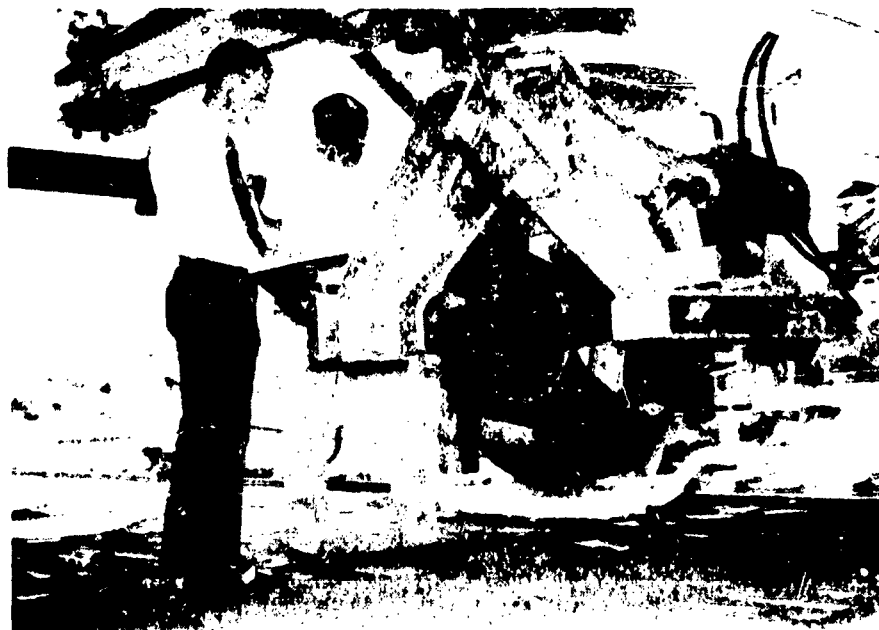
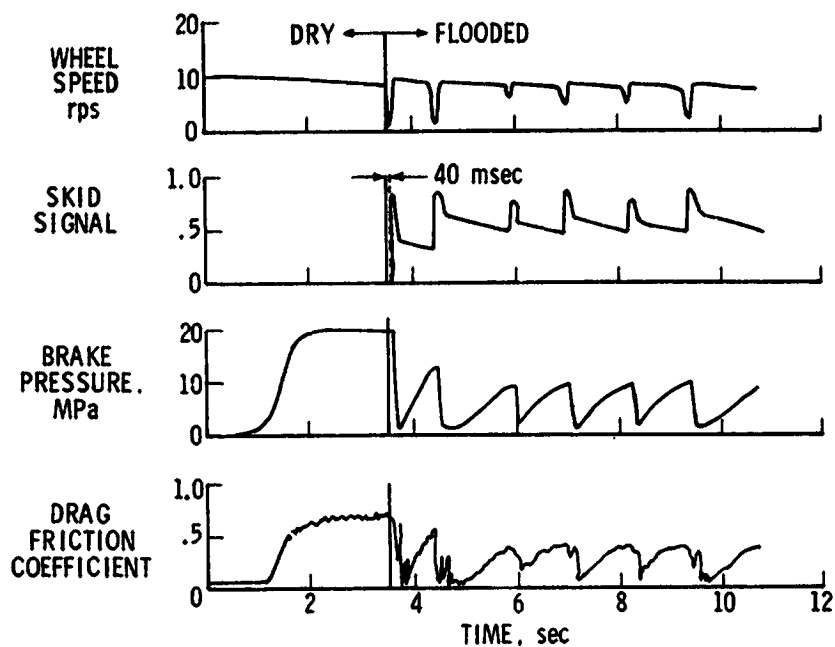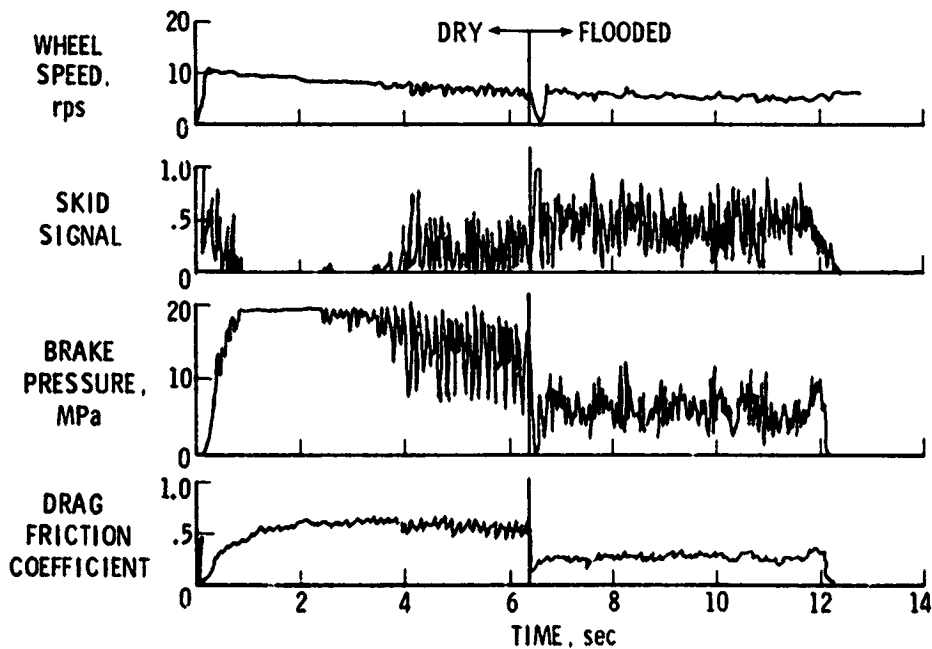Figure 2.- Test tire and instrumented dynamometer.

264
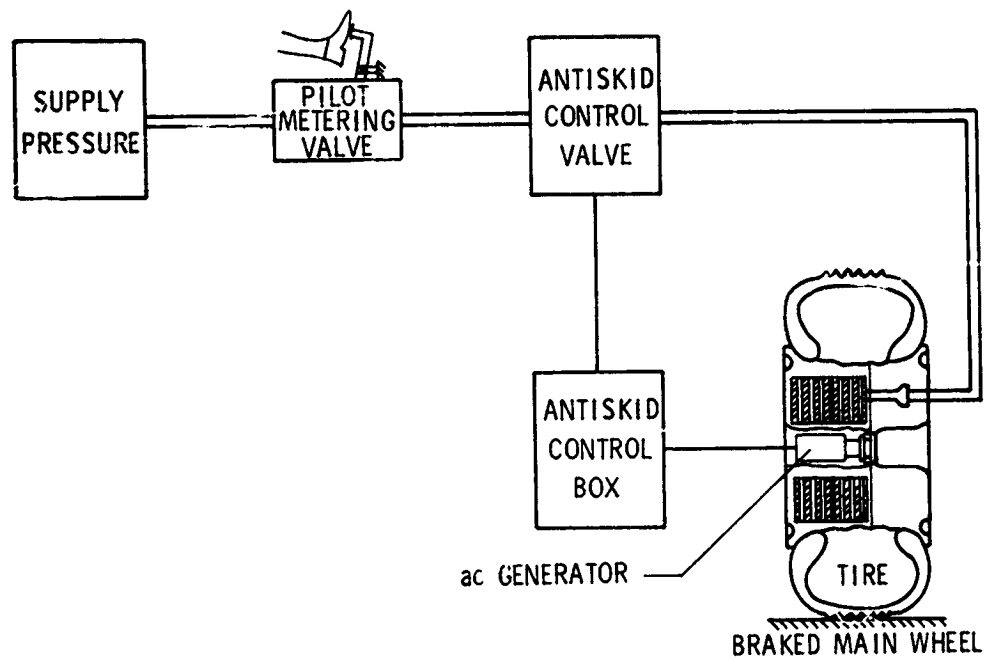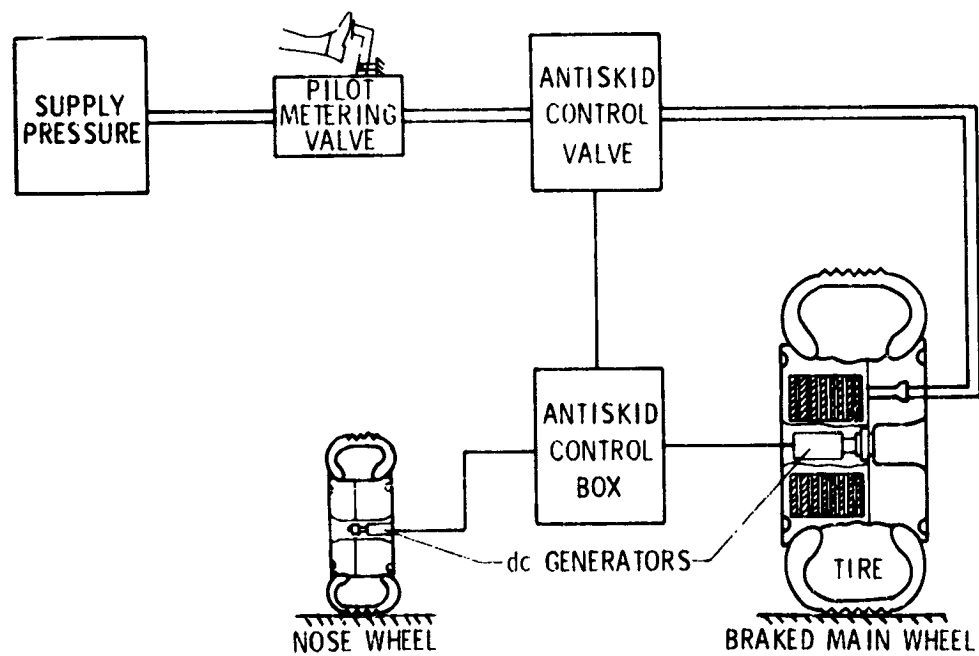
(a) System A.

(b) System B.

Figure 3.- Skid control system.

(a) Brake system A; 0° yaw; 79.2 kN vertical load; 20.7 MPa brake supply
pressure; new tread; 49 knots nominal carriage speed.

(b) Brake system B; 0° yaw; 83.2 kN vertical load; 19.0 MPa brake
supply pressure; new tread; 41 knots nominal carriage speed.

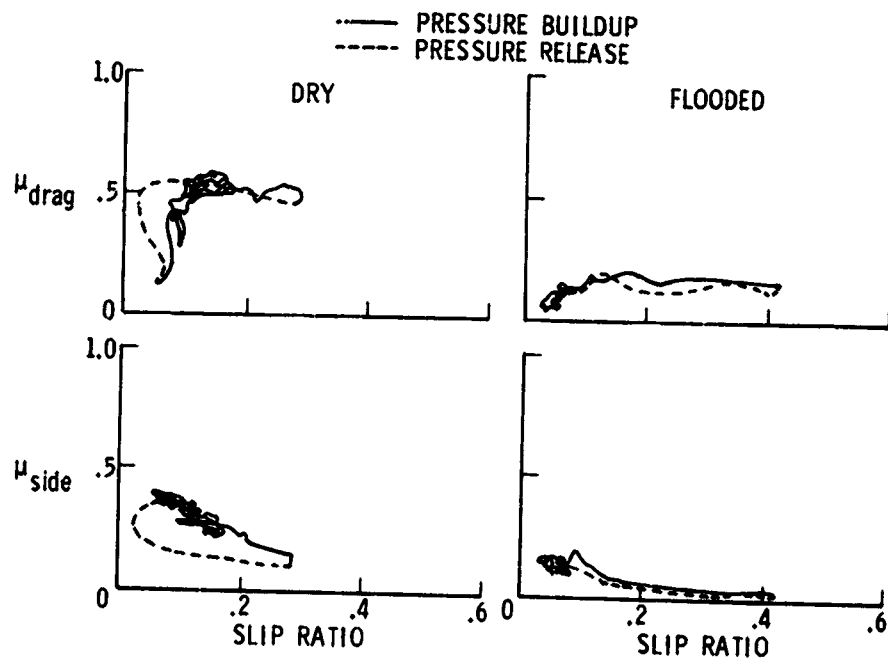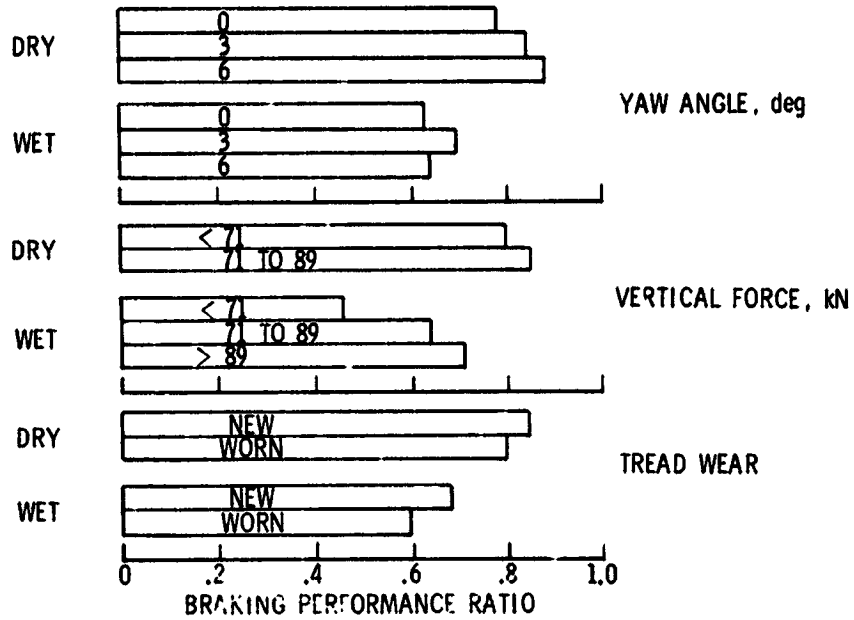Figure 4.- Typical antiskid system responses to transient runway conditions.
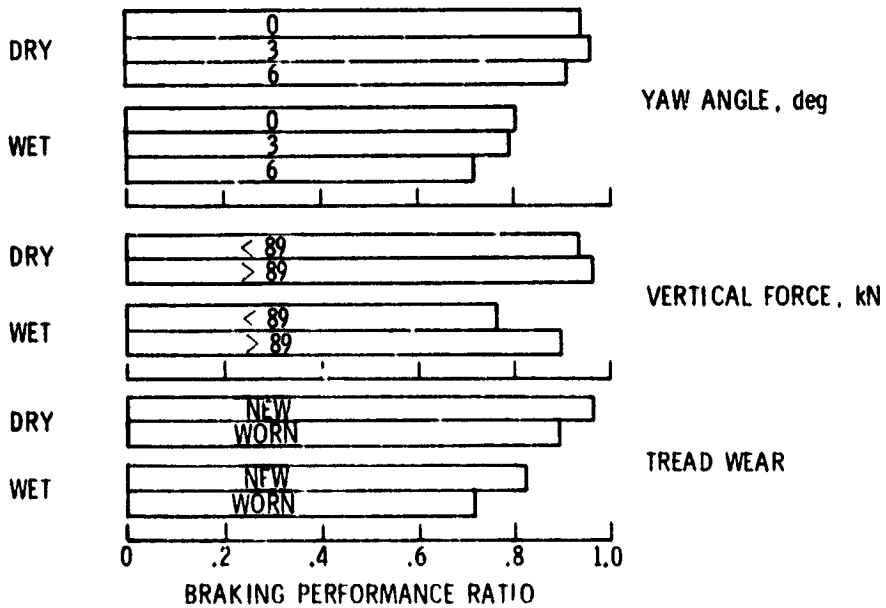
266

Figure 5.- Brake system A friction coefficients during cyclic braking. 6° yaw; 78.3 kN nominal vertical load; 20.7 MPa brake supply pressure; new tread; 75 knots nominal carriage speed.

DRY   0 / 3 / 6

WET   0 / 3 / 6   YAW ANGLE, deg

DRY   < 71 / 71 TO 89

WET   < 71 / 71 TO 89 / > 89   VERTICAL FORCE, kN

DRY   NEW / WORN

WET   NEW / WORN   TREAD WEAR

0   .2   .4   .6   .8   1.0
BRAKING PERFORMANCE RATIO

(a) Brake system A.

DRY   0 / 3 / 6

WET   0 / 3 / 6   YAW ANGLE, deg

DRY   < 89 / > 89

WET   < 89 / > 89   VERTICAL FORCE, kN

DRY   NEW / WORN

WET   NEW / WORN   TREAD WEAR

0   .2   .4   .6   .8   1.0
BRAKING PERFORMANCE RATIO

(b) Brake system B.

Figure 6.- Effect of test parameters on braking performance ratio.
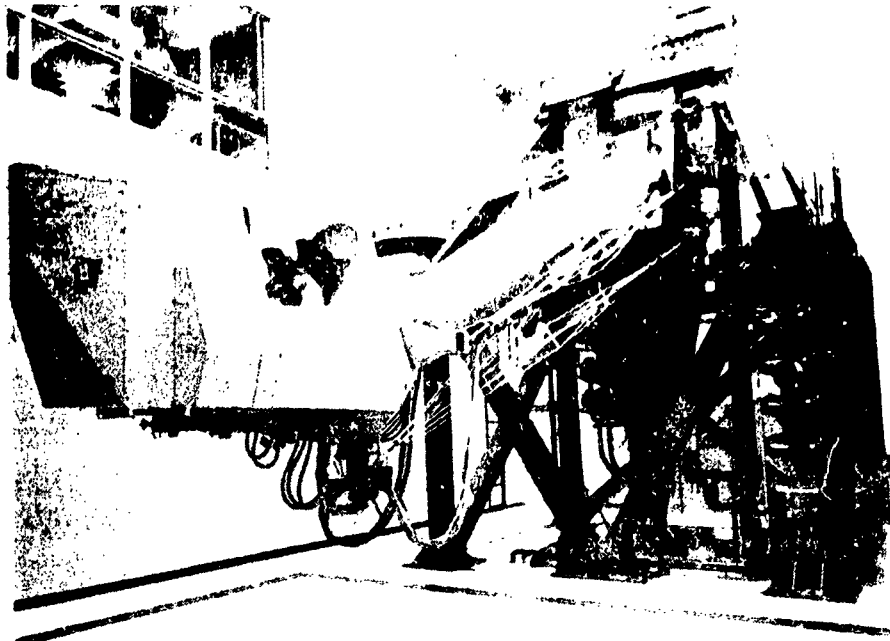
Figure 7.- Motion base simulator.

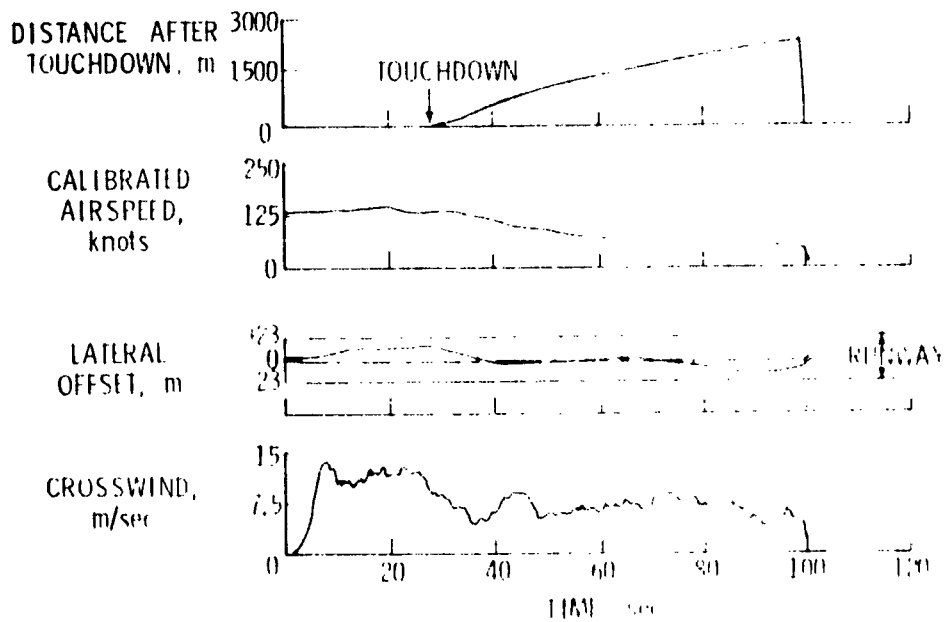Figure 8.- F-4 airplane landing on ice covers.

ATMOSPHERIC TURBULENCE POWER SPECTRAL MEASUREMENTS TO LONG

WAVELENGTHS FOR SEVERAL METEOROLOGICAL CONDITIONS

Richard H. Rhyne and Harold N. Murrow
NASA Langley Research Center

Kenneth Sidwell
The George Washington University
Joint Institute for Advancement of Flight Sciences

SUMMARY

Use of power spectral design techniques for supersonic transports requires accurate definition of atmospheric turbulence in the long wavelength region below the "knee" of the power spectral density function curve. Examples are given of data obtained from a current turbulence flight sampling program. These samples are categorized as (1) convective, (2) wind shear, (3) rotor, and (4) mountain-wave turbulence. Time histories, altitudes, root-mean-square values, statistical degrees of freedom, power spectra, and integral scale values are shown and discussed.

15

INTRODUCTION

"Gustiness" or the effect of atmospheric turbulence has always been of concern for aircraft operations. In early years individual or discrete gusts of differing shape were used to verify designs. It was always recognized that turbulence is a statistical phenomenon, however, in that single gusts are seldom if ever encountered. About 25 years ago the use of random process theory, or more commonly referred to as "power spectral analysis" techniques, began to receive significant attention as a more appropriate design analysis method. As a result of these developments, experimental turbulence sampling programs were conducted in order to provide a statistical description of the atmosphere in power spectral form. These measurements verified, in general, that the slope of the von Karman equation (given in fig. 1) of $-5/3$ is appropriate. Limitations in both instrumentation and data reduction procedures prevented the acquisition of data at wavelengths long enough to identify appropriate values of L in the von Karman equation (or to verify the validity of the equation). If L (generally referred to as the integral scale value and physically sometimes thought of as the average eddy size (ref. 1)) and σ (the root-mean-square value) are known, then the power spectrum is completely described. Regardless of the intensity or power level, each L value corresponds to a specific knee or break frequency in the power spectrum curve. Meteorological researchers therefore need appropriate L values to fill gaps in the description of the atmosphere. An example of the significance of the L value for aircraft designers is shown by the vertical bands in figure 1. (Note that log scales are used in fig. 1.) The primary effect of

response to turbulence is in the rigid body, short period, and Dutch roll modes. For subsonic aircraft such as the 707, B-52, and 747 airplanes which cruise at $M \approx 0.8$ and at altitudes of 11 to 12 km (35 000 to 40 000 ft), the primary response to turbulence is to the right of the knee of the spectral curves for all values of L in the range believed to be appropriate for consideration. However, for supersonic cruise aircraft such as are being studied presently in this country, that is, cruise $M \approx 2.7$ at approximately 18 km (60 000 ft), the predicted response is more significantly affected by the L value as can be seen in the figure. Fatigue and ride quality are also important aspects of the aircraft response to atmospheric turbulence. It was decided, therefore, that significant effort was warranted to remove this gap in the knowledge of atmospheric turbulence properties and establish a program with a primary aim of determining appropriate values of L for different meteorological conditions. As a result, special attention must be given to instrumentation and data processing in the low-frequency or long-wavelength region.

SYMBOLS

Values are given in both SI and U.S. Customary Units. The measurements and calculations were made in U.S. Customary Units.

g acceleration due to gravity, m/sec^2 (ft/sec^2)

h altitude, km (ft)

L integral scale value, meters (ft)

M Mach number

u longitudinal component of turbulence, m/sec (ft/sec)

v lateral component of turbulence, m/sec (ft/sec)

w vertical component of turbulence, m/sec (ft/sec)

      wavelength, meters (ft)

σ root-mean-square value (also standard deviation), m/sec (ft/sec)

$\sigma_u, \sigma_v, \sigma_w$ standard deviations of u, v, and w

Φ power spectral density, $\dfrac{(m/sec)^2}{cycles/meter}$ $\left(\dfrac{(ft/sec)^2}{cy \ cles/ft}\right)$

PROGRAM IMPLEMENTATION

The NASA MAT (Measurement of Atmospheric Turbulence) program was established in response to the preceding requirements. All three components of turbulence (vertical, lateral, and longitudinal) were to be measured. It was decided that two sampling aircraft would be required to cover the entire altitude range of

272

interest - one airplane covering the range of altitudes from sea level to 15 km
(50 000 ft) and a special high-altitude airplane for altitudes above 15 km.
The sensors selected required sampling to be done at subsonic speeds. A B-57B
Canberra was selected for the sampling at altitudes up to 15 km and it was
decided that a B-57F would be the preferred aircraft for use at altitudes above
15 km. Basically, the required measurements for each of the three turbulence
components involve a primary measurement on a boom forward of the aircraft (see
fig. 2) (angle fluctuations for the vertical and lateral and airspeed variations
for the longitudinal components of the turbulence) which must then be corrected
for aircraft motion. Motion corrections are provided by data from an onboard
inertial platform and from rate gyros. These corrections are especially impor-
tant, the present emphasis being on accurate data at long wavelengths. The
equations are given in reference 2. To obtain power estimates at the extremely
low frequencies required (that is, long wavelengths), narrow spectral "windows"
(bandwidths) on the order of 0.02 Hz must be used in the data processing proce-
dure. Such narrow spectral windows introduce wild statistical fluctuations in
the power estimates unless relatively long data samples can be obtained. The
statistical reliability believed to be necessary requires on the order of 24
to 30 statistical degrees of freedom for the spectral values and translates to
data samples of at least 19-minute duration. The instrumented B-57B sampling
airplane is shown in figure 3. Details concerning the power spectral algorithms
employed, and the justification for not prewhitening the time histories for long
wavelength analysis are given in reference 3. Instrumentation details and
measurement accuracies are given in reference 4. An assessment of the overall
instrumentation performance by means of inflight maneuvers, together with an
assessment of possible low-frequency trend type errors based upon postflight
performance of the inertial platform system, is given in reference 5.

Sampling flights with the B-57B were made in the March 1975 to September
1975 time period. A total of 46 flights were made, 30 in Eastern United States
within range of the airplane based at Langley Air Force Base, Virginia and 16 in
Western United States within range of the airplane based at Edwards Air Force
Base, California. A full time project meteorologist provided functions of coor-
dinating and planning flights, observing from the rear seat during the flight,
and conducting postflight analysis to document pertinent meteorological param-
eters and to define the meteorological position where turbulence was encountered.

A summary of data obtained is given in table 1 with the number of data
runs to be processed associated with various meteorological conditions. Data pro-
cessing is currently in process. Four samples (identified by asterisks in
table 1) have been selected for detailed discussion in this paper.

DATA DESCRIPTION AND DISCUSSION

The four cases selected for detailed discussion herein are categorized
according to meteorological conditions. (The mountain wave case appears to also
involve some wind shear and thus probably should not be considered to be a pure
classical case of mountain-wave turbulence.) Pertinent information for the four
cases is summarized in table 2. Run lengths are given for the four cases
and, associated with the run lengths, the statistical degrees of freedom (ref. 6)

appropriate for the resulting power spectra are also given. It was a goal in this program to achieve at least 24 statistical degrees of freedom with a resolution bandwidth of 0.02 Hz. Note that for the rotor case, the goal was not quite achieved; thus, somewhat larger random-type fluctuations can be expected in these power spectral estimates. Root-mean-square (σ) values for the three components of turbulence (longitudinal (u), lateral (v), and vertical (w)) are also given in table 11. Note that for the convective and perhaps the rotor case, the σ values are similar for the three components. However, for the wind-shear and mountain-wave cases the vertical component has a much smaller σ value than that of the lateral component by factors of 3 to 4 which indicates a lack of isotropy. This aspect will be discussed later in the paper. Data to be presented and discussed for the four cases will include time histories, power spectra, and exceedance curves.

Time histories for the convective case at an altitude of 0.3 km (1000 ft) above gently rolling terrain are given in figure 4. Because of the length of this run (19.1 minutes), the first part of the time histories is shown in figure 4(a) and the final portion in figure 4(b). As shown in table 11, the σ values are similar for the three components and are about 1.2 m/s (4 fps).

The power spectra resulting from these time histories are shown in figure 5. The curves are comparable to those of figure 1 except that the results have not been normalized; that is, the area under the curves is equal to the variance or σ^2. The abscissa values were obtained by converting frequency to inverse wavelength by use of the average true airspeed for each run. Symbols are shown for the five lowest frequency power estimates. Except for the first point, which will be discussed subsequently, the estimates are at equal increments of approximately 0.01 Hz (10 Hz/1024). On a log plot the points therefore appear closer together at higher values of $1/\lambda$. The first point is obtained from the data-reduction algorithm at zero frequency but, for convenience, is located at one-fourth the interval between zero and the next regularly obtained point at 0.01 Hz, or at 0.0025 Hz. (The value could not, of course, be shown at zero frequency on a logarithmic plot.) These zero-frequency power estimates are believed to be valid for the results presented in this paper. (See ref. 5.) Past practice has been to discard this value because of the effect of trend errors in the time histories, and because the prewhitening procedure used at that time for wide-band spectral analysis caused the value to go to infinity. Superimposed on the data are shown theoretical von Karman type curves with selected L values. Note that the slopes of the curves match at the higher frequencies. It is shown that the vertical component can be described very accurately with an L value of 300 m (1000 ft). The lateral component, however, has relatively higher power content at low frequencies and the appropriate L value is apparently in the range of 600 m (2000 ft). The longitudinal component fits well with an L value of 1200 m (4000 ft). This difference between components, of course, means that the turbulence is not isotropic in the long wavelength region. In the wavelength region where previous measurements have been made, however, isotropy would seem to prevail.

The time histories for the high-altitude wind-shear case are presented in figure 6. It should be noted that the vertical-scale sensitivities have been decreased by a factor of 2 as compared with the preceding case and that the

severity is much greater. The intensity of the turbulence for all three com-
ponents is gradually increasing with time. Such nonhomogeneous (or nonstationary)
behavior has generally been believed to be responsible for considerable rounding
or smoothing of the spectral knee. The recent work of reference 7, however,
indicates that unless the change in intensity is considerably more abrupt than
shown here, little effect should be observable in the spectra. It is obvious
that significant low-frequency power is present in the horizontal components;
this is assumed to be directly attributable to the changing horizontal wind
field. The low-frequency content can be thought of as a modulation of the mean
value with a typical high-frequency amplitude-modulated random process super-
imposed. A model of turbulence which includes mean modulation has been suggested
by Reeves (ref. 8). No pronounced low-frequency power is noted in the vertical
component. These observations are substantiated in the corresponding power
spectra shown in figure 7. Note that while an L value of 300 m (1000 ft)
appears to be appropriate for the vertical component, L values of greater
than 1800 m (6000 ft) would apply for the horizontal components directly reflect-
ing the large power content at low frequencies.

The next case to be presented was an encounter on the lee side of the
Sierra Mountains in California at an altitude approximately level with the
higher ridges. The turbulence was categorized as rotor-type turbulence. The
onboard observer reported direct correlation of turbulence severity with the
upwind terrain. Peak center-of-gravity acceleration increments of 1g were
equaled or exceeded 80 times in this traverse of the rotor region, with maximum
incremental accelerations of +2.2g and -1.8g. Time histories of the three
components of turbulence are given in figure 8. Note the segments between $4\frac{1}{4}$
and $7\frac{1}{4}$ minutes for the longitudinal component where high-frequency oscillations
are absent. This condition is caused by the sensitive airspeed measurement
system being off-scale some of the time in the negative direction; as a result,
the high-frequency fluctuations were partially lost. It can be seen that rela-
tively low-frequency wavelike oscillations are present on all three time histo-
ries, the lateral component exhibiting the most prevalent and highest amplitude
oscillations. The σ values given in table II further substantiate this obser-
vation. The spectra for this case are given in figure 9. All three spectra
continue upward with large low-frequency power; thus, if the von Karman expres-
sion is applicable in this region, L must be greater than 1800 m (6000 ft).
It should be noted that the high-frequency part of the longitudinal spectrum,
as well as σ_u, could be somewhat contaminated by the loss of the high-frequency
fluctuations as a result of the partial off-scale condition previously mentioned.
The flattening-out of the high-frequency end of the spectrum is not associated
with this problem but is a result of the use of the high-altitude restrictor
provided for the pitot-static test head. The use of two different restrictors
for flight operations above and below 9.1 km (30 000 ft) to provide the proper
damping for the sensitive airspeed measurement is discussed in reference 4. In
this particular case the high-altitude restrictor was installed, since the orig-
inal mission for this flight was to seek high-altitude mountain-wave turbulence.

The final case considered herein is categorized as lee wave-generated turbu-
lence which propagated upward and was encountered at an altitude of about 14.3 km
(47 000 ft). The time histories are given in figure 10. Notice that the vertical
component contains at least three waves and possibly four. Patches of turbulence

occur on the rising part of the last two waves; or at approximately $7\frac{1}{2}$ and 10 minutes from the start of the run. Apparently, the last two waves have not broken down into continuous turbulence as yet, or the displacement of the airplane has carried it out of the turbulent region of the wave. Inspection of the lateral and longitudinal components, where a very long wave can be seen, together with supplementary meteorological information, indicates that wind-shear effects were also present. Thus, this is not a classic case of pure mountain-wave turbulence. These time histories are of considerable interest; whether they should be used to obtain power spectra might be debatable since the turbulence is not very continuous. Power spectra were obtained, however, for the whole 12.6-minute run and are shown in figure 11. A large amount of low-frequency power is present in all three components. This case is in contrast to the wind-shear-alone case where the vertical component contained relatively little low-frequency power.

Figure 12 presents the measured exceedances of the vertical velocity component of turbulence for the four cases considered herein. The exceedances are (for each selected level) the average of the crossings of the positive and negative levels about the zero mean value for the data run. Only positive slope crossings are counted. In figure 12, the crossings per unit distance (in both km and mi) are shown on a logarithmic scale with the level of the vertical velocity component on a linear scale. The exceedances reflect the relative turbulence intensity levels of the four cases. The high intensity rotor and high-altitude wind-shear cases show significantly more crossings than the convective and mountain-wave cases; for example, at a level of 5 meters per second the difference is about two orders of magnitude.

The four exceedance curves of figure 12 show a combination of the exponential and Gaussian functional forms which are used for the analysis of atmospheric turbulence data. The exponential form of the exceedance expression has generally been found applicable for extended data samples or composites of many samples. It is the basis for development of structural design criteria for aircraft response to atmospheric turbulence for both the discrete gust approach and the random process or power spectral method. The exponential form would appear as a straight line on the semi-log plot of figure 12. From inspection of the figure, it appears that the high-altitude wind-shear case is the most nearly exponential (linear) and the rotor case would appear to be the most nearly Gaussian.

CONCLUDING REMARKS

Data have been collected for a number of turbulence encounters at altitudes between 0.3 and 15 km (1000 and 50 000 ft). The associated meteorological conditions have been identified. Four encounters were considered herein. For these cases the following observations are made:

1. The von Karman turbulence model seems to be appropriate for the vertical component in the low-altitude convective and high-altitude wind-shear cases, with an integral scale value of 300 m (1000 ft).

276

2. The lateral and longitudinal components appear to also fit the model fairly well for the low-altitude convective case when integral scale values of 600 m (2000 ft) and 1200 m (4000 ft), respectively, are used.

3. For the horizontal components in the high-altitude wind-shear case, and all three components in the rotor case, very large power obtained at the long wavelengths makes it doubtful whether the von Karman expression is applicable in this region. If it is, integral scales values greater than 1800 m (6000 ft) are required.

4. The time histories from the mountain-wave case appeared to include some effects of wind shear. All the "waves" had not broken down into continuous turbulence and were thus probably not especially appropriate for spectral representation. Very large power however was present at long wavelengths.

5. All cases exhibited the -5/3 slope of the von Karman expression in the shorter wavelength region.

6. The turbulence intensity was very severe for the rotor case and approached that of a small thunderstorm.

Data processing and further analysis are continuing. At the present time it is not known whether similar meteorological conditions will result in similar power spectra. The instrumentation system is scheduled to be installed in a B-57F aircraft later this year in order to acquire turbulence samples above 15 km (50 000 ft).

REFERENCES

1. Houbolt, John C.; Steiner, Roy; and Pratt, Kermit G.: Dynamic Response of Airplanes to Atmospheric Turbulence Including Flight Data on Input and Response. NASA TR R-199, 1964.

2. Murrow, Harold N.; and Rhyne, Richard H.: The MAT Project - Atmospheric Turbulence Measurements With Emphasis on Long Wavelengths. Proceedings of the Sixth Conference on Aerospace and Aeronautical Meteorology of the American Meteorological Society, Nov. 1974, pp. 313-316.

3. Keisler, Samuel R.; and Rhyne, Richard H.: An Assessment of Prewhitening in Estimating Power Spectra of Atmospheric Turbulence at Long Wavelengths. NASA TN D-8288, 1976.

4. Meissner, Charles W., Jr.: A Flight Instrumentation System for Atmospheric Turbulence Data. NASA TN D-8314, 1976.

5. Rhyne, Richard H.: Flight Assessment of Atmospheric Turbulence Measurement System With Emphasis on Long Wavelengths. NASA TN D-8315, 1976.

6. Otnes, Robert K.; and Enochson, Loren: Digital Time Series Analysis. John Wiley & Sons, Inc., c.1972.

7. Mark, William D.; and Fischer, Raymond W.: Investigation of the Effects of Nonhomogeneous Behavior on the Spectra of Atmospheric Turbulence. NASA CR-2745, 1976.

8. Reeves, Paul M.; Joppa, Robert G.; and Ganzer, Victor M.: A Non-Gaussian Model of Continuous Atmospheric Turbulence for Use in Aircraft Design. NASA CR-2639, 1976.

TABLE I.- SAMPLING SUMMARY OF B-57B FLIGHTS

[46 FLIGHTS WERE MADE BETWEEN MARCH 1974 AND SEPT. 1975]

(30 EASTERN U.S. AND 16 WESTERN U.S.)

TURBULENCE CATEGORY	NUMBER OF DATA RUNS	
TERRAIN RELATED, ROTOR*	14	(6 FLIGHTS)
THERMAL , CONVECTIVE*	8	(2 FLIGHTS)
NEAR THUNDERSTORMS	12	(2 FLIGHTS)
JET STREAM AND HIGH-ALTITUDE WIND SHEAR*	27	(6 FLIGHTS)
MOUNTAIN WAVES*	8	(4 FLIGHTS)
ISOLATED SITUATIONS	7	(2 FLIGHTS)

* CASES SELECTED FOR REVIEW IN THIS PAPER

TABLE II.- PERTINENT DATA FOR FOUR SELECTED CASES

METEOROLOGICAL CONDITION	ALTITUDE , km (ft)	RUN LENGTH		STATISTICAL d.f. FOR POWER SPECTRA	σ_w , m/sec (ft/sec)	σ_v , m/sec (ft/sec)	σ_u , m/sec (ft/sec)
		min	km (miles)				
CONVECTIVE	0.3 (1000)	19.1	148 (91.7)	45	1.15 (3.78)	1.18 (3.86)	1.35 (4.41)
WIND SHEAR	13.0 (42600)	12.2	137 (85.1)	29	2.45 (8.05)	7.33 (24.03)	4.48 (14.70)
ROTOR	3.9 (12800)	8.1	88.5 (55.0)	19	3.82 (12.52)	5.51 (18.09)	3.57 (11.73)
MOUNTAIN WAVE	14.3 (46800)	12.6	149 (92.4)	29	1.34 (4.41)	5.39 (17.69)	4.30 (14.11)

d.f. = f (BANDWIDTH, LENGTH)
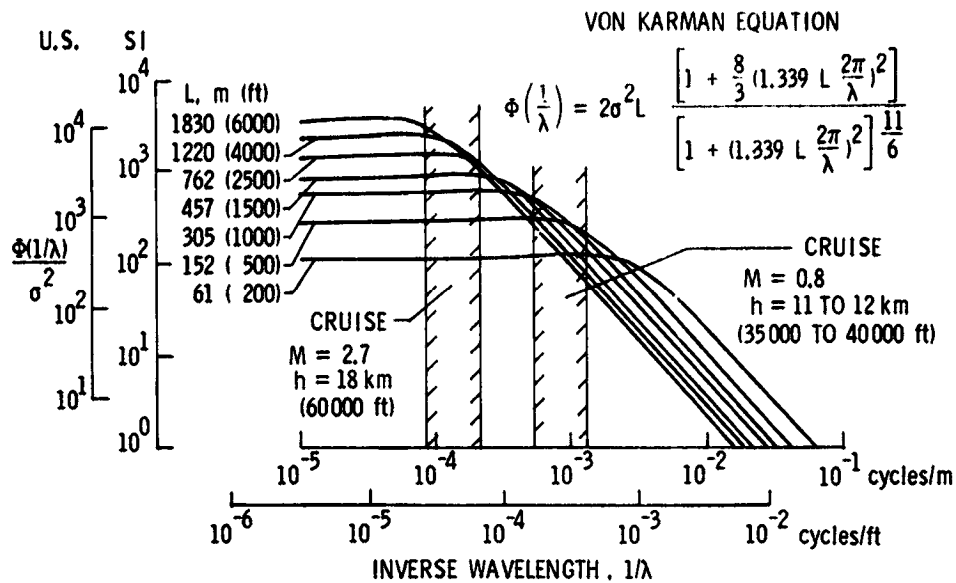
Figure 1.- Wavelength regions of primary aircraft response
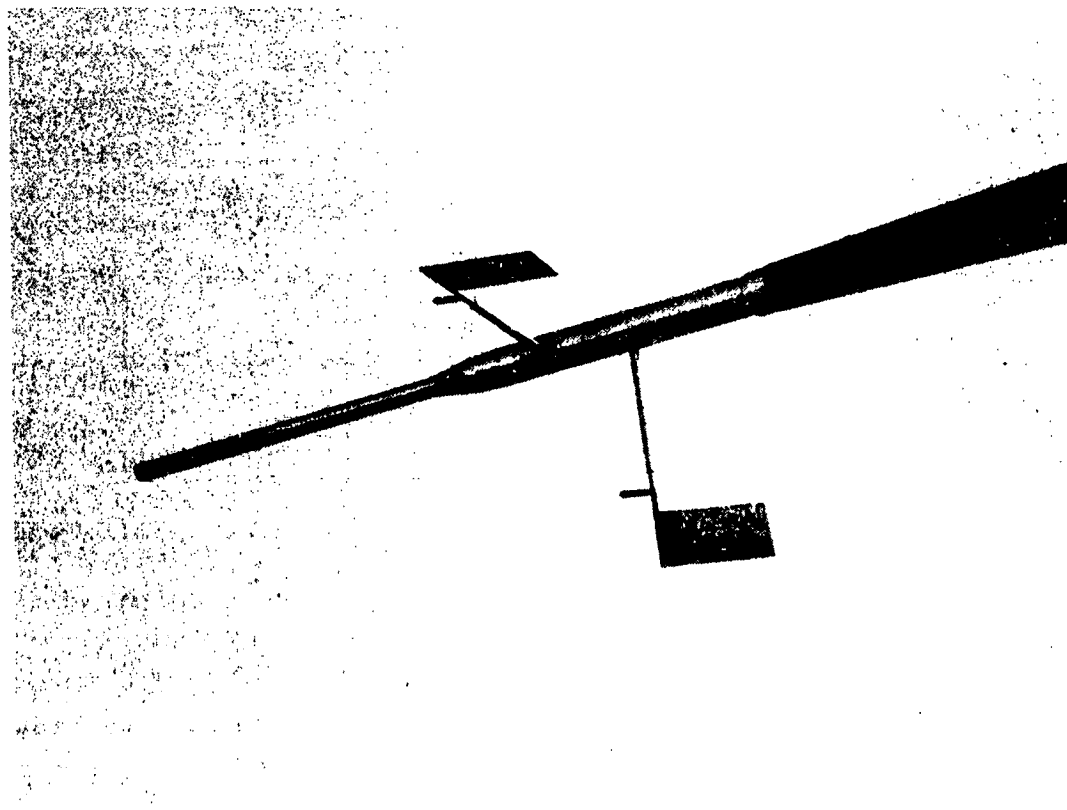shown on von Karman theoretical spectra.

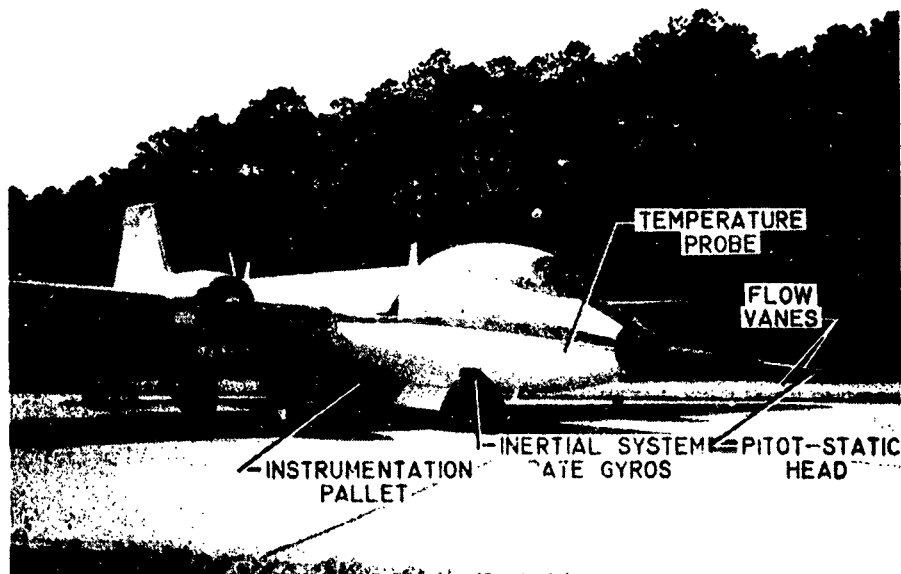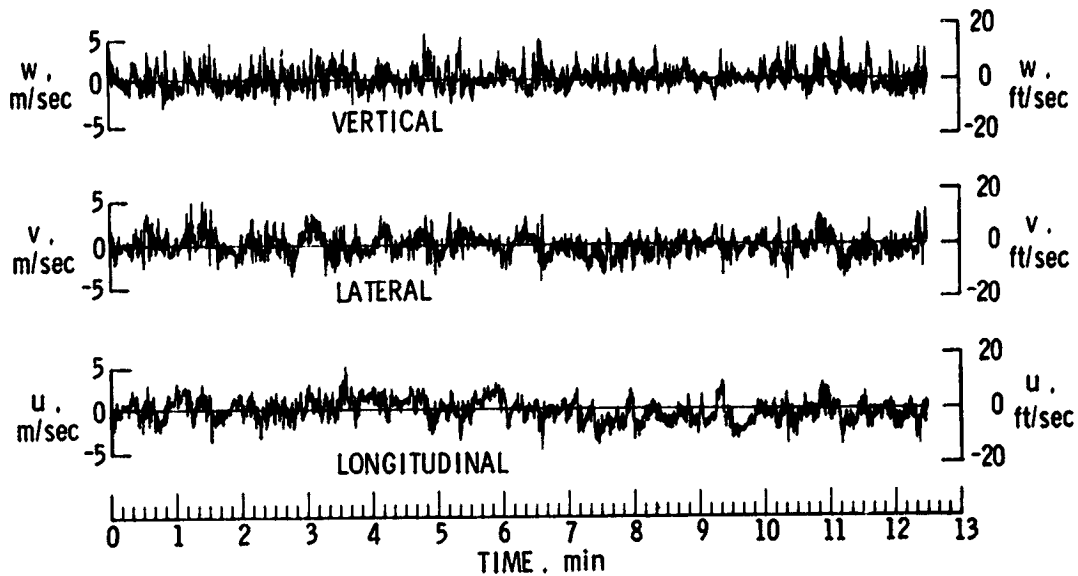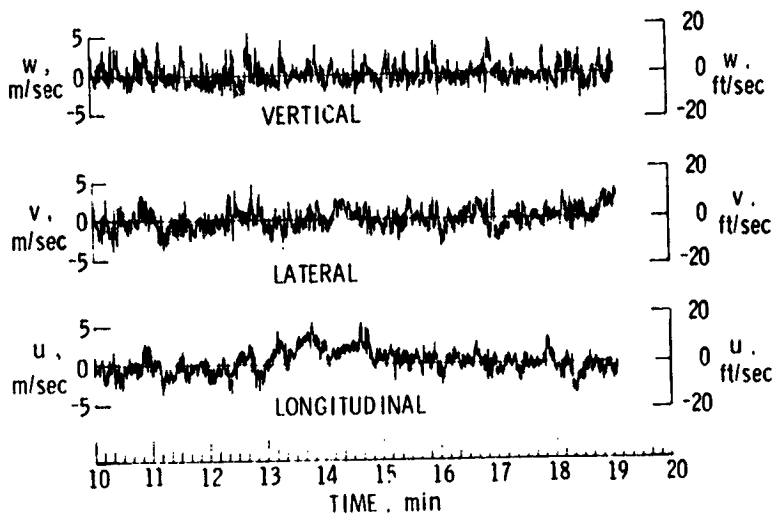Figure 2.- Head for providing three basic measurements.

Figure 3.- Instrumented airplane.

(a) Time interval, 0 to 12.5 minutes.

(b) Time interval, 10 to 19 minutes.

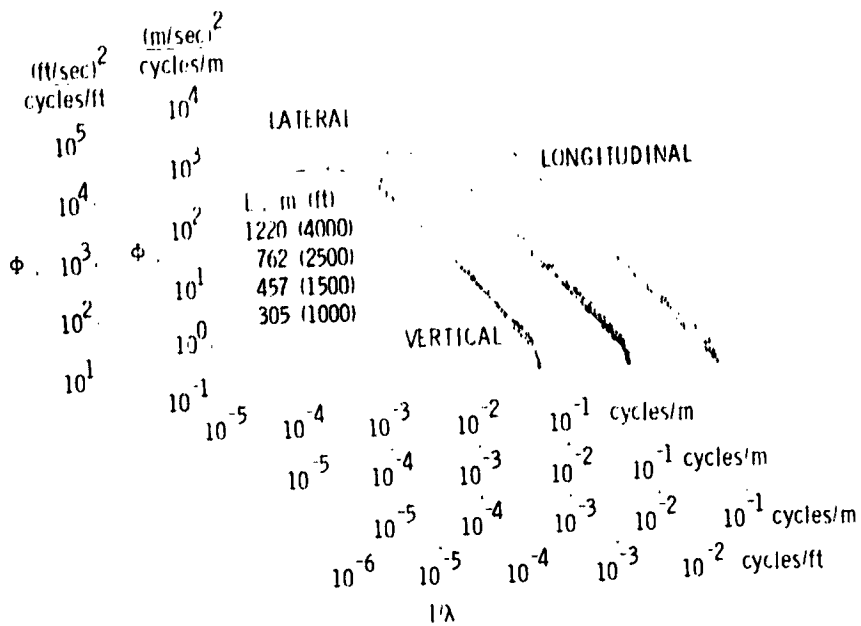Figure 4.- Turbulence component time histories. Convective case.

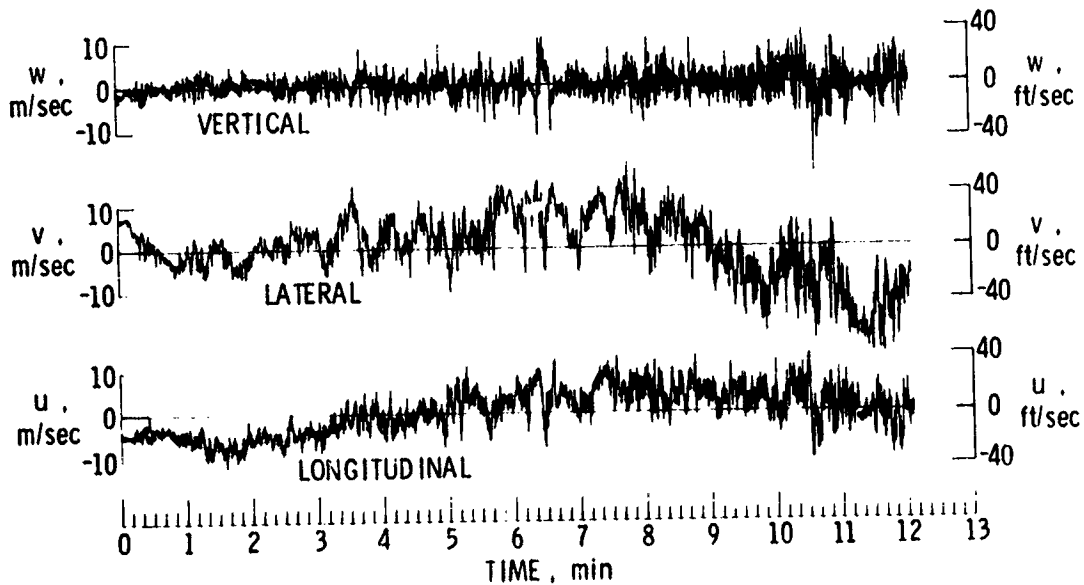Figure 5.- Power spectra of turbulence components.
Convective case.

Figure 6.- Turbulence component time histories.
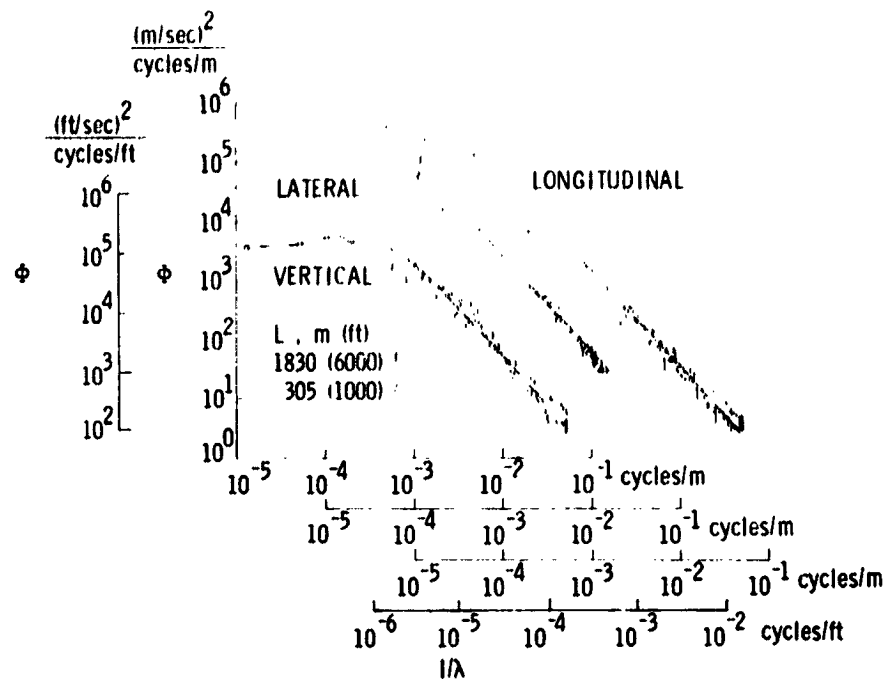High-altitude wind-shear case.

283

Figure 7.- Power spectra of turbulence components.
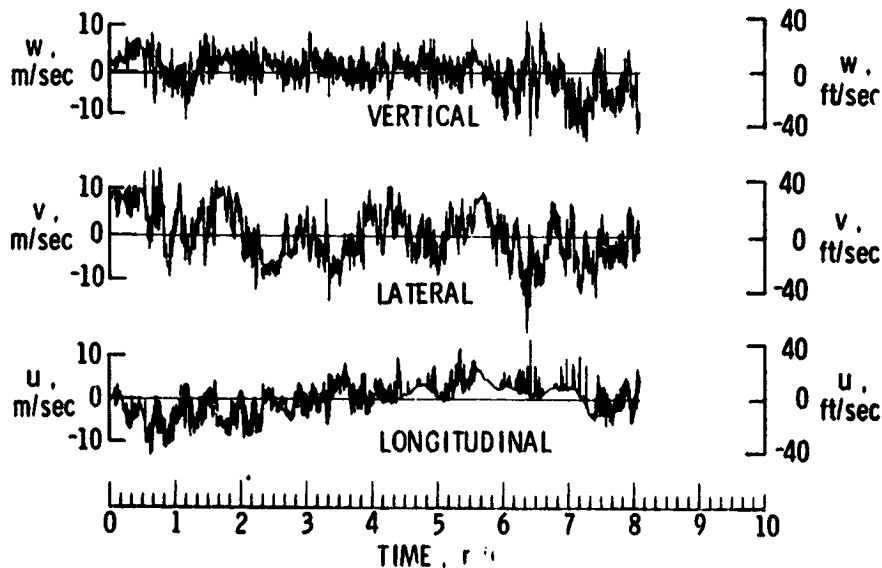High-altitude wind-shear case.

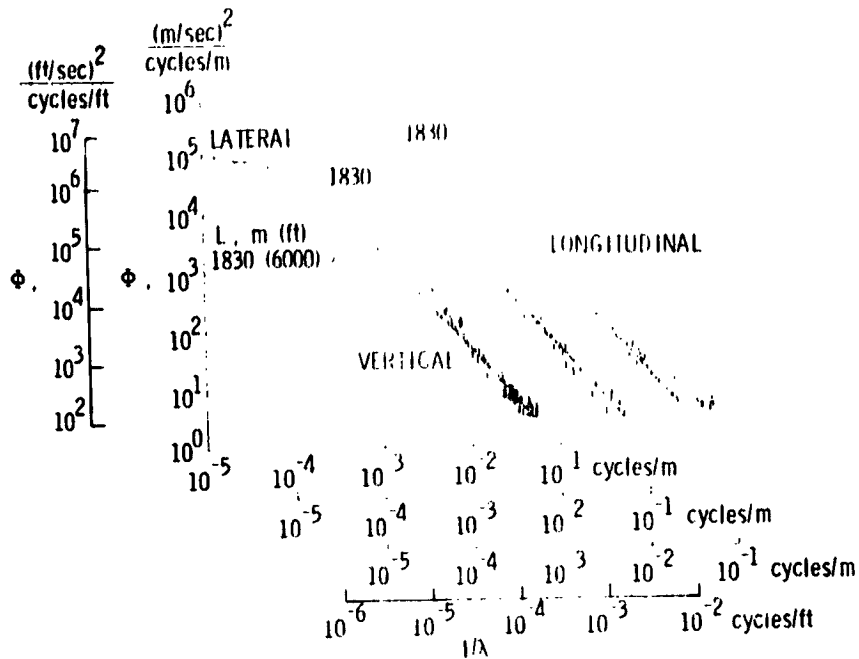Figure 8.- Turbulence component time histories.   Rotor case.

284

Figure 9.- Power spectra of turbulence components. Rotor case.
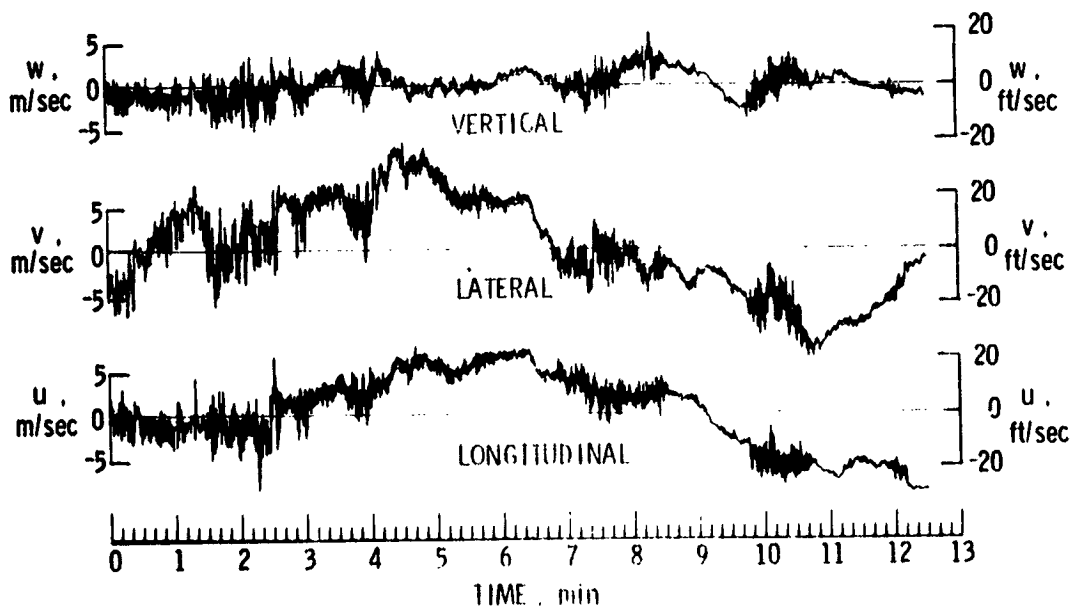

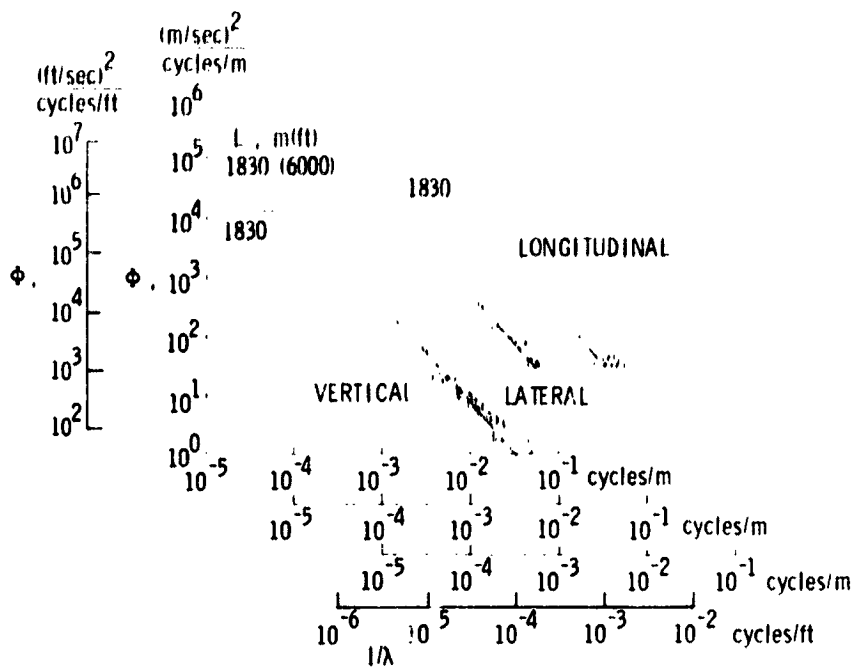Figure 10.- Turbulence component time histories. Mountain-wave case.

Figure 11.- Power spectra of turbulence components.
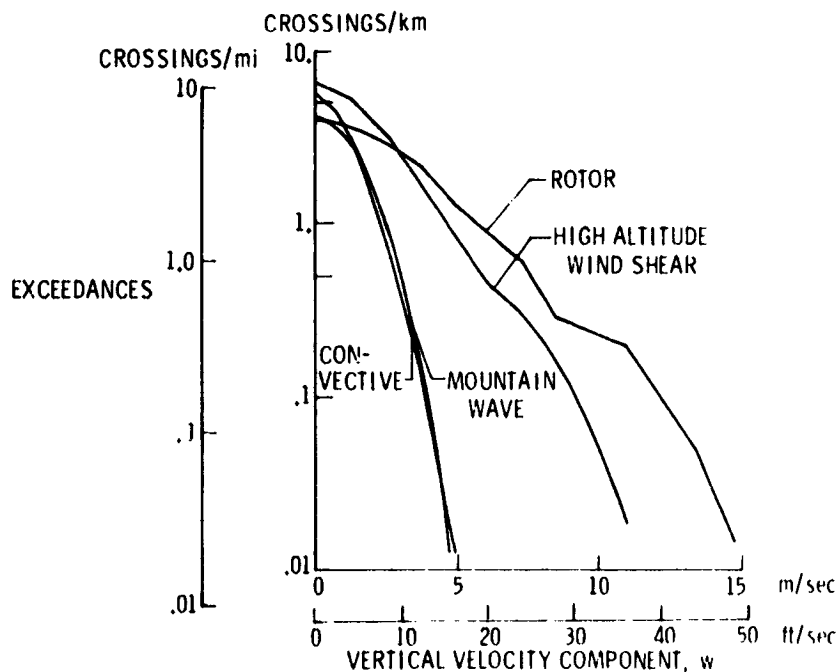Mountain-wave case.

Figure 12.- Measured exceedance frequency of vertical component
of gust velocity for four meteorological cases.

286

LASER DOPPLER TECHNOLOGY APPLIED TO

ATMOSPHERIC ENVIRONMENTAL OPERATING PROBLEMS

Edwin A. Weaver, James W. Bilbro, James A. Dunkin, Harold B. Jeffreys
NASA Marshall Space Flight Center

SUMMARY

Laser Doppler technology is being developed and applied to aviation safety problems in the atmospheric environment. The feasibility ` this technique was established when CO_2 laser Doppler ground wind data were very favorably compared with data from standard anemometers. As res of these measurements, two breadboard systems have been deve'oped fo taking research data; a continuous wave velocimeter and a ied \   system. The scanning continuous wave laser Doppler . er was developed for detecting, tracking and measuring   .. wake vortices. It was successfully tested at an airport where   located vortices to an accuracy of 3 meters at a range of 150 meters. The airborne pulsed laser Doppler system was developed to detect and measure Clear Air Turbulence (CAT). This system was tested aboard an aircraft, but jet stream CAT was not encountered. However, low altitude turbulence in cumulus clouds near a mountain range was detected by the system and encountered by the aircraft at the predicted time. The hardware is being modified to extend the performance and range. The application of these systems, data highlights and test results are presented in this paper.

INTRODUCTION

NASA is sponsoring research and development of Carbon Dioxide (CO_2) Laser Doppler System Technology and its application to aircraft operating problems that are caused by adverse natural and induced atmospheric environments. The breadboard sensors developed under this technology use basically the same principle as conventional Doppler radar. In the laser Doppler system case, coherent laser radiation is Doppler shifted in frequency when it is scattered by the natural aerosols of the atmosphere that are in motion at the velocities of the wind or turbulence. The frequency of the scattered radiation is compared to the frequency of the laser beam by photomixing. The resultant difference frequency is directly proportional to the line-of-sight velocity of the aerosols when the transmitting and receiving optics are aligned on the same axis. This principle is illustrated in figure 1.

The application of the technology to measure atmospheric winds was started at MSFC about ten years ago by Mr. Milton Huffaker, now of the Wave Propagation Laboratory, National Oceanic and Atmospheric Administration. The feasibility of the atmospheric measuring concept was demonstrated by using a CO_2 laser system to measure ground winds. The data from these measurements compared very favorably with simultaneous cup anemometer, wind-vane sensor, and hot wire anemometer data. These measurements have been discussed in several publications.

The first laser Doppler systems application to aircraft operating problems was the detection and measuring of clear air turbulence. A breadboard airborne system was developed and tested in 1972 and 1973 aboard the Convair 990 aircraft based at the Ames Research Center. During these tests the concept of an airborne laser Doppler system to detect turbulence was successfully demonstrated. Although high altitude jet stream CAT was not found, turbulence in cumulus clouds was detected and encountered by the aircraft as predicted by the laser Doppler system.

In 1969 wake vortices from a DC-3 aircraft were successfully detected by a CO_2 laser Doppler system in a cooperative effort with the Langley Research Center. The data from these feasibility tests were reported in the 1971 NASA Aircraft Safety and Operating Problems Conference. Design studies and research activities for the development of an improved breadboard system were initiated after the concept feasibility tests.

In 1973, the Federal Aviation Administration requested the NASA's Marshall Space Flight Center to develop a breadboard scanning continuous wave laser system for detecting, tracking and measuring aircraft wake vortices in the landing corridor of an airport. This system was developed and successfully tested in 1974 and 1975 at the John F. Kennedy International Airport (JFK). The tests provided vortex data and tracks on over 1600 aircraft landings. These two breadboard systems will be discussed in more detail.

There is always a concern for personnel safety when laser systems are used. These systems are designed to meet conservative safety requirements. In addition, ordinary glass and plastics will reflect the CO_2 laser radiation and therefore, will prevent eye damage.

SCANNING LASER DOPPLER VELOCIMETER FOR VORTEX MEASURING

The Scanning Laser Doppler Velocimeter (SLDV) System shown in figure 2 is capable of detecting, tracking, and measuring the velocity patterns of aircraft wing tip vortices as well as general atmospheric turbulence. The SLDV is a continuous wave, focused, coaxial optical system which operates with a CO_2 laser emitting infrared radiation at a wavelength of 10.6 micrometers. This system is installed in an equipment van and consists of a 20 watt very stable CO_2 laser, a modified Mach-Zehnder interferometer, a Bragg cell frequency translator, an F/2 cassegrainian telescope with a 30.5 cm (12 in.) aperture, an infrared detector, a versatile range and angle scanner, a signal

288

processor, a data algorithm processor, various displays and recording electronics. The system is designed to have a range coverage of 61 to 610 m (200 to 2000 ft.) and an elevation coverage of 3° to 60°. The maximum range and angle scan rates are 7 Hz and 1 Hz, respectively. The system detects Doppler velocities and discriminates those up to 61 m/s (200 ft/s) in increments of 0.55 m/s (1.8 ft/s) and provides a line-of-sight velocity spectrum for the range resolution volume in space associated with the point where the system is focused. The velocity spectrum is processed along with scanner data to provide specific information on velocity magnitude, signal position in space and signal intensity as a function of time.

Following the development of the SLDV system, aircraft wake vortices and wind profile measurements were performed with two units installed at the JFK Airport. These measurements were performed in cooperation with the Department of Transportation's Federal Aviation Administration (FAA), Transportation Systems Center (TSC) and the National Aviation Facilities Experiment Center (NAFEC).

The test site at JFK Airport was located near the middle marker on Runway 31R which is about 765 m (2500 ft.) from the end of the runway. The site was instrumented with wind anemometers, pressure sensors, acoustic radars, as well as the laser Doppler system which served as the standard for the tests. Two SLDV units were located about 121 m (400 ft.) on either side of the runway centerline as shown in figure 3. This arrangement permitted these two independent sensors to scan a common area perpendicular to the aircraft landing corridor. The area of primary coverage by the laser systems for the vortex problem was 61 m (200 ft.) on either side of the runway centerline and 65 m (215 ft.) altitude.

To cover this primary area, the range position for the focus of the radiation was continuously cycled between a 61 m (200 ft.) and 305 m (1000 ft.) as the angular position for the focus was cycled between 3° and 33°. These two simultaneous movements of the radiation focus in this area perpendicular to the aircraft approach lane mapped out a finger like pattern in elevation for each scan frame. To provide adequate data density in the scanned area, a 7 Hz range scan rate and a 0.2 Hz elevation rate were used. These rates also gave a new frame of data across the vortices every 2.5 seconds. This continuous coverage of the scanned area provided the data for vortex time histories that will be discussed later.

The Doppler shifted radiation from the scanned areas was collected and mixed with the laser beam on an infrared detector where the radiation energy was converted to electrical energy. This electrical signal was then sent to the signal processor where the velocity data were sorted into .55 m/s (1.8 ft/s) increments. This data contained information on the ground wind speeds and the vortex velocities which were generally higher than the wind data. A velocity threshold was set above the peak wind speed so that only the vortex velocities were sent to the data algorithm processor along with

associated signal intensities and the position data obtained from the scanner. These data were then screened using the vortex location algorithm to assure that sufficient data existed to locate a vortex center. Further screening of the data assured that unusable data such as noise spikes were not used. Then, to locate the first vortex, the data were processed using a centroiding technique based on the maximum signal intensity of the usable data from a single frame of the scanned area. After finding the first vortex, the data used in determining its location were eliminated and the real time algorithm proceeded to look for a second vortex. After the second vortex was located, or if a second data area could not be defined, the chosen vortex centroids were displayed in real time and the location information was stored on a disk for later transfer to magnetic tape for use in vortex behavior studies.

Typical vortex tracks are shown in figure 4. The time based plots show altitude and lateral location of the port (0) and sta board (*) vortex centroids with time. When only one vortex was found a single position (S) was denoted for that scan frame. The position of the SLDV's at the test site is shown on the right hand plots of time versus range. The top curves are from SLDV 1 (van 1) and the bottom ones from SLDV 2 (van 2). A Boeing 707 aircraft, experiencing about a 0.9 m/s (3 miles/hr.) head wind, generated the vortex tracks. Most aircraft came over this point of the test site between 35 m (115 ft.) and 55 m (180 ft.) altitude. This one was just above 37 m (120 ft.) as indicated in the plots on the left of altitude versus time. There is general agreement between the data from SLDV 1 and SLDV 2. The better agreement in the data usually occurs at distances less than 152 m (500 ft.) from the SLDV location. The tabular data used in generating these plots is printed simultaneously. Processing of the data in a post processing mode allows all of the real time displays to be regenerated plus plots of peak velocity and peak intensity shown in both altitude and range.

The unthresholded data were also recorded and are being used to determine SLDV system performance and for study of the velocity flow fields. So far, the analysis shows that the vortex locations are within a 3 m (10 ft.) tolerance at 150 m (492 ft.) range and that the SLDV performed according to the theoretical design, thereby fully meeting the sensor development objectives.

Over 1600 flights on Runway 31R at JFK airport were monitored during the tests yielding vortex information on 13 different types of aircraft. The majority of the data is from B-707's, B-727's, B-747's and DC-8's. Peak vortex velocities of 30.5 m/s (100 ft./s) were measured and the vortices were tracked to a range of 457 m (1500 ft.). The data on vortex tracks were furnished to the Transportation Systems Center shortly after it was collected for analysis of vortex behavior and other studies which were part of the FAA's wake vortex program. Along with the MSFC, the Lockheed Missiles and Space Company, M&S Computing Company and the Raytheon Company participated in the SLDV development program.

290

When vortex data were not being collected, the data algorithm processor could be configured to give wind profiles in near real time. In this mode, data from the two independent units were processed for time correlation of the scans from the two systems and then spatially correlated to meet certain spatial requirements. These data were then used to determine the vertical and horizontal velocity components associated with a given altitude. A near real time plot of the resulting average horizontal and vertical wind components in the common scan area of the plane between the two sensors is shown in figure 5. Plotted here are the horizontal(X) and vertical (Y) velocity components as a function of altitude using data collected on April 1, 1975. The time correlation for these plots is 1.25 s., with a spatial correlation of 2 m (7 ft.) and the altitude increments are 6 m (20 ft.). From the recorded unthresholded data, similar wind information is available for each of the vortex time histories. This data may be of interest to those studying vortex behavior in ground effect.

A detailed description of the SLDV development is contained in references 1, 2 and 3.

THE CAT SYSTEM

Studies for the design and development of a breadboard pulsed CO_2 laser Doppler system began in 1968. The objective of this effort, illustrated in figure 6, was to determine experimentally whether a pulsed laser Doppler system aboard an aircraft could detect and measure CAT at a reasonable distance ahead of the aircraft, to make it a suitable principle for an onboard aircraft warning system. This is further discussed in references 4 and 5. Toward this goal a breadboard system was built, given an initial checkout, and then flight tested in 1972 and 1973. Following a detailed system and component evaluation, the hardware is being modified to improve the hardware performance, to increase the range and to provide a ground wind measuring capability. Extensive ground based tests are planned. These will be followed in 1978 by a flight evaluation test for CAT.

The CAT system consists of a very stable CO_2 laser, a modulator or pulse gate, a power amplifier, a modified Mach-Zehnder interferometer, an F/3 newtonian telescope, an infrared detector, a filter bank type signal processor, appropriate displays and recording electronics.

The transmitter part of the CAT system uses a master oscillator power amplifier configuration, similar to conventional pulse Doppler radar, to achieve high power output along with the good frequency stability needed for Doppler detection. The output of a frequency stable CO_2 laser is directed to the modulator where it is pulse modulated to drive the power amplifier. The output of the power amplifier goes to a telescope and is then transmitted forward of the aircraft through a Germanium window mounted in a special fairing pod on the side of the aircraft which serves as the view port for the instrument.

291

A small portion of the transmitted energy is backscattered by aerosols to the telescope where it is then directed to the infrared detector which is also receiving a small part of the outgoing laser beam. These two beams combine to yield a signal that contains the Doppler frequencies of the aerosols with respect to the aircraft speed. This signal is processed and analyzed by a filter bank to get the velocity and turbulence information of interest.

The primary characteristics of the tested system were a wavelength of 10.6 μm, a pulse length of 1 to 10 s, a pulse rate of 110 to 200 pulses per second, a peak power of 2.2 to 3.0 kW with an average power of 1.5 to 2.5 watts, a telescope diameter of 30.5 cm (12 inches), a signal integration of 50 pulses and a turbulence resolution minimum of 0.6 m/sec (2 ft/s).

The laser and optics equipment, as installed on the aircraft, is shown in figure 7. The signal processing equipment is shown in figure 8. Two similar racks of equipment contain power supplies, timing controls, displays and recorders. The development of this equipment is discussed in reference 6. The Galileo, a Convair 990 aircraft based at Ames Research Center was the flight test aircraft for the CAT system and is shown in figure 9. A special 46 cm (18 inch) diameter fairing shown over the wing was built to house a special window for the CO_2 radiation and a forward reflecting mirror that directed the laser radiation forward along the flight path. A close view of the fairing is shown in figure 10. The reflecting surface inside the fairing is a Germanium window that is transparent to the 10.6 m radiation.

The pulsed laser Doppler equipment shown above was tested aboard the aircraft in August and September 1972 and again in January 1973. Atmospheric Turbulence Targets were located including desert thermal turbulence and mountain wave turbulence, two types of CAT. These CAT encounters came after calibration and performance data were collected.

The CAT system data discussion requires a description of the data displays which were regularly photographed during the tests. These pictures are used extensively in the data analysis. One of the displays is a Range Velocity Intensity (RVI) display on which the vertical scale is velocity, range is on the horizontal scale, while intensity shows up as different brightness levels of the data. Figure 11 shows signals received from cirrus clouds at 10 km (33000 ft.) altitude with the aircraft traveling at 890 km/hr (480 knots). The data at the top of the display shows the true air speed of the aircraft out to a range of 20.5 km (11 nautical miles.) A spread or width about this velocity line would indicate turbulence. The brightness at the left of this line shows the high intensity signals received from the clouds at close range. The bottom part of the displays, indicated by the overlapping lines, are the signals from an A scope, which is a signal intensity versus range plot of the unprocessed velocity. In figure 11b, the total range on the A scope is 1/2 the range of the RVI display, so the signals of interest in the top half of the screen, identifying the cirrus clouds are at a range twice the indicated range on the RVI display.

292

The data in figure 12 shows three well separated clouds traveling at different speeds ahead of the aircraft. The data spot on the left of the top display shows the true air speed of the aircraft. Turbulence is indicated in both figure 12a and b. The width of the spectral returns on the lower screen indicates extreme turbulence, which is defined as gust velocities above 15 m/s (50 ft/s). A turbulence velocity of 19 m/s (63 ft/s) is shown. Figure 13 is a set of data confirming the encounter by the aircraft of turbulence detected by the CAT system shortly after the time of the data in figure 12. The top plot, 13a, is a display of the turbulence signal intensity versus velocity at a Greenwich mean time of 23:53:10. For a selected range, this display shows the velocity distribution from the filter bank. The peak of the curve is at the flight velocity and when turbulence is detected the peak signal flattens and there is an increase in the width of the velocity. In this display, the measured or selected range in signal time i.e., the round trip time to the turbulence at the speed of light, is 27 μs. This corresponds to a distance of 4 km (2.2 nautical miles). With the aircraft traveling at a speed of 665 km/hr (359 knots) the estimated time to the patch of turbulence is 22 seconds. The aircraft center of gravity accelerometer data was recorded and the signal for this aircraft encounter with the turbulence is shown in figure 13b which is a plot of G load versus time. The top curve is the vertical acceleration trace and the bottom one is a horizontal acceleration trace. The accelerometer data trace starts when the turbulence ahead of the aircraft appears on the intensity velocity display. Between 20 and 30 seconds, there are major changes in the acceleration curves especially the top trace. At 22 seconds, the identified time, the accelerometer already shows a change in G load, the change having started at about 18 seconds. The maximum acceleration is over 0.5 G and occurs at 24 seconds after the turbulence was identified. This set of data indicates that it is possible to identify turbulence ahead of the aircraft with the pulsed laser Doppler system, the CAT system, before it is encountered by the aircraft.

A dust storm in the Kingman, Arizona area was found during the flight on September 6, 1972. The aircraft did not fly into the storm because of the potential damage to the aircraft and the onboard instrumentation and experiments, but the aircraft was flown near it. Strong signal returns were collected by the CAT system and are shown in figure 14. The top set of data shows the increased signal intensity and the spread that is caused by the turbulence and the increased backscattered signal resulting from the dust. As the aircraft started away from the storm the CAT system detected a wind shear as shown on the RVI display. The difference in horizontal velocity measured over 3.0 km (1.6 nautical miles) range was about 50 km/hr (27 knots). The aircraft flew through this shear and its instrumentation recorded a 40 km/hr (22 knots) shear as it passed through the region where the laser system identified the shear.

The flight test results can be summarized as follows:

1. There were no CAT system operating problems resulting from the airborne environment.

2. Nonjet stream turbulence was identified and then encountered near a dust storm and on the east side of the Sierra Mountains in many cumulus clouds. Clear air mountain wave and desert thermal turbulence were identified and en-countered.

3. Wind shear was detected, measured, and encountered near a dust storm.

4. Clear air signals, where there was no turbulence, were measured at ranges of 5 to 9 km (3 to 5 nautical miles) and up to altitudes of 6.7 km (22,000 ft.).

5. Cirrus clouds were identified at altitudes between 7.6 to 11.5 km (25,000 to 38,000 ft.).

6. Three well separated cumulus clouds were detected simultaneously ahead of the aircraft.

The pulsed CO_2 laser Doppler system discussed above has demonstrated some of the capabilities essential to meet the stated objective for this develop-ment; to determine experimentally whether a pulsed laser Doppler system aboard an aircraft can detect and measure CAT sufficiently ahead of the aircraft to make it a suitable principle for an onboard instrument. MSFC supported by the Raytheon Company has been working to find the answer to this objective. The CAT system is now undergoing modifications to improve the performance of the hardware which should result in a transmitted signal that has greater coherence and increased signal strength. These improvements will result in increased detection range to as much as 18.5 km (10 nautical miles). The equipment is also being modified to enable measurement winds from the ground. With these improvements it appears that the stated objective requirements will be met during a future flight test.

CONCLUDING REMARKS

Presented above are two of the breadboard CO_2 laser Doppler systems that have been developed to help resolve aviation safety problems. Research and development is continuing on both of these breadboard systems to advance the systems technology and to take advantage of the advances in the state-of-the-art. Studies on applying this technology to measure pollution, wind shears, and severe storm winds are part of the overall program. Experience of value to these studies was gained when a ground based CW laser system was used to collect data on dust devil velocities. The advancement of this technology may lead to other applications for measurements of the atmosphere. The interest in these advances is based on the demonstrated results to date which are now summarized.

Laser Doppler technology has been used to successfully measure natural and induced atmospheric turbulence that affect aircraft and airport operations. Two breadboard systems have been developed and tested for making atmospheric velocity measurements.

294

1. A ground based continuous wave CO_2 SLDV tracked aircraft wing tip vortices and measured ground winds at an airport providing unique high quality test data on aircraft vortices.

2. A pulsed CO_2 laser Doppler system has measured true air speed, winds aloft, non-rain cloud locations, wind shear and turbulence. These feasibility measurements have lead to special application system studies.

The technology is advancing and will result in significant reductions in hardware size weight and power requirements while increasing range capability and data handling capability and capacity. This may then lead to the commercial use of these developments in solving some aircraft safety operating problems.

REFERENCES

1. Bilbro, J. W.; Jeffreys, H. B.; Weaver, E. A.; Huffaker, R. M.; Craig, D. G.; George, R. W.; and Marrero, P. J.: Laser Doppler Velocimeter Wake Vortex Tests, NASA TMX 64988, FAA-RD-76-11, March 1976.

2. Jeffreys, H. B.; Bilbro, J. W.: Development of a Laser Doppler System for the Detection and Monitoring of Atmospheric Disturbances, NASA TMX 64981, November 1975.

3. Huffaker, R. M.; Jeffreys, H. B.; Weaver, E. A.; Bilbro, J. W.; Craig, G. D.; George, R. W.; Gleason, E. H.; Marrero, P. J.; Reinbolt, E. J.; Shirey, J. E.: Development of a Laser Doppler System for the Detection, Tracking & Measurement of Aircraft Wake Vortices, NASA TMX 66868, FAA-RD-74-213, March 1975.

4. Dahm, W. K.; Dunkin, J. A.; Weaver, E. A.: Development of a Laser Doppler System for the Detection of Clear Air Turbulence. Paper presented at MSFC Research Review, February 1973.

5. Weaver, E. A.: Clear Air Turbulence using Lasers, NASA SP270, Vol. 1, NASA Aircraft Safety & Operating Problems, May 1971, pp. 89-100.

6. Jelalian, A. V.; Keene, W. H.; Sonnenschein, C. M.: Development of CO_2 Laser Doppler Instrumentation For Detection of Clear Air Turbulence, Raytheon Company, ER70-4203, ER72-4243 Final Report, NASA Contract NAS8-24742, NASA CR-127058, June 1970, May 1972
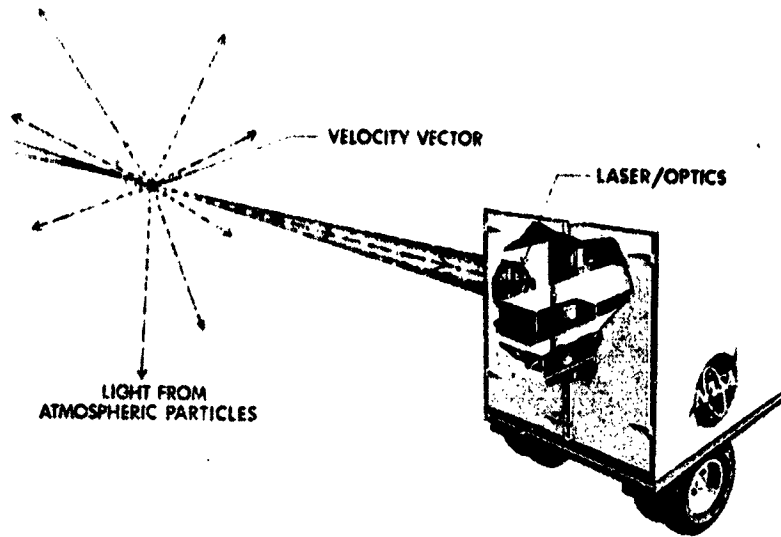
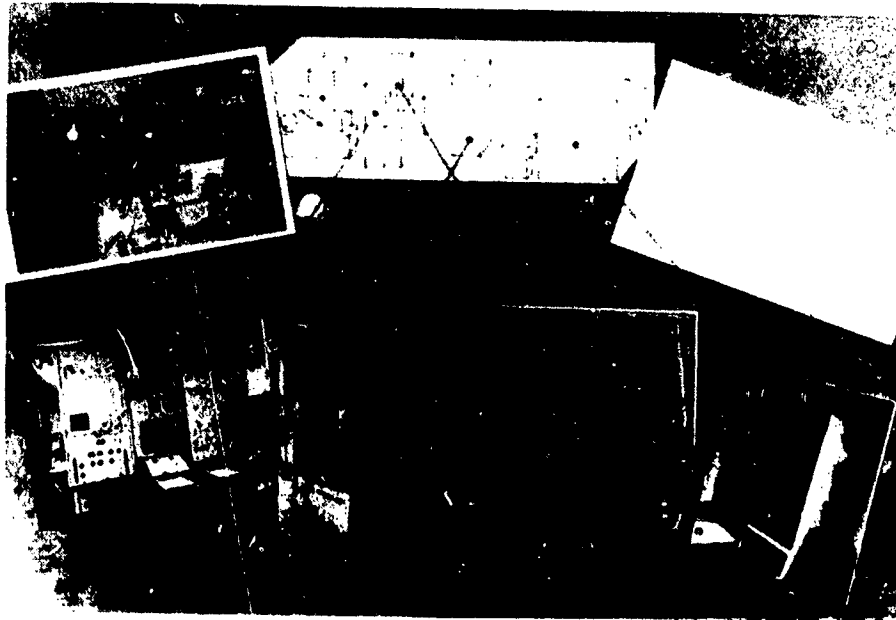Figure 1.- Laser Doppler principle.
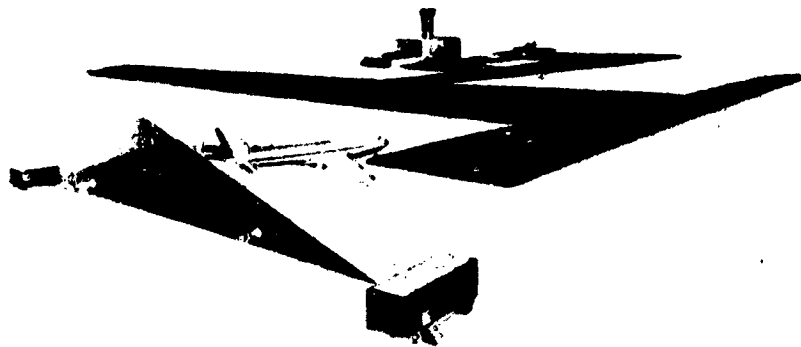

Figure 2.- Scanning laser Doppler velocimeter.

296

Figure 3.- Scanning laser Doppler velocimeter.
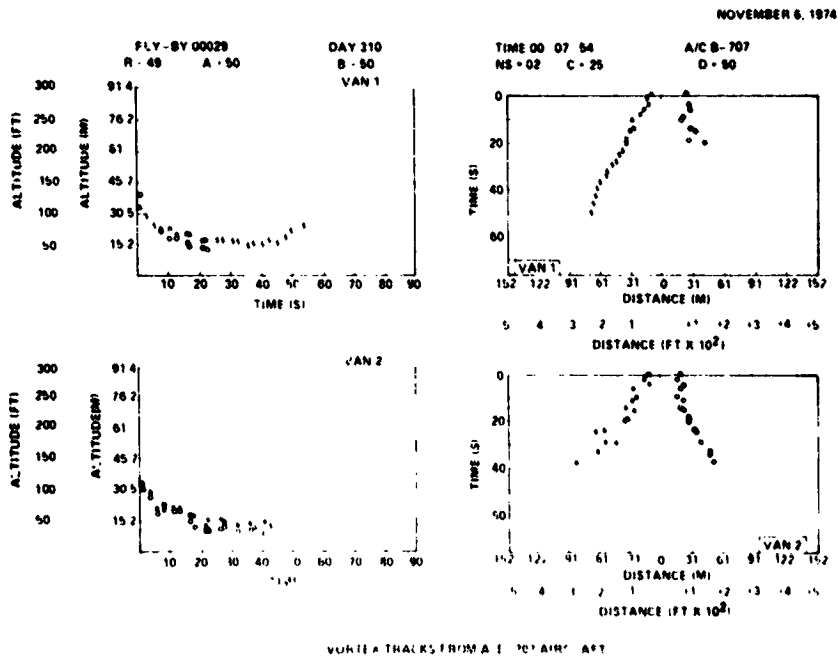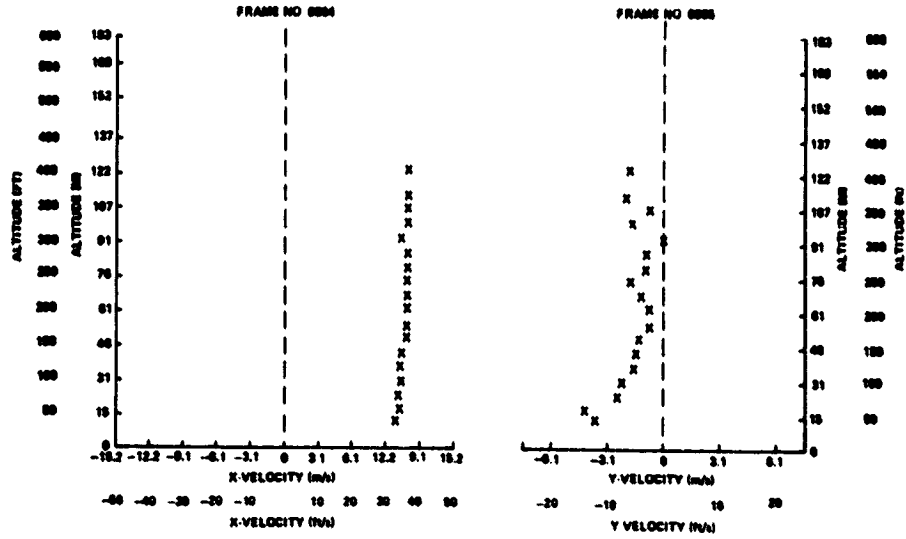JFK Airport operations.

Figure 4 - SLDV data.

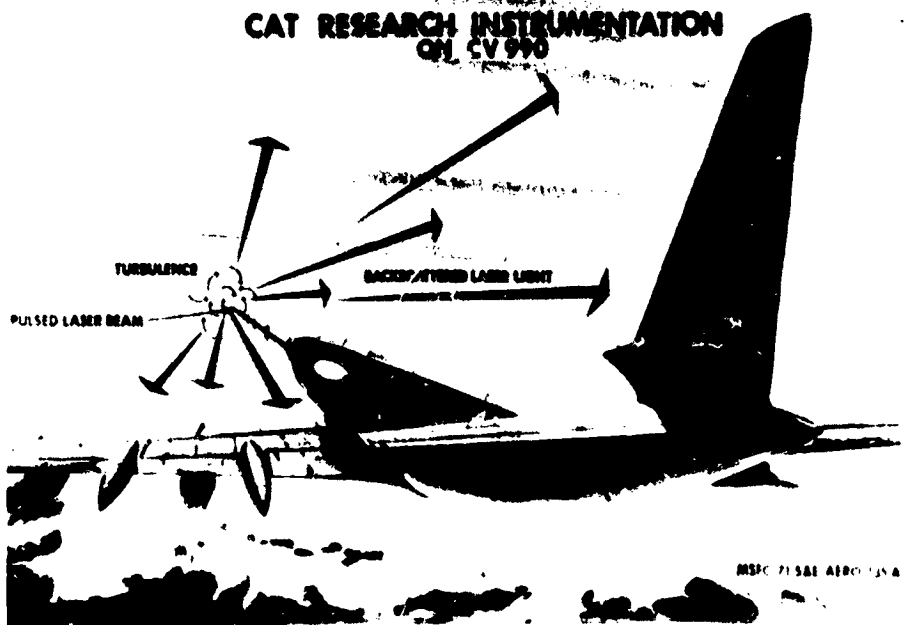Figure 5.- SLDV wind profile at JFK Airport.

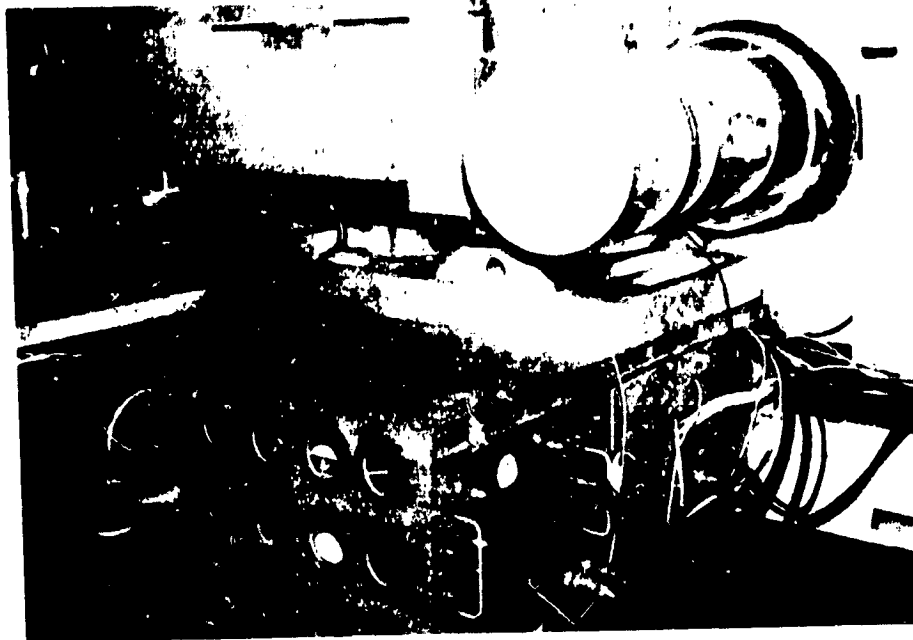Figure 6.- CAT research instrumentation on CV 990.

298

Figure 7.- CAT system, laser, optics and telescope assembly on CV 990 aircraft.
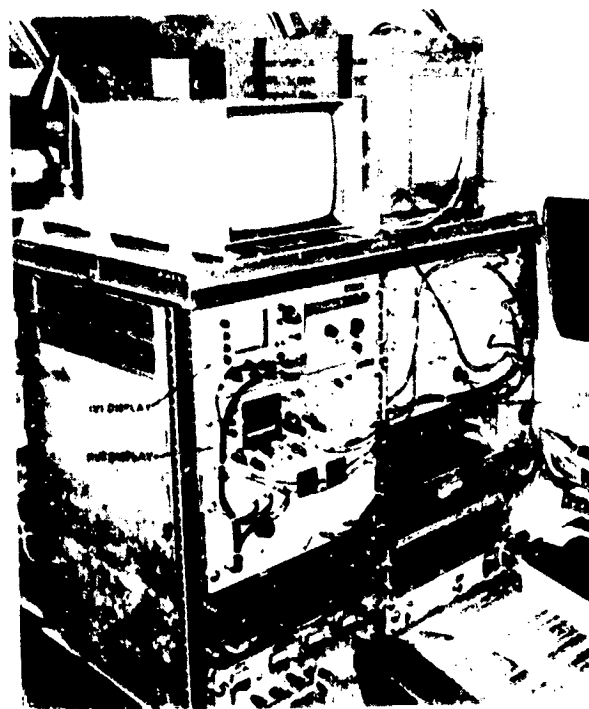

Figure 8.- CAT system signal processor and displays assembly on CV 990 aircraft.

Figure 9 - Convair 990 aircraft.

Figure 10. - CV aircraft Engine on CV 990 aircraft.
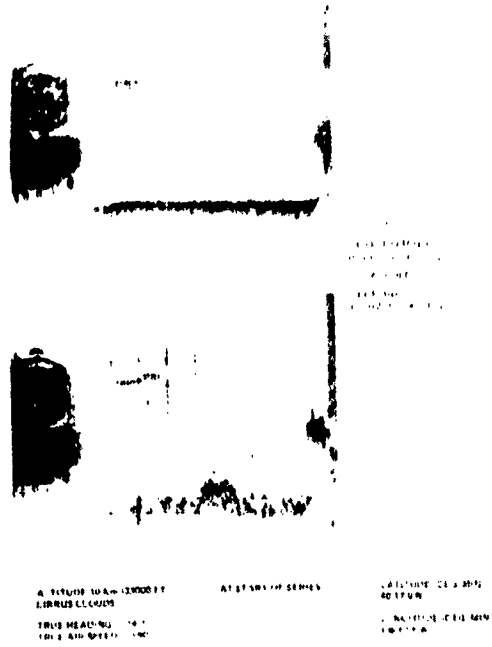
300

Figure 11.- CAT system data. Cirrus cloud returns.
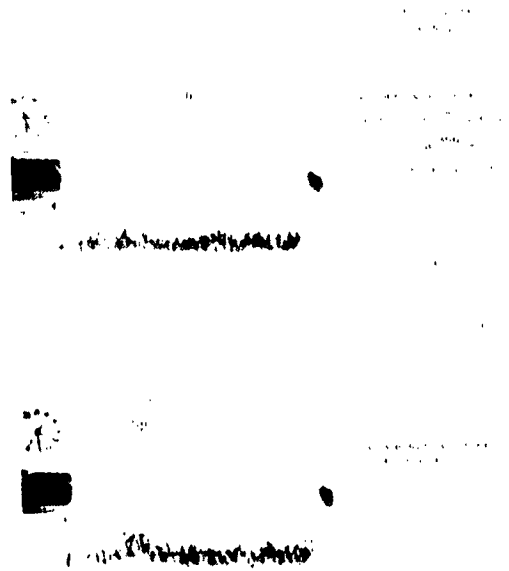
Figure 12.- CAT system data. Cumulus clouds.

301
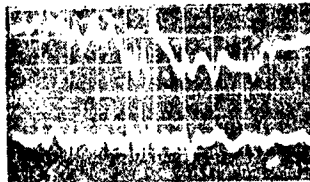
Figure 13.- CAT system data. Cloud
turbulence correlation data.
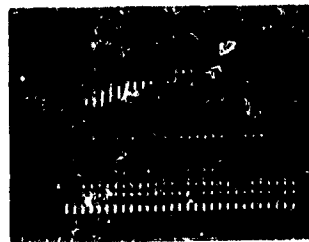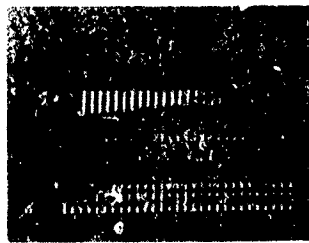

Figure 14.- CAT system data. Dust storms.

SUMMARY OF NASA WAKE-VORTEX MINIMIZATION RESEARCH

R. Earl Dunham, Jr.
NASA Langley Research Center

SUMMARY

This paper is a review of the NASA effort in the area of wake-vortex minimization and summarizes the results presented at the NASA Symposium on Wake Vortex Minimization, February 25 and 26, 1976, Washington, DC. Some additional results obtained since the symposium are also included. Theoretical and experimental techniques for assessing the effectiveness of various wake-vortex mini. zation techniques are described. Three methods of reducing the effect of aircraft trailing vortices and a preliminary assessment of the operational suitability of employing wake-vortex minimization techniques are discussed.

INTRODUCTION

Aircraft trailing vortices are one of the principal factors affecting aircraft acceptance and departure rates at airports. Minimization of the hazard posed by the vortex would allow reduction of the present spacing requirements. Such reductions would allow full utilization of advances in automatically aided landing systems (ref. 1) while maintaining or improving safety within the terminal area. For several years NASA has been conducting an intensive in-house and contractural research effort involving theoretical and experimental studies of various wake-vortex minimization techniques. This work was done in conjunction with the Federal Aviation Administration's investigation of various sensing devices for detecting the presence of vortices within the terminal area.

This paper is a brief review of NASA's effort in the area of wake-vortex minimization and summarizes the results presented at an NASA symposium on wake-vortex minimization (ref. 2). Additionally, some results, obtained since the symposium, of the application of one wake-vortex minimization technique to DC-10 and L-1011 aircraft are presented.

SYMBOLS

$b/2$ aircraft semispan, m

C_L lift coefficient

$\bar{c}$ aircraft average wing chord, m

d separation distance between vortices, m

t	time
U_∞	free-stream velocity, m/sec
X,Y,Z	orthogonal coordinate axis system with origin at wing center
Γ	vortex circulation, m^2/sec

Subscripts:

1	vortex one
2	vortex two

THEORETICAL STUDIES

Inviscid Analysis

A theoretical method used to describe the rolled-up vortex system of a lifting surface is the technique of Betz (ref. 3) which was recently reassessed and described in reference 4. The theory, based on the conservation equation for inviscid two-dimensional vortices, relates the circulation in the fully rolled-up vortex to the span loading on the lifting wing. Because of the simplicity of the method, the details of the rollup process are not described; however, the technique has been shown to be useful in predicting gross vortex character-istics behind lifting surfaces (ref. 5) and often has been found to be more accurate than more complex methods.

The rollup process of the vortex sheet from a lifting surface has been determined by calculations of the two-dimensional time-dependent motion of point vortices. This type of rollup calculation for an elliptically loaded wing is illustrated in figure 1. Point vortex computerized-rollup calculations are subject to unrealistic numerical instabilities because of the singular point at a radius of zero from the point vortex. Reference 6 discusses techniques for minimizing these errors and describes a technique for monitoring the numerical stability of these calculations. As shown in figure 1, the application of the principles described in reference 6 provides an accurate point-vortex calculation description of the rollup of an elliptically loaded wing.

The Betz modeling and the two-dimensional time-dependent point-vortex calcu-lation techniques have been used to study a variety of span-load distributions for wake-vortex minimization. Analysis has indicated that span-load alterations, in order to produce large vortex core sizes with related reductions in circum-ferential velocities, are limited in the achievable amount of vortex minimiza-tion. (See refs. 4 and 6.)

The two-dimensional time-dependent calculations have shown the possibility of achieving wake-vortex minimization through the production of a chaotic wake structure to enhance the dissipation of shed vorticity. In figure 2, the numer-ical calculations for a stepped or sawtooth span-load distribution are shown to have chaotic wake rollup. Model tests (ref. 7) of a wing having a sawtooth span

304

loading showed that the shed vortices did undergo the large-scale excursions shown in figure 2; however, several spans downstream, when vortex linking was completed, a vortex pair still remained. The model results indicate that the interaction of multiple vortex pairs in a wake brings about large disturbances to the vortex sheet. It is necessary to include viscous effects in the theoretical calculations to understand the significance of this process.

Viscous Studies

Under an NASA contract, a computer program has been developed to solve the vortex equations of fluid motion including convection and turbulent diffusion. The computer code uses a second-order closure for the velocity correlation and an invariant turbulent model. Details of the turbulent model and the second-order closure technique may be found in references 4, 8, and 9. The computer code was used to calculate the merging of two equal-strength like-sign vortices. Figure 3 indicates the pressure-intensity field during the merging process of two equal-strength like-sign vortices where minimums in pressure are designated by the darkened regions. During the merging process, considerable turbulent kinetic energy is generated and is plotted in figure 4 for the merging of two equal-strength like-sign vortices. The process of turbulence generation during vortex merging is significant because it will aid the dissipation process of the merged vortex. The merging of the vortices illustrated in figures 3 and 4 is representative of the merging which normally takes place between the wing-tip and outboard flap vortex of an aircraft in the landing configuration. The results of the viscous vortex analysis have shown that by altering the span-load distribution of a large transport aircraft so that the wing-tip and flap vortices are of nearly equal strengths with the flap vortex at the 40-percent semispan station, the turbulence produced during the merging process is maximized. Such a configuration leads to an enhanced diffusion of the trailed vorticity. Experimental results of this configuration are discussed later.

EXPERIMENTAL STUDIES

Experimental studies have been conducted to evaluate various wake-vortex minimization techniques. Primarily, the vortex minimization techniques were evaluated for the vortex-generating aircraft in the landing configuration. Vortex effects on a trailing aircraft for an in-trail type penetration (that is, one aircraft behind another) are used to infer the vortex hazard in the terminal area, since this type of encounter is most likely to occur during landing approaches. Experimental studies consisted of both flight tests and model tests of vortex minimization techniques.

Model Tests

Model tests have been conducted utilizing the test procedure illustrated in figure 5. For most of the tests, a B-747 aircraft model was used as a vortex generator, since it is representative of current wide-body jet transports. As will be discussed later, a limited number of tests were conducted by using DC-10 and L-1011 vortex-generating aircraft. The effectiveness of various vortex

minimization techniques was determined by measuring the vortex-induced rolling
moment on a smaller wing model positioned downstream of the vortex-generating
aircraft. This technique has been used in wind tunnels and towing facilities
in which both the vortex generator and the trailing wing are translated through
a fluid medium. Facilities which have been used to obtain a rolling-moment
assessment of vortex minimization concepts are the Ames 40- by 80-foot wind
tunnel, the Langley V/STOL wind tunnel and vortex flow facility, and, under
contract, a water towing tank at Hydronautics, Inc. Details concerning these
facilities and the test technique can be found in reference 10. Additionally,
laser-Doppler velocimeters (ref. 11) and hot-wire anemometers have been used
during some tests to measure vortex velocity components. Flow-visualization
studies in several facilities have proven to be a useful qualitative indication
of the vortex.

Flight Tests

Flight tests have been conducted at the Dryden Flight Research Center using
NASA's B-747 aircraft as a vortex generator while using a T-37B and the Ames
Research Center Learjet as vortex probe or trailing aircraft. Also, the Wallops
Flight Center C-54 aircraft and Langley's PA-28 aircraft have been used to
evaluate one wake-vortex minimization technique. The test technique has involved
the determination of the vortex-induced rolling moment from the measurements
obtained during the probe aircraft while making in-trail vortex penetrations.
A discussion of the flight-test procedures and examples of the data obtained
are provided in references 12 and 13. In addition to rolling moments, some
measurements of the vortex velocity distributions have been obtained by hot-wire
probes on the Learjet (ref. 12).

Flight-test measurements of the vortex-induced rolling moment have been
found to correlate qualitatively with results obtained in the model-test facil-
ities. Techniques which have been identified by model tests to minimize the
vortex upset on a trailing model have been shown to provide similar reductions
in flight tests. The results do not correlate directly in magnitude because of
differences in the level and scale of ambient turbulence and Reynold's number
between model tests and flight tests.

WAKE-VORTEX MINIMIZATION TECHNIQUES

During the course of NASA's experimental program, numerous wake-vortex
minimization concepts or ideas were investigated. Several concepts or methods
were found to provide some alteration in the detailed vortex structure without
significantly reducing the rolling moment on a trailing aircraft wing model.
These unsuccessful concepts are discussed in reference 14. For the purpose of
the following discussion, the concepts which have been found to meet the primary
program objective of a significant reduction in the vortex-induced rolling
moment on a trailing aircraft have been divided into three categories. The first
is the use of turbulence generation or injection to rapidly diffuse the vorticity.
The second is the use of vortex interaction which has been identified in the
preceding theoretical section. The third area for discussion is to combine the
effects of vortex interaction and turbulence injection.

306

Turbulence

Figure 6 illustrates a turbulence device as it was installed on a C-54 aircraft for a flight-test evaluation. The device generates considerable turbulence without affecting the wing-lift characteristics. Details concerning the development of this device can be found in reference 15. The turbulence device was found to rapidly diffuse and dissipate the vortex system from the C-54 aircraft. A flight-test evaluation using a PA-28 aircraft to probe the C-54 vortex system indicated that significant reductions in the vortex-induced rolling moment were obtained when the turbulence device was installed on the C-54 aircraft. (See fig. 7.) Model tests on a B-747 of a similar turbulence device have shown that by proper spanwise placement of the device, the vortex-induced rolling moment on a following aircraft can be reduced considerably. However, as would be expected, the operational penalties associated with the drag of such a device are significant.

The turbulence within a jet engine exhaust has been shown to provide some dissipation of the aircraft's trailing vortices. However, as shown in reference 16, the levels of thrust required to achieve a significant reduction in the vortex-induced rolling moment on a following aircraft are large. As indicated in reference 16, the thrust for significant vortex dissipation during the landing approach of a B-747 would require full power on the outboard engines and some reverse thrust on the inboard engines for flight-path control.

Vortex Interaction

Theoretical studies have indicated that turbulence is produced during the merging process of a wing-tip and flap vortex. Additional analyses have shown that the interaction phenomena produce a maximum amount of turbulence dissipation when the wing-tip and flap vortices are of nearly equal strength and the flap vortex originates at the 40-percent semispan station. This concept was implemented on a B-747 aircraft by deploying only the inboard flap segment during landing approach to achieve the desired location of the flap vortex. Details concerning the development of this concept are given in reference 17.

Figure 8 illustrates the differences in the character of the vortex interaction and merging for a B-747 aircraft in a normal landing configuration with all the flaps deployed and in a wake-vortex minimization configuration with only the inboard flaps deployed. Model-test and flight-test results of this concept indicate reductions of approximately 50 percent on the vortex-induced rolling moment on a trailing aircraft.

As indicated in reference 17, the implementation of this concept on a B-747 aircraft, in the manner described, imposed severe penalties on the pitching-moment characteristics and maximum lift-coefficient capability of the aircraft during landing approach. Additionally, the deployment of the landing gear adversely affected the vortex merging phenomena, which could only be reestablished by using a large vortex generator just aft of the wing and on either side of the fuselage. (See ref. 17.)

307

Combined Effects

The deployment of certain flight-spoiler combinations alters the span-load characteristics, sheds significant turbulence, and can be used to combine the effects of vortex merging and turbulence injection. References 18 and 19 cover the development and implementation of the spoiler concept for wake-vortex minimization. As shown in references 18 and 19, the maximum reduction in trailing-wing rolling moment behind a B-747 aircraft is achieved by deploying the two outboard spoilers (numbered 1 and 2 in fig. 9) during landing approach. Model-test results using this spoiler configuration indicate significant reductions in the vortex-induced rolling moment on a Learjet-size aircraft behind a B-747 (fig. 10). The results of reference 18 show that symmetric deployment of the two outboard spoiler panels on a B-747 aircraft increases the landing configuration drag about 20 percent while reducing the maximum lift-coefficient capability about 5 percent. Additionally, it was found during flight tests that the spoiler concept produced significant aerodynamic buffet which seriously detracts from the ride quality and may have structural implications with regard to the flap and flap-bracket fatigue life.

Model-test results of applying the spoiler concept to DC-10 and L-1011 aircraft for vortex minimization are shown in figure 11. The data show that the deployment of the proper spoiler combination on these aircraft provides a significant reduction in the vortex-induced rolling moment for a Learjet-size aircraft. The spoilers to be used on the DC-10 and L-1011 aircraft are the two most inboard flight spoilers (comparable to spoilers 3 and 4 in fig. 9). The results of the DC-10 and L-1011 aircraft have shown that the vortex-minimization techniques developed during B-747 aircraft tests are applicable to other vortex-generating aircraft. The implementation of any concept must include consideration of the differences in span loading, engine, and spoiler placement along with other configuration differences.

OPERATIONAL CONSIDERATIONS

A preliminary analysis of the operational considerations of implementing the turbulence concept by use of drag devices or engine thrust, the vortex-interaction concept by extension of only the inboard flap, and the combination of these concepts by deployment of the flight spoilers for wake-vortex minimization on a B-747 aircraft has been performed under contract. All the concepts have certain performance penalties which would preclude their use during take-off operations; consequently, they were only considered to be used during the approach and landing.

The analysis indicated that any form of turbulence injection through the use of high thrust settings on selected engines with partial reverse thrust on the other engines was operationally unsuitable. Considerable hardware would be required to implement a retractable turbulence device similar to that shown in figure 6 on a B-747 aircraft. The analysis indicated that such a device could not meet the approach-climb requirements (one engine out), but could be used during landing. Additionally, some penalties were incurred during the cruise configuration because of the hardware employed to stow the drag devices.

Because of cost and the performance penalties associated with their use, the turbulence concepts would probably be considered unsuitable for operational use.

The implementation of the vortex-interaction concept by deployment of only the inboard flap considerably reduced the static margin and restricted the center-of-gravity range severely. This technique was considered unsuitable for operational use.

The use of the spoiler concept was found to be operationally the most promising concept analyzed. The spoiler concept appears to meet most certification requirements, with the possible exception of the approach-climb requirement. An assessment of the structural penalties associated with the flight spoiler-induced buffet or possible solutions to this problem have not been conducted. As is seen in figure 10, the vortex-induced rolling moment on a trailing aircraft can be significantly reduced by using the flight spoiler but not totally eliminated. Such reductions are characteristic of all the vortex-minimization concepts evaluated. As indicated in reference 13, vortex-minimization concepts, such as the flight spoilers, can reduce the distance at which a probe aircraft can controllably fly behind a B-747 aircraft. An analysis has not been conducted to determine whether the economic gains of a reduction in separation criteria are offset by the economic penalties associated with implementing wake-vortex minimization techniques, such as would be incurred with structural changes, to withstand or reduce any flight spoiler-induced buffet.

CONCLUDING REMARKS

Considerable advances have been made in the area of theoretical analysis of wake-vortex minimization techniques. Experimental model-test and flight-test procedures have been developed for evaluating various wake-vortex minimization techniques and the model tests and flight tests have been shown to qualitatively agree. Tests have indicated that turbulence injection and vortex interaction brought about by a suitable span-load alteration can considerably reduce the trailing-vortex intensity. The use of the existing flight spoilers on a wide-body airplane utilizes both the turbulence injection and the vortex-interaction technique to bring about wake-vortex minimization. A cursory analysis of the operational feasibility of employing wake-vortex minimization techniques has been conducted. All the vortex-minimization techniques incur severe performance penalties which would preclude their use during take-off. The flight-spoiler concept was considered the most feasible candidate; however, a solution to the spoiler-induced buffet was not analyzed. Additionally, the economic penalties associated with implementing any wake-vortex minimization concept must be balanced by any economic gain in reduced separations.

REFERENCES

1. Walsh, Thomas M.; Morello, Samuel A.; and Reeder, John P.: Review of Operational Aspects of Initial Experiments Utilizing the U.S. MLS. Aircraft Safety and Operating Problems, NASA SP-416, 1976. (Paper No. 2 of this compilation.)

2. Wake-Vortex Minimization. NASA SP-409, 1976.

3. Betz, A.: Behavior of Vortex Systems. NACA TM 713, 1933.

4. Donaldson, Coleman duP.; and Bilanin, Alan J.: Vortex Wakes of Conventional Aircraft. AGARD-AG-204, May 1975.

5. Bilanin, Alan J.; and Donaldson, Coleman duP.: Estimation of Velocities and Roll-Up in Aircraft Vortex Wakes. J. Aircraft, vol. 12, no. 7, July 1975, pp. 578-585.

6. Rossow, Vernon J.: Inviscid Modeling of Aircraft Trailing Vortices. Wake-Vortex Minimization, NASA SP-409, 1976.

7. Ciffone, D. L.; and Orloff, K. L.: Far-Field Wake-Vortex Characteristics of Wings. J. Aircraft, vol. 12, no. 5, May 1975, pp. 464-470.

8. Bilanin, Alan J.; Teske, Milton E.; Donaldson, Coleman duP.; and Snedeker, Richard S.: Viscous Effects in Aircraft Trailing Vortices. Wake-Vortex Minimization, NASA SP-409, 1976.

9. Lewellen, W. S.; and Teske, M.: Turbulence Modeling and its Application to Atmospheric Diffusion. Part II Critical Review of the Use of Invariant Modeling. Rep. No. EPA/600/4-75/016b, U.S. Environ. Prot. Agency, Dec. 1975. (Available from NTIS as PB-253 451/9GA.)

10. Stickle, Joseph W.; and Kelly, Mark W.: Ground-Based Facilities for Evaluating Vortex Minimization Concepts. Wake-Vortex Minimization, NASA SP-409, 1976.

11. Ciffone, Donald L.; and Orloff, Kenneth L.: Application of Laser Velocimetry to Aircraft Wake-Vortex Measurement. Wake-Vortex Minimization, NASA SP-409, 1976.

12. Jacobsen, Robert A.; and Barber, M. R.: Flight-Test Techniques for Wake-Vortex Minimization Studies. Wake-Vortex Minimization, NASA SP-409, 1976.

13. Barber, Marvin R.; Hastings, Earl C., Jr.; Champine, Robert A.; and Tymczyszyn, Joseph J.: Vortex Attenuation Flight Experiments. Wake-Vortex Minimization, NASA SP-409, 1976.

14. Dunham, R. Earl, Jr.: Unsuccessful Concepts for Aircraft Wake-Vortex Minimization. Wake-Vortex Minimization, NASA SP-409, 1976.

15. Patterson, James C., Jr.; Hastings, Earl C., Jr.; and Jordan, Frank L., Jr.: Ground Development and Flight Correlation of the Vortex Attenuating Spline Device. Wake-Vortex Minimization, NASA SP-409, 1976.

16. Patterson, James C., Jr.; and Jordan, Frank L., Jr.: Thrust-Augmented Vortex Attenuation. Wake-Vortex Minimization, NASA SP-409, 1976.

17. Corsiglia, Victor R.; and Dunham, R. Earl, Jr.: Aircraft Wake-Vortex Minimization by Use of Flaps. Wake-Vortex Minimization, NASA SP-409, 1976.

18. Croom, Delwin R.: The Development and Use of Spoilers as Vortex Attenuators. Wake-Vortex Minimization, NASA SP-409, 1976.

19. Croom, Delwin R.: Low-Speed Wind-Tunnel Investigation of Various Segments of Flight Spoilers as Trailing-Vortex-Alleviation Devices on a Transport Aircraft Model. NASA TN D-8162, 1976.
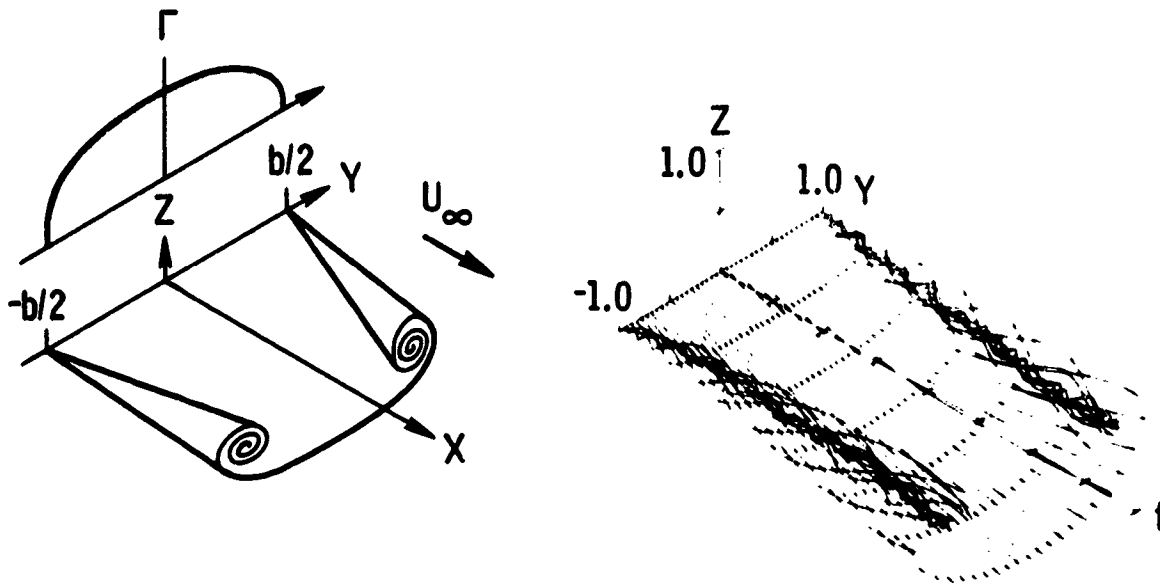
311

Figure 1.- Results of point-vortex calculations of the vortex-sheet rollup from an elliptically loaded wing. (Data from ref. 6.)
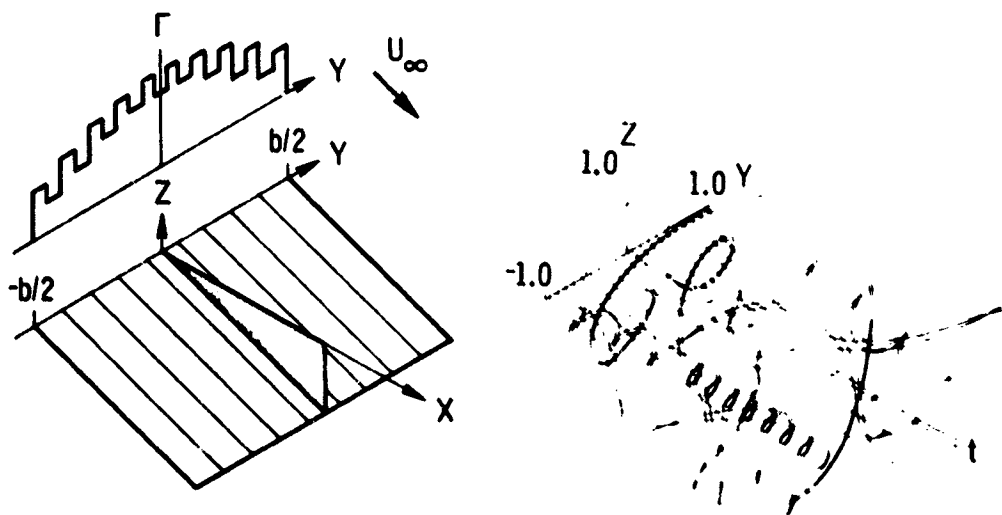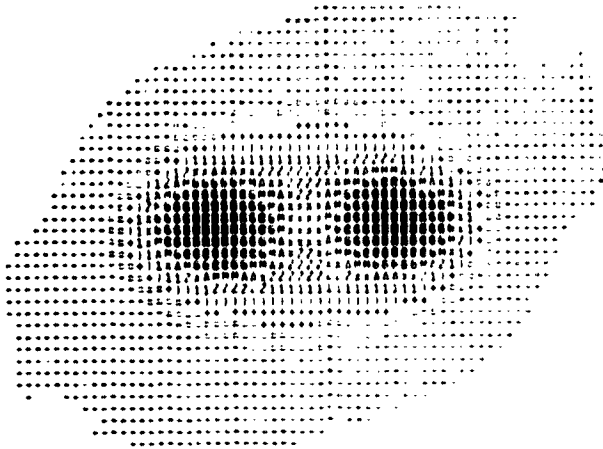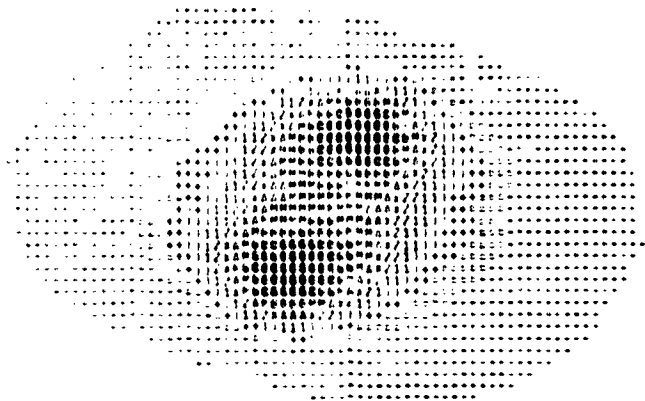

Figure 2.- Results of point-vortex calculations of the vortex-sheet rollup from a sawtooth-load distribution. (Data from ref. 6.)

312

(a) Initial setup for start of calculations.

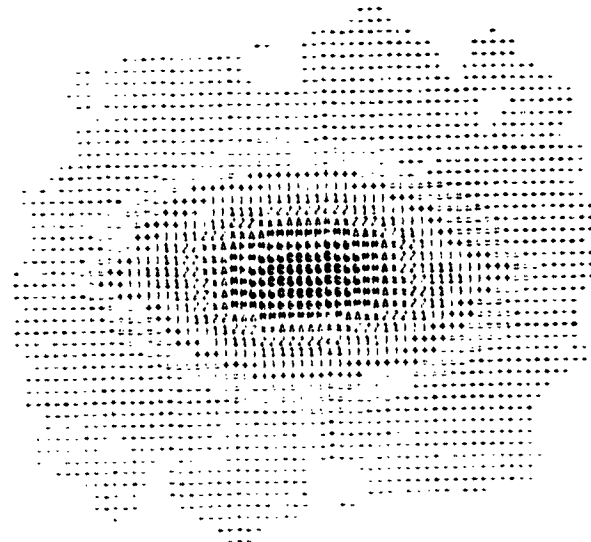(b) Pressure-intensity plot at a nondimensional time ($t\nu/d^2$) of 0.0.

(c) Pressure-intensity plot at a nondimensional time ($t\nu/d^2$) of 1.33.

(d) Pressure-intensity plot at a nondimensional time ($t\nu/d^2$) of 2.67.

(e) Pressure-intensity plot at a nondimensional time ($t\nu/d^2$) of 4.0.

Figure 3.- Illustration of merging and interaction of two equal-strength like-signed vortices. ($Re = 10^4$.)

(a) Turbulent kinetic energy at a non-dimensional time $(t\Gamma/\pi d^2)$ of 0.0.

(b) Turbulent kinetic energy at a non-dimensional time $(t\Gamma/\pi d^2)$ of 1.33.

(c) Turbulent kinetic energy at a non-dimensional time $(t\Gamma/\pi d^2)$ of 2.67.

(d) Turbulent kinetic energy at a non-dimensional time $(t\Gamma/\pi d^2)$ of 4.0.

Figure 4.- Turbulent kinetic energy intensity plots for the merging of two equal-strength like-sign vortices. (From ref. 8.)
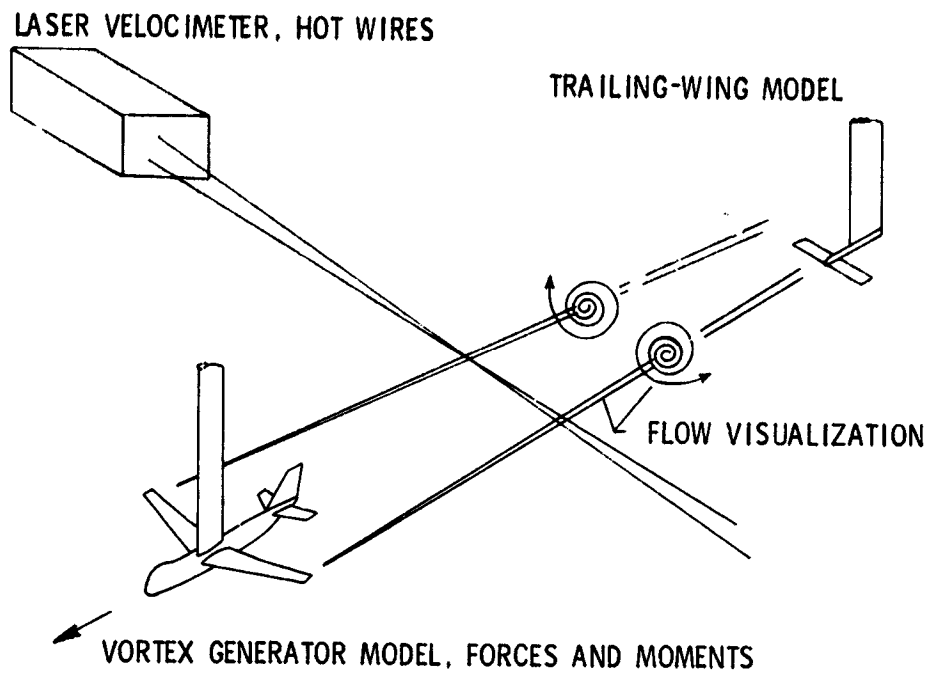
Figure 5.- Illustration of model-test procedure.
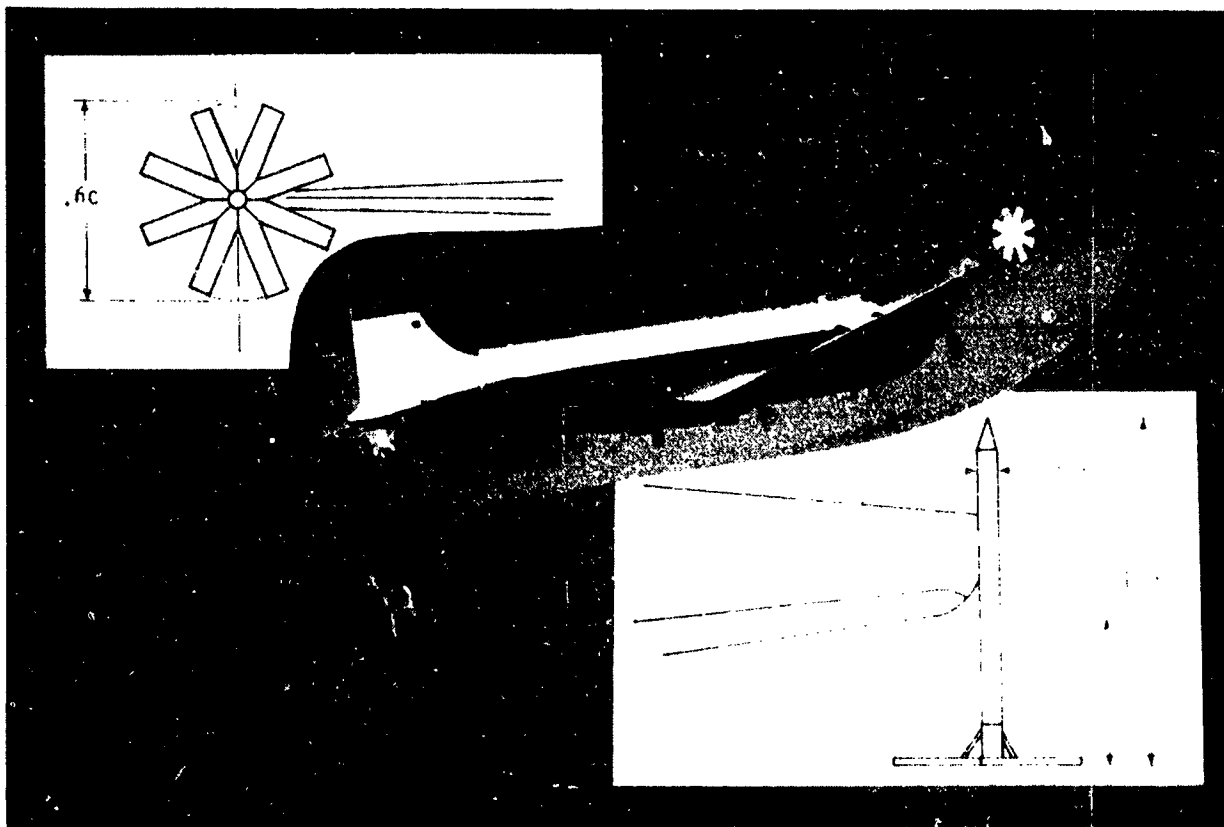
Figure 6.- Turbulence device installed on C-54 airplane for flight tests.

315
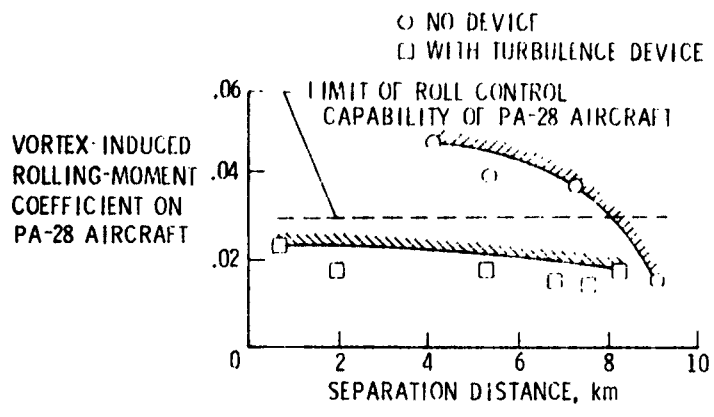
Figure 7.- Flight-test results of the turbulence device.
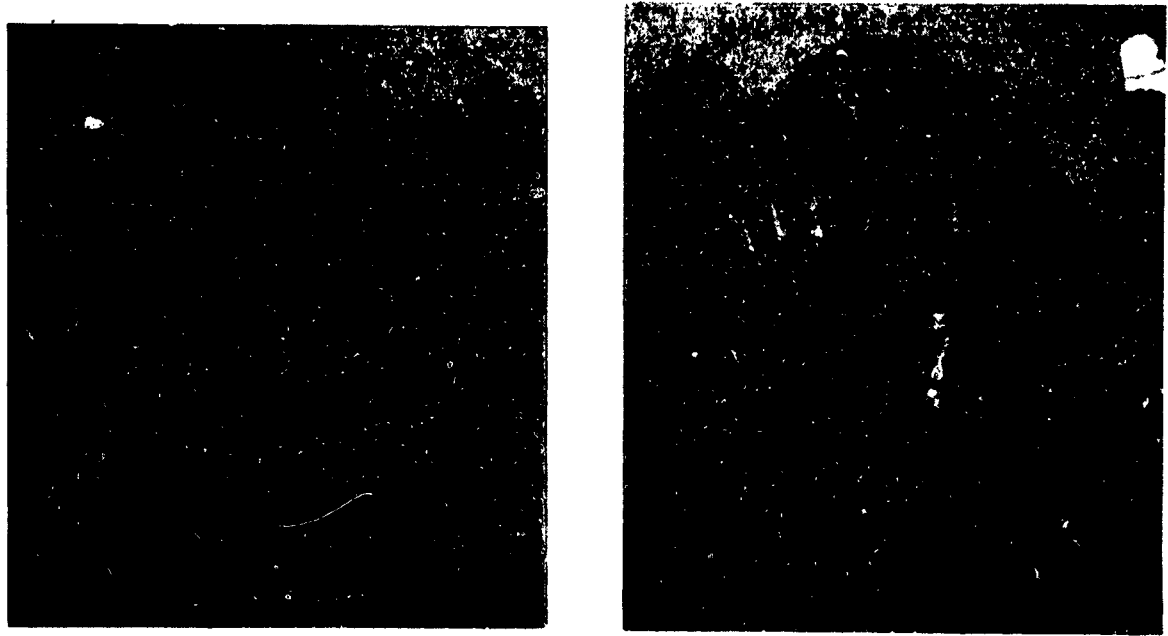
(a) All flaps extended.   (b) Only the inboard flap extended.

Figure 8.- Photographs illustrating vortex interaction.

316
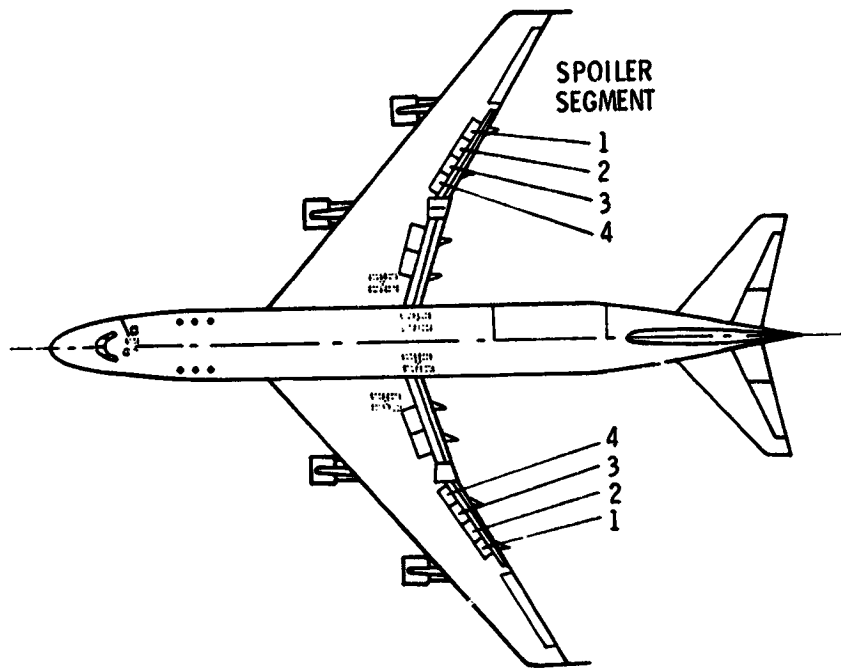
Figure 9.- Location of flight spoilers on a B-747 aircraft.

MODEL TEST RESULTS; $C_L = 1.2$
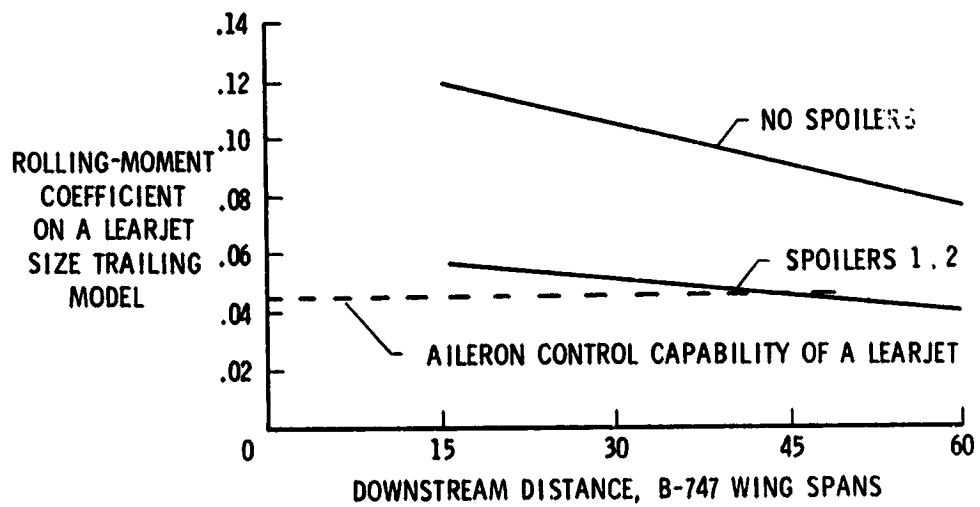
Figure 10.- Model-test results of the effect of using the flight
spoilers on   )-747 for vortex minimization.
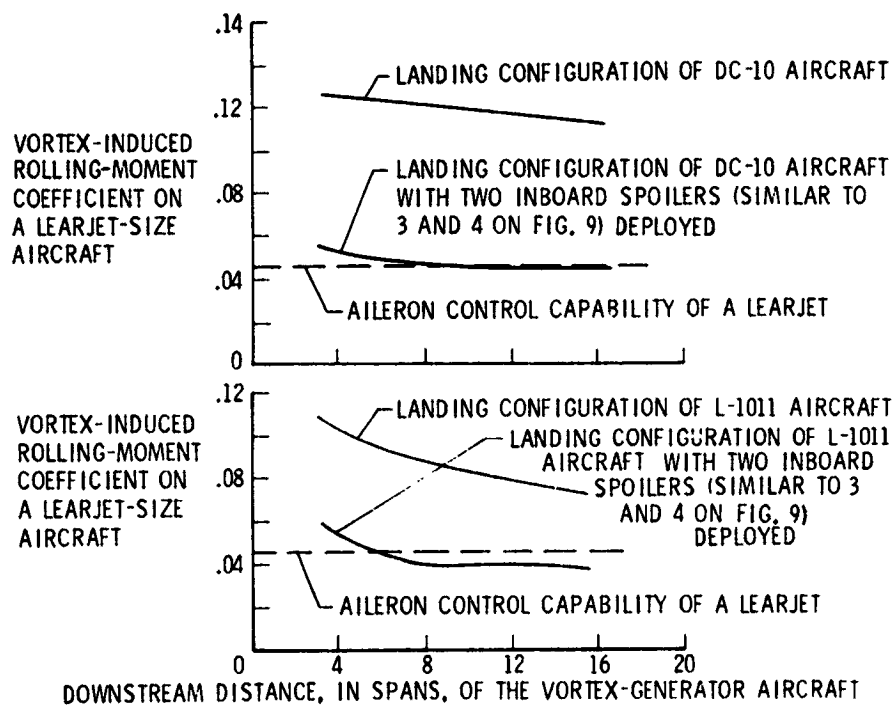
Figure 11.- Model-test results of using flight spoilers for
wake-vortex minimization on DC-10 and L-1011 airplanes.

STATUS OF NASA AIRCRAFT ENGINE EMISSION REDUCTION AND

UPPER ATMOSPHERE MEASUREMENT PROGRAMS

Richard A. Rudey and Erwin A. Lezberg
NASA Lewis Research Center

SUMMARY

NASA is conducting programs to evaluate advanced emission reduction techniques
for five existing aircraft gas turbine engines. Varying degrees of progress have been
made toward meeting the 1979 EPA standards in rig tests of combustors for the five
engines. Results of fundamental combustion studies suggest the possibility of a new gen-
eration of jet engine combustor technology that would reduce oxides-of-nitrogen (NO_x)
emissions far below levels currently demonstrated in the engine-related programs. The
Global Air Sampling Program (GASP) is now in full operation and is providing data on
constituent measurements of ozone and other minor upper-atmosphere species related
to aircraft emissions.

INTRODUCTION

This paper briefly describes some of the current NASA programs concerned with
evaluating and reducing the potential impact of aircraft operations on the atmosphere.
With the passage of the Clean Air Act in 1970, the Environmental Protection Agency
(EPA) was charged with establishing acceptable exhaust emission levels of carbon mon-
oxide (CO), total unburned hydrocarbons (THC), oxides of nitrogen (NO_x), and smoke for
aircraft engines. In response to the charge, EPA promulgated the standards described
in reference 1 in 1973. Reductions of up to sixfold from present emission levels will be
required by the EPA compliance date of January 1, 1979. NASA has responded to this
requirement with major programs to evolve and demonstrate advanced technological
capability for low-emission gas turbine engine combustors.

The climatic impact studies completed by the Department of Transportation (DOT
Climatic Impact Assessment Program (CIAP)) recommended NO_x reductions from 6- to
60-fold (ref. 2). The National Academy of Sciences (NAS) Climatic Impact Committee
(CIC) also completed their study in 1975 (ref. 3), relying heavily on the CIAP results.
The CIC study recommended 10- to 20-fold NO_x reductions. The first number in each
range reflects what was felt to be achievable within a decade. Defining quantitative val-
ues for tolerable cruise NO_x emissions is extremely difficult because baseline atmo-

319

spheric data related to the potential aircraft impact are lacking. The need for these data was responsible for the initiation of CIAP and later GASP and other related efforts.

This paper summarizes the status of emission reduction technological developments both for the local (airport) problem, which is directly related to the 1979 EPA standards, and for the projected high-altitude problem. Progress in the Global Air Sampling Program's (GASP) measurement of upper atmospheric constituents is also reviewed.

Although values are given in both SI and U.S. customary units, the measurements and calculations were made in U.S. customary units.

AIRCRAFT ENGINE EMISSION REDUCTION

The level of undesirable emissions from aircraft engines varies with engine operating characteristics, as illustrated in figure 1. Concentrations of CO and THC, expressed as grams of pollutant per kilogram of fuel burned, are the highest at the low-power (idle) condition. However, concentrations of NO_x (as well as smoke) are generally the highest at the high-power (takeoff) condition. Reducing these emissions at the discrete operating conditions as well as other intermediate conditions requires an understanding of the causes and effects in the combustion process, shown in figure 2. The low values of inlet temperature, inlet pressure, and fuel/air ratio at low power (idle) produce quenching of reactions, poor combustion stability, and poor fuel atomization and distribution. The resultant combustion inefficiency is manifested as carbon monoxide and unburned hydrocarbon emissions. Conversely, the high values of inlet temperature, inlet pressure, and fuel/air ratio that occur at high power (takeoff) cause excessive residence time, high flame temperature, and poor local fuel distribution. The result can be as high NO_x and smoke emissions.

If we evaluate the corrective approaches needed to reduce emissions, we can see that somewhat of a dilemma exists. For reducing CO and THC, the approaches (dictated by the chemical kinetics) are to burn stoichiometric mixtures to increase combustion temperature and to maximize residence time. For reducing NO_x, the approaches are to burn lean mixtures and to minimize residence time. Improving fuel atomization and distribution (eliminating zones where the fuel/air ratio is not optimum) is helpful in reducing all emissions. Thus, to effectively reduce emissions and optimize the combustion process simultaneously over the entire operating range, some form of staging or modulation of the fuel/air ratio and residence time will be needed. To reduce emissions at only one condition, such as CO and THC at low power, staging or modulation may not be necessary.

In discussing the approaches that are being evaluated to control aircraft emissions, we will consider the two flight regions of principal concern, local and upper atmo-

320

sphere, and describe the activities and progress associated with emission reduction in that region.

The Local Problem

The local problem, in terms of aircraft emissions, is described in the promulgated EPA standards (ref. 1) and is specifically associated with the pollutants emitted during a prescribed landing-takeoff (LTO) cycle, as shown in figure 3. The LTO cycle is divided into four discrete modes of operation: (1) taxi/idle (in and out), (2) takeoff, (3) climbout, and (4) approach, and is limited to flight operation below 914 meters (3000 ft). The varying time segments associated with the operating modes were established as average values and could vary from airport to airport as well as with traffic conditions. The EPA used this cycle to arrive at an EPA parameter (EPAP) for establishing standards for the various undesirable emissions. The EPAP is computed from either of the following definitions, depending on the type of engines being considered:

EPAP = Pounds of pollutant per 1000 thrust (in lbf)-hours per cycle

EPAP = Pounds of pollutant per 1000 shaft horsepower-hours per cycle

Thus, an integrated value for each pollutant over the prescribed LTO cycle is used in the standards. Based on considerations of the time in mode (fig. 3), the engine emission characteristics (fig. 1), and the fuel consumed in each mode, the most effective means of reducing CO and THC EPAP values would be to reduce the emissions at taxi/idle. Conversely, reducing NO_x at takeoff and climbout is most effective. Controlling all emissions at approach is equally important

To evaluate the potential of advanced technology to control emissions over the LTO cycle to the levels required by the standards, NASA has implemented an emission reduction technology program. The objective is to reduce aircraft engine emissions to levels consistent with the requirements of the EPA standards. The approach consists of a series of multiphased contracts covering five contemporary engines that fall within four of the specified EPA engine classes: The Garrett-AiResearch TFE731-2 engine, in class T1 (turbofan under 35 584-N (8000-lbf) thrust); the General Electric CF6-50 engine and the Pratt & Whitney JT9D-7 engine, in class T2 (turbofan over 35 584-N (8000-lbf) thrust); the Pratt & Whitney JT8D engine, in class T4, and the Detroit Diesel Allison 501-D22A engine, in class P2 (turboprop engines). In general, the contracts are structured to have three phases: (1) a first phase during which a number of advanced concepts are evaluated for emission control capability and overall performance, (2) a second phase during which the most promising concepts are refined and evaluated in terms of engine compatibility, and (3) a third phase during which one selected concept is tested in an engine to demonstrate emission and overall performance characteristics The T4 and P2 efforts were terminated at the completion of the first Phase. The T1

effort is currently in the second phase and the T2 efforts are in the third phase.

A wide variety of low-emission concepts were evaluated during the course of these contracts. Concepts ranging from minor modifications of the existing engine combustors to major changes such as staged combustion were considered. An example of a minor modification is shown in figure 4. The reverse-flow concept shown is applicable to the Detroit Diesel Allison 501-D22A engine. One part of the modification consisted of redirecting the liner cooling air in the primary zone upstream and hence recycling the CO and THC formed by quenching back into the hot combustion zone. In addition, the conventional fuel nozzle was replaced with a more efficient air-blast nozzle. These changes, which reduced the undesirable quenching effects and improved fuel-air distribution and atomization proved to be very effective for controlling CO and THC at low power. No reduction in NO_x was obtained or anticipated. Since CO and THC emissions were the major problem for this engine. this minor modification was all that was needed to meet the standards. Also, since this is a relatively simple modification that should not be difficult to adapt to the engine. the contract effort was not extended into the demonstration phases. Complete results of the contract effort are given in reference 4.

The more complex combustion concepts needed to simultaneously control all emissions are illustrated in figure 5. Figure 5(a) compares a double-annular staged concept (ref. 5) with the conventional combustor of the General Electric CF6-50 engine. This concept employs parallel staging where one stage (the pilot stage) is used at idle and is optimized to control CO and THC emissions and the second stage (the main stage) is used for full power and is optimized to control NO_x emissions. By varying the fuel split to the two stages, various degrees of control are possible. A staged concept that is adaptable to the Pratt & Whitney JT9D-7A (ref. 6) is compared with the conventional combustor in figure 5(b). The function of the two stages is the same as for the CF6-50 engine, but they are arranged in series rather than parallel. Both designs employ improved fuel atomization and fuel-air distribution in both the pilot and main stages and lean combustion and residence-time control in the main stages. Both concepts are currently undergoing engine demonstration tests that are scheduled for completion by the end of 1976 or early 1977.

The rig test results of the advanced concepts shown in figures 4 and 5 as well as the most successful concepts tested in the T1 and T4 efforts (refs. 7 and 8) are compared with the corresponding conventional combustor emissions and the 1979 EPA standards in table I. All values shown are EPA parameter (EPAP) values. All of the advanced concepts were able to meet the EPA standards for THC and smoke. The CF6-50 and 501-D22A concepts were able to meet the CO standards. The other three concepts reduced CO but still did not meet the standards. Further refinement of the TFE731-2 concept can probably produce further reductions in CO. Only two of the five concepts were capable of reducing the NO_x emissions to the standard levels. However, it is

322

significant that substantial NO_x reductions were obtained with all the concepts except the 501-D22A concept, which did not require a reduction to meet the standards.

These results indicate that the CO and NO_x EPA standards will probably not be achieved for any engine evaluated using the technology evolved in the NASA/industry program conducted to date. However, substantial reductions in all emissions are achievable and would certainly lead to beneficial reductions in local aircraft emissions if they are employed in future engines.

Many aspects of local emission reduction capability must still be evaluated. The impact of the real engine environment on emissions must and will be considered in actual full-scale engine tests. Constraints resulting from operational considerations, engine-to-engine variations, safety and maintenance considerations, and overall performance must all be evaluated before absolute achievable levels can be quantified.

The Upper-Atmosphere Problem

In the case of high-altitude emissions, the primary concern is the NO_x emissions of cruising aircraft (both subsonic and supersonic). Most of the studies conducted and sponsored by NASA to date have been aimed at determining the minimum practical level of NO_x emissions that can be obtained for future aircraft engines. In this regard, many fundamental studies have been conducted. A display of typical results is shown in figure 6. This plot illustrates the interdependency between NO_x emission index, equivalence ratio, combustion efficiency, and residence time obtained in a prevaporized-premixed combustion experiment. Extremely low levels of NO_x emissions (~0.5 g/kg) were obtained at acceptable levels of combustion efficiency for simulated cruise operating conditions. However, it must be clearly understood that these results were obtained in a very carefully controlled fundamental experiment and are not necessarily representative of the levels that may be achieved by a prevaporized-premixed combustion system in an actual engine environment. They were, however, obtained at inlet temperatures and pressures that simulated the type of conditions expected in supersonic engines and, therefore, do provide an indication of the minimum NO_x emissions possible at these conditions. The NO_x levels achieved (0.5 g/kg) represent a 40-fold reduction from current aircraft cruise values and fall within the recommended levels of the climatic impact studies (CIAP and CIC).

Based on the results obtained from the fundamental experiments and several of the advanced technology combustors from the clean combustor program described previously, estimates were made with regard to potential cruise NO_x emission reductions. The clean-combustor technology could reduce cruise NO_x emissions by about a factor of two for an engine having a 30:1 pressure ratio in an aircraft cruising at 11.3 kilometers (35 000 ft) and Mach 0.85. Achieving the levels recommended by the climatic impact

studies, a 6- to 10-fold (or greater) reduction, will require the use of prevaporized-premixed combustion.

To determine the applicability of prevaporized-premixed combustion to advanced combustors, NASA has begun a Stratospheric Cruise Emission Reduction Program (SCERP). This program will consist of in-house, contract, and university grant efforts and will use a multiphase approach. Although the program is directed toward reducing the cruise NO_x of subsonic aircraft by a minimum of 6- to 10-fold, the information obtained during the fundamental studies undertaken in the first phase (phase 1) will also be applicable to supersonic aircraft engine combustors. During phase 1, fundamental information regarding lean combustion stability, autoignition and flashback, fuel preparation, and engine-related constraints will be obtained. This information will then form the basis for developing promising conceptual designs to be evaluated in the following three program phases (phases 2 to 4), which are essentially identical to the three phases of the NASA/industry programs currently underway to evaluate advanced concepts for the local emission problem. Since the goal of this program is to meet EPA-established LTO cycle emission standards as well as to reduce cruise NO_x, it is likely that some form of staged combustion or variable geometry will be required. If a successful concept is evolved, the program is structured to provide a full-scale engine demonstration during the early 1980's.

MEASUREMENT OF UPPER-ATMOSPHERE CONSTITUENTS

The objectives of the NASA Global Atmospheric Sampling Program (GASP) are to provide baseline data for selected atmospheric constituents in the upper troposphere and lower stratosphere over a 5- to 10-year period and to analyze these data to assess potentially adverse effects between aircraft exhaust emissions and the natural atmosphere.

The approach chosen was to install automated sampling systems on Boeing-747 aircraft flying the commercial air-routes (ref. 9). The system installation is shown in figure 7. In situ monitoring instruments and the associated gas-handling system are installed in the nose section of the B-747 below the first-class passenger compartment. Four B-747 installations and an NASA CV-990 aircraft installation have been completed and the aircraft are in routine service. Two of the B-747 aircraft installations presently include single-filter samplers. The routes for the aircraft are shown in figure 8. United Airlines flies the routes over the continental U.S. and to Hawaii. Pan American World Airways flies around-the-world routes from the U.S. in the Northern Hemisphere, transpacific routes to the Far East, intercontinental routes to Central and South America, and occasionally transpacific routes to Australia. A Pam Am B-747 SP flies long-range, great-circle routes from New York and the west coast to Tokyo at altitudes up to 13.7 kilometers (45 000 ft). Coverage in the Southern Hemisphere is pro-

vided by Qantas Airways of Australia on trans-Australian flights and on flights from Australia to the South Pacific, to the U.S. west coast, and to Europe. The dashed line in figure 8 show CV-990 routes for latitudinal flight surveys scheduled for October-November 1976 and February-March 1977.

Data acquisition begins on ascent through 6-kilometer (20 000-ft) altitude and terminates on descent through 6 kilometers. GASP data are taken during a 16-second recording period at intervals of 5 minutes. Following data reduction and verification, the final data tapes are archived and are available to users at the National Climatic Center (NCC) at Asheville, North Carolina. The parameters measured on the GASP systems, along with subsidiary information added to the archival tapes, are as follows:

(1) Data-point identification - aircraft identification, date and time; and position and altitude

(2) Other flight data: wind speed and direction; static air temperature; and aircraft speed, heading, and acceleration

(3) Constituent data: ozone, water vapor, and particle concentration; filter sample composition (SO_4^-, NO_3^-, Cl^-); and analysis of whole gas samples for $CFCl_3$ (Future data will include CO, NO_x, and condensation nuclei (CN) and will expand the whole-gas-sample analysis to include CF_2Cl_2, CCl_4, and N_2O.)

(4) Subsidiary data: tropopause pressure arrays from National Meteorological Center (NMC) objective analysis.

Constituent data available on the GASP archival tapes through calendar 1975 have been limited to ozone and water vapor. Some filter analysis data and analysis of whole gas samples for $CFCl_3$ will appear on subsequent tapes following resolution of earlier problems with the analytical procedures and the cleaning and preparation of filters and sample bottles. Uncertainties in calibrating the particle counter have precluded the inclusion of particle concentration data in the archives to date. New instruments to measure CO, condensation nuclei, and NO_x are in the process of certification testing and installation on the GASP aircraft.

Some examples of ozone data and the effect of atmospheric transport on ozone profiles are shown in figures 9 and 10. Figure 9 (ref. 10) gives the ozone mixing ratio as a function of latitude for several around-the-world flights during March 1975 and includes flights in both the troposphere and the stratosphere. The data show a large scatter in ozone mixing ratio which is typical of the spring maximum. For comparison, North American, March, mean ozone distributions at 10.0 and 12.5 kilometers (32 800 and 41 000 ft) are also shown in figure 9. The two curves were calculated from tabulations of molecular concentration given in reference 11.

As an illustration of ozone variation with respect to the local tropopause as defined by the NMC objective analysis procedure, ozone mixing ratio data from several around-the-world flights during March 1975 are plotted as a function of the altitude pressure in-

crement above and below the tropopause in figure 10. The data have been separated according to the local wind vector curvature (ref. 12) as determined from aircraft-system measurements of wind direction and velocity. The differences, in terms of ozone mixing ratio scatter below the tropopause and ozone gradient below and above the tropopause, are striking when the data for cyclonic and anticyclonic wind curvature are compared. The ozone distribution for anticyclonic streamline curvature (fig. 10(a)) shows the expected steep gradient and increase of ozone in the stratosphere. The cyclonic streamline curvature (fig. 10(b)) indicates a less-steep gradient and high ozone levels below the NMC-defined tropopause. The data illustrate the greater tendency for more intense stratospheric-tropospheric exchange associated with cyclonic curvature of the wind fields.

The single-filter samplers currently installed on two of the B-747 aircraft have limited capability for providing baseline composition data since the filter can only be changed during routine servicing of the GASP systems, which occurs on the average of once every 2 weeks. These single filters will be replaced shortly with an eight-filter magazine. To date, because of limited exposure and earlier problems with analytical and filter washing procedures, limited composition data are available from the B-747's. However three filter-sampling flight series originating from Cleveland and from Holloman Air Force Base in New Mexico have been flown during the past year with the NASA Lewis F-106 aircraft using identical filter samplers. Data on sulfate and nitrate concentrations from the F-106 flights are plotted as a function of pressure altitude difference above or below the local tropopause in figure 11. Although there is considerable variation, the concentrations are low and are consistent with other aircraft sampling flights (refs. 13 and 14). Although the data illustrated represent only a very limited sample, a steep gradient and a peak are indicated above the local tropopause, with considerably lower levels in the troposphere. Sulfate and nitrate are believed to originate from the sulfuric acid aerosol layer in the stratosphere and from absorption of nitric acid vapor on the IPC (cellulose) filter material.

CONCLUDING REMARKS

NASA is conducting programs to evaluate advanced emission reduction techniques for five existing aircraft gas turbine engines. Although these programs are in various stages of completion, the results suggest that significant reductions in all pollutant emissions (carbon monoxide (CO), total hydrocarbons (THC), oxides of nitrogen (NO_x), and smoke) can be achieved. Progress has been made to varying degrees toward meeting the 1979 EPA standards in rig tests of combustors for the five engines.

Selective reductions in certain emission levels (e.g., CO and THC) can be achieved by relatively minor to moderate modifications to current engine baseline combustors.

Because of the inherent total emission control capability of staged combustor concepts, their continued development for application to future newly manufactured engines seems highly desirable. The added complexity involved in the staged concepts, however, will likely require continued development beyond the scope of the current programs. Proof-of-concept tests in full-scale engines are still needed to quantify the success of the advanced concepts in terms of their absolute level of emission reduction and to demonstrate the capability to successfully satisfy all the engine requirements.

Results of fundamental combustion studies suggest the possibility of a new generation of jet aircraft engine combustor technology that would provide emission levels far below those currently possible with the advanced technology concepts demonstrated in the engine-related programs. Considerable fundamental research is still needed, however, before the techniques being studied can be translated into useful combustors. Successful development of these techniques into operational engine combustors would provide the level of NO_x reductions desired for both local air quality and for minimizing effects on the ozone layer during high-altitude-cruise. The objective of the recently begun NASA Stratospheric Cruise Emission Reduction Program (SCERP) is to evaluate the potential of these techniques to evolve combustors for future aircraft gas turbine engines.

The Global Air Sampling Program is now in full operation. Data taken during the past 2 years on ozone have shown its extreme variability but are also providing some valuable insight into stratospheric-tropospheric exchange processes. The measurement of NO_x and CO, which may be directly related to engine emissions, has not yet been implemented but will begin shortly. The accumulation of an adequate data base for these constituents may take several years before GASP can contribute to an assessment of the potential impact of jet engine cruise operations on the upper atmosphere.

REFERENCES

1. Control of Air Pollution for Aircraft Engines - Emission Standards and Test Procedures for Aircraft. Federal Register, vol. 38, July 17, 1973, pp. 19088 - 19103.

2. Grobecker, A. J.; Coroniti, S. C.; and Cannon, R. H., Jr.: Report of Findings: The Effects of Stratospheric Pollution by Aircraft. DOT-TST-75-50, Dept. of Transportation, 1974.

3. Environmental Impact of Stratospheric Flight - Biological and Climatic Effects of Aircraft Emissions in the Stratosphere. Nat. Acad. Sci., 1975.

4. Anderson, R. D.; et al.: Pollution Reduction Technology Program, Turboprop Engines - Phase 1. (EDR-8708, General Motors Corp.; NAS3-18561) NASA CR-135040, 1976.

5. Gleason, C. C.; Rogers, D. W.; and Bahr, D. W.: Experimental Clean Combustor Program - Phase II Final Report. NASA CR-134971, G.E. 74 AEG 380, July 1976.

6. Roberts, R.; Peduzzi, A.; and Vitti, G. E.: Experimental Clean Combustor Program - Phase II Final Report. NASA CR-134969, PWA-5153, 1976.

7. Fear, J. S.: The NASA Pollution Reduction Technology Program for Small Jet Aircraft Engines - A Status Report. AIAA Paper 76-616, July 1976.

8. Roberts, R.; Fiorentino, A. J.; and Green, W.: Pollution Technology Program, Can-Annular Combustor Engines. (PWA-5394, Pratt & Whitney Aircraft; NAS3-18548) NASA CR-135027, 1976.

9. Perkins, P. J.; and Gustafsson, U. R. C.: An Automatic Atmospheric Sampling System Operating on 747 Airliners. Int. Conf. Environmental Sensing and Assessment. Vol. 2, Inst. Electr. Electron. Eng., 1975, pp. 1 26-4 to 10 26-4.

10. Holdeman, J. D.; and Lezberg, E. A.: NASA Global Atmospheric Sampling Program (GASP). Data Report for Tape VL001. NASA TM X-71905, 1976.

11. Wilcox, R. W.; Nastrom, G. D.; and Belmont, A. D.: Periodic Analysis of Total Ozone and Its Vertical Distribution. (RR-3, Control Data Corp.; NAS2-7807) NASA CR-137737, 1975.

12. Falconer, P. D.; and Holdeman, J. D.: Atmospheric Ozone Measurements Made from B747 Airliners: Spring 1975. Paper presented at the Joint Symposium on Atmospheric Ozone, Dresden, East Germany, Aug. 9-17, 1976.

328

13. Lazrus, A. L.; Gandrud, B.; and Cadle, R. D.: Chemical Composition of Air Filtration Samples of the Stratospheric Sulfate Layer. J. Geophys. Res., vol. 76, no. 33, Nov. 1971, pp. 8083–8088.

14. Lazrus, A. L.; and Gandrud, B. W.: Distribution of Stratospheric Nitric Acid Vapor. J. Atmos. Sci., vol. 31, no. 4, May 1974, pp. 1102–1108.

TABLE 1. – EMISSION REDUCTION TECHNOLOGY PROGRAM – SUMMARY OF RESULTS TO DATE (EPAP VALUES)

Engine	Emission[a]								
	Carbon monoxide			Total hydrocarbons			Oxides of nitrogen		
	Conventional combustor	Advanced technique	EPA standard	Conventional combustor	Advanced technique	EPA standard	Conventional combustor	Advanced technique	EPA standard
CF6-50 (double-annular concept)	10.8	3.0	4.3	4.3	0.3	0.8	7.7	4.2	3.0
JT9D-7 (vorbix concept)	8.6	6.5	4.3	3.9	.3	.8	4.9	2.2	3.0
JT8D-17 (vorbix concept)	16.1	8.9	4.3	4.4	.2	.8	8.2	4.1	3.0
TFE731-2 (piloted-airblast concept)	17.5	10.1	9.4	5.3	.1	1.6	5.3	3.9	3.7
501-D22A (reverse-flow concept)	31.5	4.6	26.8	15.0	.3	4.9	6.2	7.3	12.9

[a]Smoke standards should be achievable for all concepts
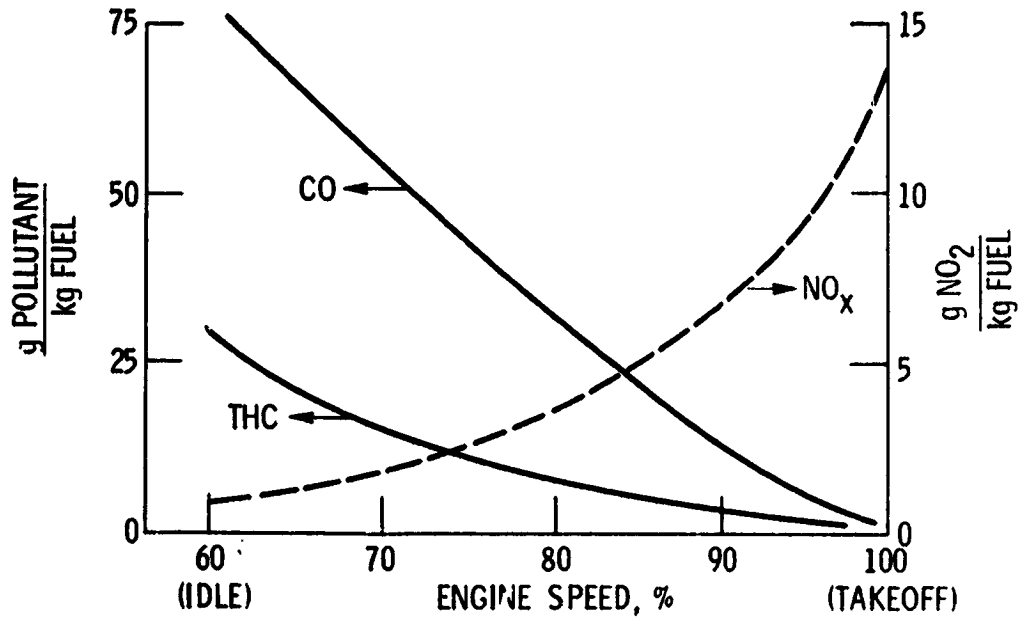
Figure 1.- Typical engine exhaust emission characteristics.
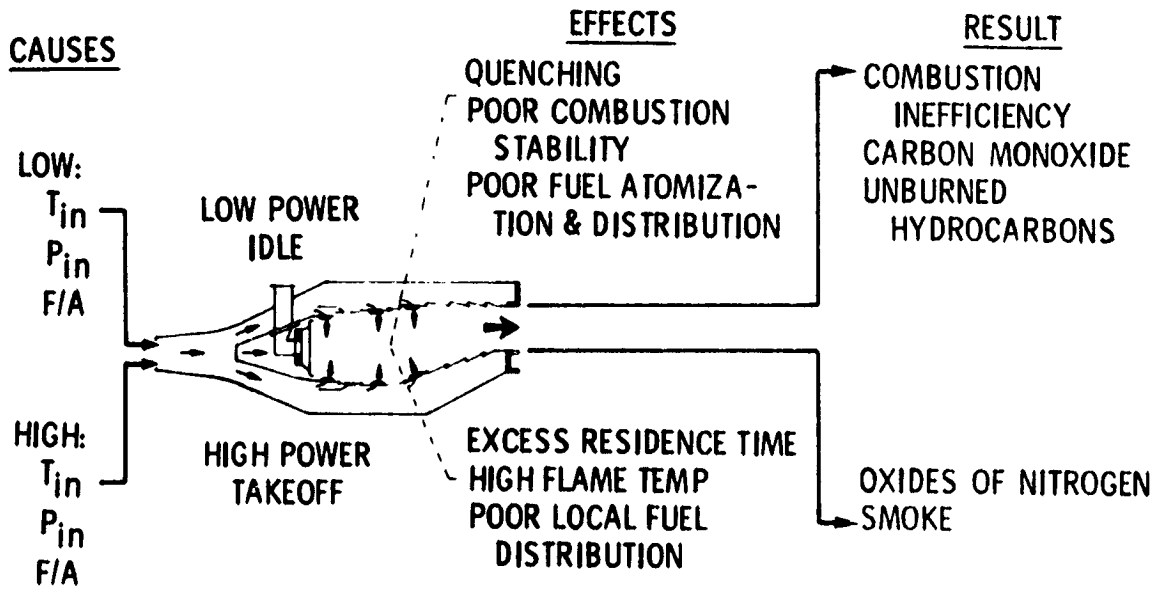

Figure 2.- Aircraft gas turbine combustor pollution considerations.
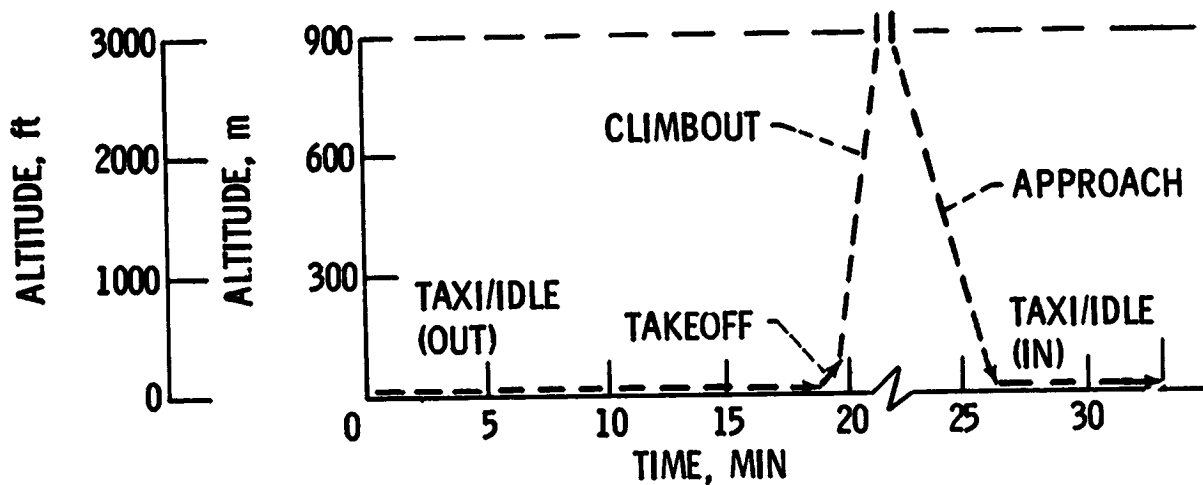
Figure 3.- EPA landing-takeoff cycle.
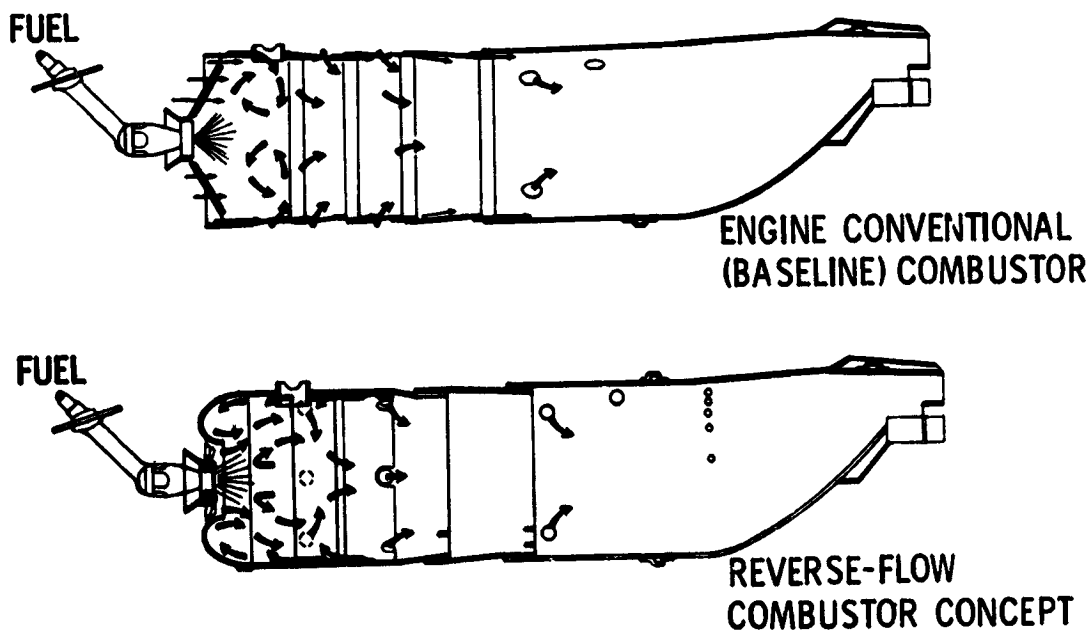
Figure 4.- Reduced-emissions combustor - minor modifications to Detroit
Diesel Allison 501-D22A engine.

331
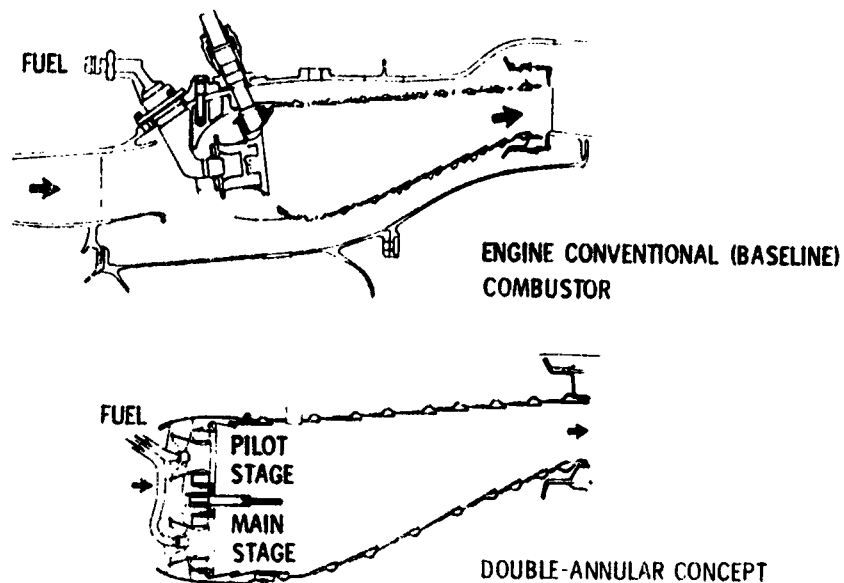
(a) Double-annular concept applied to
General Electric CF6-50 engine.
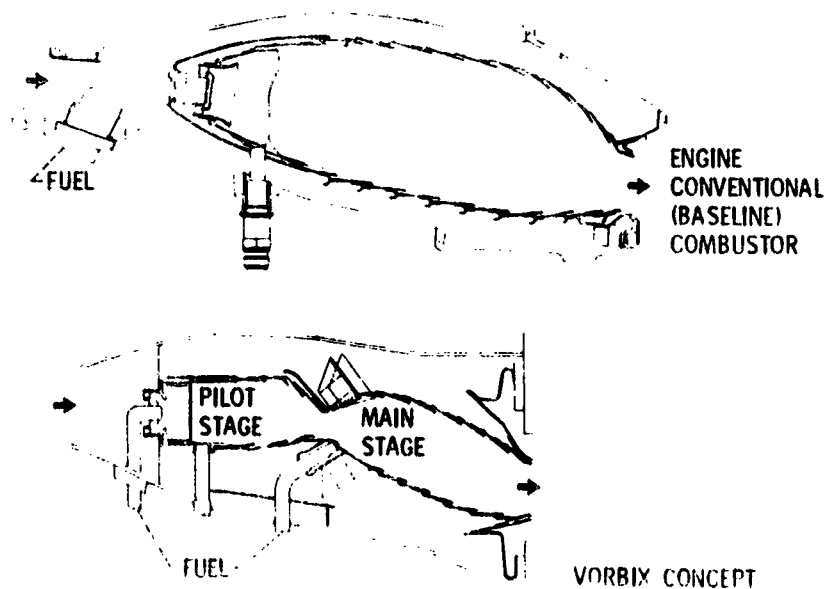
(b) Vorbix concept applied to
Pratt & Whitney JT9D-7A engine.

Figure 5.- Reduced-emissions combustor - staged concepts.

332
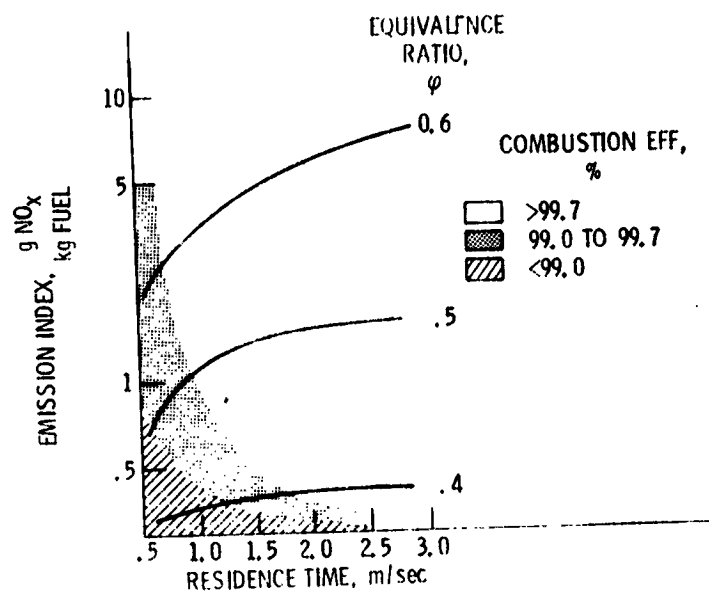
Figure 6.- Combustion efficiency and NO_x emissions.
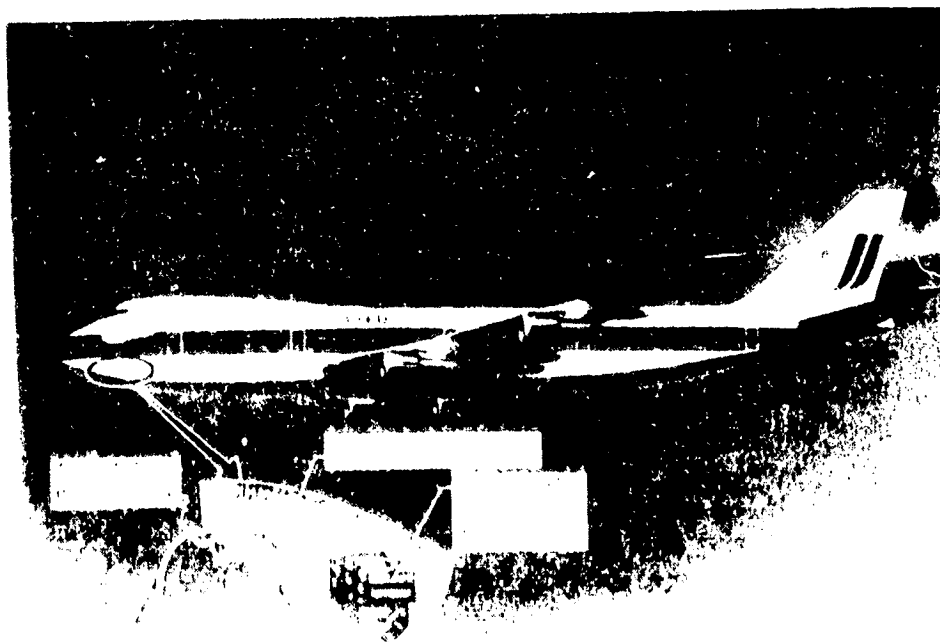
Figure 7.- CASP system installation.
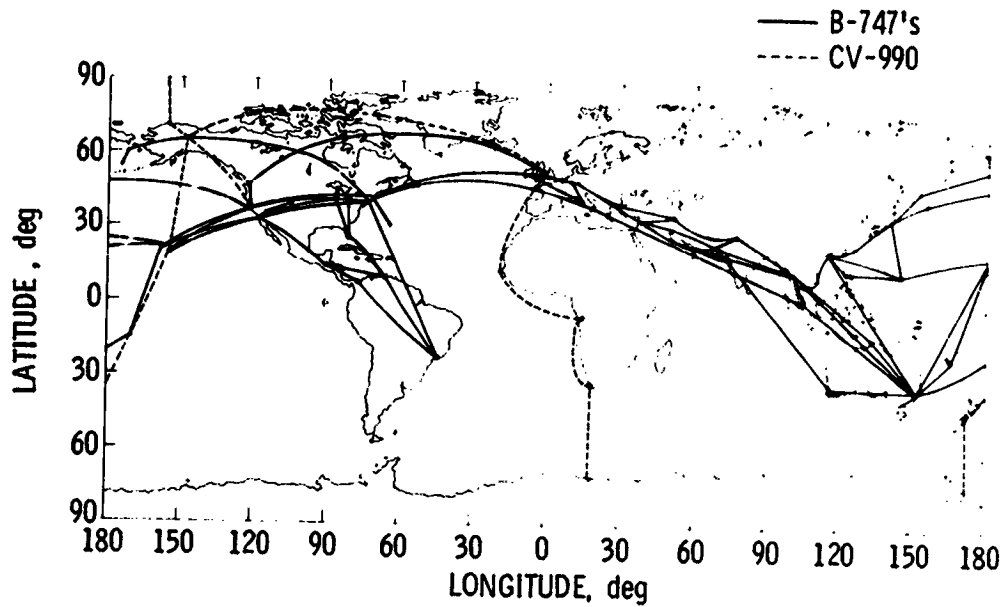
Figure 8.- GASP flight routes.
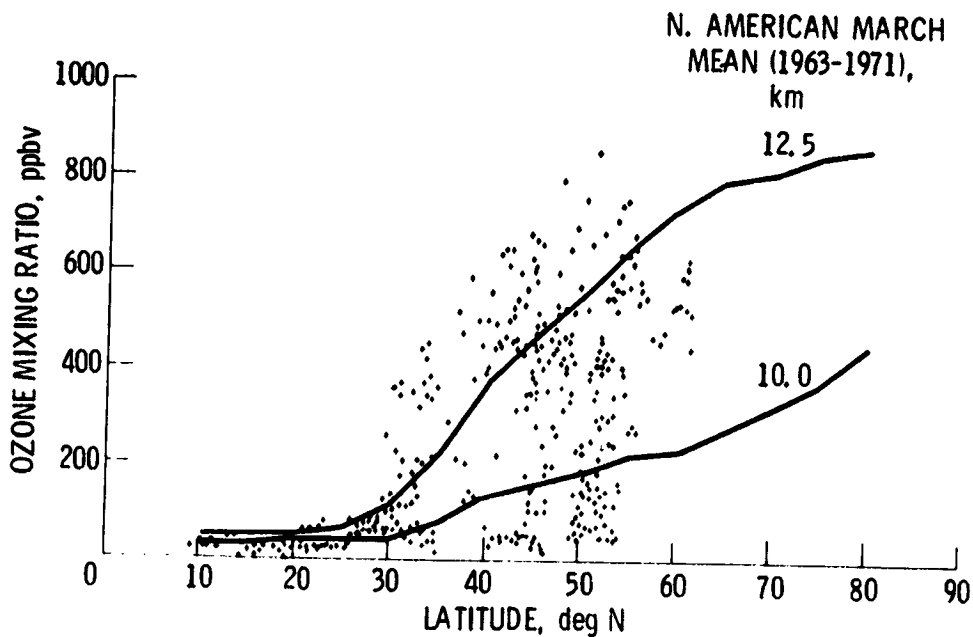
Figure 9.- Variation of ozone mixing ratio with latitude.
Altitude, above 10 kilometers; sampling period,
March 11 to 30, 1975.

334
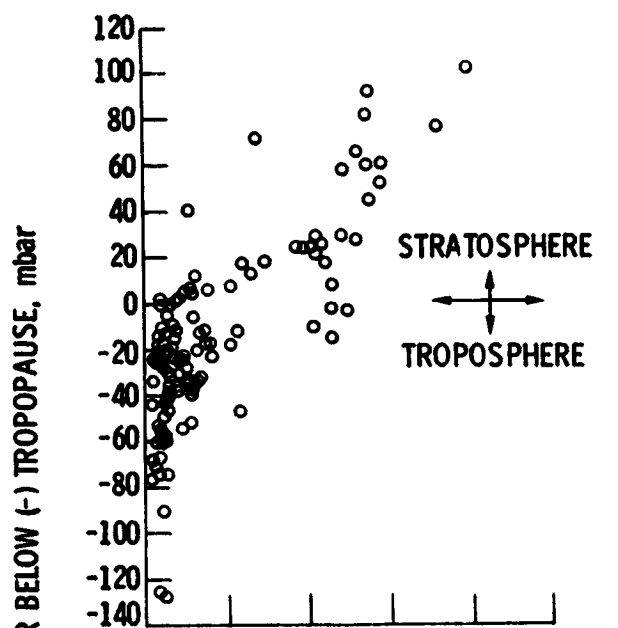
(a) Anticyclonic curvature.
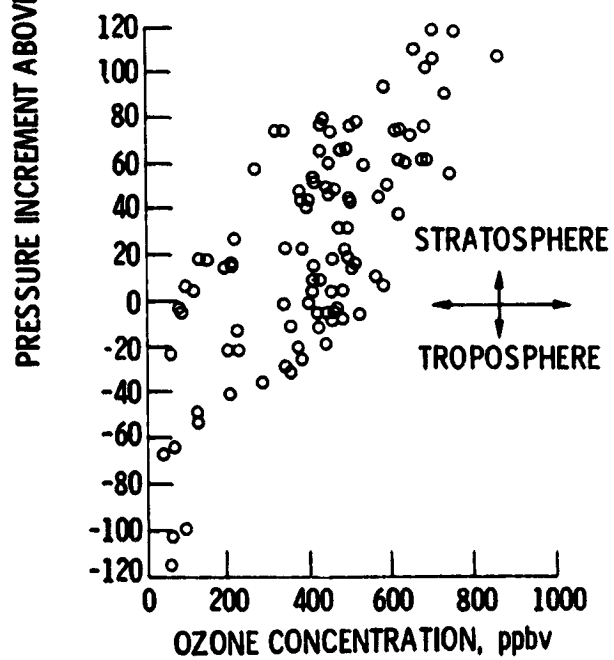
(b) Cyclonic curvature.

Figure 10.- Vertical profile of ozone
mixing ratio showing effect of wind
vector curvature. Sampling period,
March 1975.
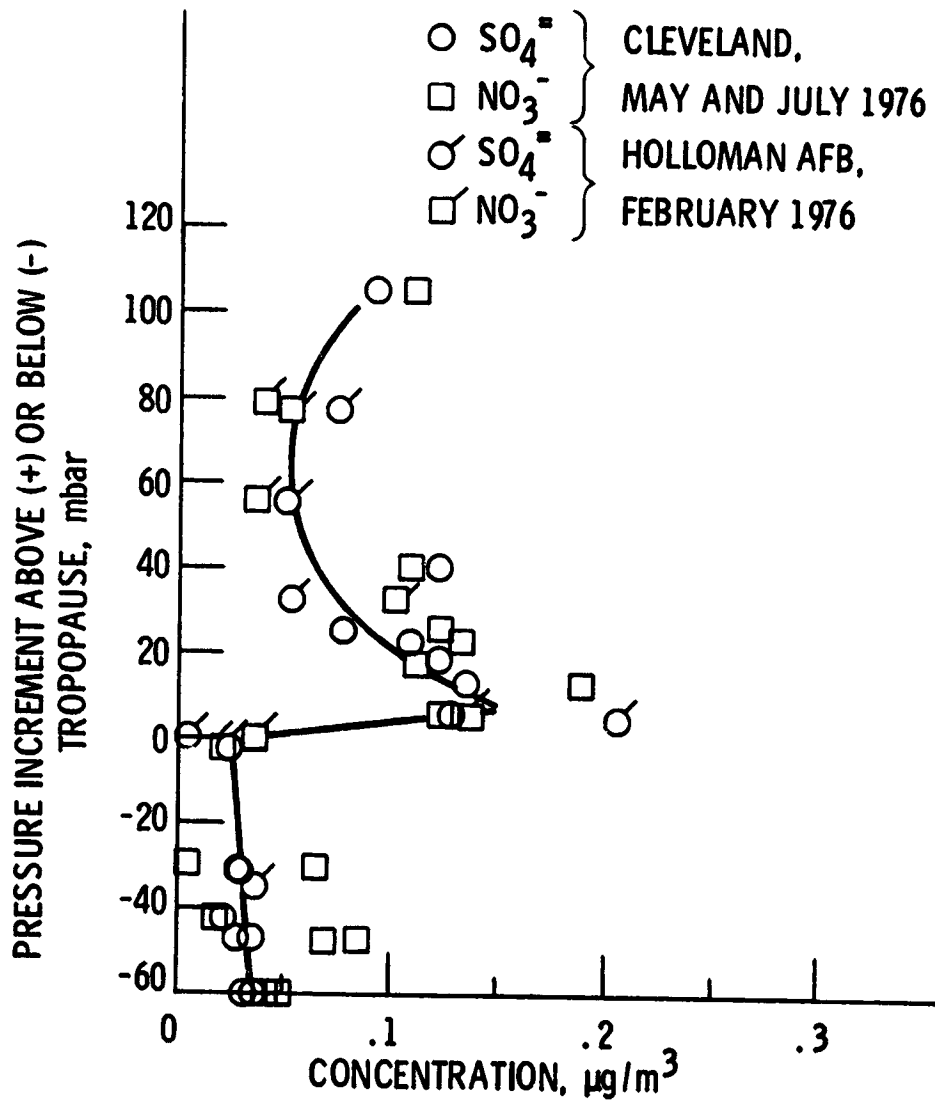
Figure 11.- Vertical profile of $SO_4^=$ and NO_3^- from F-106 filter flights.

STATUS OF RESEARCH INTO LIGHTNING EFFECTS ON AIRCRAFT

J. A. Plumer

General Electric Company

SUMMARY

Developments in aircraft lightning protection since 1938 are briefly noted. Potential lightning problems resulting from present trends toward the use of electronic controls and composite structures are discussed, along with presently available lightning test procedures for problem assessment. The validity of some procedures is being questioned because of pessimistic results and design implications. An in-flight measurement program is needed to provide statistics on lightning severity at flight altitudes and to enable more realistic tests, and operators are urged to supply researchers with more details on electronic components damaged by lightning strikes. A need for review of certain aspects of fuel system vulnerability is indicated by several recent accidents, and specific areas for examination are identified. New educational materials and standardization activities are also noted.

INTRODUCTION

The widespread concern about the effects of lightning on transport aircraft was perhaps first evidenced by the formation in 1938 of the subcommittee on lightning hazards to aircraft of the National Advisory Committee for Aeronautics (NACA). This committee numbered among its members some of the most prominent flight safety, weather, and lightning experts of the day. Among the latter was Dr. Karl B. McEachron, then director of research at the General Electric High Voltage Laboratory, who performed for the committee the first man-made lightning tests on aircraft parts and structures. During the later part of this committee's 12-year existence other organizations such as the U.S. National Bureau of Standards, the University of Minnesota, and the Lightning and Transients Research Institute (LTRI) also began to conduct research into lightning effects on aircraft. Much of this research was sponsored by the NACA and its successor the National Aeronautics and Space Administration (NASA), along with the Federal Aviation Administration, the U.S. Air Force and Navy, and aircraft manufacturers and operators.

For a long time the physical damage at the point of flash attachment to the aircraft was of primary concern. Typical of the damage were holes burned in metallic skins, puncture or splintering of nonmetallic structures, and welding or roughening of movable

19

337

hinges and bearings. The ignition of the fuel was of particular concern, as was the problem of conduction of lightning current directly inside the aircraft via long-wire antennas. A considerable amount of research was also directed toward its effects on people, such as flash blindness and electric shock.

The early research led to the development of protective devices, including fuel filler caps, which will not spark when struck by lightning; lightning arresters, which safely conduct lightning currents from antennas to the airframe; diverter bars and tapes, which minimize punctures of radomes; and static dischargers, which reduce electromagnetic interference in communications systems.

In 1963 the fuel tanks of a Pan American Boeing 707 aircraft exploded in-flight near Elkton, Maryland, after a lightning strike. The exact source of the ignition has never been established, but the explosion stimulated further research into the effects of lightning on fuel systems and fuel tank inerting systems. This research has been instrumental in the development of active surge tank protection (STP) systems for extinguishing flames ignited at vent outlets. The incorporation of much of this protection technology into the design of modern transport aircraft is a principal reason for their present excellent safety record in the lightning environment.

The lightning-safety record is not quite as good for U.S. military aircraft, several of which have been lost in recent years due to lightning strikes. The military have been a traditional proving ground for new technology, and there are several concepts reaching the application stage which may increase potential lightning hazards still further. Fortunately, most of these possibilities have been recognized and efforts are underway to develop effective protection. Since some of this new technology will eventually be used in commercial aircraft, it is appropriate to review recent developments and identify the directions in which aircraft-lightning research should proceed in the future.

SYMBOLS

C   capacitance of aircraft or lightning flash to its surroundings, F/m

e_1 induced voltage between wires, V

e_2 induced voltage between wire and airframe, V

f   frequency of traveling wave reflections at either end of aircraft, Hz

i_L lightning stroke current, A

L   inductance of the lightning current flow path in aircraft, H/m

(aircraft length, m

R   radius of electrostatic field, m

R_s resistance of an airframe, Ω

r radius of lightning channel, m

T time for a traveling wave to travel the aircraft length and back, s

t time, s

v velocity of traveling wave propagation, m/s

Z surge impedance, Ω

φ_i internal magnetic flux produced by lightning current, A/m

φ_o external magnetic flux produced by lightning current, A/m

ELECTRICAL AND ELECTRONICS SYSTEMS

In recent years it has become apparent that lightning strikes may indirectly affect electronic equipment located elsewhere in the aircraft from the point of lightning attachment. Examples of this are the interference or damage to instruments and power distribution systems summarized from a sampling of 214 airline lightning strike reports in table I. Another example which caused more alarm among safety experts was the lightning strike to the Apollo 12 vehicle which disrupted the command module power system after lift-off.

The cause of these indirect effects was thought to be the electromagnetic fields associated with lightning currents flowing through the aircraft. Research (ref. 1) began in 1967 to determine the coupling mechanisms involved and the potential impact that these indirect effects might have on equipment operation and flight safety. Briefly, it has been confirmed that, when lightning currents flow through an aircraft, magnetic fields are produced and structural voltage rises occur which couple transient voltages into the vehicle's electrical wiring (as shown in fig. 1). In some cases these voltages are high enough to damage solid-state electronic equipment to which the wiring is connected. Unlike other aspects of aircraft design, there are no specifications or standards which say what level of transient voltage a piece of apparatus must withstand or conversely, what levels the transient voltages must not be allowed to exceed in vehicle wiring. This incompatibility between the transient withstand capability of electronic devices and the transients to which they are exposed is not limited to the aerospace industry but is one which is appearing to some degree wherever solid-state electronics are used, with a wide range of unfortunate consequences.

Some idea of the actual transient voltages that lightning may produce in an aircraft's electrical circuit might be obtained by passing simulated lightning currents through an aircraft and measuring the voltages induced. Existing generators, however,

are incapable of forcing the high currents (up to 200 000 A) associated with a severe lightning strike through a test circuit as large as a complete aircraft. Even if it were possible, most owners would, understandably, hesitate to allow this much current to be passed through their aircraft. Therefore, under sponsorship of the NASA Aerospace Safety Research and Data Institute a nondestructive test called the lightning transient analysis (LTA) (ref. 2) was developed. In LTA impulse currents as low as 1/1000 of that expected in an actual lightning strike are passed through the aircraft between typical lightning attachment points. Voltages induced by these currents are then linearly extrapolated to full-scale levels. Comparison of voltages induced by LTA and full-scale test currents have confirmed that linear extrapolation is valid in most situations.

Typical wire-to-wire and wire-to-airframe voltages induced by LTA test currents in a fighter aircraft (ref. 3) wire bundle are shown in figure 2. When 300 amperes was impressed upon the airplane, the peak voltage measured between either wire and the airframe was 2.4 volts (left oscillogram). A linear extrapolation to a severe lightning stroke of 200 000 ampers would induce

$$(2.4 \text{ V}) \frac{200\ 000\ \text{A}}{300\ \text{A}} = 1600\ \text{V}$$

between these wires and airframe ground at plug P22. The measured voltage between the two wires (right oscillogram), however, extrapolates to only about 350 volts. This result illustrates the benefit of two-wire (independent return) circuits over single-wire and airframe return. The benefit comes from the smaller circuit loop through which magnetic flux may pass as compared with the single wire and airframe return. On the other hand, the two-wire method requires more wire and this may be undesirable from weight and cost standpoints.

Whether the two-wire or any other protective scheme (with other penalties) provides sufficient protection or is even necessary at all depends on the actual transient voltage levels that may be induced and the upset or damage levels of the associated electronics. Because tools to calculate expected voltage levels by analysis alone are not yet available, the LTA test has been used to tell designers what to expect in such aircraft as the NASA Flight Research Center F-8 digital-fly-by-wire airplane, the Navy – Lockheed S-3A antisubmarine warfare aircraft, and the USAF – General Dynamics F-16 Air Combat Fighter. Lightning transient analysis techniques are also beginning to be used to certify new systems being installed on present transport aircraft.

A large amount of induced voltage data has been obtained from these LTA tests. Perhaps because direct effects tests on sections of an aircraft (for which a few government specifications are available) are usually performed at the 200-kiloampere level, the LTA data have been extrapolated to this level for design purposes. This has

340

resulted in alarmingly high voltages being predicted for some critical circuits. As might be expected, the validity of these predictions is being questioned by aircraft designers who continually ask for proof that such voltages in fact occur in flight and whether 200-kiloampere strikes really occur often enough to be the design level. The increasing reliance on electronics to perform flight critical functions, as in fly-by-wire flight controls without mechanical backup, means that reliable values must be available for design purposes, since indiscriminate application of protective shielding and surge suppression devices would impose unacceptable size, weight, and cost penalties.

There are other aspects of the induced voltage problem which also are not well understood. For example, certain of the induced voltages bear a clear mathematical relationship to the lightning current which causes them. But other voltages, sometimes superimposed on the familiar ones (as shown in fig. 3), seem to bear none. While of short duration, they are often among the highest voltages measured and thus the determining factor in protection decisions. It has been suggested by Fisher (ref. 4) that these voltages are induced by traveling current wave reflections excited in the airframe when the lightning flash first strikes the aircraft. These reflections would arise because of the probable differences in the surge impedance Z of the lightning flash channel and the aircraft (fig. 4). The velocity v of the traveling waves in the aircraft would be that of light, $3 \cdot 10^8$ meters per second, and the period of oscillation would be proportional to the length of the aircraft.

The voltage of figure 3(c) was induced in an aircraft whose length ℓ is 13 meters, for which the period T of one complete down-and-back cycle would be

$$T = \frac{2\ell}{v} = \frac{26 \text{ m}}{3 \times 10^8 \text{ m/s}} = 8.67 \cdot 10^{-8} \text{ s}$$

and the frequency f of repeated cycles would be

$$f = \frac{1}{T} = 11.53 \text{ MHz}$$

If a current of this frequency had been in the airframe, it could have induced a voltage of the same frequency in the aircraft's electrical circuits. A frequency of this order is indeed evident in the induced voltage oscillogram of figure 3(c). The question is, Do these oscillations actually occur in aircraft struck in flight or are they caused only by the LTA test? The explanation of figure 4 depends on an inequality between the surge impedance of the lightning channel and that of the aircraft. Bewley (ref. 5) defines the surge impedance of a lightning stroke in terms of the radius r of the lightning channel

341

and the radius R of the electrostatic field due to the volume of the cloud that participated in the discharge, as follows.

$$Z = 60 \left(\log \frac{R}{r} - \frac{1}{2} \right)$$

And Bewley calculates values of between 100 and 600 ohms for typical strokes. The surge impedance of the aircraft is determined from its lengthwise distributed inductance L and capacitance to its surroundings C by the relation:

$$Z = \sqrt{\frac{L}{C}}$$

A conductor as large as an aircraft would have a low inductance and relatively high capacitance. Assuming the inductance to be 0.1 microhenry per meter and the capacitance to be 50 picofarads per meter, then the surge impedance of the aircraft would be

$$Z = \sqrt{\frac{0.1 \times 10^{-6} \ H/m}{50 \times 10^{-12} \ F/m}} = 44.7 \ \Omega$$

which is considerably less than that of the lightning stroke. The reflection and refraction coefficients defined by Bewley (ref. 6) for an aircraft of this impedance are calculated in figure 4, where the surge impedance of the lightning channel is taken for convenience to be 450 ohms. These calculations show that the initial peak of traveling wave current in the airframe could be 1.8 times the amplitude of the incident lightning current. A current of this magnitude and frequency might well induce the kind of voltage shown in figure 3(b).

There could be no better way of confirming the existence and severity of these voltages than by an in-flight data gathering program. Instrumentation technology has advanced to the point where it should now be possible to develop small instrument packages capable of measuring and recording the magnitudes and waveforms of actual lightning currents and the voltages they induce in aircraft circuits. Such instruments might be installed in commercial transport aircraft and monitored for several years to obtain a good sampling of data on the real life environment they experience.

342

FUEL SYSTEMS

Stimulated in part by the Elkton accident and also by the SST development program, a large amount of research was conducted during the 1960's to determine mechanisms by which lightning strikes might ignite flammable vapors in aircraft fuel tanks and to develop protective measures. Emphasis was placed on integral wing tanks and associated vent systems. The research led to the development of methods to extinguish fires that originated at vent outlets or to prevent their ignition in the first place. Successful test techniques have also been developed (refs. 7 and 8) to enable the definition of safe thickness for integral tank skins of various metals. A large amount of data such as that shown in figure 5 is on hand relating skin materials and thicknesses to the lightning environment. These protective measures and test techniques are in use today by the major airplane manufacturers and have contributed to greater flight safety.

Since 1971, however, at least three accidents involving in-flight explosion of fuel tanks and suspected lightning strikes have occurred. These accidents again bring up the issue of fuel system vulnerability. The earlier focal points of vent systems and skin punctures appear not to have been involved in these accidents (a USAF KC-135, a USAF F-4, and an Iranian Air Force B-747), yet there is evidence that lightning could have struck these aircraft at or about the time the explosions occurred. The exact mechanism of fuel ignition has not been found in any of these cases. The accidents therefore indicate a need for a reexamination of fuel system vulnerability to lightning. Whereas most earlier research dealt with ignition sources originating at the arc attachment point, less is known or documented about the effects of lightning current conduction through typical fuel tank structures and associated plumbing. Airworthiness Standards such as the U.S. Federal Aviation Regulations Part 25 (ref. 9) pertaining to fuel systems specify that the ignition of fuel vapors by stroke attachment or steaming shall be prevented, but do not appear to place equal stress on the effects of current conduction through the airframe. The lightning tests that are suggested in an associated document (ref. 10) relate primarily to proof against sparking from stroke attachment to access doors, filler caps, and the like. The emphasis in existing military standards is the same (ref. 11).

With reference to figure 6, some aspects of fuel systems that might bear further examination are

(1) Mechanical bonding - Does the bonding together of integral tank walls, ribs, spars, and skins provide adequate electrical bonding for lightning currents? Are there any conditions in present constructions that may result in an electrical spark? If not, how much margin of safety exists?

(2) Fuel system lines and fittings - How much lightning current may actually flow in the vent lines, fuel lines, hydraulic lines, etc., present in typical fuel tanks? How

343

does the current get into and out of this plumbing? Can sparks occur across joints and couplings? To what extent, if any, do procedures to prevent excessive vibration of lines and fittings (per FAR pt. 25, par. 25.993) degrade electrical bonding among sections of lines and between lines and structures?

(3) <u>Electrical sparks</u> - If electric current is flowing from one metallic element to another, what conditions of current amplitude, waveshape, contact resistance, relative motion, and corrosion must exist to cause a spark? Much is known about how much electrical <u>energy</u> must be discharged through a spark to cause ignition, but this parameter is hard to equate in terms of lightning current. How much electric <u>current</u> does it take to cause a spark sufficient to ignite fuel?

(4) <u>Electrical apparatus inside fuel tanks</u> - Are fuel tank electrical parts, such as pump motors, valves, and fuel quantity probes, really as immune to sparking as their manufacturers say they are? What about lightning-induced voltages brought to these items from electrical circuits that run outside of the fuel tanks, and which may therefore be outside of the fuel system designer's control?

(5) <u>Fuel</u> - The three aircraft mentioned above carried JP-4 fuel which has a wider flammability envelope than the aviation kerosenes commonly used by U.S. commercial airlines. How much safer is Jet A than JP-4 under the conditions in items (1) to (4) which may cause sparking?

(6) <u>Design guidelines</u> - What, if any, new design guidelines should be followed to overcome the situations in items (1) to (4) which may result in sparking?

Answers to these questions could probably be obtained from a combination of basic research into sparking mechanisms of metals in various types of contact with one another and an extensive series of carefully instrumented laboratory tests of typical aircraft fuel tanks, including, especially, integral tanks in wings. Included in these tests would be full-scale simulated lightning currents conducted through the tanks with ignitable hydrocarbon-air mixtures inside.

STRUCTURES

Recent emphasis in lightning protection of structures has been placed on the fiber-glass, boron, and graphite reinforced composites which are beginning to replace conventional aluminum in some applications. Much is now known (refs. 12 to 14) about the electrical conduction properties of these materials and the degree of damage that specific amounts of lightning currents can cause. Protective coatings have been developed to minimize this damage, and work is now underway to develop mechanical bonding and fastening techniques which can safely conduct lightning currents without sparking or loss of strength. In some applications, such as engine fan blades, wing leading edges, and fuselage skins, composites will not be exposed to direct lightning strike effects, but in

other cases these materials are being used where lightning strikes frequently attach. Initial experience has been with fiberglass and, though protected in many cases by metallic diverter bars, fiberglass wing tips, radomes, and fairings have been extensively damaged by lightning strikes as shown for example in figure 7. To date, none of this damage has caused a fatal accident, but there have been some close calls. The protective devices designed for these structures have performed well under laboratory tests, but their performance on an aircraft in flight has not been as good.

There appear to be several reasons for this poor performance. (See fig. 8.) One is the presence of anti-erosion paints which are often applied over a protective diverter on the real aircraft. Another is the way the nonmetallic part is attached to metallic substructural elements, which are outside the control of the protection designer. Still another is the continued use of the same type of electrical wiring inside the nonmetallic structure as was used satisfactorily within the metallic structure it replaced, and yet another - and possibly the most important reason - is a lack of knowledge of the basic relation between the lightning flash and the aircraft during the formative stages of the strike. This deficiency has limited our ability to simulate the real world in the laboratory and properly test protective diverters.

Improvements in understanding this situation can probably be obtained by in-flight evaluations of the performance of protective devices against laboratory predictions, and by use of more thorough instrumentation in the laboratory to obtain a better understanding of dielectric breakdown processes in typical aircraft structures.

In addition to the direct effects considered above, the potential impact on electrical and electronic systems of replacement of the aluminum skin with a composite skin remains to be learned. Whereas aluminum skins provide sufficient shielding of many of today's aircraft electronic systems, the absence of this property in a composite skin (fig. 9), will expose internal wiring to much more intense electromagnetic fields and require marked changes in electrical system design.

EDUCATION AND STANDARDIZATION

Since lightning may have some affect on nearly every system in an aircraft, succesful protection depends on many designers being aware of potential lightning problems. To improve this awareness, some educational materials are available which are worthy of note.

Educational Films

The U.S. Navy Air Systems Command has prepared four educational films (ref. 15) on the protection of aircraft against lightning. These are available from the Navy for

loan to anyone desiring to introduce the subject to aircraft designers or operators.

In response to inquiries for more detailed information on protection of fuel and electrical systems, the Navy is preparing two more films, which treat these subjects in greater detail.

Lightning and Static Electricity Conferences

The Society of Automotive Engineers (SAE) Committee AE-4 on Electromagnetic Compatibility together with (at various times) the U.S. Air Force, U.S. Navy, Royal Aeronautical Society, and Institution of Electrical Engineers has conducted international conferences on lightning and static electricity as applied to aircraft. These conferences have provided a forum for researchers to review advancements in the state of the art every 2 years since 1968. Proceedings of each conference have been published (refs. 16 to 19).

Aircraft Lightning Protection Handbook

The Aerospace Safety Research and Data Institute of NASA Lewis Research Center has sponsored a handbook on Lightning Protection of Aircraft by Fisher and Plumer of General Electric, in which the results of many research programs are digested and presented in a manner useful to aircraft designers and operators. This book is to be published as a NASA Special Publication in 1976.

Test Standards

Lightning protection has suffered in the past from a lack of lightning qualification test standards which reflect the state of the art. Those that do exist (e.g., refs. 10 and 11) apply only to a few systems or components or are impossible to perform as written and therefore are subject to individual interpretations and deviations. Accordingly, a subcommittee composed of experts in lightning laboratories, industry, and government has been formed under SAE Committee AE-4 to draft lightning test waveforms and techniques that would form the basis of new or updated government specifications. This committee has completed its work on this task with the publication of a report defining lightning test waveforms and techniques for aerospace vehicles and hardware (ref. 20). The Committee is now embarked on an additional task of recommending transient test levels for aerospace electronics equipment.

346

CONCLUDING REMARKS

One of the keys to answering the lightning effects questions raised in the preceding paragraphs is a more thorough understanding of the interaction between the lightning flash and the aircraft in flight. The instrument development work and in-flight measurement program needed for this will require the efforts of several researchers, designers, and operators of aircraft and will take a number of years to accomplish.

In the meantime, it is important that details of lightning strike incidents to aircraft flying today are recorded by the operators and made available to researchers, especially when there is interference or the malfunction of electronic equipment aboard the aircraft. For example, if an instrument is believed to be damaged by a strike, a description of any parts burned out and replaced by the repair shop would enable researchers to get some idea of the magnitude of the induced voltage surge involved and the location of the aircraft wiring in which it originated. Methods to provide protection against similar incidents could also be developed from these data. Admittedly, it is difficult to track component failure information in the midst of the other requirements imposed on operations personnel, yet these data are available now and would be extremely valuable in achieving a better understanding of the indirect effects problem and designing protection for future aircraft.

REFERENCES

1. Lloyd, K. J.; Plumer, J. A.; and Walko, L. C.: Measurements and Analysis of Lightning-Induced Voltages in Aircraft Electrical Circuits. NASA CR-1744, 1971.

2. Walko, L. C.: A Test Technique for Measuring Lightning-Induced Voltages in Aircraft Electrical Circuits. NASA CR-2348, 1974.

3. Plumer, J. A.; Fisher, F. A.; and Walko, L. C.: Lightning Effects on the NASA F-8 Digital-Fly-by-Wire Airplane. NASA CR-2524, 1975.

4. Fisher, F. A.: Analysis of Lightning Current Waveforms through the Space Shuttle. Aircraft Lightning Protection Note 75-1, General Electric Co., 1975.

5. Bewley, L. V.: Traveling Waves on Transmission Systems. Dover Publications, Inc., 1963, pp. 114-117.

6. Bewley, L. V.: Traveling Waves on Transmission Systems. Dover Publications, Inc., 1963, pp. 45-52.

7. Kester, Frank L.; Gerstein, Melvin; and Plumer, J. A.: A Study of Aircraft Fire Hazards Related to Natural Electrical Phenomena. NASA CR-1076, 1968.

8. Brick, R. O.: A Method for Establishing Lightning-Resistance/Skin-Thickness Requirement for Aircraft. Lightning and Static Electricity Conference. Part 2: Conference Papers. AFAL-TR-68-290-Pt-2, Air Force Avionics Lab., 1969, pp. 295-317.

9. Federal Aviation Regulations. Part 25-Airworthiness Standards, 1974, p. 81, par. 25.955

10. Protection of Aircraft Fuel Systems Against Lightning. FAA-AC-20-53, Federal Aviation Agency, 1967.

11. Bonding, Electrical, and Lightning Protection, for Aerospace Systems. MIL-B-5087B, Naval Publications Forms Center, Aug. 1970.

12. Fassell, W. M.; Penton, A. P.; and Plumer, J. A.: The Effects of High Intensity Electrical Currents on Advanced Composite Materials. U-4587, Philco-Ford Corp., 1969.

13. Penton, A. P.; Perry, J. L.; and Lloyd, K. J.: The Effects of High Intensity Electrical Currents on Advanced Composite Materials. U-4866, Philco-Ford Corp. (AD-876197), 1970.

14. Penton, A. P.; Perry, J. L.; and Lloyd, K. J.: The Effects of High Intensity Electrical Currents on Advanced Composite Materials. U-5018, Philco-Ford Corp. (AD-740822), 1972.

15. U.S. Navy: Lightning and Precipitation Static Causes and Effects on Aircraft, 1973. (Available from Naval Air Systems Command Hq. Washington, D.C. 20360)
    Flash and Glow, Film MN-11092A
    Damage and Protection, Film MN-11092B
    Research and Development Testing, Film MN-11092C
    Future Aircraft Design Problems, Film MN-11092D

16. Proceedings of 1968 Lightning and Static Electricity Conference. AFAL-TR-68-290, Air Force Avionics Lab., 1969.

17. Proceedings of 1970 Lightning and Static Electricity Conference. Soc. Automot. Engrs., Inc., 1970.

18. Proceedings of 1972 Lightning and Static Electricity Conference. AFAL-TR-72-325, Air Force Avionics Lab. (AD-752551), 1972.

19. Proceedings of 1975 Lightning and Static Electricity Conference. Roy. Aeronaut. Soc. (London), 1975.

20. Lightning Test Waveforms and Techniques for Aerospace Vehicles and Hardware. SAE Committee AE-4, Task F report. Oct. 1976.

TABLE I. - EXAMPLES OF INDIRECT EFFECTS IN

COMMERCIAL TRANSPORT AIRCRAFT

[214 lightning strike reports.]

System	Interference	Outage
HF Comm	--	5
VHF Comm	27	3
VOR receiver	5	2
Compass (all types)	22	9
Marker beacon	--	2
Weather radar	3	2
ILS	6	---
ADF	6	7
Radar altimeter	6	---
Fuel flow gage	2	---
Fuel quantity gage	--	1
Engine rpm gages	--	4
Engine EGT gages	--	2
Static air temperature gage	1	---
Windshield heater	--	2
Flight director computer	1	---
Navigation light	--	1
AC generator tripoff	(6 instances of tripoff)	
Autopilot	1	---

MAGNETIC FLUX
PENETRATION:

BY DIFFUSION
THROUGH
SKINS

BY PENETRATION
THROUGH
APERTURES

$$e_1 \cdot \frac{d\varphi_1}{d\tau}$$
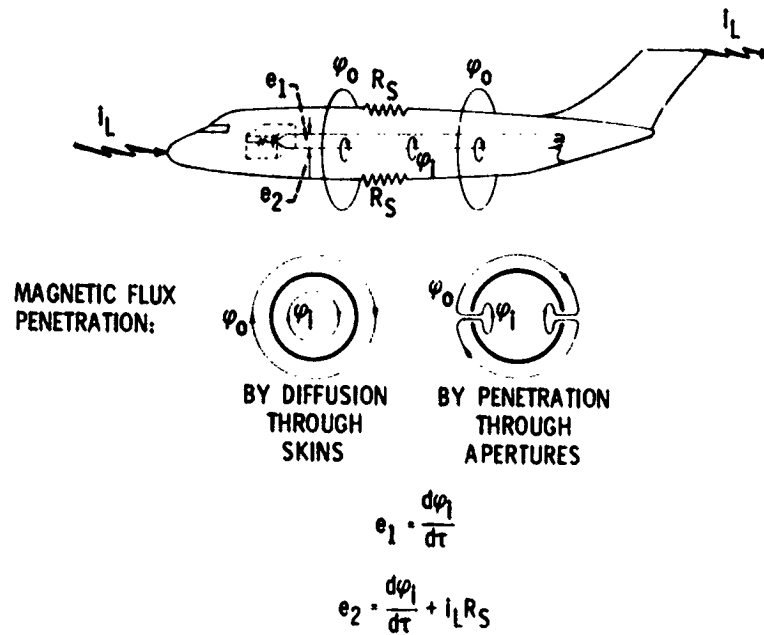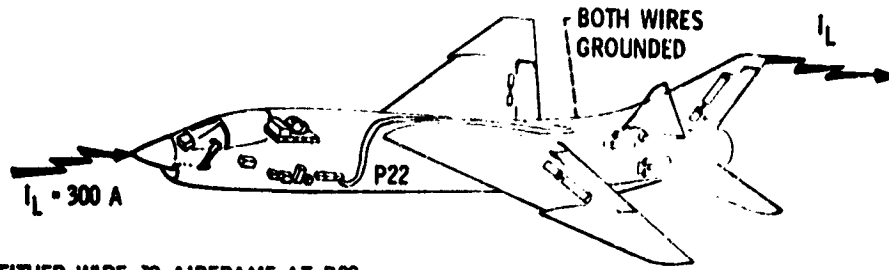
$$e_2 \cdot \frac{d\varphi_1}{d\tau} + i_L R_S$$

Figure 1.- Induced voltage mechanisms.

350

EITHER WIRE TO AIRFRAME AT P22
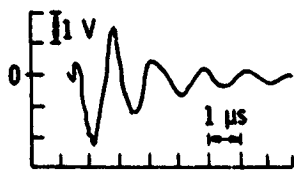
ONE WIRE TO OTHER AT P22

Figure 2.- Typical induced voltages: wire-to-wire and wire-to-airframe.

(a) Waveform of lightning current and magnetic flux.
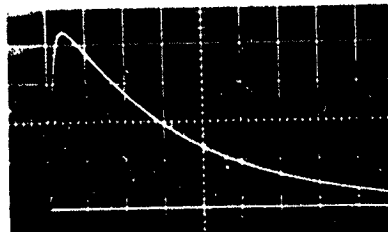
(b) Induced voltage

$$e = \frac{d\varphi}{d\tau} + i_L R_S$$

= clear relationship.
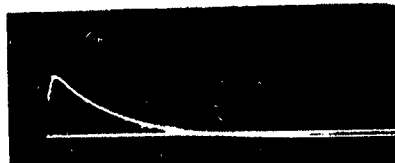
(c) Induced voltage

$e = f(?)$

• unclear relationship.
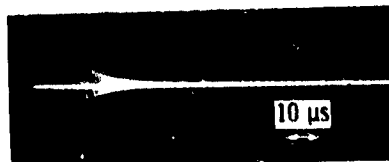
Figure 3.- Relationship between lightning current and induced voltages.

351

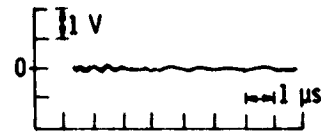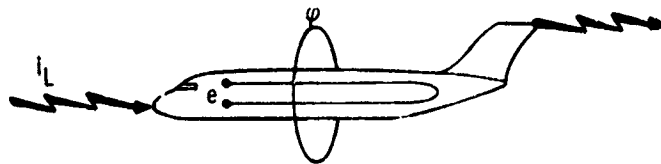Z_L 450 Ω $Z_{A/C}$ 50 Ω Z_1 450 Ω

REFRACTED CURRENT $\dfrac{2Z_L}{Z_{A/C}+Z_L}$ 1.8 i_1 $\dfrac{2Z_{A/C}}{Z_{A/C}+Z_L}$ 0.2 i_1

REFLECTED CURRENT $\dfrac{Z_L-Z_{A/C}}{Z_{A/C}+Z_L}$ 0.8 i_L $\dfrac{Z_{A/C}-Z_1}{Z_{A/C}+Z_1}$ 0.8 i_1
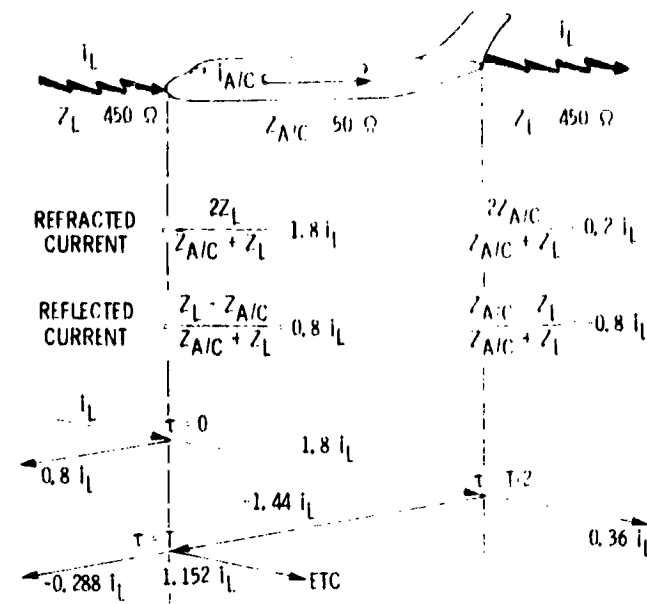
THESE REFLECTIONS CAUSE AN OSCILLATING CURRENT IN THE AIRFRAME:

Figure 4.- Traveling wave reflected in aircraft.

Figure 5.- Lightning charge required to puncture fuel
tank skins of various thickness (from ref. 8).

352

Figure 6.- Areas for reexamination for lightning
effects in fuel systems.

Figure 7.- Fiberglass structure damage by lightning.

Figure 8.- Problems in protection of composite structures.

Figure 9.- Magnetic shielding property of composites.

RATIONALE FOR STRUCTURAL INSPECTIONS

John R. Davidson
NASA Langley Research Center

SUMMARY

During the past few years, methods have been developed to predict the reliability of aircraft structures. They depend upor inspection effectiveness which, in turn, depends upon structural complexity, quality, and the percentage of the structure inspected. Reliability can be enhanced by choosing materials properly, designing damage-tolerant structures, and increasing inspection frequency. And, for fleet operations, costs can be minimized through proper inspection schedules, and enhanced reliability can be compatible with minimum cost. The methods are derived from a combination of probability theory and engineering equations.
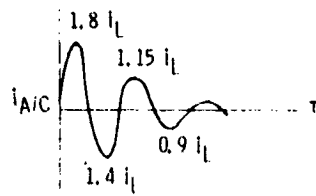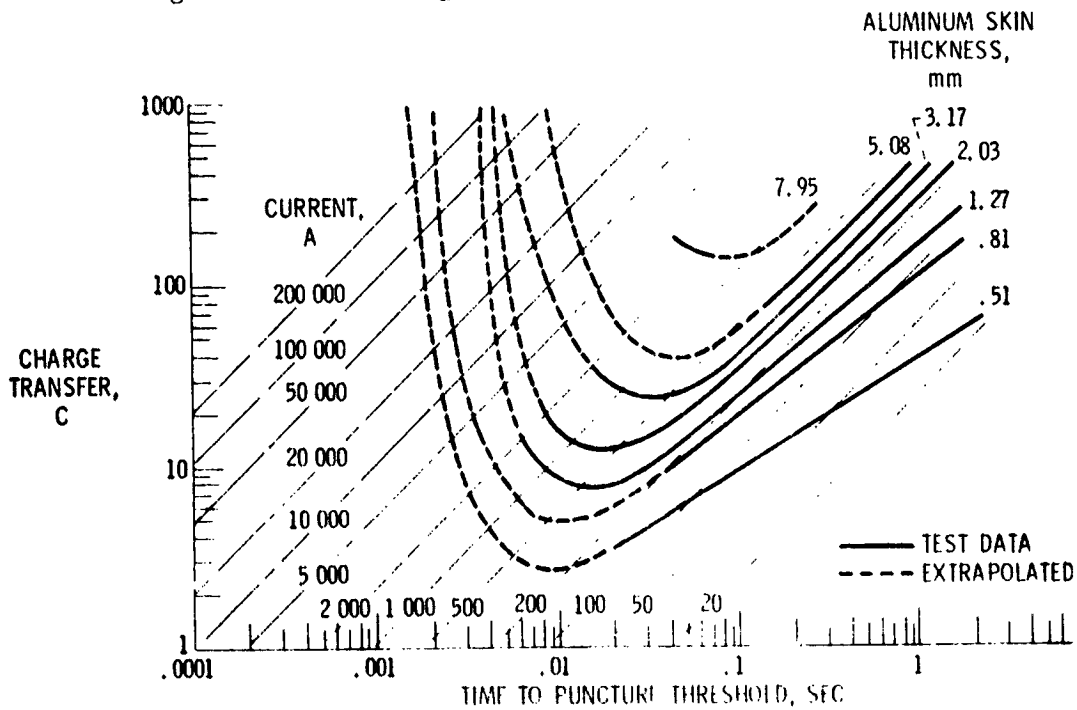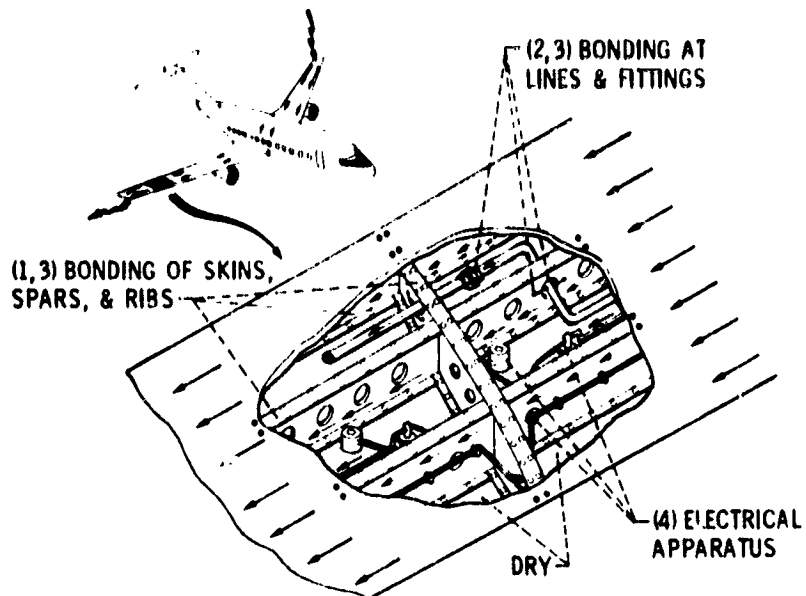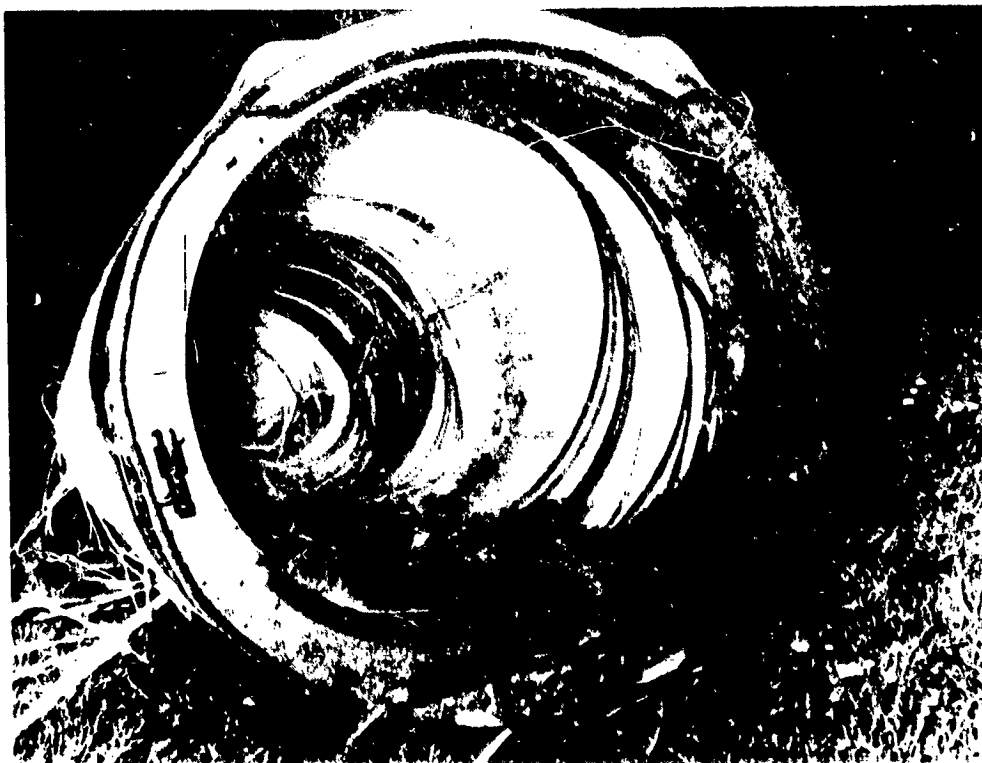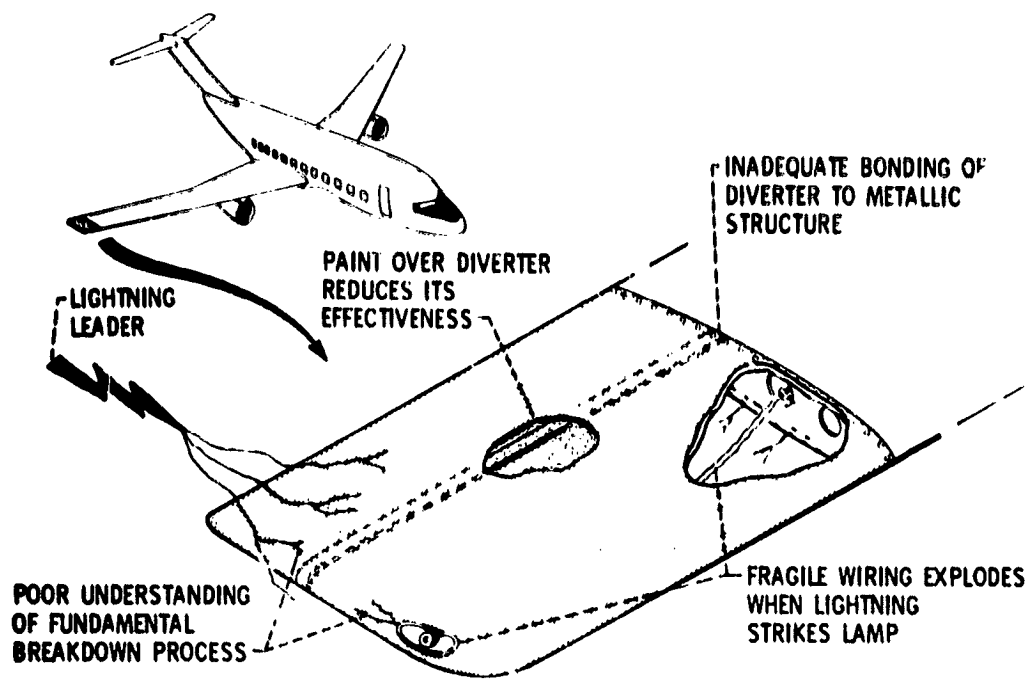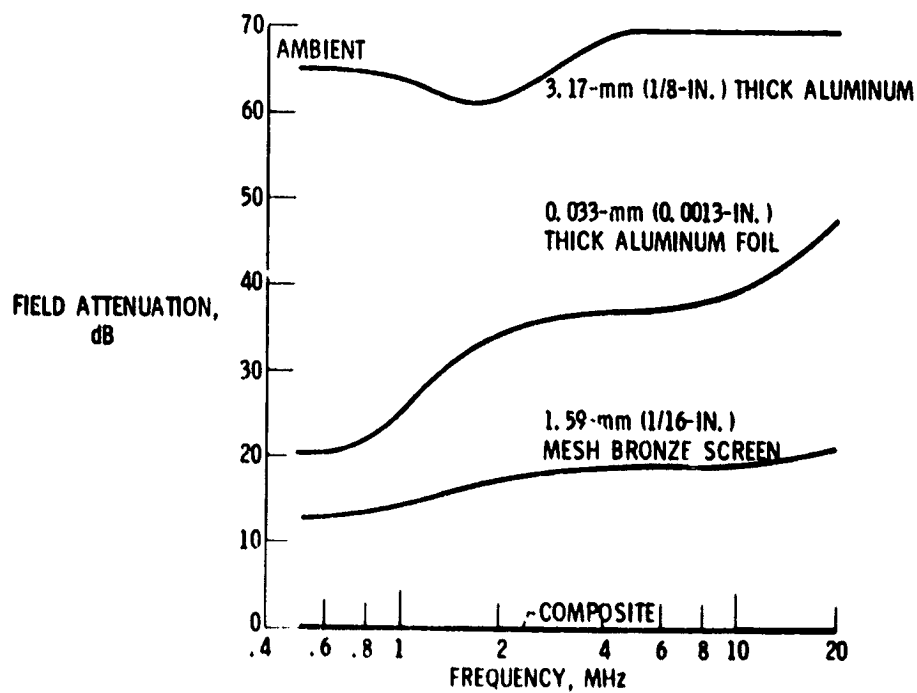
INTRODUCTION

During the past few years, methods have been developed to predict the reliability of aircraft structures. The methods are derived from a combination of probability theory and engineering equations. Their earliest application was to military aircraft operations, where the military urgently needed ways to prolong fleet life and to ensure that enough aircraft were always available for use. The purpose of this paper is to acquaint the operators of the commercial fleet with these methods and how they have been used to improve reliability and reduce the cost of operations.

The discussions in this paper are not meant to serve as "cookbook" guides to application, but only to synopsize some of the methods applicable to commercial fleet operation. Those who wish to apply these methods to their own fleet operations are urged to consult the references which discuss, in more detail, how the methods are used and what data are needed as input for the analyses.

INSPECTION

Reliability methods depend upon inspection. Figure 1 shows a typical inspection problem encountered in the laboratory. The specimen, about 5.5 cm wide, is subjected to repeated loads in tension. If a crack grows, it will start at the small drilled holes and will propagate across the width. Cracks 0.1 mm long can be found easily for two reasons: the inspector knows where to look, and the specimen is accessible.

Figure 2 is a photograph of an aircraft wing box, a much harder inspection problem. Sometimes the inspector knows where to look (for example, if

he is responding to an airworthiness directive), but, even so, cracks can occur anywhere. And a few parts of the structure are inaccessible to anything except a teardown inspection. Practical inspection and reliability methods must take into account the possibility of random flaw locations, multiple flaws, and area inaccessibility.

The reliability after inspection depends upon how well a crack can be detected. Figure 3 (refs. 1 to 3) shows some typical data for the probability of detection (solid lines). In contrast, the dashed lines show some empirical fits; they can be adjusted analytically to match reasonably smooth experimental curves fairly well. In general, the probability of detection is larger for longer cracks. Ultrasonics and dye penetrant inspections are more sensitive than X-rays, but to use them the area must be accessible. X-rays are used for inaccessible areas, but the radiation source must be positioned directly over the crack. The data in figure 3 are from detectability tests generally under laboratory conditions. Part of the reason that the experimental curves are not smooth is the paucity of data, even though these curves were obtained during an extensive and well-planned program. The unevenness of the curves illustrates a point: not much data exist yet about the inspection process, a process that includes both apparatus and inspector. A statistician, of course, would want enough data points to establish 90-percent or 95-percent bounds on the curves.

Figure 4 (ref. 4) shows one of the empirical curves. It has several features. First, if the crack is short enough, it cannot be found (detectability is 0). Second, there is a crack length that corresponds to some given detectability; here, cracks of length a and longer can be found at least 90 percent of the time. And finally the curve may never reach 1.0 because, for various reasons, even long cracks are occasionally overlooked. Sometimes the curve may not be completely defined, but for some uses, only the crack length at some percent of detectability needs to be known. Such a simple case is considered first.

With these aspects in mind, figure 5 (ref. 5) relates the reliability after inspection to the probability that the part was crack free before inspection. Reliability here has a specific meaning: a part that has passed inspection has passed because it was thought to have been crack free. Reliability after inspection is the probability that the part actually is crack free. Detectability is a parameter for the various curves. Here the inspector knows where to look, and only must decide whether one crack of some given length (such as 4 mm) or longer is, or is not, present. This is a simple inspection case. Note that all the curves lie above the no-inspection line, showing that inspections always enhance reliability. And, because they increase monotonically, high initial quality (reliability before inspection) always enhances final reliability.

However, quite frequently a crack or cracks can appear at random locations (as, for example, in the structure in fig. 2). And, in such a case, the actual number of cracks is not known. Figure 6 shows the reliability after inspection as a function of the detectability for the case where the actual number of cracks in a given piece is a random number, Poisson distributed. The mean (or average) number of cracks per piece before inspection is the parameter shown beside each curve. Cracks might be anywhere in the structure. Reliability

is significantly enhanced if detectability is high. (High detectability implies an effective inspection procedure.) If a part contains, on the average, 10 cracks before inspection, detectability must be very high if the part is to be reliable after inspection.

Figure 7 is like figure 6, except that figure 7 applies to a case where 25 percent of the structure is inaccessible for inspection. Because there is a chance that some of the randomly located cracks might be in the uninspected region, the curves in figure 7 are lower than the curves in figure 6. Note in particular that 100 percent reliability cannot be attained, even if cracks are 100 percent detectable. At mean of 1 flaw per part the highest that reliability can be is about 0.78.

Up to this point, unreliability has been defined as having an overlooked crack; unreliability has not necessarily meant that a part will fail. (Ways to build crack-tolerant structures, where the seriousness of small undetected cracks is minimized, are discussed subsequently.) Consider the case where an overlooked crack grows longer under the influence of stress changes due to gust and maneuver loads. Reliability is redefined to mean that any crack present will not grow to be "critically long" before the next inspection. A critical length may be the length at which the structure no longer supports limit loads, or some shorter length, perhaps one that only makes passengers nervous if they see it. Whatever the chosen definition, critical length is some fixed value that must not be exceeded, and the structure is reliable only if the critical length is not reached.

Figure 8 (ref. 4) illustrates a distribution function that represents crack lengths. The solid curve indicates that short cracks are likely to occur much more often than long cracks do. After some initial flights the cracks grow, so that the dashed line represents the new crack length distribution. During inspection, the longer cracks are likely to be discovered and fixed, so that the dashed-dot line represents the distribution after inspection. The dashed-dot line fairs into the dashed curve at the limit of detectability — shorter cracks are not detectable. During subsequent flights, unrepaired cracks continue to grow.

Figure 9 shows the results of an analysis that recognizes growing cracks. The two curves illustrate the relative impact of various inspection schedules. The abscissa is the frequency of inspection; it is the number of inspections scheduled during a period whose length is such that a just-detectable crack can grow to critical length. The two symbols have the following definitions: t_c is the time at which a crack just becomes critically long and t_d is the time at which the crack becomes long enough to be detectable (for example, detectable 90 percent of the time). The curve R_{02} illustrates the reliability for surviving one inspection period with no initial inspection. The curve R_{012} is for survival of one period with an initial inspection; it is higher because the extra inspection is likely to discover more cracks that could grow to critical length between inspections.

ENHANCING RELIABILITY

It is helpful of course, to know what size crack must be found to keep the structure reliable between inspections. Figure 10 shows "safe" crack lengths plotted against the normalized inspection frequency. First, look at the curve for a critical crack length a_c of 100 mm. At a frequency of two inspections during the normal period, all cracks shorter than 7.7 mm must be detected. On the other hand, if $a_c = \infty$ (in an infinitely tough material), an inspector must still find all cracks longer than 8.3 mm, so switching to a tough material does not help much when inspections are infrequent. For more frequent inspections tolerable crack lengths are longer, but also the curves separate. Tougher materials can help to alleviate an inspection detectability problem if inspections are frequent, if the structure remains strong even with moderately long cracks, then, of course, it remains reliable. Since a moderately long crack can be detected more easily than a short crack, the detectability problem is moderated, and the structure is more likely to be repaired before the crack becomes critically long.

Figure 11 (ref. 6) shows how the choice of material influences performance. For structures in tension, such as the lower wing surface, stress/density is a measure of the load-carrying ability per pound of structure. High values on the ordinate indicate efficient structures. The life requirement is the life of the aircraft, or, perhaps as in this discussion, the time between inspections. The initial flaw (crack) size is the length of a crack just a bit smaller than that which can be detected. D6ac steel is the most efficient of the three materials if very small cracks, for example, 1 mm, can be found. Titanium is best if a somewhat longer crack must be tolerated; but cracks grow relatively fast in titanium, so the useful life is not as long as for 2024-T3 aluminum which can tolerate much longer cracks than the other two materials can.

In addition to choosing the proper material, the structure itself can be made crack tolerant (ref. 7). Figure 12 is not only a graph of residual strength, it is also a sketch of a panel with riveted stringers. Only the right half of the panel is sketched; the panel is symmetric about the vertical center line (the ordinate). Only one-half of the crack is shown, it, too, is symmetric. Figure 12 shows how riveted stringers help to retain the load-carrying ability of a cracked plate. Here load-carrying ability is plotted against crack length. The dashed line shows the strength of a plate with no stiffeners. As the percentage of material in the stiffeners increases, so does the load-carrying ability. This is because the stiffeners pick up the residual load as the crack passes underneath. Some structures have integral stiffeners instead of riveted stiffeners; a panel with integral stiffeners does not have the same crack tolerance as a panel without stiffeners because the stiffeners, too, tend to crack.

Thus proper materials and construction enhance reliability because longer cracks can be tolerated, and an inspector is more likely to detect long cracks.

MINIMIZING COSTS OF OPERATION

Reliability methods can be applied to economy of fleet operation. Figure 13 (ref. 8) shows the cumulative cost of inspection and repair plotted versus design lifetimes. The data are for a fleet of fighter aircraft with a design life of 6600 flights. The aircraft are inspected every 2200 flights. The top curve is total cost, and the next is repair cost; the dash-dot curve is inspection cost. Repair cost is the major contributor to total cost. Note that the cumulative total cost and cumulative repair cost begin increasing rapidly after the aircraft has been in service for two lifetimes. Figure 14 is the same data for inspections scheduled every 1100 flights. It is cheaper to inspect and repair every 1100 flights, chiefly because cracks remain small and are cheaper to repair. For example, small cracks near holes can be fixed by reaming the hole, whereas larger cracks may lead to major rework. The lower repair cost more than offsets the larger inspection cost.

Of course, the cost of extremely frequent inspection might overwhelm the gain in repair cost, and consequently an optimum inspection frequency exists (ref. 9). Figure 15 shows how this optimum can be found. (Some commercial transport data were used in computing this figure.) The ordinate is the total operating cost, including the expected cost of failure of the aircraft, divided by the cost of failure. (The expected cost of failure is generally low, because it is the product of the cost of failure and the unreliability, and the unreliability is a very small number.) The cost of failure can include replacement cost, insurance losses, ancillary damage, lawsuits, etc. The abscissa is the number of scheduled inspections per design lifetime. The parameter for the various curves is the inspection cost divided by the cost of failure. Each curve has a minimum, located by the dashed line; at which the expected operating costs are minimized.

In figure 16 some data have been added to figure 15. The dot-dashed curve is the probability of failure, calculated by methods somewhat like those discussed previously. If operations are to be constrained to some value of unreliability, such as 10^{-3} (reliability of 0.999), then each aircraft must be inspected at least seven times during its design lifetime. Thus, for a parametric value of 10^{-3}, the aircraft must be inspected more often than it would have been to minimize expected operational costs. But for parametric values of 10^{-4} and smaller, the minimum cost number of inspections leads to reliability greater than 0.999. Thus, for certain values of the parameter, enhanced reliability and lower operational costs go together.

CONCLUDING REMARKS

To sum up, inspection effectiveness depends upon structural complexity, quality, and the percentage of the structure inspected. Reliability can be enhanced by choosing materials properly, designing damage-tolerant structures, and increasing inspection frequency. And, for fleet operations, costs can be minimized through proper inspection schedules, and enhanced reliability can be compatible with minimum cost.

359

REFERENCES

1. Eggwertz, Sigge; and Lindsjö, Göran: Influence of Detected Crack Length at
Inspections on Probability of Fatigue Failure of Wing Panel. Tech. Note
HU-1745, Part 2, Aeronaut. Res. Inst. of Sweden, 1975.

2. Packman, P. F.; Pearson, H. S.; Owen, J. S.; and Young, G.: Definition of
Fatigue Cracks Through Nondestructive Testing. J. Mater., vol. 4, no. 3,
Sept. 1969, pp. 666-700.

3. Knorr, Ekkart: Reliability of the Detection of Flaws and of the Determina-
tion of Flaw Size. Fracture Mechanics of Aircraft Structures, Harold
Liebowitz, ed., AGARD-AG-176, Jan. 1974, pp. 396-412.

4. Davidson, John R.: Reliability and Structural Integrity. NASA TM X-71934,
1974.

5. Davidson, J. R.: Reliability After Inspection. Fatigue of Composite
Materials, ASTM Spec. Tech. Publ. 569, 1975, pp. 323-334.

6. Elber, Wolf; and Davidson, John R.: A Material Selection Method Based on
Material Properties and Operating Parameters. NASA TN D-7221, 1973.

7. Poe, Clarence C., Jr.: The Effect of Broken Stringers on the Stress Intensity
Factor for a Uniformly Stiffened Sheet Containing a Crack. NASA TM X-71947,
1974.

8. Yang, J.-N.: Statistical Estimation of Service Cracks and Maintenance Cost
for Aircraft Structures. AIAA Paper No. 75-767, May 1975.

9. Yang, J.-N.; and Trapp, W. J.: Inspection Frequency Optimization for Air-
craft Structures Based on Reliability Analysis. J. Aircr., vol. 12,
no. 5, May 1975, pp. 494-496.
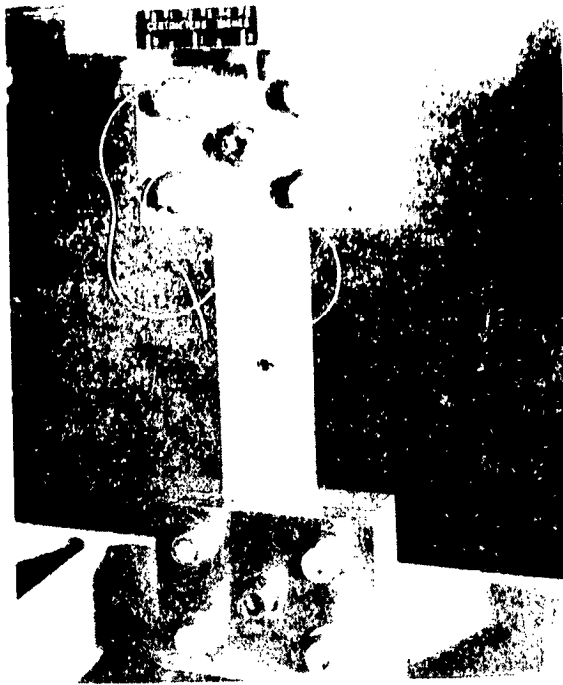
Figure 1.- Laboratory fatigue specimen.
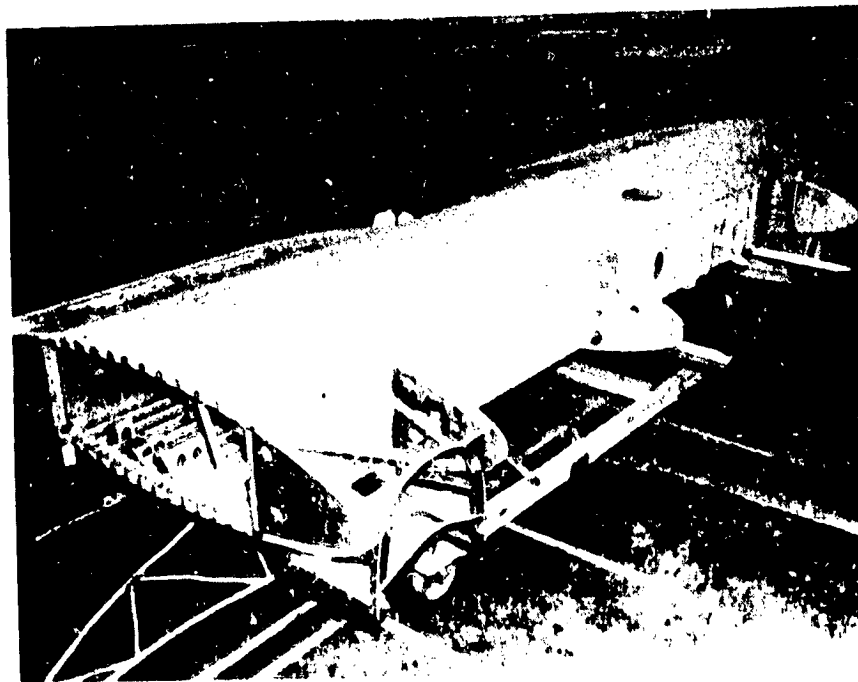
Figure 2. Aircraft wing box.

361
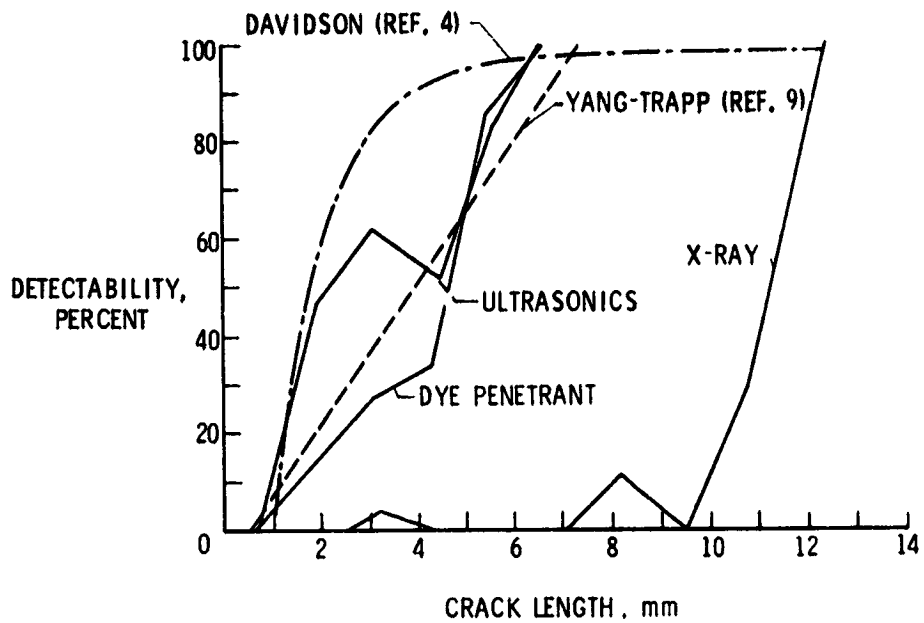
Figure 3.- Typical data and empirical curves for probability
of detection (ref. 1). Empirical curves can be adjusted
to fit experimental data.
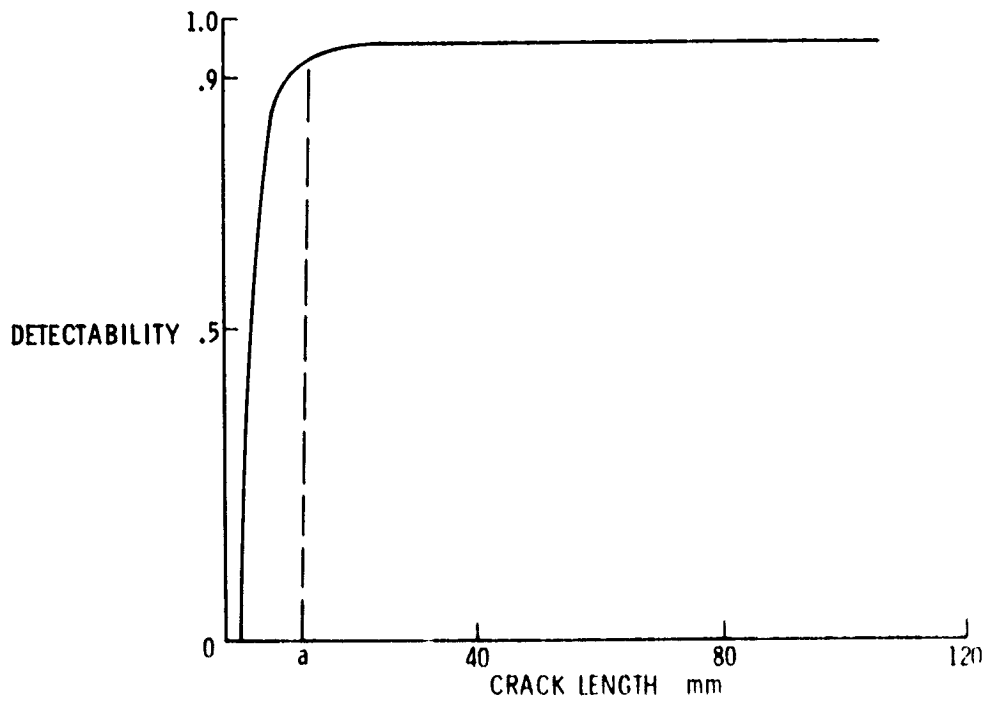
Figure 4.- An empirical curve for probability of detection.

362
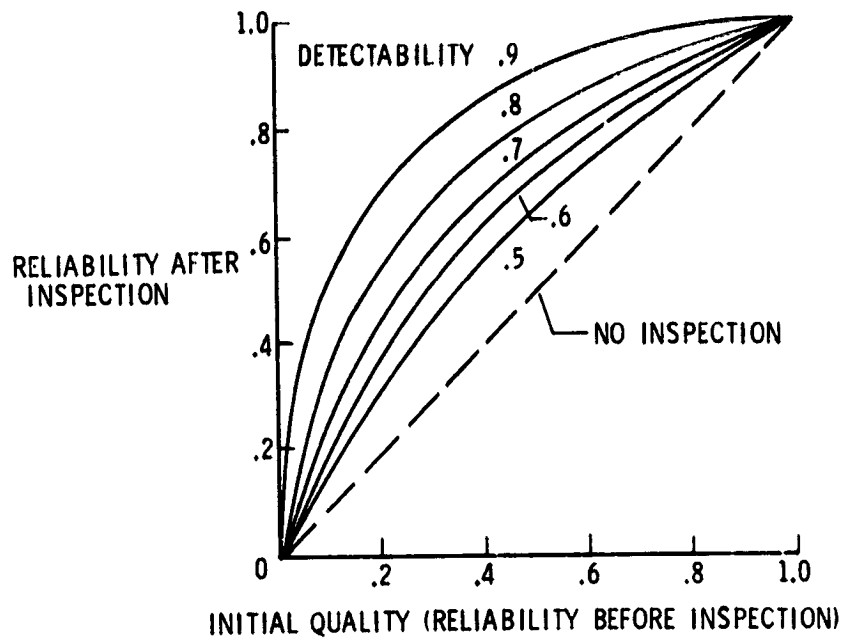
Figure 5.- Quality, detectability, and reliability.
Crack site known.
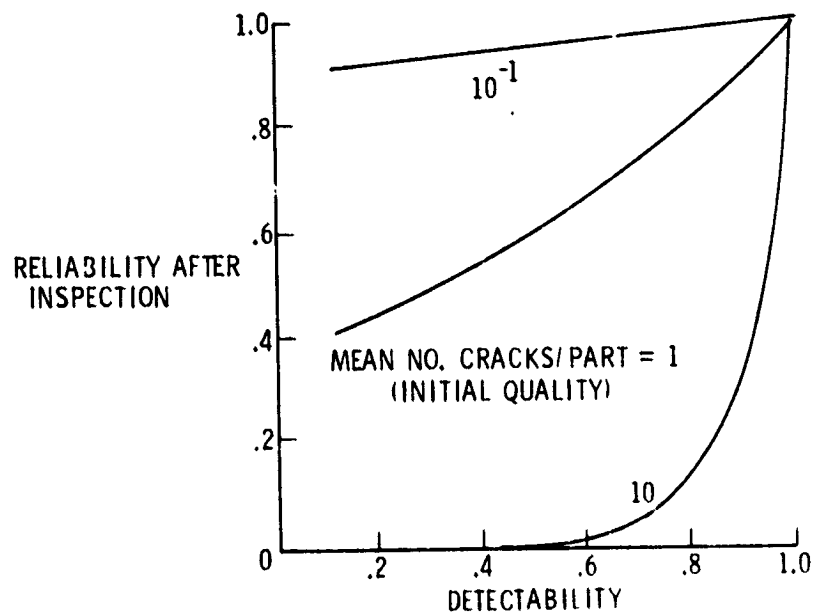
Figure 6.- Quality, detectability, and reliability.
Randomly distributed crack sites; 100 percent of
structure inspected.
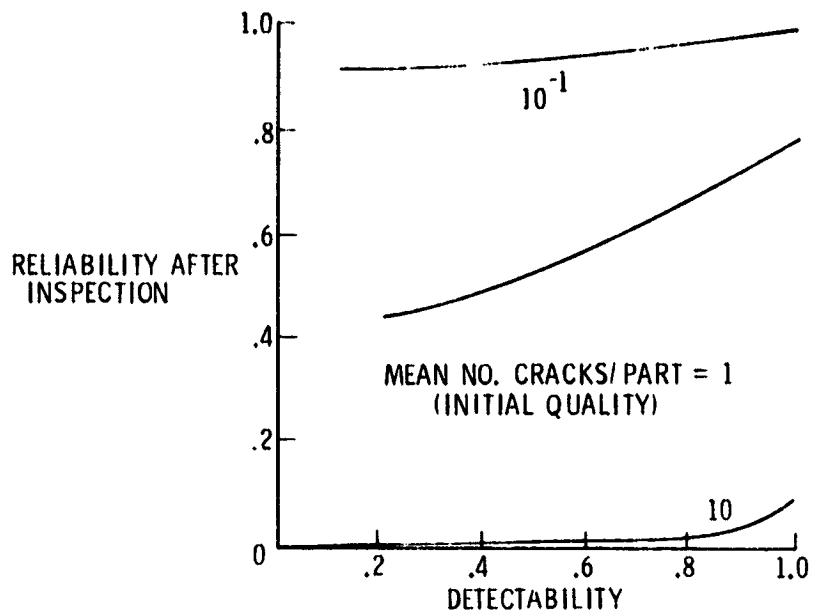
Figure 7.- Quality, detectability, and reliability.
Randomly distributed crack sites; 75 percent of
structure inspected.
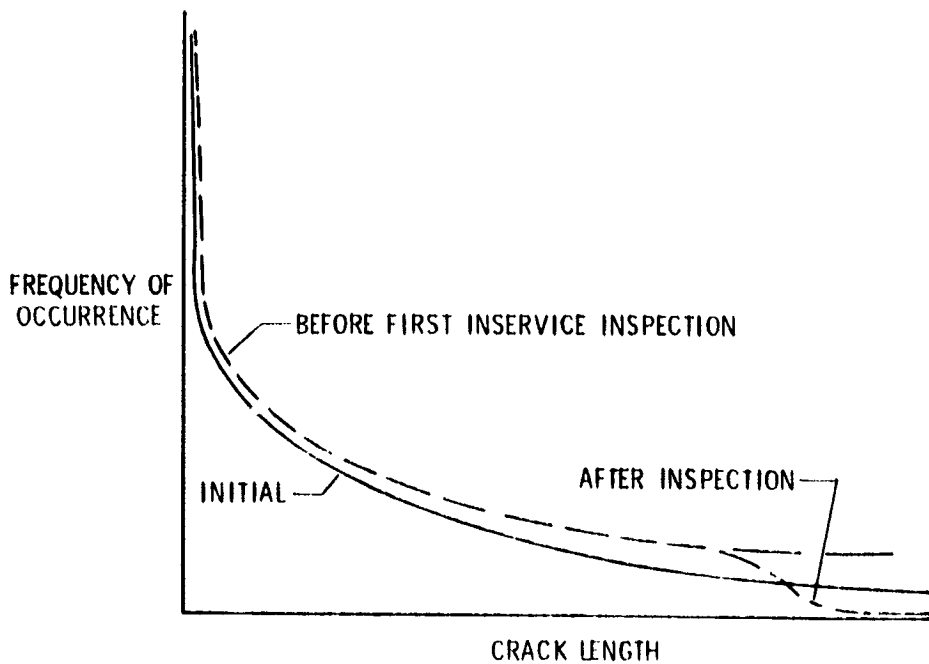
Figure 8.- Distribution functions for crack length.
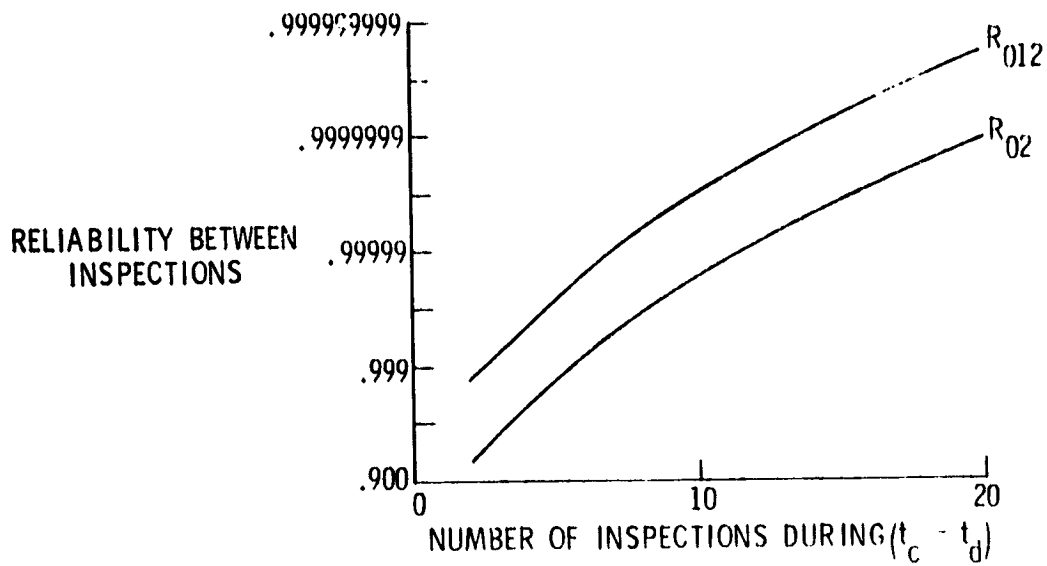
Figure 9.- Effect of various inspection schedules.
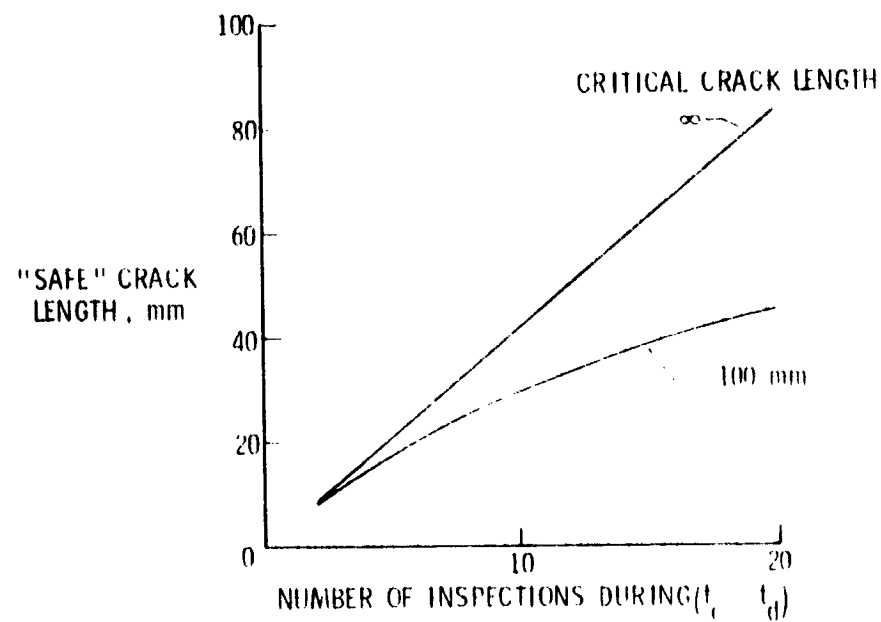
Figure 10.- "Safe" crack length and material toughness.
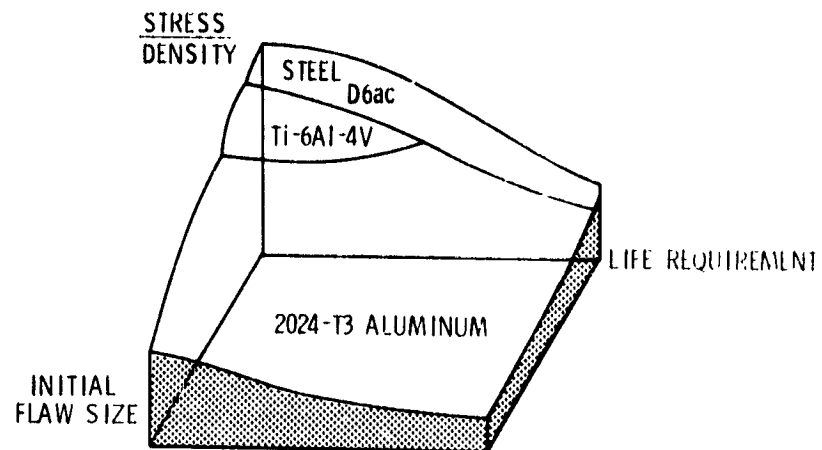
Figure 11.- Relative efficiencies of some aircraft materials.
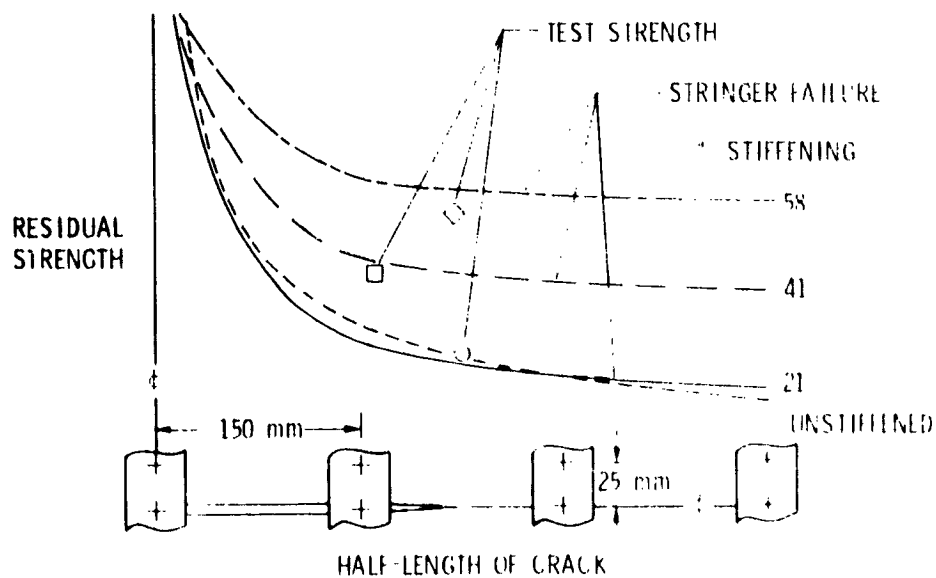
Figure 12.- Residual strength of panel with riveted stringers.
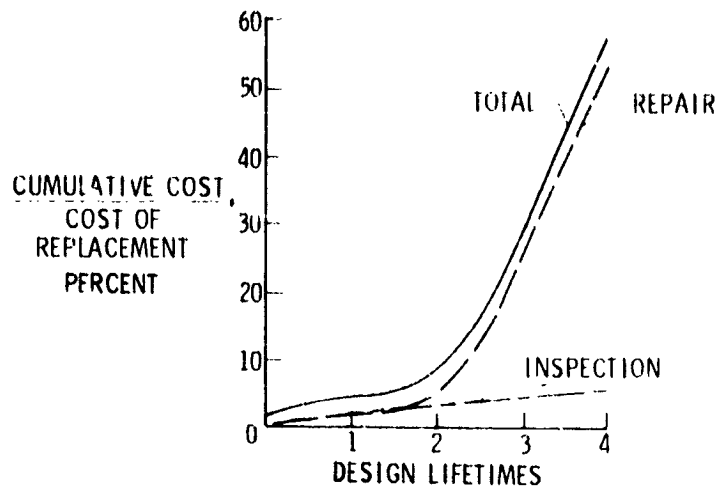
Figure 13.- Relative costs. Inspection
interval 2200 flights.
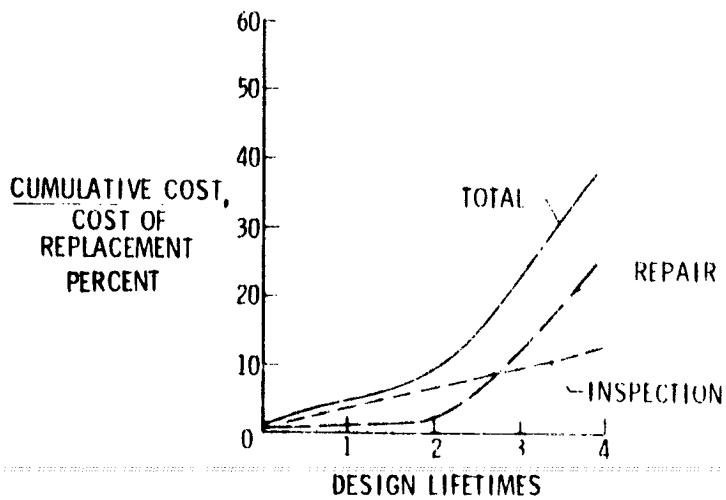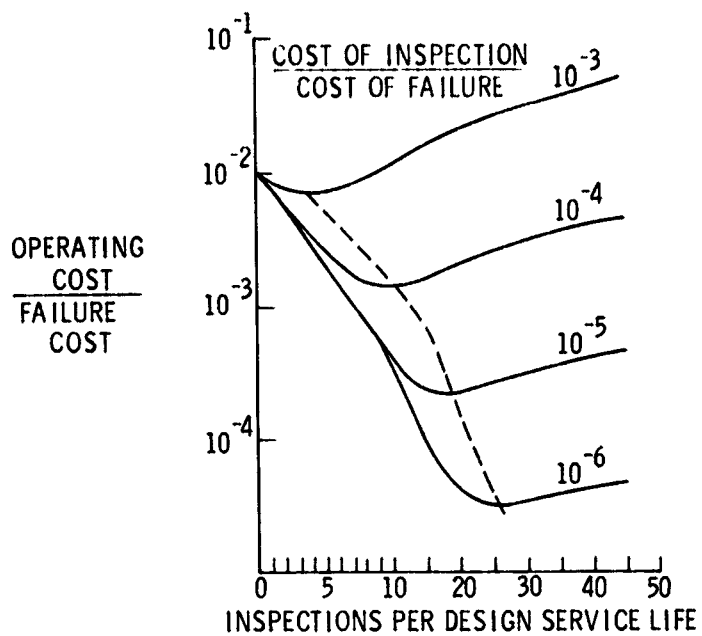
Figure 15.- Optimum number of inspections
per lifetime.
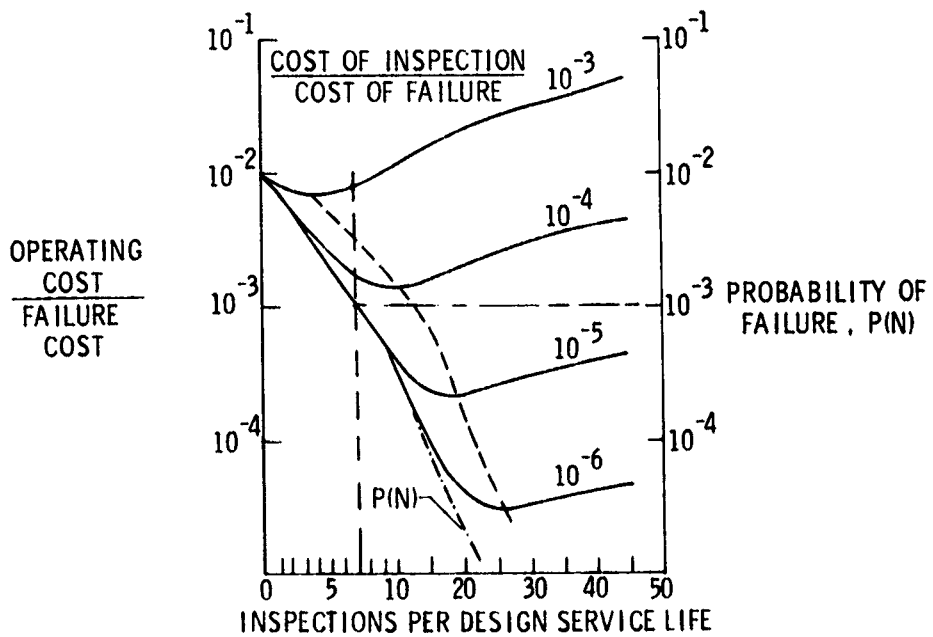
Figure 16.- Optimum number of inspections per lifetime
and probability of failure.

I N77-18101

GENERAL AVIATION CRASH SAFETY PROGRAM AT LANGLEY RESEARCH CENTER

Robert G. Thomson
NASA Langley Research Center

SUMMARY

The purpose of the Langley Research Center crash safety program is to support development of the technology to define and demonstrate new structural concepts for improved crash safety and occupant survivability in general aviation aircraft. The program involves three basic areas of research: full-scale crash simulation testing, nonlinear structural analyses necessary to predict failure modes and collapse mechanisms of the vehicle, and evaluation of energy absorption concepts for specific component design. Both analytical and experimental methods are being used to develop expertise in these areas. Analyses include both simplified procedures for estimating energy absorption capabilities and more complex computer programs for analysis of general airframe response. Under the crash safety program, these analyses will be developed to provide the designer with methods for predicting accelerations, load, and displacement histories of collapsing structures. Full-scale tests of typical structures as well as tests on structural components are being used to verify the analyses and to demonstrate improved design concepts.

INTRODUCTION

Technology for predicting aircraft dynamic response under crash loads and occupant behavior during impact is being developed by Langley Research Center (LaRC) in a joint NASA/FAA crashworthiness program. Part of the analytical and experimental program includes evaluating airframe, seat, and restraint-system concepts for mitigating crash loads imposed on occupants of general aviation aircraft. The methods used and concepts developed from these ongoing efforts will make feasible future aircraft designs that will enhance the degree of survivability under a crash condition with minimum weight and cost penalties. The total program with its goal of improved occupant survivability following an airplane accident is shown in figure 1. NASA's responsibility in this joint program is shown as shaded boxes, the FAA's role as unshaded boxes, and joint efforts as crosshatched boxes.

Crashworthiness design technology is divided into three areas: environmental, airframe design, and component design. The environmental factors consist of acquiring and evaluating actual field crash data and defining a crash envelope within which the impact parameters allow tolerable acceleration levels.

Airframe design has a twofold objective: to assess and apply current, on-the-shelf, analytical methods to predict structural collapse; and to develop and validate advanced analytical techniques. NASA's primary role

in the joint program is the development of advanced analytical techniques. Full-scale tests will be used to verify the analytical predictions, as well as to demonstrate improved crashworthy design concepts. A facility for free-flight crash testing of full-scale aircraft structures and structural components has been developed at LaRC. Airframe design also includes evaluation of novel crashworthy design concepts and their effect on structural crashworthiness.

Component design consists of exploring the development of new and innovative energy-absorbing concepts to improve performance of seats and occupant restraint systems as well as the design of nonlethal cabin interiors.

LaRC CRASH SAFETY PROGRAM

The responsibilities of LaRC in the airframe design technology portion of the joint program (see fig. 2) can be divided into three program elements: full-scale crash simulation testing, nonlinear crash impact analysis, and crashworthy design concepts.

Full-Scale Crash Simulation Testing

The full-scale crash simulation testing is being done at LaRC in the Langley impact dynamics research facility (ref. 1) shown in figure 3. This facility is the former Langley lunar landing research facility that has been modified for free-flight crash testing of full-scale aircraft structures and structural components under highly controlled test conditions. The test vehicles are suspended from the gantry and then swung pendulum fashion and released to simulate free-flight crash conditions at impact.

The facility's basic gantry structure is 73 m (240 ft) high and 122 m (400 ft) long supported by three sets of inclined legs spread 81 m (267 ft) apart at the ground and 20 m (67 ft) apart at the 66-m (218-ft) level. A movable bridge spans the top and traverses the length of the gantry.

Test method.- The method for crash testing the aircraft is shown pictorially in figure 4. The aircraft is suspended from the top of the gantry by two swing cables and is drawn back above the impact surface by a pullback cable. An umbilical cable used for data acquisition is also suspended from the top of the gantry and connects to the top of the aircraft. The test sequence is initiated when the aircraft is released from the pullback cable. The aircraft swings pendulum style into the impact surface. The swing cables are separated from the aircraft by pyrotechnics just prior to impact, freeing the aircraft from restraint. The umbilical cable remains attached to the aircraft for data acquisition, but it also separates by pyrotechnics before it becomes taut during skid out. Since the separation point is held relatively fixed near the impact surface, the length of the swing cables is used to adjust the flight-path angle from 0° to 60°. The height of the aircraft above the impact surface at release determines the impact velocity and can be varied to give impact velocities from 0 to 26.8 m/s (60 mph). It is important that, in the suspended position, the

370

force vectors of the swing cables and pullback cables act at 90° to each other and pass through the center of gravity of the aircraft. This is necessary to control aircraft pitch reaction during the swing phase. The movable bridge allows the pullback point to be positioned along the gantry to insure this force relation for various pullback heights and swing-cable lengths. The pitching velocity of the aircraft at swing-cable separation continues to change the pitch attitude of the aircraft during the free-flight phase of the test. In the 10 tests conducted to date, the pitch angle change due to this condition has never been greater than 1.75°.

A typical aircraft suspension system which is designed specifically for the aircraft configuration being tested is shown in figure 5. The swing cables attach to hard points in the main wing spar of the aircraft so that a line connecting the two hard points (dashed line in figure) passes directly through the aircraft center of gravity. The pullback cable attaches to these same hard points; thus, its force reaction also passes through the center of gravity. Two sets of pitch cables are attached to the swing cables 3 m (10 ft) above the hard points in the wings and to hard points in the fuselage fore and aft of the aircraft center of gravity. Adjustments in roll angle to about 30° can be made, without sacrificing control, by varying the length of the swing and pitch cables. Adjustments in yaw angle to about 15° can be made by varying the length of the cables in the pullback harness and the pitch cables. Adjustments in pitch to about 45° can be made by varying the length of the pitch cables in the fore and aft directions. Larger changes in pitch, yaw, and roll require redesign and/or relocation of the hard points in the aircraft. For other aircraft configurations, the hard points must be properly located and a new suspension system must be designed to maintain the swing and pullback cables at 90° to each other with their force vectors passing through the aircraft center of gravity.

Instrumentation.- Data gathering from the full-scale crash test of an aircraft is accomplished with extensive photographic coverage, both interior and exterior to the fuselage, utilizing low-, medium-, and high-rate cameras and with onboard strain gages and accelerometers. The piezoelectric accelerometers (range of 250g and 2 to 5000 Hz) are the primary data-generating instruments. A typical accelerometer layout for a test specimen experiencing zero yaw at impact is shown in figure 6. Circles indicate instruments positioned to measure accelerations normal to the fuselage's horizontal plane. Diamonds represent instruments positioned to measure accelerations both in the normal and longitudinal directions as shown in the figure. The side-view schematic also shows two dummies onboard the test specimen. There have been from one to four anthropomorphic dummies (National Highway Traffic Safety Administration Hybrid II) onboard all full-scale aircraft tests conducted to date at LaRC. Shown in figure 7 is a schematic of a typical onboard camera and restraint-system arrangement. The forward camera is located in the radio compartment in the instrument panel, the rear camera on a rear instrument shelf, and the two side cameras are cantilevered off the fuselage. These cameras are shock resistant and are mounted in a cantilever fashion. There are approximately 15 exterior cameras used during a test. The location and framing rate of these cameras are discussed in reference 1. The restraint-system arrangement and type of restraint used vary from test to test.

Tests conducted.- Full-scale crash testing of aircraft and aircraft components is being conducted at LaRC to determine a set of structural design crash parameters for which the cabin area maintains its structural integrity to the degree that it supports a livable volume throughout the crash sequence. These structural crash parameters will be supplemented by FAA field crash data to form a basis for a rational crash design envelope. In addition, the experimental crash test data will be used to ascertain the validity of analytical predictions and to test the performance of improved structural and seat concepts for crashworthiness. The initial stages of the crash test program, from February 1974 to June 1976, have been conducted using 10 twin-engine light aircraft impacting into a concrete surface.

A summary of the impact parameters associated with these 10 tests is shown in figure 8 by the shaded boxes. The flight-path angle was maintained at -15° except for two tests. These two tests had flight-path angles of -30° and -45°. The flight-path velocity has been held constant at 26.8 m/s (60 mph) except for one test at 13.4 m/s (30 mph). Two tests were performed with landing gear extended and are indicated by an asterisk. Positive angles of attack of 15° and 30° were introduced in two tests at -15° flight-path angle. In addition, two tests were conducted with negative roll angles of 30° and 15°.

Future full-scale aircraft tests, shown in figure 8 by unshaded boxes, will include twin-engine aircraft at lower impact flight-path angles but higher impact velocities (aircraft's swing velocity will be augmented with wing-mounted rocket motors). In addition, three high- and three low-wing, single-engine aircraft crash tests are planned, as well as stripped airframe tests on field terrain simulated by dirt. The matrix of full-scale crash testing is by no means complete and does not consider such secondary effects as aircraft sliding, overturning, cartwheeling, or tree and obstacle impact. However, the proposed crash tests should generate enough meaningful crash data to define single- and twin-engine structural crash test envelopes.

NASA full-scale crash test data.- Experimental acceleration time history data and structural damage assessment, generated from each of NASA's full-scale crash tests, are being analyzed for publication. The analyses consider the effects of varying one of the impact parameters only, such as, flight-path velocity, flight-path angle, angle of attack, or roll. A representative sample of the type of data to be reported is presented herein for 1 of the 10 tests shown in figure 8 (nominal test conditions of 26.8 m/s (60 mph) flight-path velocity, -15° flight-path angle, zero angle of attack, and zero roll and yaw).

Figure 9 is a sequence of photographs taken with a 20-frame-per-second camera during the second crash test. Time between frames is 0.05 second. The sequence clearly shows the free-flight condition of the test aircraft prior to impact at 26.8 m/s (60 mph) and a pitch angle of -12°. The structural damage to the fuselage occurs during two impacts: primary impact when the nose initially impacts the ground surface (third frame) and secondary impact when the cabin slams down onto the ground surface because of fuselage rotation (fifth frame). This secondary impact produces the most severe normal accelerations in the cabin area. For this particular test, structural damage was moderate with the cabin maintaining its livable volume. Rivet shear occurred

372

in the cabin along lines of overlapping skin sheet metal and interior stiffening structure. Breaks due to this rivet shear appeared in the roof at the main spar frame, along the window ledges, and in the vicinity of the door. Upon impact, the forward floor beams and nose wheel well rotated upward causing buckling of the entire nose, fire wall, and floor beams in the cockpit. The combination of downward momentum of the wings and the impact of the main spar with the ground produced twisting of the main spar and loss of wing dihedral angle. In addition, the cabin floor experienced upward heaving of the floor beams causing outboard seat rotation. Glass breakage was confined to the pilot's windscreen and side window.

Four representative sets of acceleration time histories, normal to the longitudinal axis, recorded during this full-scale crash test are presented in figures 10, 11, 12, and 13. At the top of each figure there is a side-view schematic locating the accelerometers (diamond symbols) and the four anthropomorphic dummies (pilot, copilot, and two passengers) of interest. Figures 10 and 11 are typical acceleration time histories while figures 12 and 13 are acceleration time histories with timed events from photographic data superimposed on the acceleration traces.

Figure 10 presents acceleration traces at two different locations normal to the floor beam of the fuselage. The first accelerometer is located at the initial point of impact, first fuselage frame. Acceleration trace (2) is aft of the first passenger and is not affected by the primary impact but by the secondary impact when the cabin compartment slams onto the contact surface. The fuselage direc'y below point (2) contacts the ground 0.09 second after initial ground conta . (fifth frame of fig. 9). For the nose location at the first fuselage frame (trace (1)) during the first 0.1 second after impact, the aircraft exhibits high amplitude oscillatory behavior caused by initial impact (120g negative acceleration), then rebound (42g positive acceleration) followed by another impact (40g negative acceleration) which is canceled by the action of the adjacent structure as it continues along the flight path. Although the secondary impact produces the most severe normal accelerations in the cabin area, the magnitudes of these accelerations (22g negative and 50g positive) are still substantially lower than those of the nose (impact point) accelerations and occur between 0.1 and 0.2 second after primary impact.

Figure 11 presents time history of the average of four accelerometers located normal to the base of the first passenger seat (behind the pilot) and the normal pelvic acceleration time history of the anthropomorphic dummy. The first passenger (79.3 kg (175 lb)) was seated in a standard passenger seat and was restrained by a five-point restraint system - lap belt, crotch belt, and two shoulder harnesses. The average seat input (at the base of the seat) peaks at about 0.08 second after initial impact. There is some similarity between the average acceleration trace of the seat base (3) and the first passenger pelvic trace (4) if one considers that there is a time lag of 0.02 second between the traces during which the seat cushion and dummy compress. However, little energy is dissipated by the seat structure as is evident in the small difference in maximum acceleration peaks between the seat base (3) (54g positive) and the dummy's pelvis (4) (50g negative).

In figure 12, six normal acceleration time history traces are presented with timed events from photographic data superimposed on the traces for correlation and interpretation. The six accelerometers are spaced along the floor beam of the aircraft from the first fuselage frame to the rear of the first passenger seat (see side- and top-view insert). The response of initial ground contact is felt immediately at the first frame (trace (1)) and is seen to progress rearward to the fire wall (trace (3)) with diminishing intensity and with a slight time lag associated with the rearward progression of the contact surface. Main spar ground contact (0.05 second) produces a positive acceleration or downward force in the nose of the aircraft and signals the initiation of cabin compartment excitation. The intensity of the acceleration peaks in the cabin compartment is maximum in the vicinity of the main spar and diminishes progressively from that point rearward. The secondary impact due to downward fuselage rotation produces a negative acceleration peak (or upward force) in the cabin compartment (60g on trace (4), 40g on trace (5)). The loss of wing dihedral angle and wing ground contact have little overall effect on the fuselage response except for the main spar twisting. The rivet shear failure of the fuselage in the roof at the main spar, 0.178 second after impact, concludes further significant crash effects felt in the aircraft structure.

Acceleration time history traces of the anthropomorphic dummy at the first passenger location and of the seat at the base of each leg are shown in figure 13 superimposed with timed events from photographic data. Initial ground contact, indicated by zero time in figure 13, is not felt appreciably by the first passenger. The first passenger begins downward and forward motion 0.06 second after impact at precisely the time that the front and rear legs of the seat first begin to record large localized forces. The seat then begins to rotate outboard (0.069 second). The shapes of the pulses of the two front seat legs are nearly identical as are the shapes of the pulses of the two rear seat legs. The primary pulse into each leg (the time interval between 0.07 to 0.09 second) has practically the same period but much lower amplitude in the rear legs of the seat. This primary pulse is exhibited in the pelvic region (trace (3)) of the dummy 0.025 second later. For determining a single acceleration pulse shape for seat evaluation, it appears that the simple averaging of the inputs at each leg attachment point (fig. 11) yields a satisfactory representation. Comparison of aisle leg to window leg accelerations indicates that the aisle leg negative acceleration peaks during seat rotation are higher than the corresponding window leg peaks. This difference is due to the aisle floor structure impacting first and causing outboard seat rotation. At the end of the outboard seat rotation a positive (downward) normal acceleration peak (70g and 63g) occurs in both rear seat legs as the dummy moves rearward in the seat, and at the end of dummy forward pitching, a large negative longitudinal acceleration (70g on trace (2)) occurs because of tightening of the restraint system. (The normal and longitudinal dummy acceleration traces are taken relative to a local dummy coordinate system perpendicular and parallel to the dummy's spine.) Cabin lateral expansion ends at 0.146 second, which marks the end of significant seat and dummy response. The cabin's lateral elastic recovery occurs by 0.306 second.

Nonlinear Crash Impact Analysis

The objective of the analytical efforts at LaRC is to develop the capability to predict the nonlinear geometric and material behavior of sheet-stringer aircraft structures subject to large deformations and to demonstrate this capability by determining the plastic buckling and collapse response of such structures to impulsive loadings. Two specific finite-element computer programs are being developed with attention focused on modeling concepts applicable to large plastic deformations of realistic aircraft structural components. These two programs are discussed in the following sections. Other current computer programs available for crashworthy analysis are reviewed in reference 2. This review deals primarily with modeling concepts and the relative capabilities and limitations of nonlinear computer programs for application to large plastic deformations of realistic vehicle structures.

PLANS.- For several years LaRC has been developing a rather sophisticated plastic analysis computer program (Plastic and Large Deflection Analysis of Nonlinear Structures) which includes geometric as well as material nonlinearities (refs. 3 and 4). This computer program for static finite-element analysis is capable of treating problems which include bending and membrane stresses, thick and thin axisymmetric bodies, general three-dimensional bodies, and laminated composites. The solution procedure embodies the initial strain concept which reduces the nonlinear material analysis to the analysis of an elastic body of identical shape and boundary conditions, but with an additional set of applied "effective plastic loads." The advantage of this solution technique is that it does not require modification of the element stiffness matrix at each incremental load step.

ACTION.- A nonlinear dynamic finite-element computer program (Analyzer of Crash Transients in Inelastic or Nonlinear Response (CRASH in ref. 5)) is being extended at LaRC to more realistic aircraft sheet-stringer structures. Membrane elements have been added to the initial truss and frame simulation capability to predict the transient response of frames with and without sheet coverings. This new computer program uses direct energy minimization to obtain solutions rather than the usual direct stiffness method which requires modifications of the initial stiffness matrix for plastic material behavior.

Analytical and experimental results.- These computer programs are currently being evaluated by comparison with experimental results on some simplified structures. These structures are shown in figure 14 in the order of increasing complexity: an axial compression of a circular cylinder, a tubular structure composed of 12 elements with symmetric cross sections joined at common rigid joints, an angular frame composed of asymmetric angles and bulkheads with nodal eccentricities at the rigid joints, and the same angular frame covered with sheet material. Static and dynamic analyses of these structures loaded into the large deflection plastic collapse regime are being conducted with PLANS and ACTION and are being compared with experimental data. Large deflection static analyses with corroborating experimental results, for the simplified structures shown in figure 14, are reported in reference 6.

Figure 15 is a photograph of the angular frame structure which measures 1.5 m (5 ft) in length with a base 1.3 m by 1 m (4.2 ft by 3.3 ft) tapering

375

to 0.61 m by 0.57 m (2 ft by 1.87 ft) at the tip. The frame is composed of rigid bulkheads connected longitudinally by 2.54 cm by 2.54 cm by 0.16 cm (1 in. by 1 in. by 0.0625 in.) angle. A T-beam made of two riveted 2.54 cm by 2.54 cm by 0.24 cm (1 in. by 1 in. by 0.094 in.) angles braces the rear bulkhead with a center T-beam of the same dimensions. Shown in figure 16 is a chronological sequence of computer deformation patterns for the angular frame loaded impulsively. The end (smallest) bulkhead of the angular frame was given an initial longitudinal velocity at time zero of 13.4 m/s (30 mph); the remainder of the frame was kept at rest.

Computer predictions of the subsequent deformation patterns of the angular frame obtained with the PLANS computer program are shown in figure 16 for various times (in milliseconds) after initial impact. The computer predictions indicate no appreciable collapse of the first bay of the angular frame for the 13.4 m/s (30 mph) loading. Plastic stresses and deformations are present, however, in the first bay. In igure 17 the frame is loaded impulsively (at the end bulkhead) with an initial velocity of 89.4 m/s (200 mph). The frame, under this loading condition, experiences collapse in the first bay in 0.70 millisecond. Corroboration of the analytical predictions with experimental data is to be accomplished by explosively loading the angular frame in a sequence of experimental tests with explosive sheet, detonated with fuse cord. A schematic and photograph of the test setup showing the angular frame positioned vertically with the loading on the end bulkhead are given in figure 18.

Crashworthy Design Concepts

The final area of research in the crash safety program is the development of crashworthy design concepts. The objective here is to develop structural concepts that improve the energy absorption characteristics of a structure either by modifying its structural assembly, changing the geometry of its elements, or adding specific energy absorption devices to help dissipate kinetic energy. Recent efforts in this research area at LaRC have been concentrated on the development of crashworthy aircraft seat and restraint systems. A user-oriented computer program called SOMLA (Seat Occupant Model-Light Aircraft), described in reference 7, is being used to study seat and occupant response under crash loading conditions. The computer program is based on a three-dimensional occupant and seat model in which the occupant model consists of 11 rigid mass segments. The seat model is composed of beam and membrane elements with provision for simulating plastic behavior by the use of plastic hinges. (See fig. 19.) Verification efforts of SOMLA using LaRC full-scale crash test data have resulted in the incorporation of modifications to allow for more realistic simulation of seat leg loading and occupant/restraint-system interface.

A comparison of SOMLA's computer predictions with experimental data from an aircraft section drop test is presented in figure 20. The aircraft section is a 1.5 m (5 ft) longitudinal fuselage section of a twin-engine aircraft beginning directly behind the pilot and containing the first row of passengers. (See fig. 21.) The solid curves in figure 20 are experimental accelerations for an aisle seat leg, a window seat leg, and the pelvis of the first passenger

(behind the pilot). The first passenger is seated in a standard aircraft passenger seat. The dashed curve is the computer prediction of the pelvis response for the first passenger (50 percentile male anthropomorphic dummy). The peak magnitude and duration of the pelvis response show good correlation with the experimental data. However, the experimental data exhibit an initial negative (upward) acceleration which diminishes as the seat cushion compresses, followed by a second negative peak as the occupant is loaded by the seat frame. The failure of SOMLA to predict this response is due to the occupant being loaded through node points which are time invariant.

Two-dimensional computer graphics of SOMLA's seat, occupant, and restraint-system response for the aircraft section drop test are shown in figure 22. The computer graphics show the occupant compressing the seat cushion and the slacking (gapping) of the seat belt. No shoulder harness was simulated because of the vertical test condition and the immediate flexing of the upper portion of the aircraft section, artificially unloading the test dummies' shoulder harnesses, as shown in figure 21. Computer graphic displays, as illustrated in figure 22, aid in visually interpreting the combined motions of the seat, occupant, and restraint system during the crash sequence; they are also helpful in verifying modeling techniques and data input.

CONCLUDING REMARKS

Langley Research Center (LaRC) has initiated a crash safety program that will lead to the development of technology to define and demonstrate new structural concepts for improved crash safety and occupant survivability in general aviation aircraft. This technology will make possible the integration of crashworthy structural design concepts into general aviation design methods. The technology will include airframe, seat, and restraint-system concepts that will dissipate energy and properly restrain the occupants within the cabin interior. The current efforts at LaRC are focused on developing improved aircraft components needed for crash protection, and both improved seat and restraint systems are being considered as well as structural airframe modifications. The dynamic nonlinear behavior of these components is being analytically evaluated to determine their dynamic response and to verify design modifications in structural crushing efficiency. In particular, that portion of the aircraft which surrounds the cabin area is being studied to determine methods of effectively dissipating crushing loads from three different vector directions while maintaining cabin integrity. Seats and restraint systems with deceleration devices incorporated are being studied that will absorb energy, remain firmly attached to the cabin floor, and adequately restrain the occupant from impact with the cabin interior. Full-scale mockups of structural components are being used to verify and provide corroboration to the analytical design methods.

In the development of aircraft design criteria, a set of design crash parameters are to be determined from both FAA field data and LaRC structural crash test data. The structural crash test data will include controlled crashes at velocities comparable with the stall velocity of most general aviation aircraft. Close cooperation with other governmental agencies is being maintained to provide inputs for human tolerance criteria concerning the magnitude and

duration of deceleration levels and for realistic crash data on survivability. Development of reliable crashworthiness design methods and analytical techniques for effective crash protection of general aviation aircraft is the final goal of the LaRC crash safety program.

REFERENCES

1. Vaughan, Victor L., Jr.; and Alfaro-Bou, Emilio: Impact Dynamics Research Facility for Full-Scale Aircraft Crash Testing. NASA TN D-8179, 1976.

2. McIvor, Ivor K.: Modeling and Simulation as Applied to Vehicle Structures and Exteriors. Vehicle Safety Research Integration Symposium, Rep. No. DOT HS-820 306, U.S. Dep. Transp., May 1973, pp. 5-18.

3. Armen, H., Jr.; Pifko, A.; and Levine, H. S.: Finite Element Analysis of Structures in the Plastic Range. NASA CR-1649, 1971.

4. Pifko, A.; Levine, H. S.; Armen, H., Jr.; and Levy, A.: Plans - A Finite Element Program for Nonlinear Analysis of Structures. Paper 74-WA/PVP-6, American Soc. Mech. Eng., Nov. 1974.

5. Melosh, Robert J.: Car-Barrier Impact Response of a Computer Simulated Mustang. Rep. No. DOT-HS-091-1-125-A, U.S. Dep. Transp., Mar. 1972.

6. Alfaro-Bou, E.; Hayduk, R. J.; Thomson, R. G.; and Vaughan, V. L., Jr.: Simulation of Aircraft Crash and Its Validation. Aircraft Crashworthiness, Kenneth Saczalski, George T. Singley III, Walter D. Pilkey, and Ronald L. Huston, eds., Univ. Press of Virginia, c.1975, pp. 485-497.

7. Laananen, David H.: Development of a Scientific Basis for Analysis of Aircraft Seating Systems. Rep. No. FAA-RD-74-130, January 1975.
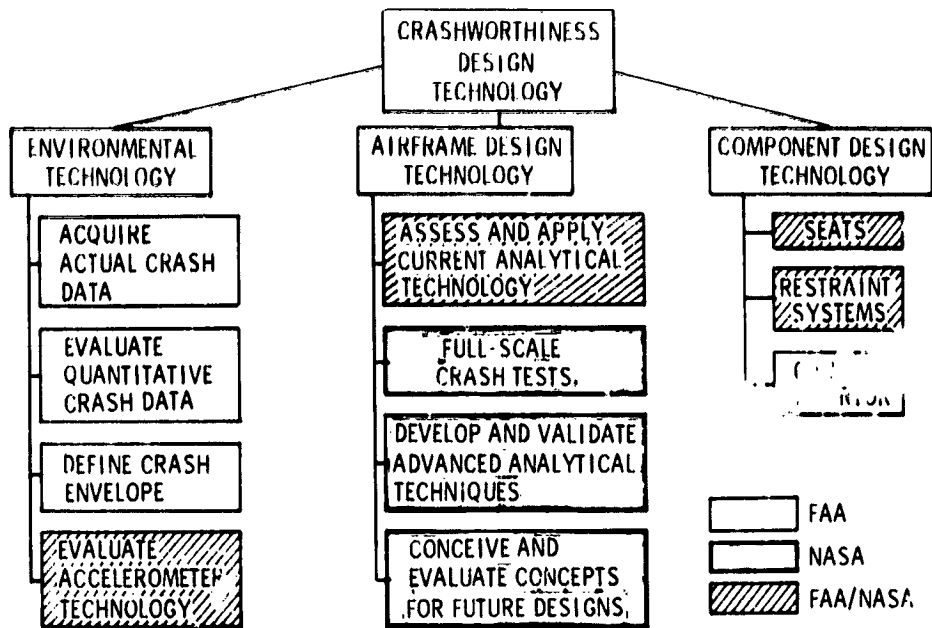
Figure 1.- Agency responsibilities in joint FAA/NASA
general aviation crashworthiness program.

CRASH SIMULATION TESTING

CRASH
SAFETY
PROGRAM
ELEMENTS

CRASHWORTHY DESIGN CONCEPTS

NONLINEAR
CRASH IMPACT ANALYSIS
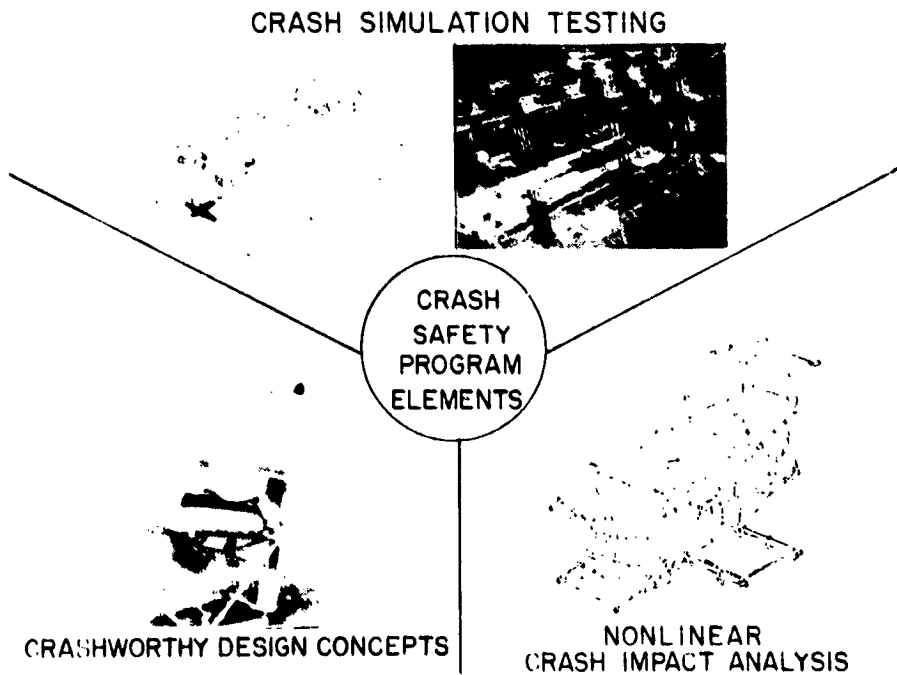
Figure 2.- Elements of LaRC crash safety program.

Figure 3.- Langley impact dynamics research facility.
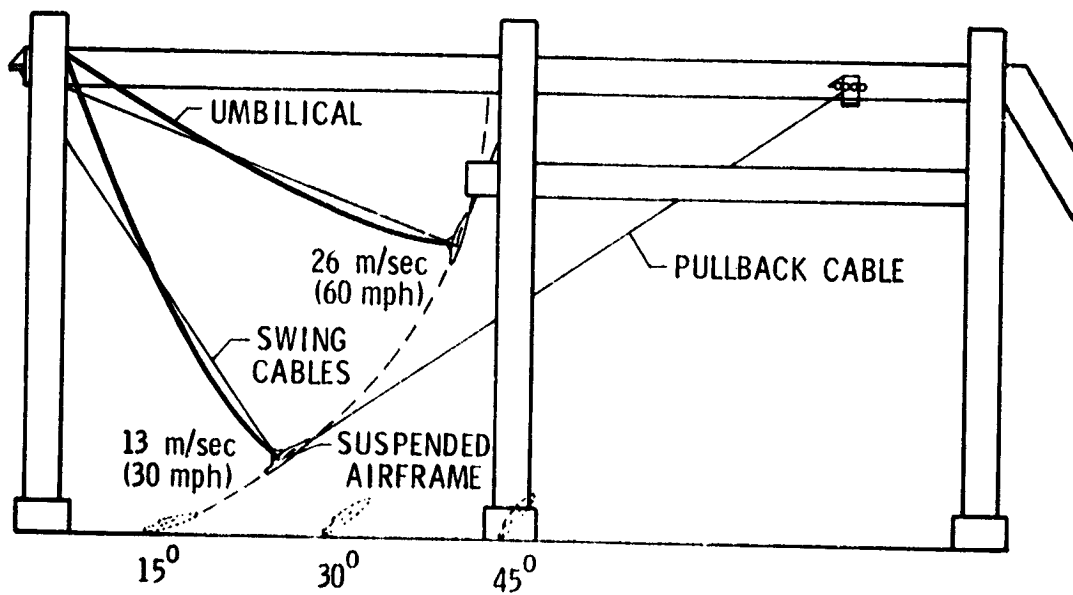
Figure 4.- Aircraft crash test method.
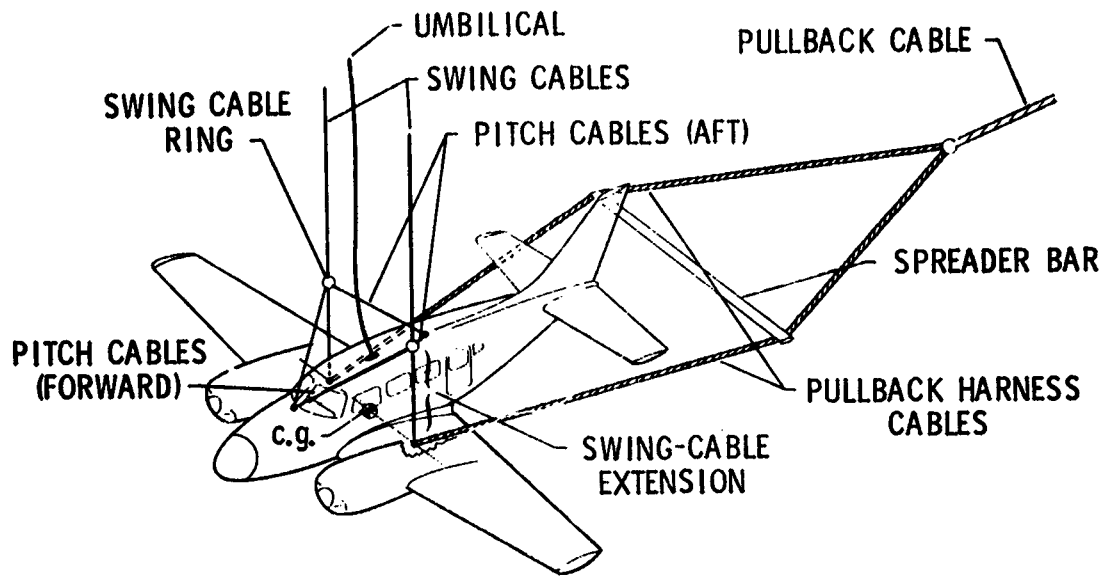
Figure 5.- Typical aircraft suspension system.

ACCELEROMETERS
○·◊ NORMAL DIRECTION
◇ LONGITUDINAL DIRECTION
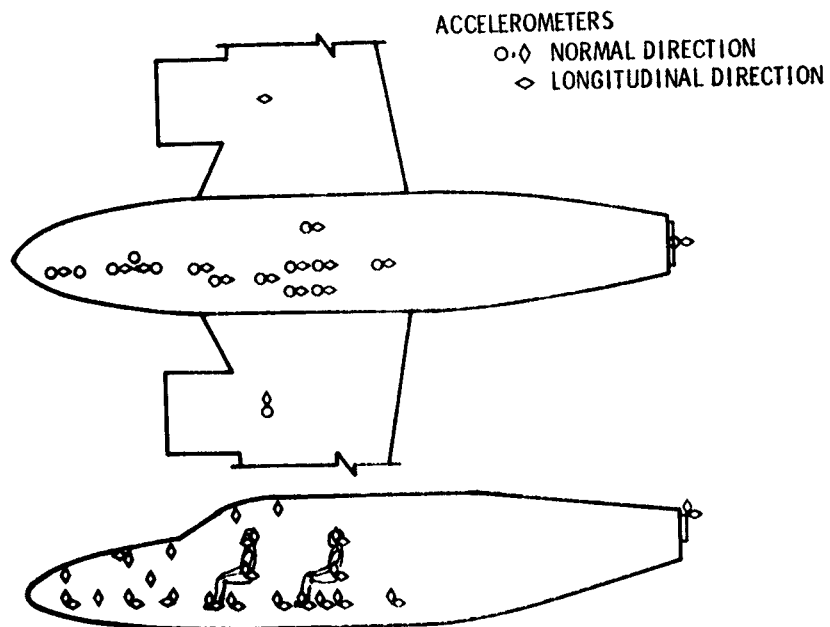
Figure 6.- Accelerometer layout for a symmetric
crash test (no yaw).
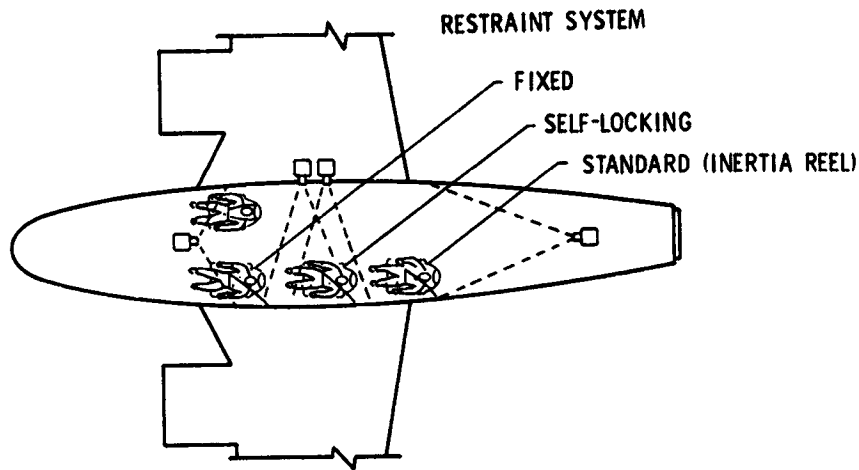
Figure 7.- Schematic of typical onboard camera and
restraint-system arrangement.

FLIGHT-PATH ANGLE , γ
ANGLE OF ATTACK , α
PITCH = θ = γ + α

ROLL ANGLE , Φ

YAW ANGLE , ψ

VELOCITY =	PITCH, θ, deg				
	13.4 m/sec (30 mph)	26.8 m/sec (60 mph)	26.8 · m/sec (60 mph)	40.2 m/sec (90 mph)	40.2 · m/sec (90 mph)
γ = - 5°				0	
γ = -15°	-15	-15	-15 / -15	-15 / -15	
		0		0	0
		15			
		-30		-30	
γ = -30°		-15			
		0			
γ = -45°		-45			
γ = -15° Φ = -15°		-15			
γ = -15° Φ = -30°		-15			

* LANDING GEAR DOWN
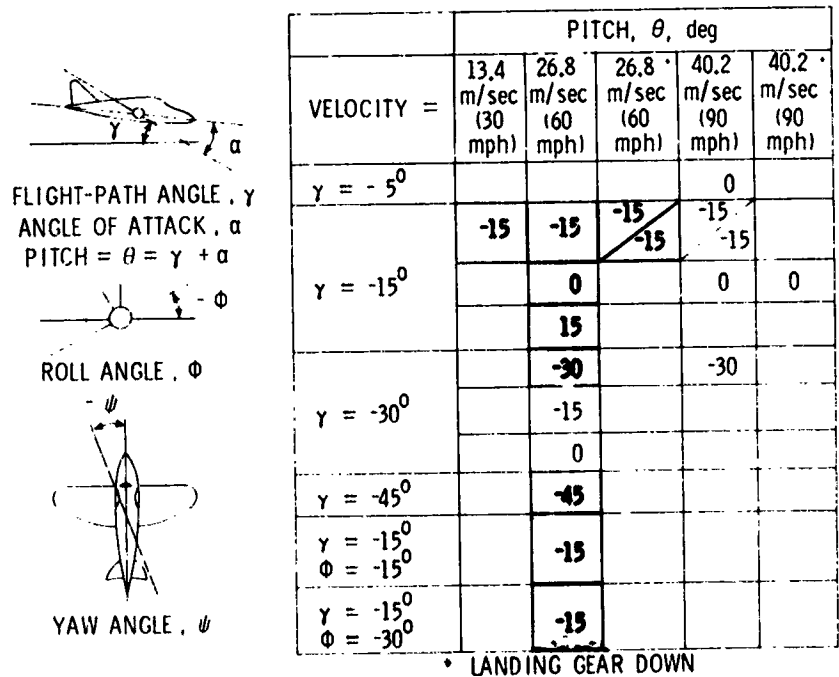
Figure 8.- Twin-engine crash test matrix. Shaded
portion indicates completed tests.
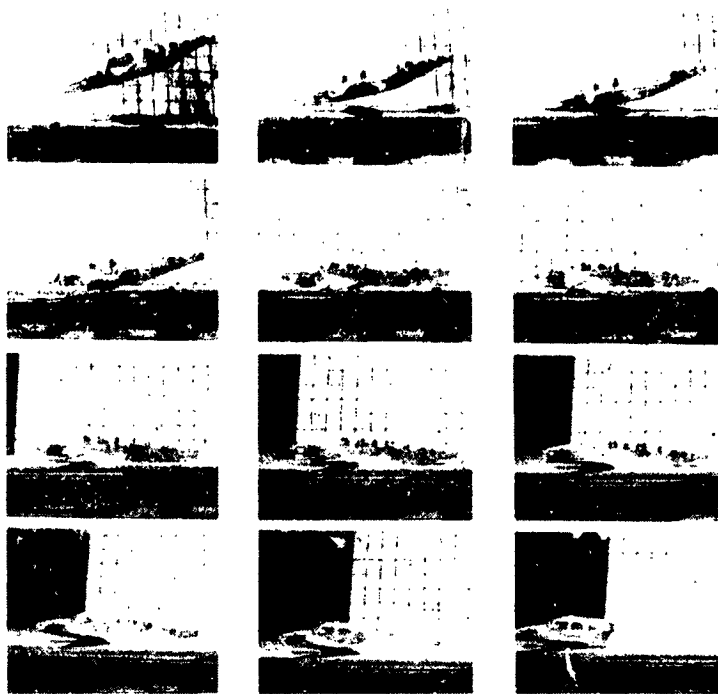
Figure 9.- Sequence of photographs taken
during full-scale crash tests.
0.05 second between frames.
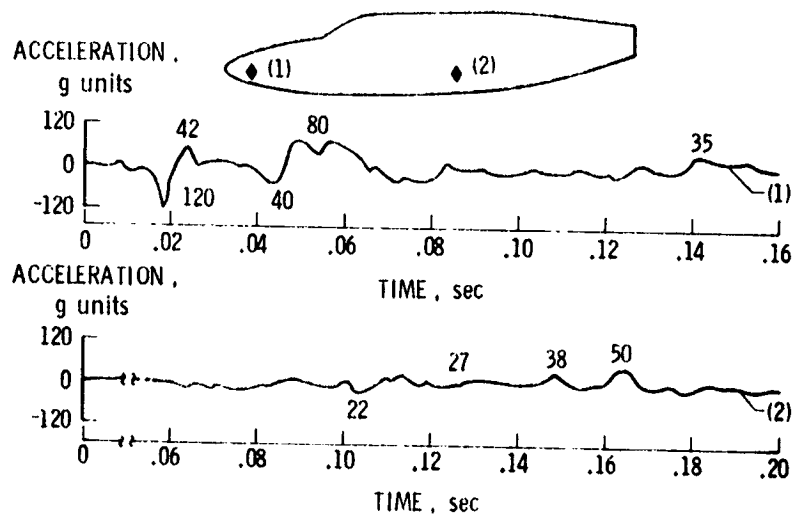
Figure 10.- Normal acceleration traces from two
extreme points on floor beam.
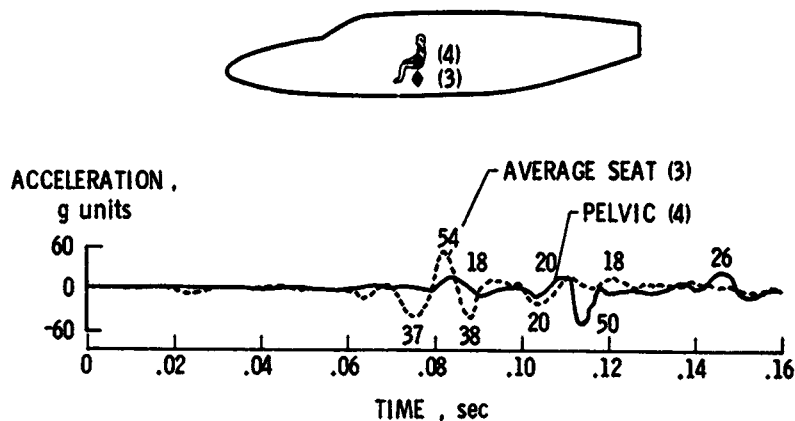
Figure 11.- Average normal acceleration at base of
first passenger seat and at dummy's pelvis.
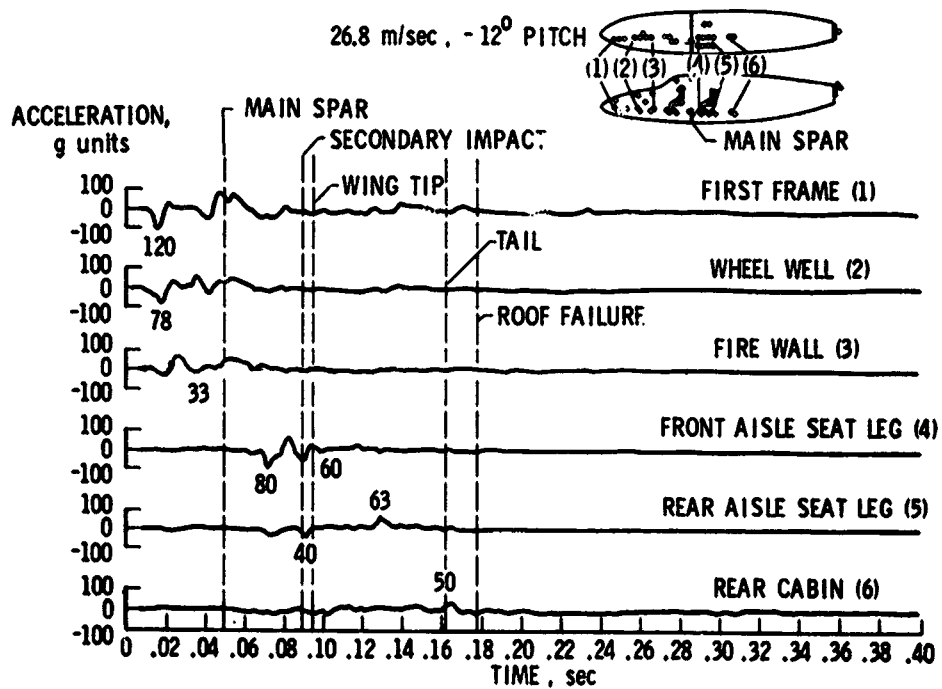
Figure 12.- Normal accelerations along fuselage floor beam.

384
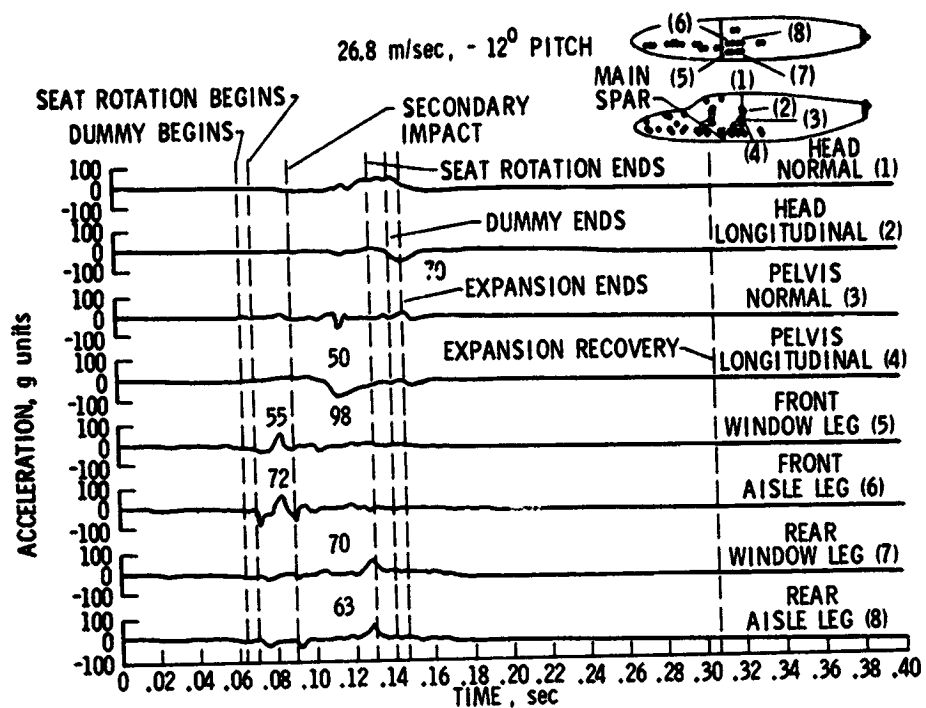
Figure 13.- Normal accelerations of first passenger seat and dummy.
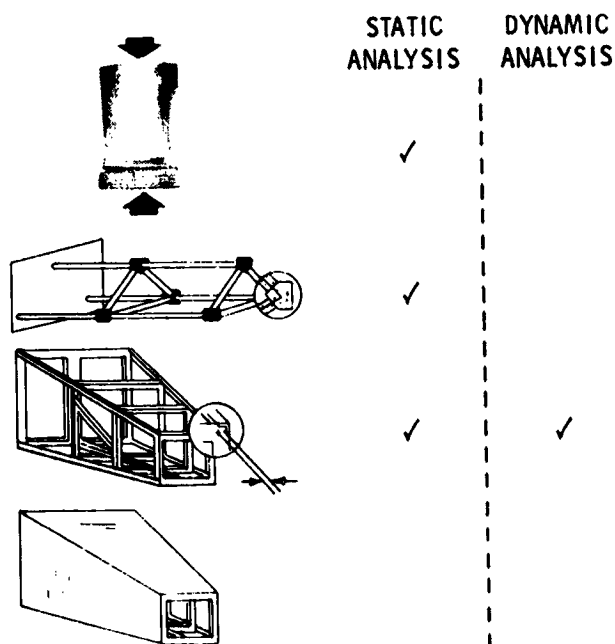
Figure 14.- Simplified structures used to corroborate experimental data with theoretical predictions.

385
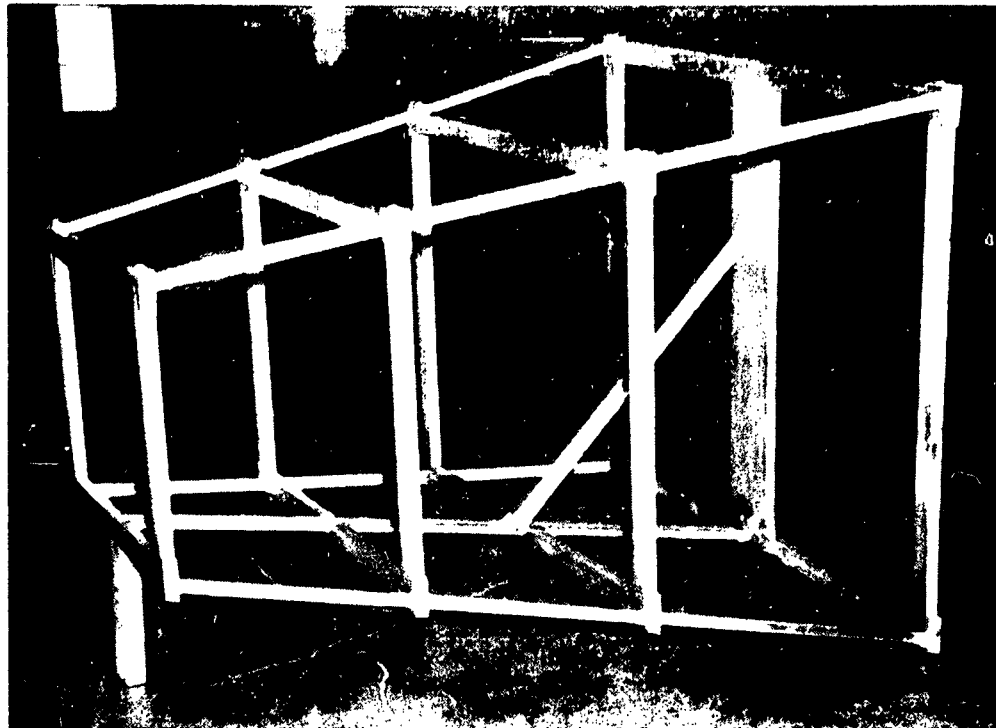
Figure 15.- Angular frame structure.
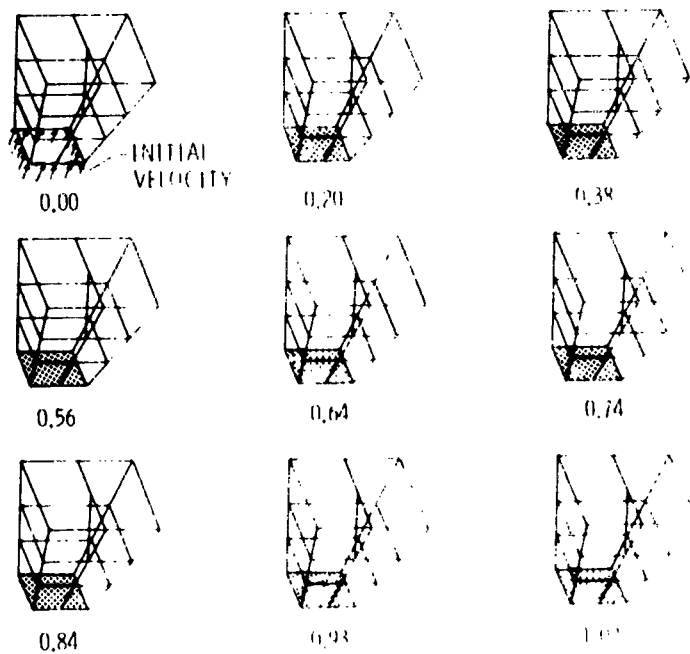
Figure 16.- Computer deformation pattern for
angular frame loaded rigid back with initial
velocity of 100 fps (30 m/s).
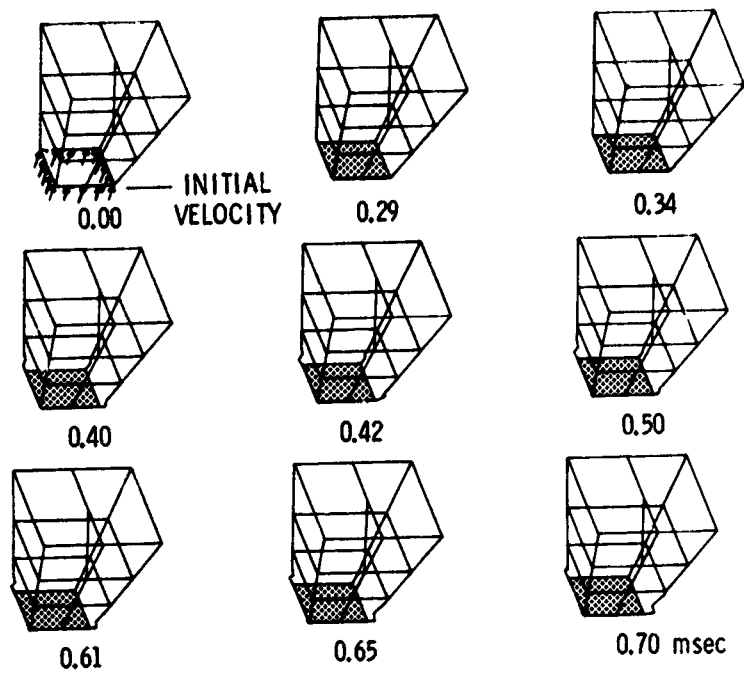
Figure 17.- Computer deformation patterns for angular frame loaded impulsively with initial velocity of 89.4 m/s (200 mph).
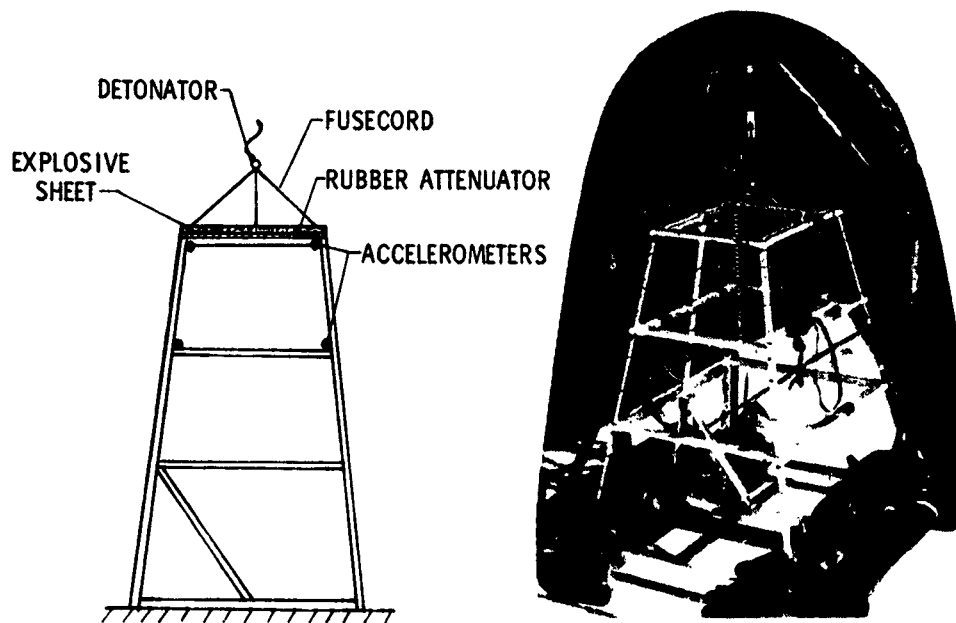
Figure 18.- Dynamic angular frame test setup.
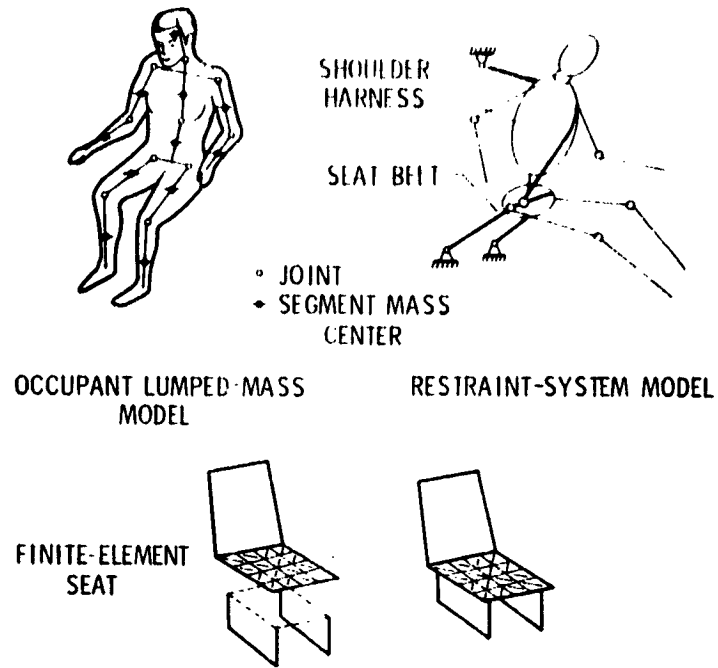
Figure 19.- Schematic of three-dimensional
seat and occupant model.
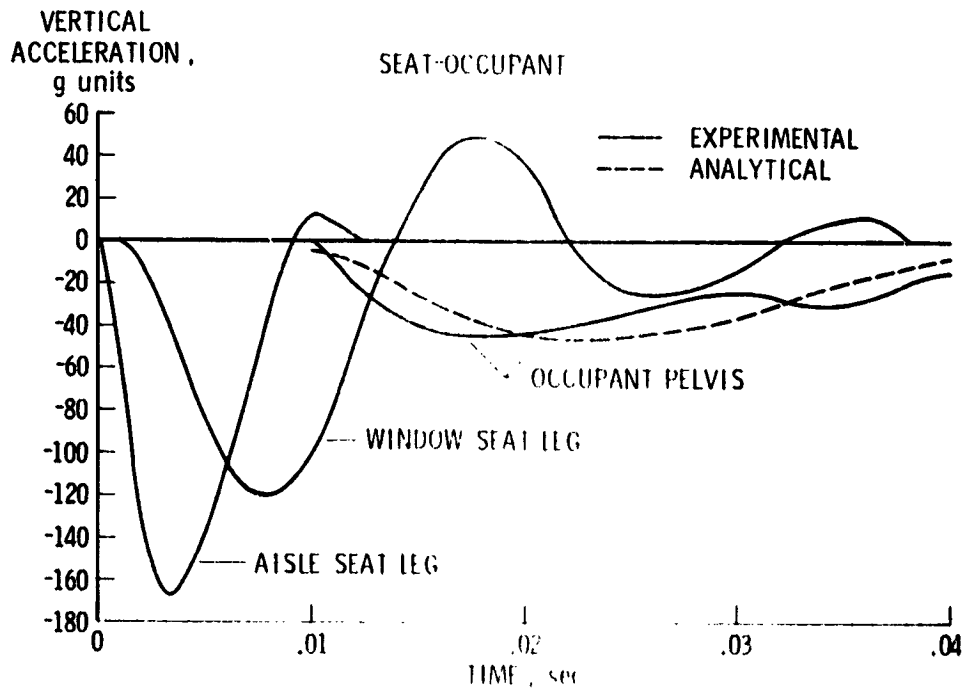
Figure 20.- Experimental data and computer predictions from
aircraft section drop test.
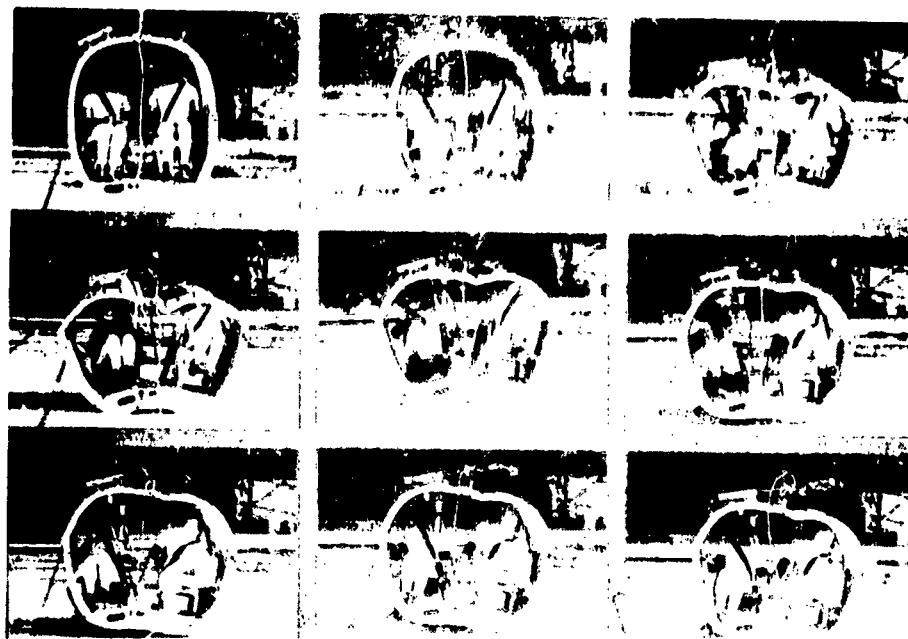
Figure 21.- Sequence of photographs taken during aircraft drop test. 0.05 second between frames.
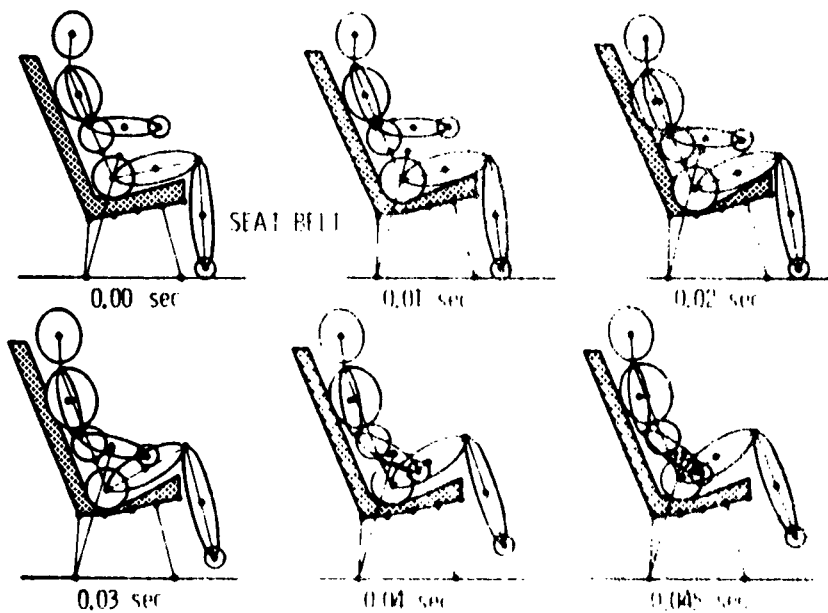
Figure 22.- Two dimensional computer graphic display of seat, occupant, and restraint system response for aircraft section drop test.

MATERIALS RESEARCH FOR AIRCRAFT FIRE SAFETY

Demetrius A. Kourtides and John A. Parker
NASA Ames Research Center

Richard W. Bricker
NASA Johnson Space Center

SUMMARY

The thermochemical and flammability characteristics of two polymeric composites currently in use and seven others being considered for use as aircraft interior panels are described. The properties studied included: (1) limiting oxygen index of the composite constituents; (2) fire containment capability of the composite; (3) smoke evolution from the composite; (4) thermogravimetric analysis; (5) composition of the volatile products of thermal degradation; and (6) relative toxicity of the volatile products of pyrolysis. The performance of high-temperature laminating resins such as bismaleimides is compared with the performance of phenolics and epoxies. The relationship of increased fire safety with the use of polymers with high anaerobic char yield is shown. Processing parameters of the state-of-the-art and the advanced bismaleimide composites are detailed.

INTRODUCTION

The purpose of this program was to assess the relative flammability and thermochemical properties of some typical state-of-the-art and candidate experimental aircraft interior composite panels, and to develop an understanding of the relationship of flammability and thermochemical properties of these systems. Specifically, aircraft interior composite panels were characterized as to their thermal stability, oxygen index of the composite components, smoke evolution from the panels, fire containment capability or fire endurance, thermal conductivity, identification of the pyrolysis effluents, relative toxicity of the degradation products and mechanical properties such as tensile strength.

As shown in figure 1, composite sandwich panels constitute most of the surface of aircraft interiors as sidewalls, partitions, ceiling panels, and overhead stowage bins. Approximately 1000 m² of the surface area of a typical wide body is made from composite panels weighing approximately 1600 kg. Currently used composite panels meet or exceed regulatory requirements (ref. 1) and offer excellent aesthetic, serviceability, maintenance, and other properties. However, additional improvements are being sought by industry, airframe manufacturers, and government agencies to reduce ignition susceptibility, fuel contribution, smoke and toxic fume emission, and to increase fire containment capability of these panels in selected areas such as lavatories and galleys (refs. 2-8).

391

Experimental composite panels that could offer improved fire resistance and smoke reduction in aircraft fires are now being developed and tested. In this program, nine different types of experimental composite panels were evaluated in terms of their flammability properties. Two of these were typical state-of-the-art interior panels and seven were experimental.

The composite panels used by most airframe manufacturers as interior paneling are sandwich panels that vary slightly in configuration, component composition, thickness, and density depending on the type of aircraft in which they are used and the specific application. In general, the panel consists of a clear polyvinyl fluoride film which is bonded to a polyvinyl fluoride decorative film bonded to a fiberglass-resin laminate. The complete laminate is bonded to an aromatic polyamide honeycomb core either when the prepreg is uncured or with a suitable adhesive film. The other side of the panel is similar except for the absence of the decorative film. The components of the panels are shown in figure 2.

SYMBOLS

The International System of Units (SI) is used.

D   percent light transmittance

Ds   specific optical density, $Ds = \dfrac{(131.58) \, Log_{10} \, 100}{D}$

Dm   specific optical density, maximum

LOI   limiting oxygen index, $O_2/(O_2 + N_2)$

TGA   thermogravimetric analysis

Yc   char yield, percent weight remaining

Td   polymer decomposition temperature

DESCRIPTIONS OF COMPOSITE PANELS

Nine types of composite panels were evaluated. Three types of resin systems were used for the fabrication of the laminates used in these composites: epoxy, bismaleimide, and various modifications of phenolic resins. The exact formulation for the phenolic resins was not available from the manufacturers. The epoxy resin used was bisphenol-A-type cured with methylene dianiline. Bismaleimide is an addition-type polyimide based on short, preimidized segments very similar in nature to those of condensation polyimides. The resin is produced by mixing a bismaleimide with a diamine at a specified ratio resulting in a resin with controlled crosslink density. The resin polymerizes thermally without loss of volatiles in contrast to the condensation polymers which cure

392

with loss of water. The general chemical structure of the laminating resins used is shown in figure 3. The components and composition of the panels are shown in tables I-III.

All composites fabricated were 2.54 cm thick. Composites 1-6 had a decorative surface of polyvinyl fluoride film printed with an acrylic ink and bonded to laminate consisting of various types of fiberglass preimpregnated with various types of phenolic resins. The laminates were adhered to the hexagonal-cell aromatic polyamide honeycomb structure using various types of phenolic resin-fiberglass adhesive ply. Composite 1 was considered a typical state-of-the-art phenolic resin panel.

Resins used in the preparation of the laminates for composites 1-6 were obtained commercially and are designated as phenolic types A through G. The decorative laminates of composites 1-6 were press-bonded to the honeycomb using an adhesive bond ply at 160° C for 12 min at 689.6 kN/M^2 pressure. The sandwich panel was then cured at 123° C for 1 hr with 50 mm Hg minimum vacuum bag pressure.

Composite 7 was composed of a laminate of bismaleimide-fiberglass adhered to the aromatic polyamide honeycomb which was filled with a poly-quinoxaline foam made from quinone dioxime. Processing of this panel is as follows: The aromatic polyamide honeycomb is coated with a pasty mixture of quinone dioxime-phosphoric acid. The amount (dry weight) of coating used is approximately 0.20-0.23 g/cm^2 (honeycomb face area) for a honeycomb structure with a 0.312-cm cell size. After application, the paste is air dried. The coated honeycomb is heated at a temperature of 150° C for 3 hr to form the carbonaceous char of polyquinoxaline, and any excess amount is removed from the faces of the honeycomb. Prepregs are prepared using the bismaleimide resin and one piece of 181 style E-glass cloth to form flat laminates. The impregnated glass cloth is dried 15 min at 80° C and then 30 min at 93° C. The prepreg is cured in a press at 180° C for 1 hr and subsequently post-cured in an oven at 250° C for 8 hr. The laminates are adhered to the filled honeycomb structure using a polyimide adhesive film using contact pressure in a heated press at 180° C for 1 hr. Processing of this type of panel has been described previously in detail (refs. 9-10). Composite 8 is a typical state-of-the-art composite panel. In general, panel consists of a decorative surface bonded to a laminate and a honeycomb core. The process for producing the decorative surface consists of silkscreening the required decor on a 0.005-cm polyvinyl fluoride film by a continuous web process. After drying, a 0.0025-cm trans-parent polyvinyl fluoride film, coated on one side with polymethyl methacrylate, is bonded to the decorative film to provide protection for the printed surface. This laminate is then bonded to one ply of epoxy-preimpregnated 181 E glass cloth which may have a canvas or other texture applied during this bonding operation. Time, temperature, and pressure vary depending on the texture applied. The current core material for sandwich paneling is a polyamide, hexagonal-cell honeycomb structure. The cell size varies 0.312 cm, 0.625 cm, or 0.937 cm depending upon strength and application requirements. The current method of bonding the skins to the core consists of using an epoxy resin-preimpregnated bond ply over which is applied the 181 E glass cloth/polyvinyl fluoride decorative laminate. The resin in the bond ply provides the adhesive to bond the skin to

393

the honeycomb and the decorative laminate to the bond ply. Curing is accomplished at 100° C with 5C cm Hg minimum vacuum bag pressure. For panels requiring decorative laminates on one side only, the bond ply provides the backside skin. Edge close-outs consist of either polyurethane foam or a phenolic microballoon-filled epoxy potting compound. Processing of this type of panel has been described previously in detail (refs. 9, 11, and 12).

The weight distribution of the panel components and some of the thermo-chemical properties of these components were determined. These included anaerobic char yield, polymer decomposition temperature, and limiting oxygen index. It can be seen in table IV that with the exception of the honeycomb and glass, the other components have a fairly low char yield and a corresponding low oxygen index.

Composite 9 was similar to composite 7 except that the bismaleimide-fiberglass honeycomb used is partially filled with a syntactic foam consisting of a mixture of carbon microballoons and bismaleimide resin. The prepregs for the facesheets are prepared in a manner similar to that described previously for composite 7. The core consists of a bismaleimide-fiberglass honeycomb filled with carbon microballoons bound with bismaleimide resin. The carbon microballoons are prepared by pyrolyzing phenolic microballoons in a nitrogen atmosphere. A stainless steel container is filled with phenolic microballoons and enclosed in a larger stainless steel container with a nitrogen inlet to provide an oxygen-free atmosphere. The assembly is placed in a larger furnace. The pyrolysis cycle is as follows: room temperature to 816° C in 4 hr, hold at 816° C for 4 hr, and cool to room temperature in 2 days. Pyrolyzed carbon microballoons must be cooled to 38° C before removal of the nitrogen blanket to prevent spontaneous ignition of the carbon microballoons. After pyrolysis, the carbon microballoons are no longer free-flowing and are agglomerated as large cakes. To break them into smaller agglomerates, the cake microballoons are placed in a container with isopropanol (ratio of 1 kg balloons/7 liters solvent) and mixed in a paint shaker for 15 min. The slurry is then screened through a 20-mesh screen to remove the larger non-separated agglomerates. The screened isopropanol/carbon microballoon slurry is now ready for core impregnation. The processing cycle for this composite is shown in figure 4.

The equipment shown in figure 5 is used to fill the cores of the fiberglass-bismaleimide honeycomb with the prepared carbon microballoons. A high-density 0.3-cm cell aluminum honeycomb is fitted and restrained on the bottom inside of the vacuum filling box. A nylon screen (120 mesh) is placed between the aluminum support honeycomb and the fiberglass-reinforced polyimide honeycomb to retain the microballoons. High vacuum is not required to effectively impregnate the honeycomb, but a high volume of air displacement is required. A vacuum reservoir chamber is pumped to a vacuum of approximately 10 mm Hg. The filled honeycomb cores, sandwiched between two nylon, fine-mesh screens and between two aluminum support honeycombs, are dried for 16 hr in an air-circulating oven at 93° C. After drying, the microballoon fill is saturated with a solution of bismaleimide resin in N-methyl-2-pyrolidone solvent. The foamed honeycomb is heated for 2 hr at 93° C and for 1 hr at 204° C to completely cure the bismaleimide binder. For the microballoon resin combination, the resin by weight is approximately 4-10 percent.

394

The assembly of the sandwich panel consists of bonding the face sheets to the microballoon-filled fiberglass bismaleimide honeycomb panel with a polyimide film adhesive. The assembly is then placed in a platen press at 204° C and cured for 2 hr at 700 kN/m². Afterward, the panel is cured for 24 hr at 254° C to remove volatile materials and to achieve reduced smoke characteristics.

TEST RESULTS AND ANALYSIS

Thermochemical Characterization of Composites

Samples of the nine types of composites were cut to a size of 2.5 cm x 2.5 cm x 2.5 cm and were ground uniformly to approximately 250 mesh. The samples were subjected to the following thermochemical studies in order to (1) determine the relative thermal stability of the samples under anaerobic and oxidative conditions, (2) determine the major volatile products produced from the pyrolysis of the samples in vacuum, and (3) determine the relative toxicity of the pyrolysis effluents by exposing animals to them.

Thermogravimetric Analyses

Thermal analyses of the composites were conducted on a DuPont 950 thermo-gravimetric analyzer (TGA) using both nitrogen and air atmospheres with a sample size of 10 mg. The thermogravimetric analyses data of 10° C/min heating rate in nitrogen is shown in figure 6.

The pyrolysis of the samples in air and nitrogen atmospheres was conducted to obtain a relative understanding of the pyrolysis of the samples in the furnace used to pyrolyze samples for assessing their relative toxicity as described later in the text. Pyrolysis in an air atmosphere is intended to approximate the environment in the pyrolysis tube at the start of the toxicity test, and pyrolysis in a nitrogen atmosphere is intended to approximate the environment in the pyrolysis tube during the test after the original air has been essentially displaced by pyrolysis effluent. The degradation products are continuously removed from the sample during thermogravimetric analysis, and in the relative toxicity test apparatus described later, they are conveyed only by normal thermal flow. The TGA data in the nitrogen atmosphere are considered more relevant because in the toxicity apparatus, the pyrolysis effluents that evolved at lower temperature have essentially displaced the original air by the time the temperature has reached 700° C.

Composite 9 is the most stable composite and gives the highest char yield in nitrogen. The thermogravimetric analyses data in air are shown in figure 7. All the composites except composite 7 were oxidized completely in air above 600° C and gave constant weight residues.

Analysis of Volatile Products

Samples of the composites were pyrolyzed to determine the degradation products. The apparatus for the pyrolysis is shown in figure 8. The samples were placed in quartz tubes that were 2.5 mm in diameter. Each sample tube was attached to a manifold and evacuated to 10^{-4} torr. A stopcock was inserted between the manifold and the sample tube so that the sample tube could be isolated while gas samples were being collected. An infrared cell was attached to the manifold via a stopcock; a mercury manometer and a trap were also attached to the manifold. At the beginning of a pyrolysis run, the stopcock to the vacuum pump was closed, and a furnace at 700° C was placed around the sample tube. At this point, a timer was started. The pressure of the gases evolved during the pyrolysis was monitored with the pressure gauge. After 5 min the furnace was removed, the stopcock to the sample tube was closed, and the stopcock leading to the infrared cell was opened allowing the pyrolysis gases to enter the infrared cell. After a pressure reading was taken, the stopcock leading from the infrared cell to the gas manifold was closed. Dry air was admitted to the infrared cell so that the total pressure was equal to atmospheric pressure. This was done so that the pyrolysis gases were always measured at the same total pressure, the main portion of which was dry air, thus eliminating the effects of pressure broadening. Infrared spectra were taken using a Perkin Elmer Model 180 infrared spectrometer. Finally, the sample tube was removed from the manifold, broken open, and the residual char was weighed.

Part of the material that was volatile at 700° C condensed on the sample tube as it was removed from the furnace. The analysis of this material is not included in the data presented.

Table V shows the results of the analysis of the volatile species in terms of milliequivalents. These results were obtained from samples that were pyrolyzed in a vacuum. A considerably different distribution of products might have been obtained had the samples been pyrolyzed in air, in which case the products would be a function of the partial pressure of oxygen at the sample, the temperature of pyrolysis, and time that it took the sample to reach the pyrolysis temperature. It can be seen that the maximum amount of volatiles analyzed accounted for only 18 percent, and additional compounds may be present either in the solid particulates or in the condensates. The same volatile products are shown in table VI in terms of milligrams of volatile compound per gram of initial sample.

Thermal Efficiency

The NASA Ames T-3 thermal test (ref. 13) was used to determine the fire endurance or fire containment capability of the composite panels. The apparatus is shown in figure 9. In this test, specimens measuring 25 cm x 25 cm x 2.54 cm thick are mounted in the chamber and thermocoupled on the backface of the specimen. The flames from an oil burner, supplied with approximately 5 liter/hr of JP-4 jet aviation fuel, provide heat flux to the front face of the sample in the range of 10.4-11.9 W/cm^2. Thermocouples are placed on the back of the

396

composite panel to determine the temperature rise as a function of time. The
heat flux produced in this burn is approximately five to seven times as high as
that which would normally be encountered in a compartment fire. The test was
primarily designed for exterior fuel-fed fires, but it is very useful in the
comparative assessment of the fire containment capabilities of aircraft interior
composite panels.

The fire endurance capability of the composite panels is compared in
figures 10, 11, and 12. The backface temperature rise of the panel is plotted
as a function of the time in minutes when the sample is subjected to this type
of fire. The dotted line is the furnace temperature in the front surface of
the panel. It can be seen in figure 12 that the backface temperature of the
conventional composite 8 reached 200° C in 2.5 min, whereas, it took as
long as 8 min for the bismaleimide composites 7 and 9 to reach a comparable
backface temperature.

Oxygen Index

The oxygen index of the components comprising the composites was determined
per American Society of Testing and Materials, Test Method D-2863. The values
indicated in table VII are for the laminated or composite components as they are
used in the sandwich composite and not for the individual polymers. It can be
seen that the laminated facesheets consisting of the bismaleimide resin offer
the highest oxygen index as compared with the phenolic and epoxy facesheets.
In addition, the filler foams utilized in the honeycomb structure have a very
high oxygen index. Among the phenolics, composite 6 exhibited the highest
oxygen index.

Smoke Evolution

Smoke evolution from the composites was determined using NBS-Aminco smoke
density chambers at two laboratories: laboratory A and laboratory B. The
procedure and test method used were essentially those described by NFPA 258-T
(ref. 14). A detailed description of the NBS smoke chamber can be found in
reference 15.

The test results obtained with the NBS smoke chamber, modified by the
incorporation of an animal module accessory (ref. 16), are presented in
table VIII. Values of specific optical density (Ds) at 1.5 min, 4.0 min, and
specific optical density maximum (Dm) are presented; standard deviations are
also given.

Composites 1 and 8 represented the state-of-the-art baseline materials.
All the other composites exhibited significantly lower smoke density values,
indicating that the phenolic and bismaleimide offer the advantage of smoke
reduction.

A comparison of the Ds values obtained by the two laboratories is presented
in table IX. In addition to possible differences in apparatus at the two

397

laboratories, the calculation procedures were slightly different. In laboratory A, the Ds values were obtained from individual test data and then averaged. In laboratory B, an average curve was generated by computer from the data of the individual tests, and the Ds values were obtained from the computer-averaged curve. The smoke density of composite panels similar to composite 8 has also been evaluated by Sarkos (ref. 17). Composition of the panel was essentially the same as composite 8 except the panel was 0.70 cm thick. The maximum smoke level, Dm (corrected) was 54 whereas the average in the present studies was 58.7.

Relative Toxicity

Efforts to obtain relative toxicity information by using the NBS smoke chamber with the animal module accessory were unsuccessful. The mice and rats exposed during the standard smoke tests showed no evidence of death or even incapacitation (ref. 16). The heat flux of 2.5 W/cm^2 used in the standard test procedure appears to be incapable of producing sufficient effluents from these high-performance materials.

Tests were conducted utilizing the NASA animal exposure chamber shown in figure 13 in order to determine the relative toxicity of the composites. The chamber is constructed from polymethylmethacrylate and has a total free volume of 4.2 liters; 2.8 liters are available for animal occupancy. The chamber is fitted with probes for pyrolysis gas sampling and for an oxygen analyzer. In addition, the temperature in the chamber is monitored utilizing the thermometer indicated.

The upper dome section is removable and is connected to the base section by means of a conventional toggle snap ring; the joint is sealed by an O-ring. The upper end of the dome section is provided with an aperture so that test gas can flow completely through the chamber if desired, using the gas inlet passage in the base as the other aperture. In these experiments, the gas outlet was connected to a bubbler to permit venting of pressure exceeding 2.54 cm of water, and to prevent entry of fresh air.

The sample material is pyrolyzed in a quartz tube, closed at one end with a cap and connected at the other end to the animal exposure chamber. A horizontal tube furnace is used for pyrolysis, and the pyrolysis effluents are conveyed to the animal exposure chamber by normal thermal flow. A perforated plate or barrier of polymethylmethacrylate prevents movement of mice into the pyrolysis or connecting tube. The chamber design and the activity of the freely moving mice promote distribution of the gases within the chamber.

A connecting tube between the furnace and the chamber is utilized which reduces the possibility of a significant temperature increase in the animal exposure chamber and reduces conduction of heat to the chamber itself, but it also represents dead space and additional travel distance and provides opportunity for condensation and absorption on the inner surface of the tube and absorption in any condensate present. The procedure for the assessment of relative toxicity has been described previously in detail (refs. 18 and 19).

398

To provide an indication of relative toxicity, 1.0 g of each of the powdered specimens of the composites was pyrolyzed at a heating rate of 40° C/min in a quartz tube to an upper temperature limit of 700° C, and the effluents conveyed by natural thermal flow into the chamber containing four Swiss albino male mice. The test was continued for 30 min, unless terminated earlier upon the death of all four animals. The highest chamber temperature recorded was 29.5° C, indicating that the pyrolysis gases were adequately cooled before entering the animal exposure chamber. Some condensation of higher boiling vapors in the connecting tube was observed, and some of the effluent gases entered the animal exposure chamber as visible heavy vapors, indicating that some higher boiling compounds did reach the animals and were not lost entirely by cooling. The lowest oxygen concentration recorded was 12 percent, indicating that hypoxia was not a significant factor in animal response. The relative toxicity to mice of the degradation products from the powdered composites when heated in this manner is shown in table X in terms of time to incapacitation and time to death.

During the 30-min exposure period, composite 9 caused no deaths in the test animals. The other composites, that is, 1-8, caused death to all of the animals in times ranging from 19.65 min to 28.31 min.

The test time-to-death was judged as the time elapsed at cessation of movement and respiration of the first test animal as judged by the observer. Time to incapacitation was judged as the time to the first observation of loss of equilibrium, collapse, or convulsions in any one of the animals, whichever came first. As a comparison, 1.0 g of wool fabric causes death to four mice in approximately 9.5 min when tested in a similar manner.

Correlation of Oxygen Index and Smoke Evolution to Char Yield

Parker et al. (ref. 20) have shown a correlation between the flammability properties of polymers and their char yield. A decrease in ease of ignition and smoke evolution was observed with high char yield polymers. The same relationship seems to exist with composites consisting of polymers and inorganic reinforcements.

The smoke density and relative anaerobic char yield of these composites was compared. It can be seen in figure 14 that in general, composites with high char yield had fairly low smoke evolution.

The limiting oxygen index of these composites was compared with their relative anaerobic char yield. It can be seen in figure 15 that in general, composites with very high char yield exhibited a high limiting oxygen index.

Thermophysical Properties

The thermophysical properties of the state-of-the-art and one advanced composite are summarized in table XI. The thermal conductivity of composite 8 was significantly higher than that of composite 9, probably due to the

absence of any insulative material in the honeycomb. The flatwise tensile strength was slightly lower.

CONCLUDING REMARKS

Composite 9, consisting of bismaleimide-fiberglass/bismaleimide honeycomb with carbon microballoons, exhibited the highest fire containment capability.

Advanced composite panels consisting of PVF/phenolic-fiberglass/aromatic polyamide honeycomb/phenolic-fiberglass (composites 2-6) and composites 7 and 9 exhibited lower smoke evolution than the state-of-the-art composite 8.

The results from the toxicity experiments indicated that the relative toxicity of the pyrolysis products of composite 9 was the lowest of all the composites tested. It should be realized, however, that these toxicity measurements are only relative, and no definite conclusions may be drawn from these studies. The methodology developed for assessing the relative toxicity is primarily designed for pure polymers and not for composite systems consisting of various polymers and fibers. Additional studies are being initiated to expose these composite constructions intact to a radiative panel heat source and thus evaluate the relative toxicity of the composite degradation products.

No definite correlation was found between the concentration of the toxic pyrolysis products of the composites and their relative toxicity to animals, indicating possibly that additional toxic species may be present both in the volatile gases, which accounted for only 18 percent of the degradation products, and in the solid particulates. Additional studies will be conducted using both gas chromatography and mass spectrometry to identify these compounds and their relative concentrations.

400

REFERENCES

1. Airworthiness Standards: Transport Category Airplanes, Federal Aviation
   Regulations. Vol. III, Part 25, Transmittal 10. Department of
   Transportation, FAA, August 1972.

2. Aircraft, Engine, and Propeller, Airworthiness, and Procedural Proposals.
   Department of Transportation, FAA. Federal Register, vol. 40,
   June 1975, Notice 75-31, pp. 6300-6305.

3. Flight Standard, Services, Transport Category Airplanes, Smoke Emission
   from Compartment Interior Materials. Department of Transportation,
   FAA. Federal Register, vol. 40, Feb. 1975, Notice 75-3, pp. 6501-6505.

4. Flight Standards Service, Compartment Interior Materials, Toxic Gas
   Emission. Department of Transportation, FAA, Federal Register,
   vol. 39, Dec. 1974, Notice 74-38, pp. 4540-4544.

5. Flaming and Self Extinguishing Characteristics of Aircraft Cabin Interior
   Materials. Final Rep. NA-68-30 (DS-68013), FAA, July 1968.

6. Gross, D.; Loftus, J. J.; Lee, T. G.; and Gray, V. E.: Smoke and Gases
   Produced by Burning Aircraft Interior Materials. Rep. NA-68-36
   (DS-68-16), FAA, June 1968.

7. Mott, D. R.; Spruance, W. W.; Danaher, D.; McGuire, R.; Kourtides, D. A.;
   Bigelow, A.; and Ault, R.: Cabin Interiors – Smoke and Fire.
   Proceedings of the 12th Annual Conference and Trade Exhibit of the
   Survival and Flight Equipment Association, Sept. 1974, pp. 114-120.

8. Gross, D.: Smoke and Gases Produced by Burning Interior Materials. NBS
   Building Science Series 18, Feb. 1968.

9. Kourtides, D. A.; Parker, J. A.; and Gilwee, W. J.: Thermochemical
   Characterization of Aircraft Interior Panel Materials. J. Fire and
   Flammability, vol. 6, July 1975, pp. 373-391.

10. Gilwee, W. J.; Parker, J. A.; Kourtides, D. A.; and Hilado, C. J.: Fire
    Resistant Low Density Composites. Proceedings of the National
    Technical Conference (NATEC) Meeting, Society of Plastics Engineers,
    Cleveland, Ohio, Oct. 4-7, 1976.

11. Kourtides, D. A.; Parker, J. A.; Hilado, C. J.; Anderson, R. A.; Tustin,
    B.; Arnold, D. B.; Gaume, J. G.; Binding, A. J.; and Mikeska, J. L.:
    Fire and Flammability, vol. 7, Jan. 1976, pp. 125-159.

12. Kourtides, D. A.; Parker, J. A.; Leon, H. A.; Williamson, R. B.; Hasegawa, H.; Fisher, F.; Draemel, R.; Marcussen, W. H.; and Hilado, C. J.: Fire Containment Tests of Aircraft Interior Panels. J. Fire and Flammability, vol. 7, Apr. 1976, pp. 257-258.

13. Riccitiello, S. R.; Fish, R. H.; Parker, J. A.; and Gustafson, E. J.: Development and Evaluation of Modified Polyisocyanurate Foams for Low-Heating-Rate Thermal Protection. J. of Cell. Plastics, vol. 7, no. 2, Mar./Apr. 1971, pp. 91-96.

14. Smoke Density Measurements, NFPA 258-T 1974, National Fire Protection Association.

15. Lee, T. G.: Interlaboratory Evaluation of Smoke Density Chamber. Tech. Note 708, National Bureau of Standards, Dec. 1971.

16. Hilado, C. J.; and LaBossiere, L. A.: Evaluation of Smoke Density Chamber as an Apparatus for Fire Toxicity Screening Tests. J. of Combustion Toxicol., vol. 3, no. 2, May 1976, pp. 356-362.

17. Sarkos, E. P.: Measurement of Toxic Gases and Smoke from Aircraft Cabin Interior Materials Using the NBS Smoke Chamber and Colorimetric Tubes. Department of Transportation, Rep. FAA-RD-76-7, FAA, Mar. 1976, pp. 15-19.

18. Hilado, C. J.: Evaluation of the NASA Animal Exposure Chamber as a Potential Chamber for Fire Toxicity Screening Tests. J. Combustion Toxicology, vol. 2, Nov. 1975, pp. 298-314.

19. Hilado, C. J.: Relative Toxicity of Pyrolysis Products of Some Foams and Fabrics. J. of Combustion Toxicology, vol. 3, no. 1, Feb. 1976, pp. 32-60.

20. Parker, J. A.; Kourtides, D. A.; Fish, R. H.; and Gilwee, W. J.: Fire Dynamics of Modern Aircraft from a Materials Point of View. J. Fire and Flammability, vol. 6, Oct. 1975, pp. 534-553.

402

TABLE I.- COMPOSITION OF COMPOSITES 1-3

Component	Composite		
	1	2	3
A. Decorative surface, cm thick, percent weight	0.002 PVF clear acrylic ink, 0.005 PVF	Same as 1-A	Same as 1-A
B. Face sheet, resin/ fabric, percent weight	Phenolic type A/7581 glass	Phenolic type C/7581 glass	Same as 2-B
C. Bond sheet, resin/ fabric, percent weight	Phenolic type B/120 glass	Phenolic type D/120 glass	Phenolic type C/120 glass
D. Core type; thickness, cm; cell size, cm; density, kg/m^3	Aromatic polyamide-paper honeycomb; 2.413; 0.31; 48.06	Same as 1-D	Same as 1-D
E. Core filler; density, kg/m^3	None	None	None
F. Same as C	Same as 1-C	Same as 2-C	Same as 3-C
G. Same as B	Same as 1-C	Same as 2-C	Same as 3-C
H. Same as A	None	None	None
Composite density, kg/m^3	72.410	79.138	70.488

TABLE II.- COMPOSITION OF COMPOSITES 4-6

Component	Composite		
	4	5	6
A. Decorative surface, cm thick, percent weight	0.002 PVF clear acrylic ink, 0.005 PVF	Same as 4-A	Same as 4-A
B. Face sheet, resin/ fabric, percent weight	Phenolic type E/7581 glass	Phenolic type F/7581 glass	Phenolic type G/7581 glass
C. Bond sheet, resin/ fabric, percent weight	Same as 4-B	Phenolic type F/120 glass	Phenolic type G/120 glass
D. Core type; thickness, cm; cell size, cm; density, kg/m^3	Aromatic polyamide- paper honeycomb; 2.413; 0.31; 48.06	Same as 4-D	Same as 4-D
E. Core filler; density, kg/m^3	None	None	None
F. Same as C	Phenolic type E	Same as 5-C	Same as 6-C
G. Same - B	Same as 4-F	Same as 5-C	Same as 6-C
H. Same as A	None	None	None
Composite density kg/m^3	76.575	76.095	70.968

404

TABLE III.- COMPOSITION OF COMPOSITES 7-9

		Composite		
	Component	7	8	9
A.	Decorative surface cm thick, percent weight	None	0.002 PVF acrylic ink, 0.005 PVF	None
B.	Face sheet, resin/ fabric, percent weight	Bismaleimide/120 glass	Epoxy type H/181 E glass B + C = 35.9 percent	Bismaleimide/ 181 E glass B + G = 14.1 percent
C.	Bond sheet, resin/ fabric, percent weight	Polyimide adhesive	Epoxy type H/120 glass	Same as 7-C C + F = 5.1 percent
D.	Core type; thickness, cm; cell size, cm; density, kg/m^3, percent weight	Aromatic polyamide-paper honeycomb; 2.413; 0.31; 48.06	Same as 7-D 2.413, 0.31; 48.06; 20.5 percent	Bismaleimide-glass honeycomb 2.413; 0.47; 80.1; 30.3 percent
E.	Core filler; density, kg/cm^3, percent weight	Quinone dioxime foam	None	Carbon micro balloons with 5 percent bismaleimide; 112; 50.5 percent
F.	Same as C	Same as 7-C	Same as 7-C F + G = 35.9 percent	Same as 7-C
G.	Same as B	Same as 7-B	Same as 7-B	Same as 9-B
H.	Same as A	None	Same as 7-A A + H = 7.7 percent	None
	Composite density, kg/m^3	110	95	130

TABLE IV.- TYPICAL PROPERTIES OF COMPONENT MATERIALS

IN STATE-OF-THE-ART PANELS

Material	Weight, percent	Char yield N_2, 700°C, percent	Polymer decomposition temperature, °C N_2	Limiting oxygen index, $\dfrac{O_2}{N_2 + O_2}$
Polyvinyl fluoride	7.6	10	400	20
Glass: SiO_2	41.9	100	—	>70
Epoxy; 4.4'-isopropylidenediphenol (bisphenol A)	30.0	23	180	21
Polyamide: poly (M-phenylene isophthalamide)	20.5	48	420	48

TABLE V.- MAJOR PRODUCTS AT 23° C FROM THE PYROLYSIS OF COMPOSITES IN

VACUUM AT 700° C FOR 5 MIN

Composite	Weight loss, percent (a)	Volatile weight loss, percent (b)	Volatiles, meq/g						E_2 (c)	Total meq/g (d)
			CO_2	CO	CH_4	HCN	C_6H_6	NH_3		
1	48.8 ± 2.1	13.8 ± 0.1	2.02 ± 0.53	0.36 ± 0.08	0.74 ± 0.04	0.24 ± 0.03	0.05 ± 0.01	—	1.63 ± 0.1	5.03 ± 0.15
2	48.8 ± 2.1	12.0 ± .8	1.54 ± .07	.54 ± .09	1.26 ± .20	.32 ± .03	.06	—	1.76 ± .32	5.64 ± .33
3	39.9 ± 2.2	12.9 ± .?	1.93 ± .14	.50 ± .03	.92 ± .24	.28 ± .02	.04 ± .01	—	2.16 ± .54	5.50 ± .40
4	41.9 ± 2.8	14.4 ± .6	2.22 ± .17	.51	1.06 ± .02	.26 ± .01	.06 ± .01	—	1.60 ± .22	5.68 ± .25
5	42.0 ± 1.3	12.6 ± .1	1.89 ± .14	.52 ± .05	.90 ± .30	.24 ± .01	.042 ± .001	—	1.94 ± .46	5.51 ± .51
6	42.6 ± 1.1	12.4 ± 1.3	1.92 ± .20	.42 ± .09	.80 ± .03	.22 ±	.062 ± .005	—	1.72 ± .23	5.02 ± .52
7	35.8 ± 7.?	10.8 ± 1.8	1.81 ± .34	.32 ± .09	.26 ± .02	.18 ± .03	.04 ± .03	0.28 ± 0.28	.16 ± .62	3.45 ± .31
8	43.6	11.6	1.95	.22	.54	.12	.053	—	.62	3.56
9	26.4 ± .3	18.6 ± .1	3.53 ± .10	.51 ± .06	.08 ± .04	.22 ± .02	—	.21 ± .12	—	4.22 ± .0?

^{a} Weight loss, percent $= \left[\dfrac{(\text{initial wt. sample}) - (\text{final wt. sample})}{(\text{initial wt. sample})} \right] \cdot 100$

^{b} Volatile weight loss, percent $= \left[\sum_i \dfrac{(\text{milliequivalents})_i \, (\text{molecular wt.})_i}{(\text{initial wt. sample}) \, (100)} \right]$

^{c} H_2 determined by difference

^{d} Total meq volatiles determined from: $\text{meq/g} = \sum \left(\dfrac{(P)(V)}{(R)(T)} \right)_i \left(\dfrac{1}{\text{initial wt. sample}} \right)$

TABLE VI.- MAJOR VOLATILE PRODUCTS AT 23° C FROM THE PYROLYSIS
OF COMPOSITES IN VACUUM AT 700° C FOR 5 MIN

Composite	Quantity[a]						
	CO_2	CO	CH_4	HCN	C_6H_6	NH_3	H_2
1	88.9	10.1	11.8	6.5	3.9		3.3
2	67.8	15.1	20.2	8.6	4.7		3.5
3	84.9	14.0	14.7	7.6	3.1		4.3
4	97.7	14.3	17.0	7.0	4.7		3.2
5	83.2	14.6	14.4	7.0	3.3		3.9
6	84.5	11.8	12.8	5.9	4.8		3.4
7	79.6	9.0	4.2	4.9	3.1	4.8	0.3
8	85.5	6.2	9.4	3.2	4.1		1.2
9	155.3	14.3	1.3	5.9		3.6	

[a]Milligrams of volatile compound at 23° C per gram of initial sample.

TABLE VII.- LIMITING OXYGEN INDEX FOR COMPOSITE COMPONENTS

Composite	Composite component	LOI @ 23° C $O_2/(N_2 + O_2)$
1	PVF, phenolic A/7581 glass, phenolic B/120 glass	27
	aromatic polyamide-paper	32
	phenolic A/7581 glass, phenolic B/120 glass	26
	average	28.3
2	PVF, phenolic C/7581 glass, phenolic D/120, glass	45
	aromatic polyamide-paper	32
	phenolic C/7581 glass, phenolic D/120 glass	32
	average	36.3
3	PVF, phenolic C/7581 glass, phenolic C/120 glass	38
	aromatic polyamide-paper	32
	phenolic E/120 glass (2 plies)	33
	average	35.3
4	PVF, phenolic E/7581 glass, phenolic F/120 glass	47
	aromatic polyamide-paper	32
	phenolic E/120 glass (2 plies)	30
	average	35.3
5	PVF, phenolic F/7581 glass, phenolic F/120 glass	44
	aromatic polyamide-paper	32
	phenolic F/120 glass (2 plies)	32
	average	36
6	PVF, phenolic G/7581 glass, phenolic G/120 glass	74
	aromatic polyamide-paper	32
	phenolic G/120 glass (2 plies)	36
	average	47.3
7	Bismaleimide/120 glass/polyimide	99
	aromatic polyamide-paper	32
	quinone dioxime foam	100
	bismaleimide/120 glass/polyimide	99
	average	82.5
8	PVF, epoxy H/181E glass, epoxy H/120 glass	29
	aromatic polyamide-paper	32
	epoxy H/181 glass, epoxy H/120 glass	28
	average	29.6
9	Bismaleimide/181E glass/polyimide	62
	bismaleimide/glass	58
	carbon microballoons/bismaleimide	85
	bismaleimide/181 glass/polyimide	62
	average	66.7

TABLE VIII.- SMOKE EVOLUTION FROM COMPOSITE PANELS[a]

Composite	Specific optical density			No. of tests
	Ds, 1.5 min	Ds, 4.0 min	Dm	
	Flaming condition			
1	44.7 ± 13.3	51.7 ± 6.9	53.3 ± 8.9	3
2	3.9 ± 3.9	5.7 ± 4.1	8.6 ± 3.0	3
3	11.6 ± .9	13.6 ± 3.2	17.1 ± 6.4	3
4	7.1 ± 5.5	7.2 ± 5.3	8.4 ± 5.8	3
5	9.2 ± 8.2	12.2 ± 8.5	15.3 ± 8.5	3
6	8.8 ± 8.2	10.3 ± 7.3	16.0 ± 6.7	3
7	1.3 ± 1.0	4.5 ± 3.5	20.4 ± 4.7	2
8	48.3 ± 7.4	58.7 ± 6.2	59.1 ± 6.4	3
9	1.0 ± .7	4.9 ± 4.0	18.2 ± 7.9	4
	Nonflaming condition			
1	11.7 ± 4.5	19.2 ± 3.1	20.2 ± 3.3	3
2	.4 ± .2	.7 ± .2	1.6 ± .2	3
3	1.0 ± .7	1.2 ± .7	2.0 ± 1.3	3
4	.7 ± .1	0.7 ± .2	1.5 ± .2	3
5	1.2 ± .2	2.6 ± .3	5.2 ± .7	3
6	2.1 ± .8	2.2 ± .6	2.7 ± .7	3
8	2.6 ± .3	11.2 ± 1.1	19.0 ± 1.9	3

[a]NBS smoke chamber, 2.5 W/cm^2

TABLE IX.- SMOKE EVOLUTION FROM COMPOSITE PANELS FROM TWO CHAMBERS[a]

	Specific optical density								
	Ds, 1.5 min			Ds, 4.0 min			Dm		
Composite	Chamber A	Chamber B	Average	Chamber A	Chamber B	Average	Chamber A	Chamber B	Average
1	44.7	--	44.7	51.7	--	51.7	53.3	--	53.3
2	3.9	10.5	7.2	5.7	15.5	10.6	8.6	19.4	14.0
3	11.6	12.7	12.2	13.6	15.9	14.8	17.9	17.4	17.6
4	7.1	11.7	9.4	7.2	13.9	10.6	8.4	16.1	12.2
5	9.2	16.7	13.0	12.2	20.7	16.4	15.3	22.8	19.0
6	8.8	13.3	11.0	10.3	16.6	13.4	16.0	.7.3	16.6
7	1.3	--	1.3	4.5	--	4.5	20.4	--	20.4
8	48.3	57.6	53.0	58.7	57.5	58.1	59.1	58.3	58.7
9	1.0	--	1.0	4.9	--	4.9	18.2	--	18.2

[a]NBS smoke chamber, 2.5 N/cm^2, flaming

411

TABLE X.- RELATIVE TOXICITY OF PYROLYSIS PRODUCTS

FROM COMPOSITE PANELS[a]

Panel	Test	Time to incapacitation, min	Time to death, min
1	1	18.1	28.31 ± 1.67
	2	21.9	25.21 ± 3.51
	3	16.3	25.83 ± 1.02
	4	18.9	22.90 ± 1.42
	Mean	18.8	25.56 ± 2.76
2	1	20.9	26.74 ± .89
	2	21.0	24.90 ± .11
	Mean	21.0	25.82 ± 1.13
3	1	19.0	24.52 ± .69
	2	22.1	25.35 ± .97
	Mean	20.6	24.94 ± .90
4	1	20.5	24.17 ± 3.01
	2	19.3	23.48 ± .31
	Mean	19.9	23.82 ± 2.01
5	1	20.3	26.18 ± 1.83
	2	19.7	22.48 ± .52
	Mean	20.0	24.33 ± 1.17
6	1	17.1	19.65 ± .31
	2	20.9	22.90 ± .96
	Mean	19.0	21.28 ± .63
7	1	22.8	27.40 ± 1.46
	2	24.8	28.28 ± .70
	Mean	23.8	27.84 ± 1.16
8	1	18.5	27.50 ± 1.86
9	1	8.7	N.D.[b]
	2	N.I.	N.D.

[a]Four swiss albino mice in 4.2 liter exposure chamber, 30 min exposure; 1.0 g powdered specimens pyrolyzed at 40 C/min to 700° C.

[b]N.D. – No deaths.

[c]N.I. – No incapacit. :ion observed.

TABLE XI.- PROPERTIES OF COMPOSITES 8 AND 9

Property	Composite 8	Composite 9
Bulk density range, kg/m^3	90–96	109–113
Flatwise tensile strength, at 23° C, kN/m^2	690	500–610
Vertical burn test	Passes	Passes
Thermal conductivity at 23° C, $W \cdot cm/cm^2 \cdot °C$	$1.296 - 1.44 \times 10^{-3}$	4.932×10^{-4}
Smoke density (specific optical density, flaming condition, 2.5 W/cm^2	Ds 1.5 min:53.0 Ds 4.0 min:58.1 Dm:58.7	1.0 4.9 18.2
Limiting oxygen index, $O_2/(N_2 + O_2)$	Epoxy-fiberglass:29 Aromatic polyamide:32 Composite: 29.6	Bismaleimide-fiberglass/ Polyimide:62 Carbon microballoons, Bismaleimide:85 Bismaleimide-fiberglass:58 Composite:66.7

413

TABLE XI.- Concluded

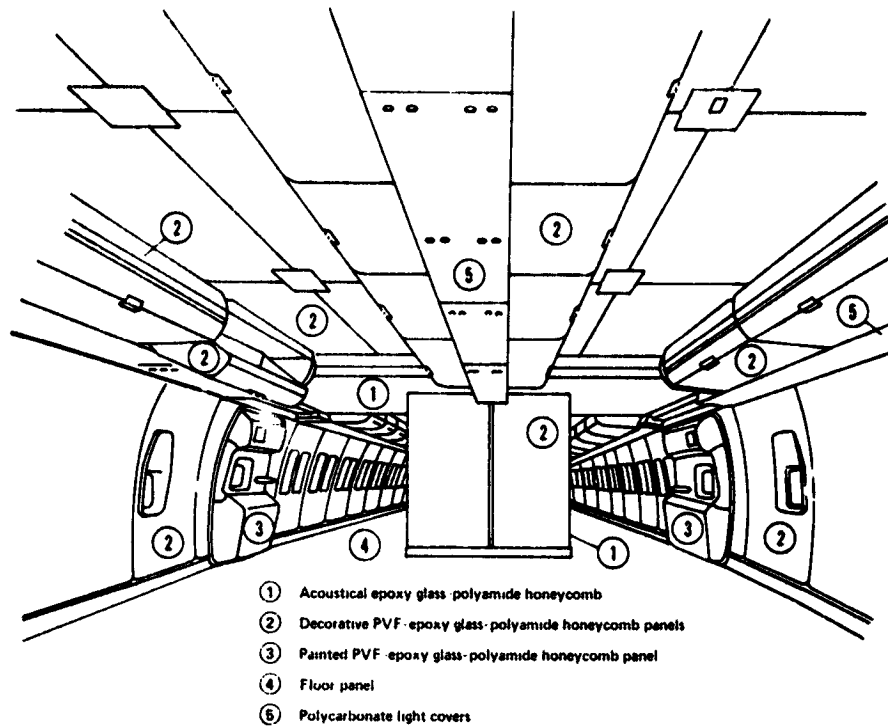| Property	Composite 8	Composite 9
Relative toxicity of pyrolysis products (1.0 g, 40° C/min to 700° C, 4 mice in 4.2 liter exposure chamber, 30 min exposure), time to incapacitation; time to death (min)	18.5; 27.5 ± 1.86	>30; >30
Fire endurance, NASA Ames T-3 test, time to reach backface temp. of 204° C at front face heat flux of 10.4–11.9 W/cm^2	2 min 20 sec	7 min 45 sec
Volatiles at 23° C from pyrolysis in vacuum at 700° C for 5 min Mg of volatile per gram of initial sample	CO_2: 85.5 CO: 6.2 CH_4: 9.4 HCN: 3.2 C_6H_6: 4.1 NH_3: -- H_2: 1.2	155.3 14.3 1.3 5.9 -- 3.6 --
TGA, percent weight remaining at 700° C (N_2, 10° C/min)	51.0	73.5

Figure 1.- Typical wide body interior materials.
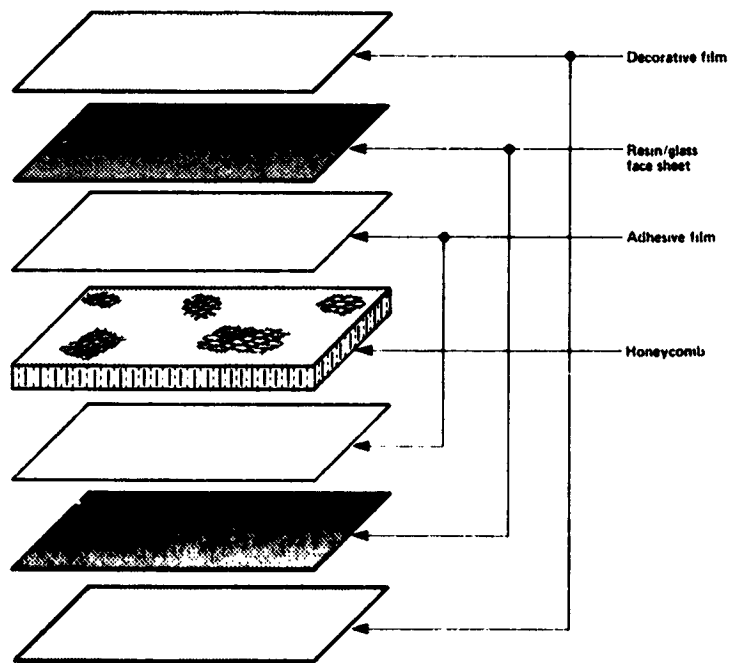
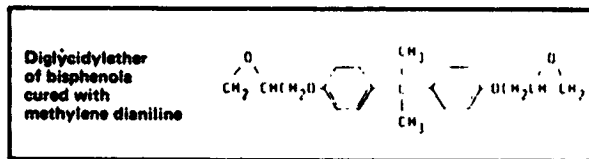Figure 2.- Typical composite configuration of aircraft interior panels.

Composites 1—6

Phenolic

Composite 8

Diglycidylether
of bisphenols
cured with
methylene dianiline
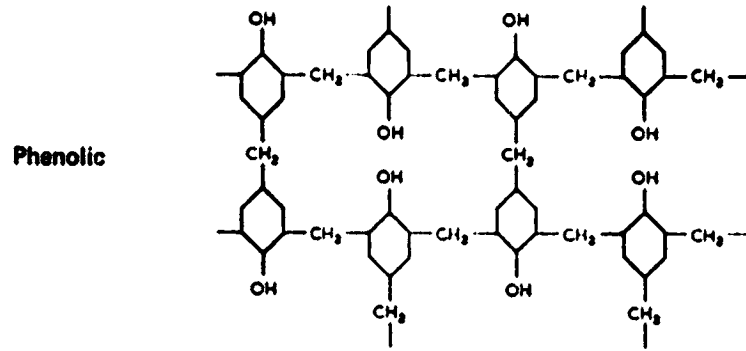
Composites 7 and 9

Bismaleimide
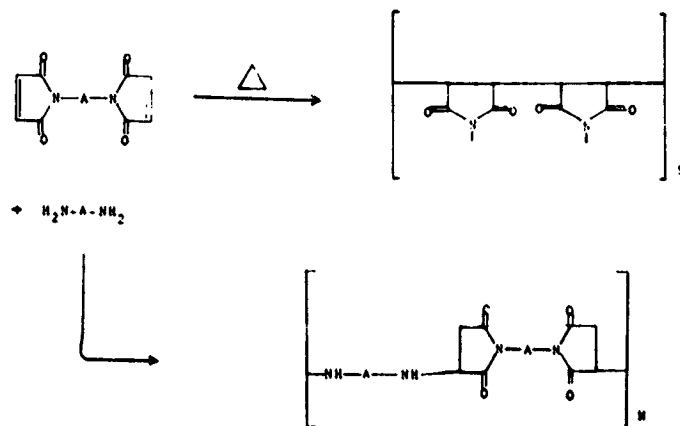
Figure 3.- Chemical structure of laminating resins.

Prepare carbon microballoons

Disperse in solvent
- Break-up caking
- Deagglomerate
- Screen

- Phenolic microballoons
- 4 hr @ 816°C
- Cool to 23°C

Impregnate honeycomb core
- Vacuum impregnate
- Dry 93°C
- Weigh

Prepare bismaleimide solution
- 50% solution in N-MP

Apply polyimide binder
- Dilute bismaleimide solution
- Brush
- Cure 2 hr @ 204°C

Prepare prepreg
- B-stage
- Resin content

Assemble panel structure
- Polyimide adhesive
- Press cure
- 177°C
- Post cure
- 2 hr @ 254°C

Cure facesheets
- Vacuum bag
- Bleeder cloth
- 1 hr @ 177°C

Figure 4.- Fabrication process for composite 9.

Polyimide honeycomb to be filled

Fine-mesh screen

Aluminum support honeycomb

Vacuum pump

Vacuum reservoir

Vacuum filling box

Solvent recovery trap
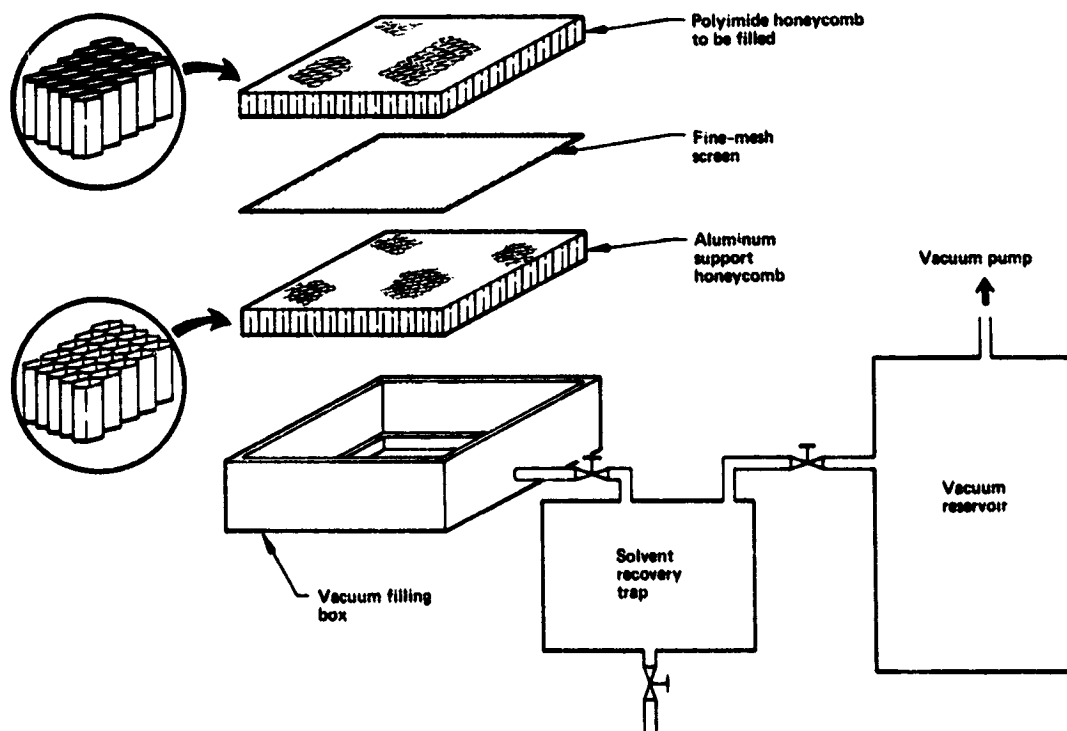
Figure 5.- Honeycomb core impregnation equipment.

417
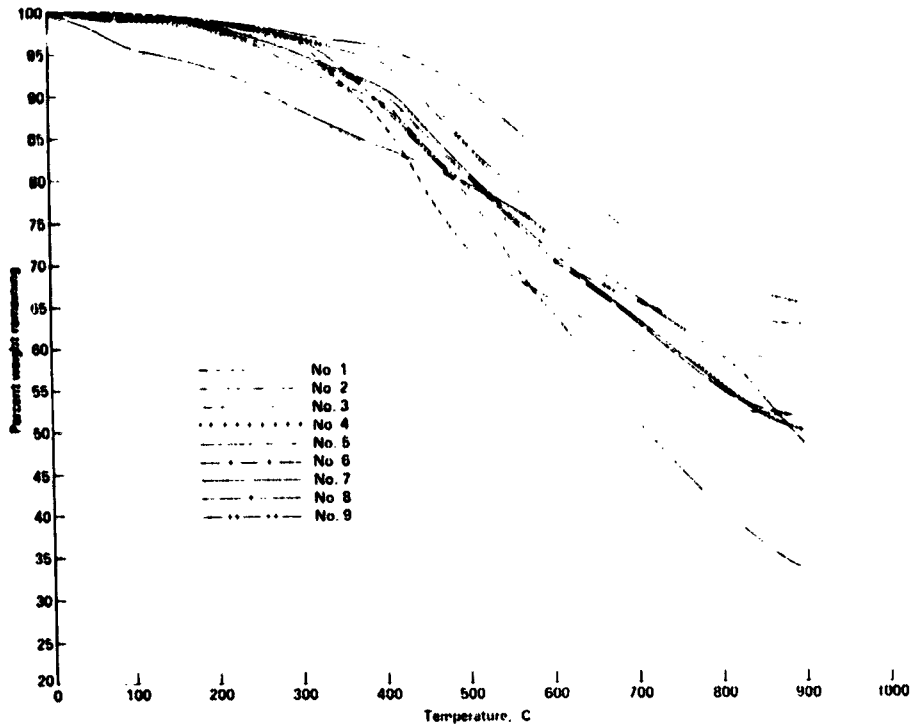
Figure 6.- Dynamic thermograph of composites 1-9 (heating rate 10° C/min, N_2).
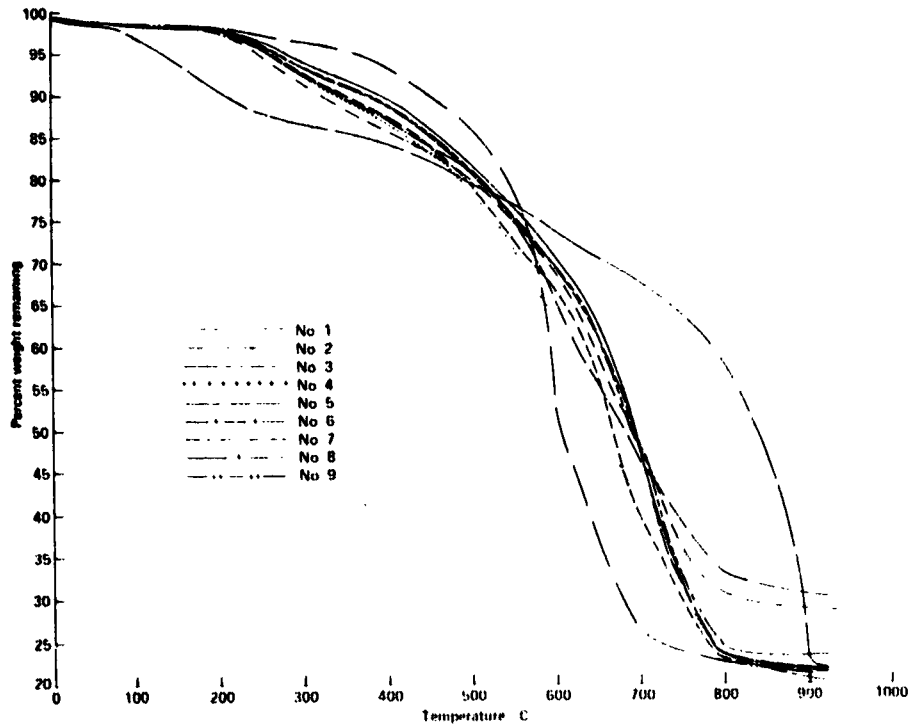
Figure 7.- Dynamic thermograph of composites 1-9 (heating rate 10° C/min, air).

418
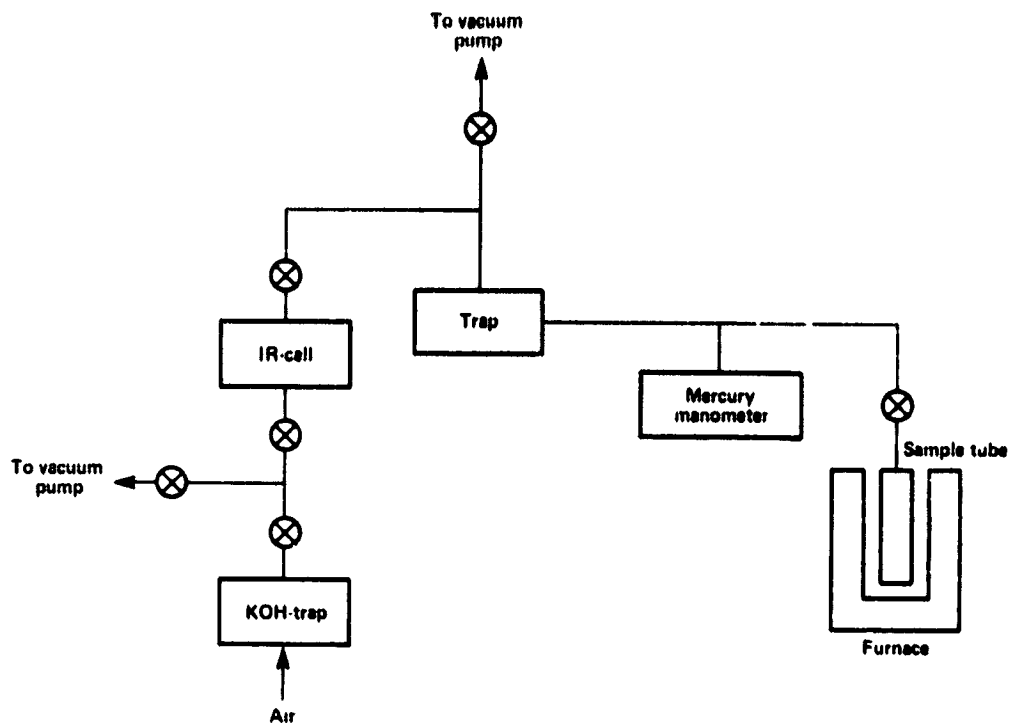
Figure 8.- Apparatus for pyrolysis of materials.

Typical heat flux at (A) 10.4 - 11.9 W/cm^2
Typical temperature at (A) 700 - 900 C

Figure 9.- NASA Ames T-3 thermal efficiency apparatus.
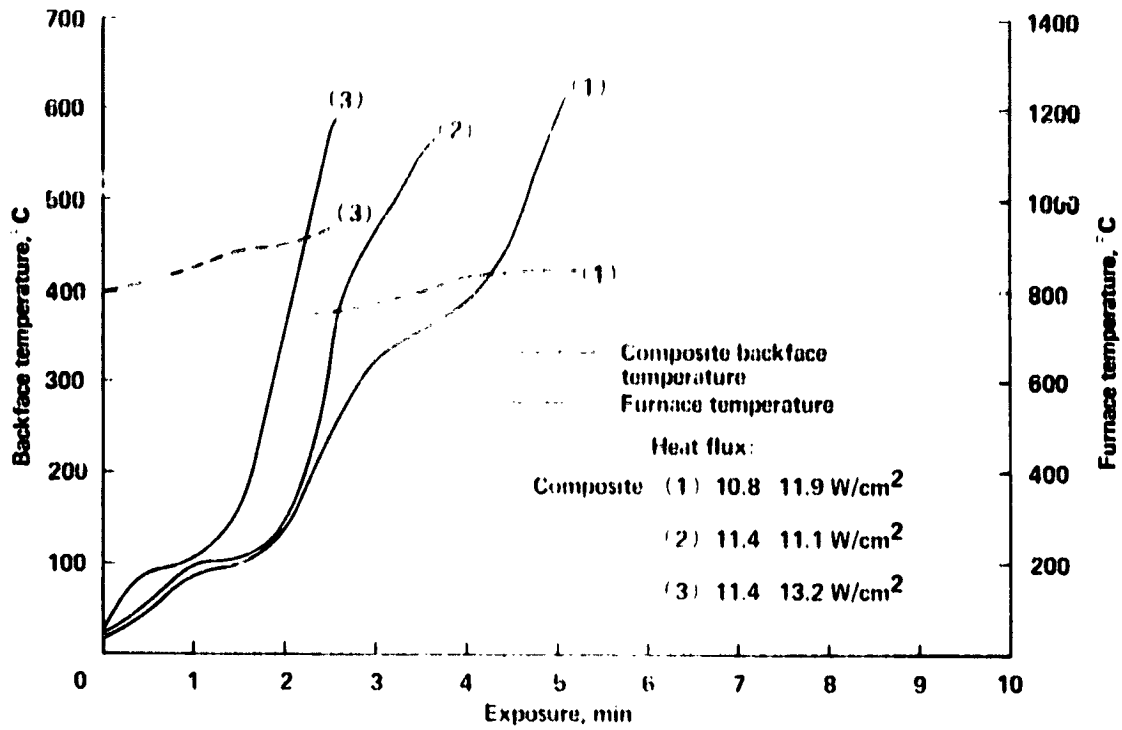
Figure 10.- Thermal efficiency of composites 1-3.

Figure 11.- Thermal efficiency of composites 4-6.

Figure 12.- Thermal efficiency of composites 7-9.

Figure 13.- Pyrolysis toxicity apparatus.

Figure 14.- Effect of char yield of composites on smoke evolution.

Figure 15.- Effect of char yield of composites on limiting oxygen index.

CONCEPTS FOR IMPROVING TURBINE DISK INTEGRITY

Albert Kaufman

NASA Lewis Research Center

SUMMARY

The trend toward higher turbine-blade tip speeds and inlet gas temperatures makes it increasingly difficult to design reliable turbine disks that can satisfy the life 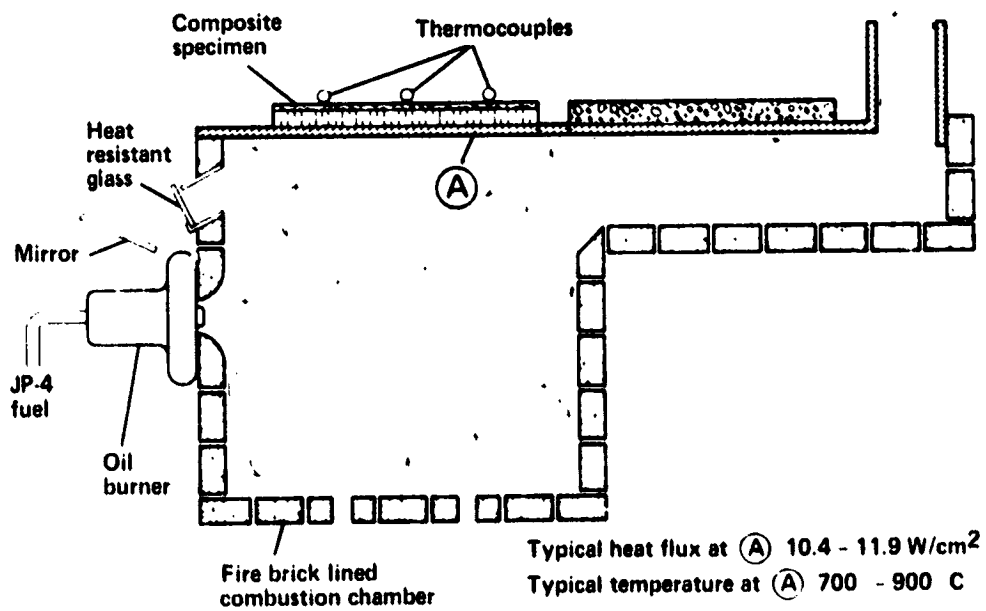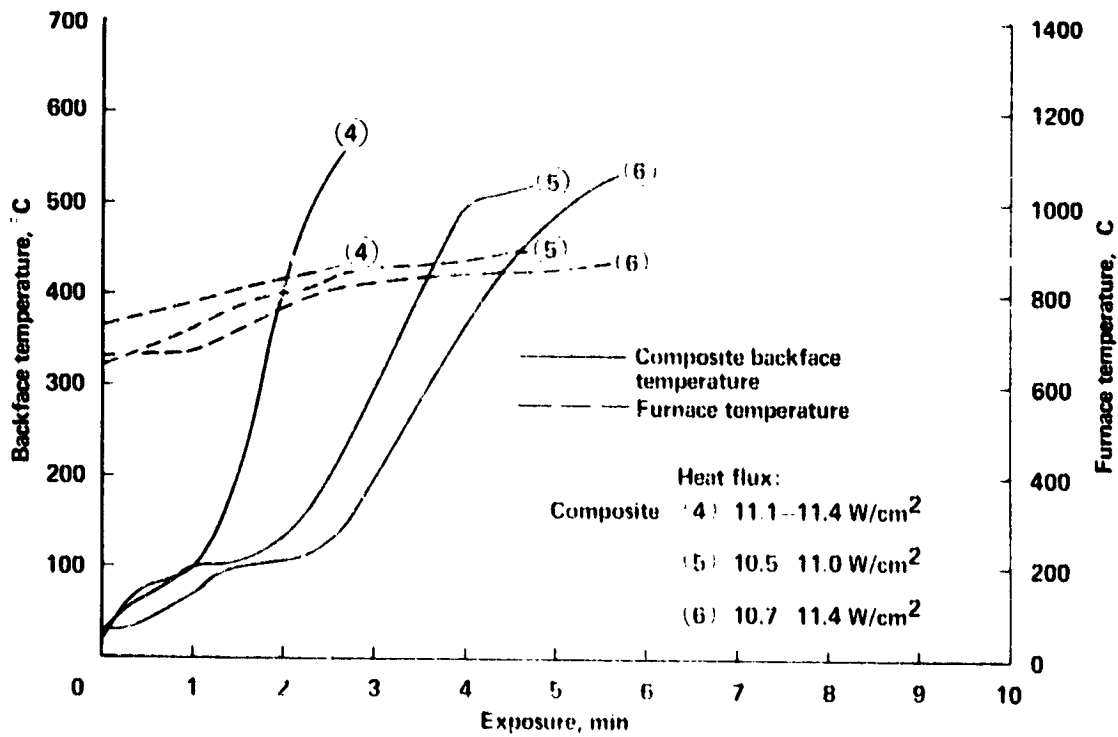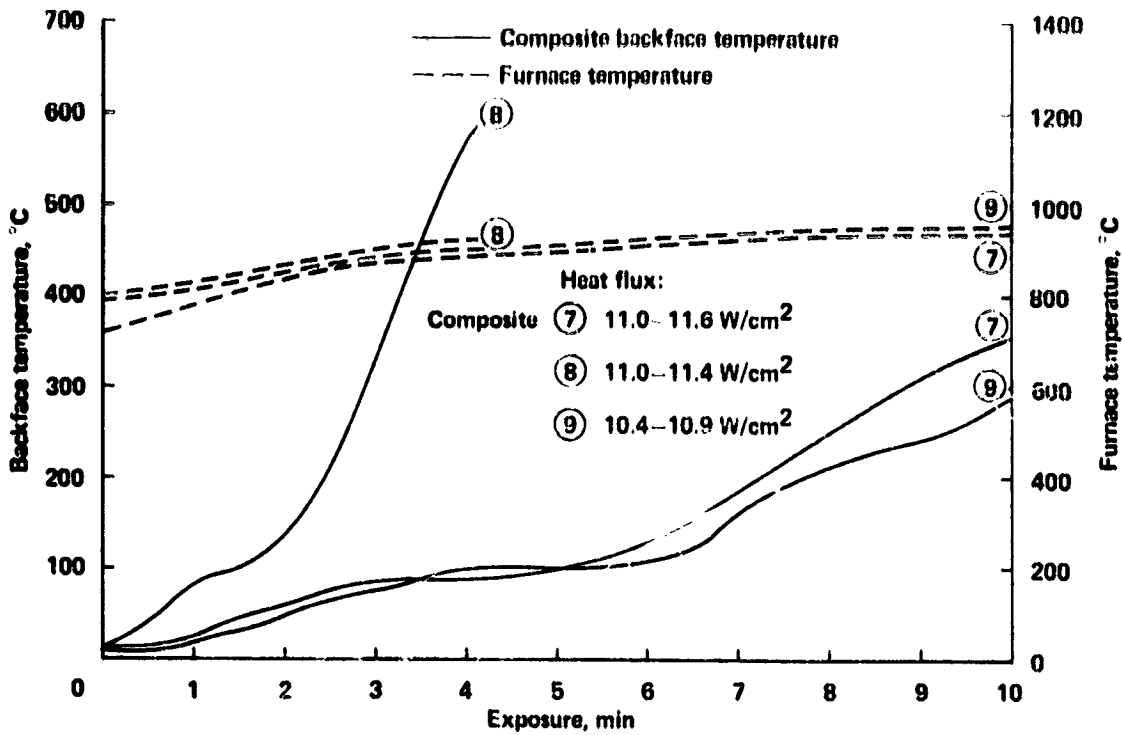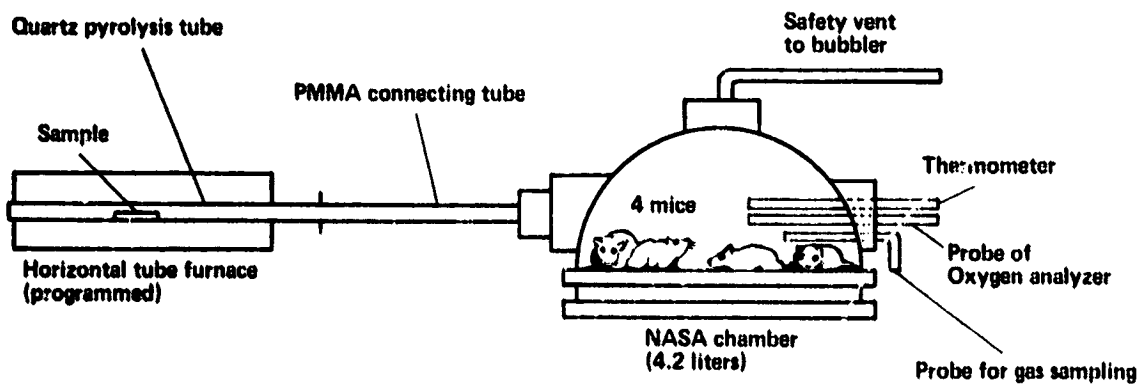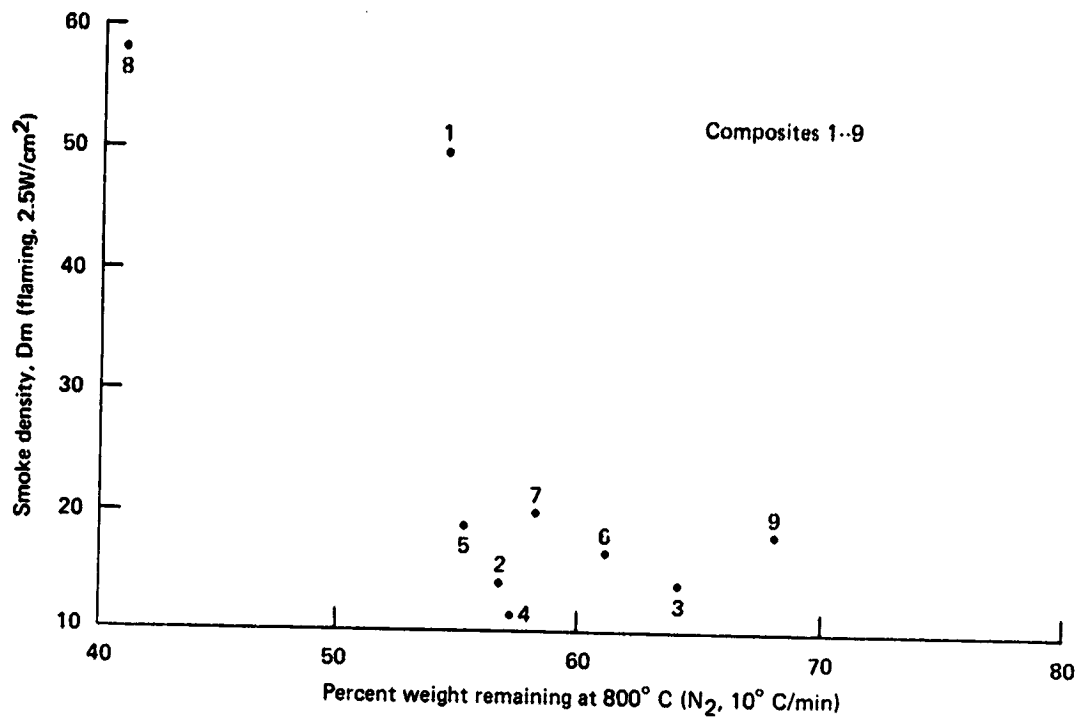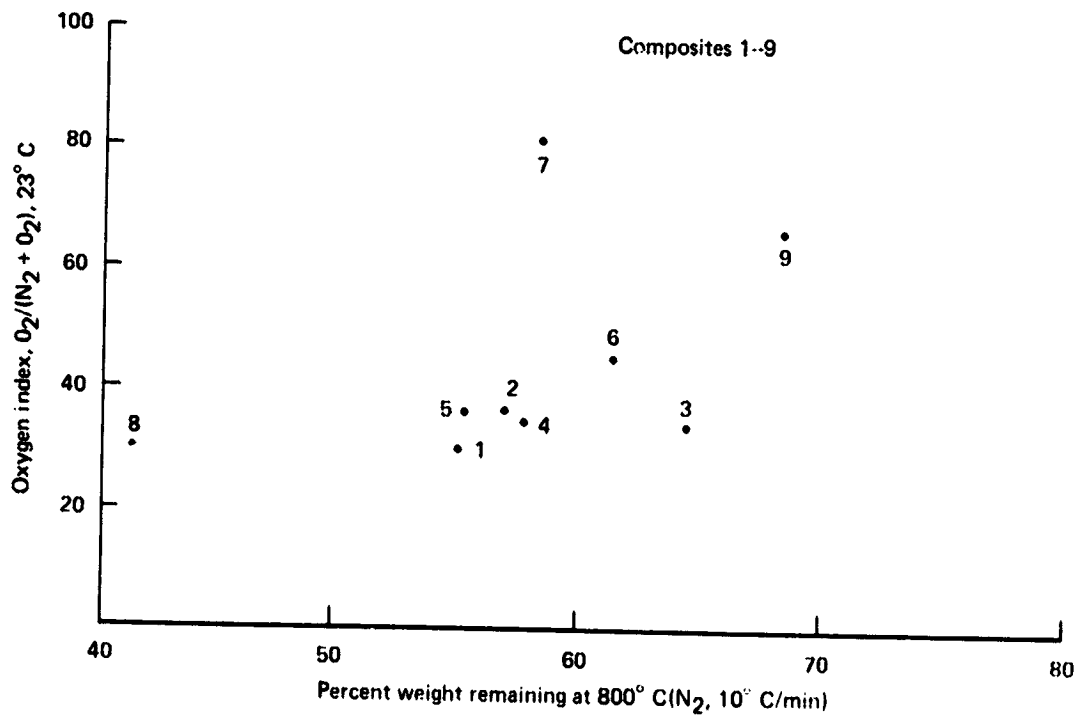and performance requirements of advanced commercial aircraft engines. Containment devices to protect vital areas such as the passenger cabin, the fuel lines, and the fuel tanks against high-energy disk fragments would impose a severe performance penalty on the engine. The approach taken in this study was to use advanced disk structural concepts to improve the cyclic lives and reliability of turbine disks. Analytical studies were conducted under NASA contracts by the General Electric Company and Pratt & Whitney Aircraft to evaluate bore-entry disks as potential replacements for the existing first-stage turbine disks in the CF6-50 and JT8D-17 engines. Results of low-cycle fatigue, burst, fracture mechanics, and fragment energy analyses are summarized for the advanced disk designs and the existing disk designs with both conventional and advanced disk materials. Other disk concepts such as composite, laminated, link, multibore, multidisk, and spline disks were also evaluated for the CF6-50 engine.

INTRODUCTION

A disk burst is one of the most catastrophic failures possible in an aircraft engine. Flight failures of disks in commercial airliners have caused fires, rupture of fuel tanks, penetration of passenger cabins, wing damage, ingestion of disk fragments by other engines, and aircraft control problems (ref. 1).

Aircraft engine companies generally endeavor to use conservative design practices and modern quality control procedures in producing turbine disks. However, failures occur because of design errors, undetected manufacturing defects, uncontrollable operating factors, errors in engine maintenance and assembly, and failure of other engine components. To attempt to design turbine disks to preclude failure from any of these causes would result in prohibitively low allowable stresses. Containment devices to protect vital areas of the aircraft against high-energy disk fragments would impose severe performance penalties on the engine.

The approach taken in this program was directed toward improving turbine disk reliability by using more advanced structural concepts to increase low-cycle fatigue life, to impede crack propagation, and to reduce fragment energies that could be generated

in the event of a disk failure. This paper reports the results of NASA-sponsored ana-
lytical studies by the General Electric Company and Pratt & Whitney Aircraft (refs. 2
and 3) to evaluate bore-entry disks as potential replacements for the existing first-stage
turbine disks in the CF6-50 and JT8D-17 engines, respectively; these engines were
selected because of their extensive use in commercial passenger aircraft. Other con-
cepts such as composite, laminated, and multidisk designs were also studied for the op-
erating conditions of the CF6-50 engines.

The bore-entry disks were compared with the existing disks (henceforth called the
"standard disks") on the basis of cycles to crack initiation and overspeed capability for
initially unflawed disks and on the basis of cycles required to propagate initial flaws to
failure. Comparisons were also made of the available kinetic energies of possible burst
fragments. All of these comparisons were also made for the standard disk with the ma-
terial of the bore-entry disk so that improvements resulting from changes in material
properties could be distinguished from those resulting from structural design changes.

DISK CONCEPTS

CF6-50 Turbine Disk Designs

The standard disk and the disk concepts considered as potential replacements are
illustrated in figure 1. The standard disk (fig. 1(a)) is machined from an Inconel 718
(Inc-718) forging. Local bosses on both sides of the disk provide reinforcement around
the bolt holes to increase the low-cycle fatigue life at the hole rims. Cooling air from
the compressor is channeled through the shaft, cools the disk bore, is pumped up
radially between the stage 1 and 2 rotors, cools the aft side of the disk between the bolt
holes and rim, and then enters the blades through openings in the dovetails.

The bore-entry disk (fig. 1(b)) is a two-part disk of integral construction. The two
disk halves are connected by radial webs for channeling coolant up the center of the disk
from the bore to the blades. Among the advantages of the bore-entry concept are im-
proved cooling effectiveness, reduced axial thermal gradients, and increased resis-
tance to crack propagation in the axial direction. One of the main attractions of the
bore-entry concept for the CF6 program was that it lent itself to a redundant construc-
tion where the disk would be overdesigned so that if half was failing, the undamaged disk
half would be able to assume a larger portion of the load and sustain the damaged part;
however, this would require a substantial increase in total disk weight. The integral
bore-entry disk would be fabricated from a single-piece forging of René 95 alloy with the
material between disk halves removed by electrochemical machining.

The composite disk (fig. 1(c)) uses high-strength filament or wire hoops to provide
most of the load-carrying ability of the disk except at the dovetail attachments. The

424

hoops would have to be pretensioned in order to assure an even load distribution among the filaments; this could be accomplished by filament winding, by interference fitting, or by the selection of filament and matrix materials so that the desired hoop pretension would be applied by differential thermal expansion under engine operating conditions.

In the laminated design (fig. 1(d)), a disk is constructed by bolting together a large number of sheet-metal laminates. A stepwise variation in thickness provides more laminates at the rim and bore but leaves gaps between laminates in the web region. In the link design (fig. 1(e)) a disk is constructed of pinned sheet-metal link segments. Both the laminate and link concepts are directed toward low-cost fabrication, isolation of propagating cracks, and generation of small burst fragments rather than toward improving disk life.

The multibore disk (fig. 1(f)) separates the highly stressed bore region into a number of circumferential ribs in order to prevent a crack or flaw at the bore from propagating axially. At the ends of the ribs, the tangential stresses due to centrifugal loading would be less and, therefore, the crack propagation rate should be slower than at the bore of the standard disk.

The purpose of the multidisk design (fig. 1(g)) is to obtain improved disk cooling and to provide for a redundant construction by transference of loads from a failed disk member to the undamaged ones through the bolts. The spline disk (fig. 1(h)) is essentially a two-piece design where the members are coupled through splines on their center faces. In order to counter the tendency of each disk half to straighten out due to the lack of axial symmetry, the splines would have to be radially interlocked through pins. The mechanical coupling of the multidisk and spline designs prevents cracks in one disk member from propagating to another.

These concepts are described in more detail in reference 2.

JT8D-17 Turbine Disk Designs

The standard disk shown in figure 2(a) is machined from a Waspaloy forging. Cooling air is bled from the combustion chamber liner and discharged at high velocity through nozzles toward the front side of the disk near the rim. The cooling air is delivered to the blades through angled holes at the disk rim. These holes result in elliptical exit openings with high stress concentrations; these are the limiting low-cycle fatigue locations.

A split-bonded, bore-entry concept was selected as a possible replacement for the standard disk. As with the integral bore-entry disk (fig. 1(b)) for the CF6-50 turbine, cooling air would be introduced at the bore, would be pumped up radially through channels formed by radial webs, and would enter the blades through openings in the bases. The two halves of the bonded bore-entry disk would be fabricated from separate forgings

425

of Astroloy and diffusion brazed together at the center surfaces of the radial webs. Dovetail broaching and final machining operations would be performed on the bonded disk assembly. The emphasis in the design of the bonded bore-entry disk was on improving the cyclic life without providing redundancy or increasing the disk weight.

DESIGN CONDITIONS

Design properties of the materials for the standard and bore-entry disks are presented in table I. The simplified flight cycles used for the cyclic heat transfer and stress analyses are shown in figure 3 for the CF6-50 engine and in figure 4 for the JT8D-17 engine. The flight cycle shown in figure 4 was the cycle used in the original design of the first-stage turbine disk for the JT8D-17 engine. The analytical methods are discussed in references 2 to 4.

DISCUSSION OF RESULTS

Preliminary Analyses of CF6-50 Disk Concepts

The results of preliminary analyses of the seven candidate design disk concepts are summarized in table II. Two of the designs, the laminated and link disks, proved to have excessive mechanical stresses and to be unsuitable for the CF6 operating conditions. The multibore design exhibited high transient thermal stresses in the region above the bore rims; therefore, the desired benefit of this design in retarding the propagation of rib flaws was not fully realized. Analysis of the multidisk design under various failure conditions revealed that the bolts could not contain a failed outer disk and that a crack in a center disk would reach critical length before the load could be redistributed to the undamaged members.

Only the bore-entry, composite, and spline disks appeared suitable for the CF6-50 turbine disk applications. From the standpoint of strength-to-density ratio, the composite disk was the most promising concept. However, the composite design is furthest removed from the current state-of-the-art of fabrication and material processing technology of any of the concepts considered. Because of the considerable fabrication development that would be required, the composite disk was not further considered. The spline disk presented special problems in analysis because the load distribution among the splines is dependent on the fabrication tolerances and it is not readily apparent how the loading would be redistributed should one disk-half fail. The integral construction of the bore-entry disk gives more assurance that the loading due to a failed disk member would be more evenly redistributed on the undamaged member. The integral bore-

426

entry concept was, therefore, selected for more detailed study to replace the CF6-50 standard disk.

Analyses of CF6-50 Standard and Bore-Entry Disks

The rim and bore average temperature responses during the flight cycle of the standard and bore-entry disks are shown in figure 5. Average effective stresses are also indicated at the start and end of takeoff, climb, cruise, and thrust reversal on descent. In both disks the maximum rim and bore temperatures occurred at the end of takeoff and climb, respectively; the maximum stresses also occurred in the bore at the end of climb.

Bore temperatures in the bore-entry disk are only slightly lower than bore temperatures in the standard disk since the bore is cooled in both cases. Rim temperatures were somewhat higher in the bore-entry disk because the coolant picks up some heat from the center faces of the disk, whereas the coolant only comes into contact with the sides of the standard disk near the rim.

Figure 6 shows the predicted cyclic lives to crack initiation in the initially unflawed standard and bore-entry disks. The limiting fatigue life of 30 000 cycles in the Inc-718 standard disk was at the aft dovetail post rabbet, where the side plate is fastened to the disk. This location was not further considered in the study because fragment generation due to failure would be limited to the dovetail post and adjacent blades. The next most critical location in the Inc-718 standard disk was at the bore with a predicted crack initiation time of 63 000 cycles. The initial FAA certified life of the first-stage turbine disk was 7800 cycles based on one-third of the minimum design life for the original design cycle, which was somewhat different from the simplified cycle used in this study; this FAA approved life is subject to increase as the result of ground tests of three fleet leader engines.

Calculated crack initiation lives for the René 95 standard and bore-entry disks were over 100 000 cycles. Since the crack initiation analyses were based on minimum guaranteed material properties, it is evident that even the standard disk is very conservatively designed provided the design conditions are not exceeded and the disks are initially unflawed.

The cyclic lives for cracks propagating from initial semielliptical surface flaws 0.635 centimeter (0.250 in.) by 0.211 centimeter (0.083 in.) to critical crack size are shown in figure 7 for the most critical locations in the three disks. Manufacturing flaws of this size should be readily detectable by modern nondestructive evaluation technique... However, in the past, large defects in turbine disks have occasionally escaped detection through human error and have caused problems in some military engines in flight.

The most critical locations for flaws were at the dovetail slot bottom in the Inc-718

standard disk and at the bore in the René 95 standard and bore-entry disks. Although the bore-entry disk showed an improvement in the minimum crack propagation life of more than 300 percent as compared with the Inc-718 standard disk, part of this increase was due to the superior strength properties of the René 95 alloy. If the effect of different materials was eliminated by comparing the bore-flawed bore-entry and René 95 standard disks, the improvement in crack propagation life resulting solely from the structural change was 136 percent.

The crack propagation lives given in figure 7 for the Inc-718 standard disk with a dovetail slot bottom flaw and the bore-entry disk with a bore flaw are only 5 and 20 percent of the FAA certified life of the disk. However, the probability of such large flaws occurring at critical locations and passing modern inspection procedures is statistically remote. Of greater significance is that a substantial improvement in the crack propagation life is added insurance against sudden catastrophic failure due to unforeseen design, manufacturing, maintenance, or operating problems. The overspeed burst margins of the bore-entry disk were 18 and 11 percent greater than for the Inc-718 and René 95 standard disks, respectively.

The redundant construction of the bore-entry disk resulted in an increase in weight of 66 percent over the standard disk. This extra weight is equivalent to an increase of 0.29 percent in installed specific fuel consumption (SFC) for an average DC10-30 aircraft flight.

The extra disk weight could also be added to the standard disk design to reduce the centrifugal stresses due to the blade loads. However, this mechanical stress reduction would probably be offset by the increased transient thermal stresses resulting from the slower thermal response of the bulkier disk. Also, a heavier standard disk would lack the redundancy of the bore-entry disk and would generate even higher fragment energies from a burst disk.

Some possible fragment patterns resulting from manufacturing flaws are illustrated in table III. The available kinetic energies that would be generated from these failures are also indicated. The highest energy fragments are caused by failures initiating at and propagating radially from the bore, as shown by the 120° disk and blade fragment pattern for the standard disk in table III. However, the redundant construction of the integral bore-entry disk would enable the undamaged member to contain such a failed part. The only possibility of a segment separating in this way would be if the radial failure propagated through a web to the opposite disk face; however, this is highly unlikely because the total thickness for all the webs is only 20 percent of the bore circumference and, as one web started failing, its load would be transferred to adjacent webs. The most likely mode of fragment generation is a rim fragment resulting from defects or crack initiation sites at the dovetail slot bottom or bolt hole rim. Based on spin pit experience, the rim-initiated crack would result in the loss of three dovetail posts and

four blades, as shown in table III. The fragment energy of the bore-entry disk rim fragment was only about 10 percent of the 120^0 disk segment that was assumed to be generated from a bore defect in the standard disk.

Analyses of JT8D-17 Standard and Bore-Entry Disks

The average temperature responses for the JT8D-17 turbine disks in figure 8 show consistently lower bore and rim temperatures throughout the cycle in the bore-entry disk as compared with the standard disk. The lower temperatures in the bore-entry disk were the result of its superior cooling effectiveness and the use of cooling air bled from the compressor midstage. Maximum temperatures and stresses occurred at the end of takeoff and climb, respectively.

Predicted cyclic lives for the initially unflawed standard and bore-entry disks are presented in figure 9. The FAA-certified life of the Waspaloy standard disk is 16 000 cycles based on the limiting low-cycle fatigue life at the exit of the cooling air hole. These results indicate an improvement in the cyclic crack initiation life of the Astroloy bore-entry disk of 88 percent over the Waspaloy standard disk and 67 percent over the Astroloy standard disk. The most critical location in the bore-entry disk was in the bore region at the entrance to the cooling air channel.

Defects and manufacturing flaws in the JT8D-17 turbine disks were considered for the critical locations indicated in figure 10. Subsurface flaws of 0.119 centimeter (0.047 in.) in diameter were assumed in the bore and web regions for all three disks; this diameter was selected because it is at the threshold of detectability by ultrasonic inspection. The web flaws shown in figure 10 were at the radius of maximum radial stress in the standard disks and at the radius of maximum axial stress at the bond surface in the bore-entry disks. The surface flaws at the disk rim or bore were assumed to be 0.081 centimeter (0.032 in.) in length.

The most critical location in the Waspaloy standard disk for a flaw was at the exit of the cooling air hole with a predicted crack propagation life of 2900 cycles. Substituting Astroloy properties for the Waspaloy reduced the calculated crack propagation life to 1150 cycles because of the lower ductility. However, there are indications that if the crack propagation data had included hold-time effects, the crack propagation life of the Astroloy standard disk would have been superior to that of the Waspaloy standard disk. This would also mean that the values given in figure 10 for the bore-entry disk are too low.

The calculated improvement in the minimum crack propagation life of the bore-entry disk over the Waspaloy standard disk was 124 percent. This improvement is significant in increasing the capability of the disk to survive uncontrollable factors that might result in catastrophic failure of conventionally designed disks. There was a

429

slight reduction in the overspeed burst margin of the bore-entry disk as compared with the standard disk because the overall disk weight was kept constant and that portion of it due to the radial webs was of small structural importance.

A substantial reduction in fragment energy is shown in table III for the JT8D-17 bonded bore-entry disk even though it was not designed for redundancy. This improvement would result from the confinement of the fragmentation from a bore flaw to one disk half; the other half would probably experience failure at the rim from the increased blade loading.

CONCLUDING REMARKS

Some advanced turbine-disk structural concepts have been analytically studied as potential replacements for the existing first-stage turbine disks in the CF6-50 and JT8D-17 engines. An integral bore-entry design was selected for more detailed evaluation for the CF6-50 engine as a result of preliminary analyses of seven disk concepts in-including composite, laminated, and multidisk designs. The integral bore-entry turbine disk was designed to improve disk life and to prevent high-energy fragmentation by using redundant construction at the expense of an increase in disk weight.

A split-bonded, bore-entry design was selected for evaluation for the JT8D-17 engine. This bore-entry disk was designed to improve disk life without redundance or an increase in disk weight.

Cyclic thermal, stress, and fracture mechanics analyses of the bore-entry and standard disks demonstrated that substantial improvements in the cyclic lives of both initially unflawed and flawed disks could be achieved with the bore-entry disk designs. The benefits of the advanced disk designs are influenced by differences in design philosophy, disk cooling method, fabrication procedure, and engine operating characteristics.

REFERENCES

1. National Transportation Safety Board Special Study: Turbine-Engine Rotor Disc Failures, 1975.

2. Barack, W. N.; and Domas, P. A.: An Improved Turbine Disk Design to Increase Reliability of Aircraft Jet Engines. NASA CR-135033 (R75AEG, General Electric Co.), 1976.

3. Alver, A. S.; and Wong, J. K.: Improved Turbine Disk Design to Increase Reliability of Aircraft Jet Engines. NASA CR-134985 (PWA-5329), 1976.

4. Kaufman, Albert: Advanced Turbine Disk Designs to Increase Reliability of Aircraft Engines. NASA TM X-71804, 1976.

430

TABLE I. - DESIGN PROPERTIES OF TURBINE DISK MATERIALS

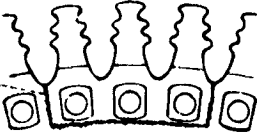| Property	CF6-50 engine		JT8D-17 engine	
	Inc-718	René 95	Waspaloy	Astroloy
Ultimate tensile strength, N/cm^2				
At 294 K	126 000	150 000	121 000	134 000
At 811 K	110 000	115 000	110 000	117 000
Yield strength (0.2 percent offset), N/cm^2				
At 294 K	101 000	116 000	86 000	97 000
At 811 K	92 000	110 000	56 000	87 000
Elongation at failure, percent				
At 294 K	20	8.5	24	19
At 811 K	30	8.5	21	14.5
1000-Hour rupture strength at 867 K, N/cm^2	68 000	103 000	79 000	84 000
Stress range for crack initiation in 10 000 cycles at 811 K (minimum stress, zero), N/cm^2	61 000	93 000	85 000	[a]85 000
Critical stress intensity factor at 894 K, $N/cm^{3/2}$	93 000	88 000	[a]68 000	[a]68 000
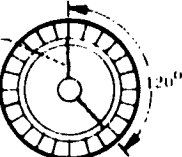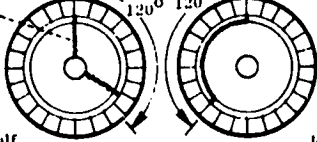
[a]Estimated.

TABLE II. - RESULTS OF PRELIMINARY ANALYSES OF CF6-50 DISK CONCEPTS

Disk concepts	Advantages	Disadvantages
Bore entry	Redundancy, improved thermal response, longer life	Increased weight to provide redundant design
Composite	Reduced stress levels, longer cyclic life	Limited material possibilities, fabrication development required
Laminated	Redundancy, low fragment energy, low cost	Excessive weight, high stresses at bolts and bolt holes, thermal mismatches between laminates
Link	Redundancy, low fragment energy, low cost	Excessive link stresses, difficult to seal disk to prevent coolant leakage
Multibore	Ribs prevent axial flow propagation at bore	High transient thermal stresses at rib outer diameter
Multidisk	Improved thermal response, some redundancy	Increased weight, bolts would fail if outer disk failed, no load shift if inner disk failed
Spline	Redundancy, longer life	Increased weight to provide redundant design, difficult to analyze load shift with one failed disk.

TABLE III - FRAGMENT ENERGIES OF TURBINE DISK DESIGNS

Disk design	Fragment pattern	Available kinetic energy J
CF6-50 standard disk	Initial flaw 120°	1 172 500
CF6-50 integral bore-entry disk	Initial flaw	110 500
JT8D-17 standard disk	Initial flaw 120°	678 600
JT8D-17 bonded bore-entry disk	Initial flaw 120° 120° Front half Rear half	513 000

432
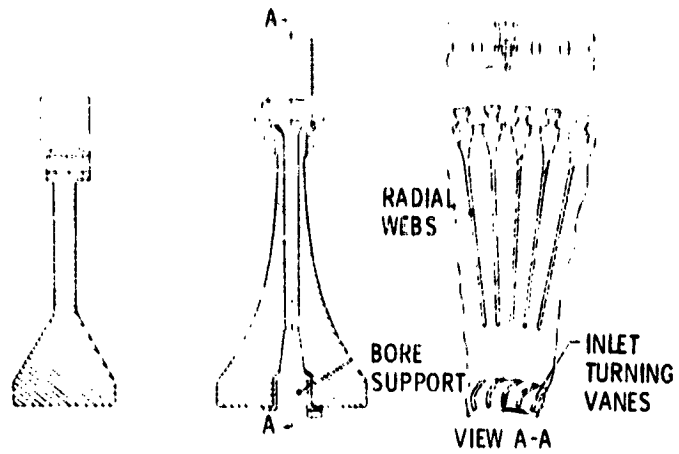
(a) Standard disk. (b) Integral bore-entry disk.
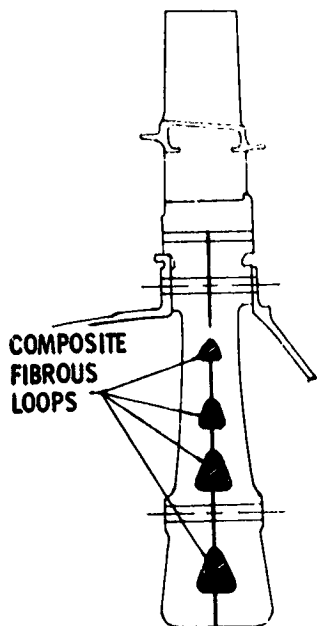
(c) Composite disk.   (d) Laminated disk.

Figure 1.- CF6-50 first-stage turbine disk designs.

433
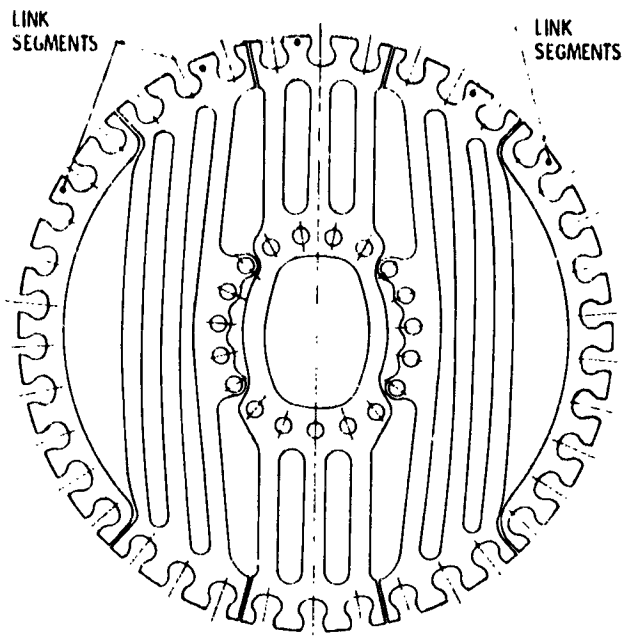
(e) Link disk (typically a disk would
    contain 20 to 40 layers each clocked
    axially relative to the next).
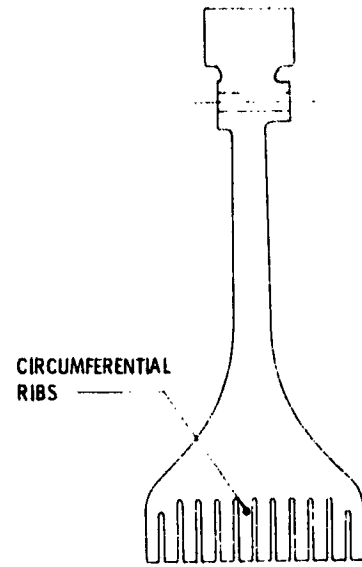
(f) Multibore disk.

Figure 1.- Continued.
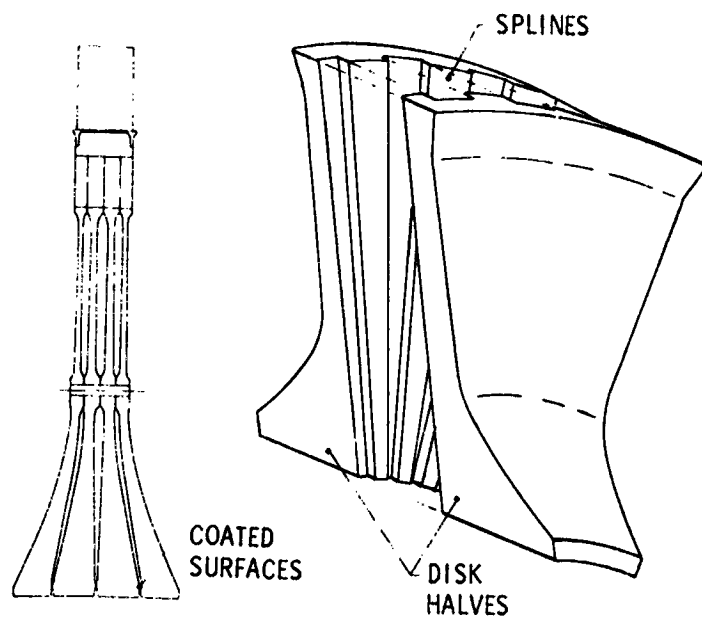
(g) Multidisk.   (h) Spline disk.

Figure 1.- Concluded.

COOLING AIR FLOW PATH

RADIAL WEBS

COOLING AIR FLOW PATH

A

A

COOLING AIR FLOW PATH

BONDED SURFACE

COOLING AIR FLOW PATH

SECTION A-A
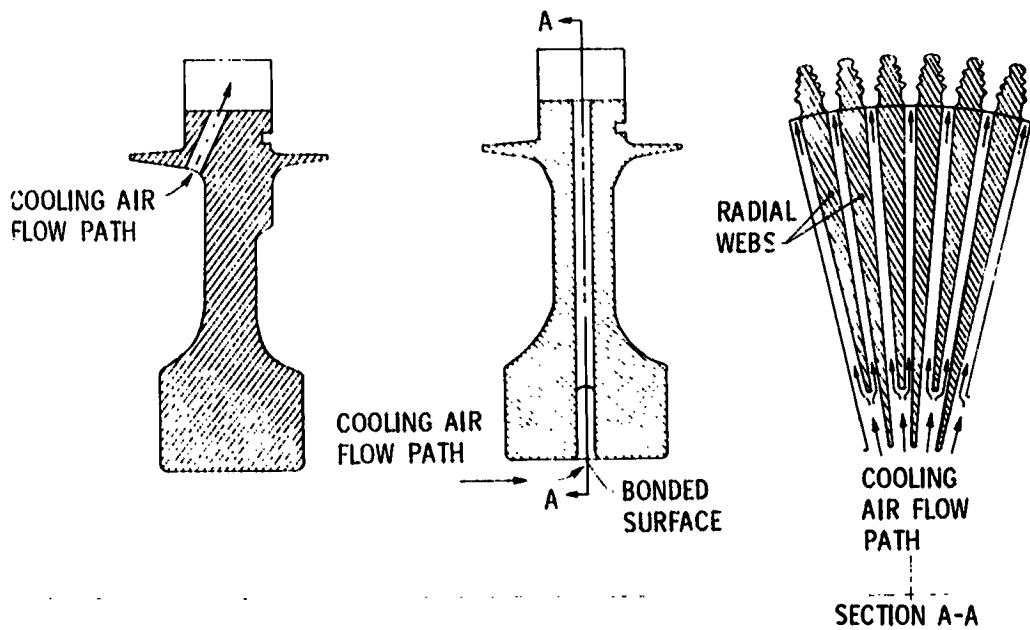
(a) Standard disk.   (b) Bonded bore-entry disk.

Figure 2.- JT8D-17 first-stage turbine disk designs.
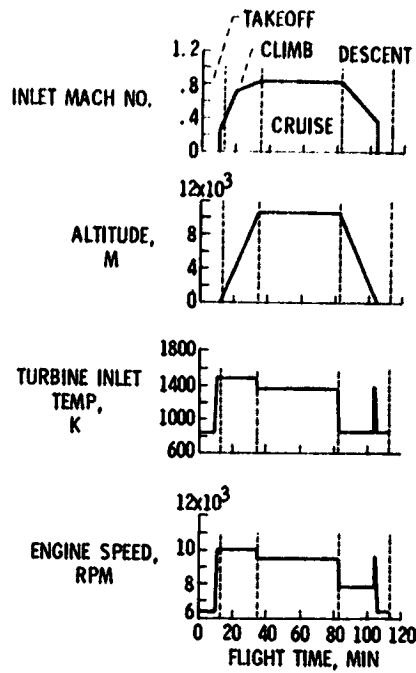
Figure 3.- CF6-50 simplified engine cycle.
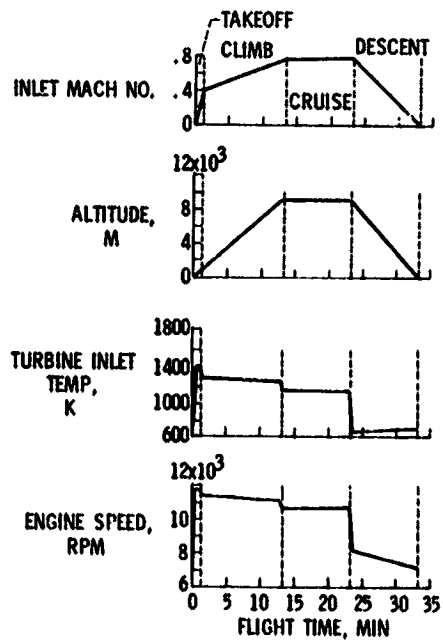
Figure 4.- JT8D-17 simplified engine cycle.
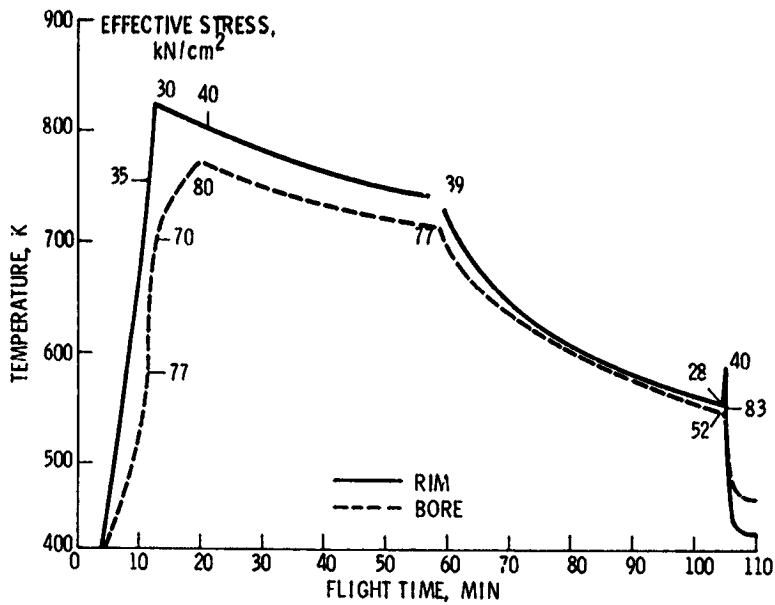
(a) INC-718 standard disk.
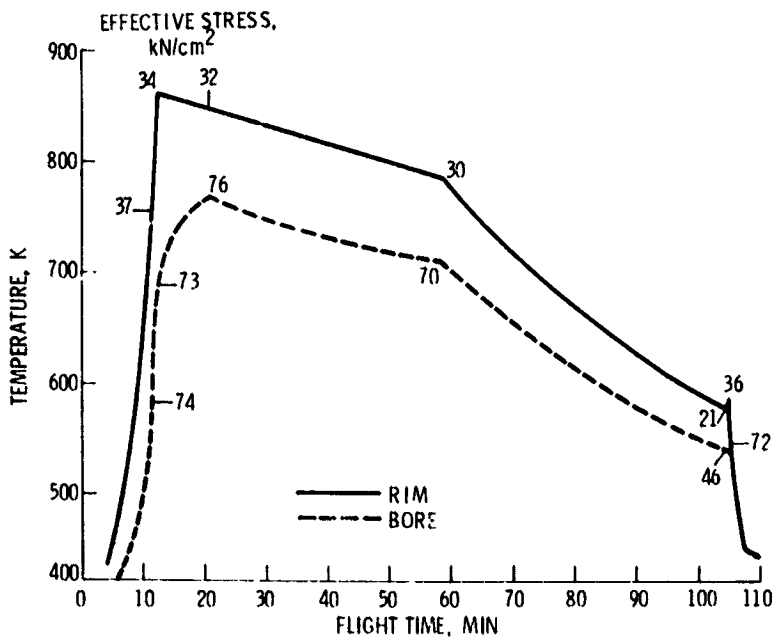
(b) Bore-entry disk.

Figure 5.- CF6-50 turbine disk temperature response.

(a) Standard disk (INC-718).   (b) Standard disk (René 95).   (c) Integral bore-entry disk (René 95).

Figure 6.- Crack initiation lives of CF6-50 first-stage turbine disk designs.

BURST SPEED, PERCENT OF MAXIMUM TAKEOFF SPEED: 126	134	149
WEIGHT CHANGE, PERCENT OF STANDARD DISK WEIGHT: ---	0	+66

(a) Standard disk (INC-718).   (b) Standard disk (René 95).   (c) Integral bore-entry disk (René 95).

Figure 7.- Crack propagation lives of CF6-50 first-stage turbine disk designs.

439
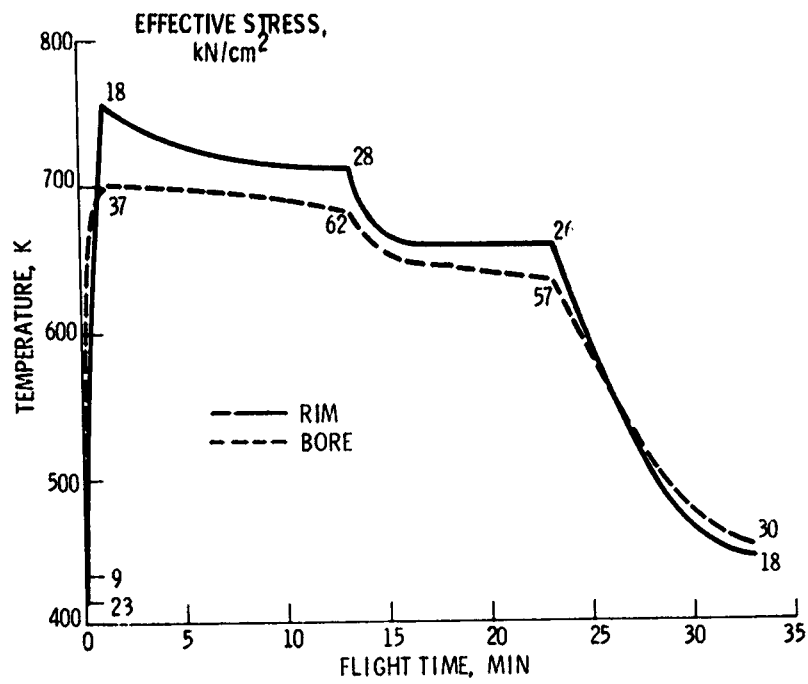
(a) Waspaloy standard disk.
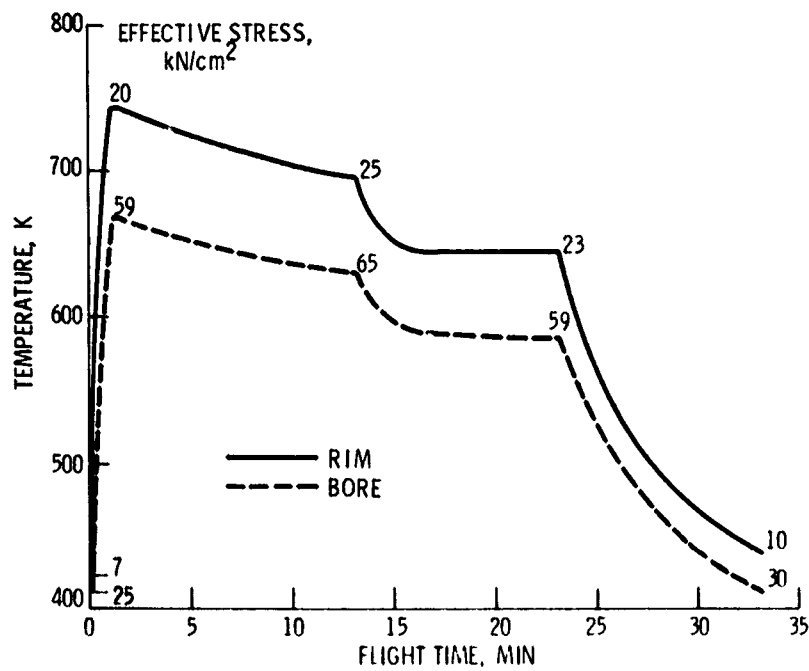
(b) Bore-entry disk.

Figure 8.- JT8D-17 turbine disk temperature response.

440
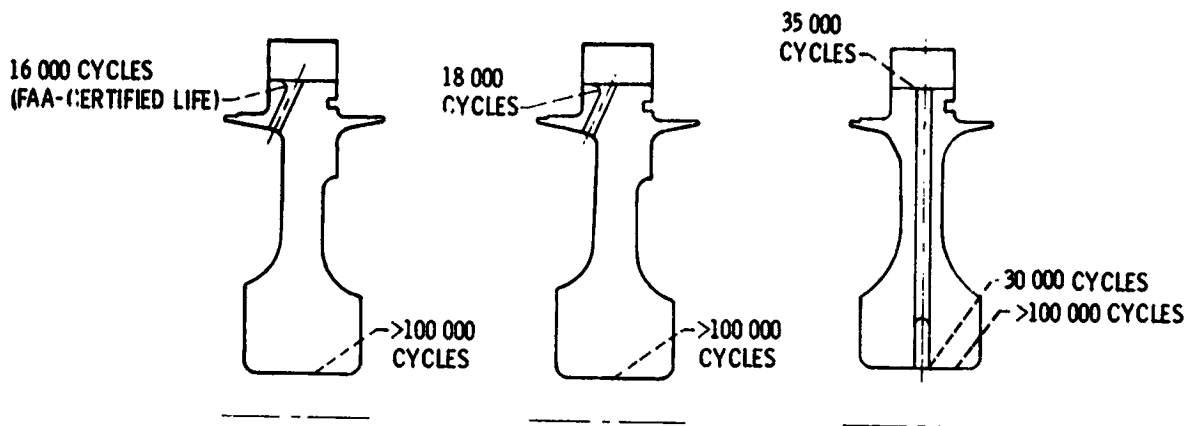
(a) Standard disk (Waspaloy). (b) Standard disk   (c) Bonded bore-entry
                                   (Astroloy).   disk (Astroloy).

Figure 9.- Crack initiation lives of JT8D-17 first-stage turbine disk designs.

(a) Standard disk   (b) Standard disk   (c) Bonded bore-entry
    (Waspaloy).   (Astroloy).   disk (Astroloy).
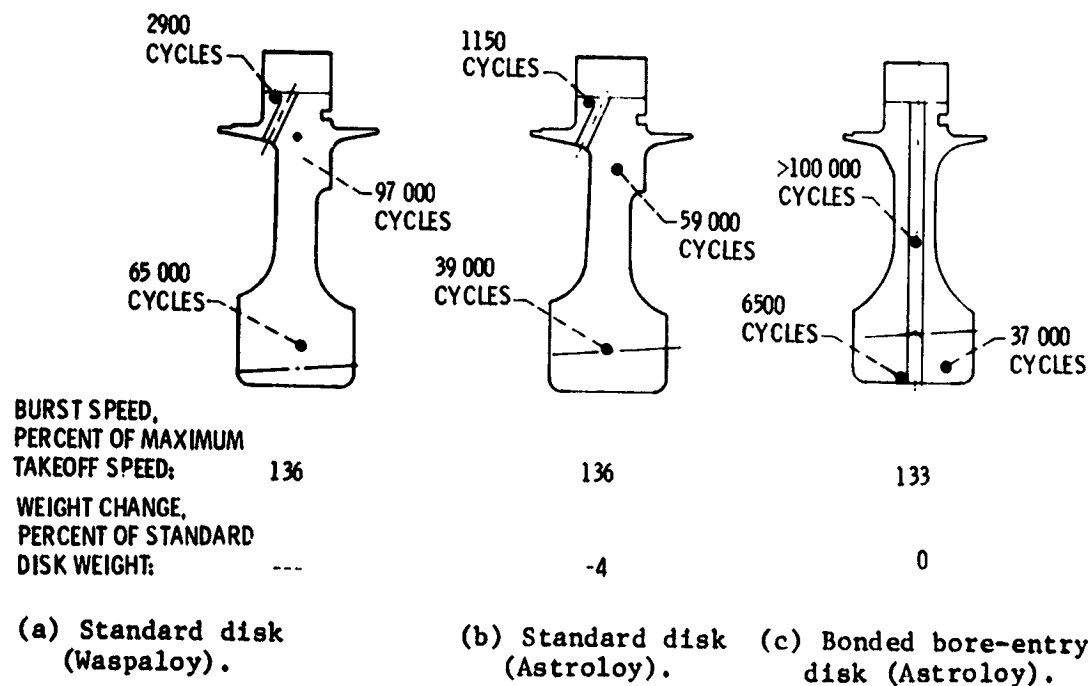
Figure 10.- Crack propagation lives of JT8D-17 first-stage turbine
                         disk designs.

441

N - 18104

AIRCRAFT ENGINE SUMP-FIRE STUDIES

William R. Loomis
NASA Lewis Research Center

SUMMARY

The problem of lubricant sump fires in aircraft engines is examined, and pertinent background subjects are discussed (i.e., the basic conditions required to start fires, the flammability limits for lubricant vapors, the importance of engine sump sealing systems, and the engine operating parameters that affect fires). Results of ongoing experimental studies are reported in which a 125-millimeter-diameter-advanced-bearing test rig simulating an engine sump is being used to find the critical range of conditions for fires to occur. Design, material, and operating concepts and techniques are being studied with the objective of minimizing the problem. It has been found that the vapor temperature near a spark ignitor is most important in determining ignition potential. At temperatures producing oil vapor pressures below or much above the calculated flammability limits, fires have not been ignited. But fires have been routinely started within the theoretical flammability range. This indicates that generalizing the sump-fire problem may make it amenable to analysis, with the potential for realistic solutions.

INTRODUCTION

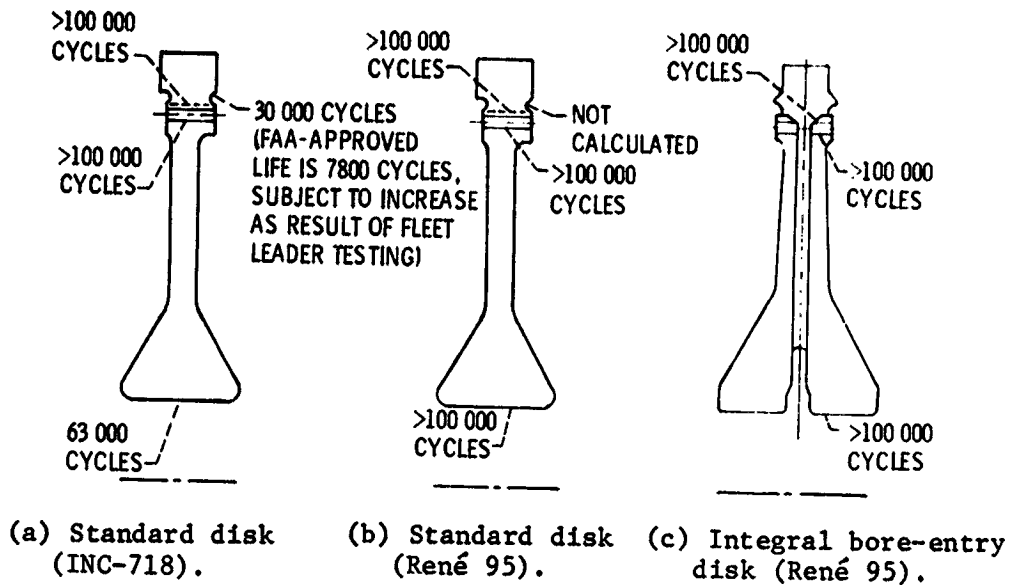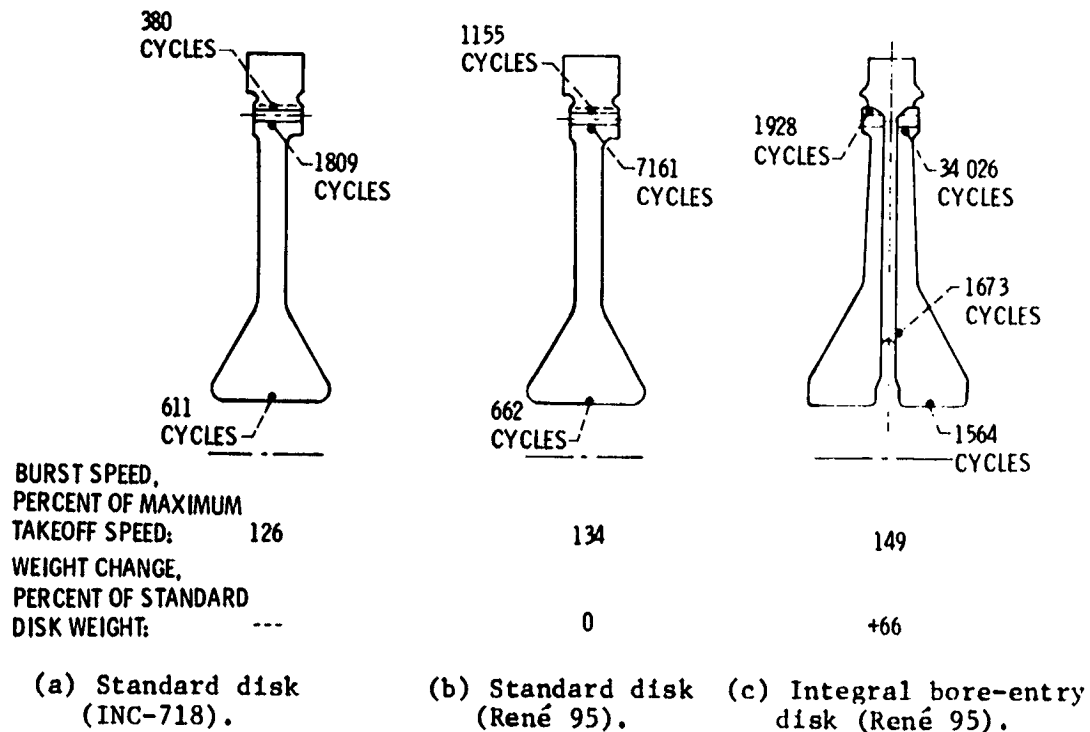Lubricant sump fires have been encountered in high-temperature operation of aircraft engines during flight, in engine ground studies, and in advanced laboratory studies of lubrication systems (ref. 1) and mainshaft seals (ref. 2). There is evidence that at least 31 incidents of sump fires or excessive heat in a bearing sump have occurred over a recent 5-year period in one widely used aircraft engine. Despite the reality of fires and near fires in operational aircraft engines, the environment found in engine sumps, with their high oil-recirculation rates, leads to the inherent contention that sumps in general are too oil rich for fires to occur in them. However, the trend toward developing engines with higher speeds and higher pressure ratios and their resulting higher energy levels suggests an impending increase in the frequency of sump fires.

Past sump fires have resulted from a number of different causes, which shows the need for study in this problem area. First, we must find the ranges of the principal operating parameters that are potential causes of sump fires and then experimentally

443

and analytically explore various operating, materials, and design concepts and tech-
ıs to reduce the fire potential. Accordingly, NASA is sponsoring a continuing re-
.rch program at SKF Industries (contract NAS3-19436) to realize these objectives,
wherein various means to mitigate sump fires are being studied on a 125-millimeter-
diameter-advanced-bearing test rig. This paper presents the status of this program
and its significant highlights.

The ultimate targets of this program are, by fiscal year 1978, (1) to acquire a
comprehensive understanding of sump-fire problems and (2) to develop methods for
eliminating, reducing, or controlling fires in current and proposed aircraft engines.

BACKGROUND

Before we discuss the past, current, and planned experimental sump-fire studies,
let us first consider background subjects important to this problem area. These in-
clude the basic conditions required for fires to start, the flammability limits for lubri-
cant vapors, the importance of the engine sump sealing systems, and, finally, those
engine operating parameters that affect fires.

Basic Conditions for Fires

Three basic conditions are required in an aircraft engine oil sump for fires to
occur. First of all, there must be a proper mixture of air and oil in vapor, mist, or
droplet form. If there is insufficient oil in the mixture (too lean) or excessive oil in
the mixture (too rich), a fire cannot start. Data taken from a report by Kuchta and
Cato of the U.S. Bureau of Mines (ref. 3) show that for an MIL-L-7808 (type I ester)
lubricant, fires cannot be ignited if air-oil weight ratios are above 29 to 1 or below
5.5 to 1.

Secondly, the air-oil mixture temperature must be above a critical value. The
mixture temperature must be above the flash point of the oil before a fire can be
ignited and above the fire point before a fire will continue to burn in the absence of an
ignition source. At temperatures above the autoignition temperature (AIT), no exter-
nal ignition source is required to start a fire. For the type II ester oil being used in
the test program the flash point, fire point, and AIT are 525 K (485° F), 558 K
(545° F), and 705 K (810° F), respectively (ref. 4).

Thirdly, there must be the presence of an ignition source of sufficient energy
level when the mixture temperature is below the AIT. Ignition sources include fric-
tional sparks and component surfaces heated by frictional rubbing, as well as hot
chamber walls and hot gases. Primary ignition sources within a sump are frictional

heating of failing seals, bearings, and other rubbing parts plus the leakage of high-temperature compressor discharge air into the sump area.

Flammability Limits for Lubricant Vapors

The concept of flammability limits for lubricant vapors is important and is illustrated in the lubricant flammability diagram shown in figure 1. At a given system temperature and pressure, there is an upper ratio and a lower ratio of oil $\underline{vapor}$ to air, known as the upper flammability limit (UL) and the lower flammability limit (LL), respectively, within which self-sustaining or self-propagating flames can be produced by an ignition source. At oil concentrations above the UL, the mixture is said to be too rich to burn; below the LL, it is too lean to burn (refs. 5 and 6).

It is worth emphasizing that it is the oil concentration in the $\underline{vapor\ state}$ that defines the flammability of the oil-air mixture. The maximum concentration of oil vapor is determined by its equilibrium vapor pressure at any given temperature. The equilibrium oil-air ratio is therefore the ratio of the vapor pressure of the oil to the air pressure in the chamber. The flow rates of air and liquid oil do not determine flammability except to the degree that they influence the temperature and thereby the vapor pressure. However, flow rates can profoundly influence the severity and propagation characteristics of a fire once it has been ignited.

Maximum burning velocity is achieved when a stoichiometric ratio C_s of oil vapor and oxygen exist in the chamber. This ratio is equivalent to the molar ratio of oil and oxygen in the balanced chemical equation for complete combustion of the oil. The stoichiometric ratio is always within the flammability range of the oil. It has been shown for many hydrocarbons that at 297 K (75° F)

$$LL_{297K(75°F)} = 0.55\ C_s \tag{1}$$

$$UL_{297K(75°F)} = 4.8\ C_s \tag{2}$$

The flammability range increases with temperature according to the following equations:

or

$$\left.\begin{aligned} LL_T &= LL_{297K}\left[1 - 7.2 \cdot 10^{-4}(T - 297)\right]\\ LL_T &= LL_{75°F}\left[1 - 4 \cdot 10^{-4}(T - 75)\right] \end{aligned}\right\} \tag{3}$$

$$\left. \begin{array}{l} UL_T = UL_{297K}\left[1 + 7.2 \times 10^{-4}(T - 297)\right] \\[8pt] UL_T = UL_{75^\circ F}\left[1 + 4 \times 10^{-4}(T - 75)\right] \end{array} \right\}$$

or   (4)

By definition, oils will not burn below their flash point. Therefore, for oils with flash points higher than 297 K (75° F), the LL and UL at 297 K (75° F), calculated from equations (1) and (2), have no physical meaning but can be used in equations (3) and (4) to estimate flammability limits above the flash point. The calculated LL line should intersect the vapor pressure-temperature curve near the flash point of the oil, and this temperature, T_L, is defined as the lower flammability temperature at equilibrium vapor pressure conditions. Similarly, an upper flammability temperature T_U exists where the calculated UL line intersects the vapor pressure-temperature curve.

The relation of calculated flammability limits to temperature for the type II ester lubricant is shown schematically in figure 1. Lubricant vapor pressure and concentration are given as a function of temperature. The region enclosed by the vapor pressure curve, the flammability limits, and the AIT line defines the temperatures and lubricant vapor partial pressure in air for which ignition sources can produce a self-propagating fire. Above the AIT, no ignition source is required.

Importance of Engine Sump Sealing

The potential fire conditions in an aircraft engine are greatly influenced by the efficiency of the engine sump sealing system. Figure 2 is a cross-sectional view of the sump for a typical engine bearing compartment. Here the essential problem is to protect the bearing sump from the hot environment, which is compressor discharge air at temperatures to 922 K (1200° F) and pressures to 242 N/cm^2 (350 psi). (The compressor discharge air is used to cool the high-pressure-turbine disks.) A buffer type of seal system is used and this requires three sets of labyrinth seals on each side of the bearing. Figure 3 is a simplified schematic of this sealing system. The buffer gas is seventh-stage compressor bleed air with a relatively low pressure of 55 N/cm^2 (80 psi) and temperature of 478 K (400° F); therefore, it can be allowed to leak through the inner labyrinth seal directly into the bearing compartment. This buffer gas thermally insulates the bearing compartment. The buffer system requires an overboard vent. The buffer gas flowing into this vent prevents the hotter compressor discharge air from getting into the bearing compartment. In some engines, the labyrinth seals next to the bearing compartment have been replaced with face-contact seals. This reduces leakage and results in lower specific fuel consumption. However, failure of either the labyrinth or face-contact seals could create conditions that would result in a

446

sump fire (i. e., a rubbing friction ignition source and a hot air-oil mixture). This fact stresses the importance of developing better and more reliable seals that could reduce the probability of sump fires occurring.

Engine Operating Parameters Affecting Fires

The basic parameters that control fire conditions in an engine bearing sump and the range of operating values that are being studied in the program are shown in table I. The parameters that can affect the ratio and temperature of a combustible mixture are

(1) Oil flow rate into the sump
(2) Oil inlet temperature
(3) Air leakage rate to the sump
(4) Air inlet temperature
(5) Shaft or bearing speed
(6) Ignition source and duration

Other parameters, such as sump volume and geometric configuration as well as bearing, shaft, seal, and housing temperatures and lubricant flammability, can also affect sump-fire susceptibility. In addition, the ratio of air leakage rate to sump volume is probably a critical parameter and should be considered for each system application.

EXPERIMENTAL ENGINE-FIRE TEST APPARATUS

In the test bearing program itself, a bearing test rig originally designed to study 125-millimeter-diameter aircraft main-shaft thrust bearings at high temperatures and speeds was modified to simulate an engine sump and to accommodate sump-fire testing. Figure 4 is a cross-sectional view of the bearing sump area. The rig was designed to create controlled rub and electric spark ignition sources and to provide for varying oil and air flows and temperatures and was instrumented to determine temperature profiles throughout the sump. Shown in figure 4 are the test bearing, a Monel baffle on the hot-air side of the bearing, the rub ignition mechanism, and the main seal life-off device that permits hot air to flow into the sump for fire ignition attempts.

RESULTS AND DISCUSSION

Preliminary Test Study

Test results from a preliminary study completed several years ago (ref. 7) had indicated that spontaneous combustion could not be obtained over the range of variables studied and that simulated engine fires could readily occur and be self-sustaining in a

wide range of parameters when an electric spark ignitor was used. A spark ignitor was used in most of the fire tests as an experimental, easily controlled means of producing fires. Other significant results are as follows:

Ignition from rubs by labyrinth seals and other component materials can cause sump fires. This was shown by the fact that fires were also obtained by using the rub ignitor mechanism in the test chamber. Bearing skidding and excessive seal interferences are potential fire sources and suggest that accidental fires in engine sumps may well arise from these causes.

Fire ignition is sensitive to location. It is likely that significant real differences in air-oil ratios exist in the various parts of the sump, which makes it difficult to achieve significant data on air-oil ratios. Indications from oil degradation products were that sump fires begin in localized and small regions of the sump and are influenced by baffles. Combustible volume grows slowly with the duration of the fire in response to local gas and oil mass flow conditions.

Nitrogen blanketing was effective in the immediate extinguishing of every test run fire once the fire had been detected.

A fire-baffle (Monel sheet) mitigation device on the hot side of the bearing not only prevented fire propagation, but also prevented bearing thermal seizure due to hot (922 K; 1200° F) gas flow directly into the bearing. Such baffles have practical significance.

Freon-113 flame snuffer injected into the lubricant flow was only marginally effective in controlling fires.

Current Test Study

In our current work in this program we are using some of the experimental techniques and testing facilities from the preliminary study. The objectives of this phase of the program are to make a more definitive determination of the critical ranges of lubricant and hot-air flow rates and other operating variables and thus find the flammability range of conditions (or envelope) where fires are likely to occur.

Results and conclusions from the current program to date are as shown in figures 5 to 7, where the basic parameters were varied over their full ranges in different combinations and a spark ignitor was used. Figure 5 presents hot-air flow rates as a function of temperature increase in the sump at a constant oil flow rate of 0.45 m³/hr (2 gal/min) and a temperature of 441 K (335° F). The higher the air flow rate, or the seal leakage, the more severe were the resulting fires. At low air flow rates, only minor fires if any were ignited. At medium air flow rates, non-self-sustaining fires were experienced, but at high air flow rates, self-sustaining fires were started. These self-sustaining fires spread more generally throughout the sump, with tempera-

448

ture increases as high as 556 K (1000° F) before extinguishment. However, fires could be ignited at all air flow rates evaluated under the proper set of conditions.

As illustrated in figure 6, where oil flow rates are plotted against air-oil mixture temperatures at a constant high air flow rate of 41 m^3/hr (24 stdft^3/min), the mixture temperature decreases with increasing oil flow rate. This suggests that more oil is mixing with the air. This difference was more pronounced at the higher air flow rates, pointing to a greater mixing of the oil and air at higher air flows.

No fires could be ignited when the mixture temperature was below the flash point temperature of the oil. However, the converse was not always true. Fires could not always be ignited when the mixture temperature was well above the flash point. (Refer again to fig. 6.) In one case, where no fire occurred when the air-oil mixture temperature was 611 K (640° F) at an oil flow rate of 0.23 m^3/hr (1 gal/min), an increase in the oil flow rate resulted in fires as the mixture temperature was decreased but not below the flash point temperature.

It is significant that all fires fell within the range of operating parameters for the flammability limits as predicted from combustion principles. If the vapor mixture temperatures can be held below the flash point of the lubricant in any regions of the engine where potential ignition sources are located, the fire problem will be much less acute, if not even eliminated.

As shown in figure 7, a series of runs were made at increasing oil inlet temperatures and with constant air flow rates as high as 41 m^3/hr (24 stdft^3/min) and air inlet temperatures as high as 814 K (1005° F). No fires could be ignited when a 0.45-m^3/hr (2-gal/min) oil flow was maintained except when oil inlet temperatures exceeded about 419 K (295° F). It should be stressed that these data are for specific stoichiometric conditions and results might differ for other combinations of air and oil flows and temperatures. If proper engine heat management can be achieved by using heat exchangers and other devices, the oil inlet temperature can be held to such a level that oil vapors will be at temperatures below the lower flammability limit.

Although there was evidence that the air-oil mixture in the sump was often too vapor rich to burn, it is presently considered that the best approach to minimizing sump fires is to design to produce mixtures too vapor lean to burn. This could possibly be done by injecting more oil (e. g., by increasing the oil recirculating rate) or by incorporating a device to provide more equal dispersion of the oil, such as baffles in the sump. The injection of more oil would have the effect of reducing mixture temperatures, which is in the proper direction to suppress fires.

Since the experimental data and the flammability theory coincide fairly well in this study, it appears that generalizing the sump-fire problem may make it amenable to analysis. If analysis can predict flow fields and temperature distribution within the sump, the presence or absence of conditions within the flammability limits can be

449

determined from lubricant vapor pressure-temperature data and combustion principles.

CONCLUDING REMARKS

As a logical extension to this work, further studies directed toward reducing sump-fire problems are planned. These include further spark ignition tests, where the effectiveness of novel sump baffles will be studied to produce excessively vapor-lean environments adjacent to the bearing, as well as a study of the effect of higher oil flow rates or perhaps a combination of the two. Also, additional rub ignitor tests will be performed using improved honeycomb seal and rub shroud materials that should reduce rub temperatures. Use of less-flammable lubricants in the system is another area of interest for this program. Also, a computerized analysis of the test results is planned to assist in assessing the effects of arbitrary engine sump geometric variations and flow patterns. The goal of this analytical study is to develop, concurrent with test procedure, a preliminary prototype analytical tool to predict sustained combustion in terms of critical flow and sump geometric parameters.

In closing, we would like to reiterate that improving seals for use in engine sumps could solve sump-fire problems by preventing the occurrence of conditions that are conducive to fires. The NASA Lewis Research Center is currently working on designs toward that purpose.

REFERENCES

1. Rhoads, W. L.; and Peacock, L. A.: Advanced Turbine Engine Mainshaft Lubrication System Investigation, Phase 2. Part 1: Background, Test Elements and Results, and Conclusions for System Performance. (AL69T016-Pt-1, SKF Industries, Inc.; NAS3-6267) NASA CR-72854, 1971.

2. Parks, A. J.; McKibbin, R. H.; and Ng, C. C. W.: Development of Mainshaft Seals for Advanced Air Breathing Propulsion Systems, Phase 1. (PWA-3161, Pratt & Whitney Aircraft; NAS3-7609) NASA CR-72338, 1967.

3. Kuchta, J. M.; and Cato, R. J.: Ignition and Flammability Properties of Lubricants. SAE Paper No. 680323, Apr.-May 1968.

4. Kuchta, Joseph M.: Summary of Ignition Properties of Jet Fuels and Other Aircraft Combustible Fluids. AFAPL-TR-75-70, Safety Research Center, Bureau of Mines, 1975.

5. Zabetakis, Michael G.: Flammability Characteristics of Combustible Gases and Vapors. Bull. 627, U.S. Dept. of the Interior, Bureau of Mines, 1965.

6. Barnett, Henry C.; and Hibbard, Robert R.: Basic Considerations in the Combustion of Hydrocarbon Fuels with Air. NACA Rep. 1300, 1957.

7. Rosenlieb, J. W.: Aircraft Engine Sump Fire Mitigation. (AL73T007, SKF Industries, Inc., NAS3-14310) NASA CR-121158, 1973.

TABLE I. - PARAMETERS THAT CONTROL FIRE

CONDITIONS IN ENGINE BEARING SUMPS

PARAMETER	OPERATING VALUES BEING STUDIED
OIL FLOW RATE INTO SUMP	0. 23-0. 45 m^3/hr (1-2 gal/min)
OIL INLET TEMP	353-441 K (175^0-335^0 F)
HOT AIR LEAKAGE RATE TO SUMP	7-48 m^3/hr (4-28 stdft^3/min)
HOT AIR INLET TEMP	739-823 K (870^0-1040^0 F)
SHAFT OR BEARING SPEED	7 000-14 000 rpm
IGNITION SOURCE & DURATION	UP TO 60 sec
OTHER PARAMETERS	-----------------------------

Figure 1.- Flammability diagram for type II ester lubricant, MIL-L-23699.
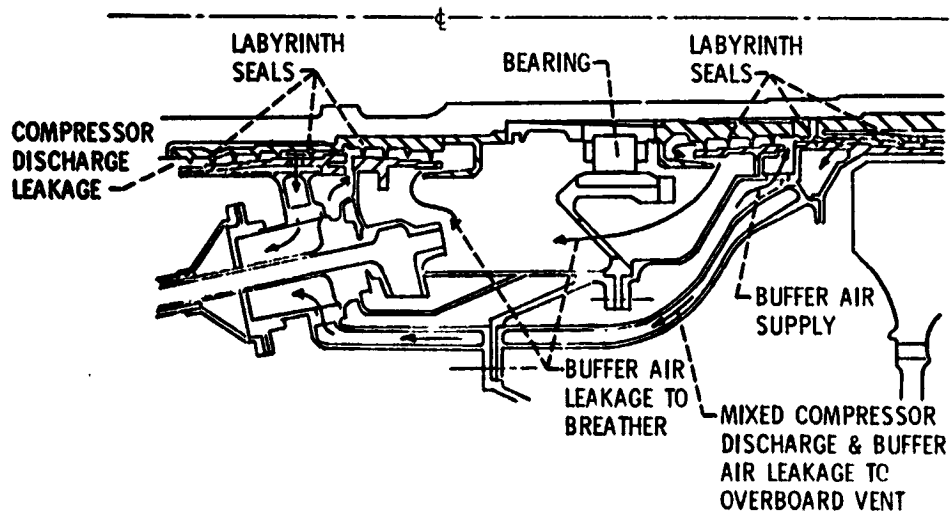
Figure 2.- Typical engine bearing sump.
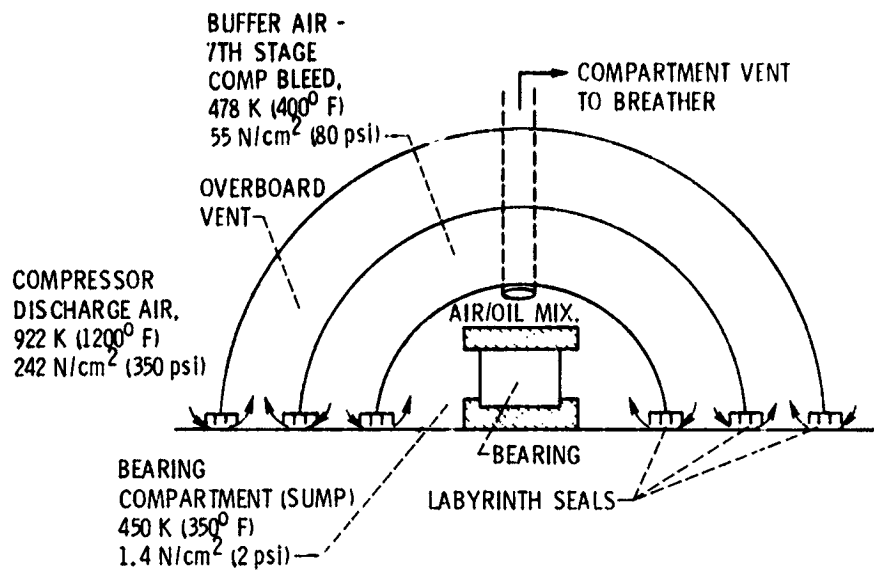
Figure 3.- Schematic of typical aircraft gas-turbine-engine
sump seal system.
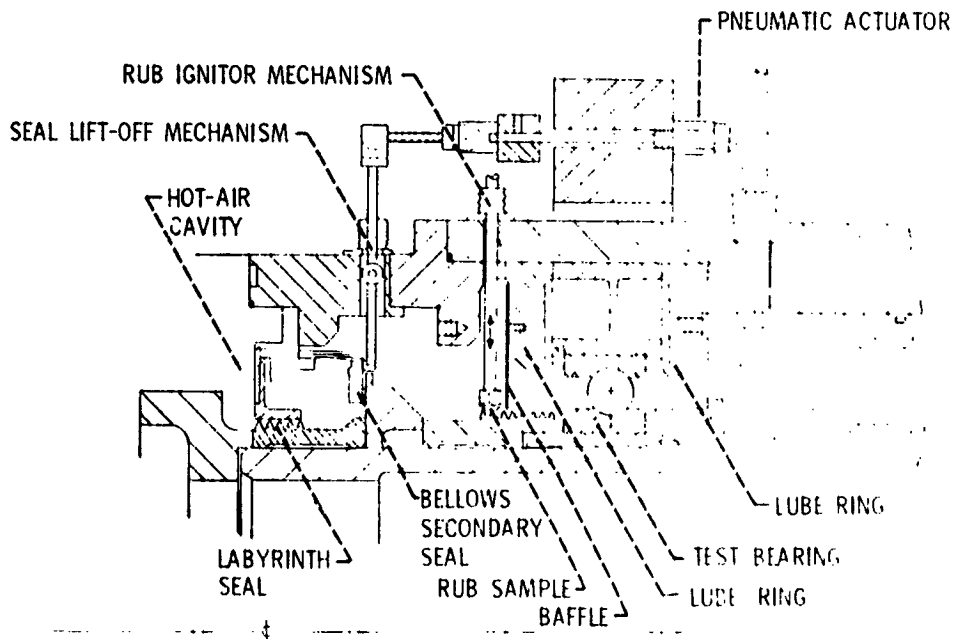
Figure 4.- Sump-fire test rig.
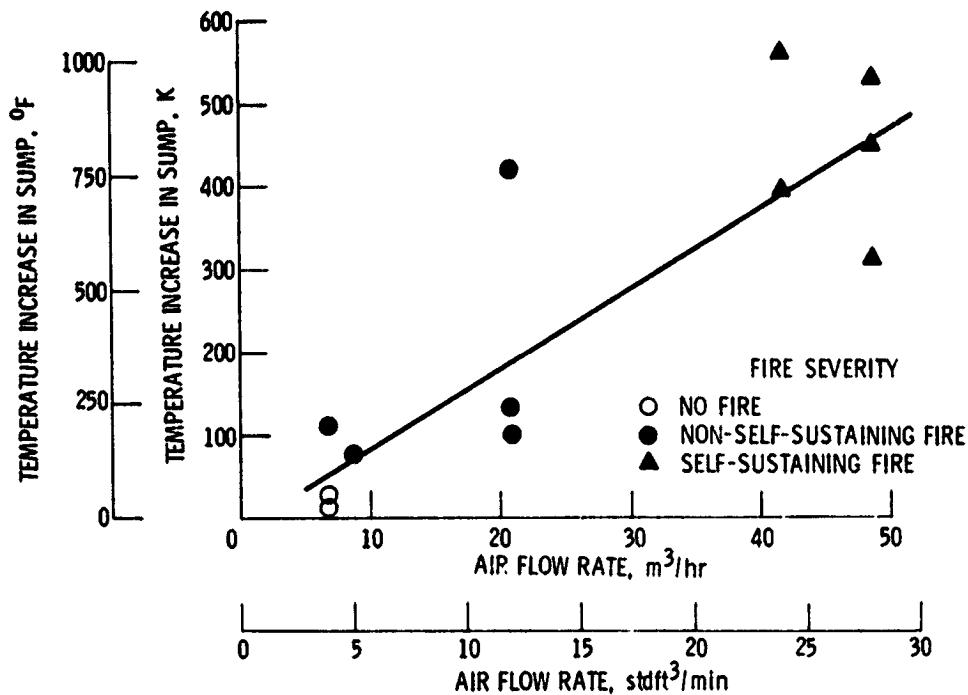
Figure 5.- Effect of air flow rate on fire severity. Oil, type II
ester; oil flow rate, 0.45 m³/hr (2 gal/min) at 441 K (335° F);
air inlet temperature, 789 to 814 K (960° to 1005° F); ignition
source, spark; speed, 14 000 rpm.
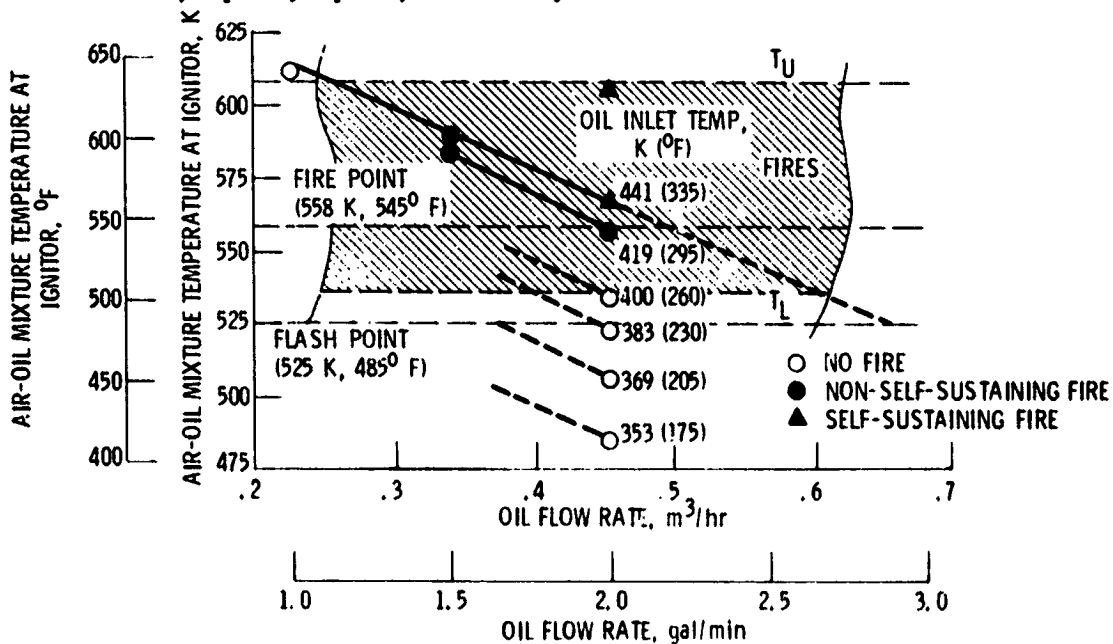
Figure 6.- Effect of oil flow rate on air-oil mixture temperature and
combustion at various oil inlet temperatures. Oil, type II ester;
air flow rate, 41 m³/hr (24 stdft³/min) at 789 to 814 K
(960° to 1005° F); ignition source, spark; speed, 14 000 rpm.

455
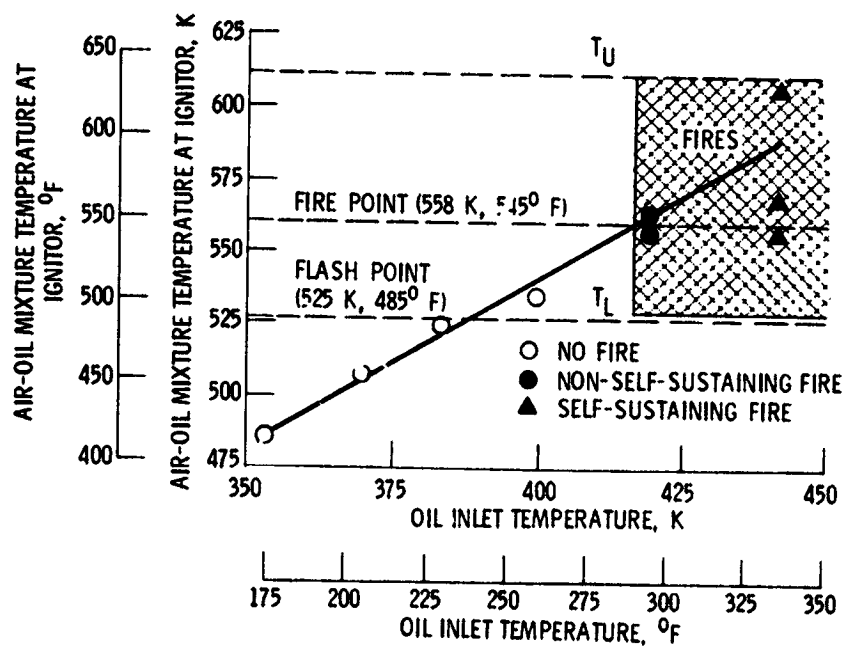
Figure 7.- Effect of oil inlet temperature on air-oil
mixture temperature and combustion. Oil, type II ester;
oil flow rate, 0.45 m³/hr (2 gal/min); air flow rate,
41 m³/hr (24 stdft³/min) t 789 to 814 K (960°
to 1005° F); ignition source, spark; speed, 14 000 rpm.

456

ALTERNATIVE AIRCRAFT FUELS TECHNOLOGY

Jack Grobman
NASA Lewis Research Center

SUMMARY

NASA is studying the characteristics of future aircraft fuels produced from either petroleum or nonpetroleum sources such as oil shale or coal. These future hydrocarbon based fuels may have chemical and physical properties that are different from present aviation turbine fuels. This research is aimed at determining what those characteristics may be, how present aircraft and engine components and materials would be affected by fuel specification changes, and what changes in both aircraft and engine design would be required to utilize these future fuels without sacrificing performance, reliability, or safety. This fuels technology program has been organized to include both in-house and contract research on the synthesis and characterization of fuels, component evaluations of combustors, turbines, and fuel systems, and, eventually, full-scale engine demonstrations. The entire effort has been integrated with a similar program being conducted by the Air Force Aero Propulsion Laboratory (AFAPL) and is being coordinated with other government agencies within the DOD and ERDA. This paper is a review of the various elements of the program and presents significant results obtained so far.

INTRODUCTION

As shown in figure 1, the fuel consumption by commercial aviation has roughly tripled during the last 15 years (ref. 1). Most forecasts predict a reduced rate of growth in air transportation. Nevertheless, the rate of increase in demand for aviation turbine fuels is expected to exceed that for automotive gasoline. Forecasts of the growth rate in fuel consumption by U.S. airlines vary from about 4 to 7 percent. Even the conservative predictions indicate a doubling of the fuel required for air transportation by the year 2000.

Presently, jet aircraft are totally dependent on petroleum derived kerosene fuels. At some time in the future, it will be necessary to obtain aviation fuels from sources other than petroleum. Domestically, these alternative sources include oil shale and coal. The most likely aviation turbine fuel derived from these alternative sources will probably be a liquid hydrocarbon that is similar to petroleum derived turbine fuels.

The relative reserves of petroleum, oil shale, and coal are illustrated in figure 2 (ref. 2). Based on the current total energy use rate, the U.S. supply of petroleum

25

will be depleted around the turn of the century. The U.S. must currently import about 35 percent of the oil that we consume. This figure could grow to over 50 percent by 1985. The reserves of oil shale and coal could supply our total energy needs for several hundred years. Both government and industry are conducting programs to exploit the conversion of oil shale and coal to a crude oil (refs. 3 and 4). These so-called "syncrudes" have properties somewhat similar to crude petroleum, with the exception that they contain a lower proportion of hydrogen to carbon and a higher concentration of undesirable impurities. Large capital expenditures will be required to launch the syncrude industry. Even with the support of government, initial production of syncrudes is not expected until about 1985, and this initial production will support only a small percentage of the total U.S. fuel demand.

The average distribution of finished products from a barrel of petroleum is shown in figure 3. The percent distribution of the various products are illustrated with the more volatile products at the top and less volatile products at the bottom of the barrel. Jet fuel, which takes most of the kerosene cut (or about 7% of the barrel), is obtained by a straight-run distillation of the crude plus a small degree of hydrotreating for sulfur removal. Distillation involves a relatively simple physical separation of the various components within the crude by a series of repeated stages of vaporization and condensation. Hydrotreating involves the chemical addition of hydrogen to unsaturated organic compounds to form saturated compounds or the removal of trace impurities such as sulfur by conversion to volatile compounds which may be more easily removed from the product. The cost of hydrotreating is directly related to the quantity of hydrogen required to process each barrel of crude. Until now, the kerosene portion of crude petroleum has been sufficient to supply the demand for aviation turbine fuels; however, as the demand for aviation turbine fuels grows faster than the demand for other petroleum products, it will become increasingly difficult to meet these demands from the kerosene cut of the barrel alone.

The alternatives to a shortened supply of aviation turbine fuel include (1) converting heavier cuts of the barrel to turbine fuel by hydroprocessing, which will result in increases in refinery cost and energy losses, (2) relaxing specifications for aviation turbine fuels, and (3) using shale oil and coal syncrudes as refinery feedstocks. Of course, another approach to alleviate the problem is fuel conservation by improving aircraft efficiency. The NASA has recently organized a program to evolve energy efficient propulsion and aerodynamic systems (ref. 2). However, this paper will concentrate on the technical problems related to the utilization of aviation turbine fuels with properties significantly different from current specification fuels.

AVIATION TURBINE FUELS TECHNOLOGY

The NASA fuels technology program is concerned with the evaluation of the potential characteristics of future jet fuels and the determination of the possible effects of these fuels on the performance and durability of engine components. The objective is to evolve any new technology required to use these fuels. The problems in using fuels with properties that are significantly different from specification aviation turbine fuels are emphasized. Research related to the effect of relaxed fuel specifications on combustors, turbines, fuel tanks, fuel system components, and materials is being conducted. The NASA effort is being conducted as part of a joint integrated fuels technology program with the Air Force Aero Propulsion Laboratory. The entire program is being coordinated with other government agencies that are involved with research on the use of shale oil and coal syncrudes.

Characteristics of Aviation Turbine Fuels

Commercial jet aircraft fuels have relatively tight specifications. As shown in figure 4, the initial boiling point of a typical commercial Jet A is generally greater than 440 K (330° F) in order to comply with the minimum specification value for a flash point of 310 K (100° F). The limiting value for flash point is set to minimize the probability of an accidental fire during fueling or following an emergency landing. The maximum final boiling point for Jet A may be as high as 570 K (570° F), but it is generally less than this value to comply with limits on freezing point.

Many of the important jet fuel properties are interrelated. An increase in final boiling point generally corresponds to an increase in both freezing point and aromatics concentration. The aromatic compounds found in petroleum products consist of a class of unsaturated cyclic hydrocarbons containing one or more benzene rings that have a wide range of boiling points. The volatility, which is related to the boiling range, must be a compromise between satisfactory combustion characteristics and an acceptable flash point. Low aromatic concentrations are desired to minimize smoke and flame radiation caused by smoke. Limits on the concentration of aromatics, olefins, and nitrogen compounds in the fuel are necessary to maintain chemical stability of the fuel so that gums, varnish, and carbon are not formed either during storage or within the heated parts of the fuel system. Olefins, which are a class of unsaturated organic compounds containing at least one double bond, are relatively reactive chemical compounds. Any nitrogen or sulfur in the fuel will be converted to undesirable oxide pollutants during combustion. Sulfur and trace metals such as vanadium, sodium, and potassium must be avoided to prevent the corrosion and oxidation of hot turbine blades. All of these elements are easily removed from petroleum derived fuels by hydrotreating.

However, the concentration of these elements in shale oil and coal syncrudes is much higher, and their removal, especially nitrogen from shale oil, is difficult (ref. 5). The freezing point and viscosity, which are generally controlled by limiting final boiling point, are important factors affecting fuel system design and reliability.

The Jet A fuel specification limits the maximum aromatic concentration to 20 percent by volume, which corresponds to a hydrogen content of about 13 to 14 percent by weight (fig. 5). As the aromatic concentration increases, the hydrogen content decreases and the tendency for smoke to be formed during combustion increases. A higher aromatic content is generally accompanied by increases in final boiling point, freezing point, and specific gravity. A higher specific gravity reduces the heat content of the fuel by weight but, correspondingly, increases heat content by volume.

Effects of Relaxed Fuel Specifications on Combustors

The effect of varying hydrogen content in a hydrocarbon fuel on the liner surface temperature of a conventional combustor is shown in figure 6 (ref. 6). The surface temperature increases with decreasing hydrogen content because the increased aromatics results in increased soot formation, which causes higher flame radiation due to increased flame emissivity. These experimental data for a single JT8D combustor can operating at simulated cruise conditions indicate that a 1-percent decrease in hydrogen leads to a 50 K (90° F) increase in liner wall temperature. Increasing liner surface temperature may reduce combustor operating life or at worst result in the gradual degradation of combustor components that could lead to further damage to the turbine.

Other data showing the effect of variations in hydrogen content on combustor performance were obtained from several experimental combustors designed to minimize exhaust pollutants (refs. 7 and 8). Two of the low-pollutant combustors being studied under a NASA contract designated as the "Experimental Clean Combustor Program" are shown in figure 7. The "Vorbix" combusor is being developed by Pratt & Whitney for the JT9D engine, and the double-annular combustor is being developed by General Electric for the CF6-50 engine. Both combustor designs consist of two combustion stages. A pilot stage burns a relatively rich fuel-air mixture at low power conditions such as idle in order to minimize hydrocarbon and carbon monoxide emissions. A main stage is used to burn a relatively lean mixture of fuel and air at high power conditions such as takeoff and cruise in order to minimize smoke and oxides of nitrogen.

Test results for these two experimental low-pollutant combustors are compared with the results for more conventional production combustors in figure 8. The maximum liner surface temperature minus the combustor inlet air temperature is shown plotted against the hydrogen content. Test data for the two conventional combustors follow a similar trend of increasing surface temperature with decreasing hydrogen

460

content. However, the experimental two-stage combustors are relatively insensitive to the hydrogen content of the fuel over the limited range of hydrogen concentrations that were studied. This effect is attributed to the fact that the main stage of the low-pollutant combustors operates at relatively lean fuel-air ratios thus producing less soot and lower flame radiation. These results thus indicate that this design might permit the use of a fuel with a higher aromatic content without suffering smoke formation penalties. Other test data obtained with these low-pollutant combustors using No. 2 diesel fuel indicate a small loss in altitude relight capability and a small increase in carbon monoxide and total hydrocarbon pollutants at idle. The effects of using No. 2 diesel fuel on combustion efficiency and combustor exit temperature profile were negligible. Future test plans include studying the effects of broad specification fuels on combustor durability at elevated pressures to simulate takeoff operating conditions.

Effects of Relaxed Fuel Specifications on Fuel Systems

The typical spread in freezing point of a hydrocarbon fuel blend as a function of final boiling point is shown in figure 9. Freezing point is somewhat of a misnomer here since a jet fuel consists of many different organic compounds, and only a pure compound solidifies at a constant and definite temperature. For jet fuels the freezing point is defined by the initial presence of solid hydrocarbon crystals in the liquid phase. The wide spread in freezing point for a given final boiling point is probably due to the variations in the types and concentrations of organic compounds found in fuels refined from different crude sources. The only difference between the specifications for Jet A and Jet A-1 is the maximum allowable freezing point, which is 233 K $(-10^0$ F) and 223 K $(-58^0$ F), respectively. The freezing point for diesel No. 2 is considerably higher and varies from about 250 to 255 K $(-10^0$ to 0^0 F).

A representative variation in tank fuel temperature over a long distance flight is shown in figure 10 (ref. 9). As a safety margin for avoiding fuel line plugging, the FAA requires that the tank fuel temperature be maintained at least 3 K $(5.4^0$ F) above the freezing point of the fuel being used. For the example shown, the tank fuel temperature will fall below the safety margin for Jet A after flying about 3700 kilometers (2000 nm). This figure thus illustrates the necessity of using Jet A-1, which has a lower freezing point for long distance flights. It is interesting to observe that the effect of initial fuel temperature on tank fuel temperature becomes negligible for long flight times.

Several flight operational methods may be considered for maintaining a fuel above its freezing point. In the event that the measured tank fuel temperature approaches the safety margin, the tank fuel temperature may be increased by increasing flight Mach

number, reducing flight altitude, or altering course to avoid cold air masses. All of these approaches penalize fuel consumption. Switching from outboard to inboard fuel tanks, which are at a slightly higher temperature, is relatively limited in effectiveness. As shown in the previous figure, preheating fuel on the ground has a negligible effect on the fuel tank temperature for a long flight. However, preheating fuel on the ground might be necessary during the winter in some regions just to transfer a broader-specification fuel such as diesel No. 2 to the aircraft.

The use of broader-specification fuel such as diesel No. 2 would require a major redesign of the airframe fuel system. Insulating the fuel tanks could provide a partial solution. However, heating the fuel in the tank during flight would probably be required to maintain the tank fuel temperature above the freezing point. Several approaches to heating the fuel during the flight could be considered. Fuel could be recirculated through the engine heat exchanger and returned to the fuel tank. This approach would probably require changes to the present design for the fuel pumps and engine heat exchanger. Another approach could be the addition of fuel tank heaters. Whatever method is used, high local fuel temperature must be avoided to prevent gumming of fuel passages due to degradation of the fuel. The problems in using a broader specification fuel with a higher freezing point are currently being studied analytically by Boeing under a NASA contract.

CONCLUDING REMARKS

Many areas of research and development will have to be explored if we are to use alternative fuels for jet aircraft. The research performed so far, in which the effects of higher aromatic content and lower volatility fuels on combustors were studied, must be extended to higher operating pressures to fully evaluate performance and durability problems. The initial low smoke and low liner temperature results obtained in experimental two-stage combustors look promising. Fuel system technology must be evolved to permit the use of fuels with higher freezing points and lower thermal stabilities. Additional fundamental data are needed to relate thermal stability to fuel composition. Data on the effects of alternative fuels on materials must be obtained, including their compatibility with both fuel system elastomers and turbine blade alloys and coatings. Any potential toxicity problems related to fuels derived from coal or oil shale must be studied, although undesirable toxic compounds will probably be removed at the refinery. Finally, extensive engine endurance testing will be required to establish the overall reliability of engines designed to use an alternative fuel.

462

REFERENCES

1. Povinelli, Frederick P.; Klineberg, John M.; and Kramer, James J.: Improving Aircraft Energy Efficiency. Astronaut. Aeronaut., vol. 14, no. 2, Feb. 1976, pp. 18–31.

2. Dugan, James F., Jr.; et al.: Fuel-Conservative Engine Technology. Aeronautical Propulsion Conference. Ch. VI, NASA SP-381, 1975, pp. 157–190.

3. Shaw, Henry; Kalfadelis, Charles D.; and Jahnig, Charles E.: Evaluation of Methods to Produce Aviation Turbine Fuels from Synthetic Crude Oils, Phase 1. GRU-1PEA-75; AFAPL-TR-75-10, Exxon Research and Engineering Co., 1975.

4. Pinkel, I. I.: Future Fuels for Aviation. AGARD-AR-93, Advisory Group for Aerospace Research and Development, 1976.

5. Antoine, Albert C.; and Gallagher, James P.: Synthesis and Analysis of Jet Fuels from Shale Oil and Coal Syncrudes. NASA TM X-73399, 1976.

6. Butze, Helmut F.; and Ehlers, Robert C.: Effect of Fuel Properties on Performance of a Single Aircraft Turbojet Combustor. NASA TM X-71789, 1975.

7. Roberts, R.; Peduzzi, A.; and Vitti, G. E.: Experimental Clean Combustor Program, Phase II, Alternate Fuels Addendum. (PWA-5370, Pratt & Whitney Aircraft Div. of United Technologies Corp., NAS3-18544.) NASA CR-134970, 1976.

8. Gleason, C. C.; and Bahr, D. W.: Experimental Clean Combustor Program, Alternate Fuels Addendum, Phase II, Final Report. (R76AEG268, General Electric Co.; NAS3-18551.) NASA CR-134972, 1976.

9. Barr N. M.; et al.: Boeing Airplane Fuel Systems at Low Temperature. D6-423286, Boeing Co., 1975.
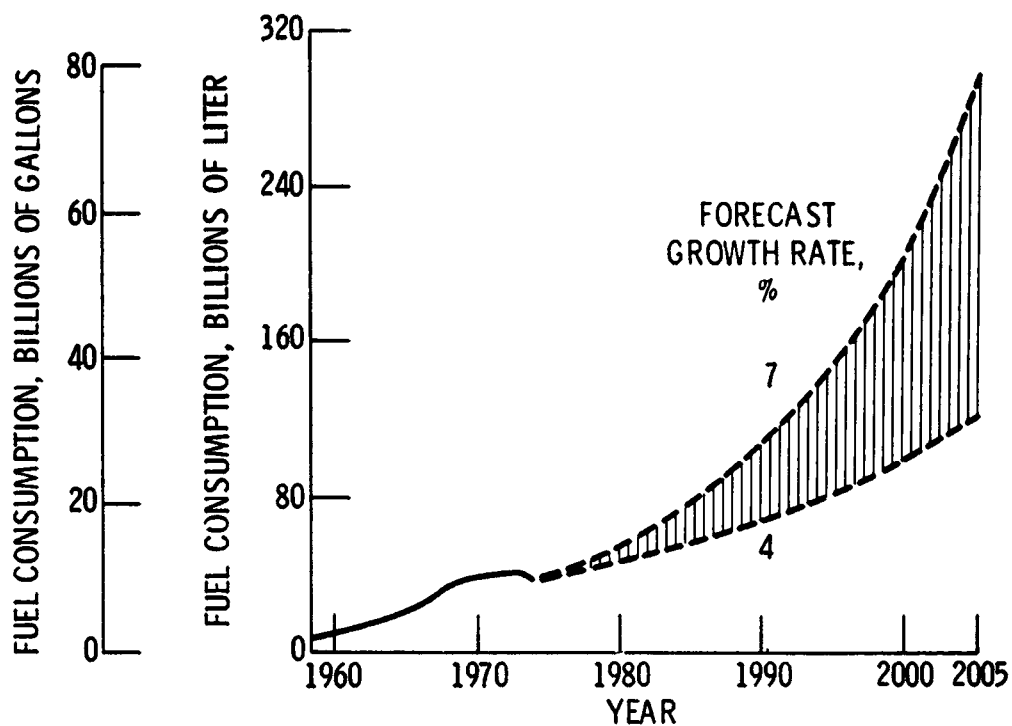
Figure 1.- U.S. air transportation fuel consumption estimates
for certificated airlines.
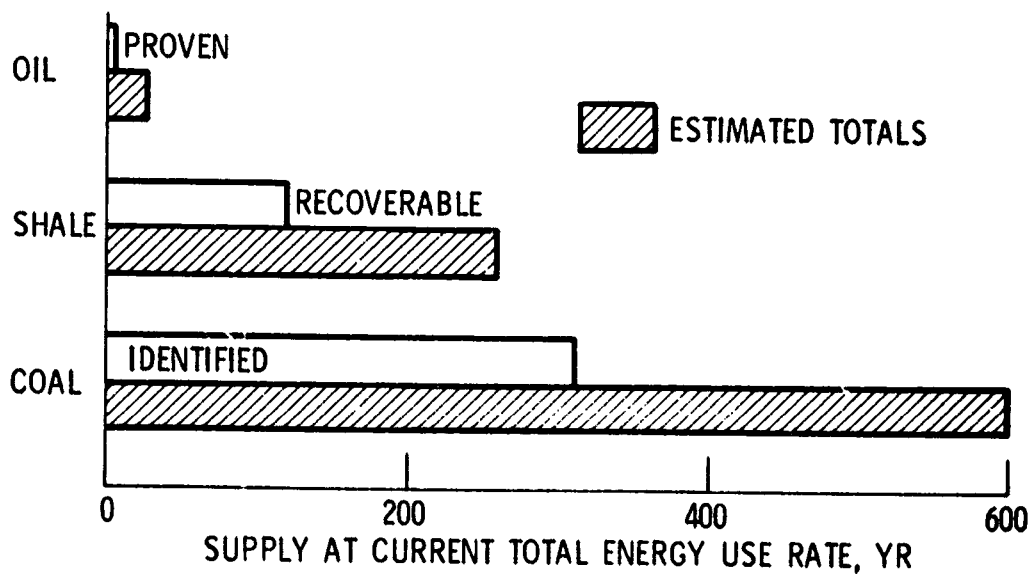
Figure 2.- Comparison of U.S. fuel resources.

	% OF TOTAL
LPG, PETROCHEMICALS	7
GASOLINE	45
JET FUEL (7%) + KEROSENE (3%)	10
DIESEL, HOME HEATING, INDUSTRIAL FUEL OILS	32
LUBRICANTS, ASPHALT, COKE	6
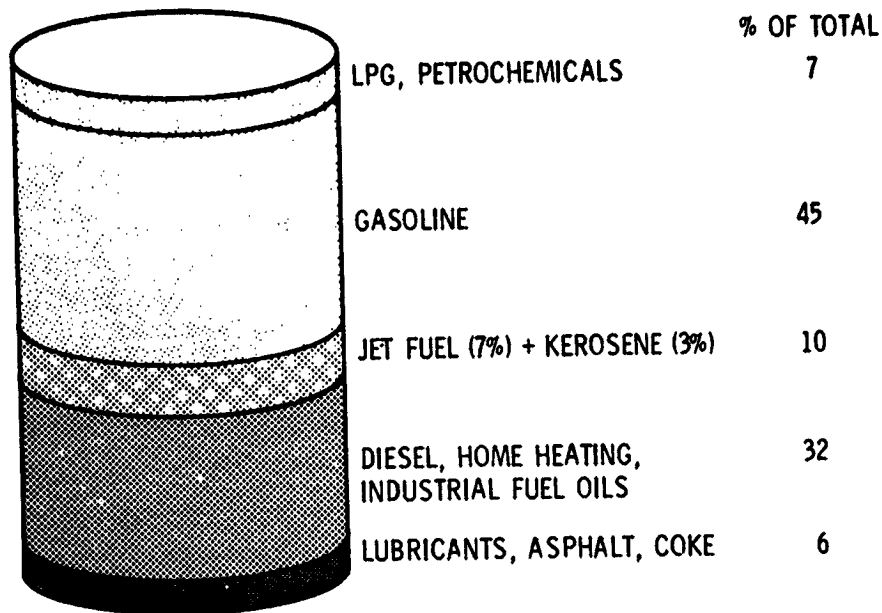
Figure 3.- Distribution of petroleum to finished products.
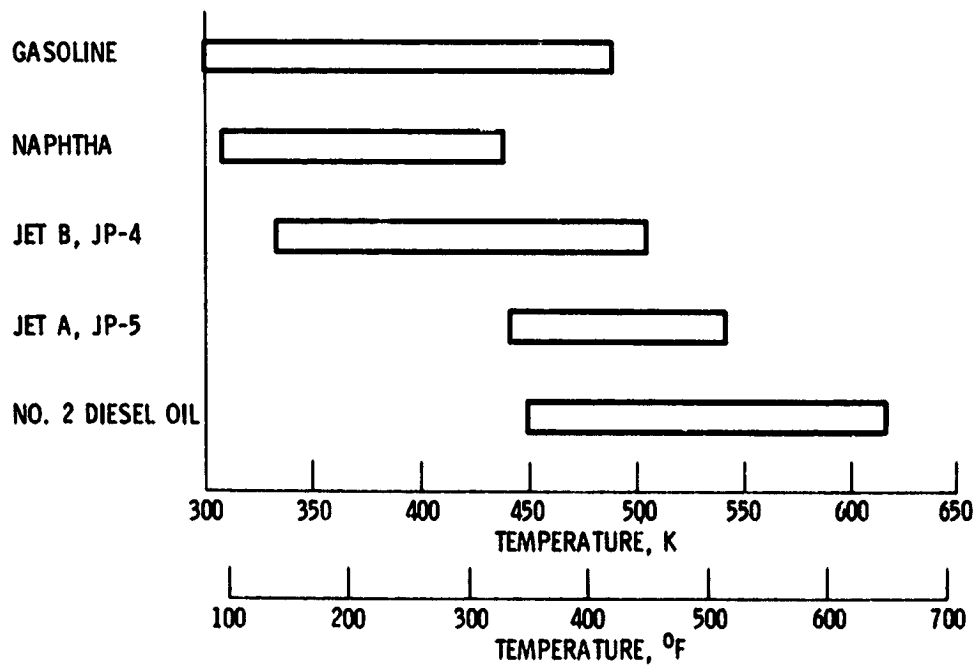
Figure 4.- Boiling range of various petroleum products.
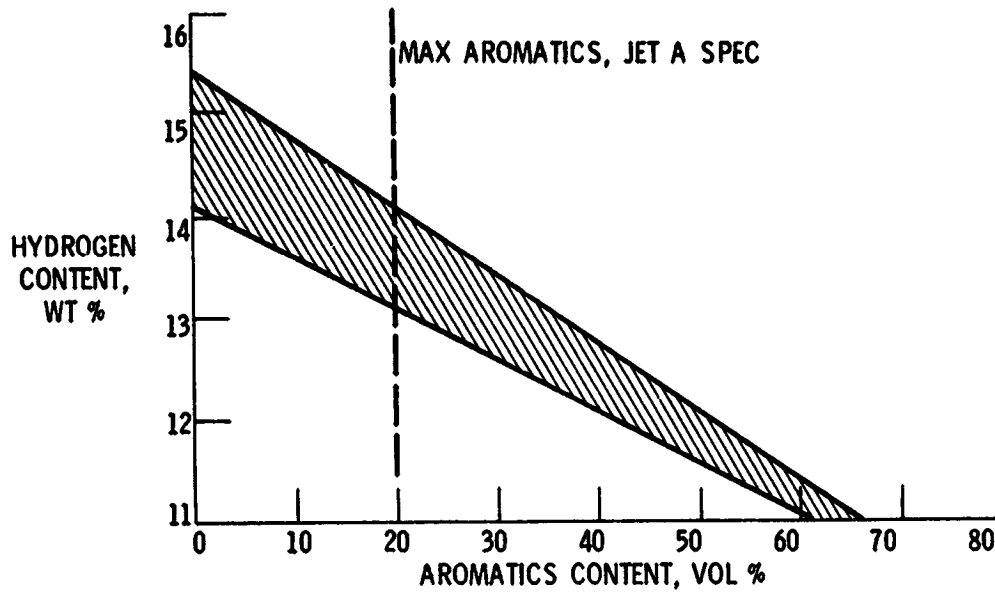
Figure 5.- Variation of hydrogen content with aromatics content.
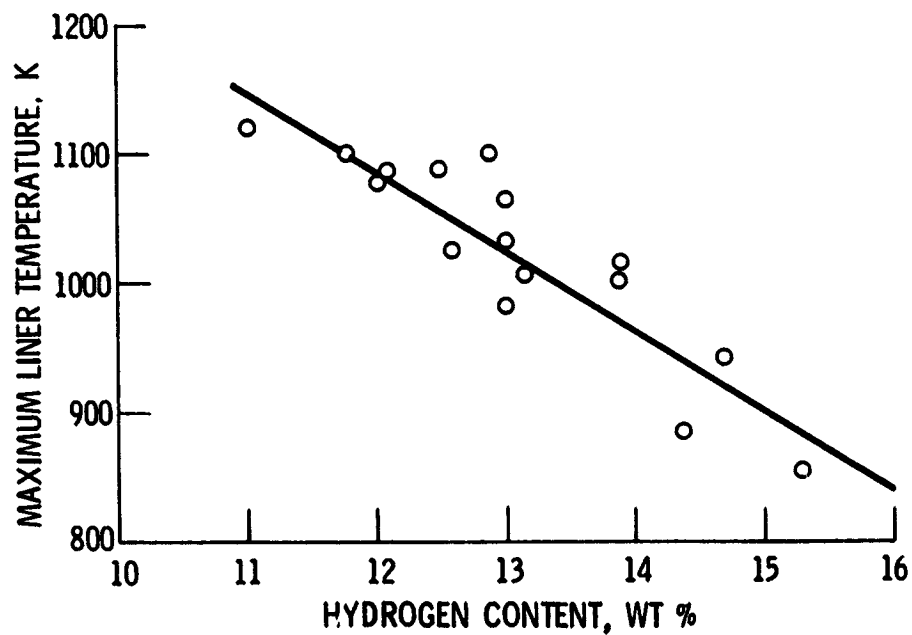
Figure 6.- Effect of hydrogen content of fuel on combustor
liner surface temperature.
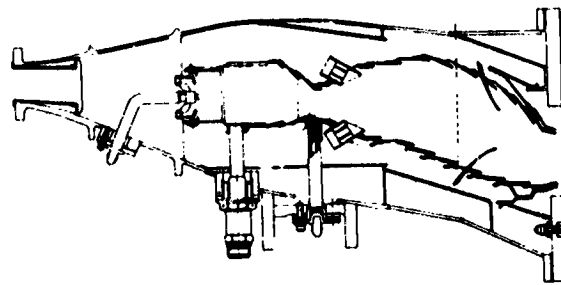
VORBIX COMBUSTOR FOR JT9D ENGINE
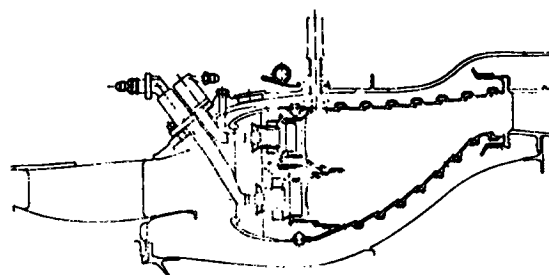
DOUBLE-ANNULAR COMBUSTOR FOR CF6-50 ENGINE

Figure 7.- Experimental clean combustor program.
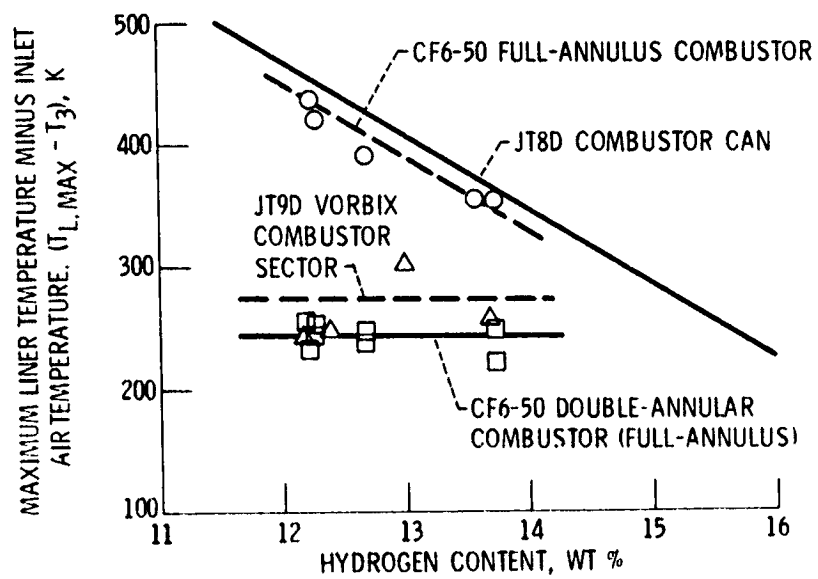
Figure 8.- Effect of hydrogen content of fuel on
combustor liner surface temperature.
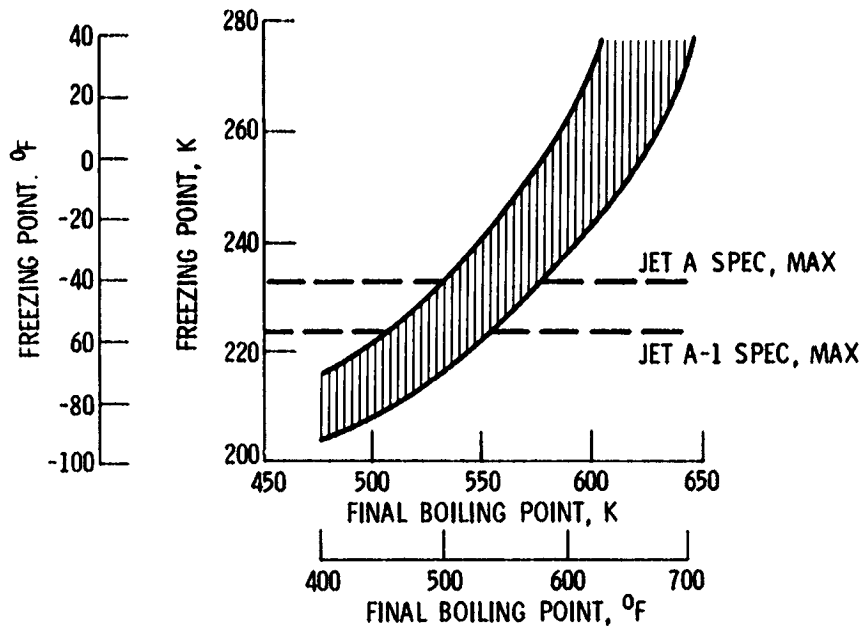
Figure 9.- Variation of freezing point with final boiling point.
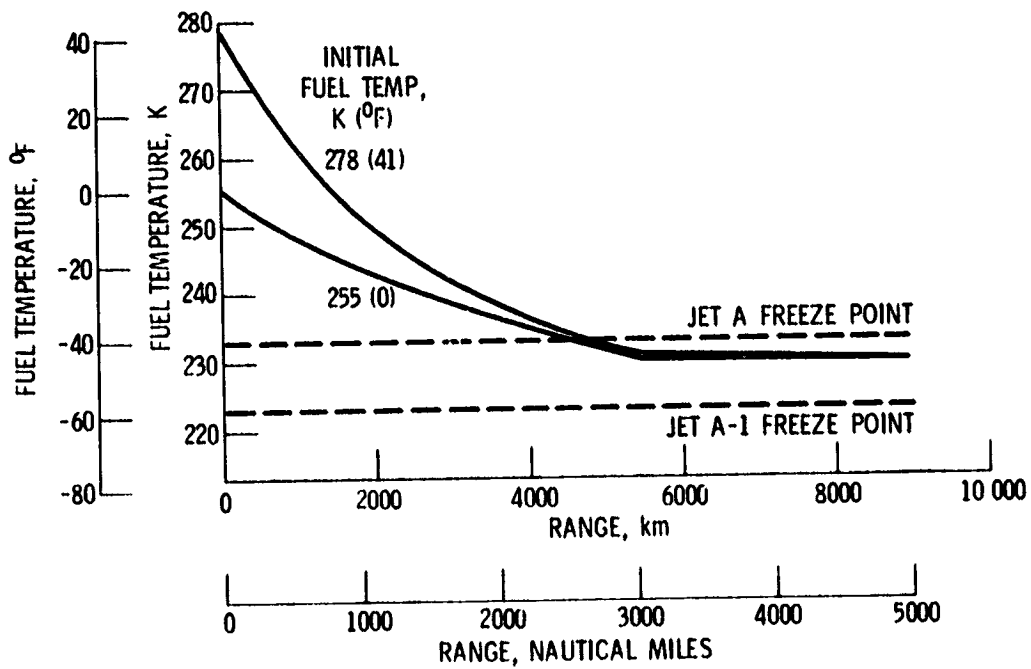
Figure 10.- Calculated minimum fuel temperature for Boeing 747 aircraft.

GAS- PATH SEAL TECHNOLOGY

John Zuk
NASA Lewis Research Center

SUMMARY

Improved gas-path seals are needed for better fuel economy, longer performance retention, and lower maintenance, particularly in advanced, high-performance gas turbine engines. Problems encountered in gas-path sealing are described, as well as new blade-tip sealing approaches for high-pressure compressors and turbines. These include a lubricant coating for conventional, porous-metal, rub-strip materials used in compressors. An improved hot-press metal alloy shows promise to increase the operating surface temperatures of high-pressure-turbine, blade-tip seals to 1450 K (2150° F). Three ceramic seal materials are also described that have the potential to allow much higher gas-path surface operating temperatures than are possible with metal systems.

INTRODUCTION

Seals present fundamental and continuing problems in gas turbine engines. Many seals are used in these engines. A large gas turbine engine, such as that shown in figure 1, has over 100 major seals and several hundred minor seals. Seals not only restrict gas leakage, but also provide thrust balancing, meter cooling gas flow, and protect bearing compartments and other mechanical components. Thus, the cumulative effect of sealing practice is appreciable. Our present concern for fuel conservation and need for much better performance retention call for improved seals. Also advanced engines will operate at higher pressures, temperatures, and speeds than current engines. These engines will have to be run "tighter" than current engines. Hence, even better seals will be required. The Lewis Research Center is working in most of the major sealing areas and has an extensive shaft sealing program that has resulted in a very successful lift-pad sealing concept. This concept is excluded from this presentation but is addressed in reference 1 and is briefly described in the sump-fire program presentation (ref. 2).

This presentation addresses the primary-gas-path seals. The main function of these seals is to keep the working fluid in the designed flow path. Thus, the working fluid can contribute to the useful work energy of the engine rather than be added to the wasted energy of leakage.

Primary-gas-path seals can be classified as either outer or inner air seals. The inner air seals are usually labyrinth seals and are the interstage or end seals (fig. 2). These seals are composed of rotating knife edges interfacing with a stationary sleeve of a rub-tolerant and erosion-resistant material. The outer air seals are blade-tip seals (fig. 2) and are located in the gaps between the blade tips and the casing shroud. The casing shroud also contains a rub-tolerant and erosion-resistant material. Of all the seals, the primary-gas-path seals have the greatest effect on performance, particularly on fuel economy.

As an example, compressor efficiency, one measure of performance, is greatly affected by the blade-tip clearance. The compressor efficiency penalty as the ratio of blade-tip clearance to blade height is increased is shown in figure 3. These data were obtained from operational and research compressors (ref. 3). Usually, the high-pressure stages of high-performance compressors have short span heights. Hence, the compressor efficiency is very sensitive to blade-tip clearance. Note in figure 3 that doubling the clearance can mean a 2-percent penalty in efficiency. In addition, stall/surge margins also depend greatly on clearance.

GAS-PATH SEALING PROBLEMS

Operating seal clearances depend on both operating conditions and installation. Operating conditions include maneuver and landing "g"-load deflections, aerodynamic surge and pressure-induced stator deflections, rotor dynamic response to rotor unbalance, thermal transient mismatch between rotating and static seal components, centrifugal growth, and engine-case distortion (ovalization) caused by engine mounting. The first two conditions depend on the operating history of the specific engine. Closer-clearance operation can be attained by using rub-strip liners with initially tight clearances and permitting the interaction of blade tips to wear in the required operating clearances. The remaining conditions are common to all engines of the same model and require basic structural and design modifications to achieve significant reductions in running clearance. We are working on such design concepts, including active clearance control.

Generally, the gas-path seal clearances change with each engine condition, such as idle, takeoff, and cruise. Dimensional changes in the seal support structure are large relative to the seal clearances. The trend toward higher engine pressures and temperatures will tend to increase both seal displacements and erosion.

Although nominally rub-tolerant materials are used today, problems arise during close-clearance operation when severe rub situations are encountered. In these situations the blade tips can wear severely.

Figure 4 shows the surface of a conventional shroud seal material after a severe

470

rub. There are two distinct regions in the wear pattern. On the far right, acceptable rubbing has occurred; on the left, the blade-tip material has been "smeared" or transferred. This smearing is undesirable because the blade tip has worn, resulting in a larger leakage path. However, an almost equally undesirable situation occurs when the shroud material transfers to the blade tip and results in a full 360° rub groove caused by this effective increase in blade height.

In addition to performance loss, poor gas-path seals cause many associated problems. Increased clearance due to rubbing or lack of erosion resistance decreases the stall/surge margin in the compressor. Severe rubbing of blade tips can initiate cracks in the blades and greatly reduce the blade life. Seal wear debris may deposit downstream and affect other components' performance. The most serious consequence of poor rub tolerance is, of course, self-destruction.

The Lewis sealing programs are fully integrated with the Department of Defense's programs on gas-path sealing.

HIGH-PRESSURE-COMPRESSOR TIP SEALS

Prior to the current jumbo jets, compressor tip seal surfaces in civilian engines were not treated with a rub-tolerant material. Because of their relatively low stage pressure ratios and more-rigid structures than current jumbo jet engines, the operating seal clearances in these older engines were set so rubs would never occur. Also fuel prices were relatively low when these engines were designed. Current jumbo jet engine designs, however, could not afford this operating penalty, and rub-tolerant surface materials had to be used. It is estimated that as much as a 4-percent increase in compressor efficiency was obtained by using rub-tolerant surface treatments.

Two classes of rub-tolerant materials are widely used today. One class includes porous metal, cermet, and composite materials. These are generally thermally sprayed or sintered, fine metal particles or metal fibers with low cohesive strength due to their porosity (fig. 5). In principle the particles or fibers are sheared off by bond fracture during a rub. A trade-off must be made between rub tolerance and erosion resistance.

As a result, present shroud seal materials may have either poor rub tolerance or poor gas erosion resistance (fig. 6). Fortunately, both good rub tolerance and good erosion resistance can be obtained through more careful control of the material-processing variables than is presently used, but much work remains to be done in this area.

In figure 6, an NASA experimental material is compared with two conventional shroud seal materials - porous metal and porous cermet. The porous metal material shows very low friction, which indicates good rub tolerance, but is badly eroded by hot

471

gas. The loss of shroud material by erosion is, of course, detrimental to performance. On the other hand, the cermet material had good erosion resistance but poor rub tolerance. Because of its high friction, the cermet blade-tip material would transfer to the shroud material. Obviously, a trade-off must be made between rub tolerance and erosion resistance.

The NASA experimental material, however, shows reasonable friction and excellent erosion resistance (fig. 6). These qualities are achieved by using a plasma-sprayed, solid lubricant coating on the conventional porous metal material. In addition, this lubricant coating is formulated to provide oxidation resistance; and further, it will reduce leakage flow through the porous structure. The photomicrograph in figure 7 is a magnified cross-sectional view of this shroud seal material, showing the plasma-sprayed, solid lubricant surface coating on the porous metal substrate.

Figure 8 shows the same view after a knife-edge rub. Knife-edge rubs are similar to blade-tip rubs. The groove indicates a clean rub, with no metal transfer from or to the knife edge. The knife edge showed no measurable wear. The coating provided a glassy phase, on the rub surface, that acted as a high-temperature solid lubricant. The preliminary results with this lubricant coating material are promising. However, further studies and additional testing, simulating a complete engine environment and operating cycle, are necessary before this material concept can be used in an engine. This work is described in references 4 and 5. A continuing Lewis in-house program is under way to study this approach further.

The other class of material is the plastically deformable surface materials. These materials are almost fully dense and are characterized by their low yield strength. During a rub these materials flow plastically and at the same time offer good erosion resistance (fig. 9). They are generally applied by thermal spray processes. One of the most serious problems with currently used materials is that the debris is not innocuous. A program (Contract NAS3-20054) has recently been started to very fundamentally investigate plastically deformable materials. The goal is to find a better substitute for the currently used materials and at the same time learn how to make more-rub-tolerant, gas-path seal materials.

HIGH-PRESSURE-TURBINE TIP SEALS

In high-pressure turbines, the currently used engine tip seals are segmented shroud seals, which are limited to gas-path surface temperatures less than 1366 K (2000° F). Because of the more severe environment in high-pressure turbines, oxidation and corrosion resistance and the ability to withstand thermal cycling are additional requirements.

As shown in figure 10, some currently used metal tip seals are merely untreated

472

shrouds composed of a cobalt-base alloy that is softer than the blade. However, the rub tolerance is minimal and only very light rubs can be accommodated. A currently used rub-tolerant surface treatment is a direct-sintered nickel-aluminum alloy. It, however, is also limited to 1366 K (2000° F) gas-path surface temperatures. Recently, contractual work (NAS-3-18905) has led to the completion of a development effort on an improved shroud seal material, a hot-pressed, slightly porous, nickel-chromium-aluminum alloy that is yttria stabilized. This alloy meets all operating requirements and extends operation to about 1450 K (2150° F). This seal material has been successfully engine tested, and presently the laboratory fabrication process is being up raded for larger volume production. Further engine tests are being conducted under this contract.

With current seal material technology, higher turbine-inlet-temper re c   ... al can only be obtained by using cooling schemes on the hot-gas sur ·   o such schemes are shown in figure 11 - transpiration cooling and "... cooling. However, the performance penalty for this additional cooling air is great, and larger clear nce operation is necessary to avoid rub smearing of the cooling holes.

Currently, ceramic turbine shrouds are being developed as a means of extending uncooled-gas-path-surf ce operating temperatures. Three ceramic material systems are being investigated - zirconia, silicon carbide, and silicon nitride (fig. 12). The zirconia system is a graded cermet. A metal-rich composition is first directly sintered to the metal supporting shroud, and then layers of progressively more ceramic-rich materials are sintered until a surface layer of 100-percent zirconia is achieved. Finally, a porous layer is bonded for rub tolerance. This work is sponsored by the Navy. A related Lewis program (NAS3-19759) is investigating plasma spraying of this cermet system. If successful, this approach would have a large cost advantage over the direct-sintering process. Also it may be applied to existing shrouds and thus extend their life and/or operating temperatures.

Two Lewis programs are studying silicon carbide and silicon nitride systems. One, under contract NAS3-20081 is investigating density variations in and structural configurations of these systems. Another program (NAS3-20082) is investigating silicon/silicon carbide substrates coupled with a series of abradable surface layers, in order to find the most optimum combination.

In addition to improved shroud seal materials studies, work is being conducted on the mating turbine blade tips. Both treated and untreated turbine tips are being stud ied. Recent work has shown that turbine blade tips can wear under certain conditions. Abrasive grits such as aluminum oxide and silicon carbide bonded to the blade tips are being evaluated.

All these ceramics approaches show much promise but must overcome many problems, particularly the thermal shock resistance common to all ceramics and the

473

attachment of the ceramic to the metal supporting structure because of differences in thermal expansion properties. Satisfactory progress is being made and we probably will see ceramic seal technology applied in the 1980's.

CONCLUDING REMARKS

Only a few of the many ongoing programs in gas-path sealing technology at the Lewis Research Center have been presented. Promising high-pressure-compressor and turbine tip seals that will make possible improved performance are being developed. Because of the necessity for conserving energy, there is a pressing need to improve and better retain engine performance in an economical, low-maintenance, and safe way. This goal can be achieved by improved seal technology, which will be even more critical in meeting the requirements of future high-performance engines.

REFERENCES

1. Ludwig, Lawrence P.: Self-Acting and Hydrodynamic Shaft Seals. NASA TM X-68214, 1973.

2. Loomis, William R.: Aircraft Engine Sump-Fire Studies. Aircraft Safety and Operating Problems, NASA SP-416, 1976. (Paper No. 24 of this compilation.)

3. Mahler, Frederic H.: Advanced Seal Technology. PWA-4372; AFAPL-TR-72-8, Pratt & Whitney Aircraft, 1972.

4. Ludwig, L. P.; and Johnson, R. L.: Sealing Technology for Aircraft Gas Turbine Engines. AIAA Paper 74-1188, Oct. 1974.

5. Shienibob, L. T.: Development of Abradable Gas Path Seals. (PWA-TM-5081, Pratt & Whitney Aircraft; NAS3-18023) NASA CR-134689, 1974.
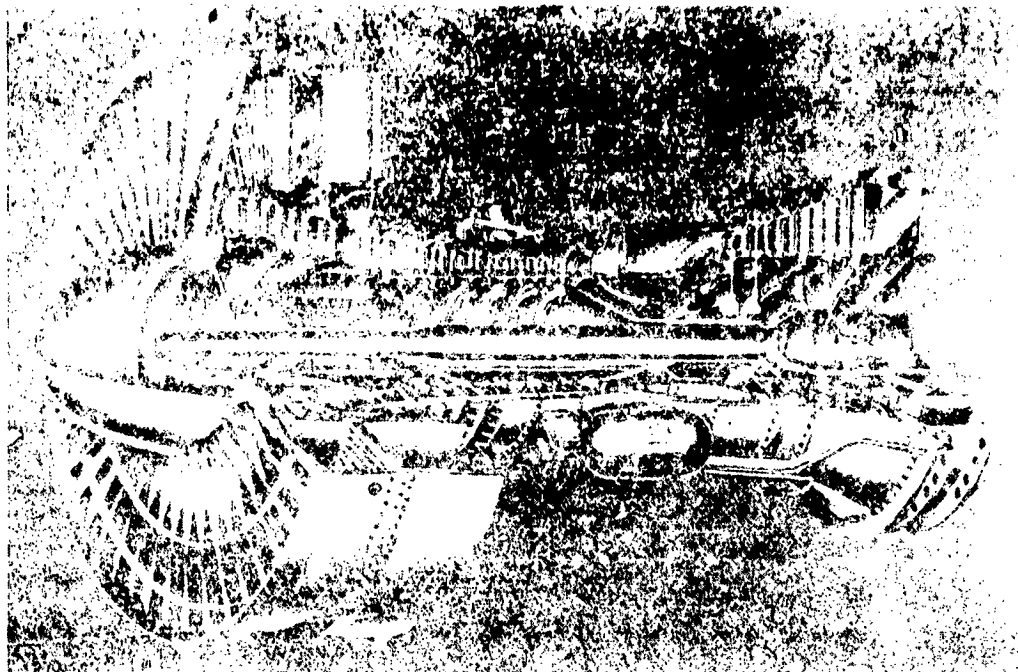
Figure 1.- Typical turbofan engine.

Figure 2.- Primary gas-path seals.
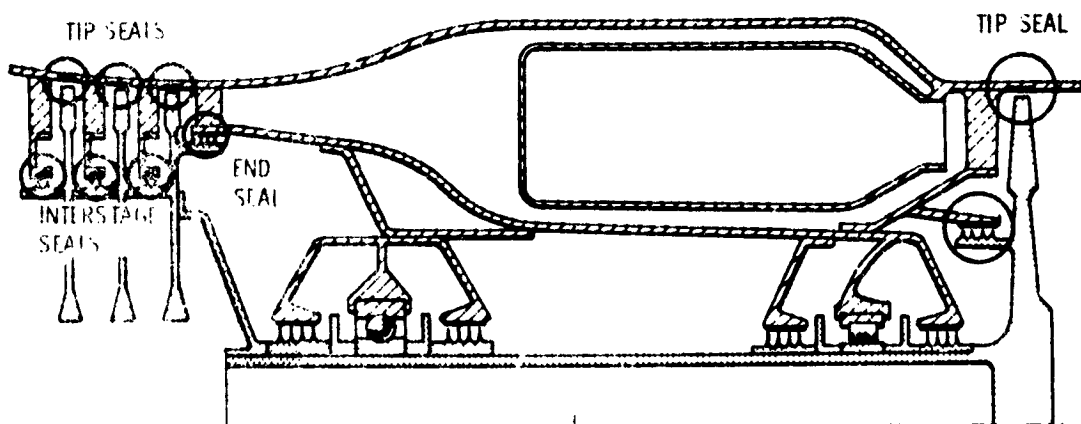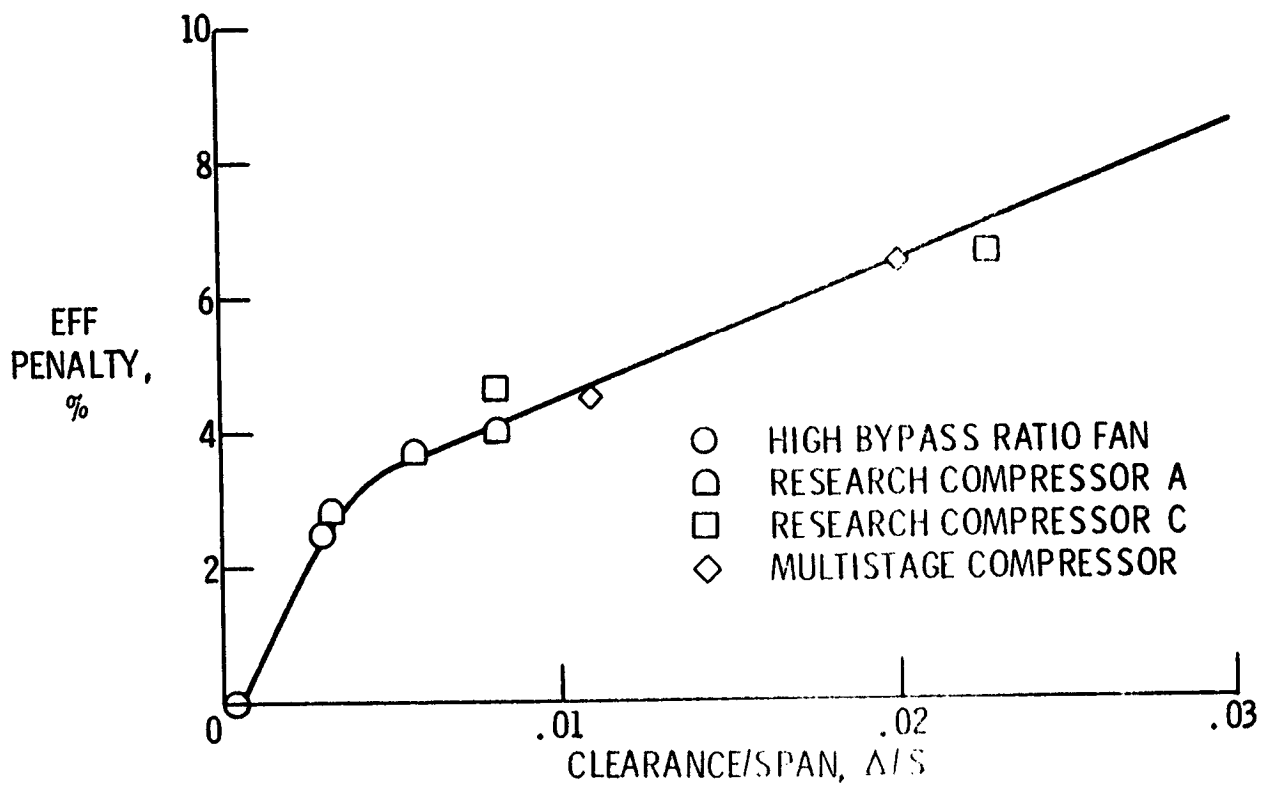
Figure 3.- Compressor performance penalty. (From ref. 3.)

Figure 4.- Shroud seal rul.

476
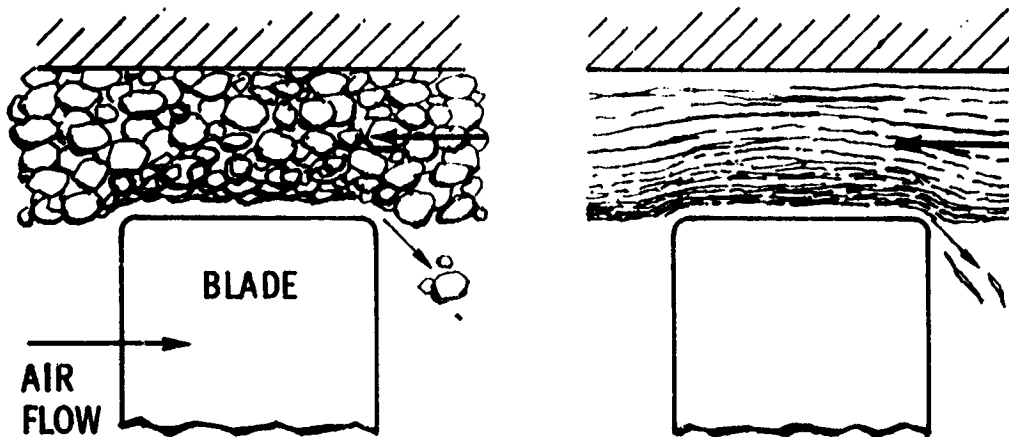
(a) Sintered metal particles.   (b) Sintered metal fibers.

Figure 5.- Compressor tip seals with porous-metal surface treatments.
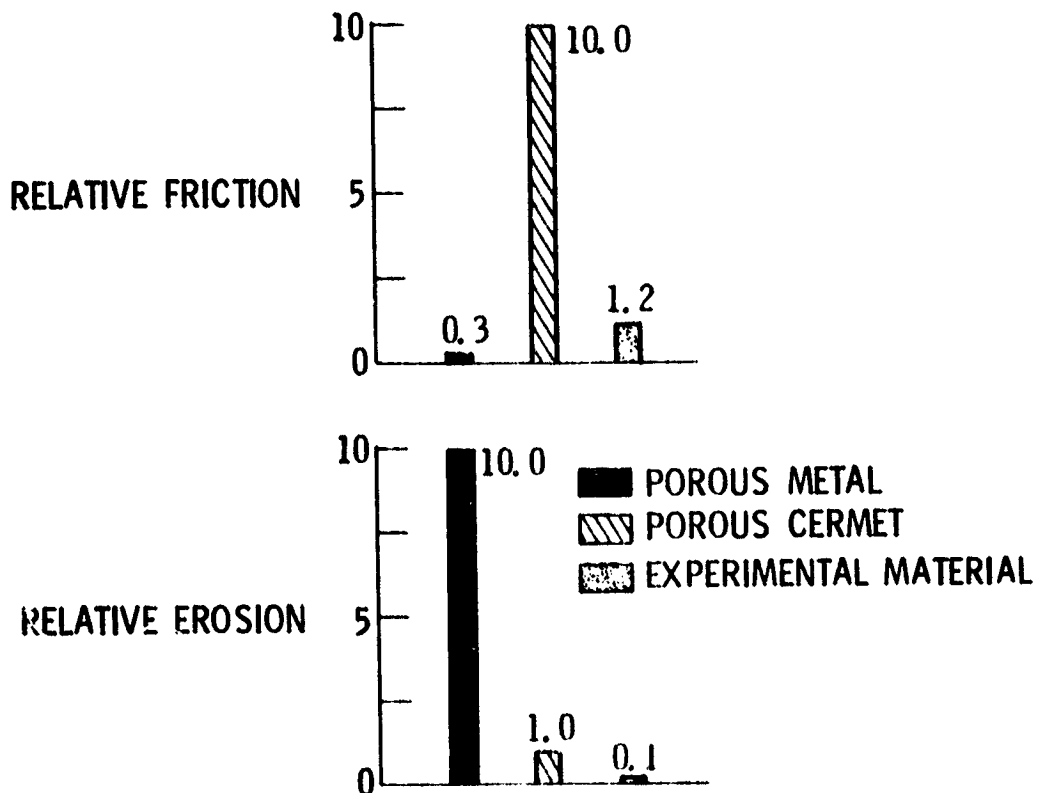
Figure 6.- Friction and erosion of shroud seal materials.
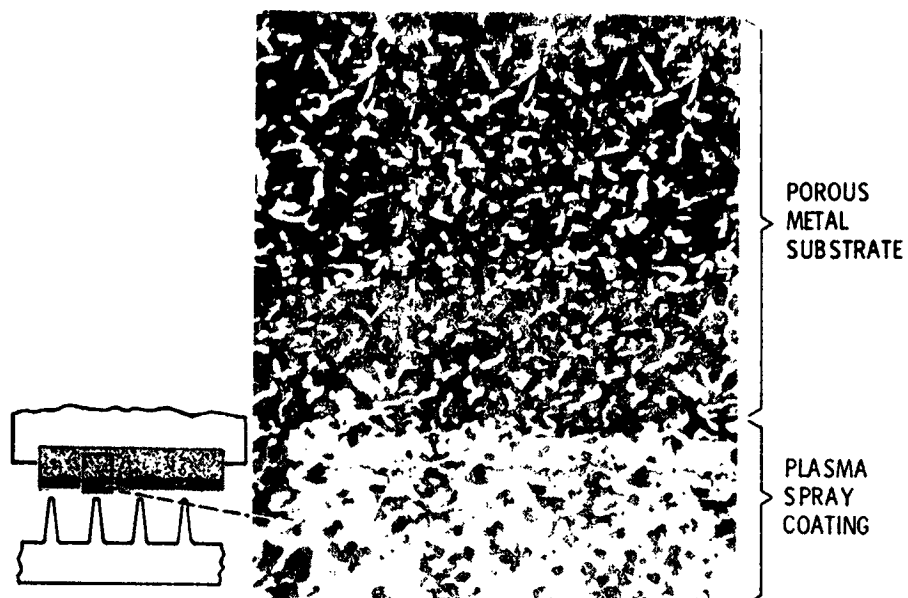
Figure 7.- Photomicrograph of NASA experimental seal material.

Figure 8.- Photomicrograph of rub groove
in NASA experimental seal material.

478
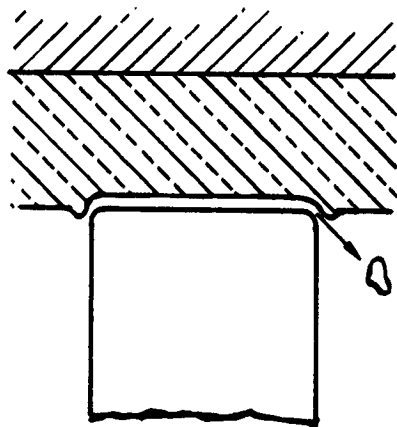
Figure 9.- Rub behavior of thermally sprayed, plastically deformable surface treatments.
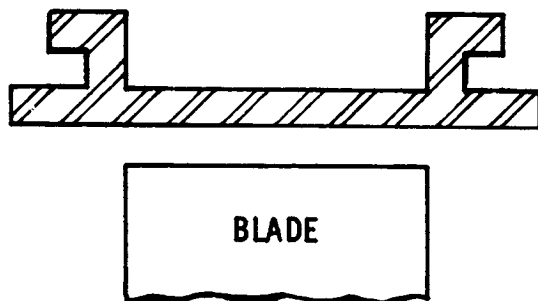
(a) Untreated cobalt-base shroud.
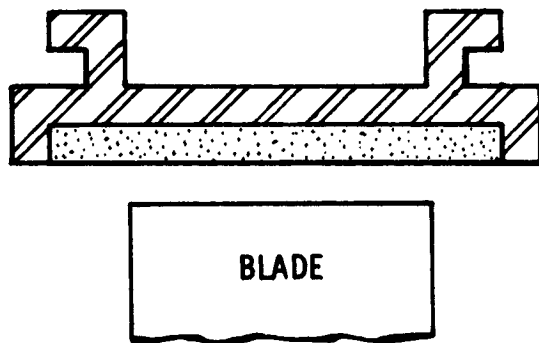
(b) Shroud with rub-tolerant surface treatment of hot-pressed Ni-Cr-Al-Y alloy or sintered NiAl alloy.

Figure 10.- Metal turbine tip seals.
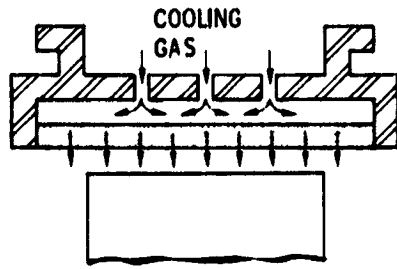
(a) Transpiration cooled.
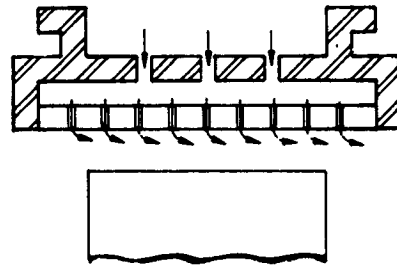
(b) Film cooled.

Figure 11.- Cooled turbine tip seals.
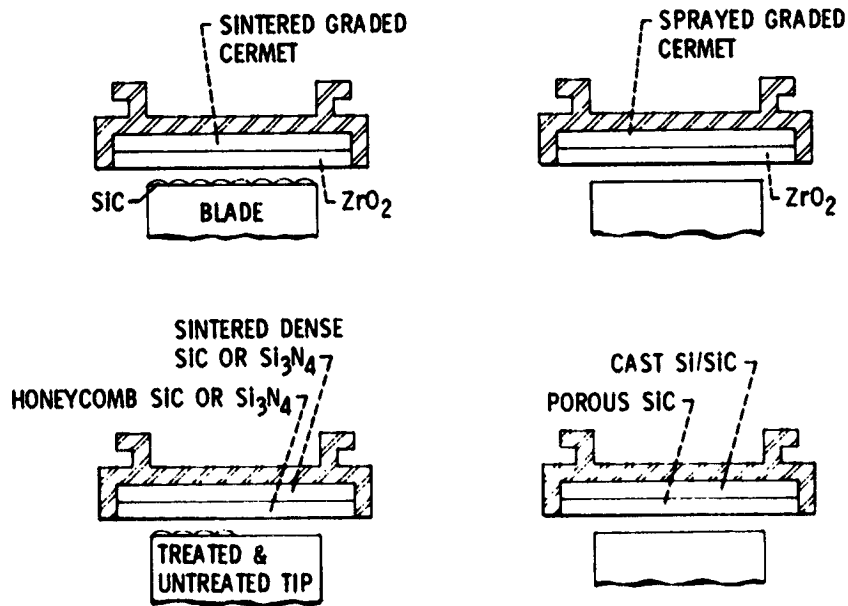
Figure 12.- Ceramic turbine tip seals.

ADVANCED INLET DUCT NOISE REDUCTION CONCEPTS

David Chestnutt
NASA Langley Research Center

Charles E. Feiler
NASA Lewis Research Center

SUMMARY

This paper is a progress report on the implications of inlet noise reduction on aircraft direct operating costs (DOC). It considers treated inlet rings, various other inlet noise reduction concepts, and forward-speed effects. The paper has been limited to relatively well-established approaches to inlet noise reduction, such as acoustic liners and fixed-geometry/high-subsonic-speed inlets which are the focus of considerable current research activity. All of the concepts discussed will be of a "passive" nature, i.e., no moving parts or electrical feedback systems. More futuristic approaches may include variable inlet geometry, inlet sprays, and in-duct cancellation. These "active" approaches may be applied at some future time after the passive approaches have been more fully exploited.

INTRODUCTION

Inlet noise is a contributor to the total noise signature of commercial jet transport aircraft that must be controlled to achieve community acceptability and to meet current and future federal noise regulations. Efforts to control inlet noise are either at the source through proper design of the rotating components so as to minimize the generation of noise or by appropriate modifications within the inlet duct so as to inhibit the radiation of turbomachinery noise from the inlet face. The last decade has witnessed efforts by the universities, the government, and private industry to identify, develop, and implement a variety of methods for inlet noise control. An imaginative research effort continues to improve on established methods and to produce new ideas.

The purpose of this paper is to present a progress report on current efforts by describing various approaches to noise control within the inlet which show promise for future applications. Included in the discussion are treated inlet rings, refracting inlets, variable impedance liners, hybrid inlets, and forward-speed effects. Not included in this paper are the more futuristic approaches to inlet noise reduction which would involve variable geometry, inlet sprays, in-duct cancellation, and the like. A summary of these concepts is given in reference 1.

481

As a reminder of the nature of the problem, a schematic example of a fan noise narrowband spectrum that may occur within an inlet is shown in figure 1. Superimposed upon a background of broadband noise are pure tones occurring at multiples of the blade passage frequency. Among the more important sources of these tones are the interaction of rotating blades and stationary vanes with upstream generated wakes, atmospheric turbulence and ground vortices, wall boundary layers, and inflow distortion resulting from crosswinds and angle of attack. On occasion combination tones can be observed which occur at the sums and differences of the harmonics of tones from multistage devices. When the relative Mach number into the fan blades becomes supersonic, shock waves created at the blade leading edges spiral down the duct to form "multiple pure tones" (MPT). This fundamental MPT occurs at the shaft speed, and there may be higher harmonics which create a very ragged sound spectrum and have a "buzz-saw" sound. In-duct levels of broadband noise on the order of 120 to 130 dB have been measured. Tones may extend 10 to 15 dB above these levels. Overall noise levels near the fan of 150 to 160 dB are not unusual. In this paper, methods of reducing fan noise within the inlet duct are described, whereas methods of reducing the noise at the source by modifications to the fan itself are not considered.

SYMBOLS AND ABBREVIATIONS

c	speed of sound
D	inlet diameter
f	frequency
l	length of acoustic treatment
m	spinning mode number
M	Mach number
BPF	blade passing frequency
DOC	direct operating cost
EPNdB	unit of effective perceived noise level
PNdB	unit of perceived noise level
PNLT	tone-corrected perceived noise level
SPL	sound pressure level

QUIET ENGINE PROGRAM

Several years ago Lewis Research Center completed the Quiet Engine Program. One of the program objectives had to do with the exploration of inlet splitter

482

rings for noise suppression. A photograph of one of these engines with three inlet rings is shown in figure 2. At that time the state of the art indicated that inlet rings were required to substantially reduce inlet noise below the standards of Federal Aviation Regulation Part 36 (FAR 36; ref. 2). This belief was based in a large part on the results from duct theory and experiments being used for noise reduction prediction. Figure 3 (ref. 3) depicts some results from this inlet ring study. Perceived noise level is plotted as a function of azimuth angle measured from the inlet axis. There was a significant reduction in noise at all angles for the wall-only treatment. The inlet with splitter rings yielded noticeable additional reductions between 10° and 50° only. A conclusion that may be drawn from these results is that adding the complexity of inlet splitter rings produced small additional noise reductions. This result may have been due to the fact that the wall treatment performed much better than expected or that perhaps a noise floor was encountered at the level reached by the wall-only treatment, thereby preventing further reduction by the rings.

Using 1972 acoustic technology from the Lewis Quiet Engine Program, acoustic and economic trade-offs were calculated by the General Electric Company as shown in figure 4 (ref. 4). The curve indicates the trade-off between DOC and noise reduction achieved by the use of acoustic treatment. This curve is based on the experience with the low fan tip speed used on Quiet Engine "A." The initial point on the curve is for the untreated engine configuration. Subsequent points are for incremental additions of acoustic treatment with the final point representing a three-ring inlet and a two-ring exhaust duct.

A result from this analysis is the penalty on DOC incurred through the use of 1972 acoustic treatment technology to achieve noise levels 10 dB or more below the standards of FAR 36. The curve indicates that the economic cost of reaching this noise level is too high. This paper will attempt to show that the slope of this curve is being changed by current research. The exact change is not known but definite improvements are indicated. Another Quiet Engine Program may be appropriate in the future to determine more precisely the new acoustic and economic trade-offs.

Figure 5 (ref. 4) shows predicted attenuation of sound power as a function of frequency based on 1972 noise source assumptions allowing only axisymmetric modes. The amount of attenuation obtainable simply depended upon the amount of treatment that could be put in an inlet, and for higher frequencies large amounts of treatment would be required to produce only modest amounts of noise reduction. The data points above this curve indicate acoustic measurements with the quiet engine, two fans, and a JT8D engine. The noise reduction results were much better than predicted. The discrepancies between the predictions and the measurements caused a re-evaluation of the duct theory assumptions. A probable explanation for the overly conservative prediction is the noise-source assumption. Figure 6 indicates schematically the actual acoustic pressure pattern generated by rotor-stator interaction or a supersonic-tip speed rotor. When these spinning mode patterns are accounted for in the theory, the maximum possible sound attenuation is increased. Figure 7 (ref. 5) shows the effect of the presence of spinning modes in the source on maximum sound power attenuation as a function of frequency. The lowest curve represents the axisymmetric

483

source assumption that was made with the previous theory. The same experimental
data has been plotted on the curves, showing that this sound description can
account for the level of experimental data. When it becomes possible to measure
the noise sources inside of these turbomachines it may become apparent how good
these new theoretical assumptions are. Work is currently underway to measure
these noise sources statically and hopefully, in the future, in a flight
environment.

ADVANCED LINER CONCEPTS

In this section consideration will be given to progress made on advanced
duct liner concepts for improving the sound absorption efficiency of nacelle
acoustic treatment. The goals of this work are to broaden the bandwidth of
absorption, to improve low-frequency absorption characteristics, and to achieve
more absorption with less weight and volume of treatment. An extensive review
of duct acoustics and duct liner concepts is given in reference 6. More recent
advances are contained in references 1 and 7.

Refracting Inlet

A relatively new noise reduction concept termed a "refracting inlet" has
been proposed in reference 8. The basic phenomenon to be exploited in this
inlet is illustrated in the sketch at the upper left of figure 8. In the
experiment depicted, a sound wave traveling upstream in the narrow portion of
the duct is seen to be refracted toward the lower wall after passing through
the throat. It is believed that this refraction is caused by the velocity
gradients present near the throat, particularly near the lower wall. The
amount of refraction is a function of sound wavelength and flow speed. This
experimental result suggests that it may be possible to use controlled refrac-
tion of sound waves to reduce inlet noise as shown in figure 9. The data of
figure 9 are based on recent laboratory tests. By suitably tailoring the
gradients in the inlet flow, noise propagating within the inlet is redirected
towards wall acoustic treatment. In another case the radiated noise could be
directed away from the ground. By directing more sound energy onto a liner,
the efficiency of acoustic treatment might be significantly enhanced. Research
is currently underway to explore more fully the performance and practicality of
the refracting inlet concept.

Variable Impedance

One approach to increasing liner absorption is the variable impedance
concept illustrated schematically in figure 10. In its simplest form, segments
of liners having different impedances are placed axially along, or circumferen-
tially around, the inlet. One can conceive of combining these two discrete
patterns and smoothing over abrupt changes in liner properties to produce a
continuous variation in impedance. The carefully designed change in impedance
is believed to break up the orderly modal structure found in a uniformly lined
duct and may redistribute some of the acoustic energy into cutoff modes. The

484

axially segmented liner has been studied theoretically and experimentally because it is an arrangement which is relatively easy to set up in a laboratory or to examine theoretically. The continuous variation of impedance may emerge as a useful concept when more sophisticated fabrication techniques and design procedures become available. In particular bulk absorbing materials are re-emerging as candidates for engine inlets because of new material availability. Bulk materials could be made to have continuously varying impedance tailored for a particular noise source.

Data on three axially segmented liners, obtained using the 30.48-cm-diameter (12 inch) research compressor in the Langley anechoic noise facility, are shown in figure 11. By placing various combinations of segmented treatment in the compressor inlet, a parametric study of segmented liner configurations was conducted in cooperation with the General Electric Company. The spectra in the figure are for a hard wall inlet, a uniform liner, and one of the acoustically better three-segment liners. It can be seen that the three-segment liner produces greater noise reduction than the uniform liner in the low- and mid-frequency range, as would be expected because of the two thicker treatment sections. Moreover, the high-frequency attenuation is maintained with the segmented liner even though a smaller amount of high-frequency treatment is present. One of the aims of current research is to expand to higher values the frequency range over which segmented treatment produces significant additional noise reduction. Data such as these suggest that multisegment liners may be superior to uniform liners and that the concept deserves further careful inves-tigation. Probably the most urgent need at the moment is for well-controlled tests of multisegment and uniform liners optimized and tested for a known noise source in order to get a true comparison of their relative merits. It will take special care to do this statically in view of what is now known about the effects of inlet turbulence on turbomachinery noise generation.

Hybrid Inlets

In a hybrid inlet both acoustic treatment and high subsonic velocity air-flow are combined to reduce noise. By operating at average throat Mach numbers somewhat less than 1.0, the aerodynamic performance penalties associated with the sonic inlet are minimized. Figure 12 (ref. 9) shows a comparison between a near-sonic inlet and a hybrid inlet for the NASA QCSEE engine. This figure indicates a relatively small reduction in total pressure recovery after treat-ment was added. In this case the noise reduction achieved as a result of the high subsonic speed airflow is augmented by sound absorption at the acoustically lined walls. These acoustic characteristics of the hybrid inlet are indicated in figure 13 which shows data for an experimental hybrid inlet compared with data for a hard-wall baseline at high subsonic Mach number inlet. In this case, the baseline inlet was found to produce SPL noise reductions of up to 20 dB at an average throat Mach number of 0.85. With the addition of wall treatment, additional noise reductions were obtained throughout the operating range as indicated by the upper curves. The full potential of the hybrid inlet concept remains to be explored. There are several directions for further research using the hybrid inlet concept, such as the combined use of segmented acoustic treat-ment to improve sound attenuation, and wind tunnel or flight testing to optimize aerodynamic and acoustic performance in the presence of forward speed.

485

Liner Design

This discussion would not be complete without mention of the some novel liner designs of L. Wirt of the Lockheed-California Company (ref. 16). Wirt's inventiveness has produced a number of unique geometrical variations of the Helmholtz resonator which are being considered as candidates for inlet treatment. Among these are Permoblique, Schizophonium, and Can a-bel. These names refer to the geometrical design of the backing cavities. They have been found to have excellent low-frequency noise reduction qualities.

FORWARD-SPEED EFFECTS

The flight noise data presented were measured by the Douglas Aircraft Company (ref. 3). The measuring technique employed included a series of ground microphones and sophisticated techniques for tracking the aircraft flight path, including the airplane position and speed relative to the observation point. Engine corrected speed was carefully controlled and atmospheric weather conditions were monitored.

The static noise data were measured on an engine test stand with far-field microphones. In order to compare static data with flight data, it was necessary to project the static data to flight conditions. The procedures used accounted for the number of engines, aircraft flight path, air speed and altitude, atmospheric absorption, Doppler shift, and acoustic path length. Appropriate corrections were also applied to the jet noise component of the spectra to account for the effect of relative velocity on this noise component.

Flight data on a CF6-6 engine were obtained on a DC-10 installation where the nacelles have fixed geometry inlets and acoustic treatment on the cowl walls. A comparison of flight and projected static PNLT time histories is shown in figure 14. For this engine, the flight data are 3 to 12 PNdB less than the static projection depending on the time or position at which the comparison is made. Figure 15 shows a spectral comparison of these data at an inlet angle of about 70°, corresponding to the peak inlet fan noise. While the static data clearly reveal the presence of the fan fundamental tone, it is absent in the flight data. At frequencies higher than the fan fundamental frequency, the projections from the static data remain higher than the flight data.

The trends of figure 15 were also observed when the spectra were compared at the maximum PNLT values. The maximum values correspond to aft-radiated noise for this engine. Thus, a major difference between flight and static data is the absence of the fan fundamental tone in the flight data. The absence of this tone probably accounts for a significant part of the reduction in flight PNLT values relative to the static projections.

The presence of the fan fundamental in the static data suggests that it had to be produced by a different noise source during static testing that was absent during flight tests. The source is thought to be inflow distortion or atmospheric turbulence.

Aside from the disturbing conclusion that static fan or engine data are to some degree unreliable because of unsteady inflows, the important conclusions from flight data are that these unsteady inflows are minimized and that acoustic "cutoff" can be realized to yield noise levels substantially less in flight than would be expected from projection of the static data to flight.

Research is currently underway (ref. 11) to explain static noise results. The product of this work will, hopefully, improve the quality of future fan and engine static tests.

CONCLUDING REMARKS

This paper has presented an overview of certain passive, advanced concepts for the suppression of noise within the inlets of gas turbine engines. A status report of research on inlet acoustic liners and high subsonic Mach number inlets has been given. Some directions for improving these suppression methods have been pointed out and certain research and operating problems have been highlighted. Attention has been drawn to several ideas which may find practical application in the future and some optimism has been shown regarding minimizing operating losses for engine noise reduction concepts. These concepts can be expected to improve the relationship between noise reduction and direct operating cost.

REFERENCES

1. Lansing, Donald L.; and Chestnutt, David: Survey of Inlet Noise Reduction
   Concepts for Gas Turbine Engines. NASA TM X-72801, 1976.

2. Noise Standards: Aircraft Type Certification. Federal Aviation Regulations,
   vol. III, pt. 36, FAA, Dec. 1969.

3. Feiler, Charles E.; and Merriman, James E.: Effects of Forward Velocity
   and Acoustic Treatment on Inlet Fan Noise. NASA TM X-71591, 1974.

4. Cornell, W. G.: Experimental Quiet Engine Program – Summary Report.
   NASA CR-2519, 1975.

5. Feiler, Charles E.; Heidelberg, Laurence J.; Karchmer, Allan M.;
   Lansing, Donald L.; Miller, Brent A.; and Rice, Edward J.: Propulsion
   System Noise Reduction. Aeronautical Propulsion, NASA SP-381, 1975,
   pp. 1-64.

6. Nayfeh, Ali Hasan; Kaiser, John E.; and Telionis, Demetri P.: The
   Acoustics of Aircraft Engine-Duct Systems. AIAA Paper No. 73-1153,
   Oct. 1973.

7. Rice, Edward J.: Acoustic Liner Optimum Impedance for Spinning Models
   With Mode Cut-Off Ratio as the Design Criterion. NASA TM X-73411, 1976.

8. Sloan, D.; and Farquhar, B. W.: The Refracting Inlet: A New Concept for
   Aircraft Inlet Noise Suppression. Paper 75-GT-21, American Soc. Mech.
   Eng., Mar. 1975.

9. Luidens, Roger W.: Inlet Technology for Powered-Lift Aircraft. Powered-
   Lift Aerodynamics and Acoustics, NASA SP-406, 1976, pp. 369-386.

10. Wirt, L. S.: Sound-Absorptive Materials To Meet Special Requirements.
    J. Acoust. Soc. America, vol. 57, no. 1, Jan. 1975, pp. 126-143.

11. Hodder, Brent K.: An Investigation of Possible Causes for the Reduction
    of Fan Noise in Flight. AIAA Paper No. 76-585, July 1976.
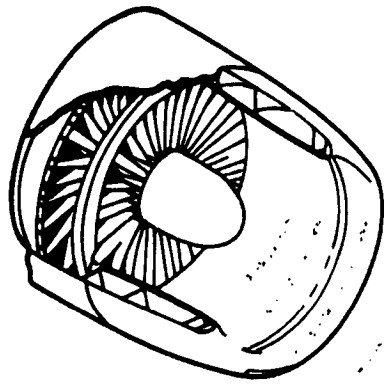
SCHEMATIC
FAN NOISE SPECTRUM

SPL, dB

BROADBAND
NOISE

LOG FREQUENCY, Hz
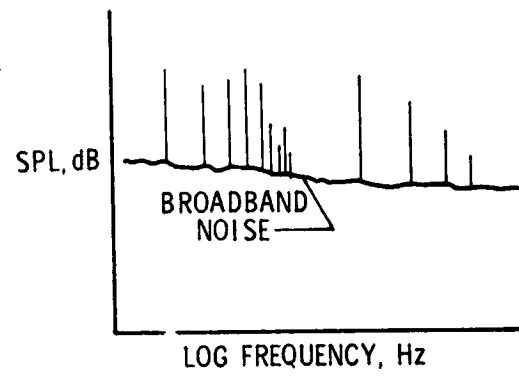
Figure 1.- Fan inlet noise.
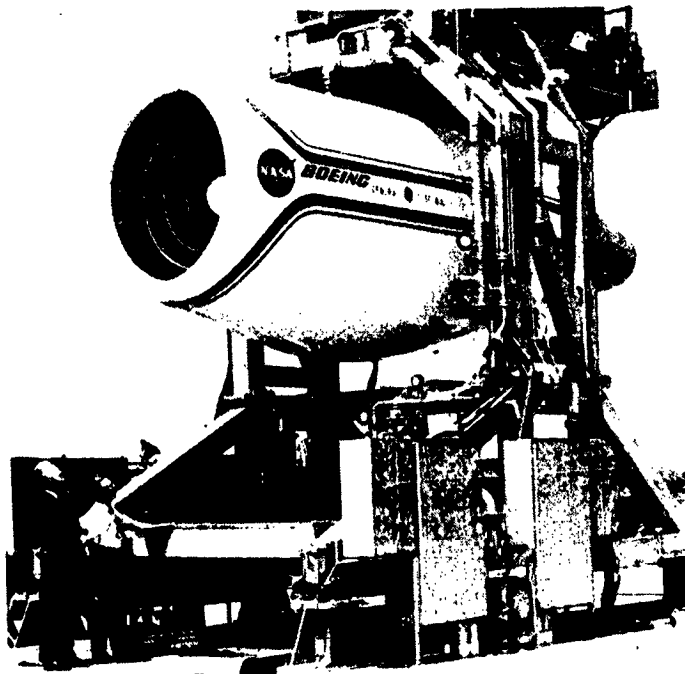
Figure 2.- NASA Quiet Engine with inlet rings.

489
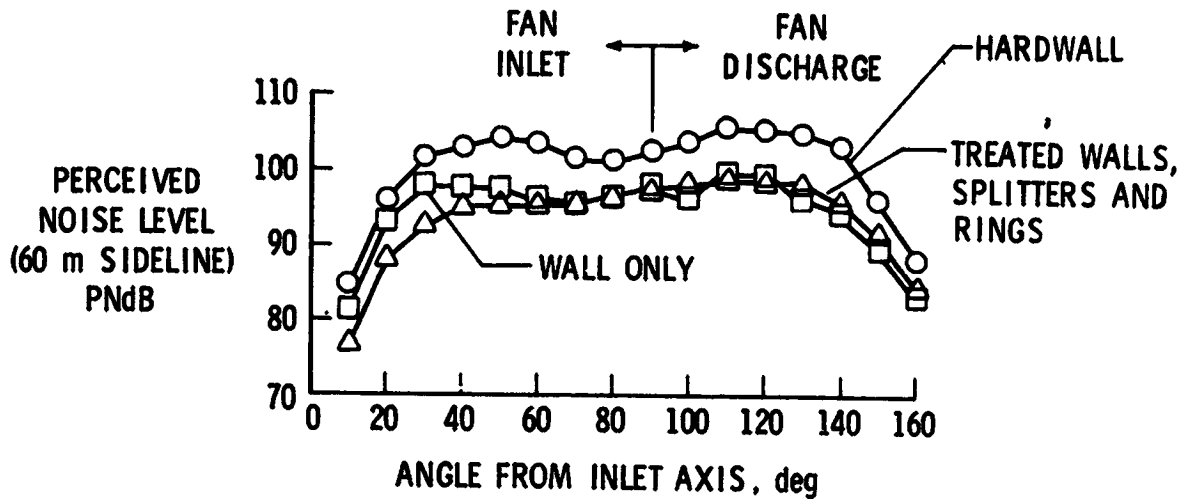
Figure 3.- Effect of inlet suppressor configuration from Quiet Engine Program.
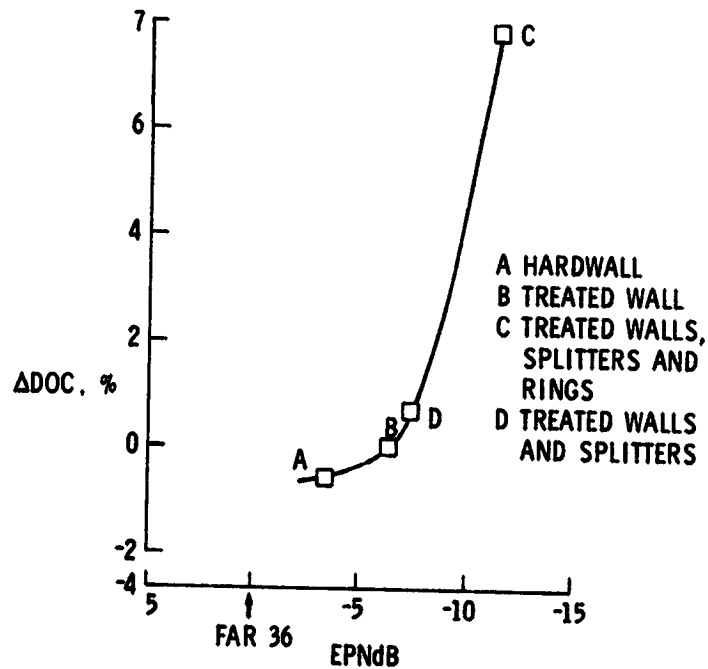
Figure 4.- 1972 relationship between estimated perceived noise level and direct operating costs from the Quiet Engine Program.

490
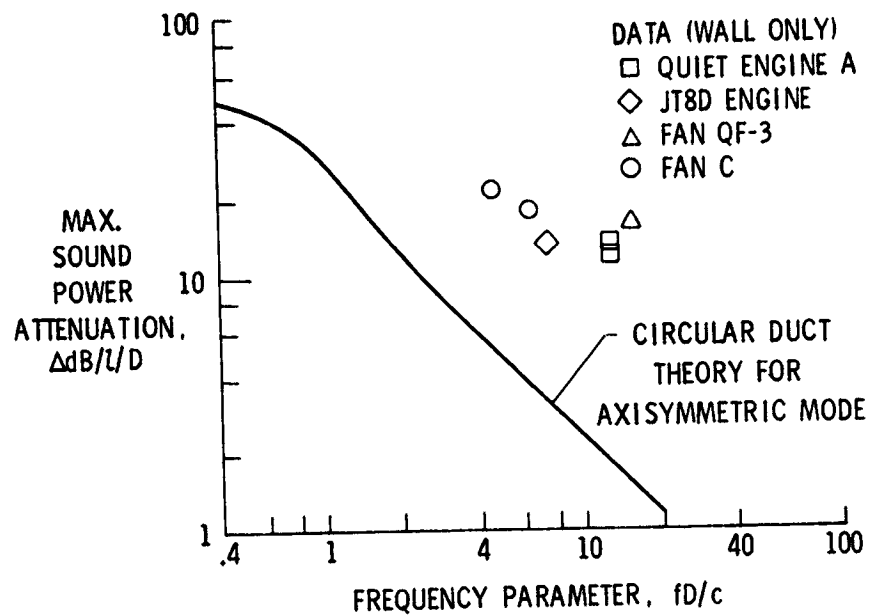
Figure 5.- Comparison of suppressor theory with data.

FOUR LOBE PATTERN, m = 4
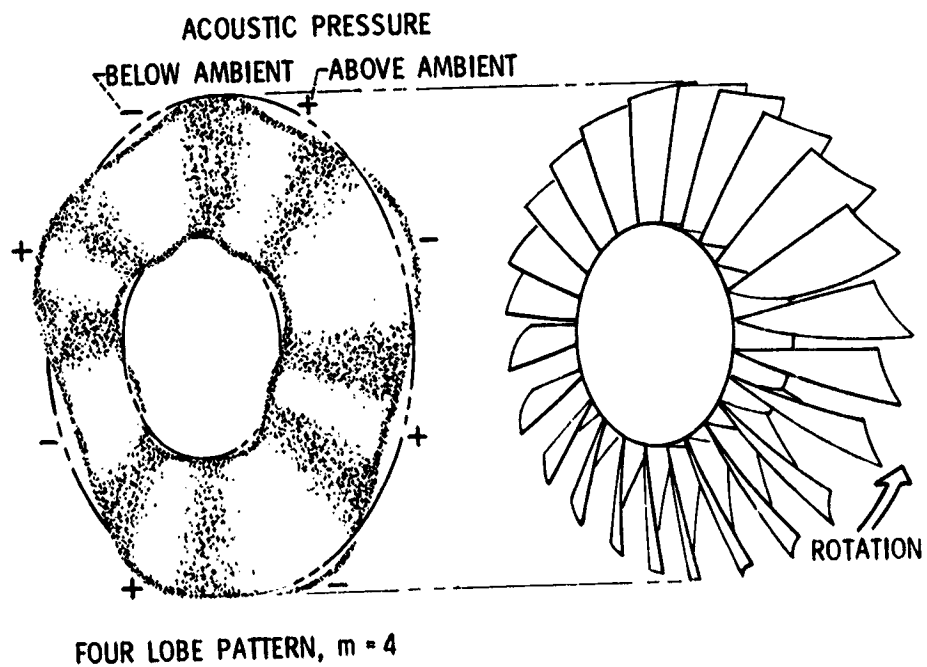
Figure 6.- Spinning lobe or mode pattern.
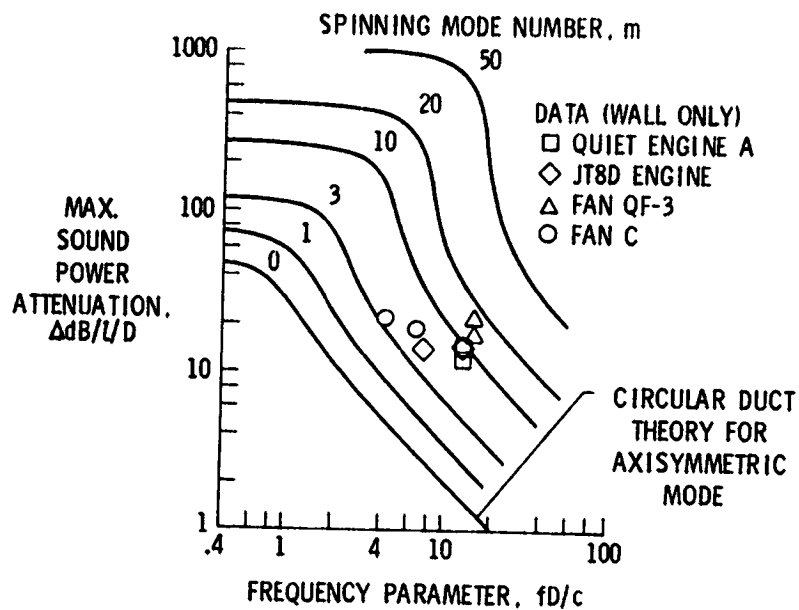
Figure 7.- Effect of spinning mode number on theoretical
maximum sound attenuation.
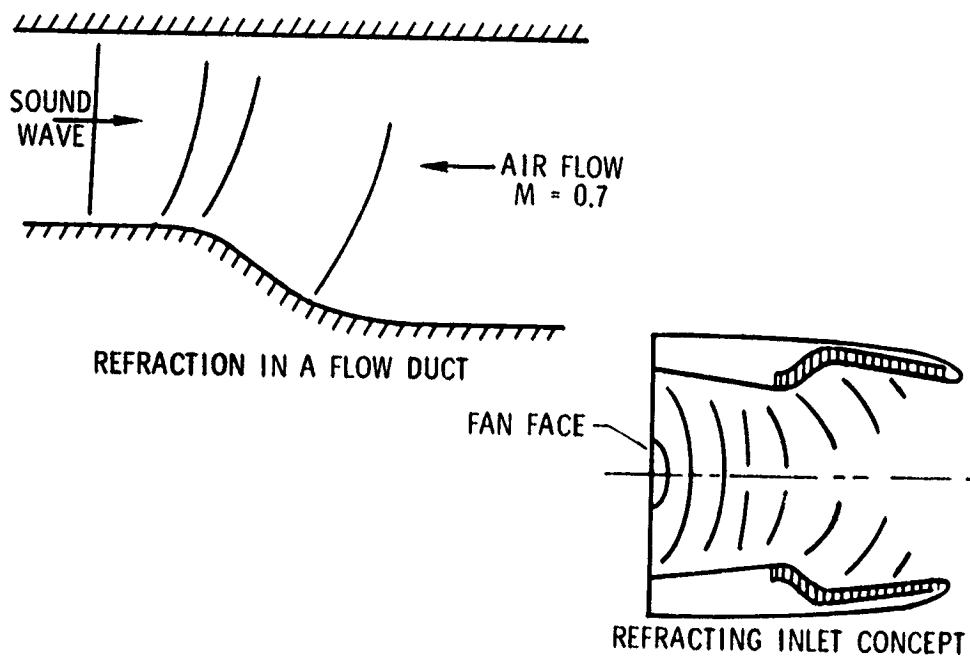
Figure 8.- Wave refraction by velocity gradients.

492
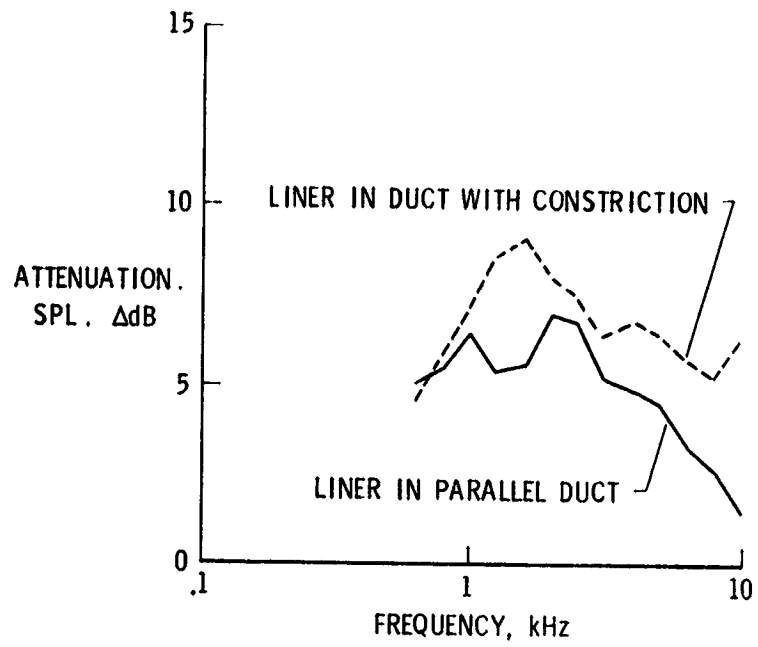
Figure 9.- Improvement of linear effectiveness
by refraction; M = 0.35.

AXIAL SEGMENTATION

CONTINUOUS VARIATION

CIRCUMFERENTIAL
SEGMENTATION
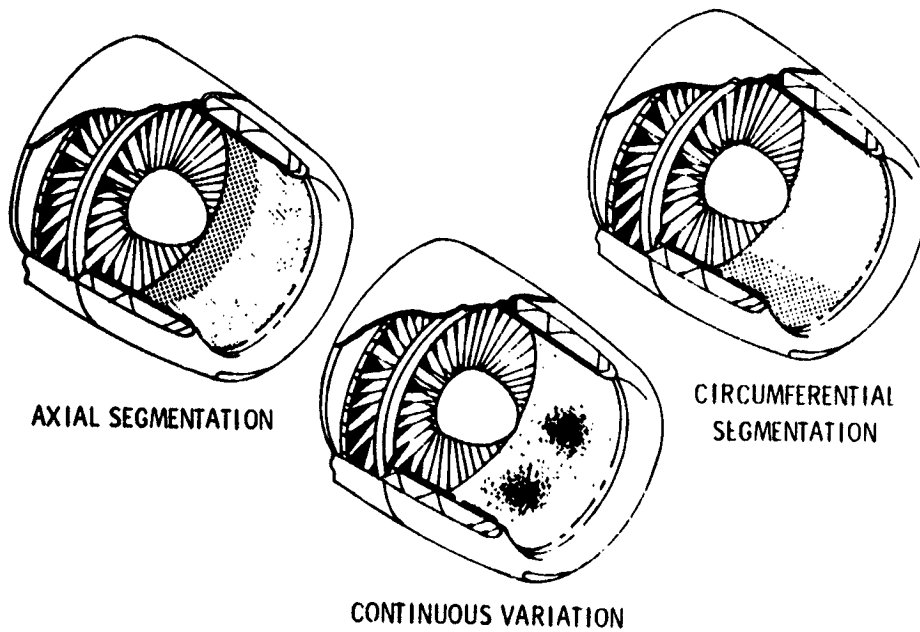
Figure 10.- Variable impedance liner concepts.
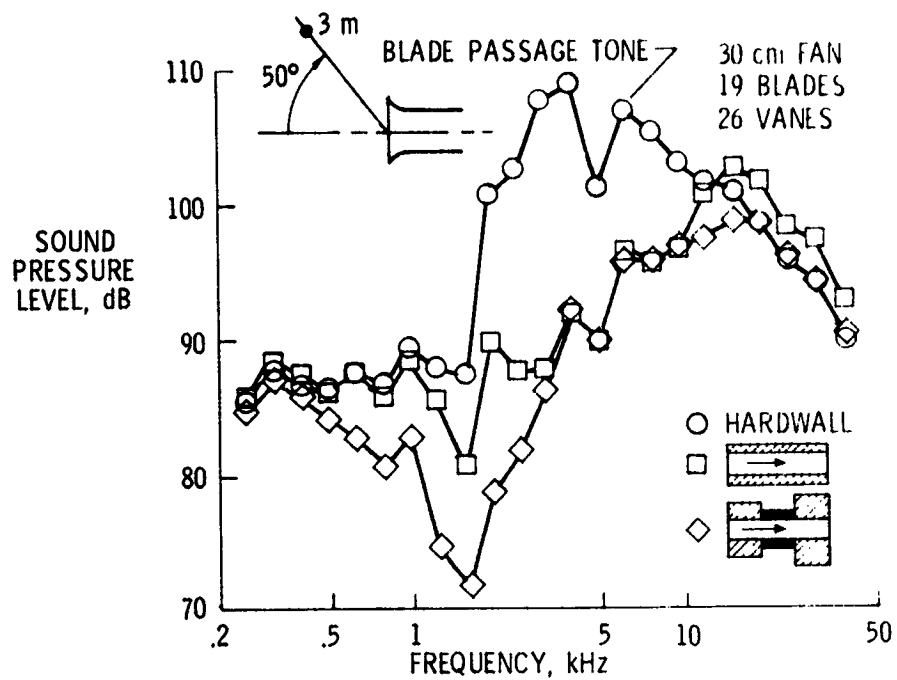
Figure 11.- Segmented liner spectra comparisons.
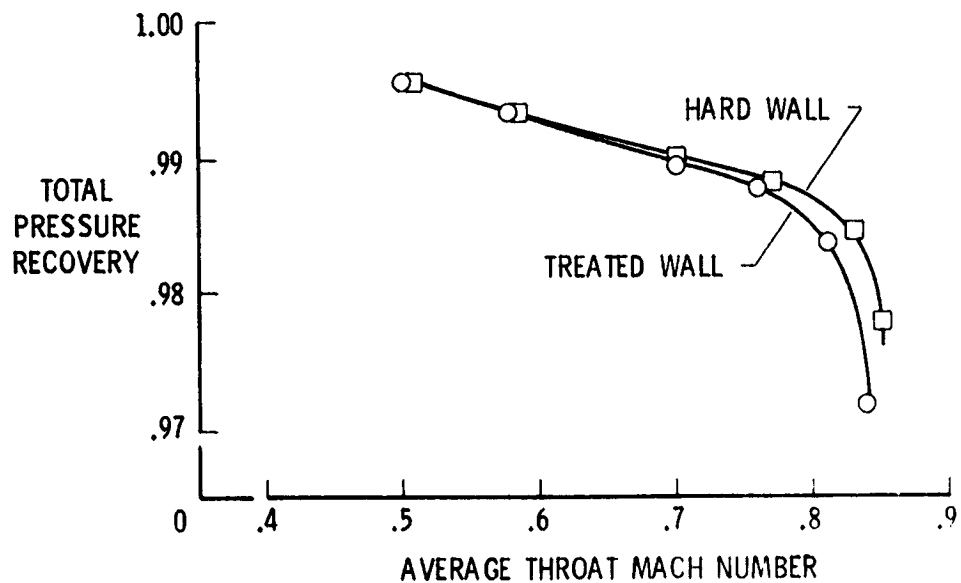
Figure 12.- Hybrid inlet aerodynamic performance for QCSEE engine.

494
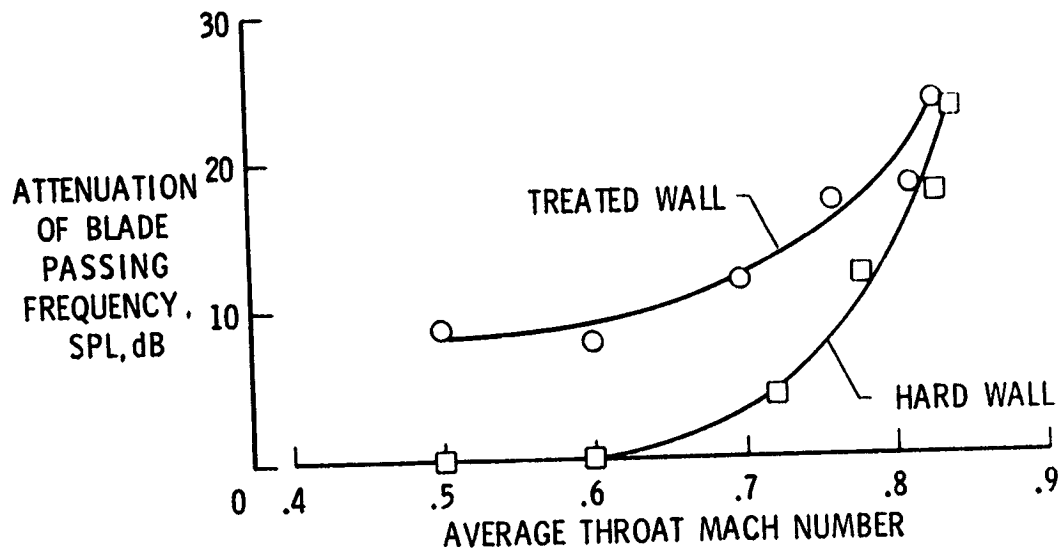
Figure 13.- Hybrid inlet acoustic performance for QCSEE engine.
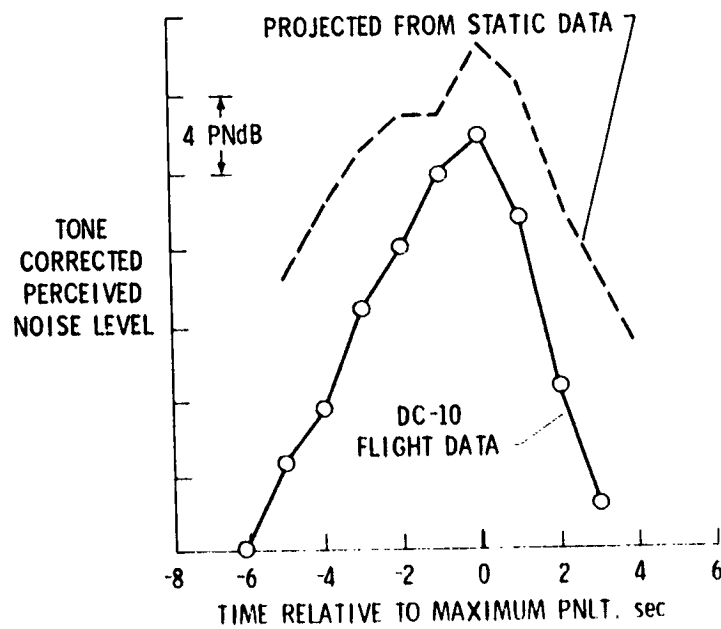
Figure 14.- Comparison of flight and projected
static noise histories for CF6-6 engine.
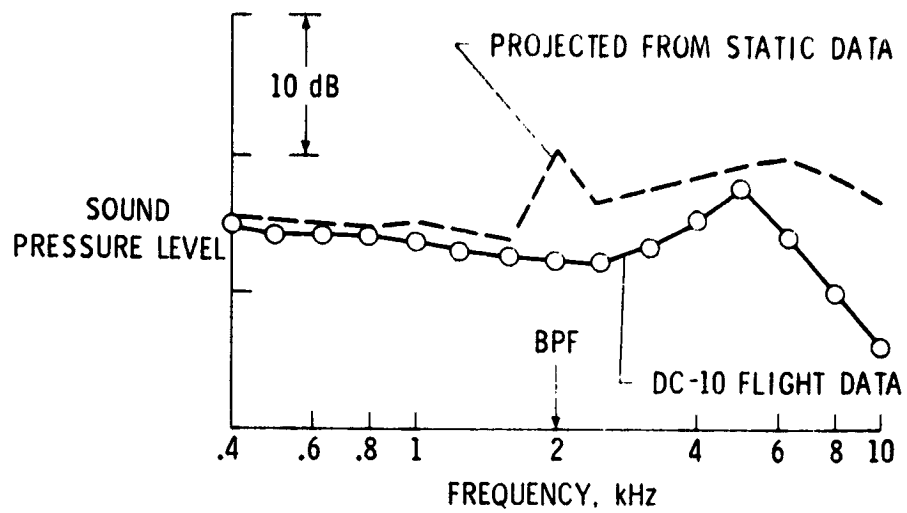
Figure 15.- Comparison of flight and projected static
  inlet sound pressure spectra for CF6-6 engine.

496

-18108

DEVELOPMENTS IN AIRCRAFT JET NOISE TECHNOLOGY

Orlando A. Gutierrez and James R. Stone
NASA Lewis Research Center

SUMMARY

This paper briefly describes significant developments in two areas of jet noise technology: the development of jet noise technology relative to coannular nozzles of all types, and a recent approach to the analysis of flight effects that appears to allow simulated flight effects results to be transformed to actual flight conditions with a high degree of confidence. The coannular nozzle section presents results applicable to high-bypass-ratio turbofan engines, as well as current work on inverted-profile coannular nozzles applicable to low-bypass-ratio turbofan engines suitable for use in future supersonic cruise aircraft.

INTRODUCTION

This paper reviews some of the progress made in jet noise technology since the Aircraft Engine Noise Reduction Conference held at the NASA Lewis Research Center 4 years ago and reported in reference 1. During this time span, Lewis in-house and contracted technology programs have been concerned with noise problems typical of a variety of aircraft, as illustrated in figure 1. These aircraft include conventional aircraft (CTOL) and powered-lift aircraft using engines located over the wing (OTW) and under the wing (UTW), all of which use medium- to high-bypass-ratio turbofan engines, as well as supersonic cruise aircraft, which use low-bypass-ratio turbofan engines. Common to all these aircraft is the use of some type of turbofan engine. This has been reflected in the emphasis placed on the study of coannular jet noise, as is described in this paper. In addition, a recent approach to the understanding of the effects of flight on jet engine exhaust noise is discussed.

Other significant jet noise work being carried out at Lewis in such fields as jet noise suppressor technology and jet-surface interaction noise have not been covered in this paper because of time limitations.

COANNULAR JET NOISE

Because turbofan engines are the primary candidates for all these types of aircraft, the study of coannular jet noise has been of cardinal importance. Figure 2 is a gener-

28

alized sketch of a coannular nozzle showing the inner, or core, nozzle surrounded by the outer, or fan, nozzle. The two exhaust streams form three regions of turbulence that are important in the generation of jet noise the region where the core flow and fan flow mix (region I); the region where the fan flow mixes with the ambient air (region II); and the region where the merged jets mix with the ambient air (region III). Each of these regions generates noise, and their relative importance to the overall jet noise signature of a particular coannular nozzle depends on the relative sizes and velocities of the two streams.

Conventional Coannular Nozzles

Over the past few years a large amount of research has been done on the jet noise characteristics of "conventional" coannular nozzles (e.g., refs. 2 and 3). Figure 3 shows the characteristics of the conventional coannular nozzles. These nozzles have large fan area to core area ratios and fan velocity to core velocity ratios less than 1.0. In this type of coannular nozzle the core-flow/fan-flow and merged-jet/ambient-air mixing regions are the significant noise-producing parts of the jet. These nozzles are applicable to high-bypass-ratio turbofan engines suitable for conventional and STOL aircraft applications, as well as to such research facilities as free jets.

Experimental work has been conducted (refs. 1, 3, and 4) on scale-model nozzles of this type, covering sufficient variations in area ratio, velocity ratio, and exit-plane offsets to permit prediction curves to be generated for this type of coannular nozzle. The results are shown in figure 4 as a change in noise from a reference level as a function of velocity ratio for a series of area ratios. The reference level, referred to as synthesis, is the antilogarithmic sum of the noise levels expected from each stream considered as a convergent nozzle acting alone and thus represents the noise level that would be observed in the absence of interaction effects. (This reference level also corresponds to the results of early jet noise prediction methods such as ref. 5.) The maximum noise reduction obtained for fan-to-core velocities ratios less than 1 increases with an increase in area ratio from an insignificant amount at an area ratio of 0.5 to 11 dB at an area ratio of 10. The velocity ratio at which the maximum reduction occurs varies between 0.5 and 0.4, depending on the area ratio. As a practical application the velocity ratios used in conventional and STOL high-bypass-ratio engines are above a value of approximately 0.7 for performance reasons, which limits the coannular reductions for practical use to between 3 and 4 dB. The reductions in noise such as shown in this figure (developed from the data of ref. 3) have been incorporated into design procedures such as the NASA Aircraft Noise Prediction Program (ANOPP) (ref. 6) and the current proposed Society of Automotive Engineers (SAE) prediction procedures. These

design procedures are not applicable to coannular nozzles with fan-to-core velocity ratios greater than 1.0.

Inverted-Velocity-Profile Coannular Nozzles

Coannular nozzles that produce inverted velocity profiles (fan velocity higher than velocity core) have become interesting candidates for application to low-bypass-ratio turbofan engines. These engines are being considered for use in future supersonic cruise aircraft. This type of nozzle, shown schematically in figure 5, is characterized by a small fan-to-core area ratio (of the order of 1.0) and a fan-to-core velocity ratio in the range of 1.5 to 2.0. With this type of nozzle, the fan-flow/ambient-air and merged-jet/ambient-air mixing regions are the dominant sources of jet noise. Therefore, the prediction methods based on conventional coannular jet data, where the core-flow/fan-flow and merged-jet/ambient-air mixing regions are dominant, do not apply. To fill this gap in jet noise technology, Lewis has been sponsoring experimental studies over the last 3 years with Pratt & Whitney Aircraft and General Electric to determine the noise characteristics of inverted-velocity-profile coannular nozzles.

The basic models tested in these contractor studies are shown in figure 6. A coannular nozzle without plug and with an area ratio of 0.75 and a fan-stream radius ratio of 0.76 is shown in figure 6(a). (This radius ratio is defined as the ratio of the fan-stream inner radius to the fan-stream outer radius.) The model shown in figure 6(b) is a coannular nozzle with a central plug and with an area ratio of 0.67 and a fan stream radius ratio of 0.90. These test models had equivalent total diameters of 13 and 15 centimeters, respectively.

Typical results. - Results from the experimental programs are plotted in figure 7 as peak perceived noise level (normalized for jet density effects)[1] as a function of fan jet velocity for cases where the fan jet velocity was at least 1.5 times the core jet velocity. The jet noise levels for the coannular nozzles are 6 to 10 perceived noise decibels (PNdB) lower than if no favorable interaction occurred between the two sets (both jets exhausting through separate conical nozzles). Between the two coannular nozzles, the configuration with the central plug, which had a higher fan-stream radius ratio, showed a 2-PNdB-greater noise reduction. The thrust losses are about 1.5 to 2.0 percent (referred to an ideal nozzle).

In addition to the base coannular configurations shown, configurations with mechanical suppressors were also tested by adding chutes, convolutions, or tubes to the fan stream, and, in some cases, including ejectors. These suppressed configurations

---

[1]The exponent at the fan jet density is based on conical nozzle results, and for the range of velocity shown here varies from 1.0 at 373 m/sec to 2.0 at velocities above 540 m/sec.

reduced the noise an additional 3 to 7 PNdB, but at the expense of relatively large thrust losses (as much as 8 percent greater than with the unsuppressed coannular nozzles).

Mission analyses (e.g., ref. 7) have shown that the noise reductions observed for the unsuppressed configurations relative to early predictions, which did not account for jet interaction effects, coupled with the low thrust losses involved (~1.5 to 2 percent) are sufficient to meet present FAR-36 noise standards. As a consequence, the technology studies have been concentrated on unsuppressed inverted-velocity-profile coannular nozzles in preference to suppressed configurations and extended to study the effects on noise and thrust characteristics of geometric variables such as radius ratio and area ratio.

Parametric trends. - The effects of velocity ratio on the noise reduction for two different-area-ratio coannular plug nozzles with constant fan radius ratio are shown in figure 8. The noise level relative to the synthesized level predicted for noninteracting jets is plotted as a function of core-to-fan velocity ratio for constant fan operating conditions. (The core velocity was changed by varying both temperature and pressure.) It can be seen that, over this range, the fan-to-core area ratio has very little effect on the noise. Maximum noise reduction occurs between core-to-fan velocity ratios of 0.3 and 0.5. As the core flow is reduced to very low values, less noise reduction is obtained, which could be attributed to the lack of sufficient inner flow to promote rapid velocity decay in the energetic fan stream. When the core flow is increased above a velocity ratio of 0.5, less noise reduction is again obtained, in this case because the core stream affects the jet noise generated in the merged-jet/ambient-air mixing region.

The effects of radius ratio on aeroacoustic performance for two velocity ratios are shown in figure 9. The noise reduction is shown in figure 9(a) as a function of fan-stream radius ratio. As the radius ratio is increased, the noise reduction is also increased, indicating the desirability, from an acoustic point of view, of designing engine nozzles with a high fan radius ratio. The noise reduction obtained with a core-to-fan velocity ratio of 0.5 was larger than for the no-core-flow case, as was previously discussed.

The effect of velocity ratio and fan radius ratio on the thrust characteristics both statically and when exposed to an external flow Mach number of 0.36 (takeoff conditions) is shown in figure 9(b). It is obvious that the thrust losses obtained with no core flow are quite severe (up to 10 percent relative to a convergent nozzle). For a velocity ratio of 0.5, losses are much lower (between 1 and 2 percent additional losses relative to a convergent nozzle). An increase in the radius ratio causes an increase in thrust losses, indicating the need, from a designer's point of view, to trade off the thrust losses with the amount of noise reduction in order to select the optimum nozzle radius ratio for an engine exhaust system.

500

Simulated flight effects. - The acoustic information presented in the preceding sections on the inverted-velocity-profile coannular nozzles has been static data. However, a most important consideration is whether these noise reductions relative to a convergent nozzle are maintained under flight conditions. Consequently, the acoustic program has also included experimental investigations of these models under simulated flight conditions in an acoustic wind tunnel. Typical results obtained with a coannular nozzle without a plug with subsonic velocities in both streams (fan-to-core velocity ratio, ~1.5) are shown in figure 10. The data are presented in terms of overall sound pressure level(OASPL) as a function of the radiation angle from the nozzle inlet. The wind tunnel results have been corrected for the shear layer and sound convection effects of the tunnel stream and converted to a flight frame of reference by the methods of reference 8. The highest curve represents the static conditions, and the lower two curves show directivities at free-stream Mach numbers of 0.18 and 0.30, respectively. Reductions in jet noise were obtained throughout the measured arc, from 60° to 150° from the inlet axis. Peak noise reduction varied from 5 to 7 dB below the static case. The most significant result was that the noise reduction due to forward velocity was the same as for a convergent nozzle, indicating that the noise reduction benefit evident under static conditions is maintained in flight.

Similar results are shown in figure 11 for a case where the fan stream was supersonic (pressure ratio, 2.5). The subsonic core conditions are the same as for figure 10, producing a 1.9 fan-to-core velocity ratio here. The results are very similar except that the peak reductions are somewhat smaller in magnitude (by about $1\frac{1}{2}$ dB) and that in the forward quadrant there is an actual increase in noise level. These changes from the subsonic case are caused by shock-generated noise. However, this forward-quadrant effect does not change the reduction in flight relative to a convergent nozzle, as the convergent nozzle is similarly affected.

DETERMINATION OF JET NOISE IN FLIGHT

The presentation of the preceding simulated flight directivity data for the coannular nozzles introduces another area of study where analytical and experimental efforts have been concentrated: the effects of flight on jet noise and the correlation of jet engine exhaust noise flight data with simulated flight model test information. It is imperative to be able to predict flight jet noise characteristics from analytical models and/or scale-model data because actual flight testing for research and development purposes is prohibitive in cost. Flight noise data from jet engines do not appear to agree with predictions based on classical jet noise theories, such as discussed in reference 9. However, these differences seem to be reconciled if the flight effects are applied to the jet mixing noise and to the internal noise of the engines as well, as suggested in refer-

ence 10. These effects of flight on jet engine exhaust noise directivity are illustrated in figure 12. In figure 12(a), flight effects on the jet mixing noise are presented for a typical turbojet engine. The solid curve represents the jet noise produced statically in terms of noise level as a function of radiation angle. The difference between the solid and the dashed lines represents the reduction in jet noise due to the source strength reduction introduced by the reduction of the relative velocity between the jet and the surrounding medium during flight. This effect is constant at all angles. The dash-dot curve represents the predicted flight noise directivity, incorporating the dynamic effect on noise as well. This dynamic effect tends to decrease the noise in the aft quadrant and increase it in the forward quadrant.

The flight effects on internal noise sources are shown in figure 12(b). Because these sources are not subjected to the relative flow field, there is no source strength reduction, but only motion or dynamic effects. These sources have no relative motion with respect to the nozzle; therefore, the velocity change has a greater effect when applied to the internally generated noise, resulting in larger increases of noise in the forward quadrant than that shown in figure 12(a) for jet noise. As with jet noise, a reduction in noise occurs in the aft quadrant.

The application of the preceding principles to the prediction of jet engine exhaust noise directivity for a hypothetical turbojet engine are shown in figure 13. The static case is illustrated in figure 13(a). The shock-free jet noise, shown by the dashed curve, is greater than the internally generated noise (dash-dot curve). The total exhaust noise (solid curve) is the antilogarithmic sum of the jet noise and internal noise levels and is dominated by the jet mixing noise for all angles. When the flight effects are included, as shown in figure 13(b), the reduction of jet noise at all angles is counteracted by the increased contribution of the internal noise in the forward quadrant. The total exhaust noise is now dominated by internal noise in the forward quadrant; jet noise continues to dominate in the aft quadrant. Total noise statically and in flight is compared in figure 13(c). For this case the flight effect has increased the jet exhaust total noise in the forward quadrant and reduced it in the rear quadrant.

Application of this method of flight analysis of jet mixing and internal noise to the exhaust noise of two actual engines is shown in figure 14. The engines selected had dissimilar levels of internal noise, and in the figure the actual flight data are compared with calculated values. The results for a "high"-internal-noise engine, the Viper 610 in an HS-125 airplane are shown in figure 14(a). Both the calculated OASPL values (shown by the curves) and the data (shown by the symbols (ref. 11)) show the increase of noise level in flight in the forward quadrant discussed previously (figs. 12 and 13). Also shown, both calculated and measured, are the noise reductions in the aft quadrant. The results from a similar evaluation for a "low"-internal-noise engine, the NASA Lewis-sponsored refanned JT8D engine on a DC-9 airplane, are shown in figure 14(b).

502

In this case, both data and calculations indicate a reduction of exhaust noise in flight throughout all angles. A very significant conclusion to be drawn from these results is that engine exhaust noise in flight can be predicted if the internal noise of the engines is properly accounted for.

CONCLUDING REMARKS

This paper has very briefly described signif. nt developments in two areas of jet noise technology that have great impact: jet noise reduction and the prediction of flight effects. Coannular nozzles including those with inverted velocity profiles, have been shown to offer significant noise reductions with little thrust loss. These results are particularly applicable to supersonic cruise aircraft. It was also shown that flight effects on jet engine exhaust noise can be predicted if the internal engine noise is properly accounted for.

APPENDIX - SYMBOLS

A_{CORE}	core jet area, m^2
A_{FAN}	fan jet area, m^2
A_j	jet (single stream) area, m^2
C_V	thrust coefficient, dimensionless
c_a	ambient sonic velocity, m/sec
L	sideline distance, m
M_0	free-stream Mach number, dimensionless
OASPL	overall sound pressure level, dB re 20 $\mu N/m^2$
$OASPL_{COANN}$	OASPL for coannular nozzle, dB re 20 $\mu N/m^2$
$OASPL_{CORE+FAN}$	OASPL for synthesized coannular nozzle (antilogarithmic sum of core jet and fan jet OASPL's), dB re 20 $\mu N/m^2$
PNL_{pk}	peak perceived noise level, PNdB
R_i	inner radius of fan stream, m
R_o	outer radius of fan stream, m
T_{CORE}	core jet total temperature, K
T_{FAN}	fan jet total temperature, K
V_{CORE}	core jet velocity, m/sec
V_{FAN}	fan jet velocity, m/sec
V_j	jet (single stream) velocity, m/sec
θ	angle from nozzle inlet axis, deg
ρ_{FAN}	fan jet density, kg/m^3
ρ_{isa}	ambient density at standard conditions, kg/m^3
ω	density correction exponent

504

REFERENCES

1. Aircraft Engine Noise Reduction. NASA SP-311, 1972.

2. Williams, T. J.; Ali, M. R. M. H.; and Anderson, J. S.: . oise and Flow Characteristics of Coaxial Jets. J. Mech. Eng. Sci., vol. 11, no. 2, April 1969, pp. 133-142.

3. Olsen, W.; and Friedman, R.: Jet Noise from Co-axial Nozzles over a Wide Range of Geometric and Flow Parameters. NASA TM X-71503, 1974.

4. Olsen, W. A.; Gutierrez, O. A.; and Dorsch, R. G.: The Effect of Nozzle Inlet Shape, Lip Thickness, and Exit Shape and Size on Subsonic Jet Noise. AIAA Paper 73-187, Jan. 1973.

5. Jet Noise Prediction. Aerospace Information Report 876, SAE, 1965.

6. Stone, James R.: Interim Prediction Method for Jet Noise. NASA TM X-71618, 1974.

7. Whitlow, John B., Jr.: Effect of Airplane Characteristics and Takeoff Noise and Field Length Constraints on Engine Cycle Selection for a Mach 2.32 Cruise Application. NASA TM X-71865, 1976.

8. Amiet, Roy K.: Correction of Open Jet Wind Tunnel Measurements for Shear Layer Refractions. AIAA Paper 75-532, Mar. 1975.

9. Ffowcs Williams, J. E.: The Noise from Turbulence Convected at High Speed. Philos. Trans. R. Soc. London, Ser. A, vol. 255, no. 1061, Apr. 1963, pp. 469-503.

10. Stone, James R.: On the Effects of Flight on Jet Engine Exhaust Noise. NASA TM X-71819, 1975.

11. Brooks, J. R.; and Woodrow, R. J.: The Effects of Forward Speed on a Number of Turbojet Exhaust Silencers. AIAA Paper 75-506, Mar. 1975.
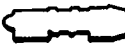
CONVENTIONAL (CTOL)		HIGH-BYPASS TURBOFAN
POWERED LIFT	OVER THE WING (OTW)	HIGH-BYPASS TURBOFAN
	UNDER THE WING (UTW)	VERY HIGH-BYPASS TURBOFAN
SUPERSONIC CRUISE AIRCRAFT		TURBOJET LOW-BYPASS TURBOFAN

Figure 1.- Types of aircraft and engines affected by developments in jet noise reduction technology.
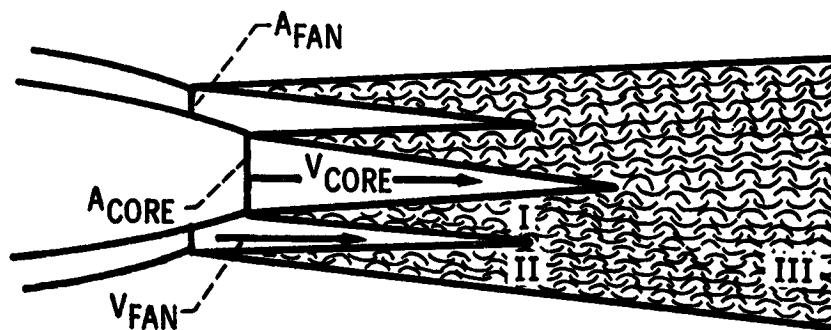
THREE NOISE-PRODUCING REGIONS:

I. CORE-FAN MIXING

II. FAN-AMBIENT MIXING

III. MERGED-JETS - AMBIENT MIXING

Figure 2.- Noise-producing regions in coannular jets.
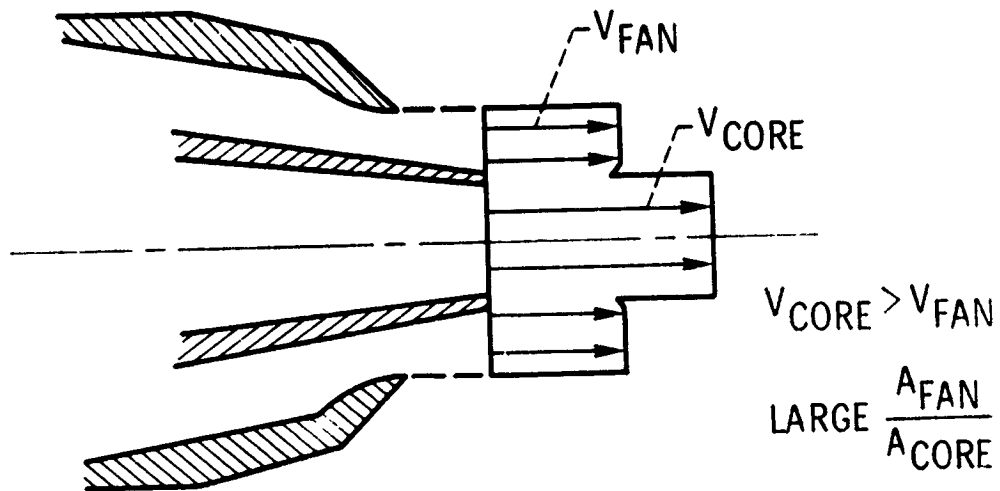
Figure 3.- Conventional coannular nozzles typical of high-bypass-ratio turbofans applicable to CTOL and STOL aircraft.
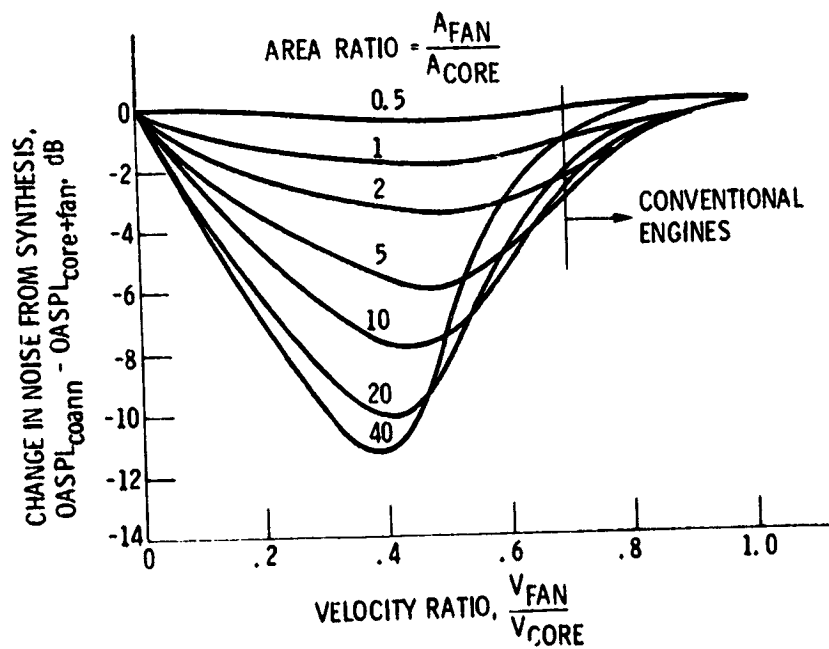
Figure 4.- Coannular noise reduction for conventional coannular nozzles.
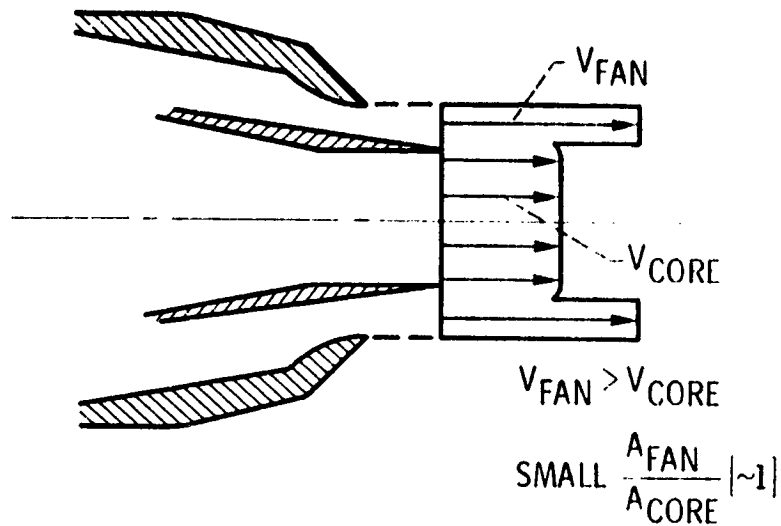
Figure 5.- Inverted-velocity-profile coannular
nozzles typical of low-bypass-ratio turbofans
applicable to supersonic cruise aircraft.

$$\frac{A_{FAN}}{A_{CORE}} = 0.75$$

FAN RADIUS RATIO = 0.76

(a) Without plug.

$$\frac{A_{FAN}}{A_{CORE}} = 0.67$$

FAN RADIUS RATIO = 0.90

(b) With plug.
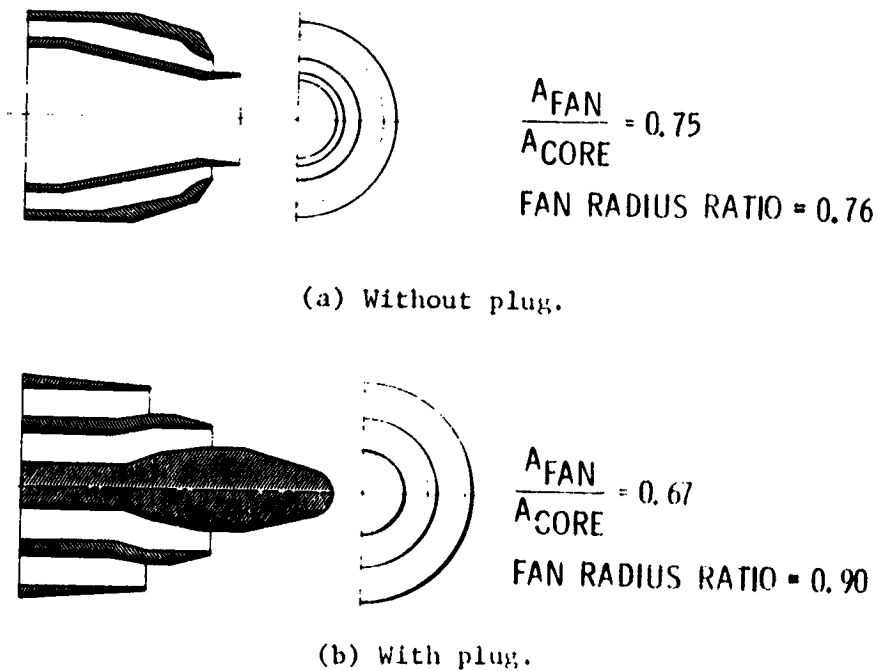
Figure 6.- Typical test models of inverted-velocity-profile
coannular nozzles.
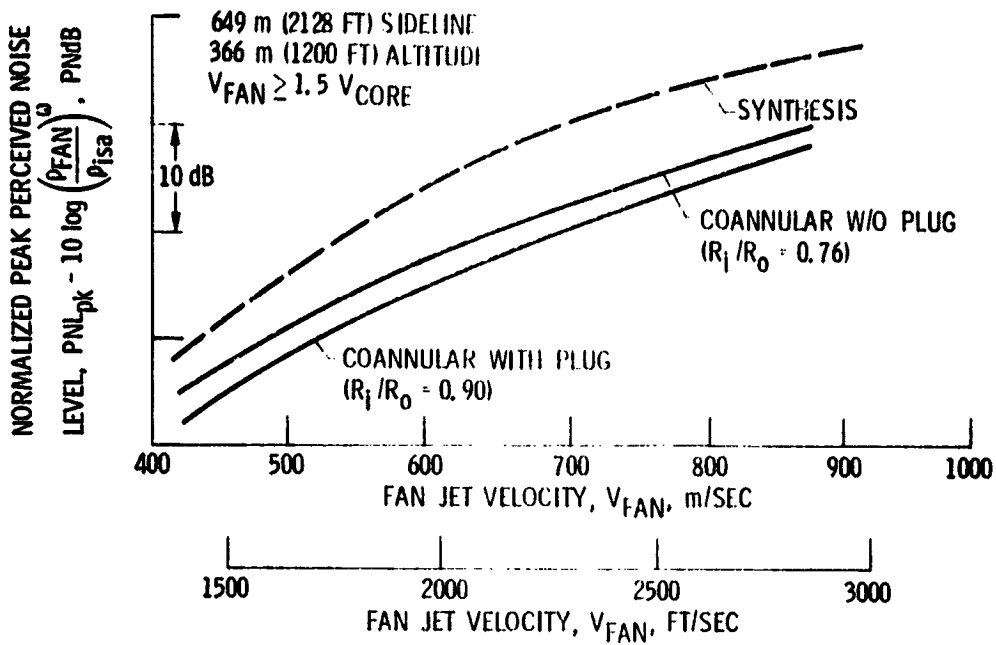
Figure 7.- Peak noise as function of jet velocity for typical
inverted-velocity-profile coannular nozzles.
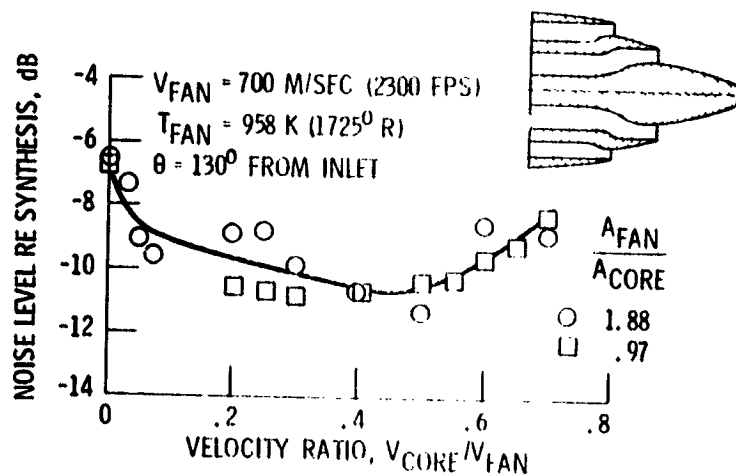
Figure 8.- Effect of velocity ratio on noise reduction
of inverted-velocity-profile coannular nozzles.
Ratio of inner to outer fan-stream radius, R_i/R_o,
0.90.

(a) Acoustic.　　　　　　　(b) Aerodynamic.
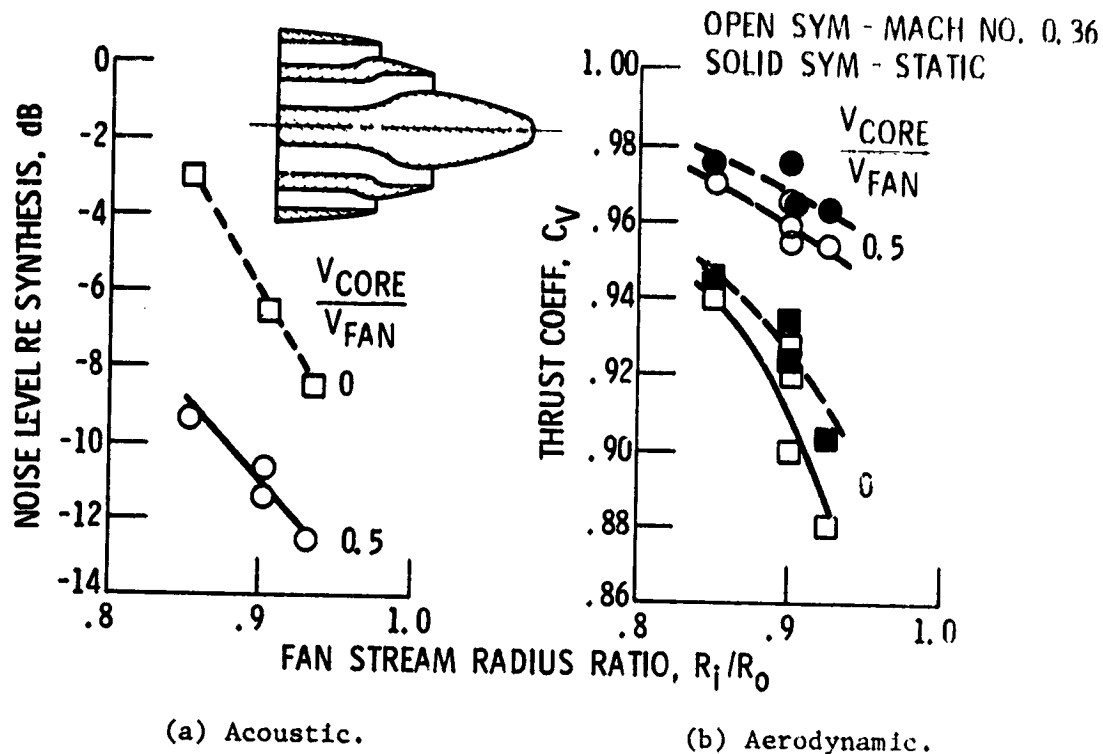
Figure 9.- Effect of radius ratio on aeroacoustic performance of
inverted-velocity-profile coannular nozzles.
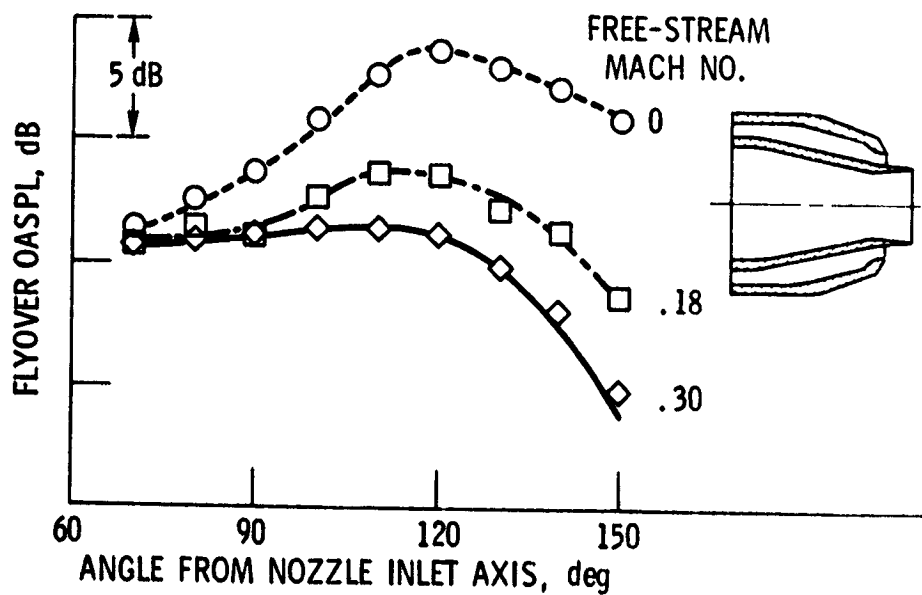
Figure 10.- Static and simulated flight directivities for
inverted-velocity-profile coannular nozzles with sub-
sonic fan stream (fan pressure ratio, 1.8).
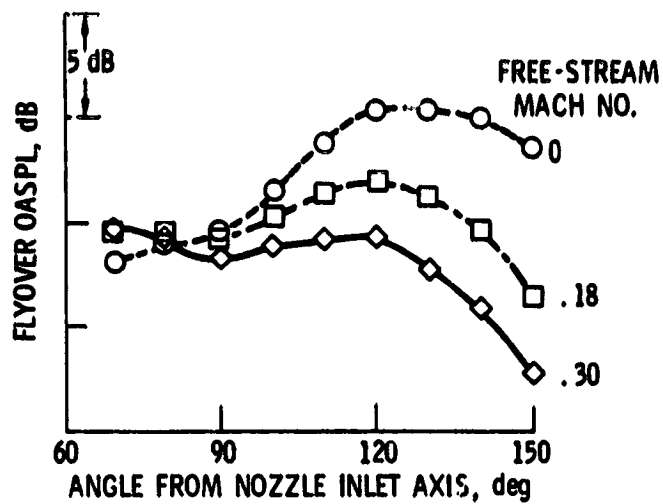
Figure 11.- Static and simulated flight directivities for inverted-velocity-profile coannular nozzles with supersonic fan stream (fan pressure ratio, 2.5).

(a) Shock-free, jet-mixing noise.

(b) Internally generated noise.
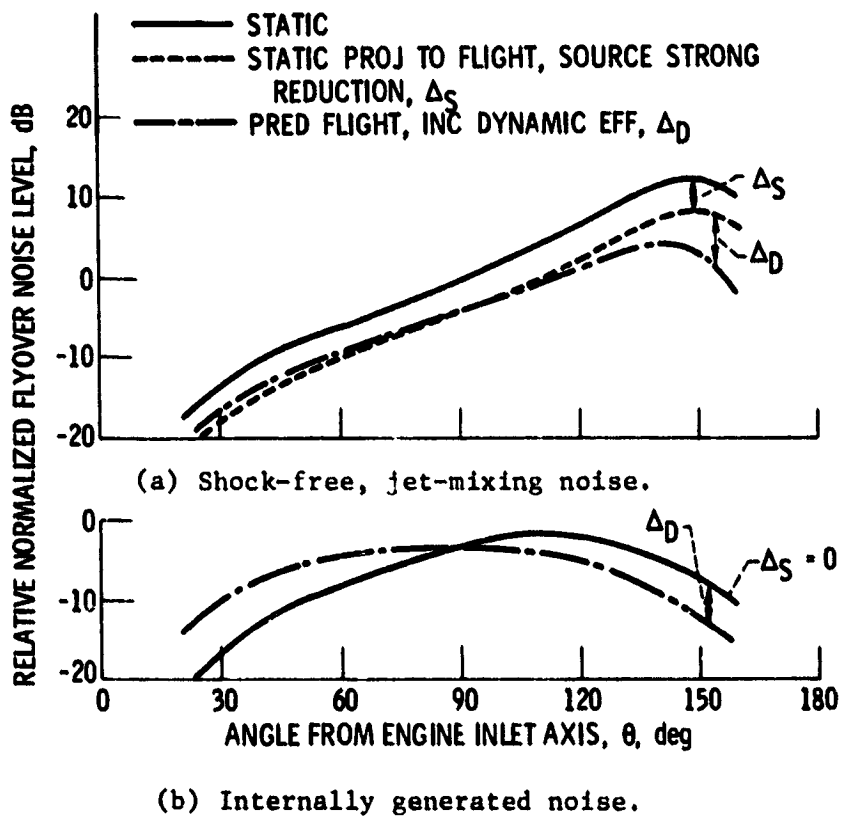
Figure 12.- Typical effects of flight on jet engine exhaust noise.

(a) Static, $M_0 = 0$.

(b) In-flight, $M_0 = 0.35$.

(c) Flight effect on total noise.
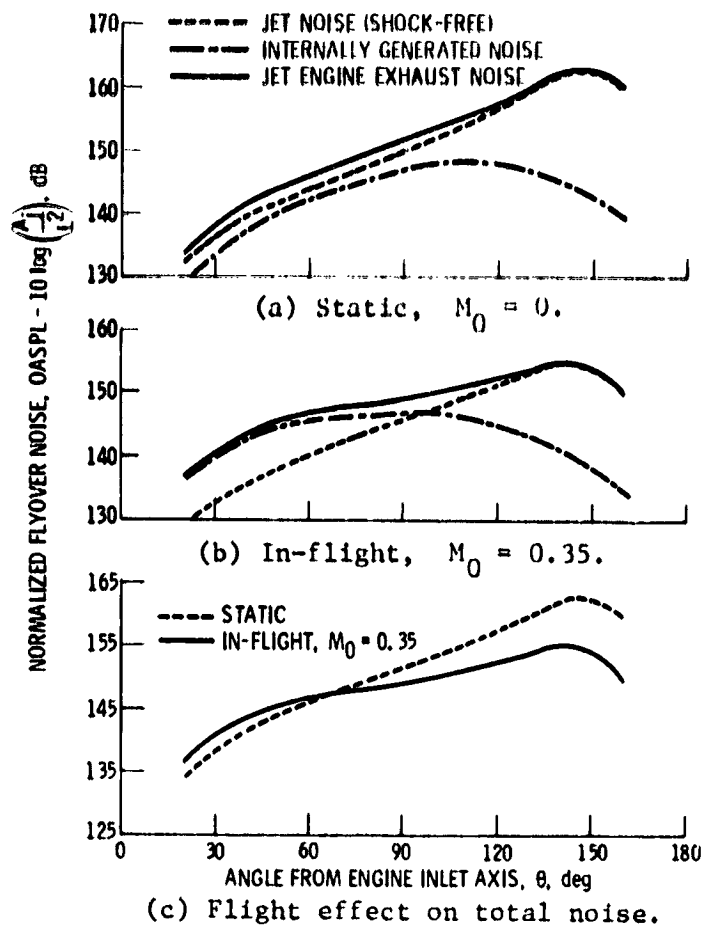
Figure 13.- Synthesis of jet engine exhaust noise directivity for hypothetical jet engine with ratio of jet velocity to ambient sonic velocity V_j/c_a of 1.80.

(a) High internal noise (Viper 610 engine in HS-125 airplane).

(b) Low internal noise (refanned JT8D engine on DC-9 airplane).
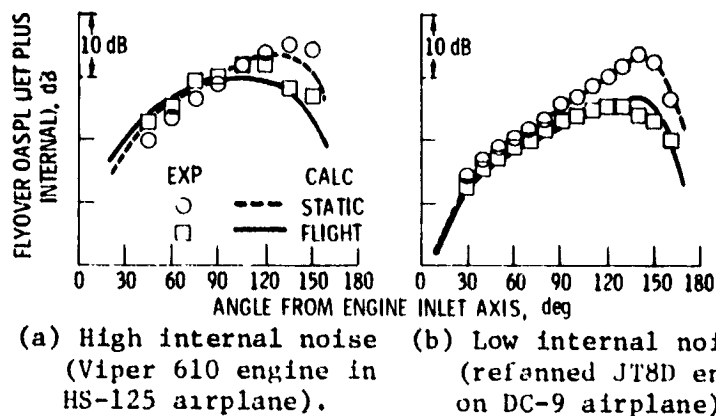
Figure 14.- Comparison of calculated and measured static and flight directivities for engines with different levels of internal noise relative to jet noise.

512

EFFECTS OF AIRCRAFT NOISE ON FLIGHT AND GROUND STRUCTURES

John S. Mixson, William H. Mayes, and Conrad M. Willis
NASA Langley Research Center

SUMMARY

Structural vibrations caused by aircraft noise can lead to damage of the structure or to transmission of noise and vibration that reduces the comfort of occupants. This paper discusses three examples involving structural response to aircraft noise. Acoustic loads measured on jet-powered STOL configurations are presented for externally blown and upper surface blown flap models ranging in size from a small laboratory model up to a full-scale aircraft model. The implications of the measured loads for potential acoustic fatigue and cabin noise are discussed. Noise transmission characteristics of light aircraft structures are presented. The relative importance of noise transmission paths, such as fuselage sidewall and primary structure, is estimated. Acceleration responses of a historic building and a residential home are presented for flyover noise from subsonic and supersonic aircraft. Possible effects on occupant comfort are assessed. The results from these three examples show that aircraft noise can induce structural responses that are large enough to require consideration in the design or operation of the aircraft.

INTRODUCTION

Noise generated by aircraft propagates into the aircraft itself and through the atmosphere to structures on the ground. In the aircraft, the noise can generate vibratory stresses that lead to acoustic fatigue, or can propagate through fuselage walls and cause uncomfortably high cabin noise levels. On the ground, aircraft noise can cause building vibrations that may lead to damage or to increased discomfort of the occupants. Penalties associated with noise effects on aircraft structures can take the form of excess weight required to prevent fatigue and to lower noise levels, of maintenance required to repair fatigue failures, or of passenger complaints of excessive noise. Penalties associated with noise effects on ground structures can range from unfavorable publicity to community actions (such as curfews) that restrict the use of airports. To minimize such penalties, it is important to assess possible noise effects early in the development of new aircraft types, especially those with increased performance, so that noise-reduction methods can be developed.

In this paper, examples of noise effects are discussed for three classes of aircraft for which increased performance is being sought. The topics discussed are: STOL aircraft acoustic loads, light aircraft noise transmission, and building response to aircraft noise. The emphasis of the

discussion is on the response of the structure to the noise. Implications of
the results for possible structural damage and occupant annoyance due to
noise are discussed.

SYMBOLS

Measurements were made in U.S. Customary Units, and are presented in both
the International System of Units (SI) and U.S. Customary Units.

d diameter of nozzle exit

f frequency, Hz

g acceleration of gravity

P_{rms} root mean square of the fluctuating component of pressure

q_0 dynamic pressure of the engine exhaust flow at the nozzle exit

U_0 velocity of the engine exhaust flow at the nozzle exit

Abbreviations:

AMST   advanced medium STOL transport

EBF   externally blown flap

FPL   fluctuating pressure level

OAFPL   overall fluctuating pressure level

rms   root mean square

SPL   sound pressure level

STOL   short (runway) take-off and landing

USB   upper surface blown

Reference level for FPL, OAFPL, and SPL is 20 µPa.

STOL AIRCRAFT ACOUSTIC LOADS

Configurations and Sources

In order to obtain STOL performance of jet aircraft using the powered-lift
concept, a particular arrangement of the aircraft components has been developed.
Some features are illustrated in figure 1. Powered lift is obtained by
deflecting the engine exhaust flow downward using wing and flaps. To obtain

514

such interaction, the engine must be located forward of the wing, either under the wing (externally blown) or over the wing (upper surface blown). In both cases, the direct impingement of the high velocity, turbulent, exhaust flow subjects the wing and flaps to intense fluctuating loads (in the presence of high static loads and temperatures) that may cause excessive acoustic fatigue. To minimize rotational moments when operating with an engine out, the STOL aircraft's engines are located nearer to the fuselage than are conventional aircraft engines. The location of the engines in a forward and inboard position exposes larger areas of the fuselage to more intense acoustic pressures than conventional locations. These high external acoustic pressures may cause excessive interior noise levels. In addition, the exterior noise of STOL aircraft when operating in the powered-lift mode (take-off and landing) is expected to be of extended duration as well as at high levels. These long durations at high levels increase the likelihood of unfavorable noise effects on the aircraft.

The two powered-lift systems currently under development (externally blown flap and upper surface blown flap) are fundamentally different from each other so that acoustic loads information on one system may not necessarily apply to the other. Therefore, parallel programs are underway on both EBF and USB systems to develop acoustic loads information through measurements on small-scale models, large-scale models, and full-scale aircraft in flight. The objectives of these programs are to develop methods for predicting acoustic loads on aircraft in flight (using model tests and scaling laws) and to provide acoustic loads data on actual aircraft for use in ongoing developments. Some results from these research programs are presented in the following discussion.

USB Flap Studies

Acoustic loads have been measured on USB configurations including small laboratory scale models, several 8.9-kN (2000-lb) thrust engine models, and a full size 220-kN (50 000-lb) thrust aircraft engine configuration. Preparations are underway to measure acoustic loads on the YC-14 AMST aircraft. Comparisons are presented in references 1 and 2 between results from small-scale models, using air jets to simulate engine exhaust, and from large-scale models having actual jet engines. In figure 2, results are shown from tests of a full-scale YC-14 ground test rig and a 1/4-scale model of that ground test. The full-scale YC-14 rig includes a CF6 engine and many systems that are to be flown on the aircraft; the test included checkout of several flight systems, including the flow-turning aerodynamic performance of the flap system and the fluctuating pressure measurement system. The scale model uses a 8.9-kN (2000-lb) thrust engine and was designed to geometrically scale the important features of the full-scale setup. The tests included aerodynamic measurements of flow turning and thrust, so the acoustic loads results shown were measured on models that were operating in a flight-type powered-lift condition. In figure 2, overall fluctuating pressure levels at three positions on the flap and fuselage are shown as a function of the average velocity of the exhaust jet at the nozzle exit. Full-scale data are taken from reference 2. Figure 2 shows that the levels of the acoustic loads are 135 to 160 dB on the fuselage (gages 7 and 20) and up to 165 dB on the wing (gage 34). These levels are high enough that

substantial effort will be required to provide satisfactory acoustic fatigue life and interior noise environments. Full-scale results are about 3 dB higher than model results. The overall agreement between model and full-scale results shown in figure 2 is sufficiently good to give confidence that model results can be used to predict full-scale characteristics. Additional analyses of the results obtained on the 1/4-scale model tests are underway for comparison with the full-scale model results. Current plans include measurements of acoustic loads on the wing, flaps, and fuselage of the YC-14 AMST aircraft to determine actual flight levels and effects due to forward speed, and to obtain results for comparison with values predicted from ground tests.

EBF Studies

Acoustic loading information has been measured on the three EBF configurations shown in figure 3 (ref. 3). Data from the small-scale model and the TF34 model (using an 36-kN (8000-lb) thrust engine) are intended to be used with scaling laws to provide predictions of acoustic loads for full-scale flight situations. Measurements on the YC-15 AMST aircraft are intended to aid the development of the scaling law prediction technique, and to provide acoustic loads data in an aircraft flight situation for an EBF STOL configuration. Data from the small-scale model are compared with results from the TF34 model in figure 4.

In figure 4, values of the dimensionless fluctuating pressure level (FPL) are presented as a function of Strouhal number. Data for two flap settings are shown at two positions on the flaps. The data for the TF34 model include engine exhaust velocities ranging from a Mach number of 0.33 to 0.59. The fact that these data all fall within the narrow dotted region indicates that FPL and Strouhal number are appropriate dimensionless quantities to account for the effects of velocity on FPL and frequency. The figure shows that for three of the four conditions there is good agreement between the results from the small-scale model (nozzle diameter of 5.08 cm (2 in.)) and from the TF34 engine (nozzle diameter of 96.52 cm (38 in.)). This agreement suggests that acoustic loads can be scaled, at least over the range of variables represented by these two tests.

An indication of the magnitude of the acoustic loads on the EBF configuration is given in figure 5. In this figure, overall fluctuating pressure levels (OAFPL) are shown for seven transducers, two flap positions representing expected flight positions, and five engine exhaust velocities covering the range from low to full engine power. Examination of the table (note the four circled values) shows that the pressure levels range from 143 dB to 163 dB. Previous experience with acoustic fatigue of structures suggests that when levels are in the 140-dB range, some acoustic fatigue may be expected, and when the levels rise to the 160-dB range, substantial problems may be anticipated.

Estimates of the interior noise levels that might be expected on passenger-carrying versions of both the EBF and the USB aircraft have been made using data such as are shown in figures 2 and 5 and current sidewall noise reduction technology. These estimates suggest that new developments either in reduction of exterior noise levels or in improvement of fuselage sidewall noise reduction are needed to provide a satisfactory cabin noise environment.

516

LIGHT AIRCRAFT NOISE TRANSMISSION

Test Description

Flight measurements of interior noise in light aircraft (refs. 4 and 5) have shown that the levels are high enough that noise reduction efforts are needed to provide a noise environment that is comfortable and similar to the environment that passengers have come to expect from their experiences in modern jet aircraft. In order to carry out noise reduction, it is necessary to know the sources of the noise and the transmission properties of current aircraft structures. Studies on light aircraft (refs. 6 and 7) have suggested that propellers and engines are important noise sources, and that possible noise transmission paths include the exterior air and fuselage sidewall (referred to herein as the "airborne" path) and the primary structure (referred to herein as the "structureborne" path) through which interior noise is transmitted in the form of structural vibration that may originate, for example, in the engine. In order to study the characteristics of these two noise transmission paths, a light aircraft fuselage was set up and tested in the reverberation chamber of the Langley aircraft noise reduction laboratory, as shown in figure 6. A sound field was generated by speakers, and the chamber characteristics provided a reverberant uniform noise field over the complete exterior of the fuselage. Three microphones in the chamber (shown in fig. 6) were used to measure the noise field exterior to the fuselage. Readings from these three microphones during testing were nearly the same, indicating that the exterior noise field was uniform. Noise was measured inside the fuselage by the two microphones shown in figure 6 for the reverberant noise field to determine airborne noise. Noise transmitted through the structureborne path was determined by attaching a mechanical shaker to the engine support structure at the front of the aircraft and taking measurements with the two microphones inside the fuselage with no exterior noise field. A broadband spectrum, having nearly constant level over the frequency range from about 100 Hz to 1000 Hz for the mechanical input and from about 100 to 4000 Hz for the acoustic input, was used.

Airborne and Structureborne Transmission

Some results from these tests are shown in figure 7, where interior noise levels measured with exterior noise alone and with vibration input alone are shown. The data shown in figure 7 indicate that the interior noise level SPL varies with either exterior noise level or mechanical input in a linear trend with 45° slope. Based on the logarithmic scales used in these figures, this result indicates that the interior noise level is a linear function of either exterior noise or mechanical vibration input. This result was anticipated and indicates that analytical programs for prediction and control of interior noise can be based on tractable linear relations. The graph of interior noise as a function of exterior noise indicates that the interior levels are about 21 dB lower than the exterior levels, indicating that the fuselage is providing a significant overall noise reduction (averaged over frequency and the various transmitting structures such as windows and sidewall panels). Further reduction of the fuselage sidewall noise is desirable and might be accomplished by means of analytical methods to optimize the distribution of mass, stiffness, and damping while retaining minimum weight.

517

Figure 7 also shows that vibration inputs are an efficient mechanism of interior noise generation. For example, 8.9 N (2 lb) of vibration force input results in an interior noise level of about 82 dB. The exterior noise level required to induce 82 dB of interior noise is about 103 dB. This result suggests that interior noise resulting from vibrations transmitted through structural paths (from vibration sources in the engine, for example) can be significant. Control of such structureborne noise might be accomplished by use of vibration isolation devices such as shock mounts or integral damping treatments in the engine support structure.

RESPONSE OF BUILDINGS TO AIRCRAFT NOISE

Study Plan

The airport community noise problem has been a major concern of airport planners and the aircraft manufacturers and operators for many years. This concern was highlighted with the proposed introduction of the Concorde supersonic transport service into this country. A major public concern was expressed in the environmental impact statement (ref. 8) about the expected Concorde noise-induced vibratory response of historic buildings and homes near the airport in terms of structural damage and annoyance. As a result of this concern, measurements of noise-induced building vibrations have been conducted by Langley Research Center near the Dulles International Airport as part of the total Department of Transportation program of assessment of Concorde.

The approach to the assessment of Concorde noise-induced building vibrations involves the following steps: (1) measurement of vibratory response of windows, floors, and walls of selected buildings, including historical ones; (2) development of functional relationships ("signatures") between the vibration response of building elements and the range of outdoor and/or indoor noise levels associated with events of interest; (3) comparison of the Concorde-induced response with the response associated with other aircraft as well as with common domestic events and/or criteria. It should be noted that criteria are not well established particularly with respect to building damage.

Test Site Description

Figure 8 is a map of the Dulles International Airport and surrounding community areas. Also shown on the map are the nominal departure flight paths of Concorde and the locations of the test sites where structural response was measured. The test sites include one historic building (Sully Plantation) which is located on the airport boundary about 2.2 km (1.4 miles) from the end of the closest runway. Also monitored were three residential houses of families who had registered complaints concerned with building vibrations due to Concorde operations. These houses, located in Montgomery County, Maryland, range from about 21 to 32 km (13.1 to 19.9 miles) from the airport.

518

Window and Wall Response

Sample vibratory response data and associated outdoor noise levels are presented in figures 9 and 10. The functional relationship between the measured vibration response of a window and wall of Sully Plantation is shown in figure 9 for the range of outdoor SPL measured during take-off operations of Concorde and subsonic aircraft (refs. 9 and 10). The data cluster about a single line and show a linear relationship between response and noise level. Both the Concorde noise levels and induced responses exceed the levels due to subsonic aircraft by about 10 dB or a factor of 3. Also, the response of the wall is lower than the window which would be expected because of the larger mass and stiffness of the wall. Of particular significance is the fact that the vibratory response is a function of pressure amplitude and virtually independent of aircraft type. Thus, the inference of references 8 and 11 that Concorde-induced building response will be greater because of the low-frequency content of the Concorde spectrum is not supported by the data shown in figure 9.

Sample vibratory response data obtained in the residential communities of Montgomery County (ref. 12) are shown in figure 10 for both Concorde and subsonic take-off operations for test site 3. A functional relationship between the vibratory response and noise levels similar to those obtained at the Sully Plantation is again observed. Both the noise levels and vibration response due to Concorde are higher than the levels associated with subsonic aircraft operations. However, the difference between the maximum levels of noise and vibration for Concorde and for the subsonic aircraft is about 26 dB or a factor of 20. The reason for the greater difference between responses of Concorde and of subsonic aircraft at this location as compared with those measured closer to the airport at Sully Plantation is believed to be due to differences in aircraft operational procedures.

The linear response relationship observed in figures 9 and 10 is significant in that it not only gives the absolute response of the aircraft as recorded but enables extrapolation to other runway cases, flyover distances, or house locations if a noise data base is available. The acceleration levels induced by the aircraft are shown to be high enough to cause small objects to rattle, perhaps resulting in increased annoyance.

CONCLUDING REMARKS

This paper presents three examples of situations where structural responses are caused by aircraft noise. Acoustic loads measured on externally blown and upper surface blown flap STOL configurations are shown to be sufficiently high that acoustic fatigue and cabin noise require careful consideration for possible commercial applications. Laboratory studies of the noise transmission into a light aircraft fuselage indicate that interior noise can enter the fuselage through both the fuselage sidewall transmission path and the primary structure (vibration) transmission path. Accelerations measured on the windows and walls of a historic building and a residential home indicate that noise from a supersonic aircraft causes acceleration levels high enough to be perceptible by occupants, and that the noise and vibration levels due to the supersonic aircraft

are higher than those due to subsonic aircraft by a large enough factor to present a clear contrast that draws attention to the supersonic aircraft.

REFERENCES

1. Morton, Jeffrey B.; Haviland, J. K; Catalano, G. D.; and Herling, W. W.: Investigations of Scaling Laws for Jet Impingement. Powered-Lift Aerodynamics and Acoustics, NASA SP-406, 1976, pp. 445-463.

2. Sussman, M. B.; Harkonen, D. L.; and Reed, J. B.: USB Environment Measurements Based on Full-Scale Static Engine Ground Tests. AIAA Paper No. 76-624, July 1976.

3. Schoenster, James A.; Willis, Conrad M.; Schroeder, James C.; and Mixson, John S.: Acoustic-Loads Research for Powered-Lift Configurations. Powered-Lift Aerodynamics and Acoustics, NASA SP-406, 1976, pp. 429-443.

4. Howlett, James T.; Williams, Lousie H.; Catherines, John J.; and Jha, Sunil K.: Measurement, Analysis, and Prediction of Aircraft Interior Noise. AIAA Paper No. 76-551, July 1976.

5. Gilbert, Gordon: Cabin Noise Levels. Bus. & Commer. Aviat., July 1976, pp. 80-82, 84, 86.

6. Catherines, John J.; and Mayes, William H.: Interior Noise Levels of Two Propeller-Driven Light Aircraft. NASA TM X-72716, 1975.

7. Catherines, John J.; and Jha, Sunil K.: Sources and Characteristics of Interior Noise in General Aviation Aircraft. NASA TM X-72839, 1976.

8. Concorde Supersonic Transport Aircraft. Final Environmental Impact Statement - Volume I. FAA, Sept. 1975.

9. Staff, Langley Research Center: Concorde Noise-Induced Building Vibrations for Sully Plantation, Chantilly, Virginia. NASA TM X-73919, 1976.

10. Staff, Langley Research Center: Concorde Noise-Induced Building Vibrations, Sully Plantation - Report No. 2, Chantilly, Virginia. NASA TM X-73926, 1976.

11. Wesler, J. E.: Comparative Noise and Structural Vibration Levels From Concorde and Subsonic Aircraft. Proceedings of the Technical Program, NOISEXPO - National Noise and Vibration Control Conference, c.1975, pp. 344-350.

12. Staff, Langley Research Center: Concorde Noise-Induced Building Vibrations, Montgomery County, Maryland - Report No. 3. NASA TM X-73947, 1976.

520
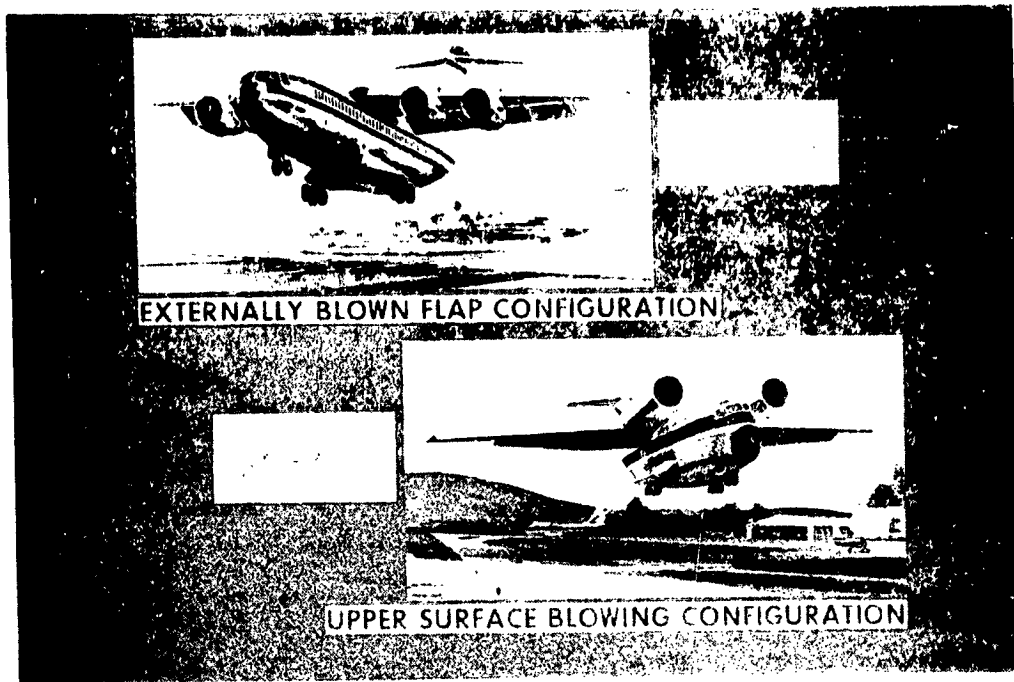
Figure 1.- Artist's concepts of commercial STOL transports
using powered-lift systems.
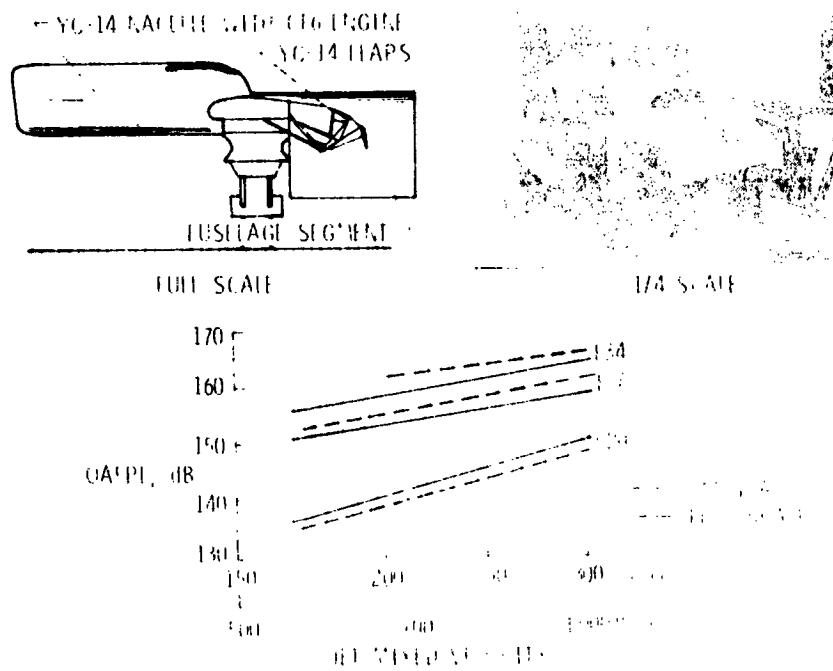
Figure 2.- Fluctuating pressures on 1/4 models.
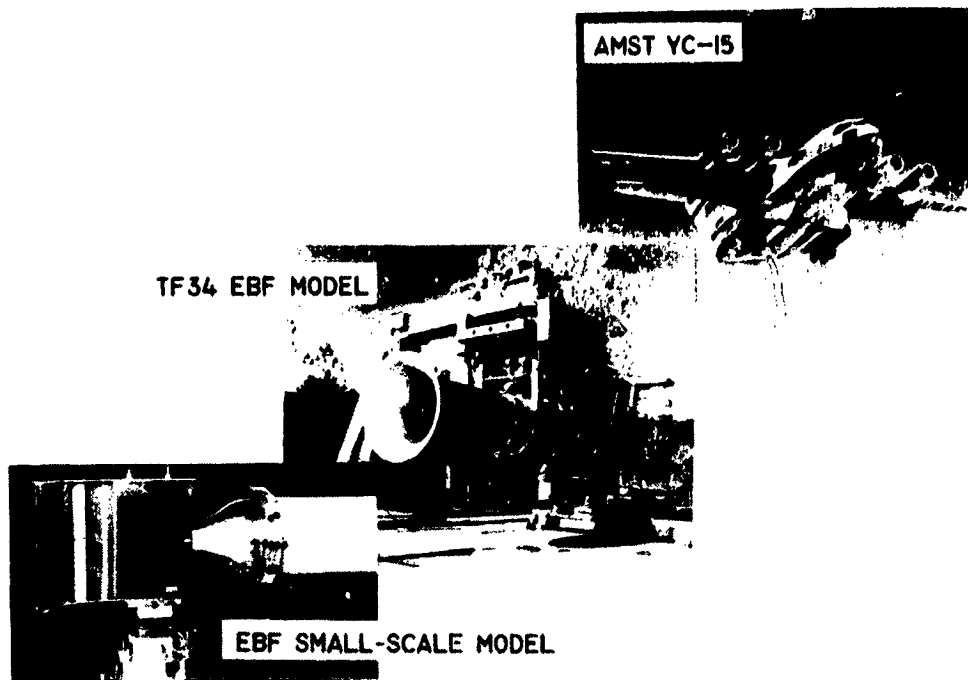
Figure 3.- Test configurations for EBF fluctuating loads studies.
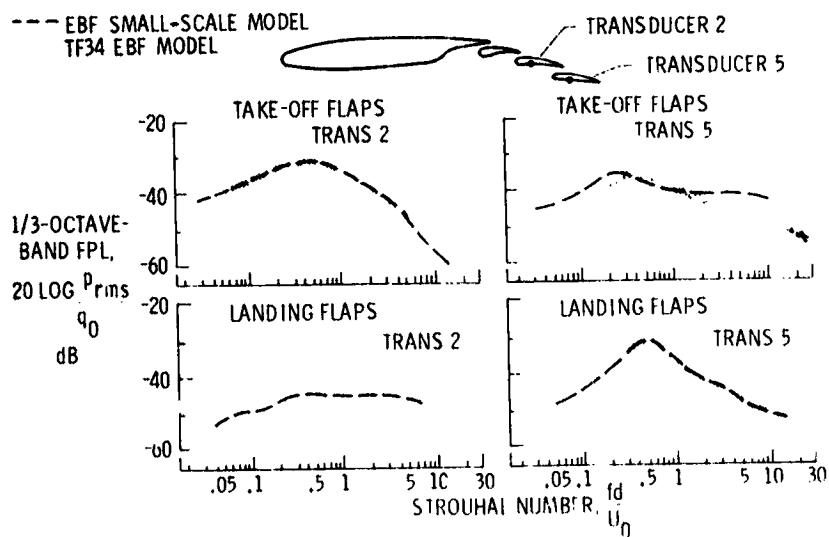
Figure 4.- Fluctuating pressures on large- and
small-scale EBF models.

OAPPL dB

MACH NUMBER	TAKE OFF (0 20 40°)					LANDING (15 35 55°)				
	0.33	0.45	0.51	0.57	0.59	0.33	0.44	0.49	0.55	0.59
T 1	149	155	156	158	159	150	156	158	160	162
R 2	151	157	159	160	161	148	154	156	159	160
A 3	152	158	160	162	163	148	153	155	157	159
N S 4	149	154	156	159	160	146	152	153	156	157
D 5	145	150	152	155	156	147	152	154	156	156
U C 6	143	143	150	152	153	158	154	155	156	157
E R 7	144	149	151	-	154	148	153	155	157	157
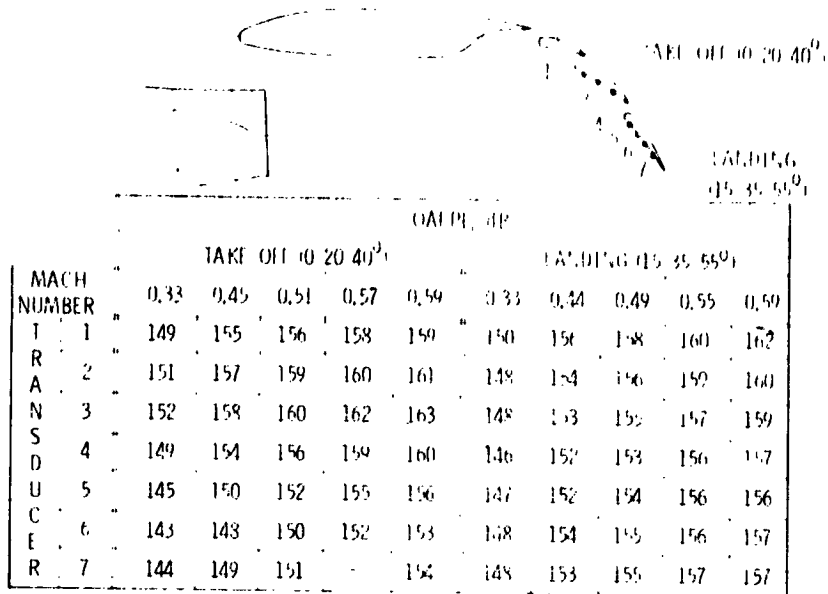
Figure 5.- Overall fluctuating surface pressure
levels on TF34 EBF model.
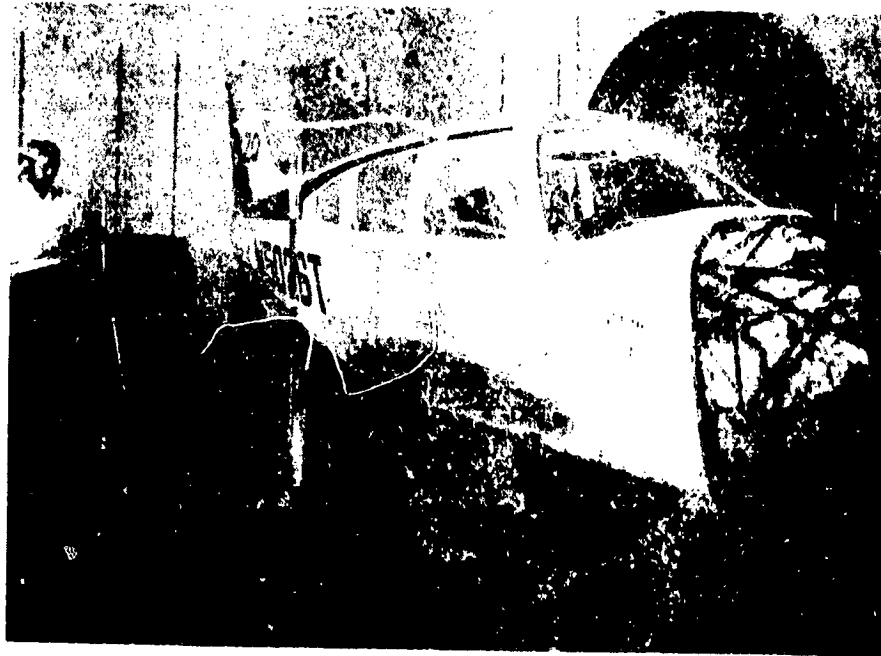
Figure 6.- Noise transmission test set up in
reverberation chamber.
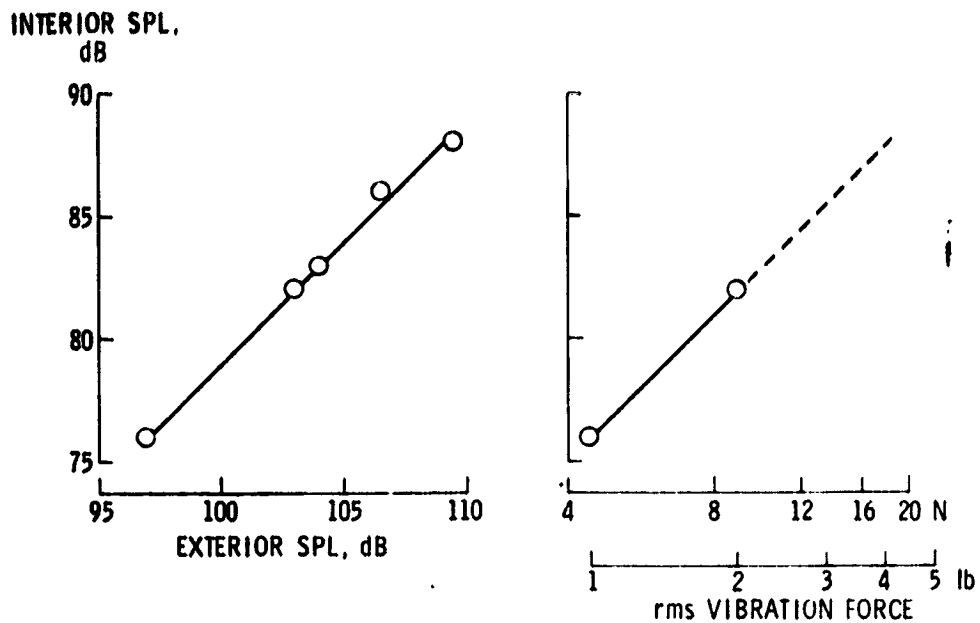
Figure 7.- Airborne and structureborne interior noise
of light aircraft fuselage in reverberation chamber.
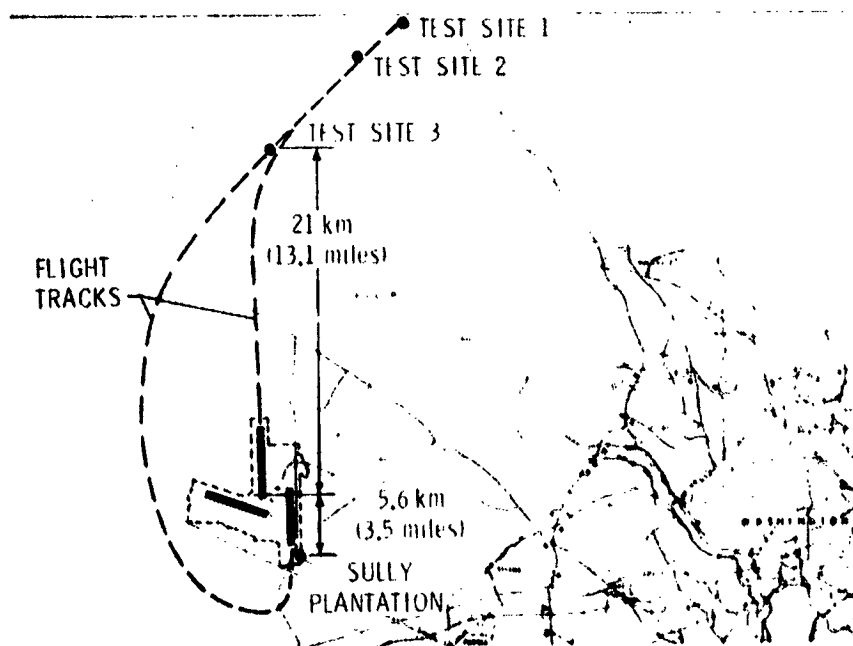
Figure 8.- Test sites for building response study.
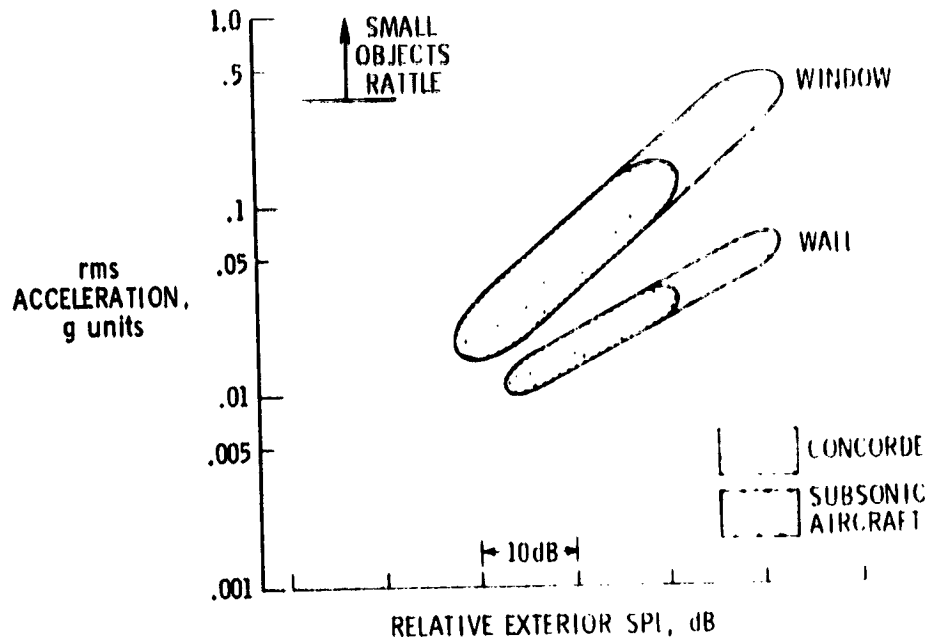
Figure 9.- Response of wall and window to aircraft noise
at Sully Plantation.
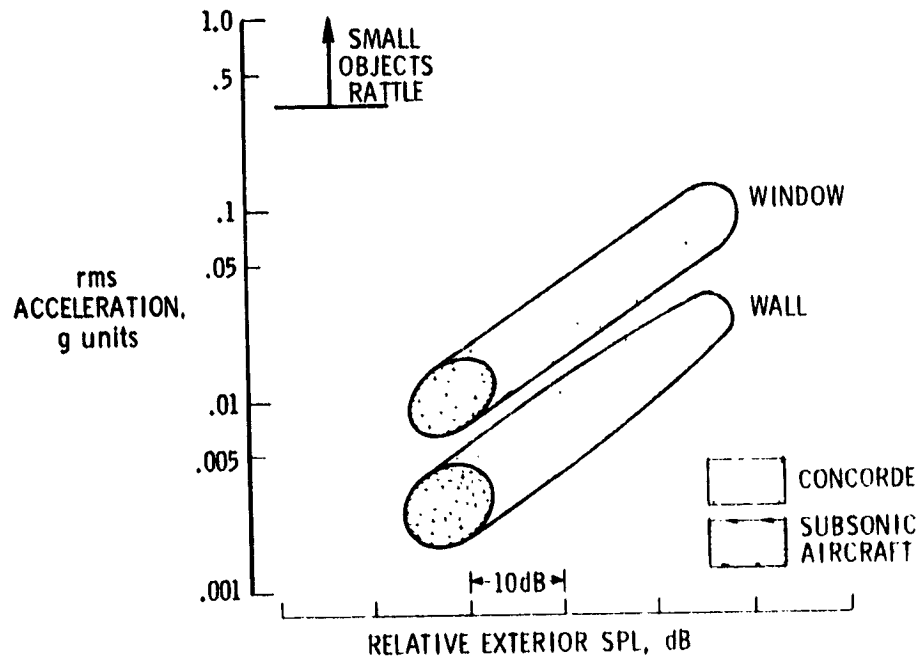
Figure 10.- Response of wall and window to aircraft noise
at test site 3.

AIRFRAME NOISE

A DESIGN AND OPERATING PROBLEM

Jay C. Hardin
NASA Langley Research Center

SUMMARY

A critical assessment of the state of the art in airframe noise is presented in this paper. Full-scale data on the intensity, spectra, and directivity of this noise source are evaluated in light of the comprehensive theory developed by Ffowcs Williams and Hawkings. Vibration of panels on the aircraft are identified as a possible additional source of airframe noise. The present understanding and methods for prediction of other component sources - airfoils, struts, and cavities - are discussed. Operating problems associated with airframe noise as well as potential design methods for airframe noise reduction are identified.

INTRODUCTION

The importance of airframe noise as the "ultimate noise barrier" to the reduction of noise levels produced by future commercial aircraft was recognized just 4 years ago as a result of NASA sponsored research on the Advanced Technology Transport. (See ref. 1.) This work included preliminary calculations, based upon sailplane data, which indicated that the nonpropulsive noise produced by a large subsonic aircraft on landing approach lay only approximately 10 EPNdB below the FAR 36 certification levels (ref. 2). The significance of the surprisingly high intensity of this hitherto neglected noise source lies in its impact on future noise regulations. Since it would be counterproductive to require engine noise levels much below those of nonpropulsive sources, the potential for further overall aircraft noise reductions is limited unless nonpropulsive noise generation can be controlled.

For this purpose, airframe noise research was begun, with the goals of understanding the generation and propagation of aircraft nonpropulsive noise as well as its reduction at the source. The first such attempts were empirical in nature, involving correlations of airframe noise measurements with gross aircraft parameters such as weight, velocity, and aspect ratio. (See ref. 3.) Such studies led to useful prediction schemes but did little to identify and rank-order the sources of the noise. Gradually, however, some understanding of the actual sources and their relative importance began to emerge. For the "clean" (cruise-configured) aircraft, it is now generally conceded that the primary sources are associated with the interactions of the wake of the wing with the wing itself, while for the "dirty" (landing-configured) aircraft, noise generated by the flaps and the

landing-gear—wheel-well combination becomes dominant. This paper presents an appraisal of the state of knowledge of airframe noise in an attempt to assess its impact on aircraft operations as well as to identify potential methods for its reduction. Also, included is an evaluation of full-scale data regarding levels, spectra, and directivity of airframe noise which suggests that airframe noise is more complex than had previously been assumed. Thus, the early empirical airframe noise prediction techniques are giving way to more refined analyses which view the total sound radiation as a summation of noise generation by individual components such as airfoils and flaps, wheel wells, and landing gear. Noise generation mechanisms for these individual component sources are discussed and methods for their reduction identified.

SYMBOLS

A	ratio of area elements
EPNdB	effective perceived noise level
J	Jacobian of transformation
K	wave number
M_r	Mach number in observer direction
OASPL	overall sound pressure level
R	Reynolds number
S	surface
SPL	one-third octave band sound pressure level
S_w	wing area
T_{ij}	Lighthill stress tensor
U	flow or aircraft speed
V	volume
V_{ed}	eddy volume
a	speed of sound
d	cylinder diameter
h	aircraft altitude
l_s	streamwise correlation length

n_j	components of normal vector
p	acoustic pressure
P_{ij}	compressive stress tensor
r	observer distance
r_{ed}	distance of center of eddy from edge
s	sideline distance
t	time
u	turbulent intensity
v_n	normal velocity
$\vec{x}$	observer position
x_i, x_j	components of position vector
ϵ	observer angle
$\vec{\eta}$	source position
θ	angle between flight path and observer directions
θ_o	angle between mean flow and trailing-edge directions
λ	directivity angle in flyover plane
ν	kinematic viscosity
ρ_f	far-field density
ρ_o	ambient density
ϕ	angle between trailing edge and observer directions
ω	circular frequency
$\Delta OASPL$	increment in overall sound pressure level

A bar over a symbol indicates time average.

AN OVERVIEW OF AIRFRAME NOISE

There are many potential sources of airframe noise on an aircraft, as shown schematically in figure 1. Each of these sources is believed to have its own

529

characteristic amplitude, spectrum, and directivity. If one measures the overall airframe noise produced by an aircraft, one sees the resultant produced by the summation of these individual sources. Although this may be confusing from the standpoint of defining and evaluating mechanisms, it is nevertheless the noise field of ultimate interest. Thus, it may be useful to review available overall airframe noise measurements.

Intensity

Overall airframe noise measurements directly beneath the flight path of the aircraft have been made for a number of years. Tables listing 65 data points published prior to 1975 have been compiled by Hardin, Fratello, Hayden, Kadman, and Africk (ref. 4). However, many of these early data were obtained by using less than optimum measurement and analysis techniques. Microphones were often pole mounted in order to compare results with certification levels, determination of the aircraft position and velocity was crude, and only minimal efforts to remove the effects of residual engine noise were made. Recently, however, two studies which attempt to overcome these objections were published. (See refs. 5 and 6.)

The first of these studies (ref. 5) presented measurements of Aero Commander, Jetstar, CV-990, and B-747 aircraft. The microphones were mounted flush with the ground to remove spectral distortion produced by reflection and radar was employed to track the aircraft as it flew a nearly constant airspeed glide slope over the microphone array.

Airframe noise data on the British aircraft H.P. 115, HS. 125, BAC 111, and VC. 10 were obtained by Fethney (ref. 6). This study employed flush-mounted microphones and a kine-theodolite system for precise position tracking, repeat flights to reduce statistical variability in the data, and extensive efforts to determine and remove residual engine noise from the data.

On the basis of these data, Fink (ref. 7) has developed a semiempirical prediction scheme for airframe noise produced by aircraft in the clean (cruise) configuration. The overall sound pressure level directly below the aircraft is given by

$$OASPL = 10 \log_{10}\left[\left(\frac{U}{100}\right)^5\left(\frac{S_w}{h^2}\right)\right] + 108.3 \text{ dB} \tag{1}$$

where

U   aircraft speed, meters per second

S_w wing area, meters^2

h   altitude, meters

530

All sound pressure levels in this paper will be referenced to 20 μPa. Note that this relation implies a dependence of clean airframe noise on velocity to the fifth power. A comparison of this prediction with measured data from a number of cruise-configured aircraft is shown in figure 2.

The airframe noise levels generated in the landing configuration are believed to be more dependent upon the detailed design of the aircraft than those of the cruise configuration. Several additional components such as leading-edge slats, trailing-edge flaps, landing gear, and wheel wells are deployed during landing whose relative contributions to the overall noise may vary considerably from aircraft to aircraft. Further, these sources are not necessarily independent, but may interact with each other due to changes in the total flow field. Although it is difficult to directly measure the effects of the individual components on the airframe noise, Fethney made some estimates based upon measurements for the VC. 10 in reference 6. The data shown in figure 3 for comparison are decibel increases over the clean-configuration overall sound pressure level as produced by several different flight conditions. The total change in airframe noise level from the cruise to approach configurations for this aircraft was 11 dB. Either flap deployment or landing-gear deployment with open wheel well is estimated to account for about 9 dB individually. The difference in noise level between open and shut undercarriage doors is estimated to be about 4 dB; this seems to indicate that substantial noise may be generated by large open cavities which suggests a method for noise reduction on those aircraft whose undercarriage doors normally remain open after gear deployment.

In reference 7, Fink has also developed a prediction scheme for airframe noise produced by aircraft in the dirty (or approach) configuration. The overall sound pressure level below the aircraft is given by

$$\text{OASPL} = 10 \ \log_{10} \left[\left(\frac{U}{100}\right)^6 \left(\frac{S_w}{h^2}\right) \right] + 116.7 \ \text{dB} \tag{2}$$

A comparison of the prediction by this relation with data from several aircraft in the approach configuration is shown in figure 4. Although most of the data appear to be well predicted by this relation, two of the aircraft, the H.P. 115 and the BAC 111, exhibit substantially lower levels corresponding better to the clean airframe prediction of equation (1) because of design peculiarities of these aircraft which, when better understood, should yield design methods applicable to other aircraft.

Fink's relations have been employed to predict cruise and approach noise levels for modern aircraft comprising most of the current commercial fleet. The results are shown in figure 5. The approach airframe noise lies at approximately the FAR 36 - 10 dB level.

531

Spectra

Based upon early measurements, Healy suggested that airframe noise directly below an aircraft produced a "haystack" type spectrum which peaked at a constant Strouhal number based on airspeed and a characteristic wing thickness. (See ref. 8.) More recent measurements indicate a much more complex spectrum. Figure 6 displays the peak one-third octave band spectra normalized to equal overall sound pressure levels for the clean Jetstar, CV-990, and B-747 aircraft as measured by Putnam, Lasagna, and White (ref. 5). Although such measurements are complicated because the moving source produces a nonstationary signal, third-octave analyses are generally reliable as long as short averaging times are employed. Note that the spectra exhibit two peaks, a lower one in the vicinity of 200 Hz, which corresponds roughly to the frequency predicted by Healy's Strouhal relation, and a higher one near 1250 Hz. However, reference 5 stated the surprising result that the shape of these spectra and the position of the peaks showed no consistent change with airspeed. Spectra for the H.P. 115, HS. 125, and BAC 111 obtained by Fethney (ref. 6) display the same shape and peak location.

The change in spectrum shape for the VC. 10 in going from the clean configuration to the dirty configuration is illustrated by the data of figure 7. The characteristic double-peaked spectrum for the clean configuration is not discernible for this aircraft. The major difference in the spectrum for the dirty configuration is a broadband increase in level, particularly at the low-frequency end.

Directivity

The directivity of airframe noise has only recently begun to be explored and only a modest amount of data exists in the open literature. Figure 8 portrays the reductions in measured overall noise levels (over those directly below the aircraft) with sideline distance for the four aircraft tested by Fethney (ref. 6). These data are compared with predicted reductions based upon consideration of the total aircraft either as a point monopole (solid curve) or as a point dipole (dashed curve) oriented in the lift direction. The fact that the data cluster about the solid curve indicates a monopolelike falloff to the side. Similar behavior has been observed by Lasagna and Putnam for the Jetstar aircraft in the landing configuration. (See ref. 9.) This result is important in its implications for the source type dominant in airframe noise as well as for the airframe noise "footprint" and will tend to make airframe noise more important on the sideline than had previously been assumed.

Figure 9 shows airframe noise measurements in the flyover plane for a clean DC-10 aircraft (ref. 10). The data have been corrected for an inverse square falloff with distance and are plotted as a function of λ, the angle of the approaching aircraft with respect to the horizontal. (Before normalizing, the airframe noise peaked slightly before the aircraft was directly overhead.) These measured data are compared with calculated values of the sum of two dipoles oriented, respectively, in the lift and drag directions. Note that the main directivity features of the measurements are supported by the calculations.

532

The best agreement between the measured data and this theoretical approach is obtained when the dipoles are negatively correlated.

A THEORETICAL BASIS FOR AIRFRAME NOISE

The most inclusive theoretical basis for the study of sound production by the airframe is that developed by Ffowcs Williams and Hawkings (ref. 11) who extended the Lighthill-Curle theory of aerodynamic sound generation (refs. 12, 13, and 14) to include arbitrary convection motion. For this case, the wave equation governing the generation and propagation of sound admits the general solution

$$4\pi a^2 \left(\rho_f(\vec{x}, t) - \rho_o \right) = \frac{\partial^2}{\partial x_i \, \partial x_j} \int_V \left[\frac{T_{ij} \, J}{r \, |1 - M_r|} \right] d\vec{\eta}$$

$$- \frac{\partial}{\partial x_i} \int_S \left[\frac{P_{ij} n_j A}{r \, |1 - M_r|} \right] dS(\vec{\eta}) + \frac{\partial}{\partial t} \int_S \left[\frac{\rho_o \vec{v}_n}{r \, |1 - M_r|} \right] dS(\vec{\eta})$$

(3)

This solution implies that the sound sources may be represented by a quadrupole distribution related to the Lighthill stress tensor T_{ij} within the volume of turbulence, a surface distribution of dipoles dependent upon the compressive stress tensor P_{ij}, and a surface distribution of monopoles produced by the normal velocity of the surface v_n. Ffowcs Williams and Hawkings further showed that, for a rigid surface, the monopole distribution degenerates into a distribution of dipoles and quadrupoles throughout the volume contained within the surface. (See ref. 11.)

In the majority of airframe noise research to date, the aircraft has been assumed to be rigid. Application of this assumption in the theory discussed in the preceding paragraph implies that airframe noise consists of a distribution of dipoles and quadrupoles. Further, at the low Mach numbers of interest (approximately 0.3 for landing approach), the quadrupole distribution has been neglected. Thus, airframe noise sources have been considered as dipole in nature. These dipole sources have also been assumed to be compact and, often, replaced by equivalent point dipoles acting at the center of the distribution.

Several aspects of experimental data regarding airframe noise are difficult, if not impossible, to explain in terms of such a theory.

Firstly, the velocity dependence of airframe noise has consistently been found to be less than the sixth power which would be expected of an aerodynamic dipole. This result has led to considerable interest in the theories of Ffowcs Williams and Hall (ref. 15) and Powell (ref. 16). They considered the radiation from a volume of turbulence near the edge of a rigid half-plane and found that

533

the sound production of quadrupoles with axes in a plane normal to the edge was enhanced such that the far-field sound intensity varied as the fifth power of the typical fluid velocity. However, there was no enhancement of quadrupoles with axes parallel to the edge.

Secondly, the definite monopolelike sideline directivity of airframe noise, which has been observed by independent research groups, is hard to understand on the basis of a purely dipole theory. Certainly it is possible for three mutually perpendicular dipoles to masquerade as a monopole. However, this requires them to be statistically independent and of equal amplitude. Although it is not hard to imagine the overall fluctuating lift and drag forces on an aircraft to be the same order of magnitude, a fluctuating side force of equal strength is more difficult to visualize. About the only place where such a force could exist in the clean configuration is on the vertical tail. However, since it is much smaller in area than the wing surface, much higher fluctuating pressures on its surface would be required.

Finally, the source of the high frequency peak in the airframe noise spectrum (fig. 6) is puzzling. This peak, which was observed by the authors of both references 5 and 6, is higher in frequency than that expected from known wing noise mechanisms and seems to be relatively insensitive to airspeed. Since the frequency of an aeroacoustic source ordinarily scales on airspeed, the presence of this peak suggests the possibility of radiation from fundamental vibratory modes of the aircraft structure. Although such vibration has not previously been considered as a source of airframe noise, just such a spectral peak has been observed by Davies in reference 17, who investigated sound produced by turbulent-boundary-layer excited panels. Davies found that the frequency of this peak was reasonably independent of flow speed.

A similar spectrum has also been observed by Maestrello (ref. 18) who reported interior measurements in an unupholstered Boeing 720 airplane. Shown in figure 10 are spectra of panel acceleration as well as sound pressure level close to the panel for the airplane in flight at a Mach number of 0.87 and an altitude of 7700 meters. Also shown are the changes in these spectra with cabin pressure. Maestrello notes that the sound pressure level varies as the fifth power of velocity. He further observes that most sound radiation comes from the edges of the panels and demonstrates methods for noise reduction by stiffening the panel boundaries. If panel vibration is truly responsible for the high frequency peak observed in airframe noise radiation, Maestrello's techniques offer a direct method of noise reduction.

More recently, Wilby and Gloyna (ref. 19) made similar measurements on a Boeing 737 airplane. Again the 1-kHz peak was observed which was taken as evidence that the panel structure acts as a filter with that center frequency. Correlation of the vibration data was high in the longitudinal direction but low in the circumferential. Adjacent panels were essentially uncorrelated.

These phenomena emphasize the necessity of a closer look at the assumptions employed in the theory of airframe noise. While it is wise to recall that there are many absolutely equivalent formulations of aeroacoustic sources, the enhancement of quadrupole sources in the vicinity of an edge as predicted

534

by Ffowcs Williams and Hall (ref. 15) and Powell (ref. 16) suggests that quadrupole terms in any theoretical formulation should not be dismissed lightly. Further, the evidence cited previously which indicates that vibration may be a source of airframe noise brings into question the assumption of rigidity. If the surface vibrates, the monopole source term in equation (3) may dominate which would explain the monopolelike sideline directivity that has been observed. Of course, there is still no mass addition to the flow but, due to the size of the body, each point on the surface may be acting as a baffled piston unable to interfere effectively with its mate of opposite phase elsewhere. The large size of the body also sheds doubt on the assumption of compactness. The spatial extent of the source region is of the order of the span of the aircraft while a typical frequency of interest has a wavelength of 0.5 m. It is possible to take into account the correlation length of the source distribution and replace each correlated region by a point source as suggested in reference 20. However, even the correlation length may be of the order of, or larger than, the wavelength. Thus, the assumption of compact sources cannot be rigorously justified. Further, this "component source technique" neglects diffraction of the sources by the fuselage which may be important in airframe noise and could be partially responsible for the observed directivity pattern.

COMPONENT SOURCES OF AIRFRAME NOISE

As noted earlier in this paper, airframe noise is the resultant of many different noise generating mechanisms. Thus, in order to render the research problem more manageable, it is prudent to identify and evaluate these individual sources.

The work of Curle (ref. 14), who extended Lighthill's theory (refs. 12 and 13) to include the case where rigid bodies are present within the field of interest, showed that the sound generation in the presence of a body could be expressed by a distribution of dipoles over its surface in addition to the usual volume integral. The strength of these dipoles is related to the fluctuating pressure experienced by the surface. This theory is exact and highly useful for computational purposes. However, it has led to a certain amount of confusion about the roles of surfaces in sound generation. Actually, a rigid surface can produce no sound, as can be seen by noting that the acoustic energy flux must approach zero close to a rigid surface (ref. 21). Thus, the true sources of sound are disturbances within the flow field itself and the surface can act only in changing the strengths of these volume sources and in reflecting and diffracting the sound they produce. The fact that the flow disturbances generate the fluctuating pressures on the surface is responsible for the alternate description of the sound production. The importance of this result is that it emphasizes the vital role played by the local flow field about the airframe components. Little is known about such flows.

The many different noise-generating mechanisms which comprise airframe noise can be crudely classed in terms of three simple models, that is, noise generation by cylinders, streamlined bodies, and cavities.

535

Cylinders

Perhaps the simplest and best understood of all examples of sound generation by flow-surface interaction is that of a cylinder in a flow. Fortunately, this is also a useful example as the entire undercarriages of aircraft are constructed essentially of cylinders of various lengths and orientations. As the flow attempts to negotiate the cylindrical contour, it separates from the surface creating a turbulent wake. This wake is highly vortical which results in a solenoidal velocity field that induces fluctuating forces on the cylinder in the streamwise and normal directions. The situation is shown schematically in figure 11.

The exact nature of the wake and, thus, the sound produced is highly dependent upon the Reynolds number ($R = \frac{Ud}{\nu}$, where U is the flow speed and d is the cylinder diameter) of the flow. Typical Reynolds numbers for aircraft undercarriage components during landing approach are in the range of 10^5 to 10^6. In this range, the classical periodic Von Karman vortex street breaks down and the wake becomes random. The most relevant work in this area is that by Fung (ref. 22) who studied the fluctuating lift and drag forces on cylinders for the range $3 \times 10^5 < R < 1.4 \times 10^6$. He found the spectrum of the fluctuating lift to peak at a Strouhal number based on strut diameter near 0.1. The spectrum of the fluctuating drag peaks at twice this frequency.

For a cylindrical component of an aircraft, if it is assumed that wavelengths of the sound produced are large compared with the dimensions of the cylinder, retarded time differences in the source region may be neglected and the sound calculated as if from a moving point dipole through the theory of Lowson (ref. 23). However, if the principal landing-gear struts are oriented such that their lift and drag dipoles yield a null below the aircraft, the strut-generated sound is not a tremendously important source of community noise. Nevertheless, the struts may be significant in generating turbulence which impinges on other surfaces of the aircraft to create substantial noise.

Streamlined Bodies

The most fundamental (in the sense of being omnipresent) component source of airframe noise is produced by the flow over the streamlined surfaces of the aircraft. Taking such surfaces to be rigid (i.e., neglecting any radiation due to panel vibration which was indicated as a possible source earlier in the paper), a dipolelike sound generation may still be observed which can be related to the fluctuating forces experienced by the surface. There are three mechanisms by which such forces may be developed: The pressure field arising in the turbulent boundary layer over the surface, force fluctuations induced by vorticity shed from the surface, and the action of any turbulence present in the incident stream. (See ref. 24.) However, these phenomena are not equally efficient in noise generation and, of course, their relative contributions vary with the characteristics of the flow field in which the surface is placed.

Boundary-layer turbulence.- The question of sound generation by boundary-layer turbulence has been effectively resolved by Powell (ref. 25) who used the "reflection principle" to show that the major surface dipoles vanish on

536

an infinite, flat, rigid surface leaving only the viscous dipoles with axes lying in the surface itself. Since such viscous stresses can only become significant at Reynolds numbers much smaller than those developed on commercial aircraft, direct radiation from the turbulent-boundary layer is a much less efficient source of direct radiation than others present even for moderately curved surfaces (as long as no separation occurs). This result remains valid for finite surfaces when the surface is larger than the sound wavelength - which is usually true of airframe noise - except near the edges. This "edge-noise" source is discussed later.

In reference to the panel vibration source proposed earlier in this paper, it might be mentioned that Laufer, Ffowcs Williams, and Childress (ref. 26) have considered the case where the surface is flexible and able to respond to the boundary-layer excitation. They remark that for surfaces of limited extent, wall motion becomes equivalent to a simple source system of high acoustic efficiency and can quickly become the most important feature of the practical boundary-layer noise problem. Thus, it appears that the boundary-layer pressure fluctuations are not major sources of noise, but the aircraft surface may generate sound through vibration and may reflect sound produced by other sources. Both of these roles require further research for better understanding.

Wake vorticity.- Sound generation by force fluctuations induced by vorticity shed from the surface is probably the primary cause for the experimentally observed fact that aerodynamic surfaces radiate predominantly from slender strips along their edges. At the edge of an aerodynamic surface, the flow must separate shedding vorticity into a wake. This vorticity will induce fluctuating surface pressures which fall off with distance from the vortex. Thus, the largest pressures will occur close to the edge. In addition, non-cancellation of boundary-layer fluctuations also occurs in this region. Which of these effects is dominant is not known at this time, although wake-induced pressures normally should be more intense. However, both point to edge noise as a primary source of airframe sound generation.

The present understanding of this source is well depicted by figure 12 which is taken from a report by Siddon (ref. 27). Siddon suggests that alternate vortex shedding, with a fairly narrow band of preferred frequencies, leads to a time-dependent relaxation of the Kutta condition at the trailing edge. The "stagnation streamline" switches cyclically from the upper to the lower surface; thus, a fluctuating-force concentration is induced near the edge. Note that this is exactly the same mechanism responsible for the production of strut noise as discussed earlier.

There has been extensive work on the prediction of this edge-noise source and numerous, sometimes conflicting, theories have been produced. (See ref. 4.) Again, the generation process is highly dependent upon Reynolds number. Much recent work (e.g., refs. 28 and 29) has dealt with the intense tones which can be produced by isolated airfoils with laminar boundary layers. However, such tones require Reynolds numbers based on airfoil chord of less than about 2×10^6 whereas commercial aircraft ordinarily exhibit Reynolds numbers of many millions. At these higher Reynolds numbers, a transition similar to the collapse of the classical Von Karman street behind a cylinder apparently occurs and a more broadband radiation results.

Fink, in reference 30, has experimentally evaluated the various theories for trailing-edge noise generation. He concludes that the best present theories are those by Ffowcs Williams and Hall (ref. 15) and Powell (ref. 16). The first of these papers considers the scattering of sound generation by Lighthill-type quadrupoles due to the presence of a half-plane in the flow. The results show that sound output of quadrupoles associated with fluid motion in a plane normal to the edge is increased by a factor $(Kr_0)^{-3}$ where $K = \omega/a$ is the acoustic wave number and r_0 is the distance of the center of the eddy from the edge. There is no enhancement of sound from longitudinal quadrupoles with axes parallel to the edge. According to this theory, the mean square pressure produced by a single eddy near the trailing edge is

$$\overline{p^2}(r,\theta,\phi) \approx \frac{\rho_0^2 \, U^5 \, u^2 \, V_{ed}^2 \, \sin\phi \, \sin^2\theta_0 \, \cos^2\theta/2}{\pi^2 \, a \, l_s \, r_{ed}^3 \, r^2} \tag{4}$$

where

u   turbulent intensity

V_{ed} eddy volume

l_s streamwise correlation length of eddy

θ angle between streamwise and observer directions

θ_0 angle that mean flow makes with trailing edge

ϕ angle between trailing edge and observer directions

This expression can then be summed at the observer location over all the (independent) eddies near the trailing edge. Note that this theory implies a dependence on the fifth power of velocity and the square of turbulence intensity. It also gives rise to a directivity pattern in a plane normal to the edge dependent upon $\cos^2\theta/2$. Finally, the theory predicts that a "swept" trailing edge (relative to the mean flow direction) would produce less noise due to the $\sin^2\theta_0$ dependence.

Inflow turbulence.- The final mechanism by which fluctuating forces may be developed on an aerodynamic surface is through the action of incoming turbulence. Although atmospheric turbulence is ordinarily of too large scale and too low intensity to be important in this regard, airframe components, such as flaps, which lie in the wake of other portions of the aircraft, may generate noise through this mechanism.

Although several different approaches to the analysis of this noise source have been devised (ref. 4), it is useful to observe that, since the work of Ffowcs Williams and Hall (ref. 15) is purely concerned with scattering of sound near an edge, it is equally applicable to this case as well. In other

538

words, their theory makes no distinction between incoming turbulence impinging on a leading edge and turbulence being shed from a trailing edge. Thus, equation (4) can be employed to calculate the level and directivity of this leading-edge source as well. The same concerns about source distribution apply, with the only change being, perhaps, the characteristics of the eddies themselves.

One possible means of reducing both the incident turbulence and trailing-edge noise on streamlined bodies is through use of porous surface treatment such as has been developed for high lift configurations. This application has recently been considered by Hayden in reference 31. Figure 13 shows the noise reduction produced by porous trailing-edge treatment on an NACA 0012 airfoil at 4^0 angle of attack. This airfoil was in the Reynolds number range where a narrow band tone can be generated which is not the case for commercial aircraft. However, it can be seen that the lower frequency trailing-edge noise is also significantly reduced. Such treatment may also be utilized on the leading edge although maintainance of aerodynamic performance is difficult.

Cavities

The final component source of airframe noise to be discussed in this section is sound generation by cavities in the surface of the aircraft. Recent data (ref. 6) indicate that one of the most intense sources of airframe noise on landing approach is produced by the wheel cavities of the aircraft since a significant increase in the broadband noise spectrum is observed when the wheel wells are opened. (See fig. 3.) This phenomenon is shown in figure 14 which is a compendium of cavity noise data from actual aircraft produced by Heller and Dobrzynski (ref. 32). It can be seen that the larger the cavity, the higher in intensity and lower in frequency is the sound produced. Of course, the larger cavities generally contain more landing-gear assemblies which may also be a factor. Although it is not yet clear whether this noise increase is due to the cavity itself or to a change in the flow field around the wing-flap system, considerable research into noise generation mechanisms of cavity flow has been stimulated.

The flow field within cavities has been of interest for several years because of fatigue and buffeting problems. Thus, extensive data on cavity flow fields have been obtained and methods for the reduction of internal pressure oscillations have been developed. (See ref. 33.) Unfortunately, however, few measurements of far-field sound generation by cavities exist due to the difficulty of making such measurements in present day flow facilities.

The "basic" (this author's terminology) cavity noise mechanism is a fairly complex interaction between the shear layer over the cavity and the volume within it. The shear layer apparently has fundamental modes of instability which act as a forcing function to produce oscillation of the air within the cavity. However, the efficiency of this forcing function in producing sound depends upon how well it couples with the fundamental acoustic modes of the cavity. If the coupling is strong, very intense tones can be produced. These tones have been studied by Block and Heller (ref. 34).

539

This basic cavity noise mechanism is primarily a low frequency phenomenon, occurring for Strouhal numbers less than about 2.5. Further, it is also critically dependent upon the cavity shape. Recent tests of a circular cavity conducted at the Langley Research Center produced much less tonal noise radiation than a square cavity of side length equal to the diameter of the circular cavity. This is important as the cavities on real aircraft are much different in shape from the simple rectangular model. (See ref. 35.) Finally, of course, this tonal mechanism cannot be responsible for the observed broadband radiation of real aircraft cavities. Thus, it is necessary to consider other potential cavity noise mechanisms.

There are at least two other possible sources of cavity noise. The shear layer shed from the leading edge of the cavity will induce fluctuating pressures on the edge resulting in an edge-noise source as discussed previously. Further, the turbulence in the shear layer will impinge on the back wall of the cavity resulting in an incident turbulence source similar to that mentioned earlier. Thus, there is the potential for a "trailing-edge" source at the leading edge of the cavity and a "leading-edge" source at the trailing edge of the cavity. Both these sources may be analyzed by the theory previously developed and both will produce a more broadband noise. The analysis is simplified by the fact that these sources will appear compact.

A potential design and operating problem might be pointed out here. The noise generation by these component sources is intimately related to the flow around them which also determines their drag. In fact, Revell (ref. 36) is attempting to predict airframe noise from steady drag measurements. If it turns out that there exists a one-to-one relation between airframe noise and drag, a general drag cleanup of the aircraft in landing approach would be necessary. This might well imply higher landing speeds, perhaps requiring longer runways, and cause consternation among pilots who prefer high drag on approach.

CONCLUDING REMARKS

This paper has presented a critical assessment of the state of the art in airframe noise. Full-scale data on the intensity, spectra, and directivity of this noise source were evaluated in light of the comprehensive theory developed by Ffowcs Williams and Hawkings. Vibration of panels on the aircraft was identified as a possible additional source of airframe noise. The present understanding and methods for prediction of other component sources - airfoils, struts, and cavities - were discussed. Operating problems associated with airframe noise as well as potential design methods for airframe noise reduction were identified.

REFERENCES

1. Gibson, John S.: The Ultimate Noise Barrier - Far Field Radiated Aero-
   dynamic Noise. Inter-Noise 72 Proceedings, Malcolm J. Crocker, ed.,
   Inst. Noise Control Eng., c.1972, pp. 332-337.

2. Noise Standards: Aircraft Type and Airworthiness Certification. Federal
   Aviation Regulations, pt. 36, FAA, June 1974.

3. Morgan, Homer G.; and Hardin, Jay C.: Airframe Noise - The Next Aircraft
   Noise Barrier. J. Aircraft, vol. 12, no. 7, July 1975, pp. 622-624.

4. Hardin, Jay C.; Fratello, David J.; Hayden, Richard E.; Kadman, Yoran;
   and Africk, Steven: Prediction of Airframe Noise. NASA TN D-7821, 1975.

5. Putnam, Terrill W.; Lasagna, Paul L.; and White, Kenneth C.: Measurements
   and Analysis of Aircraft Airframe Noise. AIAA Paper 75-510, Mar. 1975.

6. Fethney, P.: An Experimental Study of Airframe Self-Noise. Aeroacoustics:
   STOL Noise; Airframe and Airfoil Noise, Ira R. Schwartz, ed., American
   Inst. Aeronaut. & Astronaut., c.1976, pp. 379-403.

7. Fink, Martin R.: Approximate Prediction of Airframe Noise. AIAA
   Paper No. 76-526, July 1976.

8. Healy, Gerald J.: Measurement and Analysis of Aircraft Far-Field Aero-
   dynamic Noise. NASA CR-2377, 1974.

9. Lasagna, P. L.; and Putnam, T. W.: Preliminary Measurements of Aircraft
   Aerodynamic Noise. AIAA Paper No. 74-572, June 1974.

10. Munson, A. G.: A Modeling Approach to Nonpropulsive Noise. AIAA
    Paper No. 76-525, July 1976.

11. Ffowcs Williams, J. E.; and Hawkings, D. L.: Sound Generation by Turbulence
    and Surfaces in Arbitrary Motion. Philos. Trans. R. Soc. London, ser. A,
    vol. 264. no. 1151, May 8, 1969, pp. 321-342.

12. Lighthill, M. J.: On Sound Generated Aerodynamically. I. General Theory.
    Proc. R Soc. (London), ser. A, vol. 211, no. 1107, Mar. 20, 1952,
    pp. 564-587.

13. Lighthill, M. J.: On Sound Generated Aerodynamically. II. Turbulence as
    a Source of Sound. Proc. R. Soc. (London), ser. A, vol. 222, no. 1148,
    Feb. 23, 1954, pp. 1-32.

14. Curle, N.: The Influence of Solid Boundaries Upon Aerodynamic Sound.
    Proc. R. Soc. (London), ser. A, vol. 231, no. 1187, Sept. 20, 1955,
    pp. 505-514.

15. Ffowcs Williams, J. E.; and Hall, L. H.: Aerodynamic Sound Generation by Turbulent Flow in the Vicinity of a Scattering Half Plane. J. Fluid Mech., vol. 40, pt. 4, Mar. 1970, pp. 657-670.

16. Powell, Alan: On the Aerodynamic Noise of a Rigid Flat Plate Moving at Zero Incidence. J. Acoust. Soc. America, vol. 31, no. 12, Dec. 1959, pp. 1649-1653.

17. Davies, Huw G.: Sound From Turbulent-Boundary-Layer-Excited Panels. J. Acoust. Soc. America, vol. 49, no. 3, pt. 2, Mar. 1971, pp. 878-889.

18. Maestrello, L.: Use of Turbulent Model To Calculate the Vibration and Radiation Responses of a Panel, With Practical Suggestions for Reducing Sound Level. J. Sound & Vib., vol. 5, no. 3, May 1967, pp. 407-448.

19. Wilby, J. F.; and Gloyna, F. L.: Vibration Measurements of an Airplane Fuselage Structure. I. Turbulent Boundary Layer Excitation. J. Sound & Vib., vol. 23, no. 4, Aug. 22, 1972, pp. 443-466.

20. Hayden, Richard E.; Kadman, Yoran; Bliss, Donald B.; and Africk, Steven A.: Diagnostic Calculations of Airframe-Radiated Noise. AIAA Paper 75-485, Mar. 1975.

21. Ribner, H. S.: Aerodynamic Sound From Fluid Dilatations - A Theory of the Sound From Jets and Other Flows. UTIA Rep. No. 86 (AFOSR TN 3430), Inst. Aerophys., Univ. of Toronto, July 1962.

22. Fung, Y. C.: Fluctuating Lift and Drag Acting on a Cylinder in a Flow at Supercritical Reynolds Numbers. J. Aerosp. Sci., vol. 27, no. 11, Nov. 1960, pp. 801-814.

23. Lowson, M. V.: The Sound Field for Singularities in Motion. Proc. R. Soc. (London), ser. A, vol. 286, no. 1407, Aug. 1965, pp. 559-572.

24. Sharland, I. J.: Sources of Noise in Axial Flow Fans. J. Sound Vib., vol. 1, no. 3, July 1964, pp. 302-322.

25. Powell, Alan: Aerodynamic Noise and the Plane Boundary. J. Acoust. Soc. America, vol. 32, no. 8, Aug. 1960, pp. 982-990.

26. Laufer, John; Ffowcs Williams, John E.; and Childress, Stephen: Mechanism of Noise Generation in the Turbulent Boundary Layer. AGARDograph 90, Nov. 1964, pp. 20-29.

27. Siddon, Thomas E.: Noise Source Diagnostics Using Causality Correlations. Noise Mechanisms, AGARD-CP-131, Mar. 1974, pp. 7-1 - 7-13.

28. Patterson, R. W.; Vogt, P. G.; Fink, M. R.; and Munch, C. L.: Vortex Noise of Isolated Airfoils. AIAA Paper No. 72-656, June 1972.

542

29. Tam, Christopher K. W.: Discrete Tones of Isolated Airfoils. J. Acoust. Soc. America, vol. 55, no. 6, June 1974, pp. 1173-1177.

30. Fink, Martin R.: Experimental Evaluation of Theories for Trailing Edge and Incident Fluctuation Noise. AIAA J., vol. 13, no. 11, Nov. 1975, pp. 1472-1477.

31. Hayden, Richard E.: USB Noise Reduction by Nozzle and Flap Modifications. Powered-Lift Aerodynamics and Acoustics, NASA SP-406, 1976, pp. 283-305.

32. Heller, Hanno H.; and Dobrzynski, Werner M.: Sound Radiation From Aircraft Wheel-Well/Landing Gear Configurations. AIAA Paper No. 76-552, July 1976.

33. Heller, Hanno H.; and Bliss, Donald B.: The Physical Mechanism of Flow-Induced Pressure Fluctuations in Cavities and Concepts for Their Suppression. AIAA Paper 75-491, Mar. 1975.

34. Block, Patricia J. W.; and Heller, Hanno: Measurements of Farfield Sound Generation From a Flow-Excited Cavity. NASA TM X-3292, 1975.

35. Bliss, Donald B.; and Hayden, Richard E.: Landing Gear and Cavity Noise Prediction. NASA CR-2714, 1976.

36. Revell, James D.: Induced Drag Effect on Airframe Noise. AIAA Paper 75-487, Mar. 1975.

INFLOW TURBULENCE { HORIZONTAL TAIL / FLAPS / INLINE WHEELS   WAKE VORTICITY { FUSELAGE / WING / EMPENNAGE

BOUNDARY LAYER

NOSE-GEAR WHEEL WELL AND DOORS

MAIN-GEAR WHEEL WELL AND DOORS

FLAPS, SLATS, etc.
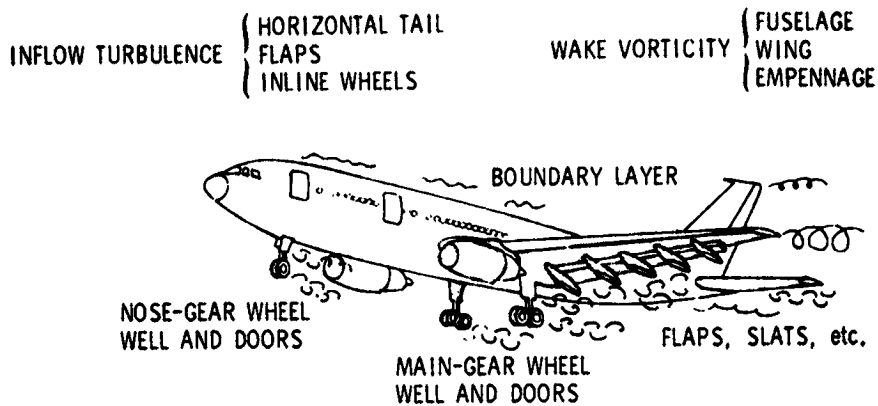
Figure 1.- Schematic diagram illustrating potential sources of airframe noise.

AIRCRAFT
- ○ CONVAIR 240
- □ DC-3
- △ AERO COMMANDER
- ◁ SCHWEIZER 2-33
- ▷ C-5A
- ◁ LIASON
- ◇ HS. 125
- ◁ VC. 10
- ◿ JETSTAR

$$OASPL = 10 \log\left[\left(\frac{U}{100}\right)^5\left(\frac{S_w}{h^2}\right)\right] + 108.3$$

OASPL - 10 log (S_w/h^2), dB

U, m/sec
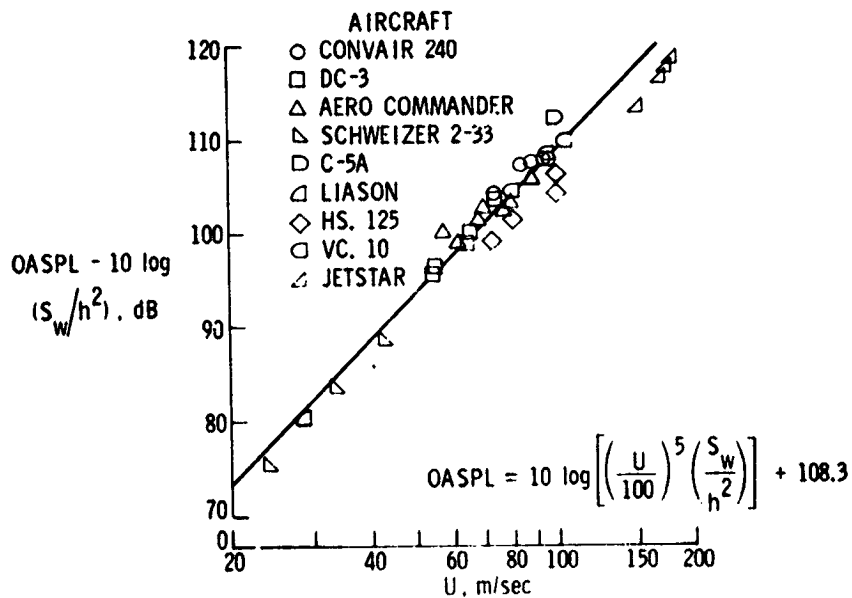
Figure 2.- Measured and calculated maximum OASPL for conventional airframes with retracted gear and flaps.

544
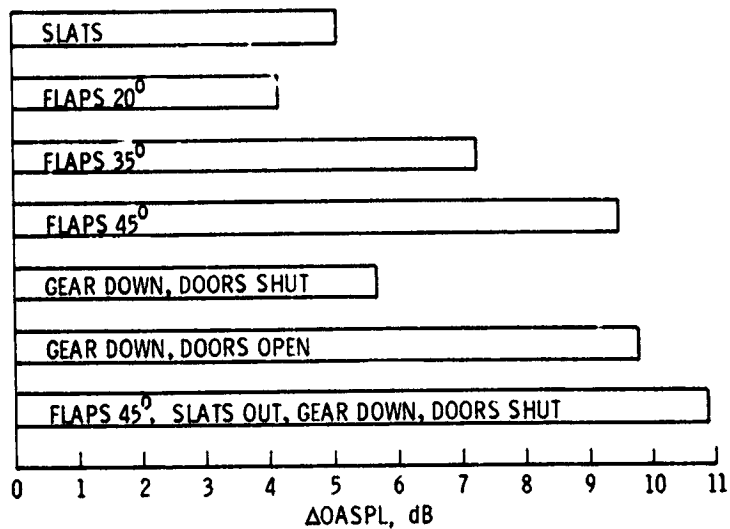
Figure 3.- Estimated nonpropulsive noise increase due to changes from the cruise configuration for the VC. 10 airplane.
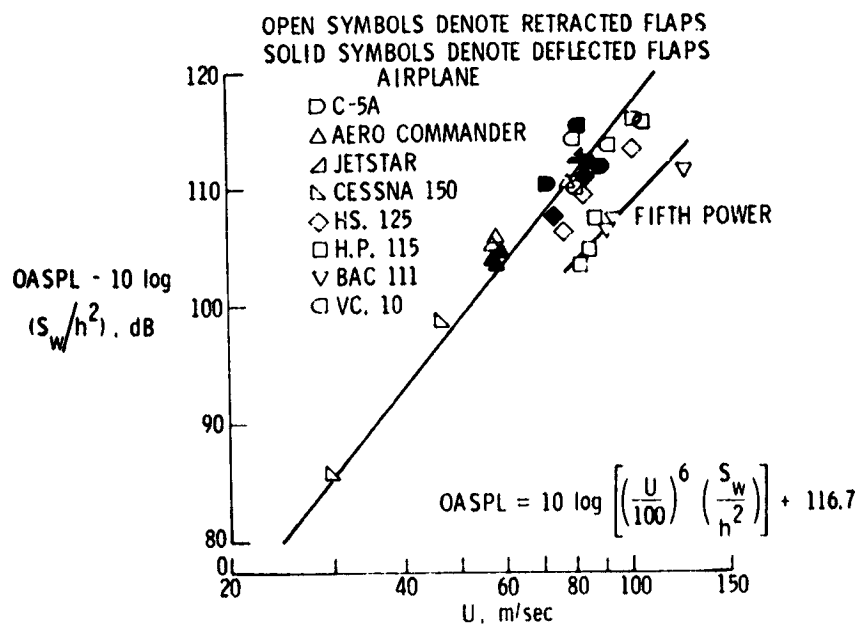
Figure 4.- Measured and calculated maximum OASPL for airframes with extended landing gear.

545
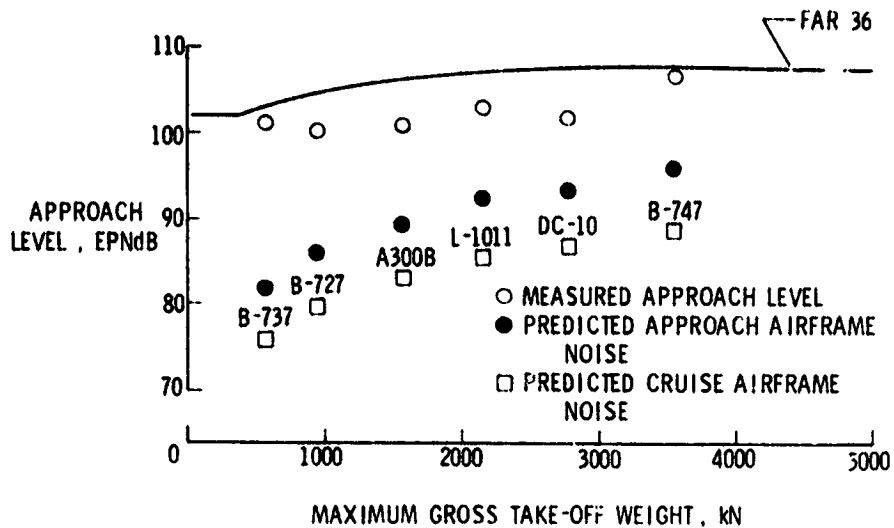
Figure 5.- Comparison of predicted approach and cruise airframe noise levels with FAR 36 certification standard (ref. 2).
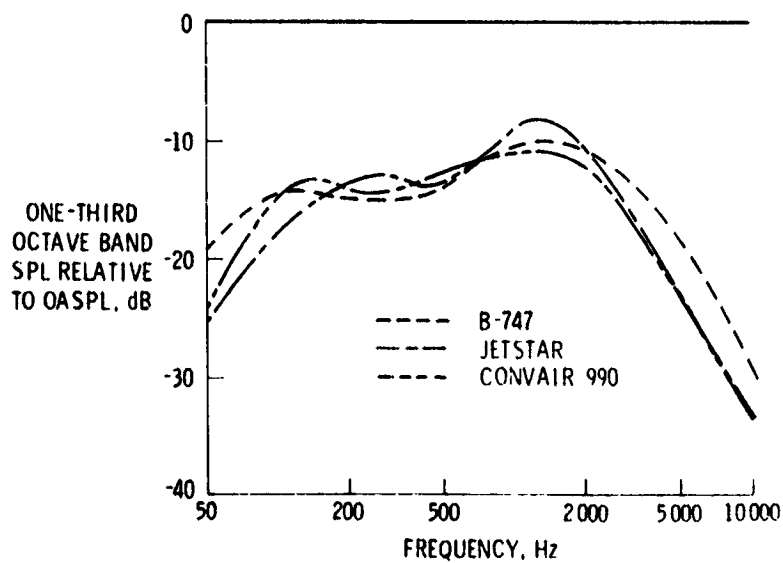
Figure 6.- Clean configuration airframe noise spectra directly below aircraft normalized to equal overall sound pressure level.
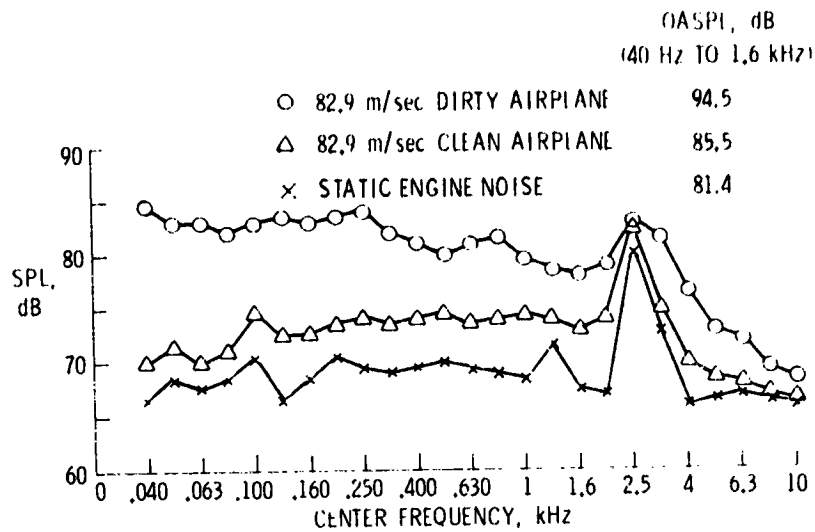
Figure 7.- Comparison of one-third octave band airframe noise spectra for dirty and clean configurations of VC. 10 airplane flying overhead at 183 m.
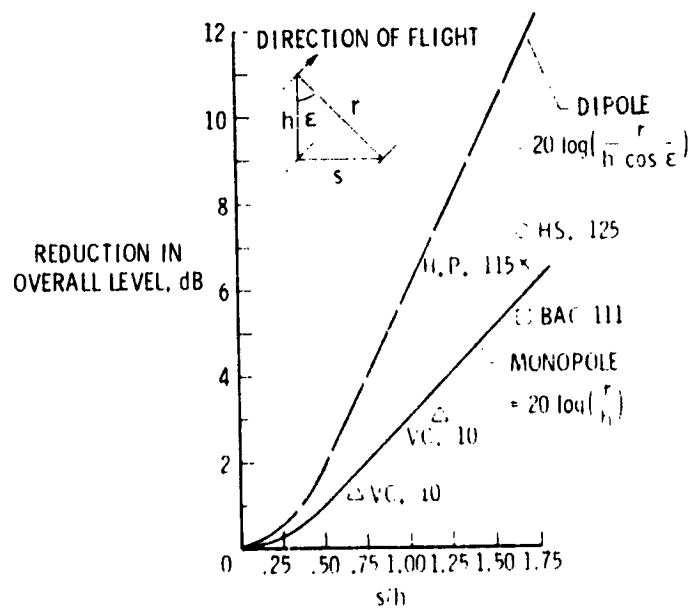
Figure 8.- Measured and predicted reduction in sideline OASPL for four aircraft in clean configuration.

OVERALL SOUND
PRESSURE LEVEL, dB
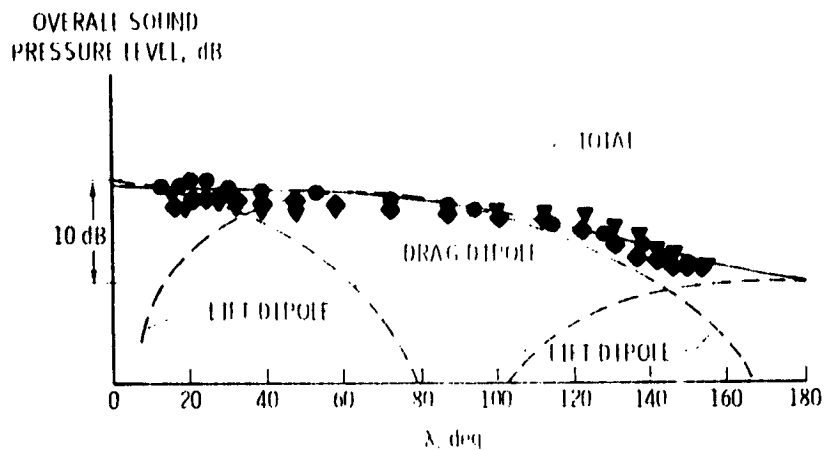
Figure 9.- Directivity pattern of DC-10 airframe noise
in flyover plane compared with that calculated for
dipoles oriented in lift and drag directions.
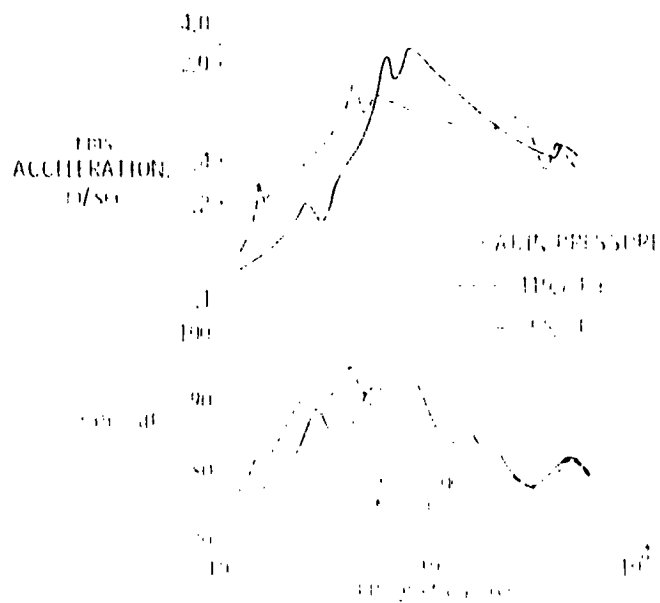
Figure 10.- Radiated sound pressure levels and skin
acceleration levels of DC-10 airplane fuselage
panel for two different values of cabin pressure.

NORMAL FORCE FLUCTUATION

WAKE
VORTICITY

FLOW DIRECTION

RIGID STRUT
ELEMENT

STREAMWISE FORCE
FLUCTUATION
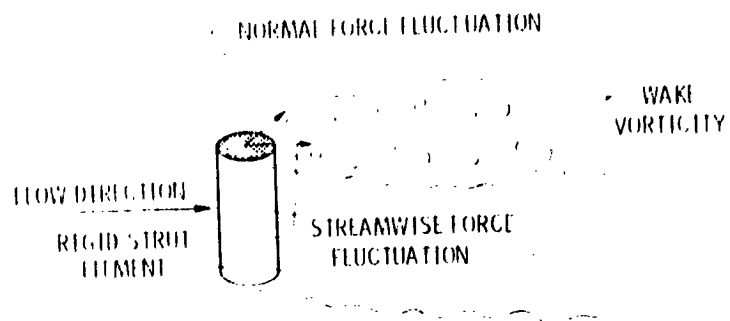
Figure 11.- Schematic diagram of wake-generated
forces on a cylindrical segment in an airstream.

$+$

$-$
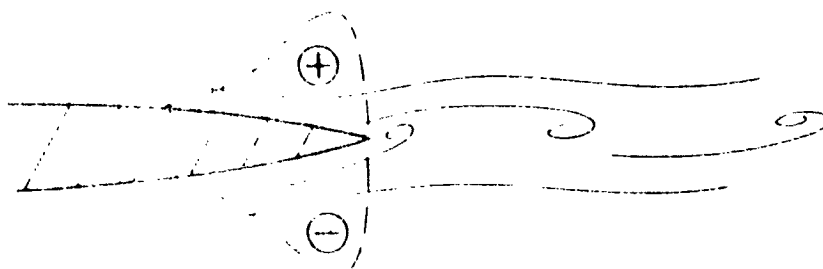
Figure 12.- Schematic diagram of flow field near a trailing
edge and wake-induced instantaneous pressure loading.
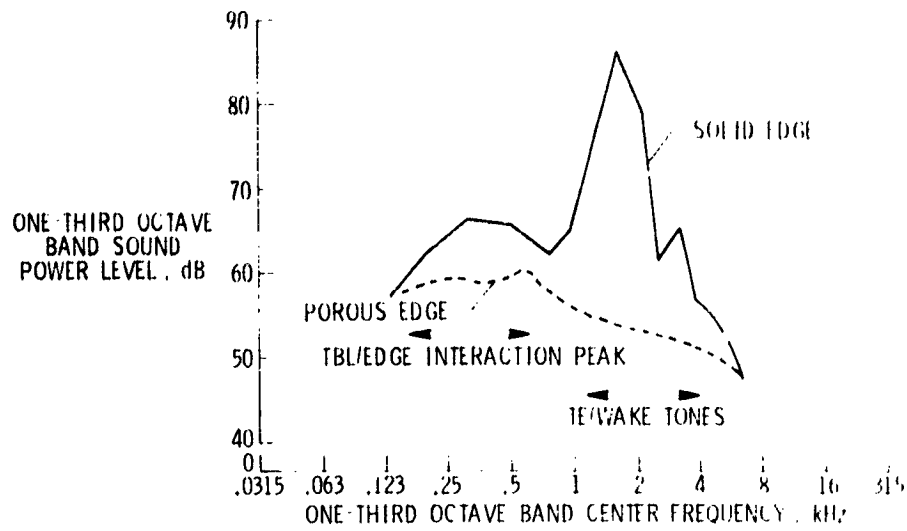
Figure 13.- Airfoil edge source reduction. NACA 0012 airfoil; chord, 0.15 m; span, 0.5 m; $\iota = 4^o$; U = 30 m/sec.
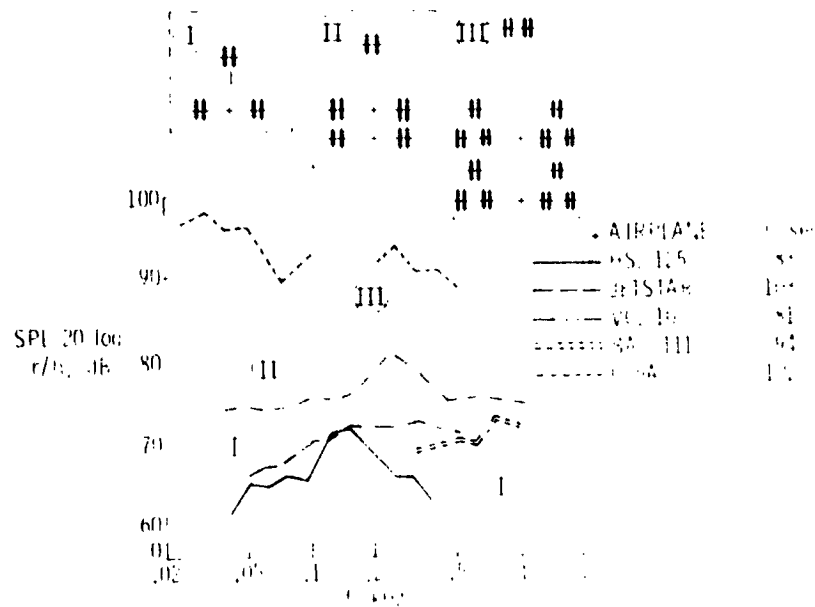
Figure 14.- Maximum landing-gear noise at flight altitude of 100 m.

N 77-18 1

INSIGHTS INTO THE NATURE AND CONTROL OF ROTOR NOISE

Robert J. Pegg
NASA Langley Research Center

SUMMARY

This paper summarizes the present understanding of four important far-field rotating blade noise sources and highlights techniques for noise reduction. These four noise areas include the role of unsteady blade surface loads on rotational noise, the effect of turbulent inflow on the radiated broadband noise of an airfoil, the influence of the trailing vortex on impulsive noise and tail rotor noise, and the effect of blade geometry on high-speed impulsive noise. These noise mechanisms occur to varying degrees on both helicopter rotors and propellers.

Considerable theoretical work has been done in the area of high-speed impulsive noise resulting from the geometry of the rotating blade system. Both model and full-scale experimental correlation of helicopter and propeller high-speed noise are presented. The effect of blade number and airfoil thickness distribution in reducing the high-speed noise is shown. The ideas presented in this paper should be of special interest in light of the proposed federal helicopter noise certification rulings.

INTRODUCTION

In the V/STOL and short-haul aircraft market of the future, the helicopter and propeller-driven aircraft will comprise a significant part of the overall population. Noise requirements such as those currently being proposed for helicopters, which are dictated by operations into densely populated or quiet surburban areas, require that the designer have a better understanding of the complex noise-generating mechanisms.

Rotating blade noise is the primary noise component for these aircraft. For general aviation propeller-driven aircraft, engine exhaust noise could also become a dominant noise source. This paper, however, will deal with the noise problems associated with helicopters. This type of aircraft can have several significant noise sources. These sources are shown in figure 1. Even though the operating conditions vary widely for the various types of rotating blade propulsion systems, a generalized noise spectrum represents the radiated noise. This generalized spectrum is shown schematically and indicates in figure 2 the primary sources of interest. The first source is associated with steady blade loads which do not vary as a function of time or azimuth position. These loads are related to the torque, thrust, coning, and blade thickness. The second source is that due to the incoherent loads on a blade moving through the air and is referred to by Wright (ref. 1) as "self-noise." These latter nonperiodic noises are related to the viscosity

effects of the air and arise from such phenomena as inflow turbulence, boundary
layer, separated flows, and vortex shedding. The noise generated by the steady
loads and the self-noise are components which are considered to be unavoidable
with the operation of conventional rotating blades and thus constitute the
minimum noise of the system (ref. 1). A third component of noise is termed
"excess noise" and results from unsteady loading due to interaction with natural
atmospheric turbulence, interaction with shed vortices, or blade operation in
the transonic speed regime. These latter noises generally occur at a blade
passage frequency in a range which is critical to detection and community
annoyance.

Numerous investigations have established the effect and relationships of
steady loads (ref. 2 to 4) and incoherent loads (self-noise) (refs. 5 and 6)
on the radiated noise. The purpose of this paper is to identify the mechanisms
and possible noise control approaches associated with the noise resulting from
unsteady loading on helicopter rotor blades.

UNSTEADY NOISE

Role of Fluctuation Pressure

Fluctuating blade loads can be categorized broadly as both periodic and
nonperiodic. These loads may arise from such phenomena as blade vibrations,
cyclic blade input, localized shock effects, and potential field interactions.
By using current rotational noise prediction techniques, improved agreement
between predicted and measured noise requires a knowledge of these high-frequency
fluctuating aerodynamic blade loads. Figure 3 shows highlights of tests con-
ducted on the Langley helicopter rotor test facility (ref. 7). These tests
included simultaneous measurements of high-frequency fluctuating surface pres-
sures and far-field radiated noise made on a full-scale nontranslating rotor
system. Spectral characteristics of measured blade surface pressures were
then applied to the existing compact rotational noise theory and compared with
measured far-field noise. A comparison of the calculated and measured rotational
noise showed that good agreement was obtained by using a 40-percent chordwise
integration of the measured fluctuating blade loads acting at a single point
on the blade. Reliable information concerning the variation of these fluctuating
loads with flight condition is still not available.

Vortex Interaction

Main rotor.- The effect of free air turbulence on the discrete noise from
rotating blade devices having skewed inflow is apparently small. Skewed-inflow
rotating blade devices (helicopter rotors and tilt rotors), however, are affected
by the rapid pressure fluctuations caused by a shed vortex passing close to a
lifting surface. One of the largest contributions to helicopter noise, when
it occurs, results from the interaction of the shed blade tip vortex and the
following blade. This "slapping" noise can be very significant from an annoy-
ance and detectability standpoint. In figure 4, vapor condensation shows the
shed vortices for a hovering commercial helicopter. In forward flight and at
certain rates of descent these vortices go through the rotor disk and interact

552

with the rotor blades and result in rapid pressure fluctuations and impulsive
noise. Figure 5 presents schematically the regions of helicopter impulsive
noise due to vortex interaction and high-speed effects. High-speed effects are
treated in a later section. This figure is a means of mapping the flight regions
(rate of descent and airspeed) where impulsive noise becomes a problem. The
blade slap boundary map has been used to determine flight path management tech-
niques to reduce terminal area noise levels (ref. 8).

The lack of adequate experimental acoustic data, which can be used to iden-
tify the basic noise mechanisms and the radiation patterns of helicopter impul-
sive noise, can be traced to a variety of measurement difficulties; this lack
of data forced past investigators to utilize qualitative observations and limited
measurements to judge the extent of the blade slap problem. The most common
method of measuring impulsive noise is to station a microphone at a fixed posi-
tion on or above the ground and fly the helicopter along nominal trajectories
at selected forward-flight conditions. Under ideal conditions, a quantitative
assessment of the character of the noise is possible. However, when one tries
to compare, in detail, the noise produced by the same aircraft under different
flight conditions, or to develop directivity patterns of the radiated noise
holding all other pertinent variables constant, such as distance to the micro-
phone, azimuth angle, and ambient wind effects, the technical problems and sta-
tistical uncertainties combine to make the data-gathering task very difficult.

Several inflight techniques for obtaining impulsive noise measurements have
been developed. The inflight acoustic measurement system (IFAMS) is a research
tool designed to study these phenomena. Typical pressure time histories mea-
sured with IFAMS are shown in figure 6. By providing a microphone array close
to the acoustic source, source location, near-field spectral characteristics,
and pressure signatures can be obtained. The data on the left of figure 6
show a pressure time history and spectrum from the advancing side microphone,
and data on the right are from the retreating side. The flight conditions are
36 m/sec (70 knots) airspeed and 183 m/min (600 ft/min) rate of descent. The
advancing side pressure time history shows discrete amplitude spikes attributable
to main-rotor blade and vortex interaction at main-rotor blade passage frequency.
The retreating side pressure time history shows no distinguishing pressure peaks
and is about 20 dB below the noise level of the advancing side.

Another inflight measurement technique utilizes a quiet, fixed-wing aircraft,
instrumented with a microphone, and flown to maintain a fixed relative position
with the test helicopter. Results of flight tests using this method are reported
in reference 9. This technique can be used to obtain far-field noise measure-
ments without Doppler shift.

Various attempts to modify the tip vortex and thereby reduce the vortex-
induced excess noise have been tried. These attempts have been both passive
(blade tips) and active (air mass injection). The results of an investigation
with a linear air mass injection system on a 2.1-m diameter (7 ft) wind-tunnel
model are shown in figure 7. The objective of this investigation was to deter-
mine whether the accelerated vortex aging by the air injection would reduce the
noise. The left-hand pressure time history and spectrum come from the rotor in
a descent condition that results in the maximum interaction impulsive noise.
The interaction peaks in the pressure time history are clearly visible. When

air is introduced at the blade tips into the vortex core, the resulting pressure time history is obtained as shown on the right-hand side. The interaction peaks on the pressure time history have been substantially reduced, and the overall sound pressure level has been reduced approximately 5 dB(A).

Tail rotor.- In addition to the effect of the vortex of a following main-rotor blade, the effect of the vortex plays an important part in the noise generated by the tail rotor. A research model was constructed, and a wind-tunnel investigation was conducted to determine the effect that the shed vortex from the main rotor had on the noise generated by the tail rotor. Figure 8 shows a picture of the model and some initial test results. The model has the capability of independent rotor speed control, variable thrust on both rotors, variation of the direction of tail-rotor rotation, and placement of tail rotor relative to the main rotor.

The spectra shown in figure 8 indicate the effect of main-rotor wake on the tail-rotor noise at increasing airspeeds. The predominant discrete harmonics are those due to the tail rotor. It can be seen that the general overall noise level increases with increasing airspeed. As airspeed is increased, tail rotor and vortex interactions occur at different positions on the tail-rotor disk and thus affect different harmonics. In addition, it was ascertained that tail-rotor noise was sensitive to the location of the vortex interaction on the tail-rotor disk, the direction of tail-rotor rotation, the lateral fin-rotor spacing, and the thrust direction of the tail rotor. Tail-rotor noise was found to be insensitive to the main-rotor thrust coefficient, longitudinal spacing of tail rotors, and the tail-rotor ratios of rotational speed to main-rotor rotational speed. The results of this study offer several approaches to reduce the noise of the tail rotor.

High-Speed Flow

Impulsive noise from helicopters can also originate from compressibility phenomena. Figure 5 schematically indicates that part of the flight regime where this type of noise becomes an increasing problem. Certain techniques can be used to push this boundary to higher speeds, but will never eliminate it. If the operational emphasis is on high-speed flight, then this source of noise will be important in determining en route flight limitations.

The two main sources for high-speed noise are the periodic pressure distributions due to unsteady shock formations on the advancing side and the monopole noise due to blade thickness and planform.

A recent theoretical prediction technique (ref. 10) based on a noncompact acoustic source model is directly applicable to high-speed propellers and rotors. Figure 9 shows a comparison of measured and calculated pressure time histories of a helicopter flying at 165 knots over a microphone. The advancing tip Mach number is 0.89. The two time histories agree very closely; the calculated pressure signature is based only on thickness noise. The effect of the tail rotor can also be seen in the measured pressure time history. By using this theory for high-speed rotating blade noise, an analytical tool exists for developing means of reducing high-speed rotor noise. An example of the use of the theory

for noise reduction is highlighted in figure 10. Pressure signatures were calculated for three nonlifting rectangular planform blades with different airfoil sections. The airfoil sections are a biconvex parabolic arc, a NACA four-digit symmetrical airfoil, and a supercritical airfoil, all with a 9.3-percent thickness ratio. The flight conditions were held constant for all three airfoil cases. From this figure, it is obvious that reduced noise levels have been achieved with the biconvex airfoil section. Camber shape does not enter into the analysis of thickness noise, but does govern airfoil lift characteristics; therefore, one can theoretically obtain suitable aerodynamic characteristics and lower high-speed impulsive noise by controlling the airfoil thickness distribution.

NOISE CONTROL TECHNIQUES

There are several basic approaches for the control of the unsteady load noise sources. These techniques can be categorized into three major areas: those involving detailed design changes such as rotor blade tip design, those involving overall configuration changes such as an increase in the number of blades, and those pertaining to changes in operation procedures. Table 1 outlines these noise control approaches for the four primary noise sources.

CONCLUDING REMARKS

It has been pointed out that the general noise spectra for a number of free, rotating blade systems are the same and that the excess noise is the primary contribution to annoyance and detectability. The excess noise is made up of various sources of unsteady loads such as the ingestion of natural atmospheric turbulence, vortex and lifting surface interaction, and transonic flow phenomena.

The effect of shed vortex modification (reduced strength, etc.) has a significant effect on reducing the impulsive noise associated with helicopters operating in the terminal area. Lastly, it was shown that by careful attention to blade airfoil and planform, the high-speed impulsive noise boundary can be pushed to higher flight speeds; thus the helicopter could cruise more economically.

REFERENCES

1. Wright, S. E.: The Acoustic Spectrum of Axial Flow Machines. J. Sound & Vib., vol. 45, no. 2, Mar. 22, 1976, pp. 165-223.

2. Gutin, L.: On the Sound Field of a Rotating Propeller. NACA TM 1195, 1948. (From Physik. Zeitschr. der Sowjetunian, Bd. 9, Heft 1, 1936, pp. 57-71.)

3. Garrick, I. E.; and Watkins, Charles E.: A Theoretical Study of the Effect of Forward Speed on the Free-Space Sound Pressure Field Around Propellers. NACA Rep. 1198, 1954. (Supersedes NACA TN 3018.)

4. Wright, S. E.: Sound Radiation From a Lifting Rotor Generated by Asymmetric Disk Loading. J. Sound & Vib., vol. 9, no. 2, Mar. 1969, pp. 223-240.

5. Stowell, E. Z.; and Deming, A. F.: Vortex Noise From Rotating Cylindrical Rods. NACA TN 519, 1935.

6. Clark, P. J. F.; and Ribner, H. S.: Direct Correlation of Fluctuating Lift With Radiated Sound for an Airfoil in Turbulent Flow. J. Acoust. Soc. America, vol. 46, no. 3 (pt. 2), Sept. 1969, pp. 802-805.

7. Hosier, R. N.; Ramakrishnan, R.; and Pegg, R. J.: The Prediction of Rotor Rotational Noise Using Measured Fluctuating Blade Loads. J. American Helicopter Soc., vol. 20, no. 2, Apr. 1975, pp. 2-11.

8. Halwes, Dennis R.: Flight Operations To Minimize Noise. Vertiflite, vol. 17, no. 2, Feb. 1971, pp. 4-9.

9. Boxwell, D. A.; Schmitz, F. H.; and Hanks, M. L.: In-Flight Far Field Measurement of Helicopter Impulsive Noise. Paper presented at the First European Rotorcraft and Powered Lift Aircraft Forum (Southampton, England), Sept. 22-24, 1975.

10. Farassat, F.; Pegg, R. J.; and Hilton, D. A.: Thickness Noise of Helicopter Rotors at High Tip Speeds. AIAA Paper 75-453, Mar. 1975.

TABLE 1.- NOISE CONTROL SUMMARY

NOISE SOURCE	NOISE CONTROL APPROACH		
	DETAIL DESIGN	OVERALL CONFIGURATION	OPERATIONAL PROCERURES
NONUNIFORM INFLOW		✓	
MR VORTEX INTERACTION	✓		✓
MR/TR VORTEX INTERACTION	✓	✓	
HIGH-SPEED THICKNESS	✓		✓

TURBULENT
INFLOW

HIGH
SPEED EFFECTS

MAIN ROTOR
VORTEX
INTERACTION

TAIL ROTOR
VORTEX
INTERACTION
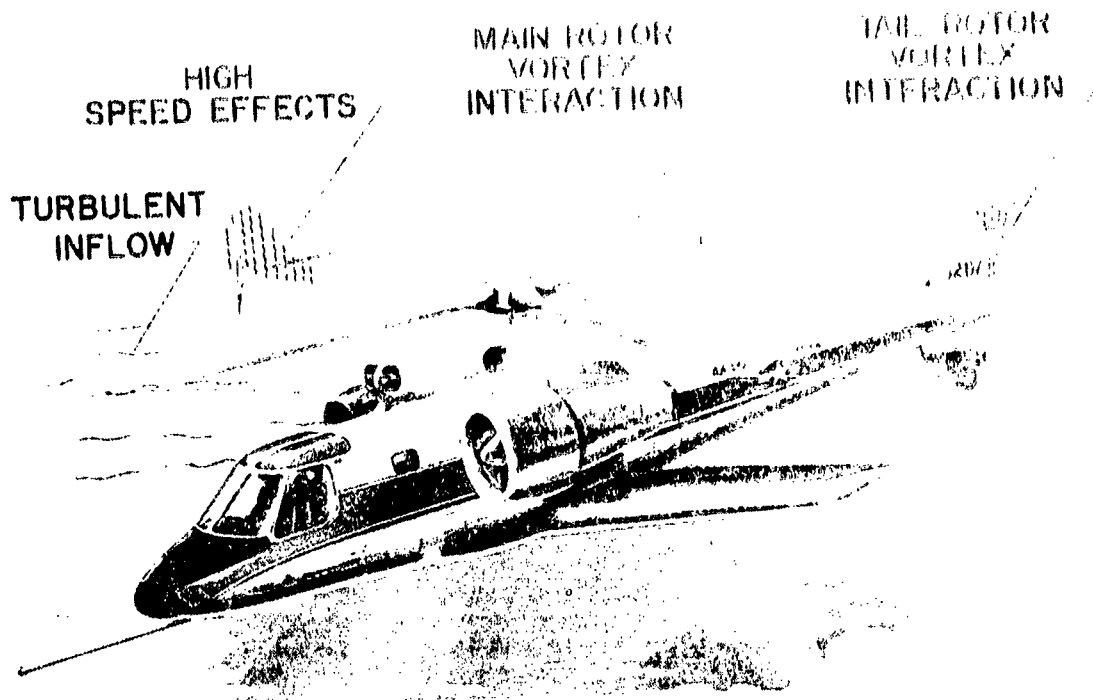
Figure 1.- Pictorial representation of rotor noise sources.

NOISE DUE TO STEADY LOADS

NOISE DUE TO UNSTEADY LOADS
(EXCESS NOISE)

NOISE
LEVEL

NOISE
DUE TO
INCOHERENT
LOADS
(SELF-NOISE)
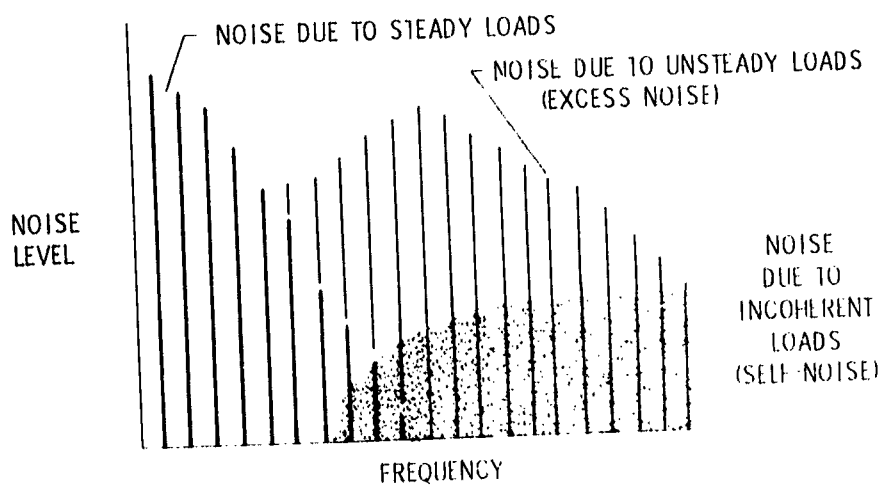
FREQUENCY

Figure 2.- Generalized acoustic spectrum for rotors.

ROTATIONAL NOISE = f(STEADY LOADS) + g(FLUCTUATING LOADS)

HELICOPTER ROTOR TEST FACILITY   CHORDWISE SURFACE PRESSURE
                                             TRANSDUCERS

AERODYNAMIC LOADING SPECTRUM   ACOUSTIC SPECTRA
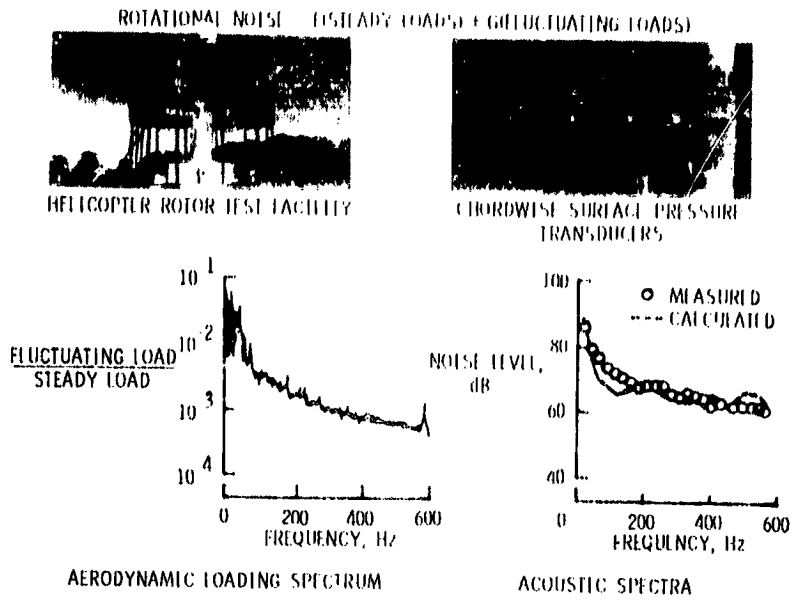
Figure 3.- Comparison of measured and calculated
noise spectra using high-frequency fluctuating
airloads.
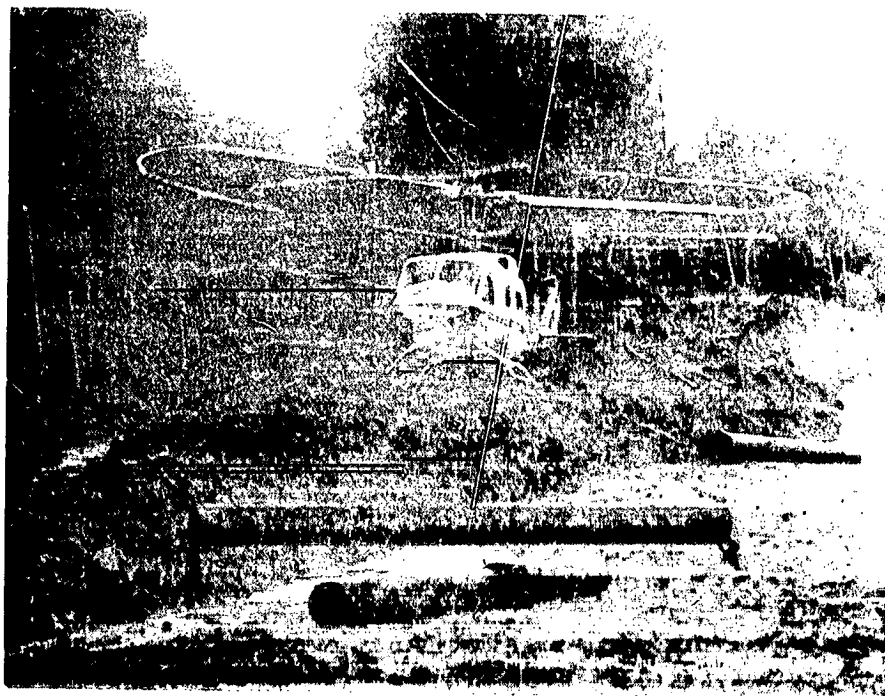
Figure 4.- Main-rotor vortex flow visualization
for a hovering helicopter.
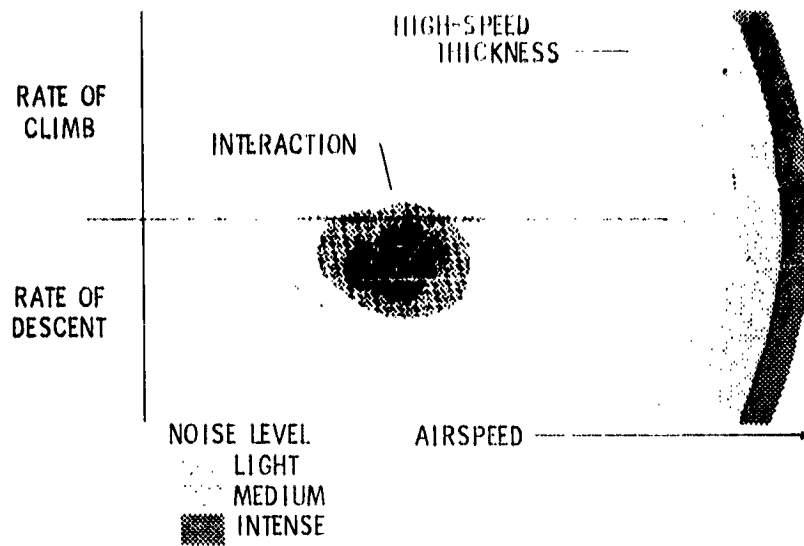
Figure 5.- Regi ̄s of flight where helicopter impulsive ɔise can be expected.

$V = 70$ kts, $R/D = 600$ ft /min

ADVANCING BLADE SIDE

RETREATING BLADE SIDE
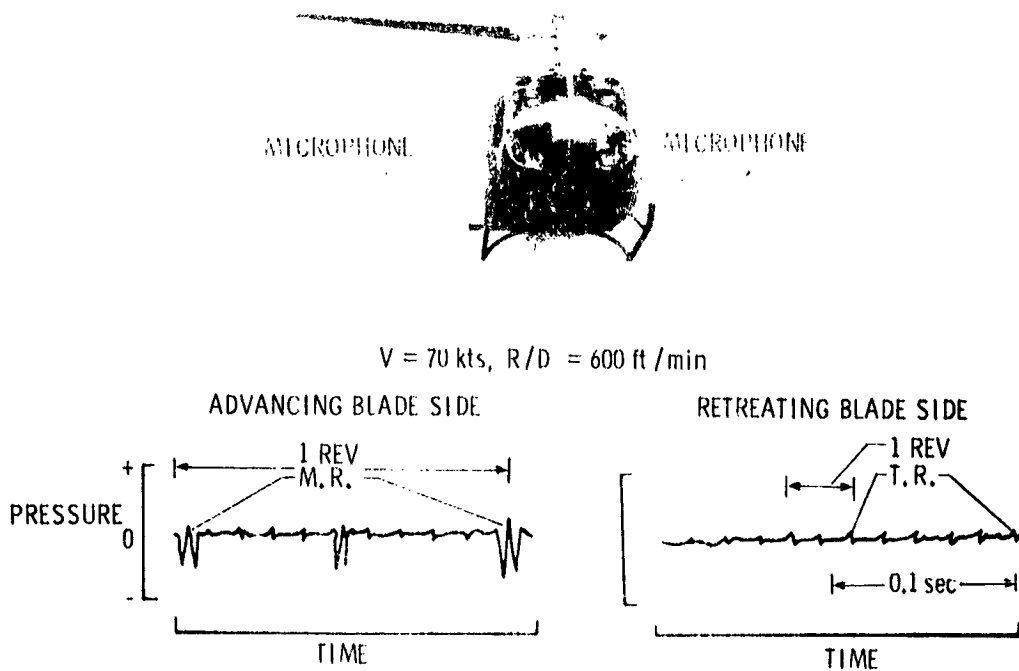
Figure 6.- Near-field measured acoustic pressure waveforms on the advancing and retreating side of a helicopter in descending flight.

DIRECTION OF ROTATION •   LEADING EDGE   ROTOR BLADE

VORTEX INTERACTION AIR JET

PRESSURE   dB(A) = 115   dB(A) = 111

0   0

TIME   TIME

AIR MASS INJECTION OFF   AIR MASS INJECTION ON
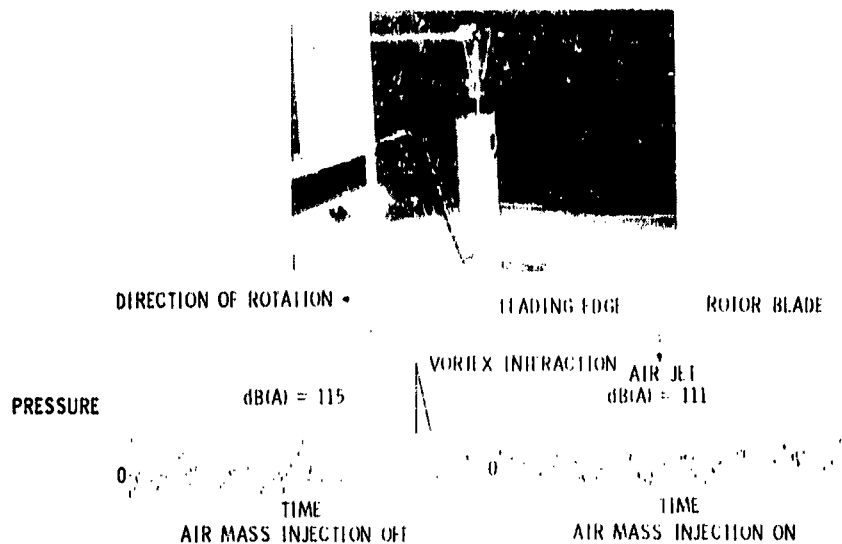
Figure 7.- Wind-tunnel verification of the effect
of vortex modification on rotor impulsive noise.

MAIN-ROTOR/TAIL-ROTOR (MARTAR) MODEL
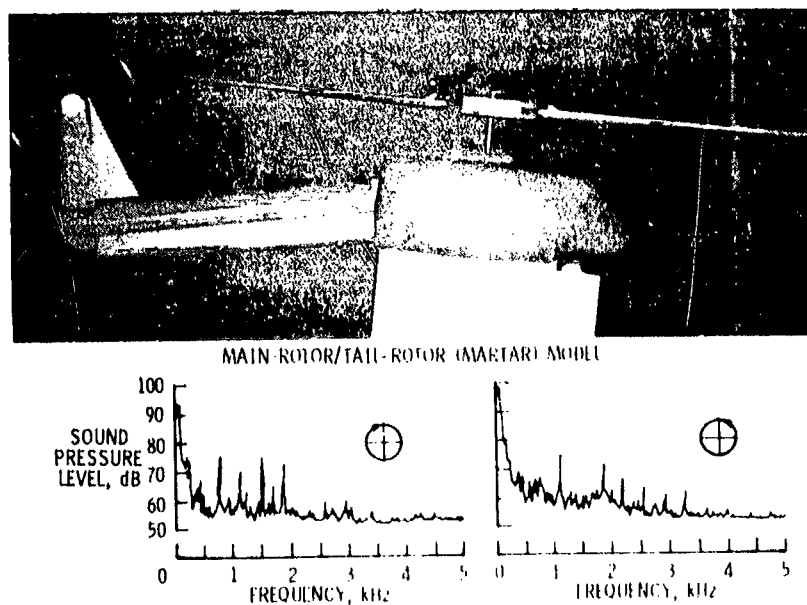
Figure 8.- A preliminary result obtained from the
main-rotor/tail-rotor model showing the effect
of tail rotor rotation and wake interaction on
tail-rotor noise.

561
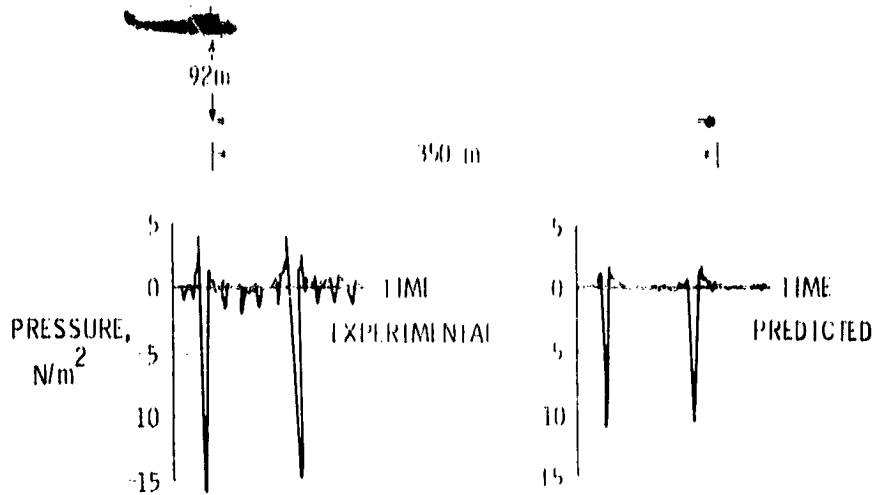
Figure 9.-- Comparison of measured and calculated sound pressure signatures for high-speed helicopter rotors.

$M_t = .9$, $t/c = .093$, (SYMMETRICAL AIRFOILS), NO LIFT
$V = 170$ kts
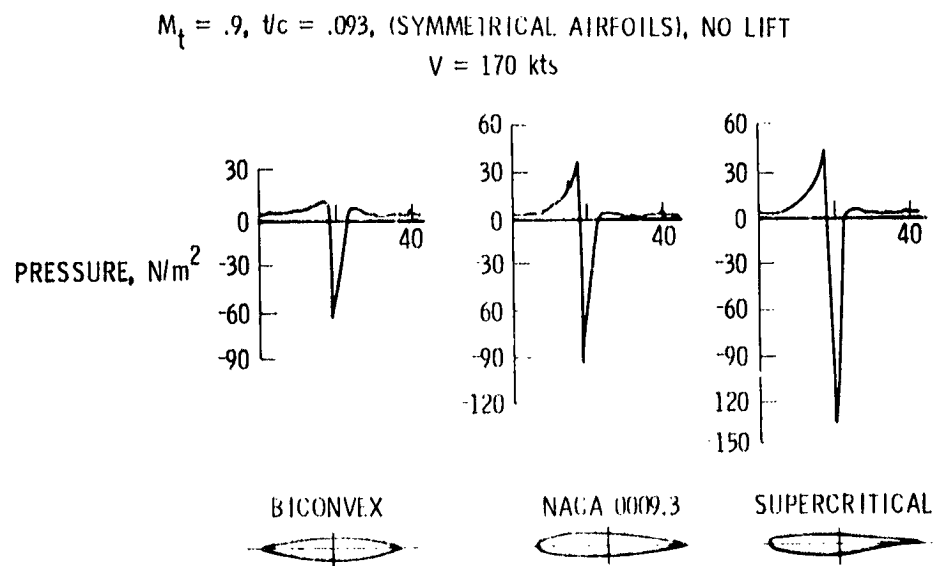
Figure 10.- Calculated sound pressure signatures of a rotor showing the effects of three different airfoil thickness distributions.

562

PASSENGER RIDE COMFORT TECHNOLOGY FOR

TRANSPORT AIRCRAFT SITUATIONS

D. William Conner
NASA Langley Research Center

Ira D. Jacobson
University of Virginia

SUMMARY

A brief overview is given of NASA research in ride comfort and of the resultant technology. Three useful relations derived from the technology are presented together with five applications of these relations to illustrate their effectiveness in addressing various ride comfort situations of passenger transports.

INTRODUCTION

Passenger ride comfort can have a significant influence in determining acceptance and use of various modes of air transportation. The definition of ride comfort as used in the present paper is expressed as the impact on the passenger of all aspects of the vehicle physical environment that affect his acceptance of the ride. The time has arrived when some reasonable level of comfort is expected by the traveling public. Advent in the late 1950's of jet transports, cruising at high altitude where the air is generally smooth, made possible levels of ride comfort in long-haul transportation far superior to anything previously attainable. Many situations still arise, however, where ride comfort can be adversely affected if special attention is not given in the design and/or operations of the aircraft. (See ref. 1.) To address these situations, ride comfort technology is required, but until a few years ago, key portions of this technology involving human factors was only poorly understood. At that time NASA initiated research effort directed toward identifying the various critical factors and toward providing quantitative relations to account for these factors in problem situations.

Aircraft situations which can lead to ride comfort problems fall into three general categories: input environments to the vehicle; aircraft operations; and aircraft configurations. Four example problem situations are listed as follows:

Environments
  Wind shears and gusts
  Turbulence
  Trailing-vortex wakes
  Runway roughness and waviness

Operations
   Cruise at low altitude
   Terminally configured vehicle maneuvers
   Excessive rate of change of cabin pressure
   Cabin temperature too warm

Configurations
   Unswept wings and/or low wing loadings
   Outsize fuselage/empennage surfaces
   Propulsion systems producing noise/vibration
   Marginal size seats and legroom

Input environments which influence the ride-motion environment consist of both naturally occurring phenomena such as gusts or turbulence and man-generated phenomena such as trailing-vortex wakes or runway roughness. Incidentally, runway roughness will become an increasingly important factor with the advent of aircraft such as supersonic transports having relatively flexible fuselages and high take-off speeds. Aircraft operations influence ride environments in the form of motions caused by maneuvers, of pressure changes caused by rapid descents, or of too high temperature. Finally, aircraft configurations influence the ride environment by size and shape of external surfaces which generate aerodynamic perturbing forces; by onboard equipment, such as power plant noise and vibrations; and by passive equipment which directly interface the passengers such as marginal size seats with limited elbowroom and legroom.

The present paper has two primary objectives: (1) presentation of a brief overview of NASA ride comfort research effort and (2) description of useful relations derived from the technology together with several applications of these relations to illustrate their usefulness in addressing air transport ride problems situations.

SYMBOLS

a   acceleration

C   comfort rating on a 7-point scale

dB(A)   A-weighted noise level, dB

E   event (given ride situation)

g   acceleration of gravity, 9.8 m/sec^2

$\dot{h}$ rate of change in altitude, m/min

ℓ seat legroom, cm

p   roll rate, deg/sec

S   satisfaction

564

T	temperature, $^\circ C$
V	indicated airspeed, knots
w	seat width between armrests, cm
γ	flight-path angle, deg
δ	Kroneker δ
θ	pitch angle, deg
σ_a	standard deviation of acceleration, g units
ϕ	roll angle, deg

Subscripts:

cm	compound maneuver
dc	descent or climb maneuver
E	event
env	environmental (factors other than maneuvers, seating space)
$\dot{h}$	rate of change in altitude
l	longitudinal direction
man	maneuver
max	maximum
mot	motion
no	noise
po	pitchover
rms	root-mean-square value
seat	seating space
T	temperature
t	transverse direction
trip	total trip
turn	turning maneuver

v   vertical direction

z   normal direction to cabin floor

RESEARCH PROGRAM

Analysis Method

A schematic of the analysis method (ref. 2) to assess ride comfort is illustrated in figure 1. A vehicle forcing function (e.g., turbulence and maneuvers) is converted into a ride-motion environment for the passenger using the appropriate transfer function for the vehicle system being analyzed. This environment together with other inputs (e.g., noise and temperature) provides a total ride environment from which a comfort evaluation is obtained using a transfer function which represents the passenger. Since response to a given ride environment can vary widely between subjects, a statistical approach is employed wherein the evaluation is expressed as a mean subjective comfort response. The calculated comfort evaluation is then related by a subjective value transfer function to a satisfaction evaluation of the flight in the context of the overall trip. Since trip satisfaction can also be influenced by factors other than ride comfort (e.g., cost, time, schedule, and safety), the subjective value transfer functions for ride comfort are not independent of other factors. Thus, the satisfaction model presented herein represents satisfaction in the context of a particular type operation (e.g., U.S. commuter operation).

Selection of Research

At the beginning of NASA research in transport aircraft ride quality in the early 1970's, the level of technology varied substantially for the several components of the analysis method shown in figure 1. Turbulence environment forcing functions to the aircraft had been measured and reasonably well quantified in statistical terms (refs. 3 and 4) as a function of factors such as altitude, terrain, and time of year. Vehicle transfer functions had been derived (e.g., ref. 5) and for the larger transport airplanes were generally well quantified because of other needs (e.g., aircraft dynamic stability and structural dynamics). Factors significant in affecting subjective reaction were not well defined both in regard to identification and to quantification of their character and magnitude (ref. 6). The subjective transfer function was poorly defined with prior research efforts generally limited to laboratory studies of vertical and transverse sinusoidal motions (e.g., ref. 7). Much of the work had been directed toward tolerance and task performance level and had dealt with relatively high motion magnitudes in the discomfort regime (these were, in fact, the type of data that subsequently provided the basis for ISO standard ISO-2631 (ref. 8), which offers provisional guidance for ride comfort vibration levels). Consequently, ride comfort evaluation technology was generally qualitative in character. Subjective value function technology was limited to only a few areas (costs and trip time), whereas ride comfort effects were a relatively unknown quantity.

Overall evaluation of the state of the art of ride comfort technology then existing (e.g., ref. 9) indicated that implementation of the analysis method

566

outlined in the previous section would require inputs and quantitative relations which could only be obtained from additional data generated by carefully structured experiments.

Experimental Effort

The approach taken in generating experimental data appropriate for ride comfort modeling is illustrated in figure 2. In this approach, subjective evaluations of ride comfort were obtained and compared with the measured ride environment. These evaluations were obtained for both fare-paying passengers and experienced test subjects traveling onboard scheduled air carriers (ref. 10) and for test subjects in controlled experiments on research aircraft (refs. 11 and 12) or ground-based simulators (e.g., refs. 13 and 14). On air carriers, test subjects gave subjective ratings periodically during the flight plus an overall rating for the total flight, while simultaneously, fare-paying passengers gave an overall rating at the conclusion of the flight. Data from air carriers were particularly useful in qualitatively identifying both the environmental factors important in real-world situations (see list at top of fig. 2) and the nature and magnitude of these environmental factors.

Controlled experiments using research aircraft were carried out to systematically investigate situations of interest (e.g., maneuvers) which would not normally be experienced in any significant amount during air carrier operations. Controlled experiments using simulators were carried out to gain a detailed understanding of the influence of factors or factor components on discomfort. Examples (refs. 13 to 20) include effects of single-degree-of-freedom vibrations with either sinusoidal or random frequency content and of various degrees of freedom alone or in combination; effects of single frequency or random noise, with and without vibrations; and effects of seat transmissibility on response to input vibrations through the floor.

Information generated by the various experimental studies has been used to model (relate) passenger comfort as a function of various ride environment inputs. These models range in complexity from simple relations for single-degree-of-freedom motion inputs (e.g., ref. 17) obtained from simulator data to complex relations for multiple-degree-of-freedom random inputs obtained by regression analysis of flight data (ref. 21). While present models are useful as illustrated later, there is yet no fully comprehensive and reliable model to meet all situations. As technology builds, considerable improvement in comfort models can be expected.

Those interested in obtaining a more detailed understanding of NASA research and resultant technology are referred to the proceedings of NASA-sponsored ride quality symposia held in 1972 and 1975 (refs. 22 and 23). These proceedings also contain much valuable information concerning research outside NASA both in the United States and in the United Kingdom plus a description and critique of ISO-2631 (ref. 8).

Ride comfort research presently underway or envisioned by NASA centers in two areas. The first area concerns vehicle-unique phenomena of unusual

environments (such as single-tone noise in civil helicopters) which will peri-
odically arise with advent of either new transport vehicles or new vehicle
operations. The second area includes various individual effects items (see list
above the Ground-Based Simulators photograph of fig. 2) where detailed informa-
tion is required to gain a better understanding of ride comfort phenomena and to
refine comfort-rating models.

USEFUL RIDE COMFORT RELATIONS

Three ride comfort relations which are useful in addressing transport air-
craft problem situations have been developed as follows from NASA research
technology:

    (1) Comfort Model Relation — to provide the subjective transfer function
         for relating ride environment to ride comfort (see fig. 1)

    (2) Ride Satisfaction Relation — to provide the subjective value function
         for relating ride comfort to trip satisfaction (see fig. 1)

    (3) Response Integration Relation — to provide a method for appropriately
         weighting and summing the series of local comfort ratings (experiences)
         of a trip to obtain an overall evaluation of comfort and satisfaction

Although the complexity and content of the relations are subject to individual
judgment and to the data base available, the present state of the art is con-
sidered sufficiently advanced to define each relation in reasonably meaningful
terms.

Comfort Model Relation

From the several comfort rating models developed during the course of the
research effort, a composite model has been developed which is comprised of the
more important ride environmental factors in a relatively simple form. This
model, shown schematically in figure 3, was derived from flight data primarily
of small to medium size (15 to 60 passenger) turboprop airplanes in short-haul
type operations and, thus, may not be fully applicable to other transport situa-
tions. The model provides a numerical rating of subjective comfort response C,
where C has the following descriptors:

    1 = Very comfortable
    2 = Comfortable
    3 = Somewhat comfortable
    4 = Neutral
    5 = Somewhat uncomfortable
    6 = Uncomfortable
    7 = Very uncomfortable

The model lists in parallel the three groupings of maneuver factors, environmen-
tal factors (motion, noise, temperature, and pressure), and seating-space

568

factors, inasmuch as data analysis to date indicated little additive or cross-coupling effects between these three groups. Relations for the maneuver-factors group are based on regression analysis of controlled-experiment results (1920 test-subject data points) carried out by NASA in-house effort using the USAF Total In-Flight Simulator (TIFS) research aircraft. (See ref. 24.) Relations for the environmental factors group and for the seating-space factors group are based on results of scheduled air carrier surveys (2976 test-subject data points) carried out by the University of Virginia.

According to the model, the mean subjective comfort rating for a unique ride event (situation) is the maximum value provided by any of the three factor groups for that event:

$$C_E = \max\left(C_{env}, \ C_{man}, \ C_{seat}\right)$$

The model relates the mean subject comfort to the factors of each factor group as follows:

Environmental Factors Group:

$$C_{env} = 2 + C_{mot} + C_{no} + C_{\dot{h}} + C_T$$

where

$$C_{mot} = 18.9\sigma_{a,v} + 12.1\sigma_{a,t} \qquad\qquad \left(\sigma_{a,v} \gtrsim 1.6\sigma_{a,t}\right)$$

$$= 1.62\sigma_{a,v} + 38.9\sigma_{a,t} \qquad\qquad \left(\sigma_{a,v} < 1.6\sigma_{a,t}\right)$$

$$C_{no} = 0.19(dB(A) - 85)$$

$$C_{\dot{h}} = 0.005(\dot{h} - 90)\delta_{\dot{h}} \qquad\qquad \left(\begin{array}{l} \delta_{\dot{h}} = 1 \ \text{ for } \ \dot{h} > 90 \text{ m/min} \\[6pt] \delta_{\dot{h}} = 0 \ \text{ for } \ \dot{h} \leq 90 \text{ m/min} \end{array}\right)$$

$$C_T = 0.054(T - 20.5)\delta_T \qquad \left(\begin{array}{l} \delta_T = 1 \ \text{ for } \ 2 + C_{mot} + C_{no} + C_{\dot{h}} > 3.4 \\[6pt] \delta_T = 0 \ \text{ for } \ 2 + C_{mot} + C_{no} + C_{\dot{h}} \leq 3.4 \end{array}\right)$$

Maneuver Factors Group:

$$C_{man} = C_{turn} \ \text{ or } \ C_{po} \ \text{ or } \ C_{dc} \ \text{ or } \ C_{cm} \qquad \text{(depending on type maneuver)}$$

where

$$C_{turn} = 0.293 + 0.0665 \left| \phi_{max} \right| + 0.07 \left| p_{max} \right| + C_{no} + C_{\dot{h}} + C_T$$

$$C_{po} = 1.75 + 22.1a_{z,rms} + C_{no} + C_{\dot{h}} + C_T$$

$$C_{dc} = 0.151 + 0.098 \left| \theta_{max} \right| - 0.118\gamma_{max} + 0.0195V_{max} + C_{no} + C_{\dot{h}} + C_T$$

$$C_{cm} = 1.48 + 12.3\sigma_{a,l} + 32.8\sigma_{a,t} + 11.62\sigma_{a,v} + 0.022\dot{h}_{rms} + C_{no} + C_{\dot{h}} + C_T$$

Seating Space Group:

$$C_{seat} = 1 + \left[0.0077(63 - w)^2 + 0.16(30 - \ell)^2 \right]^{1/2}$$

$$\text{for} \quad 30 < w \leq 63 \quad \text{and} \quad 18 < \ell \leq 30$$

The equations presented are intended to provide first-order evaluations of ride comfort. More detailed evaluations must await further advancements in the technology to resolve presently open issues, including the importance of spectral content for noise and motion, the ability of more complex models to account for increased variance, and the validation of models through acquisition of test data appropriate for establishing model accuracy for all types of transports (e.g., fixed-wing commuter, helicopters, and wide-body jets).

Ride Satisfaction Relation

Comfort judgments need to be related to a more value-oriented variable to provide assessment of the influence of ride comfort on traveler acceptance and use of a system. The value-oriented variable chosen was the percentage of passengers satisfied with the ride, that is, the fraction of passengers who, when querried at the conclusion of a flight, said they would be willing to take another flight at least without hesitation. Based on passenger questionnaire data (861 passenger samples) from air carrier surveys, the satisfaction relation shown graphically in figure 4 was established (ref. 25). This relation can be applied to subjective comfort response data to obtain the probability of satis-fying a given percentage of the passengers. Implicit in the output, however, are all the system input variables to the subjective value function as illus-trated in figure 1. Research to date has made no attempt to separately quantify the effects of each input variable; however, such quantification is ultimately needed to trade-off comfort with other system components.

570

Response Integration Relation

During an aircraft flight, a series of unique ride environment events is experienced by the passengers. While the mean comfort rating for each of these events can be established by application of the comfort rating model described, the problem remains concerning the manner in which these "local" comfort ratings (experiences) can be integrated to obtain an overall response for the entire flight. This problem was addressed by employing comfort rating data obtained from the special group of test subjects who rode scheduled airlines. To a high degree of accuracy, the overall comfort ratings of these subjects were found to be related to the mean overall response of the passengers onboard the same aircraft (ref. 26). An approximate relationship was established for weighting the series of local comfort ratings (obtained periodically) of the test subjects into a rating which closely matched their overall trip comfort rating. For a series of local ride events of equal time duration

$$E_1, E_2, E_3, \ldots, E_n$$

the corresponding weighting factors to be applied to the event comfort rating can be expressed as

$$1^{3/4}, 2^{3/4}, 3^{3/4}, \ldots, n^{3/4}$$

This relationship, a 3/4-power weighting function, is assumed appropriate for weighting any series of local mean comfort rating experiences into an expected total trip mean reaction of passengers. This weighting implies that a memory decay occurs (events at the beginning of a flight being less important than events at the end) such that a passenger's overall reaction to the flight is a stronger function of the latter portions of the flight than the beginning. The total trip comfort rating in equation form is

$$C_{trip} = \frac{\sum\limits_{E=1}^{n} E^{3/4} C_E}{\sum\limits_{E=1}^{n} E^{3/4}}$$

TECHNOLOGY APPLICATIONS

The three ride comfort relations described in the previous section when integrated into the analysis method previously outlined provide the predictive method shown in figure 5. This figure gives inputs to the aircraft and to the comfort-rating model identified to date as important. The rating value provided by the comfort-rating model for a given ride situation is shown as input either to the ride satisfaction relation for determining ride event satisfaction or to the event weighting/summing relation for determining total trip comfort and total trip satisfaction. The method shown in figure 5 or selected portions thereof can be used to address a variety of transport aircraft problem situations. Example applications will be presented to illustrate various uses to meet different types of needs.

571

Evaluation of Uprigged Spoiler

One of the simple applications of the technology is in evaluating the ride comfort for a given measured environment within the aircraft. One such application was carried out in evaluating the effects of uprigged spoilers on ride comfort during landing approach. Use of such uprigged spoilers during landings is a promising approach for reducing the magnitude of trailing vortices from large transports and, thereby, reducing hazard of vortex-caused upset to following aircraft (ref. 27).

Since the deployment of spoilers is known to worsen the ride environment in aircraft, an exploratory ride comfort investigation was carried out at the NASA Dryden Flight Research Center by the University of Virginia to evaluate ride effects. Portable equipment for measuring and recording the motion environment was placed onboard the Boeing 747 airplane for one flight of simulated landings at high altitude ($\approx$3000 m) during which uprigged spoilers of various deflections were deployed (fig. 6). The dynamic motion ride environment was measured and typical results are shown in the lower portion of the figure. These results were used as inputs to the C_{mot} equation of the comfort-rating model to provide mean comfort ratings for various amounts of spoiler deflection and for sideslip at a single spoiler deflection. A scale of percent passengers satisfied, obtained from the ride satisfaction relation of figure 4, is also shown in figure 6. The results indicate that use of uprigged spoilers would degrade the number of passengers satisfied with the ride by 10 to 15 percent depending on spoiler deflection. For real landings at much lower altitude, where a higher level of air turbulence can be expected, use of uprigged spoilers could possibly have a somewhat greater adverse effect on ride comfort.

Identification of Key Factor in Complex Maneuver

A combination of ride environment factors, experienced either simultaneously or in close succession, can result in an uncomfortable ride without direct indication of which factor or factors contributed most to discomfort. Such a situation occurred in a research aircraft investigation (ref. 24) by NASA of a curved decelerating descent typical of that which could be employed, using advanced navigation aids, for localizer/glide-slope capture in a relatively short distance. A mean comfort rating of 4.8 (somewhat uncomfortable) was given by test subjects who rode in the aircraft. Use of the comfort-rating model was employed to identify which factor or factors in the maneuver provided the greatest adverse influence on ride rating.

As shown in figure 7, the approach followed was to divide the complex maneuver into simple segments which could be individually analyzed. Generally each segment had only one dominant ride environment factor. For each segment, the maneuver ride input was quantified and the comfort rating for that input was determined by use of the maneuver motion component of the comfort-rating model. Finally the comfort rating was converted to expected ride satisfaction through use of the satisfaction relation. As can be seen from the results of figure 7, the key segment identified was that which involved a 3.2-degree-per-second pitchover of the aircraft in which the predicted ride rating was 5.1 and

572

predicted passenger (PAX) satisfaction was 61 percent. The negative normal acceleration experienced in this pitchover was quite unpleasant to passengers. Deceleration before pitchover, such as was carried out during the turn, rather than after pitchover was a wise choice since it reduced as much as possible the magnitude of the negative normal acceleration.

Derivation of Equicomfort Levels of Environments

The comfort-rating model and ride satisfaction relation can be used not only to evaluate passenger response to a given input environment (as illustrated in the previous example) but also to derive an upper boundary of the magnitude of a ride environment which could be expected to provide a given level of passenger satisfaction. Since a ride environment consists of a combination of various environmental components, information on component combinations is desirable. The present example (fig. 8) considers three environmental components: vertical random motion, transverse random motion, and noise. For many ride event situations, these three components are often the most important factors affecting comfort in transport aircraft.

The approach used was to determine the mean comfort-rating value (from fig. 4) which corresponded to the desired value of percent passengers to be satisfied. The comfort-rating model was then evaluated to provide information for constructing the graphs shown in figure 8. The graphs present levels of environment combinations consistent with obtaining either of two levels of number of passengers satisfied: 70 percent or 90 percent. In applying any such information to an aircraft situation, the user should remember that the levels of both the motion and noise environment generally are significantly higher in the rear portion of transport aircraft than in the forward cabin.

The approach described could be used to generate such relations for any component combination of the comfort-rating model. Such ride comfort relations should prove useful in carrying out cost-benefit trade-offs between alternate approaches for improving the ride comfort of a given aircraft design.

Importance of Wing Loading

Ride comfort technology can be used to provide the designer direct trade-off information on ride comfort effects of varying any particular aircraft parameter which affects the vehicle transfer function. To illustrate, the effects on ride comfort of varying the wing loading of a commuter-type aircraft have been addressed. (See fig. 9.) The ride situation selected was that of a 5670-kilogram (12 500-pound) unswept wing aircraft cruising in straight and level flight and experiencing the atmospheric turbulence inputs found at a 900-m altitude over mountainous terrain. Noise, temperature, and seating space were considered to be satisfactory. The vertical and lateral responses of the aircraft to the probabilistic distribution of atmospheric turbulence were first calculated for a range of wing loading conditions to provide the expected ride environment. The comfort-rating model and ride satisfaction relations were

573

then used to convert the calculated ride environment into a ride satisfaction evaluation expressed in terms of the cumulative probability of achieving a given percent of passengers satisfied with the ride situation.

The cumulative probability curves for four wing loadings are shown in figure 9. At both ends (final few percent) of the probability curves, the satisfaction values and trends should not be considered to be particularly accurate because of limitations in the comfort data analysis and modeling (e.g., linear regression analysis and linear modeling). Over most of the range, however, and including the knee of each of the curves, the probability characteristics should be significant and reasonably valid. In the range of 80 to 90 percent passengers satisfied, very significant improvements are evidenced as wing loading is progressively increased from 972 N/m^2 (about 20.3 lb/ft^2) to 2510 N/m^2 (54.2 lb/ft^2). The trends also indicate that further increase in wing loading would not be overly beneficial.

Prediction of Total Trip Ride Characteristics

Full exercise of the method presented in figure 5 is required to predict total trip ride comfort and passenger satisfaction. Further details are outlined in figure 10 wherein the trip is divided into equal time segments of segment time duration appropriate for addressing each ride environment event. For each event situation, inputs to the aircraft need to be established. Some inputs, such as turbulence, are random in nature and are a function of altitude, geographic features, and time of day. Other events, such as maneuvers, are more controlled in nature but still can have random variations. Inputs therefore need to be described in terms of probabilistic distribution of intensity. With these inputs, the vehicle transfer characteristics, and the ride relations described earlier, a Monte Carlo type approach can be used to calculate the probable ride comfort rating and passenger satisfaction for each segment of the trip. These results can then be weighted through use of the memory decay relation, summed and normalized to provide values for the total trip.

The approach described above was used to calculate the ride characteristics for a commuter airline demonstration project. This project, the Canadian Airtransit STOL Demonstration Program, was considered to be particularly attractive for such study because of

(1) Addition of comfortable seats with generous seating space to an aircraft otherwise considered to have a nonluxury ride

(2) Use of STOL terminal area operations

(3) Opportunity for comparison with U.S. commuter ride experience

(4) Tailoring of trip to enhance business traveler acceptance (high frequency schedule, downtown-to-downtown time saving, and total trip service approach)

574

(5) Trip situation (aircraft configuration, flight operations, type travelers) was considered to be sufficiently different from the model development data-base situations to check model validity

As shown at the top of figure 11, ride environment measurements and passenger ratings of the trip were obtained on 61 flights of the DHC-6-300 aircraft used by Airtransit. The average duration of each flight was 52 minutes. The analytical prediction of ride used 26 2-min event segments (2 climb, 2 turn, 20 straight and level at 1050-m altitude, and 2 descent) and included effects of temperature, noise, and seating, as well as of motions and maneuvers. Take-off and landing ride on the runway was not included. Further description of the Airtransit operations and of the associated ride comfort study is given in reference 28.

Comfort rating results are presented in the lower portion of figure 11 in terms of cumulative probability of achieving given values of comfort based both on prediction and on actual passenger surveys. The predicted probability of achieving a given comfort rating agreed with survey data for the higher rating values and was conservative (predicted a lesser probability) for the lower rating values, with the predicted curve displaced toward the uncomfortable direction a maximum of 0.7 rating point. This degree of agreement is considered to be very good.

Total trip satisfaction results are presented in figure 12 in terms of cumulative probability distribution, based both on predication and actual passenger survey responses. Agreement was fair over the knee of the curve. Also included in figure 12 are calculated results for the Airtransit situation but with two differences typical of a U.S. commuter operation using DHC-6 aircraft: use of conventional 19-passenger seating rather than 11-passenger seating, and use of estimated turbulence conditions associated with cruise at 600-m altitude rather than at 1050 m. The predictions are in very good agreement with passenger survey data from a U.S. commuter operating over a trip length approximating that of Airtransit. The difference in both predicted and survey results for the two operations indicates that the combination of different seating and turbulence factors does have a very significant influence on passenger satisfaction. Comparison of the end-point passenger survey results for the two carriers indicates a surprisingly large difference in probability of satisfying (willing to take another trip having the same ride) all passengers on a trip. The probability was over 60 percent for the Airtransit situation but less than 10 percent for the U.S. commuter. Very likely, the high fraction (93 percent) of the business-trip commuters on the Airtransit flights liked the special operational features incorporated to enhance business traveler acceptance (see item (4) mentioned previously) and they were not as adversely influenced by a less than comfortable ride as predictions would indicate. Better predictive treatment of trip satisfaction must await the development of a good disaggregate demand model in which ride comfort is included as only one of the number of factors (e.g., trip cost, trip time, and schedule frequency) believed to have significant influence.

575

CONCLUDING REMARKS

A brief overview has been given of NASA research in ride comfort and of the resultant technology together with reference to key technical publications. The research has resulted in the collection of a very substantial amount of ride environment and ride comfort data. Three relations, derived from these data, which are considered particularly useful for addressing transport aircraft ride comfort situations, have been described with sufficient quantitative definition for practical application. Five applications of these relations have been presented to illustrate their effectiveness and limitations in addressing various ride problems or situations in aircraft design and system operations.

REFERENCES

1. McKenzie, J. R.; and Brumaghim, S. H.: User Evaluation of Ride Quality Technology Research. NASA CR-2746, 1976.

2. Jacobson, Ira D.; Kuhlthau, A. R.; and Richards, L. G.: Application of Ride Quality Technology To Predict Ride Satisfaction f·r Commuter-Type Aircraft. 1975 Ride Quality Symposium, NASA TM X-3295, DOT-TSC-OST-75-40, 1975, pp. 45-64.

3. Elderkin, Charles Edwin: Experimental Investigation of the Turbulence Structure in the Lower Atmosphere. Ph. D. Thesis, Univ. of Washington, 1966.

4. Gunter, D. E.; Jones, G. W.; Jones, J. W.; and Monson, R. R.: Low Altitude Atmospheric Turbulence LO-LOCAT Phases I & II. ASD-TR-69-12, U.S. Air Force, Feb. 1969.

5. Etkin, Bernard: Dynamics of Flight. John Wiley & Sons, Inc., c.1959.

6. Stone, Ralph W., Jr.: Ride-Quality Overview. Symposium on Vehicle Ride Quality, NASA TM X-2620, 1972, pp. 1-22.

7. Roth, Emanuel M.; and Chambers, A. N.: Compendium of Human Responses to the Aerospace Environment. Volume II. NASA CR-1205 (II), Section 8, 1968.

8. Guide for the Evaluation of Human Exposure to Whole-Body Vibration. ISO 2631-1974 (E), Int. Organ. Stand., July 1, 1974.

9. Jacobson, Ira D.: Environmental Criteria for Human Comfort — A Study of the Related Literature. NASA CR-132424, 1974.

10. Gruesbeck, Marta G.; and Sullivan, Daniel F.: Aircraft Motion and Passenger Comfort Data From Scheduled Commercial Airline Flights. NASA CR-2612, 1976.

11. Jacobson, I. D.; and Kuhlthau, A. R.: Flight Research Experiments on Ride Quality. Tech. Rep. 403907 (NASA Grant No. 47-005-202), Univ. of Virginia, Oct. 1975. (Available as NASA CR-145984.)

12. Schoonover, W. Elliott, Jr.: Aircraft Motion and Passenger Response Data From TIFS Ride Quality Flight Experiments. NASA TM X-73944, 1976.

13. Stone, Ralph W., Jr.: Ride Quality — An Exploratory Simulator Study and Criteria Development. NASA TM X-71922, 1974.

14. Dempsey, Thomas K.: A Model and Predictive Scale of Passenger Ride Discomfort. NASA TM X-72623, 1974.

15. Stone, Ralph W., Jr.: Human Comfort Response to Random Motions With a Dominant Longitudinal Motion. NASA TM X-72746, 1975.

16. Leatherwood, Jack D.: Vibrations Transmitted to Human Subjects Through Passenger Seats and Considerations of Passenger Comfort. NASA TN D-7929, 1975.

17. Dempsey, Thomas K.; and Leatherwood, Jack D.: Experimental Studies for Determining Human Discomfort Response to Vertical Sinusoidal Vibration. NASA TN D-8041, 1975.

18. Dempsey, Thomas K.; Leatherwood, Jack D.; and Drezek, Arlene B.: Passenger Ride Quality Within a Noise and Vibration Environment. NASA TM X-72841, 1976.

19. Leatherwood, Jack D.; and Dempsey, Thomas K.: A Model for Prediction of Ride Quality in a Multifactor Environment. NASA TM X-72842, 1976.

20. Dempsey, Thomas K.; and Leatherwood, Jack D.: Vibration Ride Comfort Criteria. Presented at the Sixth Congress of the International Ergonomics Association, July 1976.

21. Kuhlthau, A. R.; and Jacobson, I. D.: Analysis of Passenger Acceptance of Commercial Flights Having Characteristics Similar to STOL. Canadian Aeronaut. & Space J., vol. 19, no. 8, Oct. 1973, pp. 405-409 and M-1 — M-6.

22. Symposium on Vehicle Ride Quality. NASA TM X-2620, 1972.

23. 1975 Ride Quality Symposium. NASA TM X-3295, DOT-TSC-OST-75-40, 1975.

24. Schoonover, Ward Elliott, Jr.: Passenger Comfort During Terminal-Area Flight Maneuvers. M.S. Thesis, George Washington Univ., 1976.

25. Richards, L. G.; Kuhlthau, A. R.; and Jacobson, I. D.: Passenger Ride Quality Determined From Commercial Airline Flights. 1975 Ride Quality Symposium, NASA TM X-3295, DOT-TSC-OST-75-40, 1975, pp. 409-436.

26. Richards, Larry G.: Ride Quality Evaluation I: Questionnaire Studies of Airline Passenger Comfort. Ergonomics, 1975, vol. 18, no. 2, Mar. 1975, pp. 129-150.

27. Croom, Delwin R.: Low-Speed Wind Tunnel Investigation of Various Segments of Flight Spoilers as Trailing-Vortex-Alleviation Devices on a Transport Aircraft Model. NASA TN D-8162, 1976.

28. Jacobson, Ira D.: Construction and Verification of a Model of Passenger Response to STOL Aircraft Characteristics. [Preprint] 760525, Soc. Automot. Eng., May 1976.

578
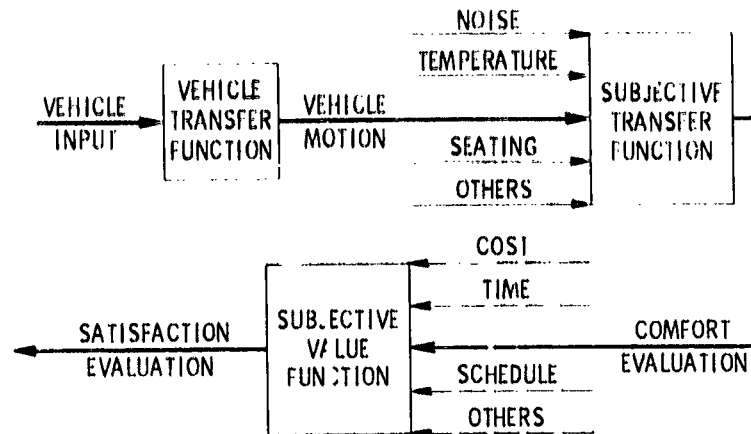
Figure 1.- Analysis method employed to assess ride comfort.
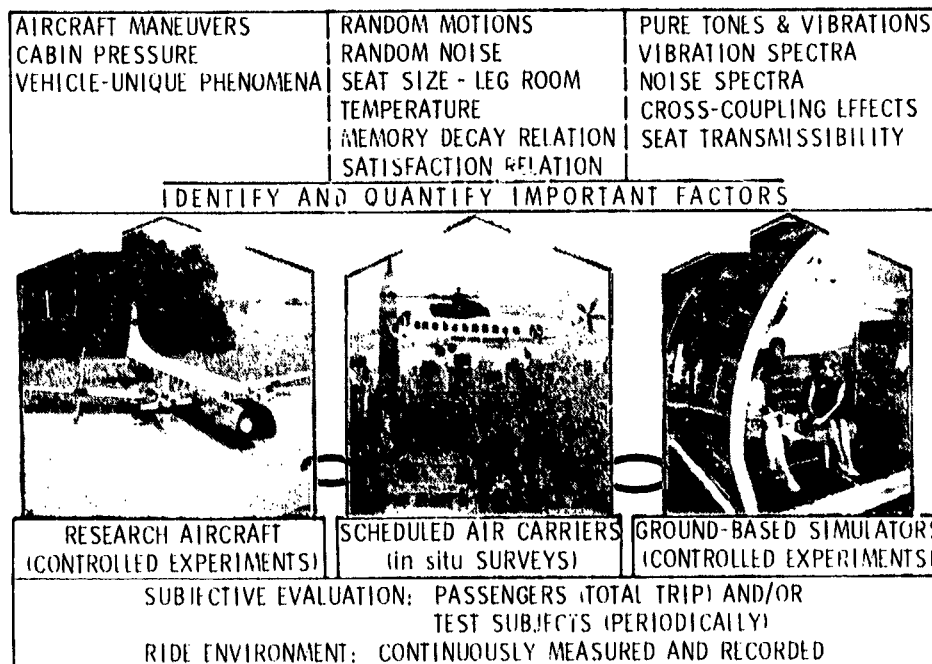
Figure 2.- NASA ride comfort research program.
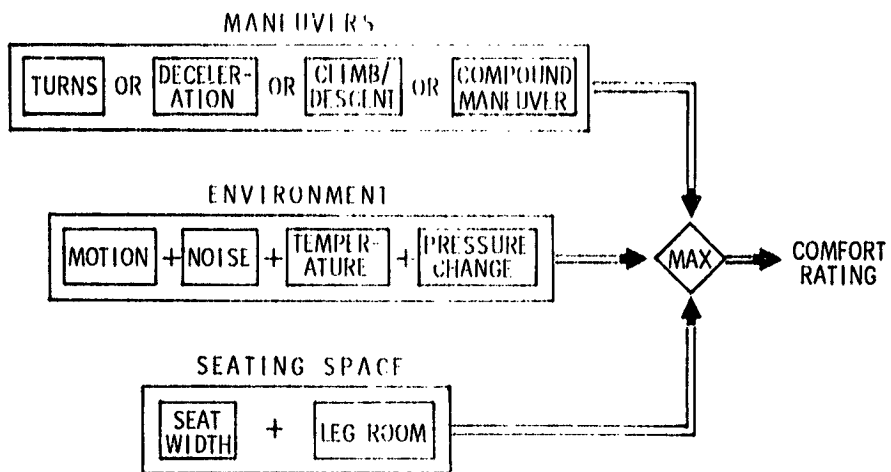
Figure 3.- Block diagram of comfort rating model for use as the subjective transfer function.
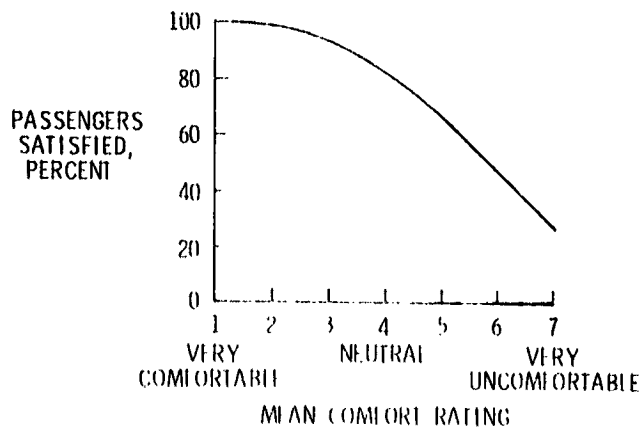
Figure 4.- Ride satisfaction relation.
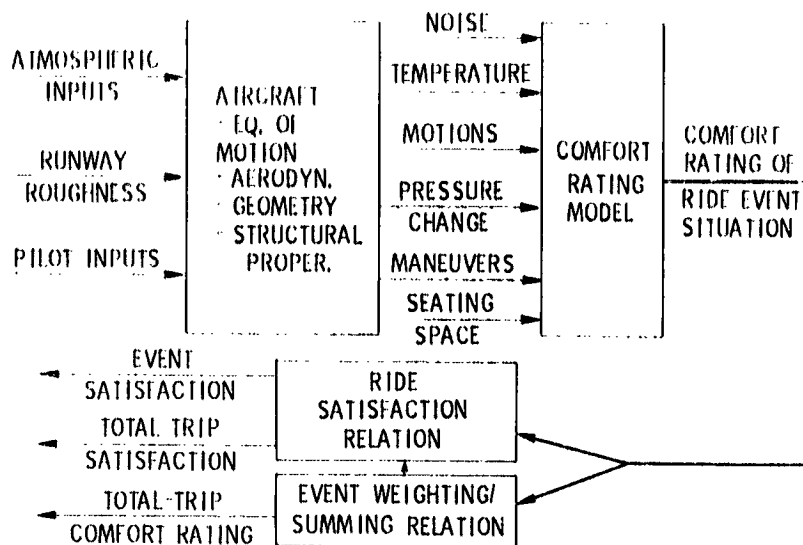
Figure 5.- Predictive method for ride comfort and passenger satisfaction as developed to date.
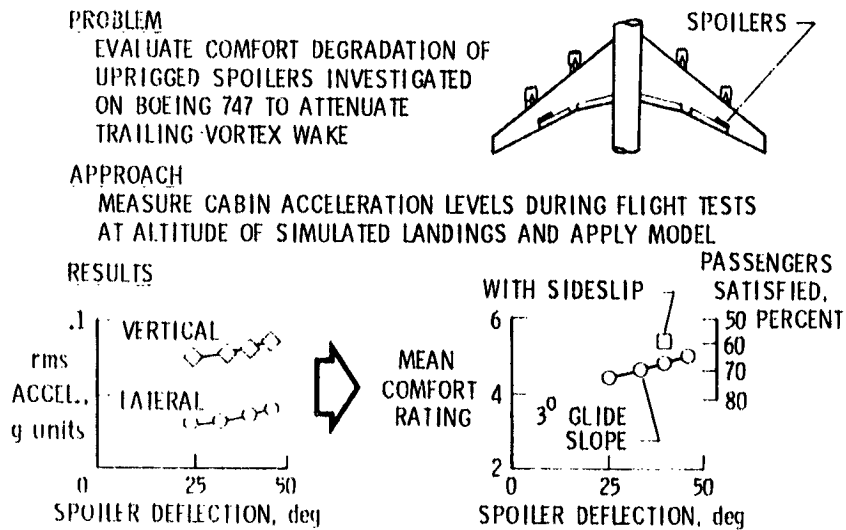
Figure 6.- Ride evaluation of aircraft using uprigged spoilers during simulated landings.

PROBLEM
  IDENTIFY KEY FACTOR(S) INFLUENCING THE "SOMEWHAT UNCOMFORTABLE"
    RATING GIVEN BY TEST SUBJECTS

APPROACH

	STRAIGHT AND LEVEL	TURN ENTRY	DECEL. IN 20^0 TURN	TURN EXIT	PITCH-OVER	STEADY DESCENT
• DIVIDE COMPLEX MANEUVER INTO SIMPLE SEGMENTS	STRAIGHT AND LEVEL	TURN ENTRY	DECEL. IN 20^0 TURN	TURN EXIT	PITCH-OVER	STEADY DESCENT
• QUANTIFY MANEUVER RIDE INPUT	NONE	8^0/sec ROLL	0.08 g LONG.	10^0/sec ROLL	-3.2^0/sec PITCH	-5^0 PITCH/ 550 m/min
• APPLY COMFORT RATING MODEL	2.0	2.4	2.0	2.6	5.1	3.2/4.3
• APPLY SATISFACTION RELATION (% PAX)	98	96	98	94	61 ↑ KEY FACTOR	89/76

Figure 7.- Ride evaluation of a complex maneuver.
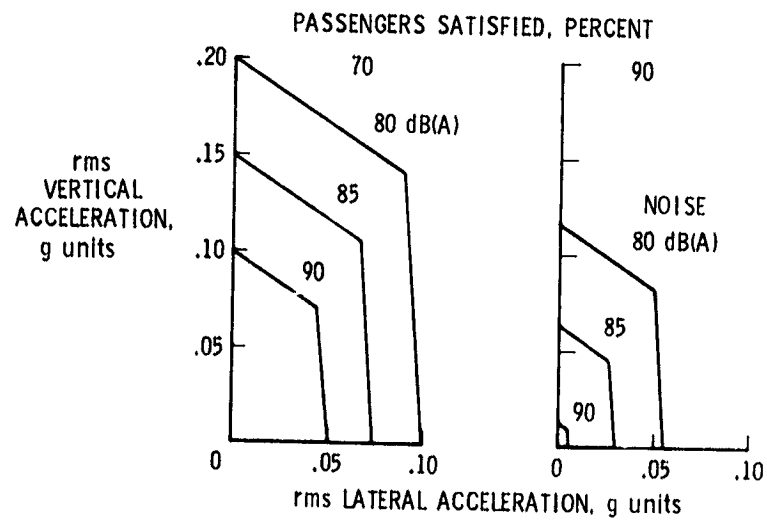
Figure 8.- Equicomfort combinations of motion and noise.
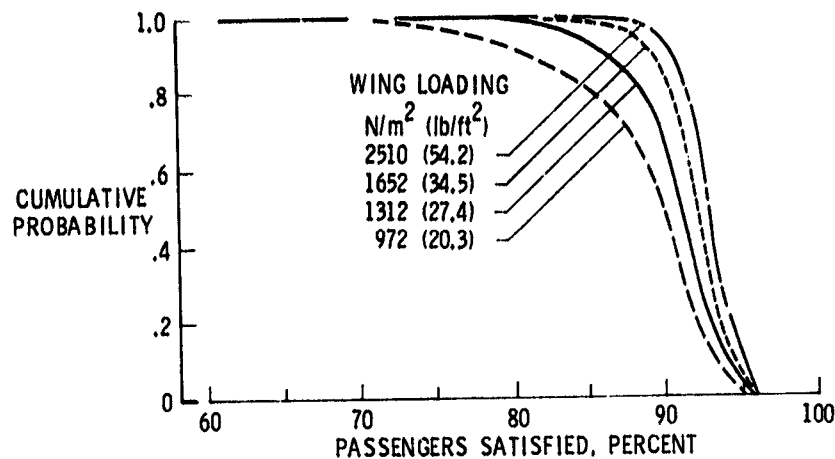
Figure 9.- Effect of variation of wing loading on ride
satisfaction of commuter-type transport aircraft.
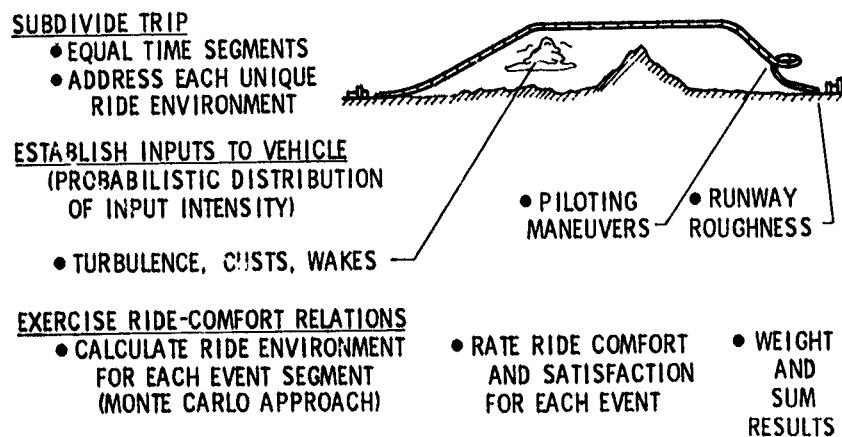
Figure 10.- Approach for total trip prediction of
ride comfort and satisfaction.

- STOL OPERATIONS OF MODIFIED
  COMMUTER AIRCRAFT BETWEEN
  OTTAWA AND MONTREAL

- RIDE ENVIRONMENT MEASURED
  AND PASSENGER TRIP-RATINGS
  OBTAINED ON 61 FLIGHTS

- ANALYTICAL PREDICTION BASED ON
  26 2-MINUTE EVENT SEGMENTS
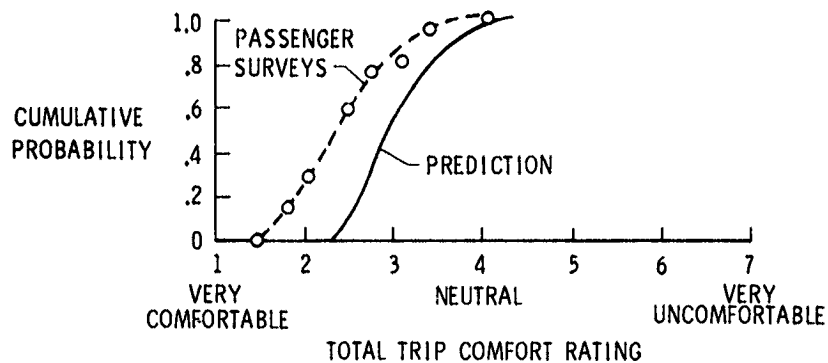
Figure 11.- Total trip ride comfort for STOL
demonstrator transport.
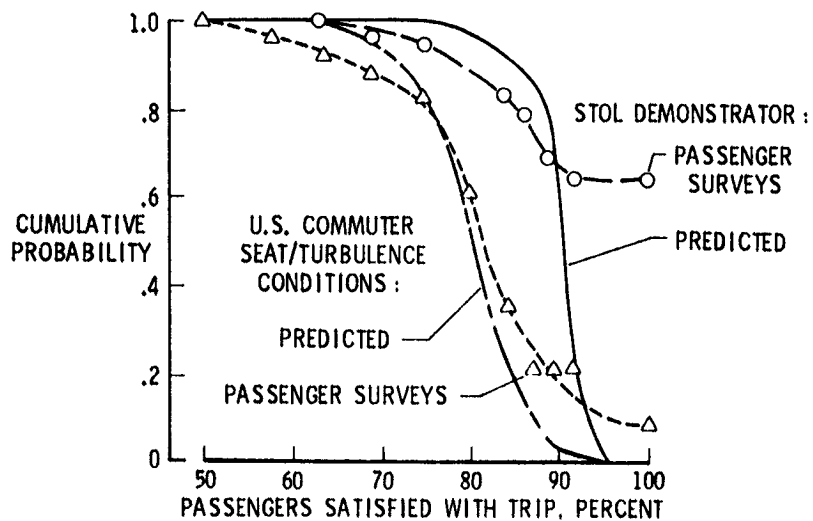
Figure 12.- Total trip satisfaction for STOL
demonstrator transport.

RETROSPECTIVE STUDIES OF OPERATING PROBLEMS IN AIR TRANSPORT

C. E. Billings, J. K. Lauber, G. E. Cooper,
and H. P. Ruffell-Smith
NASA Ames Research Center

SUMMARY

Studies of human factors in aircraft accidents provide a substantial yield of human errors which contributed to those accidents. It is probable, however, that accidents are the least common of the outcomes which can follow a human error in the aviation system. An epidemiological model for the study of human errors in aviation is presented. In this approach, retrospective data are used as the basis for formulation of hypotheses as to system factors which may have contributed to such errors. Prospective experimental studies of aviation operations are also required in order to prove or disprove the hypotheses, and to evaluate the effectiveness of intervention techniques designed to solve operational problems in the aviation system.

INTRODUCTION

This paper is designed to accomplish two objectives. Its first intent is to present human error in aviation in terms of an analogy which may be useful in attacking the problem of human errors and their effects upon aviation safety. Its second purpose is to present a systematic methodology for the attack upon this omnipresent problem.

BACKGROUND

Studies of aviation safety over the years have nearly all had certain common attributes. Nearly all such studies have focused upon aircraft accidents. Nearly all have been essentially descriptive, though the recent study by Kowalsky et al. at the Lovelace Foundation utilized sophisticated analytic techniques in an attempt to elucidate factors associated with the sample of accidents under study. Most of these studies, like most accident investigations, have had to rely heavily upon inference to determine what went on prior to the accident itself.

There have been many studies of accidents in other forms of transportation and in industry. They have given rise to various theories about the persons nd circumstances in which accidents are especially likely to occur, but none, to our knowledge, has withstood the test of time. Is it possible that attempts to improve accident statistics have not been more successful because attention has been focused upon the wrong phenomenon, or upon only one facet of the overall problem?

Since the introduction of turbojet aircraft into civil transport, between 60 and 70% of all fatal accidents in airline transport have been attributed in whole or part to human error. The figures for general aviation are substantially higher. The problem of human error, then, is clearly the most serious one facing the aviation industry.

Yet while case studies of aircraft accidents are a convenient and highly productive method of collecting instances of human error in aviation, it is less generally acknowledged that an accident is only one — and the least common — of the outcomes which can result from a human error in the aviation system. A human error may cause a perturbation in the aviation system, but under circumstances which allow time and space for recovery. More frequently still, the error may occur, be detected, diagnosed and corrected or compensated for without a significant perturbation in the system. There is an analog to this in clinical medicine, in which symptoms and sometimes signs of illness may occur. They may progress to a fatal outcome; they may herald a significant illness from which recovery occurs, or they may appear, be compensated for by the physiological reserves of the body and disappear without a significant disturbance of overall function.
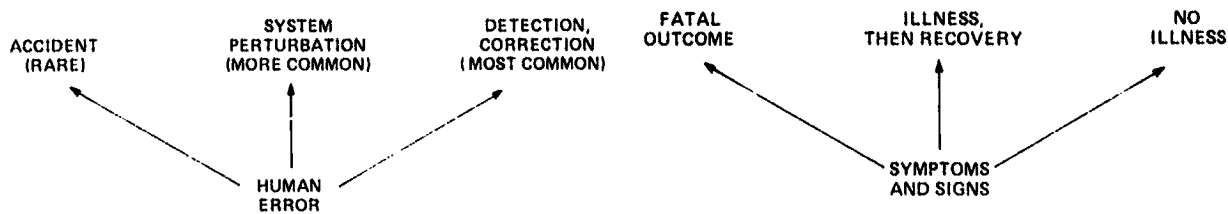
If one is to understand the problem of human error, it would seem necessary to examine cases in which recovery occurred, as well as those which had a fatal outcome. What factors differentiate these classes of errors? Or are they but one class occurring under different sets of circumstances? Or to different sorts of people who respond differently?
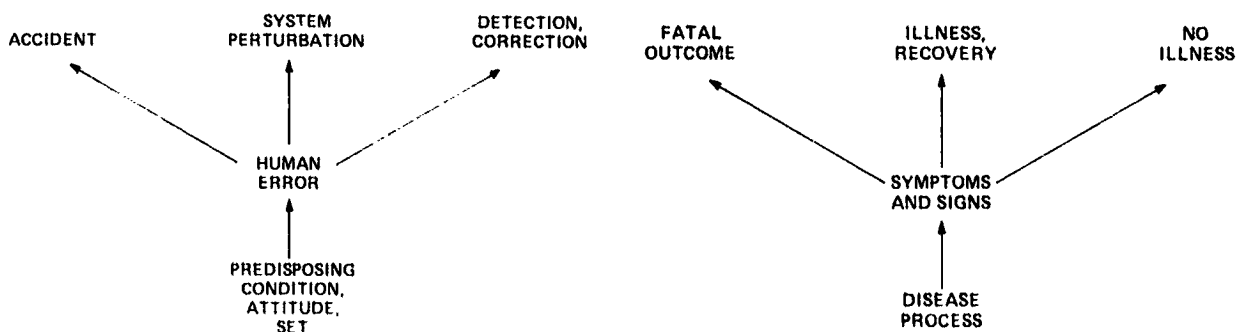
More important still is the question of what a human error is. Is it a spontaneous phenomenon — an intermittent disorder which affects people at random? Or can its occurrence be predicted? If so, by what criteria? Or is an error but a manifestation — a symptom — of some underlying disorder in the human mind or body? If so, can we gain an insight into the disease, or diseases, which give rise to these ubiquitous symptoms?

586

OUTCOME   ACCIDENT   SYSTEM PERTURBATION   CORRECTION   FATAL OUTCOME   ILLNESS RECOVERY   NO ILLNESS   OUTCOME

MANIFESTATIONS   HUMAN ERROR   SYMPTOMS AND SIGNS   MANIFESTATIONS

DISORDER   PREDISPOSING CONDITION, ATTITUDE, MENTAL SET   DISEASE PROCESS   DISORDER
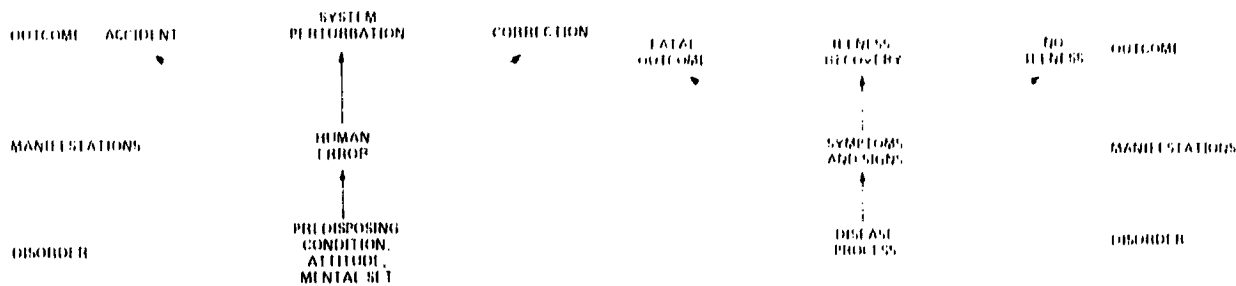
It is instructive to consider human error as a manifestation, or sympton, occurring in the presence of a variety of human conditions, which by virtue of its occurrence produces at least a potential perturbation of the man-machine system of which the human is a part. That perturbation may lead to any of a variety of outcomes. Viewed in this manner, it becomes possible to examine the human attributes and attitudes which give rise to errors. More important, it becomes possible to look beyond the human to the environment in which he is operating, in order to discern factors which may make it more likely that he will err, or less likely that he will recover given an error.

ACCIDENT   SYSTEM PERTURBATION   CORRECTION   FATAL OUTCOME   ILLNESS, RECOVERY   NO SIGNIFICANT ILLNESS

HUMAN ERROR   SYMPTOMS AND SIGNS

PREDISPOSING CONDITION, ATTITUDE, MENTAL SET   DISEASE PROCESS

OPERATIONAL ENVIRONMENT   PHYSICAL ENVIRONMENT   SOCIAL ENVIRONMENT   PHYSICAL ENVIRONMENT
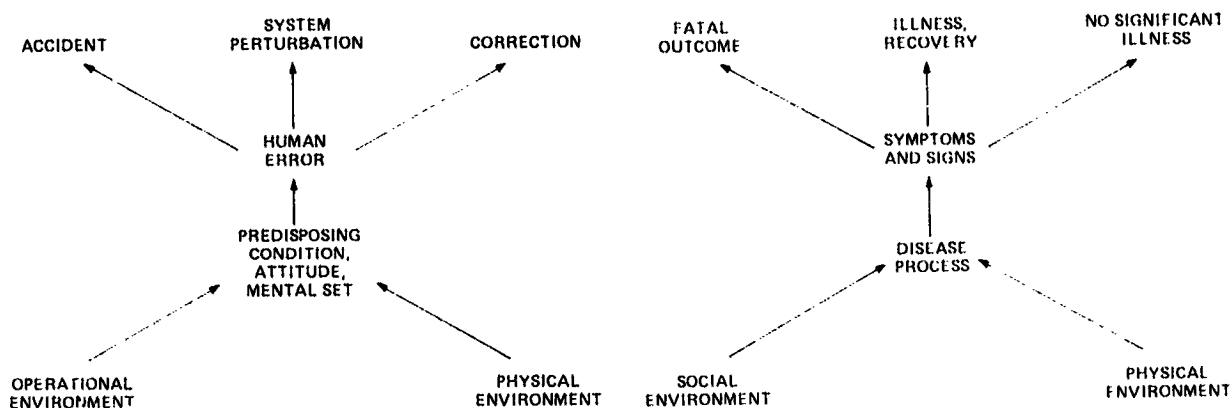
There is a powerful methodological tool for dealing with this sort of problem. Epidemiology is conventionally thought of as a tool for dealing with point-source epidemics of disease, but it is much more. Epidemiological methods have been used successfully for over a century to examine factors in the environment which contribute to a great variety of problems which beset man and animals; present concerns under concerted attack using these methods include the problems of heart disease, cancer, alcoholism and drug addiction, among non-infectious illnesses. Using epidemiological methods, it is possible to examine symptoms in terms of the diseases which produce them, and to study diseases in terms of the factors which determine their incidence, prevalence and often their outcome.

METHODOLOGY

When one is investigating a fatal aircraft accident, it is often necessary to infer the behavior which preceded it. It is more difficult still to infer with any accuracy the attitudes or attributes which may have determined

587

OCCURRENCES		ACCIDENTS
HISTORY	OUTCOME	OBSERVATION
	↑	
OBSERVATION	ERROR	(INFERENCE)
	↑	
HISTORY	PREDISPOSING CONDITIONS	(INFERENCE)
	↑	
(INFERENCE)	ENVIRONMENTAL FACTORS	(INFERENCE)
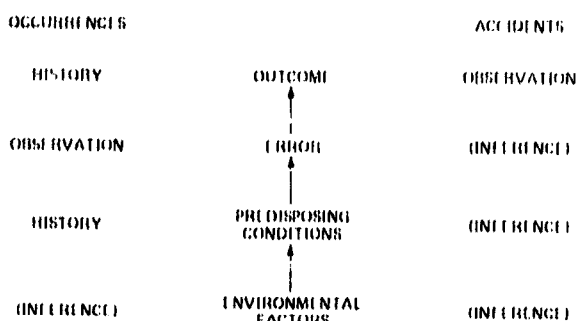
or contributed to the behavior which presumably caused the accident. Even with cockpit voice recorders, helpful though they have been, the retrospective view of the cockpit is at best clouded and fragmentary. It must also be pointed out that hindsight is not necessarily better than foresight. They are fundamentally different processes. The occurrence of a certain outcome following the demonstration of a particular phenomenon does not necessarily indicate that the outcome was causally related to the phenomenon, tempting as it may be to draw that conclusion.

It is possible to minimize bias due to this sort of reasoning by examining errors which did not lead to fatal accidents, though the possibility exists that the errors are of different classes, and therefore, not comparable. One very effective way to do this is by direct contact with the pilots and air traffic controllers who have committed the errors. While results with this method are not free of bias, injected either by the reporter or the interviewer, it is possible under the right circumstances to determine fairly precisely what occurred, how it occurred, and sometimes why it occurred. It is usually possible to gain an appreciation of the environment in which the error took place. Sometimes, though by no means always, one can gain an understanding of the psychosocial setting and background of the occurrence.

The NASA Aviation Safety Reporting System, and the flight crew interview studies which preceded it, are attempts to collect a large and comprehensive sample of occurrences in the aviation system, with enough detail about how and why they happened to permit reasonable inferences to be drawn about system factors associated with such occurrences. This voluntary, confidential reporting system was implemented in April, 1976. The System is designed to collect, analyze and disseminate information regarding potential hazards in the aviation system so that appropriate action can be taken to correct problems and thus prevent aircraft accidents. In its first six months of operation, the Aviation Safety Reporting System has received over 2900 reports describing potential threats to aviation safety.

Preliminary analysis of these reports indicates that a considerable fraction of them describe human errors, often in great detail. It has been learned that those who live and work in the aviation system will discuss mistakes they have made, often in exhaustive depth. There is great willingness to examine and analyze the possible reasons for these mistakes. It is also clear that "trivial" errors, given enough of them, may have catastrophic outcomes; study of accidents suggests that no type of human error in aviation should be considered too trivial for detailed study.

Using these techniques, it can be inferred that certain problems in the aviation environment are commonly associated with human errors in aviation operations. Problems in the transfer of information to those responsible

588

for tactical decision-making, as an instance, appear in nearly 50 percent of the human error incidents examined in detail to date. This, in turn, has led to questions about the types of information which are necessary for efficient operations, the ways in which such information can best be made available to those who need it, and the best ways to present it when it is called for.

But inference is not enough, and historical data, however provocative, proves only that an association exists between a factor and a manifestation. It remains to be proven whether that factor is causally, or non-causally, related to the phenomenon under study. Especially in a very complex man-machine system such as the aviation system, where many factors are inter-dependent and therefore correlated, it is necessary to take a rigorous approach toward the question of cause and effect, for manipulation of the wrong variable in search of a solution is expensive and may cause more problems than it solves. There is evidence that this has occurred in the area of alerting and warning systems.

It is necessary to construct a rigorous set of hypotheses and to design experiments with great care if one is to be able to sort out the various factors which may have produced or contributed to a particular unwanted effect in the aviation system. Even then, it may be difficult to partition out the variance associated with uncontrolled variables in the complex environment of aviation

OBSERVATION		OUTCOME
↓		↓
DESCRIPTION		ERROR
↓		↓
ANALYSIS	← INTERVENTION →	PREDISPOSING CONDITIONS
↓		↓
HYPOTHESIS ←		
	PROOF	ENVIRONMENTAL FACTORS
EXPERIMENT		

operations. It has become clear, however, that such experiments are absolutely necessary, that they can be performed in a setting which has face validity, and that they can contribute measurably to our understanding of the root causes of human errors in the aviation system. The report which follows (ref. 1) describes a first effort to examine the question of information transfer in the airline cockpit. It illustrates the concepts, techniques, and some of the problems involved in such epidemiological research.
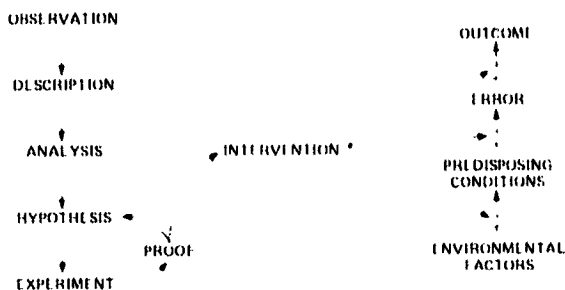
RÉSUMÉ

To summarize, then: several assumptions have been made in order to try to understand more clearly the problem of human error in aviation operations. It has been assumed, first, that errors do not "just happen." They are rather manifestations of the human condition, attitude or mental set at a particular time. That condition is in turn the result of a considerable number of internal and external, or environmental, factors.

ACCIDENT	SYSTEM PERTURBATION	CORRECTION
↘	↑	↗
	HUMAN ERROR	
	↑	
	PREDISPOSING CONDITION ATTITUDE MENTAL SET	
OPERATIONAL ENVIRONMENT		PHYSICAL ENVIRONMENT
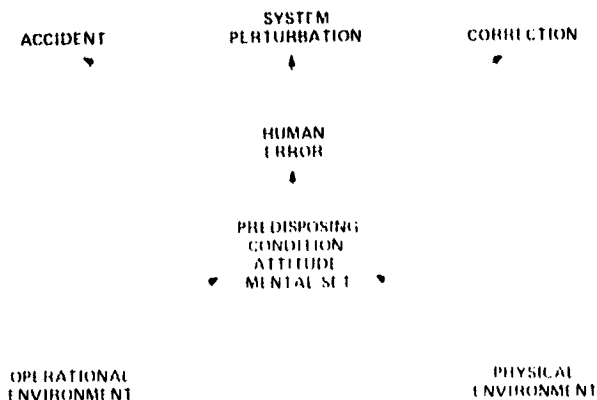
It has been assumed further that the best, albeit an imperfect, source of information about the factors contributing to human error is the person who committed the error. We are aware that the reporter may bias his report, but we know of no more authentic source.

We have assumed that persons in the aviation system who volunteer information in circumstances which do not involve personal risk do so for fundamentally altruistic motives. They will therefore attempt to be truthful in their reporting. We are concerned about certain facets of the Aviation Safety Reporting System which require reporting as a prerequisite to avoidance of disciplinary action, for we have been unable thus far to evaluate possible bias due to this factor. We hope in the near future to conduct a study which may shed some light on this problem.

We have assumed that the population of errors from which our sample is drawn contains also the errors which under specific circumstances can lead to aircraft accidents. While there is suggestive evidence that this assumption is justified, there may be specific types of errors which we are not sampling and our conclusions may be biased by the nonrepresentativeness of the population and, therefore, of our sample. The study to which we referred will examine this question as well.

Finally, we have assumed that the concepts and methods of classical epidemiology are appropriate tools for this research. We have assumed that if we choose appropriate hypotheses to explain the phenomena we are examining and inject the appropriate factors in a valid simulated operational setting, we shall be able to observe the phenomena of interest. In at least one experiment thus far, this appears to have been true. If we can now design an appropriate and specific intervention technique to neutralize the hypothesized effect of these factors, repeat the experiment and observe a change in the effect, we believe we shall have reasonably firm evidence that the factor causes the effect, together with some data regarding ways of mitigating the effect 'n aviation operations.

This is the task we have set ourselves: to attempt, by understanding the factors which cause human errors, to remove or ameliorate the unwanted effects of those factors and thus, hopefully, to make it less likely that serious errors will be committed. We also believe that an understanding of the causes of human error can enable us to design better and more rational methods of coping with the errors when they do occur, in order to improve the likelihood of a uniformly successful outcome. There are many potential points of attack upon a disease once the genesis and course of that disease are understood. Without such understanding, it is nearly impossible to provide more than symptomatic relief from its effects.

REFERENCE

1. Lauber, John K.; Billings, Charles E.; Stevenson, James L.; Ruffell-Smith, H. P.; and Cooper, George E.: Simulation Studies of Air Transport Operational Problems. Aircraft Safety and Operating Problems, NASA SP-416, 1976. (Paper no. 34 of this compilation.)

SIMULATION STUDIES OF AIR TRANSPORT OPERATIONAL PROBLEMS

John K. Lauber, Charles E. Billings, James E. Stevenson,
H. P. Ruffell-Smith, and George E. Cooper
NASA Ames Research Center

SUMMARY

An experimental evaluation of the monitored approach procedure for conducting low visibility instrument approaches is described. Four airline crews each flew 16 approaches using the monitored procedure and 16 using a modified "standard" procedure in a DC-10 simulator under various conditions of visibility, wind shear and turbulence, and radar vectoring scenarios.

In terms of system measures of aircrew performance, no major differences were found. Pilot opinion data indicate that there are some desirable characteristics of the monitored procedure, particularly with reference to the increased role of the flight engineer in conducting low visibility approaches. Rationale for developing approach procedures is discussed.

INTRODUCTION

The research described in this paper grew out of some of the concerns expressed by airline pilots during the preliminary pilot interview studies mentioned in the previous paper (ref. 1). Specifically, many pilots felt that the approach procedures they were using were less than optimal with regard to two major items: (a) the integration of all three cockpit crewmembers into the approach procedure; and (b) the callouts required of the various crewmembers during an approach.

The critical demands placed upon pilots during the last one or two hundred feet of an approach are well known. Many accidents have occurred during this critical phase of flight, and in many of these it appears that one of the major contributing factors was the inadequate or inappropriate design of approach procedures, including crew integration and callouts. In many cases sufficient information to prevent the impending disaster was present within the cockpit, yet the crew failed to utilize this information. Once the flying pilot has changed to flight by visual reference, deviations from the desired flight path might not be readily discernible from outside visual cues. These deviations will, however, invariably show up on the cockpit instrumentation; increased sink rate, deviations below glide slope, or low airspeed — all so-called killer items — will be displayed inside the cockpit. It is necessary that this information be transferred to the flying pilot if an accident is to be prevented.

There are two ways of performing this task: (a) the physical environment can be modified, making the information available in the pilot's visual field

via the use of VASI or a Head-Up display, for example; or, (b) the operational environment can be modified by using autoland or by the adoption of new callouts and monitoring procedures.

Figure 1 illustrates the relationship between the present experiment and the epidemiological model described in the previous paper by Billings et al. (ref. 1). The primary interest was in the effects of manipulation of the operational environment, specifically low visibility approach procedures, upon aircrew and aircraft performance.

Although approach procedures used by airlines vary widely, it is possible to discern two basic philosophies which have been used to structure these procedures. One of these, the standard procedure, is basically this: one pilot is responsible for flying the approach and landing, or missed approach if that should be necessary, and the other crewmembers are assigned monitoring and callout duties. The decision to land or to go around is made by the flying pilot on the basis of his assessment of the visual situation following the transition from heads-down flying. Variations of this basic procedure are used by virtually all U.S. air carriers.

One alternative to the standard procedure is one called the monitored approach by several of the foreign carriers who have developed these techniques. Basically, using this procedure, one pilot, usually the copilot, is responsible for flying the heads-down portion of the approach; the other pilot is responsible for monitoring this portion of the approach and is the individual who decides whether the outside visual cues are sufficient for the landing. If they are, this pilot, who is usually the captain, takes physical control of the aircraft and proceeds with the landing. At the transition, the copilot assumes responsibility for monitoring the remainder of the approach and landing, remaining head down until sometime during the landing roll.

Intuitively, this monitored approach procedure has some appealing features, particularly in the way the transition from instrument reference to visual reference flight is made. The captain is given sufficient time to assess the visual situation and reach a decision and can do so without the additional burden of flying the aircraft. Furthermore, more emphasis is placed upon continuous monitoring of the critical final portion of the approach and landing. However, there are also some characteristics of this procedure which appear to be less desirable, particularly those having to do with the physical transfer of aircraft control at very low altitudes.

In attempting to resolve these and other issues, it soon became apparent that there is little, if any, objective data pertaining to the relative effectiveness of these two basic philosophies for conducting low visibility approaches. On the basis of the accumulated operational experience of those carriers who have used the monitored procedure, it can be concluded that the idea has considerable merit. However, because of the fundamental importance of approach procedures for the safety of aircraft operations, decisions to utilize this approach, or any other for that matter, should be based on more

rigorous, objective performance data obtained from line pilots operating under a wide variety of realistic conditions.

In summary, the major objective of the experiment was to compare aircraft and aircrew performance during low visibility approaches using either the standard or the monitored approach procedure. A secondary objective was to develop full mission simulation research techniques for use in other research.

METHOD

Development of Approach Procedures

Because the carrier who participated in the study used a variant of the standard procedure, it was necessary to develop a modified standard procedure in order to control for the possible effects of crew familiarity with the standard procedure. To accomplish this, the approach procedures and callouts used by another U.S. carrier were used. This set of procedures was sufficiently different from those used by the participating carrier, that the likelihood that familiarity influenced the results of this study is minimal. This set of procedures is summarized in figure 2.

Two major criteria were used during the development of the monitored procedure which was used in this experiment: (a) the flight engineer should be fully and completely integrated into the approach procedure; and, (b) there should always be a clear-cut division of responsibilities — pilot flying, primary monitor, and backup monitor — as shown in figure 3. In other words, at any given point during an approach, each crewmember should be assigned one of these three functions, and whenever there is a change in one crewmember's function, there should be a corresponding, compensatory change in another crewmember's function. Thus, for example, when the flight engineer calls out, "Approaching minimums," the captain verbally acknowledges this callout and changes to outside visual reference. Simultaneously, the flight engineer assumes the primary monitoring duties inside the cockpit, and the first officer continues to function as the flying pilot. When the captain announces, "Land," the first officer now assumes primary monitor duties, the flight engineer resumes his role of back-up monitor, and of course, the captain becomes the pilot flying.

Callouts were constructed with regard to the three major functions which callouts can perform: (a) they serve to transmit information about the state of the aircraft; (b) they serve to check for subtle pilot incapacitation — if a pilot misses a callout, or fails to acknowledge one, the other pilots should check to make sure the quiet one is still with them; and finally, (c) callouts can be used to help enforce heads-down discipline. If we want to maximize the probability that a pilot will remain on the instruments during the last stages of an approach, we can assign him specific callout duties during that period of time.

Missed approaches were automatic; if the captain had not taken control of the aircraft when it reached the missed approach point, the first officer initiated the missed approach procedure, and the captain came back inside the cockpit to resume the role of primary monitor. If it became necessary to go around after the captain had decided to land, the captain called out, "Missed approach," and the first officer resumed control of the aircraft and announced, "I have the airplane." This procedure was chosen because it was reasoned that the first officer, being continuously heads down, was in the best position to assume rapid and precise control of the aircraft.

Figure 4 shows the work sheet which was provided to the flight engineer when using the monitored procedure. Before each approach was begun, the flight engineer was given an approach plate by the pilot so that he could determine the information shown on the worksheet. This information was used subsequently by the flight engineer for cross checking and for callouts. In addition, the flight engineer was assigned very specific monitoring duties and guidelines for calling out deviations from the desired flight profile.

Subjects

Because the study involved training airline pilot subjects on the use of an approach procedure which was not the approved procedure used by their company, training pilots, rather than line pilots, were used for this experiment. It was felt unwise to risk the possibility of training someone to the point where, if he were by chance to fly an actual low visibility approach shortly after his participation in this study, he might revert to the experimental procedures rather than use the approved procedure.

Eight current instructor pilots and four current flight engineer instructors served as subjects for this experiment. These instructors were assigned to one of four crews. The flight experience of each of the subject pilots is summarized in table I.

Simulation Facilities

The simulator used for this experiment was a DC-10 simulator equipped with a six-degree-of-freedom motion platform and a TV, model-terrain-board visual system. Modifications were made to the simulation software to allow control of the experimental conditions from the instructor's CRT display and control panel located in the cockpit, and to allow real-time recording of simulator data on digital magnetic tape. Additionally, provisions were made for recording communications, cockpit voice, and observer comments. Experimental sessions, each four hours long, were inte[ted into the normal simulator training schedule.

Simulator Scenarios and Experimental Design

Since one of the primary areas of concern with the monitored procedure centers around the question of transfer of control of the aircraft at low

594

altitudes, only hand-flown approaches were used. Autopilot use and its interaction with approach procedures is a separate question which was not addressed in this study.

Possible interactions between the kind of approach and the approach procedures were also of interest. Therefore both non-directional beacon (NDB) and instrument landing system (ILS) approaches were flown. All 'S approaches were flown using the Flight Director and manual throttles. All NL approaches were flown using raw data only.

Each crew flew a total of 32 approaches during the data collection phase of the experiment, sixteen using the monitored approach procedure, and sixteen using the standard procedure.

Since one of the characteristics of a good set of approach procedures is to better enable crews to cope with difficult operational situations, the effects of a variable called "Stress and Workload" on crew performance were evaluated. To accomplish this, radar vectoring techniques, wind shear, and turbulence were used to generate high and low stress and workload conditions. The low workload condition involved no turbulence, no wind shear, a five-knot crosswind from either the right or left, and radar vectoring service that was nearly ideal -- timely, accurate, and such that the aircraft would intercept the final approach course well outside the final approach fix at the proper altitude and airspeed. In contrast, the high workload condition involved a forty-knot head or tail wind which sheared to a direct crosswind of ten knots by 61 m (200 ft) above ground level (AGL), some turbulence, and radar vectoring of the kind too often encountered in the real world — late descent clearances, late turn-ons, and delayed speed reductions. These vectoring scenarios were chosen such that, if flown precisely, the aircraft would intercept the glide slope and final approach course right at the final approach fix (FAF) for the ILS approaches, and 1.6 km (1 mi) outside the final approach fix for the NDB approaches. These were difficult scenarios to fly, and they were chosen deliberately because instructor pilots are extremely proficient simulator pilots and it was necessary to ensure that there was ample opportunity for deviations from profile to develop.

Each approach (as shown in fig. 5) was begun from identical conditions: downwind heading, 1542 m (5000 ft) AGL, 250 knots, and with the aircraft in a clean configuration from a position 16 km (10 mi) abeam (either right or left) of the final approach fix. After a preliminary briefing during which the approach location and type were specified, the simulator was released, and the Experiment Controller, a qualified DC-10 instructor pilot who worked with us for the duration of the study, proceeded to give radar vectors according to the preselected scenario. Standard company operating procedures, including checklists, were used for all approaches.

An approach was terminated during the landing rollout, or upon reaching 150 m (500 ft) AGL during the missed approach. For half of the approaches, the simulated visibility was set to zero (below minimums). For the remaining half, the visibility was set at the appropriate minimums for the approach type. Daylight conditions were simulated in all circumstances.

Two crews flew the monitored approach procedures first, followed by the standard procedure. The order was reversed for the remaining two crews.

Data collection was proceeded by a 2-hr ground school session during which two crews were briefed regarding the approach procedures they were about to fly. Following ground school, the pilots were given a 1-hr, 15-min simulator training session during which 4 ILS and 4 NDB approaches were flown utilizing the appropriate set of procedures. The entire sequence of ground school, simulator training, and data collection was repeated for the alternate set of approach procedures. Upon completion of the last data collection run, an extensive debriefing session was held during which comments, observations, and suggestions of the pilots were sought.

RESULTS

For the purposes of analyzing the tracking data recorded during this study, each approach is arbitrarily divided into two segments. The initial approach segment is that portion of the approach between the Final Approach Fix and a point 10 sec prior to reaching the missed approach point. The remainder of an approach to a landing is termed the final approach segment. Landings and missed approaches were analyzed separately from the initial approach data. This division was necessary to enable the analysis to focus clearly upon the critical last 100 m of an approach. For all practical purposes, there is little difference between the two kinds of approach procedures prior to the missed approach point. It is at the point where the control of the aircraft is transferred from one pilot to the other that major differences would be most likely to appear. ILS and NDB approaches were analyzed separately.

Initial Approach Segment

Tracking data were transformed into rms lateral error, rms glide-slope error, and airspeed variability measures, and were subjected to an Analysis of Variance. As expected, the stress and workload variable did significantly affect airspeed, localizer and glide-slope tracking for the ILS approaches, and lateral course error and airspeed control for the NDB approaches. No other factor, including the set of approach procedures used, produced any significant differences in aircraft performance.

Final Segment

One measure, lateral error during NDB approaches, was significantly different as a function of approach procedure — lateral tracking was more variable using the monitored procedure. This was one of only two instances where the approach procedure variable resulted in a significant difference in performance.

596

Landing Data

Landings were analyzed using lateral and longitudinal error and sink rate at touchdown as measures of landing performance. There were no significant differences observed for any landing measures.

Missed Approach Data

Missed approach performance was evaluated using peak deviation below MDA/DH (where MDA is minimum descent altitude and DH is decision height), and the square of peak deviation to give emphasis to the larger and presumably more dangerous deviations. In addition, the time integral of total flight path below MDA/DH was analyzed. The average peak deviation below MDA for NDB approaches was significantly larger using the monitored approach procedure. No other significant differences were observed.

Debriefing Interview Results

Pilot reaction during the training sessions to the monitored procedure was largely negative, and virtually all subjects expressed concern about the transfer of control of the aircraft. These negative attitudes were modified after the subjects had experience with the experimental set of procedures; however, it is still necessary to characterize the prevailing attitude as "concerned." Most pilots, however, did concede that there were some positive benefits to using the experimental procedure, particularly in reference to the increased monitoring discipline achieved with this procedure.

There was universal acclaim from the subjects for the increased emphasis on involving the flight engineer in the approach. It was the concensus that this one aspect of the experimental procedure was by far the most important and valuable.

DISCUSSION AND CONCLUSIONS

In some ways the lack of major significant difference between the two procedures was a disappointing outcome. However, in retrospect, there are some encouraging aspects as well.

First, with respect to the question of the superiority of one set of procedures over another, it is necessary to conclude on the basis of results obtained here, that crews can perform equally well using either set of procedures. There is no clear-cut reason to select one set of procedures over another on the basis of system performance measures used in this experiment. Put another way, the choice of which of the basic approach procedures to be used should be based upon other factors. Particularly important here is the accumulated experience of a company with one set of procedures; the difficulties encountered in changing from one set of procedures to another may far

outweigh the potential advantages obtained by adopting an alternate set of procedures.

Another conclusion is that regardless of which basic approach procedure is used, it is important that the flight engineer be fully integrated into the approach. The callouts and monitoring duties which were assigned the flight engineer are largely independent of the approach procedure adopted. Although not directly supported by the tracking data obtained in this study, there is little doubt that this is the most important single consideration in the development of low visibility approach procedures.

And finally, we can conclude that simulator evaluations of approach procedures are feasible.

In summary, this first experiment was a preliminary attempt to assess the effects of selected operational factors on pilot performance, in this case with largely negative results. In a second study, the experience accumulated during this first study was used to refine procedures and techniques in an attempt to understand how certain perturbations in the operational environment can affect aircrew behavior. The preliminary results are highly encouraging, and it is intended to pursue the leads generated by those data in an attempt to see if techniques can be developed which will help airline pilots to cope with such disturbances.

REFERENCE

1. Billings, C. E.; Lauber, J. K.; Cooper, G. E.; and Ruffell-Smith, H. P.: Retrospective Studies of Operating Problems in Air Transport. Aircraft Safety and Operating Problems, NASA SP-416, 1976. (Paper no. 33 of this compilation.)

TABLE I.- PILOT DATA

CREW	SUBJECT	TOTAL TIME	DC-10
	1	9000 hr	600 hrs
A	2	14000	400
	3	1500	400
	4	14000	400
B	5	13000	400
	6	6000	700
	7	9000	600
C	8	11000	400
	9	15000	300
	10	7600	500
D	11	6000	500
	12	6900	(2.5 yr)
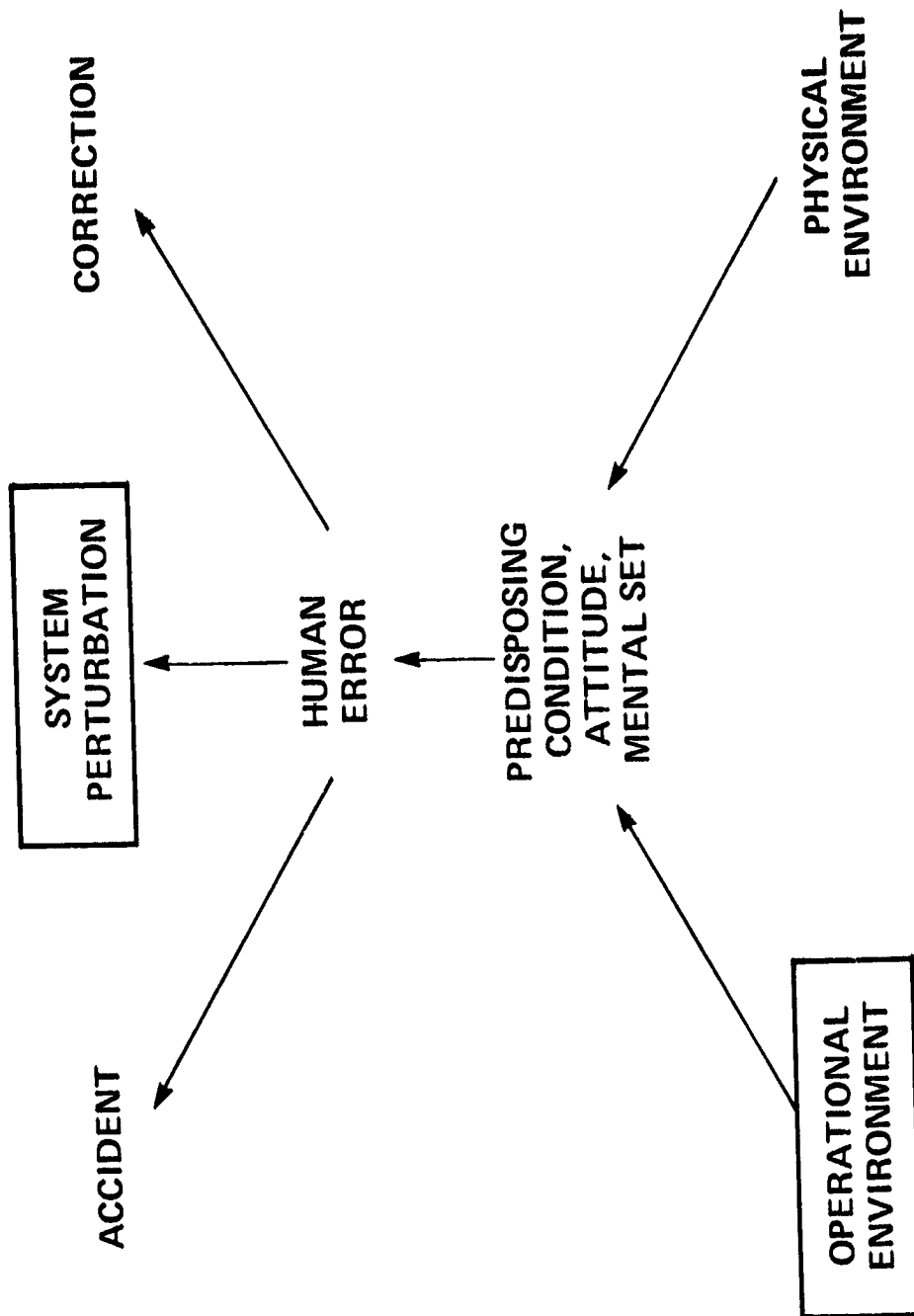
Figure 1.- Epidemiological model.

CAPTAIN

FIRST OFFICER

SECOND OFFICER

PILOT FLYING

PRIMARY MONITOR

BACKUP MONITOR

FINAL APPROACH FIX   CALLOUTS: "100 feet "MINIMUMS"
                                      ABOVE ..."

Figure 2.- Standard approach procedure.

CAPTAIN

FIRST OFFICER

SECOND OFFICER

PILOT FLYING

PRIMARY MONITOR

BACKUP MONITOR

FINAL APPROACH FIX   CALLOUTS: "100 feet "MINIMUMS"
                                      ABOVE ..."

Figure 3.- Monitored approach procedure.

601

Figure 4.- Flight engineer's worksheet.

Figure 5.- Approach profile.

PRELIMINARY REPORT ON AIRLINE PILOT SCAN PATTERNS

DURING SIMULATED ILS APPROACHES

Amos A. Spady, Jr.
NASA Langley Research Center

SUMMARY

A series of ILS approaches using seven airline-rated Boeing 737 pilots in an FAA qualified simulator have been conducted. The test matrix included both manual and coupled approaches with and without atmospheric turbulence in Category II weather. A nonintrusive oculometer system was used to track the pilot's eye-point-of-regard throughout the approach. The results indicate that, in general, the pilots use a different scan technique for the manual and coupled conditions; however, the introduction of atmospheric turbulence does not greatly affect the scan behavior in either case. A comparison is made between the objective measures of the instrument scan (oculometer data) and the pilots' opinions of their instrument use. The data show a high degree of consistency among pilots for both the quantitative data and the qualitative data (pilots' opinions). However, there is a slightly lower agreement between the quantitative and qualitative measures.

INTRODUCTION

The scanning patterns used by pilots during various phases of flight have been of extreme interest for a number of years. A number of techniques have been developed to measure subject lookpoint; however, each has either intruded on the pilot or been difficult to correlate with the state of the aircraft. For this study a nonintrusive real-time oculometer system, which allows the subject 0.03 m^3 (a cubic foot) of head motion, was used.

The purpose of this study was twofold. The first objective was the measurement of the pilots' scan patterns to provide a better understanding of how airline pilots use the existing flight instruments and to provide a data base for ILS approach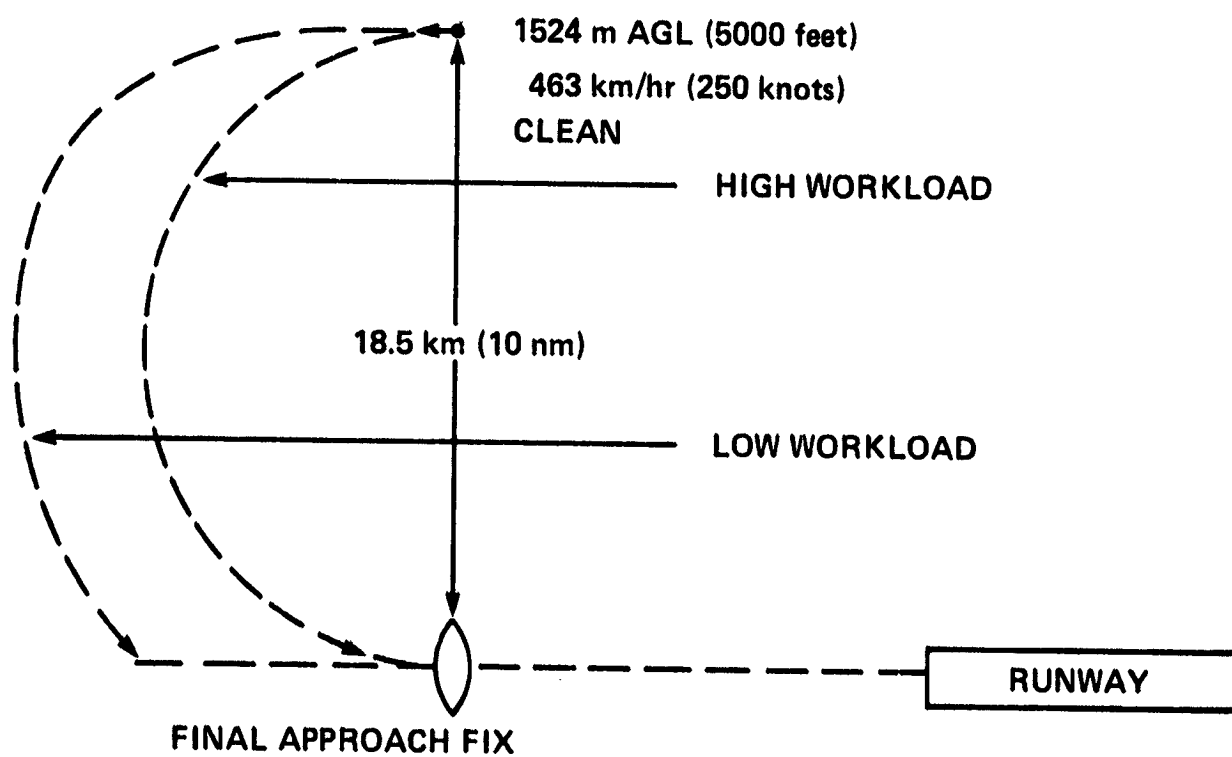es against which advanced flight displays can be compared. The second objective was to determine to what degree pilots can describe their behavior and to compare these descriptions with the quantitative data of eye-movement recordings.

The study used airline pilots flying a FAA certified Boeing 737 flight simulator at Winston-Salem, North Carolina. Both manual and coupled (automatic without auto throttle) ILS approaches from approximately 13 km (8 miles) out to a 30 m (100 ft) decision height were investigated. The data obtained give information on the pilots' scan patterns while monitoring the automatic controls and while manually flying the aircraft during which

control input decisions must be made to carry out the ILS approach. Control inputs and aircraft parameters were recorded to obtain the strategy of the individual pilots during the two modes of operation, but those data have not been analyzed.

ABBREVIATIONS

ADF   automatic direction finder (also called RMI (radio magnetic indicator))

AS   airspeed indicator

BA   barometric altimeter

FAA   Federal Aviation Administration

FD   flight director (also called ADI (attitude direction indicator with
          command bars))

HSI   horizontal situation indicator (also called CI (course indicator))

ILS   instrument landing system

RA   radar altimeter

SEG()   flight segment as defined in figure 5

T   in oculometer tracking region

n/T   out of oculometer tracking region

VSI   vertical speed indicator

EQUIPMENT

The Boeing 737 simulator used is a FAA certified initial and recurrent training facility operated by Piedmont Airlines. The only changes to the system were the incorporation of the oculometer optical head which was mounted below the ADF behind the instrument panel (fig. 1) and the addition of TV cameras behind the pilot (fig. 2) to monitor the instrument panel and a TV monitor located behind the pilot's seat to allow the test conductor to monitor the pilot lookpoints during the tests.

A modified Honeywell Mark 3 oculometer was used for the study. The oculometer has two primary subsystems: the electro-optical head and the signal processing unit. The electro-optical system generates a beam of infrared light which is directed through a beam splitting mirror toward the subject's eye. Reflections from the eye are directed by the beam splitter to an infrared-sensitive TV camera. The high reflectivity of the human retina for infrared leads to a backlighting of the pupil, so that the camera sees the pupil of the

604

eye as a bright, circular area (fig. 1). It also sees a small bright spot due
to reflection at the corneal surface. The relative positions of the center of
the pupil and the corneal reflection depend on the angle of rotation of the
eyeball with respect to the infrared beam. The signal processing unit uses the
signal from the TV camera to compute this angle of rotation and the coordinates
of the lookpoint on, for instance, an instrument panel. The output of the
signal processor is a set of calibrated digital or analog signals representing
the subject's lookpoint coordinates and pupil diameter. The modification to
the system consists primarily in a redesign of the electro-optical head result-
ing in a unit one-fourth the original size and simplification of the operating
system.

Several constants were set in the aircraft program as follows: (1) the
simulated aircraft weight was 42 640 kg (94 000 lbm) throughout all approaches;
(2) the visual scene was set for Category II conditions (30 m (100 ft) ceiling,
366 m (1200 ft) runway visual range); (3) there were zero wind conditions; (4)
turbulence when used was the maximum available on the simulator (pilots rated
this turbulence as moderate); (5) at no time were emergency conditions imposed
on the pilots. It should be noted that the airplane was not equipped with
autothrottle; therefore, in the coupled mode the pilot was required to control
airspeed.

Thirty-two channels of data were recorded. The data included oculometer
information, aircraft state variables, pilot inputs, and simulator motion
inputs. The data were recorded at a rate of 32 times a second and are in a
format that can be handled by a Control Data Corporation 6600 computer.

The oculometer was capable of tracking lookpoints within the envelope
shown in figure 1. The engine management percent times are estimated by
determining the time the subject spent looking to the right of the area covered
by the oculometer since the primary reason for looking to the center console
is engine management.

PROCEDURES AND SUBJECTS

The test conditions, as given in the following table, were designed to
investigate the pilot's scan during operations as a monitor in the coupled
approaches and as a controller in the manually controlled approaches.

Condition	Approach	Turbulence	Category
1	Manual	No	II
2	Coupled	No	II
3	Manual	Yes	II
4	Coupled	Yes	II

605

The test conditions also included the effect of atmospheric turbulence on the scanning behavior for both modes of operation. Approximately four runs for each condition were flown by each of the seven pilots. The order of runs was randomized based on a random number table. All tests were conducted in simulated Category II weather. The airport simulated was Smith-Reynolds at Winston-Salem, North Carolina. A Vital II out-of-the-window system was used to provide the pilots the visual information needed to land.

All test runs were started at 19 km (12 miles) from runway threshold (fig. 4). The first 6 km (4 miles) were used by the pilot to stabilize the aircraft on the correct flight path and to check the oculometer calibration. At 13 km (8 miles) data recording was started and continued until touchdown or until the run had been aborted as a result of the pilot choosing to go around.

All airline pilots used in the program were qualified Boeing 737 pilots who fly for a scheduled airline. Prior to starting the test program each pilot was given a briefing on the operation of the oculometer, as it was the only thing different in the cockpit. Also, the pilots were asked to assume that they were flying an aircraft full of passengers, and if they would normally elect to go around, they should do so. At the end of the test period, the pilots were asked to fill out a questionnaire concerning how they felt they had used the instruments.

All tests were conducted using the same instructor pilot as a copilot. The copilot functioned in the same manner as he would in a normal approach and provided all required callouts.

RESULTS AND DISCUSSIONS

The scanning patterns of pilots are expected to differ between pilots, and even from run to run for the same pilot; however, there should be a consistency in terms of the primary information scanned for a particular type of run. In order to establish this consistency, this report will deal only with the summary data obtained from three runs for each condition by all seven pilots. Data on aircraft state variables, pilot inputs, etc. are not dealt with, as additional work is needed in order to correlate the information.

Observation of the pilot scan patterns during the test indicated that the pilots used the center of the flight director as the primary lookpoint and moved from there to an instrument and then came back to the center of the flight director. Only rarely did a pilot check more than one instrument before returning to the center of the flight director. This is demonstrated in figure 5 which is a time history of one pilot's scan from approximately 213 m (700 ft) altitude down to 30 m (100 ft) altitude. Figure 5(a) shows the manual case (with no turbulence), and figure 5(b) shows the coupled case with no turbulence. The ordinate indicates the instruments at which the pilot was looking, with the flight director being broken in to its information blocks as indicated in figure 6. The abscissa indicates flight time in seconds. The sections T and n/T indicate eye tracking (upper level) and not tracking (lower level). As can be seen from the time histories the pilot changes fixations more rapidly and looks

606

at more instruments in the coupled mode as compared with the manual mode. The majority of the out-of-track time was caused by the pilot looking at the center console engine instruments.

The bar graphs presented in figure 7 show a comparison of the percent time spent (dwell fraction) on the instruments for both the manual and coupled modes with no atmospheric turbulence. Each grouping contains the summary data (S) over the entire run and the data for each flight segment (1 to 4) defined in figure 4. The crosshatched section defines the mean percent time spent on the instrument while the open section on top defines the standard deviation. The clock, radar altimeter, and ADF are not included in this figure as they are basically not used by the pilot. Of particular interest is the comparison of percent time spent in the flight director (approximately 73 percent for the manual mode as compared with 50 percent for the coupled mode, as indicated by the crosshatched area). Therefore, for all the other instruments the percent time is down in the manual mode compared with the coupled mode. The segmented data indicate small deviations in percent time but, in general, they do not grossly deviate from the summary data. The purpose for including it here is to indicate the type of analysis or data breakdown which is possible but an extensive look at the segment data is beyond the scope of this report. The scan rate (the number of instruments fixated on per second) also reflects this. For the manual mode, it is 1.2 per second and for the coupled mode, it is up to 1.7 per second.

The area covered by the oculometer (fig. 1) did not include the center console, where the engine and fuel management instruments are located. A check of the TV film made of the subjects' eyes indicated that they spent up to 5 percent of their time in the manual mode and up to 10 percent of their time in the coupled mode checking either fuel flow or engine pressure ratio.

A comparison of the summary of percent time spent on instruments for the manual mode with no atmospheric turbulence and with turbulence is given in figure 8. A slight increase of about 3 percent in flight director percent time is noted in the summary bar with turbulence; however, changes in the other instruments, while present, are small. Additional data analysis is needed to determine the significance of the effect of turbulence on scan. The introduction of turbulence caused a slight increase in scan rate from 1.2 to 1.4 fixations per second.

The effect of turbulence in the coupled mode is shown in figure 9. In this case additional time is spent in both the flight director and the airspeed indicator with slight decreases for the BA, HSI, and VSI. However, all the changes are small. The average scan rate increased slightly as a function of turbulence from 1.7 to 1.9 fixations per second.

The standard deviations shown by the open bars above the means in figures 5 to 7 are small, particularly for the FD and AS (which account for most of the percent time on instruments), indicating that the pilots are consistent in terms of the use of these instruments.

The mean dwell time and standard deviation of mean dwell time in seconds for the manual and coupled approaches for conditions with no turbulence are

607

given in figure 10. Of interest is the reduction in dwell time for the FD from approximately 1.6 sec in manual mode to approximately 0.8 sec in the coupled mode. However, the mean dwell time for the other instruments increased slightly in the coupled case. The standard deviations of mean dwell are large compared with the mean dwell. Additional analysis is needed to determine the dwell time distributions and correlate them to actual conditions of the aircraft and techniques of control used by the individual pilots.

The flight director was broken down into information areas as indicated in figure 6. The percent time spent in the flight director areas for the manual and coupled cases with no turbulence is presented in figure 11. It should be noted that these values are percentages of the time spent in the flight director, as indicated in figure 7, and not of total flight time. Basically, the data indicate (fig. 11) that the pilots spent a smaller percentage of their time in the center of the flight director in the coupled mode than they did in the manual mode. The rest of the time is distributed fairly evenly among the other areas for both modes, with the exception of the roll indicator. The majority of the pilots did not look at the roll indicator area at all. In this airplane the speed bug of the FD is not operative; however, the airspeed indicator (located to the left of the FD) is a bug instrument. Additional studies are needed to verify a hypothesis that the pilots are gleaning information from the airspeed indicator peripherally while still in the speed bug area. The scan rate within the flight director for the manual approach was 1.9 fixations per second as compared with 2.9 fixations per second for the coupled approach.

It is evident from the oculometer data that in terms of the percent time on instrument data (figs. 7 to 9) the ranking of instruments (the most to least percent time) changes relatively little either between pilots or between conditions. The oculometer data indicated that the FD, AS, and HSI ranked 1, 2, and 3, respectively; the VSI and BA were approximately equal for 4 and 5 rank; and the ADF and RA (not shown) ranked 6 and 7, respectively. A review of the pilot questionnaire indicated that while the pilots basically agreed with each other, their rankings did not agree with the oculometer data for the HSI, which the pilots generally ranked fifth, and for the BA, which is ranked third. It is presumed that the pilots reported those things which concerned them most and not necessarily their actual behavior. Therefore, ranking instruments strictly according to percent time spent (as measured by the oculometer) may, in fact, not reflect actual instrument priorities.

A great deal of additional analysis of the data is needed to develop a basic understanding of the strategy used in controlling or monitoring an ILS approach.

CONCLUSIONS

The results obtained from the study provide a data base on how pilots scan the existing flight instrument during simulated Category II ILS approaches. A preliminary look at the data indicates that:

1. Pilot mean percent time on the various instruments remained relatively constant throughout the approach to 30 m (100 ft).

2. The standard deviation of the percent time on instruments was relatively low.

3. Pilots spend less time in the flight director during the coupled approach than during the manual approach. Most of the difference was used on airspeed.

4. Pilots percent time on instruments varied little with the introduction of turbulence.

5. Mean dwell time on the flight director for the coupled mode was half that for the manual mode.

6. Standard deviations of dwell time are large compared with mean dwell time.

7. Pilots were consistent in ranking the instruments in terms of most to least used. However, the ranking obtained from the oculometer data in terms of percent time on instruments did not agree with pilot opinion with regard to the horizontal situation indicator and barometric altimeter.
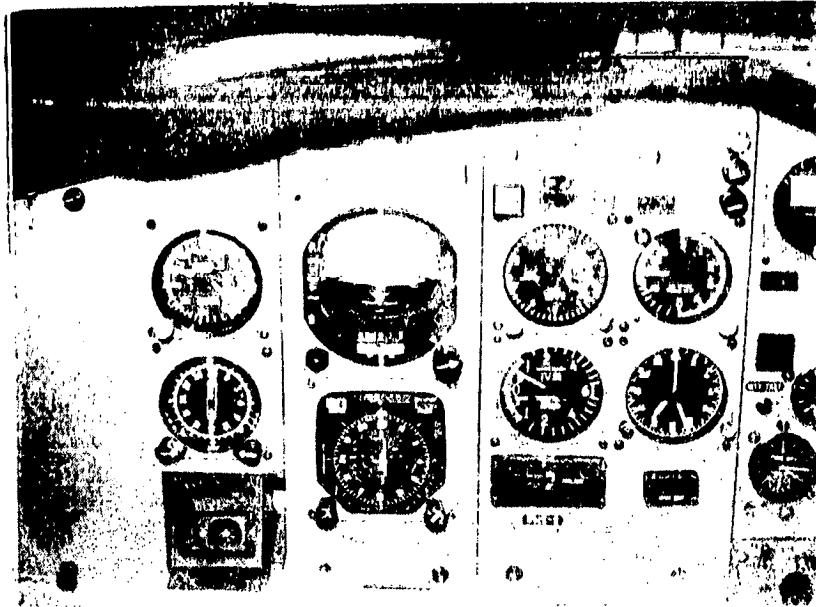
Figure 1.- Instrument panel with oculometer optical
head in place.
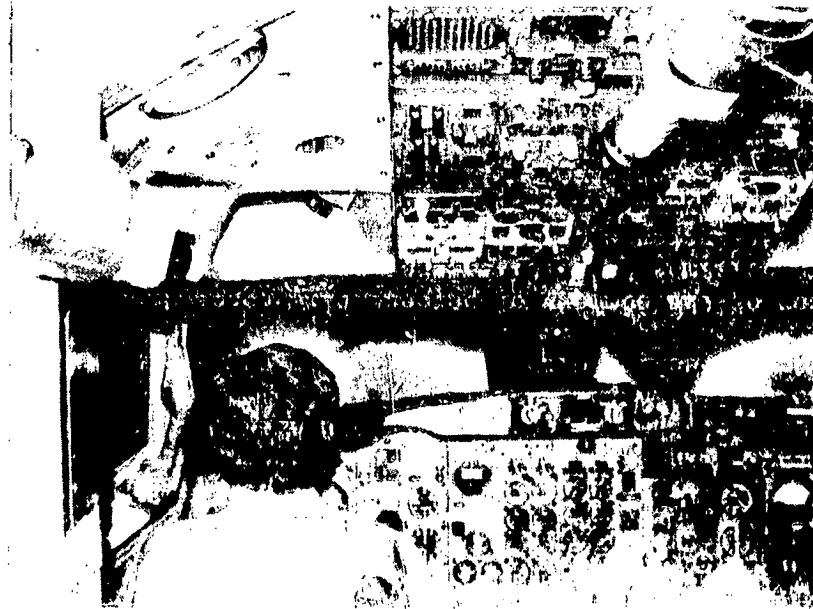
Figure 2.- Camera used to monitor pilot instrument
panel, and copilot

610
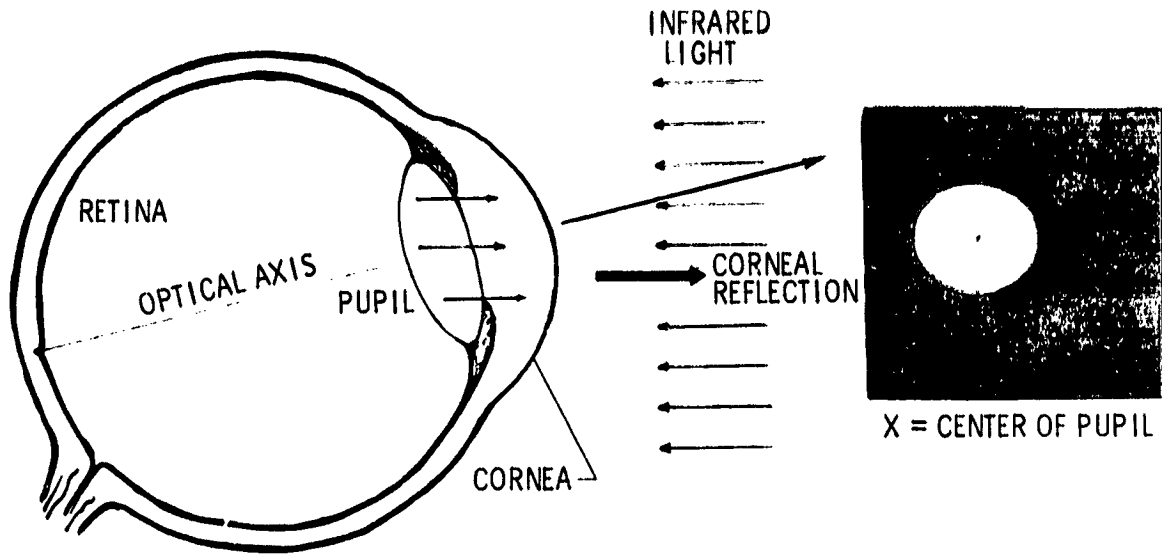
Figure 3.- Basic sensing principle.
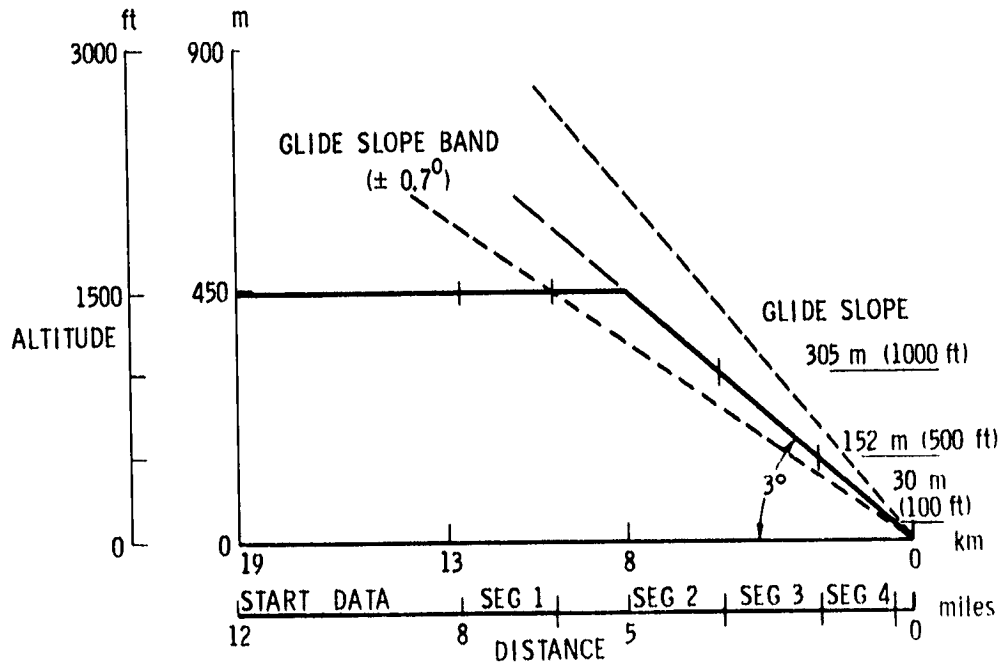
Figure 4.- Flight profile.
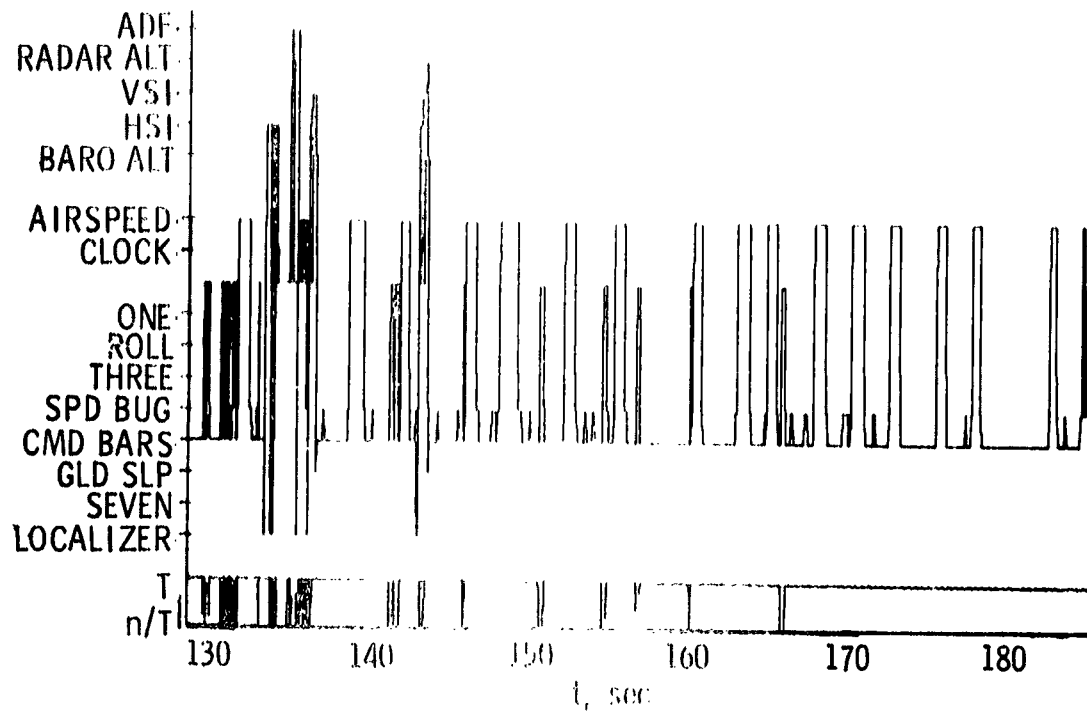
(a) Manual approach.
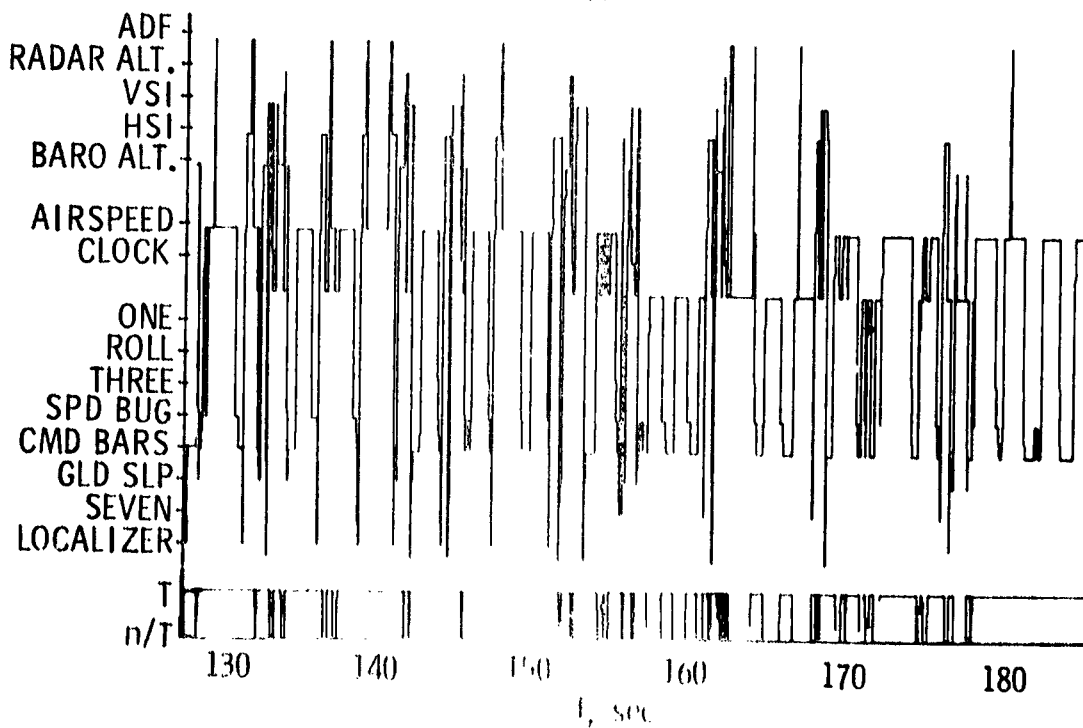
(b) Coupled approach.

Figure 5.— Time histories of one pilot's scan. 213 m (700 ft) to minimum decision altitude of 30 m (100 ft) above ground level.

612
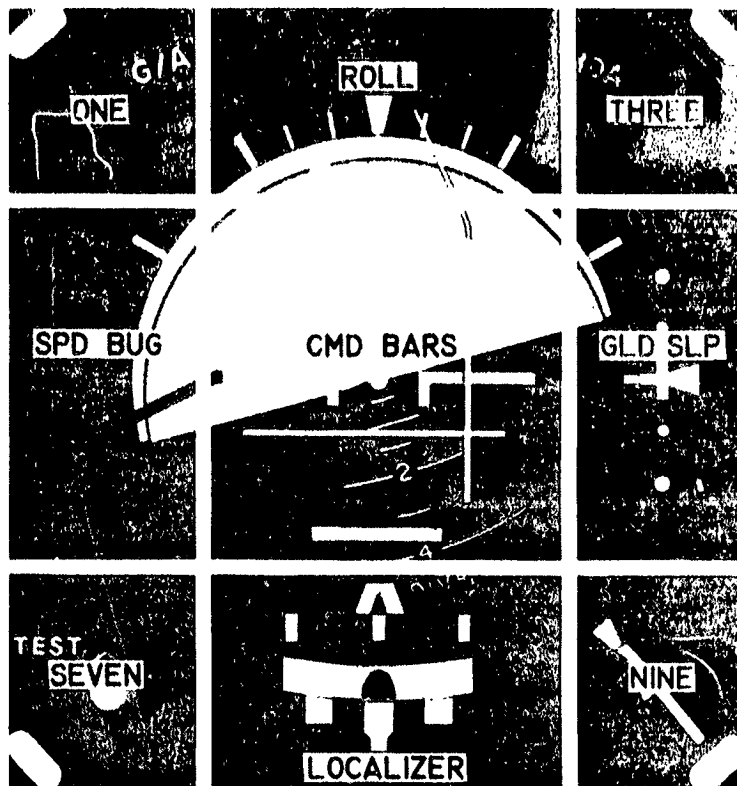
Figure 6.- Flight director breakdown.
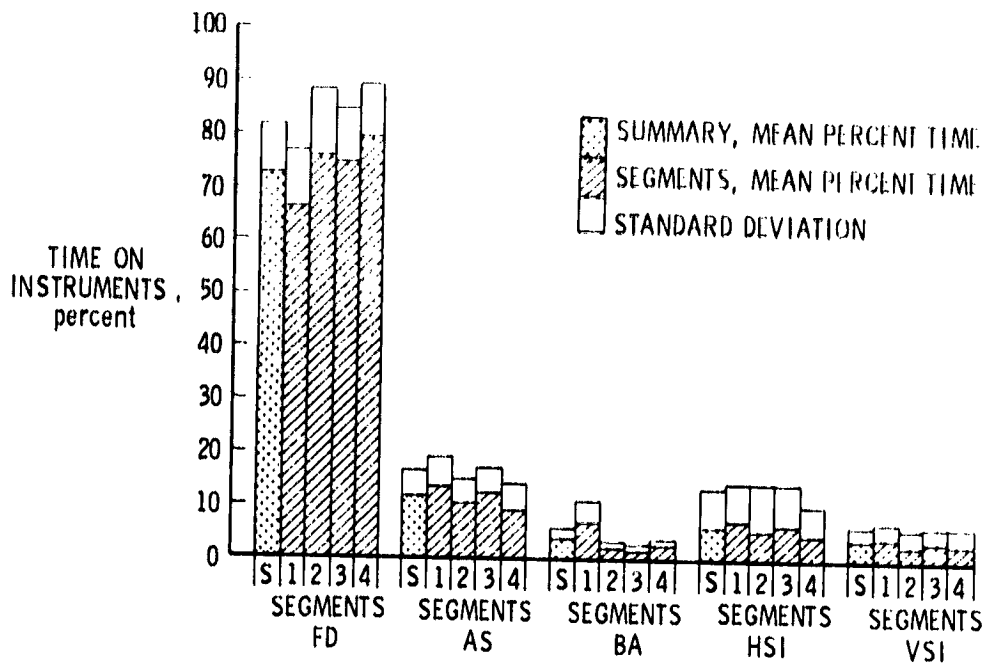
(a) Manual approaches.
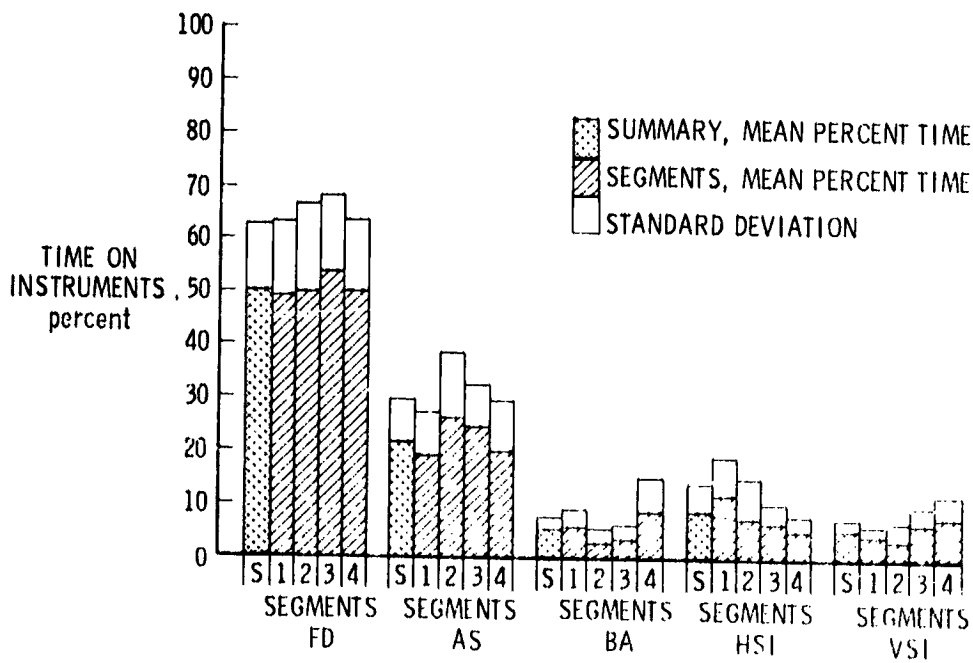
(b) Coupled approaches.

Figure 7.- Percent time on individual instruments
(7 pilots, 3 runs each).
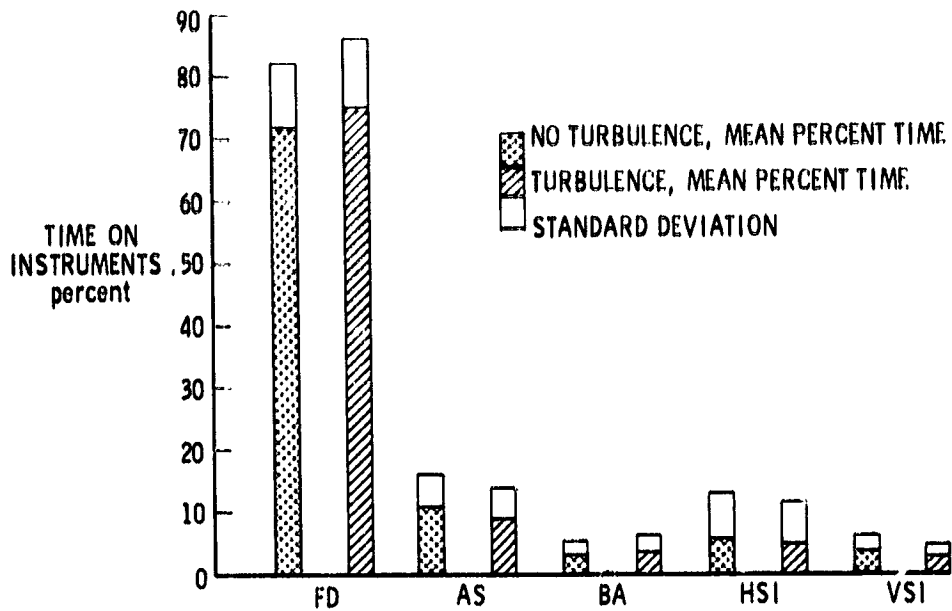
Figure 8.- Percent time on individual instruments for manual
ILS approaches with and without turbulence (7 pilots,
3 runs each).
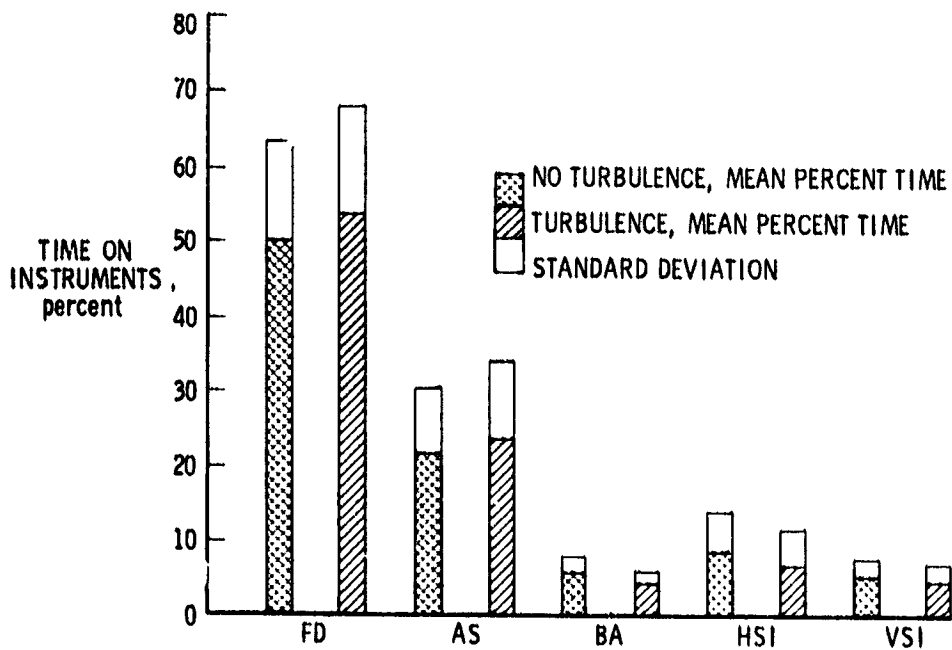
Figure 9.- Percent time on individual instruments for coupled
ILS approaches with and without turbulence (7 pilots,
3 runs each).

615
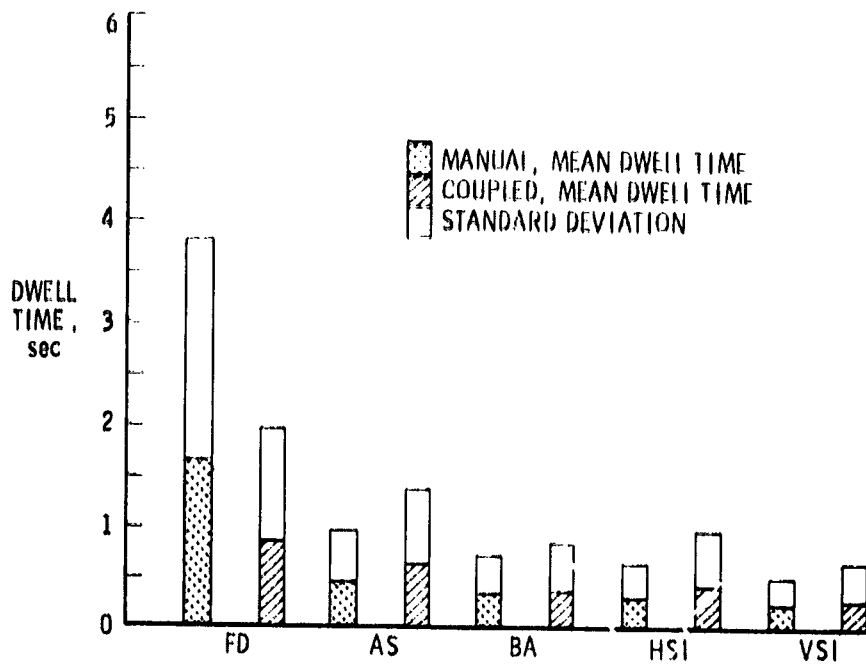
Figure 10.- Dwell time on individual instruments for
manual and coupled ILS approaches (7 pilots,
3 runs each).
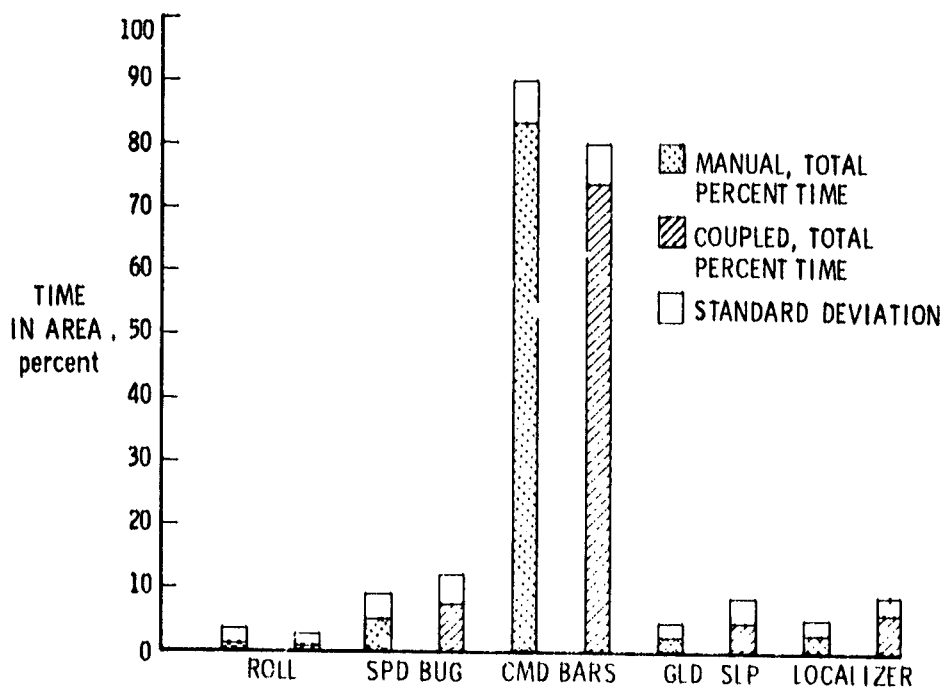
Figure 11.- Percent time on flight director areas
(7 pilots, 3 runs each).

616

A SYSTEMATIC APPROACH TO ADVANCED COCKPIT WARNING SYSTEMS FOR

AIR TRANSPORT OPERATIONS: LINE PILOT PREFERENCES*

Douglas H. Williams and Carol A. Simpson
NASA Ames Research Center

SUMMARY

Fifty line pilots (captains, first officers, and flight engineers) from 8 different airlines were administered a structured questionnaire relating to future warning system design and solutions to current warning system problems. This was followed by a semantic differential to obtain a factor analysis of 18 different cockpit warning signals on scales such as informative/distracting, annoying/soothing. Half the pilots received a demonstration of the experimental text and voice synthesizer warning systems before answering the questionnaire and the semantic differential. A control group answered the questionnaire and the semantic differential first, thus providing a check for the stability of pilot preferences with and without actual exposure to experimental systems. It was hypothesized that preferences for warning method and cancellation method would vary as a function of warning urgency or priority and as a function of expected false-alarm rate. It was also thought that age and position flown might influence pilot preferences. There were no significant differences between the two groups for overall preferences for text and voice warnings compared to other warning methods, suggesting a high degree of stability and reliability of pilot preferences for warning methods. Warning urgency and expected false-alarm rate did produce significant differences in pilot preferences for some, but not all, warning methods. Warning urgency also produced significant differences in preferred cancellation methods for some warning methods. Generally, the preference data obtained revealed much consistency and strong agreement among line pilots[1] concerning advance cockpit warning system design.

INTRODUCTION

There seems to be substantial agreement among members of the aviation community that current cockpit warning systems for commercial jet transports suffer from a wide range of human factors design problems. In a recent study by the Boeing Company (ref. 1), funded by the Federal Aviation Administration, Vietengruber documented the warning systems in aircraft now current in the fleet. He found insufficient standardization of warning signals between

[1]The term "line pilots" refers to pilots who regularly fly commercial transport aircraft. It does not include airline check pilots, chief pilots, or instructor pilots.

aircraft types and even for the same aircraft type between airlines. He also noted a trend toward increasing numbers of different warning signals in both the visual and auditory modes. George Cooper (personal communication), under contract to the National Aeronautics and Space Administration, conducted structured interviews with foreign and domestic aircraft and avionics manufacturers in order to document current philosophies and to identify specific guidelines which might assist in improving warning system design. He found general agreement that cockpit warning systems are inadequate and may be adding to cockpit workload at times when this is already heavy due to additional demands on crew attention. While general agreement was found for many guidelines, the Cooper study also revealed some major points of disagreement among the parties interviewed regarding preferred methods of alerting, that is, tones, bells, voice, alphanumerics, labeled lights, and tactile warnings such as the stick shaker. However, a need for improved standards or guidelines was recognized.

There are a number of proposals that define general approaches to cockpit warnings and assign particular alerting methods to particular hazardous conditions. Aeronautical Radio, Inc. (ARINC) has a project paper (ref. 2) that outlines specifications for airborne audible warning generators. By assigning specific aural alerts to specific hazardous conditions, they have attempted to standardize the "meanings" that pilots would have to learn to associate with each of the different types of sounds. They also recommend a visual annunciator that would remain on until an existing fault is corrected. They provide for the possibility of voice warnings in place of or in addition to the nonspeech aural warnings. The Society of Automotive Engineers (SAE-7) Steering Committee on cockpit design is currently working on design standards for future warning systems. British Airways, in a paper for the International Air Transport Association (ref. 3), presented strong arguments against the use of nonverbal aural alerts, pointing out that such alerts are limited in the amount of information they can transmit and often are startling and distracting. They suggest audio alerts, preferably voice, for high priority, quick-action dangers and visual warnings, color coded for priority, for all priorities of warnings. They recommend that high priority voice warnings be noncancellable while providing for a cancel button for lesser priority voice warnings. Clearly, there is no industry-wide consensus regarding the types of alerting signals or the system logic that should be used for cockpit warning systems.

One type of data frequently overlooked is objective measurements of user preferences. All too often, experimental systems are designed and tested in the simulator first, with pilot debriefings afterwards. Perhaps this approach is popular because of a belief that there is little agreement among pilots concerning new cockpit displays and therefore little to be gained by asking them what they want in advance. This deprives an investigation of the vast resource of flying experience of the pilots who are destined to use and depend on the new system until *after* major commitments have been made to particular design elements or types of systems. This study had the dual purpose of sampling line pilot preferences for cockpit warning system design and also providing data that would be useful in guiding subsequent flight simulation research aimed at the determination of design principles for warning systems for air transport aircraft.

618

For this investigation, only U.S. Customary Units were used in the test booklets; therefore, the equivalent values in SI Units are given as follows:

3/4 in. = 1.9 cm

3/8 in. = 0.95 cm

HYPOTHESES

Some general hypotheses regarding pilot preferences for warning systems were derived from pilot debriefings in connection with previous research on Area Navigation (RNAV) CRT displays (ref. 4) and on voice warning system design (ref. 5). Additional input was derived from flight deck observations made during a series of flights as part of an ongoing collaborative research project with American Airlines Flight Training Academy on synthesized speech displays.

During discussions with pilots on the Ground Proximity Warning System (GPWS), it was observed that they seemed to have a generally negative attitude toward voice warnings and used the GPWS to illustrate their opinion. This observation was supported as well by various articles appearing in publications written for and read by airline pilots Connes, 1975, and Rawlings, 1976 (refs. 6 and 7). However, when pilots were asked if voice warnings with extremely low false-alarm rates would be acceptable, many responded that voices could be very useful for high priority warnings if one could depend on them to be accurate. This suggested that pilots would not be pro- or anti-voice warning per se, but would instead want voice only under conditions of high priority and low false-alarm rate. To test this, it was hypothesized that pilot preferences for warning method would depend both on the urgency or priority of the problem signaled by the warning and on the expected false-alarm rate.

Another point that pilots emphasized in the earlier discussions was the difficulty created by loud sounds and voices that continued during decision-making and intracrew communication. The engine fire bell was frequently given as an example of a signal that prevented or disrupted attention to the decision-making process and masked crew checklist callouts and other important auditory events. On the other hand, pilots gave two types of comments about cancellation of visual warnings. Some wanted to cancel all lights and other visual warnings as soon as they occurred to prevent distraction from other visual displays. Others wanted visual signals to remain as long as the hazardous conditions remained. From these observations came the hypothesis that preferences for warning cancellation would depend on both warning urgency and on the warning method used (i.e., auditory, visual, tactile). In addition, it was hypothesized that a limited priority assignment scheme for visual signals would satisfy the majority of pilots.

It was also expected that age and position flown might have an effect on pilot preferences for warning system design. However, no specific predictions concerning these possible effects were formulated. To summarize, then, the hypotheses were that

619

1. Pilot preferences for warning method will depend on the urgency of the problem signaled and on the expected false-alarm rate.

2. Preferences for warning cancellation will depend on warning urgency and the warning method.

3. A limited priority assignment scheme for visual signals would satisfy most pilots.

4. Age of pilots and crew position flown might produce differences in preferences.

METHOD

Often, when a pilot preference survey is proposed, resistance is encountered because of supposed characteristics of pilot preferences. In fact, these characteristics, if they do exist, can be allowed for in the construction of the measuring instrument.

First, it is often stated that pilots have too many opinions to be adequately measured: "There are as many opinions as there are pilots." To solve this, subjects were offered reasonable alternatives to rate or rank or were offered forced choices among alternatives. In most cases, they were also offered spaces for free responses where they could write in their own opinions or suggest their own system, if they thought the ones offered were totally inadequate. If this alternative was used by a significant proportion of respondents, it would be evidence of an unmanageable diversity of opinion among pilots, inadequate test items, or both.

Further, it is often suggested that pilot opinions are too changeable because they consider whatever new system they saw last to be best. This problem was handled by splitting the sample group into two subgroups and then by making a vigorous effort to convince one of the subgroups of the usefulness and potential of two types of systems, CRT or voice, which would then be represented in the test measures. Any significant differences between the responses of the subgroups on these two systems would be evidence for changeability of the pilot preferences obtained.

Measuring Instrument

The measuring instrument was a 32-page booklet to be filled out by each test subject. It consisted of 2 pages of biographical information and 30 pages of free response, rating scale, preference grid, and ranking items. There was a second, optional test, the semantic differential, in a separate booklet. It consisted of judgments of 18 concepts on 17 polar opposite scales. It was only administered to subjects who finished the first booklet within the 3 hr allowed for the complete session. If administered, it took approximately 15 min to complete.

Subjects

Subjects were line captains (13), first officers (20), or flight engineers (14) currently flying transport aircraft or recently furloughed (3). The oldest was 60, the youngest 27, with a mean age of 41.3 years. Total time averaged 9300 hr, and 8 airlines were represented. (See table 1.) This sample was not randomly chosen, and so may not represent a true cross section.

Procedure

Subjects were obtained in sets of 1 to 9 persons. They were drawn from a pool of airline pilots based in the San Francisco Bay Area who had expressed interest in participating in research at Ames Research Center. They were paid for their participation. Each set was randomly assigned to treatments, except that the last set was picked to exactly complete the group sample size of 25.

Demonstration-first group — Sets of pilots who were assigned to the "demonstration-first" group were offered coffee and a short, purposely vague introduction[2] to the purpose of the study, and assurance that their name and airline could not be connected to their individual responses on the test items. They then participated in a 20-min experiment that exposed them to synthesized speech warning messages. Following that, they were shown a video tape of various possible CRT display warnings, and then color slides of this type of CRT system and another type of alphanumeric warning system in several simulators, aircraft, and artists' conceptions. Finally, they were given the two test booklets and allowed to work on them at their own pace, for a maximum of 3 hr. Most completed them in less time.

Questionnaire-first group — The "questionnaire-first" pilots were given the short introduction, coffee, anonymity assurances, and told they would have 2 1/2 hr to complete the test booklets, after which they were given the synthesized speech experiment and the video and slide demonstrations.

The experimenters were always present during administration of the test booklets to answer questions. Discussions were not allowed to become established. If opinions were offered spontaneously, subjects were politely encouraged to write them in the appropriate spaces on the booklets. Motivation was good, and subjects willingly worked on the booklets without complaint. Spontaneous comments offered at the end of the session were encouraging. All subjects were offered an opportunity to fill out a name and address sheet to receive a copy of the report on the study. More than two-thirds of them chose to do so; 41 of the 50 also chose to do the optional semantic differential. These are rough indications of good motivation and interest.

---

[2]The introduction was left vague to prevent biasing subjects. If any particular system was even mentioned in a positive or negative statement, it could have influenced their responses.

RESULTS AND DISCUSSION

In the following, whenever a result is presented or a conclusion offered, assume that the "demonstration-first" and the "questionnaire-first" groups were *not* significantly different, and the data were combined after the significance test had been run. The few instances when there was a significant difference are indicated. The term "pilots" is used to describe any of the subjects, whether they were captains, first officers, or flight engineers.

Throughout this paper, there are repeated references to priority (= urgency) levels, 1 through 5. These were adapted from a priority assignment scheme developed by the Boeing Company and were presented to subjects in the form shown in table II. Warning methods are repeatedly referred to, and these were initially presented to the subjects as shown in table III. Subsequently, they were referred to in an abbreviated form.

Warning Method Preferences

The preference grid shown in table IV was repeated four times, once for each of four false-alarm rates: 50 false:1 real alarm, 1 false:50 real alarms, 1 false:1000 real alarms, and 1 false:1,000,000 real alarms. Pilots were asked, for each of these rates, to place an X under the system or systems they would want for warnings of that urgency, given that the system false-alarm rate could be no better than stated. Results are shown in figure 1. There is much information in this figure, but it will reward close study. First consider one cell concerned with voice warnings for priority 1 problems (fig. 2). Note that with the high false-alarm rate, 50:1, few respondents will accept the voice warning, but as the false-alarm rate improves, more and more pilots are willing to accept this method of warning for priority 1 situations. Returning to figure 1, the larger histogram, note, in the row for voice warnings, that for the lower priority situations, the number of pilots desiring voice warnings declines, regardless of the false-alarm rate. In short, pilots do not want voice for "information only" or low priority warnings, and they do not want them if the false-alarm rate is high. But they are willing to accept voice warnings for very important, high priority warnings if the false-alarm rate is low.

Now consider the row "text message." Note that it is generally acceptable no matter what the false-alarm rate is, as shown by the evenness of the histograms within cells. But also note the slightly greater concentration of responses within the cell for urgency level 3. This would tend to indicate that text messages are seen as more valuable for moderate priority items.

Two further observations can be made from this figure. For the auditory warnings (top three rows), responses are concentrated in the higher priority columns, indicating that pilots want sounds only for important problems. A χ^2 test for the effect of false-alarm rate is also consistent ($\chi^2 = 22.6$, df = 12, $p < 0.05$).

622

Now consider visual displays. A relative insensitivity to false-alarm
rates and urgency level is shown. These responses suggest that visual warnings
can be more easily ignored if they are a false alarm, and that they can be
tailored to suit the urgency of the situation. χ^2 tests were performed on the
data for each false-alarm rate to test the relation of warning method to
urgency level. For all false-alarm rates, significance levels of p < 0.05 or
better were obtained. Inspection of the tabled data showed that the auditory
methods, particularly "other sound" and "voice," were preferred for the more
urgent warnings provided the false-alarm rate was low. Visual methods, par-
ticularly "labeled light" were preferred for moderate and less urgent warnings
for all false-alarm rates and were also preferred for level 1 and 2 urgency,
"action now" warnings when the false-alarm rate was high.

When differences between the responses of the "questionnaire-first" and
"demonstration-first" groups were tested on this item, none of the expected
ones were found, despite this being one of the most likely sections of the
questionnaire to show such differences.

Warning Cancellation

Part of matching a warning to a situation is providing a way to cancel the
warning when it is no longer wanted. Responses were collected by means of a
preference grid with cancellation options and warning methods, given different
priorities. The results are shown in figure 3. For clarity, one cell is shown
in figure 4, voice warnings for priorities 1 and 2. (For brevity on the ques-
tionnaire, priorities 1 and 2 were combined as were priorities 3 and 4.) For
these, "cancel button" is the method most preferred, and this is a general
finding.

Note the very small number of "noncancellable" responses, which indicates
that the respondents *do* want to be able to cancel a voice warning. This is
true for nearly all auditory warnings. Also, few subjects checked "don't use"
for this warning method, for this priority, indicating that they *do* find voice
warnings acceptable. Figure 3 also shows that "noncancellable" is very fre-
quently checked for lights, text messages, and flags; therefore they should
stay on until the problem is solved. When χ^2 tests were applied to test for
a statistically significant relation between urgency and cancellation prefer-
ences, they were significantly related (p < 0.001) for auditory warning methods
but not for visual methods (p > 0.20).

Finally, figure 3 shows that as priority decreases, there are many more
"don't use" responses for audio displays, the trend being reversed for
unlabeled lights and flags.

System Logic

Another question at issue in the design of warning systems is the assign-
ment of priorities for the warnings and filtering or inhibiting them. This

problem was assessed in the context of a single-channel warning system that could not present multiple simultaneous warnings. Pilots were asked to rate the following systems:

A. An onboard computer decides priority, presents the most urgent warning until the condition is removed, then presents the next most urgent, etc.

B. A primary display presents the most urgent warnings; a subsidiary display presents any others which occur simultaneously.

C. Priorities are not assigned—warnings are presented on the primary display as they occur.

D. A warning is presented for 5 seconds on the primary display then replaced with another warning, until all warnings in the stack are exhausted; then the entire thing repeats until all conditions requiring warnings are removed. All warnings are also displayed on a subsidiary display.

E. An onboard computer analyzes the pattern of warnings, then presents the crew with the best course of action in command format.

Two primary display systems were to be considered — an "alphanumeric display block of 3/4-in.-high letters"[3] or a "synthesized voice display in earphones and speakers." Results are presented in figure 5. In all cases, the visual warning was slightly more desirable. System B is the clear favorite. The other systems have mean ratings of 3, "no preference" or worse, so the pilots seem to indicate that they do not like any of these other systems very much. Clearly, more thought must be given to priority assignment schemes; perhaps system B could be used as a starting point.

Text Displays With and Without Alerting Tone

The next item concerned the use of a flashing versus a nonflashing display and the use of an auditory alerting tone. A grid was presented showing different systems and urgency levels (table V). Subjects went through the grid twice, first making an X for any systems they would want for warnings of a given urgency level, and the second time making an A for any systems they would want for a given urgency level if a single audio alerting tone were presented at the same time. The results for a warning on the bottom line of a CRT are shown in figure 6. The "not flashing" version is most desired for low-urgency warnings, while the audio tone is not considered particularly helpful for any priority. When the same warning is flashing, however, the preferences move to priority 2 with audio alerting and to priority 3 without.

Next consider figure 7, "warning on whole CRT screen." When this is not flashing, the preferences center around priority 2; but when it is flashing, the preferences move to priority 1, the most urgent flight safety items. For these, the audio alerting tone also becomes more desirable.

---

[3]All material enclosed in quotation marks is a direct quotation from the questionnaire.

Figure 8 shows the results for a "single line of twelve 3/4-in.-high alphanumerics." Again, when not flashing it is viewed as a device for presenting normal information or less vital warnings, priority 3 or below; in this case, no audio alert is wanted. When flashing, these alphanumerics can be used for the highest priority items. In this case, the audio tone becomes acceptable as an alerting device. It should be noted that some of the demonstration given to the subjects consisted of illustrations of exactly these three systems. They were shown by video tape on a 12.7-cm (5-in.) by 14.0-cm (5.5-in.) CRT monitor and by color slides of the 12-alphanumeric block used in flight on the CV-990 at Ames Research Center. Surprisingly, no significant differences in responses were noted between the "demonstration-first" and "questionnaire-first" groups for these items.

Voice Warnings

Another group of questions concerned voice warning systems. A technologically possible future system was described in which each of the present aural warnings would be replaced by a voice warning with a different voice message for each different malfunction. The description is reproduced below.

> It would be possible to replace all of the current aural warnings with voice warnings. Such a system would be able to have different voice warnings for unsafe conditions which are now signaled by the same aural warning, e.g. TAKE-OFF warning and CABIN PRESSURE warning. Such a system would also include a volume control to adjust to different listening conditions. The warnings would be presented to your headset at the same volume as your own adjusted volume level for ATC communications. As a back-up, the warnings would also be presented over a speaker with their volume automatically adjusted to be just sufficiently above the volume of the ambient cockpit noise so you would hear them clearly -- as the noise level changed, the volume of the warnings would be automatically adjusted up or down. A visual status display would also be included to display all unsafe conditions as long as they continued to exist. You would have the option of leaving the visual display on continuously or turning it on only when you wanted to look at it. There would be a cancel button for voice warnings.

In response to the question, "Would you want such a system in your cockpit?", far more pilots said they would want the proposed voice warning system. Eighty-two percent of the 50 pilots gave a "yes" or a "qualified yes" response while only 18 percent responded "no." This difference was highly significant as tested by the 50-Percent Probability test ($x = 9$, $n = 50$, $p < 0.002$).

The pilot responses to the proposed voice warning system were potentially among the most susceptible to possible influence from the demonstration of experimental synthesized speech and text displays. In figure 9, the responses of the questionnaire-first group are shown on the left, and those of the demonstration-first group are shown on the right. The proportions of "yes" (including "qualified yes") to "no" responses were nearly identical for the two

groups. The only possible difference between the two groups might be in the proportion of "qualified yes" responses given. A smaller percentage of "yes" responses for the demonstration-first group were "qualified yes" responses. The pilots in the questionnaire-first group, however, were responding on the basis of no prior experience with the capabilities of electronic voice warning systems. In this context, it would be reasonable to find a higher degree of uncertainty concerning the characteristics of a proposed voice warning system. This, in turn, could have caused more of these pilots to give a "qualified yes" response compared to the demonstration-first group. However, this apparent difference between the two groups was not significant as shown by Fisher's test ($a = 8$, $b = 3$, $c = 12$, $d = 18$, $p > 0.05$).

The next question was designed to determine which features or components of the proposed voice warning system were responsible for producing "yes" or "qualified yes" responses to the system. Figure 10 shows the percentage of "essential" judgments received by each voice warning system component. These responses were given by the 41 pilots who had responded affirmatively to the proposed system. Each pilot placed a check beside each component he thought was essential to make the voice warning system acceptable. The differences in numbers of "essential" judgments for the different components were highly significant ($\chi^2 = 54$, df = 6, $p < 0.005$). Clearly, the two most essential components are the voice cancel button (65 percent) and the visual status display (63 percent). We interpret this to mean that pilots want voice warnings only if they can cancel them and only if they have a visual status display that will continue to make the warning information available. Each of the remaining components received some "essential" judgments, but in each case, from less than 50 percent of the pilots. These other components should certainly be regarded as desirable. In contrast, the voice cancel button and the visual status display have to be included in any voice warning system.

Figure 11 also supports the finding that pilots want to be able to cancel voice warnings. In this question, they were asked to choose among several types of voice warning repetition; 77 percent of the pilots wanted the warnings to repeat until they pressed a cancel button or the problem was corrected, whichever happened first. This compares to only 19 percent who wanted the warnings repeated a fixed number of times — once, twice, r three times — and a mere 4 percent who thought voice warnings should be noncancellable. These differences were highly significant by χ^2 tests ($\chi^2 = 44.8$, df = 2, $p < 0.001$).

The pilots as a group expressed no strong preference on the question concerning the effect of warning urgency on the type of voice warning repetition. Figure 12 shows that 39 percent of the pilots thought the type of repetition should depend on urgency level, while 61 percent thought urgency should not affect the repetition of voice warnings. This difference was not significant as tested by the 50-Percent Probability test ($x = 18$, $n = 46$, $p > 0.10$). (Four pilots did not respond to this question.) Those pilots who felt voice warning repetition should depend on warning urgency wanted more repetitions and/or more stringent cancellation conditions for high priority warnings than for lower priority warnings.

The pilots also gave their preferences for the uses of voice warnings (fig. 13). First, the number of pilots who responded affirmatively to one or more of the proposed uses for voice — alerting, specific problem, immediate action, or "other" — was compared to the number of pilots who responded "don't use" voice. This gave a ratio of 43 pilots responding affirmatively to only 3 pilots responding "don't use." This difference was highly significant as tested by the 50-Percent Probability test ($x = 3$, $n = 46$, $p < 0.002$).[4] Note that the 6-percent "don't use" responses compare roughly with the responses to the proposed voice warning system where 18 percent of the 50 pilots responded "no." This can be taken as an internal crosscheck of the earlier finding that pilots generally are in favor of the concept of voice warnings.

A three-way comparison of pilot affirmative responses to the three proposed functions of voices — alerting, tell specific problem, and tell immediate actions — also resulted in significant differences in preferences ($\chi^2 = 6.75$, $df = 2$, $p < 0.05$). Mostly, the pilots wanted voice warnings to tell them the specific problem (78 percent). In addition, 64 percent wanted an alerting word such as "warning." Only 36 percent wanted to be told immediate action items. Under "other" uses (12 percent), suggestions were made by a few pilots that checklist items or immediate action items should be available on demand by voice or CRT display. These responses imply that a voice warning format consisting of an alerting word followed by a statement of the specific problem would be acceptable to most pilots.

Age and Position Flown

Neither age nor position flown resulted in significant differences for acceptability of the proposed voice warning system nor in the pilot ratings of the proposed text warning systems. Fisher's test for differences between younger (21 to 40 yr) and older (41 to 60 yr) pilots for the number of "yes" and "no" responses to the voice warning system yielded $a = 5$, $b = 3$, $c = 19$, $d = 23$, and $p > 0.05$. Similarly, a χ^2 test for position flown (captain, first officer, or flight engineer) by number of "yes" and "no" responses yielded $\chi^2 = 1.09$, $df = 2$, $p > 0.10$.

The sums of individual pilot ratings for the five proposed visual text systems were also compared for the same younger and older pilot groups using Wilcoxon's sum of ranks test ($n_A = 16$, $n_R = 16$, $n_B = 24$, $R = 305$, $z = 0.63$, $p > 0.10$). And, finally, a 3×2 comparison of position flown by low (7 to 13) versus high (14 to 19) sums of ratings for the proposed visual text systems resulted in no significant effect for position flown ($\chi^2 = 4.45$, $df = 2$, $p > 0.10$).

---

[4]Four of the 50 pilots did not respond to this item. Assuming they had checked "don't use" the ratio of 43:7 would still have been significant at the 0.002 level.

627

Semantic Differential

The analysis of pilot responses to the semantic differential also revealed strong agreement among pilots regarding the features of the different warning concepts. For those readers unfamiliar with this instrument, the semantic differential is a technique pioneered by Osgood in 1957 (ref. 8). It is generally useful for finding related concepts in a diverse collection. In use, each concept or item to be judged is placed at the top of a page which has a number of polar opposite scales. The concepts used here were all warning-related items (table VI). The scales are shown in table VII. Subjects were given a 19-page booklet, 1 page of instructions and 18 pages, each with one concept. They placed an X on each 7-point scale, closer to one of the polar opposite adjectives or the other, depending on the one they felt the concept was most closely related to. If it was unrelated, or related to both adjectives by the same amount, they placed an X in the middle space on the scale.

Data from the semantic differential are usually analyzed several ways. The analyses presented here involve mean responses of all pilots on each scale for each concept. Two-way comparisons between pairs of warning concepts are shown in figures 14(a) through (g). Figure 14(g), for example, shows that when "VASI lights" is compared to "Whoop, whoop, pull up, pull up," the lights are less startling, more informative, far more beautiful, more valuable, more passive, far more quiet, and far more soothing. The useful conclusion, then, is that to startle and annoy one would use "whoop, whoop, pull up." To present informative unobtrusively, one would use VASI lights.

Further use of the semantic differential for evaluation of experimental cockpit warning systems seems warranted. Factor analysis techniques are expected to extract groups of warnings that have similar values on the 17 polar opposite scales and to determine how factors such as evaluation, utility, and intensity characterize the different types of warnings. The aim is to standardize a set of semantic differential scales which could be used to characterize a new warning system in relation to existing systems merely by having pilots fly a simulation of the new system and then fill out a semantic differential booklet.

CONCLUDING REMARKS

Several conclusions can be drawn from the data analyzed and presented. It was shown that preferred warning methods depend on urgency or priority of the warned condition, and that false-alarm rate has a major impact on the preferred presentation mode. For example, these data would indicate that, if a system has an inherent high false-alarm rate, a visual warning method such as labeled lights or a CRT is preferable to any audio system. If a low false-alarm rate can be achieved, the audio systems, particularly voice, are preferable to visual systems for high priority warnings.

It can be inferred from these data that pilots would like a limited priority assignment scheme, that all warnings which are current should be displayed somewhere, and that the pilot should decide the course of action rather than

being told what to do. However, within these broad guidelines, much more work
must be done to define the priority assignment schemes and to optimize the
warning displays. Candidate schemes and displays must be thoroughly tested in
simulations and in flight before they are recommended for airline use.

It has also been shown that preferred cancellation options depend on
whether the warning is auditory, visual, or tactile, as well as on the priority
or urgency of the warning. The data in figure 3 will allow a choice of the
preferred cancellation option, given the priority and warning mode.

Finally, the results of this study show that a systematic, objective mea-
surement of pilot preferences for warning system design reveals consistency
and strong agreement among this sample of line pilots. While the user cannot
entirely dictate the system design, especially in airline cockpits where regu-
latory and cost considerations are so important, it would seem useful to
include input from experienced line pilots in the development of aircraft
warning systems for civil transport aircraft. The subjects whose collective
opinion is represented by the data presented here have much and varied experi-
ence .lying in different environments and aircraft types, and this should be
given due regard in the design of future warning systems.

REFERENCES

1. Vietengruber, James E.: Collation and Analysis of Alerting Systems Data,
   Midterm Review, FAA Contract DOT-FA73WA-3233 (MOD II), The Boeing Co.,
   Seattle, Washington, June 1976.

2. Audible Warning System, ARINC Characteristic 577-1. Prepared by the Airlines
   Electronic Engineering Committee, Aeronautical Radio, Inc., 2551 Riva Road,
   Annapolis, Maryland, first published March 15, 1975, revised March 31,
   1975.

3. Warning Systems. Part I, Voice Warnings; Part II, A General Consideration
   of Audible Warnings. Paper presented by British Airways at the Inter-
   national Air Transport Association, 20th Technical Conference, Istanbul,
   Turkey, Nov. 10-15, 1975.

4. Williams, Douglas H.: Comparison of Numeric Keyboard and CRT Line-Labeled
   Buttons for Information Access. NAECON '76 Record, May 1976, pp. 419-423.

5. Simpson, Carol A.: Effects of Linguistic Redundancy on Pilots' Comprehension
   of Synthesized Speech. 12th Annual Conference on Manual Control, NASA
   TM X-73,170, 1976.

6. Connes, Keith: The Coming of TWIT. Air Progress, Aug. 1975, p. 18.

7. Rawlings, Barney: SQUAWKS: Super-Quick Universal Aural-Warning Kibitz
   System. Airline Pilot, Aug. 1976, p. 28.

8. Osgood, Charles E.; Suci, George J.; and Tannenbaum, Percy H.: The Measure-
   ment of Meaning. Univ. of Illinois, Urbana, 1957.

TABLE I.- BACKGROUND AND EXPERIENCE OF 50 PILOTS

POSITIONS FLOWN		AIRLINES		ROUTES FLOWN
CAPTAIN	13	AMERICAN	20	INTERNATIONAL
FIRST OFFICER	20	PAN AM	8	DOMESTIC
FLIGHT ENGINEER	14	UNITED	7	SHORT HAUL
OTHER	3	WESTERN	5	CHARTER
		FLYING TIGERS	4	FREIGHT
		TWA	2	FERRY
		HUGHES AIR	1	
		BIRDAIR	1	
		OTHER/FURLOUGH	2	

AGE (yr)			TOTAL TIME (hr)		
YOUNGEST	MEAN	OLDEST	LEAST	MEAN	MOST
27	41.3	60	500	9,300	30,000

TABLE II.- URGENCY SCALE USED IN QUESTIONNAIRE

LEVEL	TYPE OF PROBLEM
1	IMMEDIATE ACTION REQUIRED BY CREW TO SAVE AIRCRAFT
2	IMMEDIATE ACTION REQUIRED BY CREW AS SOON AS AIRCRAFT IS STABLE
3	ACTION REQUIRED AS SOON AS TIME AVAILABLE
4	ACTION REQUIRED LATER IN THE FLIGHT· FLIGHT PLANNING MAY BE AFFECTED
5	ABNORMAL EVENTS SIGNALED FOR INFO ONLY; NO ACTION REQUIRED MAY AFFECT FLIGHT PLANNING

630

TABLE III.- WARNING METHODS AS DEFINED IN QUESTIONNAIRE

TYPE	EXAMPLES
MUSICAL SOUNDS	TONES, CHIMES, CHORDS
OTHER NON-SPEECH SOUNDS	BELLS, CLACKERS, HORNS, BUZZERS
VOICE	ELECTRONIC SPEECH (LIKE HAL IN 2001 OR LIKE GPWS VOICE)
LIGHTS WITH LABELS	LIGHTS WITH PRINTED LABELS, ALL COLORS, STEADY OR FLASHING
LIGHTS WITH NO LABELS	PLAIN, UNLABELED LIGHTS, ALL COLORS, STEADY OR FLASHING
TEXT MESSAGES	ALPHANUMERIC WARNINGS ON A TV-LIKE SCREEN OR AN ALPHANUMERIC DISPLAY BLOCK
FLAGS	MECHANICAL FLAGS IN FLIGHT INSTRUMENTS, DISPLAY COVERS, DOLL'S EYES
TACTILE	STICK SHAKERS, RUDDER SHAKERS, SEAT BOUNCERS

TABLE IV.- TYPICAL PREFERENCE GRID FOR WARNING METHODS

50 FALSE ALARMS PER 1 REAL ALARM

URGENCY LEVEL	MUSICAL SOUND 1	OTHER SOUND 2	VOICE 3	LABELED LIGHT 4	UNLABELED LIGHT 5	TEXT MESSAGE 6	FLAG 7	TACTILE 8
1 IMMEDIATE ACTION TO SAVE AIRCRAFT								
2 IMMEDIATE ACTION AFTER AIRCRAFT STABLE								
3 ACTION WHEN POSSIBLE								
4 ACTION LATER								
5 NO ACTION/ INFORMATION ONLY								

TABLE V.- PREFERENCE GRID USED FOR FLASHING/NOT FLASHING
AND AUDIO ALERT QUESTION

WARNING SYSTEM	1 IMMEDIATE ACTION	2 ACTION WHEN STABLE	3 ACTION WHEN STABLE	4 ACTION LATER	5 INFO ONLY
WARNING ON BOTTOM LINE OF CRT- -NOT FLASHING					
WARNING ON BOTTOM LINE OF CRT- -FLASHING 3/sec					
WARNING ON WHOLE CRT SCREEN- -NOT FLASHING, BUT WHATEVER WAS DISPLAYED BEFORE IS REMOVED					
WARNING ON WHOLE CRT SCREEN- -FLASHING, AND WHATEVER WAS DISPLAYED BEFORE IS REMOVED					
SINGLE LINE OF 12 3/4" HIGH ALPHANUMERICS- -NOT FLASHING					
SINGLE LINE OF 12 3/4" HIGH ALPHANUMERICS- -FLASHING 3 TIMES/sec					

TABLE VI.- SEMANTIC DIFFERENTIAL CONCEPTS USED

Altitude alert tone
3/4-in.-square yellow light, flashing
3/4-in.-high alphanumeric display, not flashing
3/4-in.-diameter red light, flashing
3/4-in.-square yellow light, not flashing
Synthesized speech
3/4-in.-diameter red light, not flashing
3/8-in.-high lettering on a CRT
Whoop, whoop, pull up, pull up
ATC controller
Mechanical flag in glideslope indicator
Engine fire bell
3/8-in. blue light, not flashing
Stick shaker
SEL CAL tone
VASI lights
REIL lights
Gear horn

TABLE VII.- SEMANTIC DIFFERENTIAL SCALES USED

Startling   --- Tranquilizing
Informative   --- Distracting
Good   --- Bad
Ugly   --- Beautiful
Soft   --- Hard
Strong   --- Weak
Worthless   --- Valuable
Loud   --- Soft
Unpleasant   --- Pleasant
Hot   --- Cold
Nice   --- Awful
Dark   --- Bright
Active   --- Passive
Noisy   --- Quiet
Safe   --- Dangerous
Alerting   --- Imperceptible
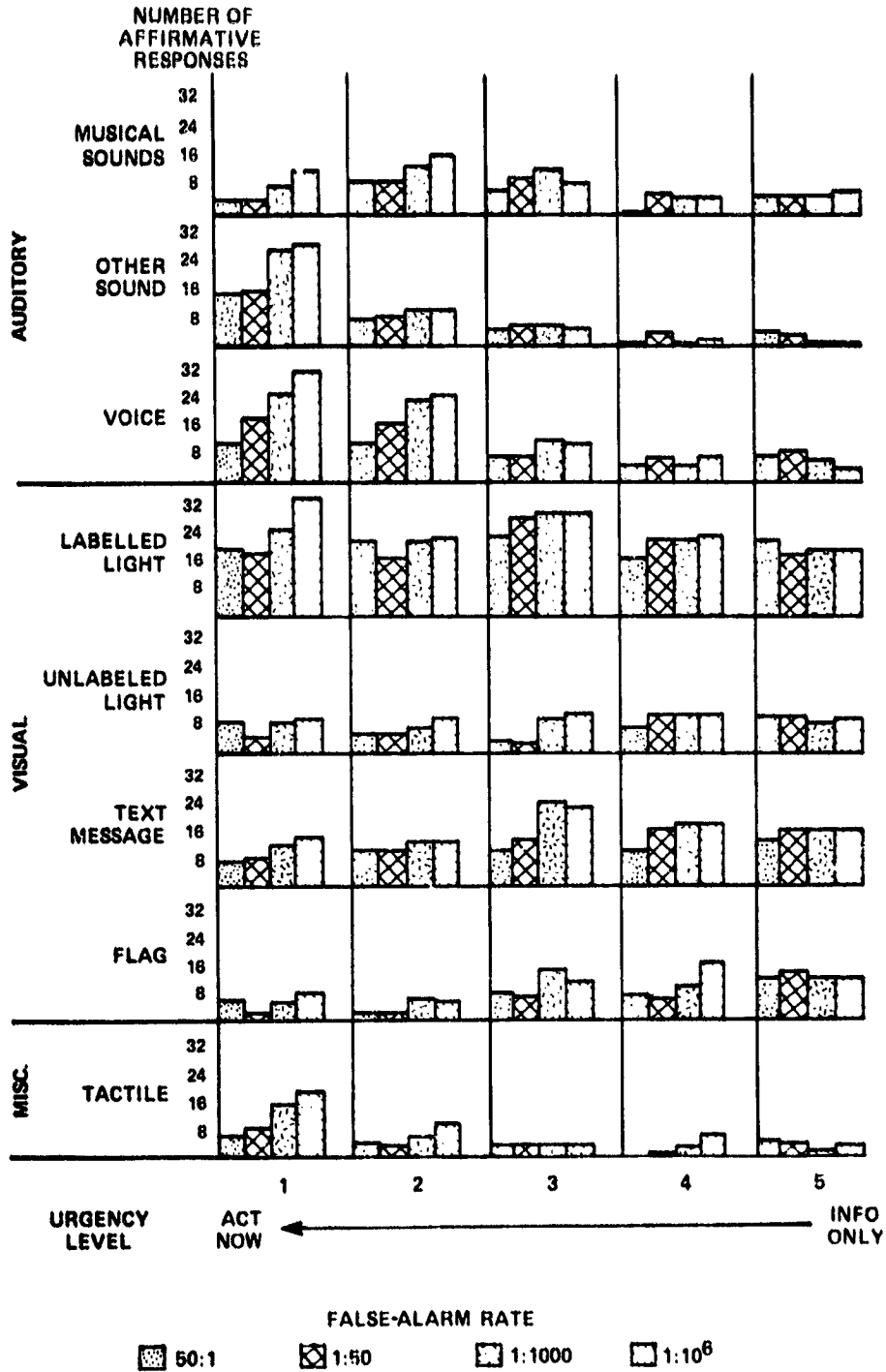Annoying   --- Soothing

632

Figure 1.- Number of affirmative responses to warning methods
as a function of warning urgency and false-alarm rate.

VOICE WARNING
PRIORITY 1 — ACTION NOW
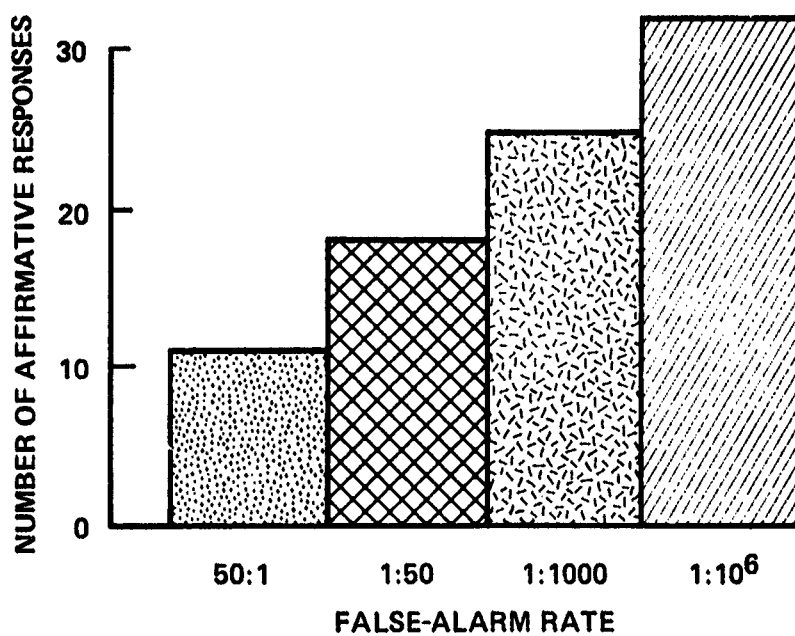
Figure 2.- Voice warning — priority 1 cell of warning
method preferences figure.
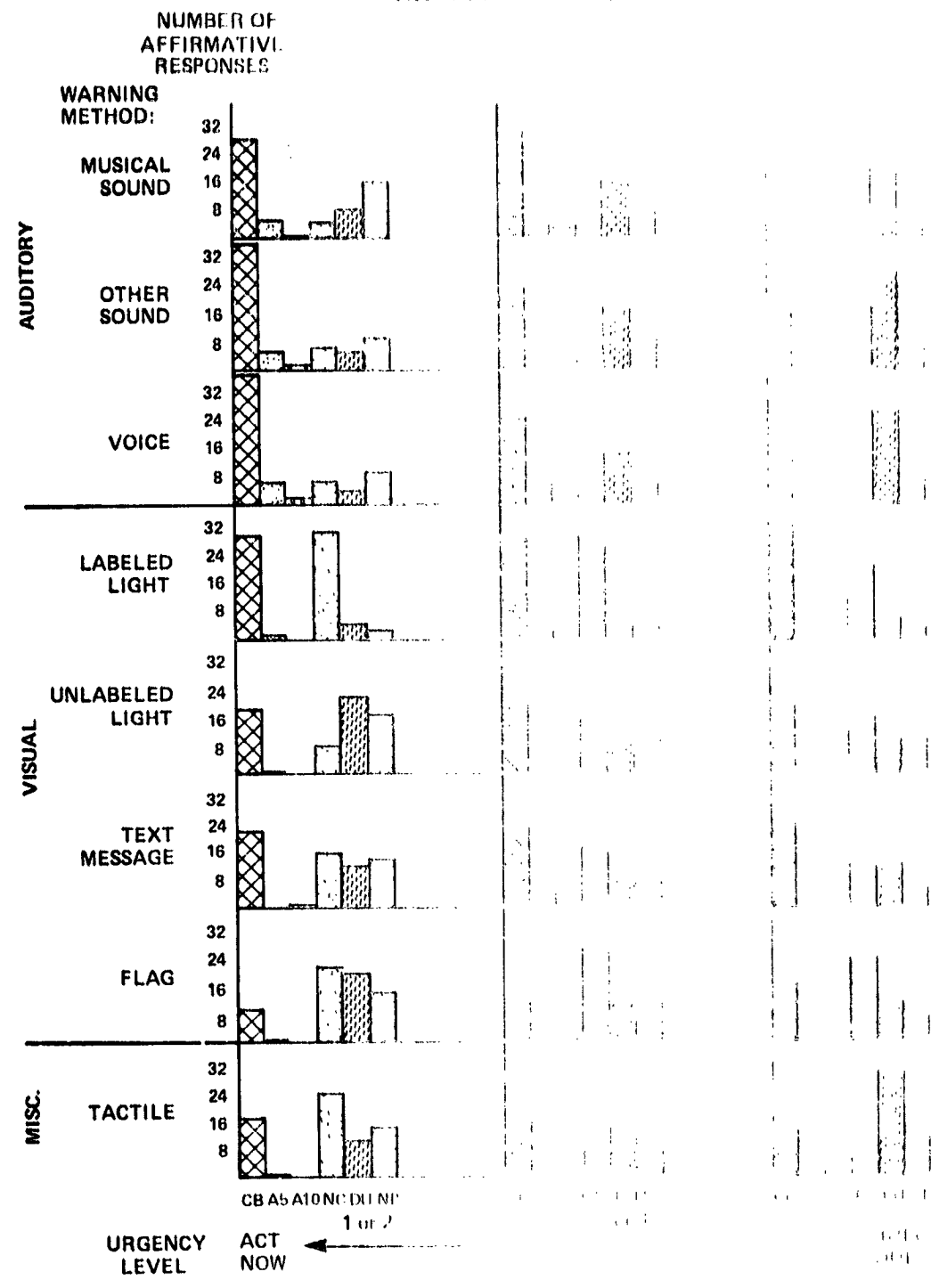
Figure 3.- Number of affirmative responses as a function of warning method

VOICE WARNING

PRIORITY 1 — ACTION NOW
PRIORITY 2 — ACTION NOW
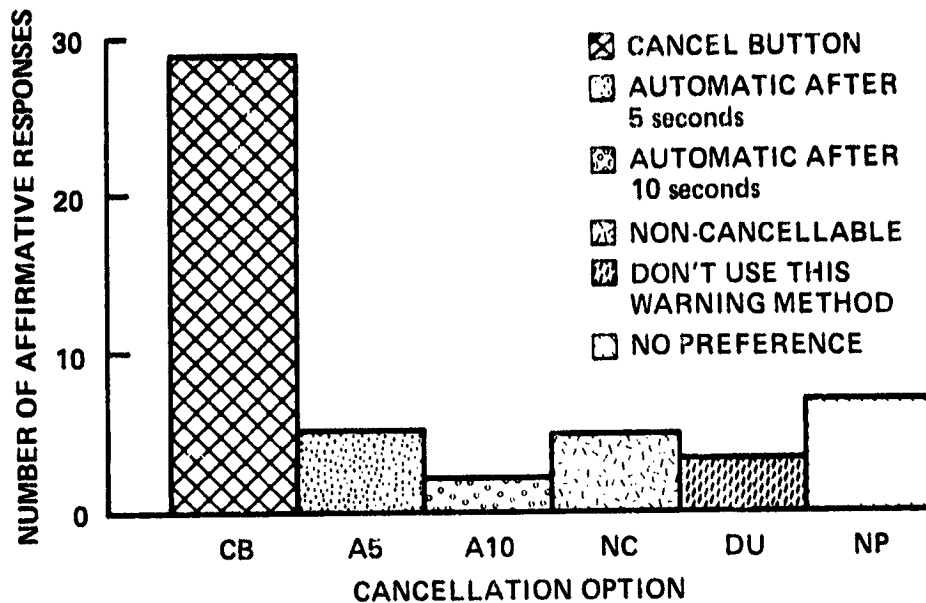
Figure 4.- Voice warning — priority 1 or 2 cell of cancellation options figure.
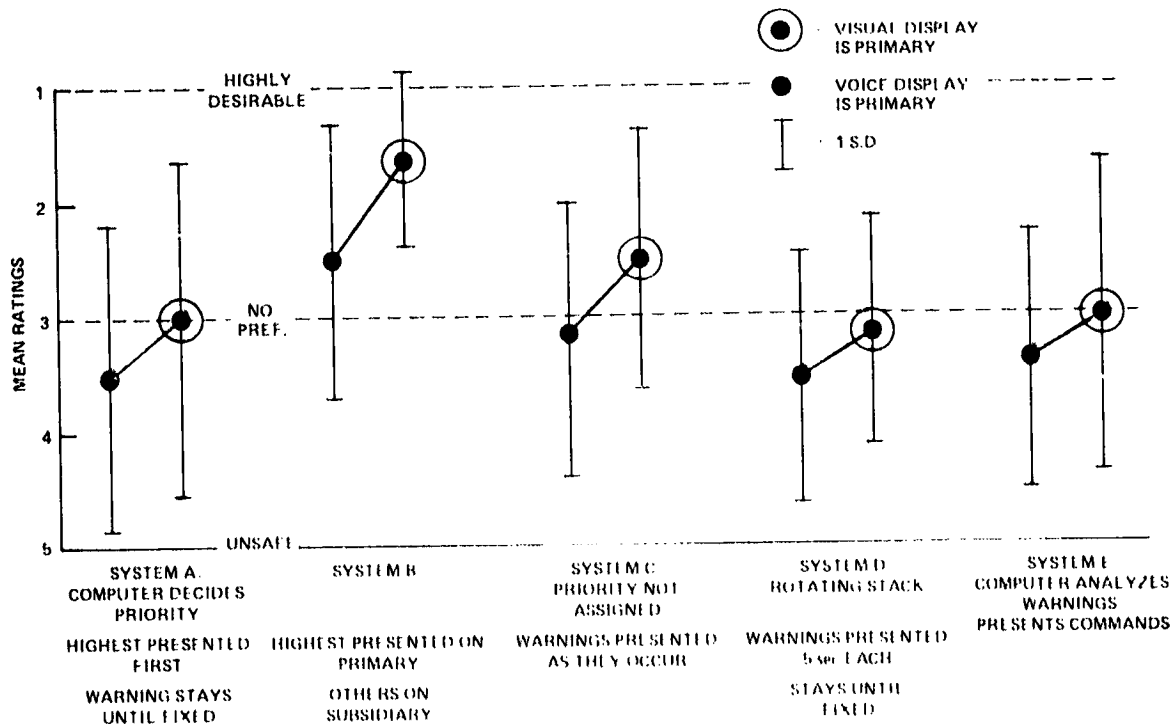
Figure 5.- System logic preferences.
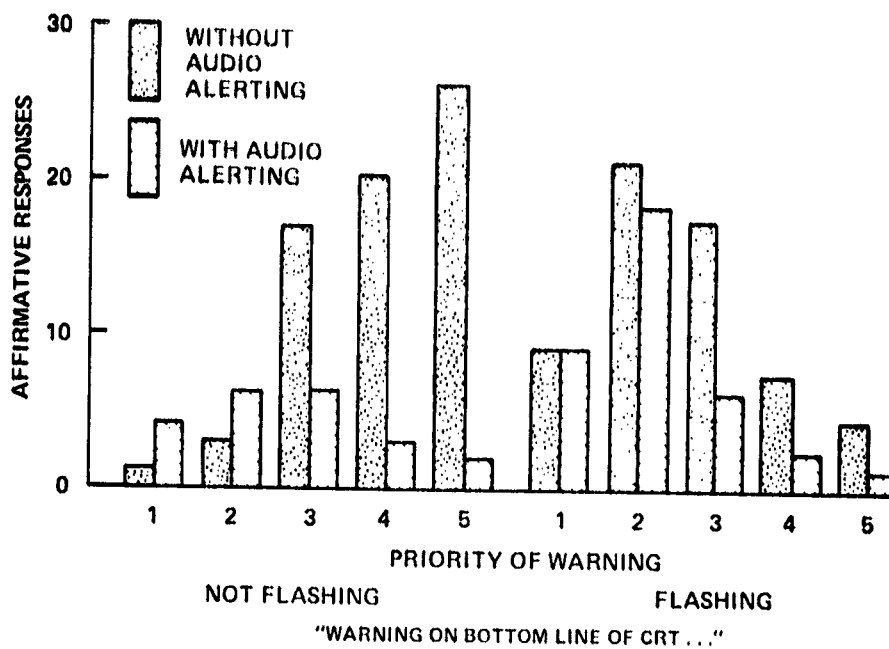
Figure 6.- Preferences for CRT line warning.
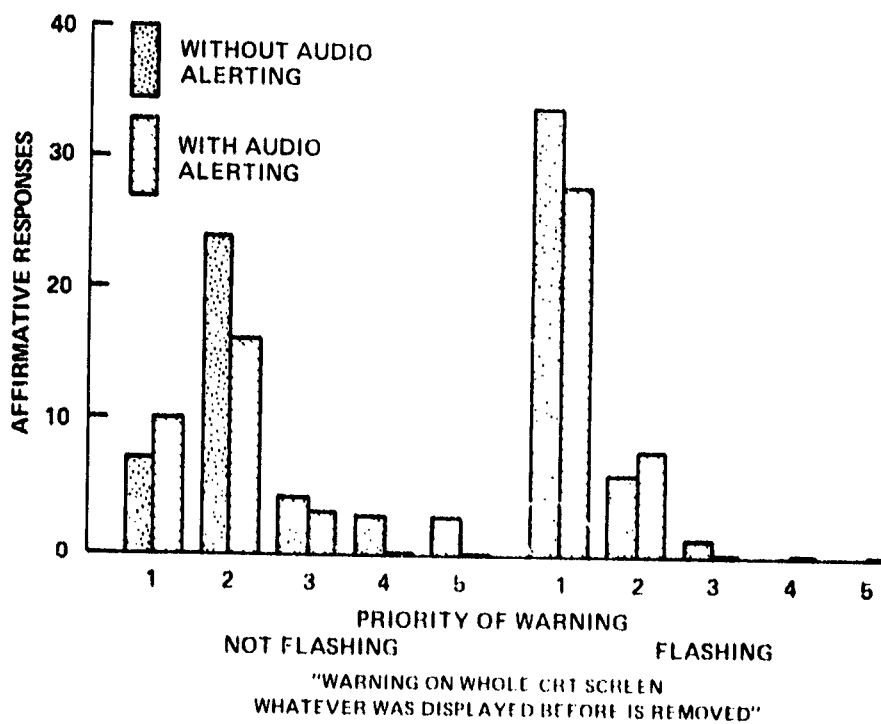
Figure 7.- Preferences for whole CRT screen warning.

637
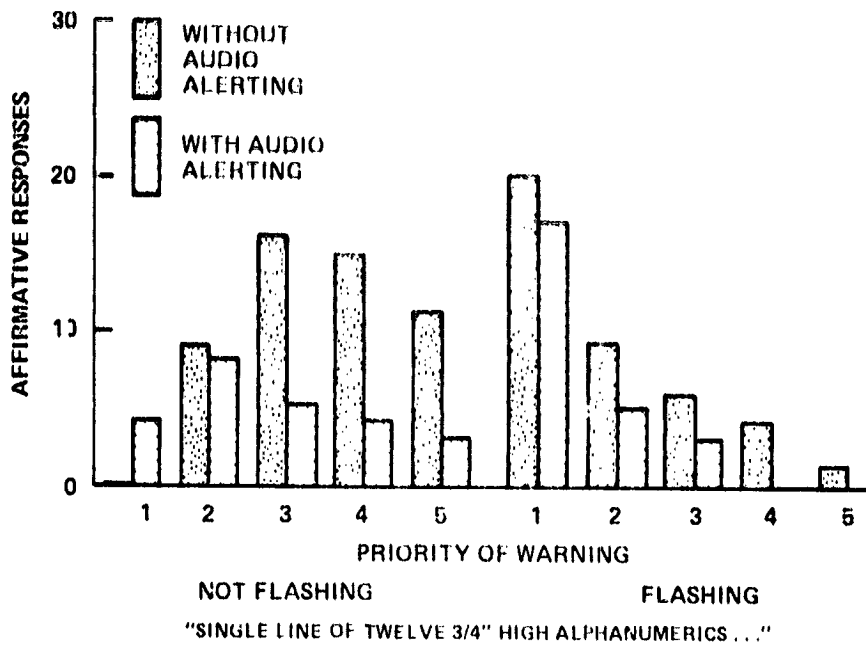
Figure 8.- Preferences for single line of alphanumerics.
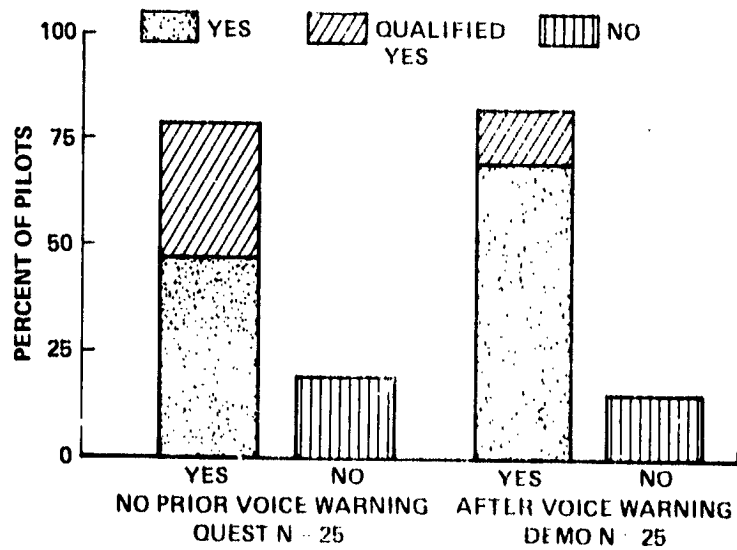
Figure 9.- Pilot acceptability of proposed
voice warning system.
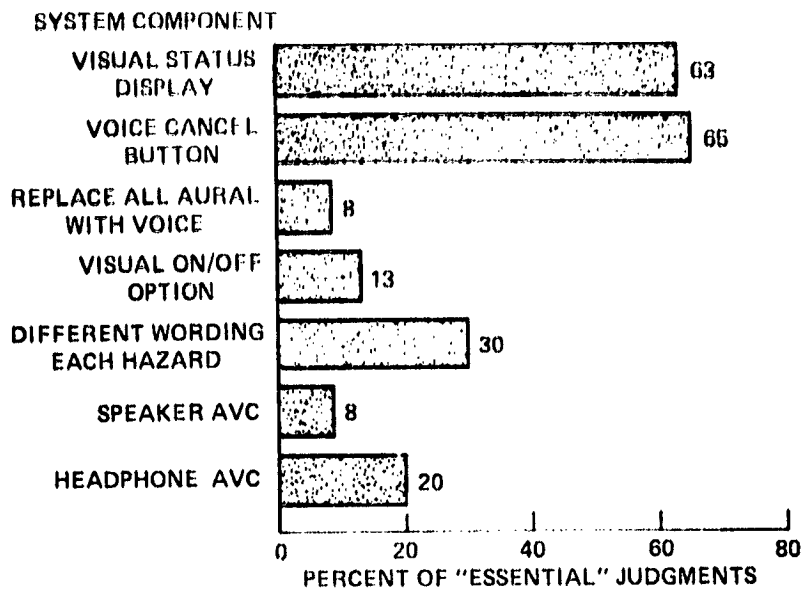
Figure 10.- Percent of "essential" judgments for each component of proposed voice warning system.
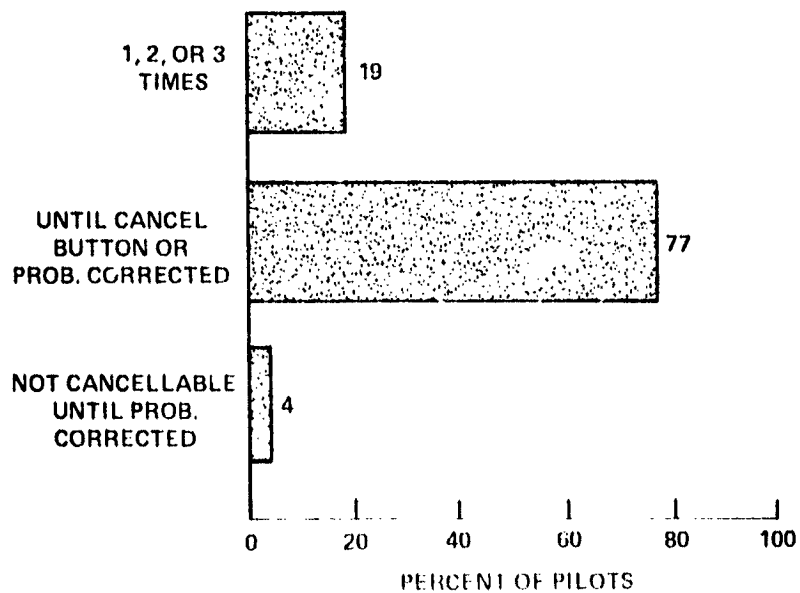
Figure 11.- Pilot preferences for repetition of voice warnings, N = 50.

639

REPETITION OF WARNINGS SHOULD DEPEND ON URGENCY–PRIORITY
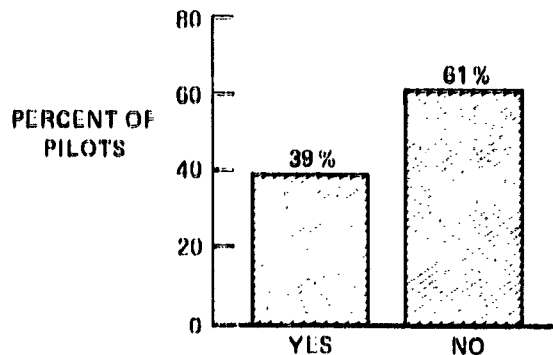
Figure 12.- Percent of "yes" and "no" responses for question regarding effect of warning urgency on preferred type of voice warning repetition.
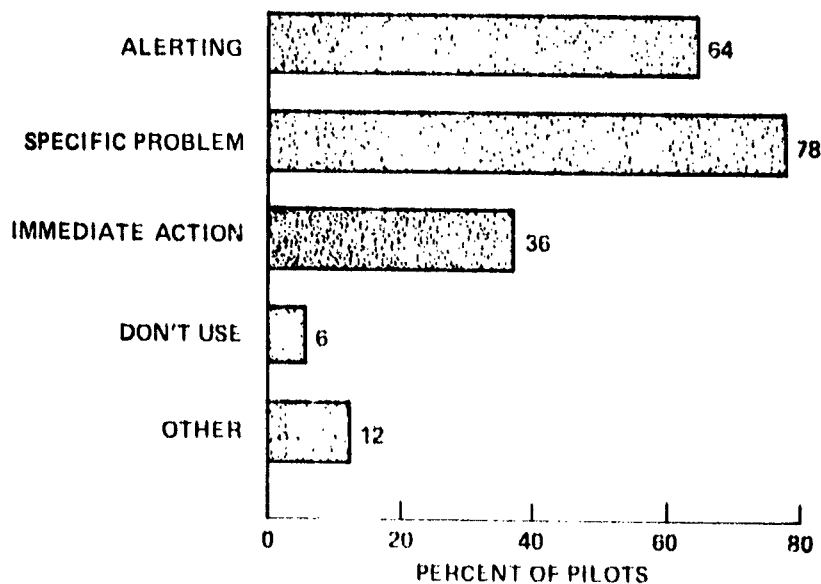
Figure 13.- Pilot preferences for uses of electronic voice in cockpit.
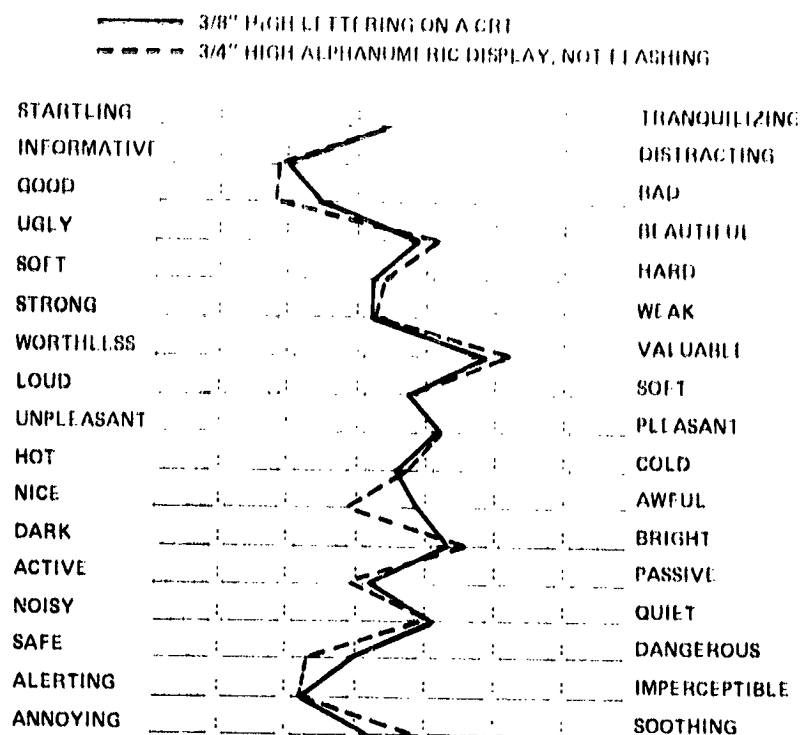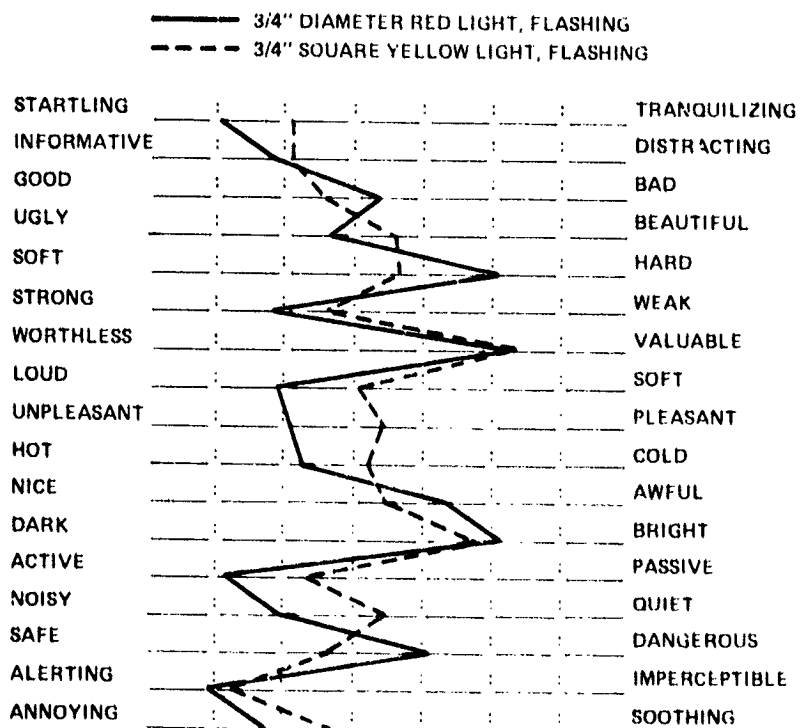
Figure 14.- Semantic differential average responses, N = 41.

TRANQUILIZING

DISTRACTING

BAD

BEAUTIFUL

HARD

WEAK

VALUABLE

SOFT

PLEASANT

COLD

AWFUL

BRIGHT

PASSIVE

QUIET

DANGEROUS

IMPERCEPTIBLE

SOOTHING

(a)

ENGINE FIRE BELL
WHOOP WHOOP, PULL UP, PULL UP

TRANQUILIZING

DISTRACTING

BAD

BEAUTIFUL

HARD

WEAK

VALUABLE

SOFT

PLEASANT

COLD

AWFUL

BRIGHT

PASSIVE

QUIET

DANGEROUS

IMPERCEPTIBLE

SOOTHING

continued.

STARTLING		TRANQUILIZING
INFORMATIVE		DISTRACTING
GOOD		BAD
UGLY		BEAUTIFUL
SOFT		HARD
STRONG		WEAK
WORTHLESS		VALUABLE
LOUD		SOFT
UNPLEASANT		PLEASANT
HOT		COLD
NICE		AWFUL
DARK		BRIGHT
ACTIVE		PASSIVE
NOISY		QUIET
SAFE		DANGEROUS
ALERTING		IMPERCEPTIBLE
ANNOYING		SOOTHING

(e)

STARTLING		TRANQUILIZING
INFORMATIVE		DISTRACTING
GOOD		BAD
UGLY		BEAUTIFUL
SOFT		HARD
STRONG		WEAK
WORTHLESS		VALUABLE
LOUD		SOFT
UNPLEASANT		PLEASANT
HOT		COLD
NICE		AWFUL
DARK		BRIGHT
ACTIVE		PASSIVE
NOISY		QUIET
SAFE		DANGEROUS
ALERTING		IMPERCEPTIBLE
ANNOYING		SOOTHING

(f)

Figure 14.- Continued.

(g)

Figure 14.- Concluded.

ATTENDEES

ADAMS, Horace O.	Federal Aviation Administration
ANDERSON, Gary L.	United Airlines
ANDERSON, Willard W.	NASA Langley Research Center
BAGINSKY, Walter	Air Force Geophysical Laboratory
BALCERAK, John	RASA
BEARD, M. Craig	Federal Aviation Administration
BEASLEY, Gary P.	NASA Langley Research Center
BERRY, Donald T.	NASA Dryden Flight Research Center
BERUBE, Roy A.	National Airlines, Inc.
BILLINGS, Charles E.	NASA Ames Research Center
BIRD, King	CALSPAN Corporation
BLAKE, Charles L.	Federal Aviation Administration
BLUMENTHAL, Vaughan L.	Boeing Commercial Airplane Company
BORGER, John G.	Pan American World Airways, Inc.
BOSWINKLE, Robert W.	NASA Langley Research Center
BOWER, Robert E.	NASA Langley Research Center
BRADY, Frank B.	Air Transport Association of America
BRAY, Richard S.	NASA Ames Research Center
BROCKMAN, Philip	NASA Langley Research Center
BRUNETTI, Anthony W.	The Flying Tiger Line, Inc.
BRYDE, William A.	Douglas Aircraft Company
CAMP, Dennis W.	NASA Marshall Space Flight Center
CARR, Edward J.	Federal Aviation Administration
CASTER, Herman P.	U.S. Naval SWC
CHEELY, James W.	NASA Langley Research Center
CHESTNUTT, David	NASA Langley Research Center
CHRISTIANSEN, John	Lockheed-California Company
CLARKE, Martyn V.	National Transportation Safety Board
CONNER, D. William	NASA Langley Research Center

COOPER, George E.   NASA Ames Research Center (Ret.)
COSGROVE, Benjamin A.   Boeing Commercial Airplane Company
COULBERT, Clifford D.   Jet Propulsion Laboratory
CRAWFORD, Daniel J.   NASA Langley Research Center
CROOM, Delwin R.   NASA Langley Research Center

D'AIUTOLO, Charles T   NASA Langley Research Center
DALTON, William S.   Federal Aviation Administration
DANIELS, Tom R.   United Airlines
DAVIDSON, John R.   NASA Langley Research Center
DE LOACH, Richard   NASA Headquarters
DI CARLO, Daniel J.   NASA Langley Research Center
DONALDSON, Coleman   Aeronautical Research Associates
                                 of Princeton, Inc.
DONELY, Philip   NASA Langley Research Center (Ret.)
DOUGHERTY, James E.   Federal Aviation Administration
DUFFY, Robert T.   NASA Wallops Flight Center
DUNHAM, R. Earl, Jr.   NASA Langley Research Center

EASTBURN, Mack W.   American Airlines, Inc.
EDWARDS, Frederick G.   NASA Ames Research Center
EMERY, Major Jay O.   4500th ABWg, Langley AFB
ENDERS, John H.   Federal Aviation Administration

FALLON, William L.   Federal Aviation Administration
FANNING, William M.   National Business Aircraft
                                 Association
FARBRIDGE, Joseph E.   DeHavilland Aircraft of Canada
FARRAR, William E.   Lockheed Aircraft Company
FAULCON, Nettie   NASA Langley Research Center
FELLER, Donald   NASA Wallops Flight Center
FICHTL, George   NASA Marshall Space Flight Center
FISCHER, Robert H.   Federal Aviation Administration
FISHER, Bruce D.   NASA Langley Research Center
FLORSHEIM, Bruce H.   The Boeing Company

646

FOX, Roy G.   Bell Helicopter Textron
FRANKLIN, James A.   NASA Ames Research Center
FULLER, William H., Jr.   NASA Langley Research Center

GARDNER, William A.   Sandia Labs
GEE, Shu W.   NASA Dryden Flight Research Center
GILBERT, Glen A.   Gilbert and Associates
GIVLER, R. N.   Boeing Aerospace Company
GODWIN, Gene E.   NASA Wallops Flight Center
GOETZ, Robert C.   NASA Langley Research Center
GOODE, Maxwell W.   NASA Langley Research Center
GOOLSBY, Lee D.   NASA Headquarters
GORHAM, John A.   Gorham Associates
GORMAN, Lt. Col. W. T.   Air Force Systems Command
GOULD, Donald G.   National Research Council, Canada
GRAFTON, Sue B.   NASA Langley Research Center
GRIFFIS, Carl L.   NASA Kennedy Space Center
GRISWOLD, Roger W., II   Flightcraft, Inc.
GRISWOLD, Lt. Col. T. L.   AFSC Liaison Office, Langley AFB
GROBMAN, Jack S.   NASA Lewis Research Center
GUITIERREZ, Orlando A.   NASA Lewis Research Center

HAINLINE, Bernard C.   Boeing Commercial Airplane Company
HALL, Albert W.   NASA Langley Research Center
HALL, James R.   NASA Langley Research Center
HAMMOND, A. Dudley   NASA Langley Research Center
HASTINGS, Earl C.   NASA Langley Research Center
HEARTH, Donald P.   NASA Langley Research Center
HECKENDORF, Marvin H.   NASA Kennedy Space Center
HELDENFELS, Richard R.   NASA Langley Research Center
HEMMEN, Delbert G.   Swearingen Aviation Corporation
HERNDON, William K.   Pan American World Airways, Inc.
HERSH, Ronald S.   Federal Aviation Administration
HESS, Robert V.   NASA Langley Research Center

HEWES, Donald E.	NASA Langley Research Center
HOCKER, Col. Jesse S.	Strategic Air Command, Offutt AFB
HODGE, Kenneth E.	NASA Headquarters
HOFFMAN, Sherwood	NASA Langley Research Center
HOLLAND, Robert W., III	General Electric Company
HORMUTH, Maj. John E.	AFALD, Wright-Patterson AFB
HORNE, Walter B.	NASA Langley Research Center
HORONJEFF, Robert	University of California
HUNTER, William W., Jr.	NASA Langley Research Center
HYNES, Charles S.	NASA Ames Research Center
INNIS, Robert C.	NASA Ames Research Center
IVANKO, Theodore	Avco-Lycoming Division
IVERSON, James D.	Iowa State University
JACOBSEN, Ira D.	University of Virginia
JANSEN, G. R.	Douglas Aircraft Company
JEWEL, Joseph W., Jr.	NASA Langley Research Center
JOHNSTONE, Paul M.	Eastern Airlines
JOHTANI, Takesi	All Nippon Airways
KAUFMAN, Albert	NASA Lewis Research Center
KELLEY, Wendell W.	NASA Langley Research Center
KENNAH, Lt. Col. R. B.	Aeronautical Systems Division
KING, Charles B.	NASA Langley Research Center
KNOX, Charles E.	NASA Langley Research Center
KOLANKIEWICZ, Ted	Federal Aviation Administration
KOURTIDES, Demetrius A.	NASA Ames Research Center
KURBJUN, Max C.	NASA Langley Research Center
LAMAR, John E.	NASA Langley Research Center
LANDER, Clayton H.	Collins Radio Group
LANGER, Hart	Pan American World Airways, Inc.
LANSING, Donald L.	NASA Langley Research Center

648

LAUBER, John K.   NASA Ames Research Center
LE BEL, James R.   Western Airlines
LEZBERG, Erwin A.   NASA Lewis Research Center
LIBERATO, Frank A.   Vought Corporation
LICHTENSTEIN, Jacob H.   NASA Langley Research Center
LOCKETT, Bascom N., Jr.   Federal Aviation Administration
LOFTIN, Laurence K., Jr.   NASA Langley Research Center (Ret.)
LOOMIS, William R.   NASA Lewis Research Center
LORENZ, Steve   NASA Langley Research Center
LOVING, Donald L.   NASA Langley Research Center
LOWN, E. C.   Goodyear Aerospace Corporation
LYMAN, E. Gene   NASA Headquarters

MAYES, William H.   NASA Langley Research Center
MC CARTY, John L.   NASA Langley Research Center
MC DOUGAL, R. L.   Lockheed-Georgia Company
MC GOWAN, William A.   NASA Headquarters
MC KISSICK, Burnell T.   NASA Langley Research Center
MC NAIR, Col. C. H., Jr.   Department of the Army
MELSON, Walter E., Jr.   NASA Wallops Flight Center
MILLER, G. Kimball, Jr.   NASA Langley Research Center
MILLER, R. L.   Lockheed-California Company
MIXSON, John S.   NASA Langley Research Center
MORELLO, Samuel A.   NASA Langley Research Center
MORGAN, Homer G.   NASA Langley Research Center
MORRIS, Dana J.   NASA Langley Research Center
MORRIS, Garland J.   NASA Langley Research Center
MOUL, Martin T.   NASA Langley Research Center
MURACA, Ralph J.   NASA Langley Research Center
MURPHY, Lt. Comdr. A.   Naval Safety Center

NASH, Brig. Gen. E. J.   Military Airlift Command
NICHOLS, Mark R.   NASA Langley Research Center (Ret.)

NICKS, Oran W.	NASA Langley Research Center
NORRIS, Eugene	Flight Safety Foundation
O'Bryan, Thomas C.	NASA Langley Research Center
O'CONNER, William Y.	General Electric Company
OLSON, William L.	Federal Aviation Administration
ORTNER, Lt. Col. A. J.	U.S. Army AVSCOM
PARKER, Loyd C.	NASA Wallops Flight Center
PARNELL, S. M.	Piedmont Airlines
PATTEN, Paul H.	McDonnell Douglas Corporation
PATTON, James M.	NASA Langley Research Center
PAULSEN, Gunnar	Ministry of Transport, Canada
PERRY, Boyd III	NASA Langley Research Center
PHANEUF, Roger J.	Air Line Pilots Association
PHILLIPS, William H.	NASA Langley Research Center
PIERPONT, W. G.	Beech Aircraft Corporation
PLUMER, J. Anderson	General Electric Company
POLK, Charles	National Science Foundation
POSEY, Joe W.	NASA Langley Research Center
PRIDE, Richard A.	NASA Langley Research Center
PRITCHARD, Reuben T.	NASA Headquarters
QUEIJO, Manuel J.	NASA Langley Research Center
QUINLIVAN, William J.	Lockheed-California Company
REEDER, John P.	NASA Langley Research Center
RHYNE, Richard H.	NASA Langley Research Center
RICHARDSON, Donald W.	Champlain Technology Industries
RIDDELL, Frank	Avco Lycoming Division
RILEY, E. G.	D.G.A. International, Inc.
RIMSON, Comdr. Ira J.	Naval Air Systems Command
ROBERTS, Leonard	NASA Ames Research Center
ROBERTSON, William A.	Air Line Pilots Association

ROSCOE, Stanley N.	University of Illinois
RUMMEL, Robert W.	Trans World Airlines, Inc.
RYAN, Col. William J.	Air Force Systems Command
SALMIRS, Seymour	NASA Langley Research Center
SANDOZ, Paul L.	Boeing Commercial Airplane Company
SAULS, Col. George M.	Hq., Tactical Air Command
SCHADE, Robert O.	NASA Langley Research Center
SCHEIMAN, James	NASA Langley Research Center
SCHELP, Donald A.	Boeing Commercial Airplane Company
SCHMIDT, Harold W.	NASA Lewis Research Center
SCOTT, Barry C.	Federal Aviation Administration
SCOTT, R. C.	Gates Learjet Corporation
SHANKS, Robert E.	NASA Langley Research Center
SHAUGHNESSY, John D.	NASA Langley Research Center
SIEBERG, Fred R.	Lockheed-California Company
SIDWELL, Kenneth W.	The George Washington University, Joint Institute for Advancement of Flight Sciences
SIMPSON, Carol A.	NASA Ames Research Center
SINGH, Jag J.	NASA Langley Research Center
SINGH, R. P.	Computer Sciences Corporation
SLEEMAN, William C.	NASA Langley Research Center
SMITH, Ronald J.	American Airlines, Inc.
SNYDER, C. Thomas	NASA Ames Research Center
SOULE, Hartley A.	NASA Langley Research Center (Ret.)
SOUTHALL, William A.	NASA Langley Research Center
SPADY, Amos A., Jr.	NASA Langley Research Center
SPANGLER, Roman M.	National Aviation Facilities Experimental Center
SPROULL, Royce H.	NASA Langley Research Center
SQUIRES, Wade	Sperry Flight Systems
STAUFFER, Warren A.	Lockheed-California Company
STEIN, Bland A.	NASA Langley Research Center
STEINMETZ, George G.	NASA Langley Research Center
STEPHENS, David G.	NASA Langley Research Center

STEWART, George F.	Naval Safety Center
STICKLE, Joseph W.	NASA Langley Research Center
STITT, James E.	NASA Langley Research Center
STONE, A. C.	Eastern Airlines
STOUGH, H. Paul	NASA Langley Research Center
STRAETER, Terry A.	NASA Langley Research Center
STUBBS, Sandy M.	NASA Langley Research Center
TANNER, John A.	NASA Langley Research Center
TAYLOR, Col. John P.	National Research Council
TAYLOR, Marion K.	U.S. Army AMRDL-Eustis Directorate
TAYLOR, Robert T.	. 3A Langley Research Center
THIBODEAUX, Jerry J.	NASA Langley Research Center
THOMSON, Robert G.	NASA Langley Research Center
TREECE, Lloyd L.	United Airlines
TREMBLAY, David B.	Aeronautical Systems Division
TYMCZYSZYN, Joseph J.	Federal Aviation Administration
VARANYAK, James E.	New Jersey Department of Transportation
VERSTYNEN, Harry A., Jr.	Federal Aviation Administration
VRETAKIS, Nicholas G.	AFSC Liaison Office, Langley AFB
WAGNER, John O.	Pratt and Whitney Aircraft
WAGNER, Richard D.	NASA Langley Research Center
WALLACE, F. L.	Pan American World Airways, Inc.
WALLER, Marvin C.	NASA Langley Research Center
WALSH, Thomas M.	NASA Langley Research Center
WEAVER, Edwin A.	NASA Marshall Space Flight Center
WEISS, Solomon	NASA Lewis Research Center
WEST, Lt. Col. T. C.	Federal Aviation Administration
WESTCOTT, Col. R. G.	Air Force Systems Command
WESTPHAL, George W.	Grumman American Aviation Corporation
WILCOCK, Trevor	British Defense Staff
WILLIAMS, Douglas H.	NASA Ames Research Center

WILLIAMS, James R.	NASA Langley Research Center
WILSON, F. J.	Lockheed-Georgia Company
WINGROVE, Rodney C.	NASA Ames Research Center
WOOD, Col. Richard H.	Air Force Inspection and Safety Center
WOOD, William D.	Transportation Systems Center
YAGER, Thomas J.	NASA Langley Research Center
YOUNG, Douglas C.	NASA Wallops Flight Center